MST 10 Tenth International WORKSHOP

On technical and scientific aspects of MST Radar

Piura, Peru - May 13-20, 2003

PROCEEDINGS OF THE TENTH WORKSHOP ON TECHNICAL AND SCIENTIFIC ASPECTS OF MST RADAR

EDITED BY Jorge Chau, Jaime Lau and Jürgen Röttger

Acknowledgments

The organizing committee thanks the support provided by:

- Scientific Committee on Solar-Terrestrial Physics (SCOSTEP)
- International Union of Radio Science (URSI)
- National Science Foundation (NSF), USA
- Atmospheric Radar System (ATRAD), Australia
- Genesys Software, Australia
- Modular antenna radar designs of Canada (MARDOC), Canada
- Consejo Nacional de Ciencia y Tecnología (CONCYTEC), Perú

The International Steering Group of MST10 is conformed by: J. Röttger (Chair, Germany), J. Chau (Peru), S. Fukao (Japan), E. Kudeki (USA), and R. Woodman (Peru).

Adherent to the International Steering Group are the Chairpersons of the MST Radar Permanent Working Groups: P. Chilson (USA), D. Holdsworth (Australia), G. Nastrom (USA), P.B. Rao (India), and M. Yamamoto (Japan).

Honorary Members of the International Steering Group are: M.F. Larsen (USA), C.H. Liu (Taiwan), A.P. Mitra (India).

The National Organizing Committee of MST10 consists of: R. Woodman (Chair, Instituto Geofísico del Perú -IGP-), J. Chau (Jicamarca Radio Observatory –JRO/IGP-), Antonio Mabres (Universidad de Piura –UDEP-) and Martin Sarango (JRO-IGP).

The Local Organizing Committee of MST10 consists of: Rodolfo Rodriguez (Chair, UDEP), William Ipanaque (UDEP), and Sergio Balarezo (UDEP).

The Program Committee, besides members of International Steering Committee, include the topical Conveners K. Gage (USA), W. Hocking (Canada), D. Hysell (USA), H. Luce (France), A. Muschinski (USA), R. Palmer (USA), I. Reid (Australia), D. Riggin (USA), and D. Thorsen (USA).

PUBLISHED BY
Radio Observatorio de Jicamarca, Lima, Peru
Universidad de Piura, Piura, Peru
December 2003

Copies and CDs can be requested to mst10@jro.igp.gob.pe

Edited Jorge Chau, Jaime Lau and Jürgen Röttger

MST 10 Group Picture

May 15th, 2003 - Piura Peru

Courtesy of Koko Zavala, Oficina de Información, UDEP.

Most countries are based on institutions, not nationalities.

1 **Jenn-Shyong Chen** (Taiwan)
2 **Peter Hoffmann** (Germany)
3 **Iain Reid** (Australia)
4 **Raymond Morris** (Australia)
5 **Arturo Peña** (Cuba)
6 **Danny Scipión** (Peru)
7 **James Avery** (USA)
8 **Denise Thorsen** (USA)
9 **Marius Zecha** (Germany)
10 **Christos Haldoupis** (Greece)
11 **Ralph Latteck** (Germany)
12 **Yves Barbin** (France)
13 **Jean-Luc Caccia** (France)
14 **Richard Ney** (France)
15 **Eric Boyer** (France)
16 **Jorge Chocos** (Peru)
17 **Alexander Praskovsky** (USA)
18 **Catherine Gaffard** (UK)
19 **Richard Wilson** (France)
20 **Hubert Luce** (France)
21 **Anna Hocking** (Canada)
22 **Wayne Hocking** (Canada)
23 **Aditi Kolatkar** (USA)
24 **Jun-ichi Furumoto** (Japan)
25 **Jann-Yenq 'Tiger' Liu** (Taiwan)
26 **Chung Chen** (Taiwan)
27 **Yen-Hsyang Chu** (Taiwan)
28 **David Hysell** (USA)
29 **Gerald Lehmacher** (USA)
30 **Mrs. Van Zandt** (companion, USA)
31 **Chris Meek** (Canada)
32 **Mrs. Bénech** (companion, France)
33 **Bruno Bénech** (France)
34 **Thomas Van Zandt** (USA)
35 **Susumu Saito** (Japan)
36 **Werner Singer** (Germany)
37 **Brian Fuller** (Australia)
38 **Christopher Lucas** (Australia)
39 **Siegfried Vogt** (Germany)
40 **Eddy Hermawan** (Indonesia)
41 **Raj Kumar Choudhary** (Canada)
42 **Nikolai Gavrilov** (Russia)
43 **Martin Sarango** (Peru)
44 **Francis Dalaudier** (France)
45 **Toru Sato** (Japan)
46 **Jürgen Röttger** (Germany)
47 **Donald Farley** (USA)
48 **Ronald Woodman** (Peru)
49 **Eleanor Praskovskaya** (USA)
50 **Corinne Morse** (USA)
51 **Noriyuki Kawano** (Japan)
52 **D. Narayana Rao** (India)
53 **Kenneth Gage** (USA)
54 **David Hooper** (UK)
55 **Tatsuhiro Yokoyama** (Japan)
56 **Mrudula G** (India)
57 **Richard Doviak** (USA)
58 **Adrian McDonald** (New Zealand)
59 **Michihiro Teshiba** (Japan)
60 **Otto Castillo** (Peru)
61 **Paul Johnston** (USA)
62 **Brenton Vandepeer** (Australia)
63 **Elias Lau** (USA)
64 **Ken Takahashi** (Peru)
65 **Robert Silva** (Australia)
66 **Glenn Hussey** (Canada)
67 **Frank Lind** (USA)
68 **Ramsey Gitany** (companion, France)
69 **Jorge Chau** (Peru)
70 **Erhan Kudeki** (USA)
71 **Shoichiro Fukao** (Japan)
72 **Hasan Bahcivan** (USA)
73 **Jose Fernandez** (USA)
74 **Julio Urbina** (USA)
75 **Robert Palmer** (USA)
76 **Yoshiaki Shibagaki** (Japan)
77 **Bok-Haeng Heo** (South Korea)
78 **Monique Petitdidier** (France)
79 **Gernot Hassenpflug** (Japan)
80 **David Fritts** (USA)
81 **Karanam Kishore Kumar** (India)
82 **Philipp Currier** (France)
83 **John Sahr** (USA)
84 **Ben Balsley** (USA)
85 **Dennis Riggin** (USA)
86 **Cesar La Hoz** (Norway)
87 **Gabriel Michhue** (Peru)
88 **Hiroyuki Hashiguchi** (Japan)
89 **Tadahiko Ogawa** (Japan)
90 **Masaki Tsutsumi** (Japan)
91 **Yasuko Umemoto** (Japan)
92 **Jaime Lau** (support, Peru)
93 **Toyoshi Shimomai** (Japan)
94 **Paco Lopez Dekker** (USA)
95 **Rodolfo Rodriguez** (Peru)
96 **Wilmer Pulache** (Peru)
97 **Leonardo Fernandez** (Cuba)
98 **Wallace Clark** (USA)
99 **Marco Milla** (Peru)
100 **Pablo Reyes** (Peru)

TENTH INTERNATIONAL WORKSHOP ON TECHNICAL AND SCIENTIFIC ASPECTS OF MST RADAR - MST10
FIRST ANNOUNCEMENT

Piura, Peru
May 20-27, 2003 (or May 13-20, 2003, tbd)

The international workshop on MST radar, held about every 2-3 years, is a major event gathering together experts from all over the world, engaged in research and development of radar techniques to study the mesosphere, stratosphere, troposphere (MST). It offers also excellent opportunities to young scientists, research students and also new entrants to the field for close interactions with the experts on all technical and scientific aspects of MST radar techniques.

The tenth MST radar workshop - MST10 -, as the previous MST workshops, will focus on the following topics

- Radar scattering processes in the neutral atmosphere
- D, E, and F region coherent scattering (PMSE, Es, EEJ, ESF)
- Winds, waves and turbulence in the lower and middle atmosphere
- Meteorological phenomena and applications.
- Operational aspects and recent system developments

As a new approach, the workshop MST10 will consist of two major parts:
- Standard workshop papers presented orally or as posters (4 days), and
- A brain-storming meeting (1.5 days) with the aim to highlight open questions and potential solutions, to produce proposals for innovative approaches, define new programs and prepare recommendations.

The latter bases on the Permanent Working Groups of the MST radar community on:
(1) System Calibrations and Definitions,
(2) Data Analysis, Validation and Parameter Deduction Methods
(3) Accuracies and Requirements for Meteorological Applications
(4) International Collaborations
.
The workshop MST10 will be held at the wonderful campus of the Universidad de Piura (UDEP, http://www.udep.edu.pe) in northern Peru. This site is known due to its operation of ST and boundary layer radars, which are part of the activities of the Instituto Geofísico del Peru, operating the Jicamarca Radio Observatory (JRO), in collaboration with international institutions like the University of Colorado (via CIRES) and NOAA (via the Aeronomy Lab). Included in the workshop activities are site-seeing tours and a visit of the Jicamarca Radio Observatory (http://jro.igp.gob.pe) in Lima.

The International Steering Group of MST10 consists of: J. Roettger (Chair, Germany), J. Chau (Peru), S. Fukao (Japan), E. Kudeki (USA), and R. Woodman (Peru). Adherent to the International Steering Group are the Chairpersons of the MST Radar Permanent

Working Groups: P. Chilson (USA), D. Holdsworth (Australia), G. Nastrom (USA), P.B. Rao (India), and M. Yamamoto (Japan).

Honorary Members of the Steering Group are: M.F. Larsen (USA), C.H. Liu (Taiwan), A.P. Mitra (India).

The National Organizing Committee of MST10 consists of: R. Woodman (Chair, IGP), J. Chau (ROJ-IGP), Antonio Mabres (UDEP) and M. Sarango (Ciencia Internacional).

The Local Organizing Committee of MST10 consists of: Rodolfo Rodriguez (Chair), William Ipanaque, and Sergio Balarezo.

The Scientific and Technical Program Committee will be established before the circulation of the Second Circular

The Tenth International Workshop on Technical and Scientific Aspects of MST Radar - MST10 - is an activity sponsored by the Scientific Committee on Solar Terrestrial Physics (SCOSTEP), the Instituto Geofísico del Peru (IGP) and the Universidad de Piura (UDEP). Further sponsors, such as URSI, Ciencia Internacional, and other agencies and foundations are expected.

If you are interested in attending the MST10 and like to receive the Second Circular of MST10 please send an e-mail to: mst10@jro.igp.gob.pe

by August 15, 2002, including in your message
1. Your name and affiliation
2. Full mailing address
3. Telephone and fax numbers including the international code
4. e-mail address
5. An indication whether you are planning to present paper(s)
6. Potential topic of your paper(s)

Table of Contents

PREFACE **11**

REPORTS **18**

REPORT ON SESSION I.1 18

REPORT ON SESSION I.2 20

REPORT ON SESSION I.3 23

REPORT ON SESSION I.4 27

REPORT ON SESSION I.5 30

REPORT ON SESSION II 31

REPORT ON THE THIRD INTERNATIONAL SCHOOL ON ATMOSPHERIC RADAR – ISAR-3 – HELD AT THE ABDUS SALAM INTERNATIONAL CENTER FOR THEORETICAL PHYSICS IN TRIESTE, ITALY, 25 NOVEMBER – 13 DECEMBER 2002 34

RESOLUTIONS **36**

RESOLUTION on Coordinated Hemisperic and Interhemispheric Observations of Polar Mesosphere Summer Echoes (PMSE) 36

RESOLUTION on Educational Issues 37

RESOLUTION on a Network on Tropical Radars 39

RESOLUTION on *E*-Region 40

SESSION I.1: RADAR SCATTERING PROCESSES IN THE NEUTRAL ATMOSPHERE **41**

I.1.3 RETRIEVAL OF ATMOSPHERIC STATIC STABILITY FROM MST RADAR RETURN SIGNAL, *D. A. Hooper, J. Arvelius and K. Stebel* 42

I.1.524 TROPOPAUSE EROSION BY MOUNTAIN WAVE BREAKING, *D. A. Hooper and E. Pavelin* 46

I.1.12 COHERENT RADAR IMAGING AND THE EFFECTS OF REFLECTIVITY FIELD VARIATIONS AND BIOLOGICAL CLUTTER, *B. L. Cheong, M. W. Hoffman, R. D. Palmer, H. Tong, V. Tellabati, S. J. Frasier and F. J. López Dekker* 50

I.1.9 ABOUT MULTIPLE LAYERING AND ASPECT SENSITIVITY OF POLAR MESOSPHERE SUMMER ECHOES, *J. Röttger* 54

I.1.4 ASPECT SENSITIVE CHARACTERISTICS OF RADAR BACKSCATTERERS AT VHF: STUDIES USING SIMULTANEOUS OBSERVATIONS OF GADANKI MST RADAR AND GPS SONDE, *A. K. Ghosh, Siddarth Shankar Das, A. K. Patra, D. Narayana Rao, V. K. Anandan and A. R. Jain* 58

I.1.10 HIGH-RESOLUTION ATMOSPHERIC PROFILING USING SIMULTANEOUS MULTIPLE RECEIVERS AND MULTIPLE FREQUENCIES, *T.-Y. Yu and W. O.J. Brown* 62

I.1.501 ATMOSPHERIC REFRACTIVITY PROFILES OVER PIURA ST RADAR, *R. Rodríguez, F. Sosa and M. Carrión* 66

I.1.505 VHF-RADAR OBSERVATIONS OF TEMPERATURE SHEETS IN THE STRATOSPHERIC-TROPOSPHERIC REGION, *Siddarth Shankar Das, K. Kishore Kumar, A. R. Jain, D. Narayana Rao, A. K. Ghosh and K. Nakamura* 70

SESSION I.2: D, E AND F REGION COHERENT SCATTERING 75

I.2.1 RECENT OBSERVATIONS OF *E* REGION FIELD-ALIGNED IRREGULARITIES AT LOW LATITUDES, *J. L. Chau, D. L. Hysell and M. A. Milla* 76

I.2.5 THE ROLE OF UNSTABLE SPORADIC-E LAYERS IN THE GENERATION OF MIDLATITUDE SPREAD-F, *C. Haldoupis, M. C. Kelley, G. C. Hussey and S. Shalimov* 86

I.2.6 STUDY OF A LOW E-REGION QUASI-PERIODIC EVENT FROM CAMP SANTIAGO, PUERTO RICO, *J. Urbina, E Kudeki and S. J. Franke* 90

I.2.10 INTERFEROMETER OBSERVATIONS OF THE BEHAVIOR OF E-REGION IRREGULARITIES IN THE MID-LATITUDE WITH THE CHUNG-LI VHF RADAR, *C. L. Chen and C. J. Pan* 94

I.2.12 IN BEAM RADAR IMAGING OF IONOSPHERIC IRREGULARITIES, *D. L. Hysell, M. F. Larsen and J. L. Chau* 98

I.2.18 FURTHER OBSERVATIONS OF PMSE IN ANTARCTICA, *M. F. Sarango, R. F. Woodman, L. A. Flores and S. Villegas* 102

I.2.20 EISCAT AND SOUSY SVALBARD RADAR OBSERVATIONS OF PMSE – DIFFERENCES AND SIMILARITIES, *J. Röttger, K. Kubo and S. Fukao* 106

I.2.21 PHASE DIFFUSION FORMULATION OF TURBULENT SCATTER SPECTRA, *H. Bahcivan and D. L. Hysell* 110

I.2.501 MORPHOLOGICAL STUDY OF THE FIELD-ALIGNED E-LAYER IRREGULARITIES OBSERVED BY THE GADANKI VHF RADAR, *C. J. Pan and P. B. Rao* 114

I.2.502 CONTINUOUS WAVE INTERFEROMETER OBSERVATIONS OF MIDLATITUDE E REGION BACKSCATTER, *C. Haldoupis, A. Bourdillon, A. Kamburelis, G. C. Hussey, and J. A. Koehler* 118

I.2.506 HF DIGISONDE AND MF RADAR MEASUREMENTS OF E-REGION BRAGG SCATTER DOPPLER SPECTRAL BANDS UNDER THE SOUTHERN POLAR CUSP, *R. J. Morris, D. P. Monselesan, D. A. Holdsworth, P. L. Dyson, M. R. Hyde and D. J. Murphy* 122

I.2.507 ROCKET OBSERVATION OF ELECTRIC FIELD CONDUCTED IN THE SEEK-2, *T. Yokoyama, M. Yamamoto, S. Fukao and R. F. Pfaff* 126

I.2.510 MULTITAPER SPECTRAL ANALYSIS OF ATMOSPHERIC RADAR SIGNALS, *V. K. Anandan, T. Rajalakshmi, G. Ramachandra Reddy and C. J. Pan* 130

I.2.512 OBSERVATIONS OF METEOR-HEAD ECHOES USING THE JICAMARCA 50 MHZ RADAR IN INTERFEROMETER MODE, *J. L. Chau, R. F. Woodman, and M. A. Milla* 134

I.2.517 RANGE IMAGING OBSERVATIONS OF PMSE USING THE EISCAT VHF RADAR: PHASE CALIBRATION AND FIRST RESULTS, *J. R. Fernandez, R. D. Palmer, P. B. Chilson, I. Häggström and M. T. Rietveld* 138

I.2.520 PMSE, NLC AND TEMPERATURE OBSERVATION DURING THE ROMA-2001 CAMPAIGN, *M. Zecha, J. Röttger, F. Lübken, J. Höffner, C. Fricke-Begemann and A. Müllemann* 142

I.2.521 RESULTS OF SEVERAL YEARS MSE OBSERVATION AT KÜHLUNGSBORN (54°N), *M. Zecha, J. Bremer and P. Hoffmann* 146

SESSION I.3: WINDS, WAVES AND TURBULENCE IN THE LOWER AND MIDDLE ATMOSPHERE AND THE LOWER THERMOSPHERE..... 151

I.3.3 WIND AND TURBULENCE MEASUREMENTS BY THE MIDDLE AND UPPER ATMOSPHERE RADAR USING UCAR-STARS METHOD, *A. Praskovsky, E. Praskovskaya, G. Hassenpflug, M. Yamamoto and S. Fukao*..... 152

I.3.4 STANDARD DEVIATIONS OF CORRELATION LENGTHS IN SPACED ANTENNA OBSERVATIONS USING THE MU RADAR, *G. Hassenpflug, M. Yamamoto S. Fukao* 156

I.3.9 OBSERVATIONS OF THE QUASI 2-DAY WAVES IN THE MESOPAUSE OVER WUHAN, CHINA, *J. Xiong, W. Wei, B. Ning and L. Liu*..... 160

I.3.10 SPORADIC E LAYER DEPENDENCE ON PLANETARY WAVES. AN EVENT STUDY SHOWING AN INDIRECT RELATIONSHIP TROUGH MODULATED ATMOSPHERIC TIDES, *C. Haldoupis and D. Pancheva* 164

I.3.11 RADAR, OPTICAL AND SATELLITE STUDIES OF CLIMATOLOGY AND EFFECTS OF ATMOSPHERIC GRAVITY WAVES AND TURBULENCE, *N. M. Gavrilov*..... 168

I.3.13 STUDIES ON ATMOSPHERIC GRAVITY WAVE ACTIVITY IN THE TROPOSPHERE AND LOWER STRATOSPHERE OVER A TROPICAL STATION AT GADANKI, *D. Narayana Rao, I. V. Subba Reddy, A. Narendra Babu, M. Venkat Ratnam and S. Vijaya Bhaskara Rao* 177

I.3.16 STUDIES ON WINDS AND MOMENTUM FLUXES USING UHF RADAR OBSERVATION OVER GADANKI (13.5°N, 79.2°E), *D. Narayana Rao, B. Vasantha, N.V.P. Kiran Kumar and I.V. Subba Reddy*..... 181

I.3.19 DEEP PENETRATIVE CONVECTION AND GENERATION OF WAVE OSCILLATION OBSERVED WITH THE CHUNG-LI VHF RADAR, *J. Röttger, M. L. Hsu, W. C. Tsai, C. J. Pan and J. Wu*..... 185

I.3.22 A BRIEF OVERVIEW OF GRAVITY WAVE BREAKING THEORY, *G. P. Klaassen*.... 189

I.3.25 TURBULENT DIFFUSIVITY INFERRED FROM MST RADAR MEASUREMENTS: A REVIEW, *R. Wilson*..... 194

I.3.26 SIMULTANEOUS OBSERVATIONS OF ATMOSPHERIC TURBULENCE IN THE LOWER STRATOSPHERE FROM BALLOON SOUNDINGS AND ST RADAR MEASUREMENTS, *R. Wilson and F. Dalaudier* 204

I.3.27 NEW MST RADAR METHODS FOR MEASURING THE TURBULENT KINETIC ENERGY DENSITY, *T. E. VanZandt, G. D. Nastrom, J.-I. Furumoto, W. L. Clark and T. Tsuda* 208

I.3.28 MEASUREMENTS OF ATMOSPHERIC TURBULENCE WITH THE DUAL-BEAMWIDTH METHOD USING THE MST RADAR AT GADANKI, INDIA, *G. D. Nastrom, P. B. Rao and V. Sivakumar* 210

I.3.33 FAST AND ACCURATE CALCULATION OF SPECTRAL BEAM-BROADENING FOR TURBULENCE STUDIES, *W. Hocking* 214

I.3.34 POSSIBLE CROSS-TROPOPAUSE TRANSPORT PROCESSES IN THE TROPICS, *M. K. Yamamoto, M. Fujiwara and S. Fukao* 218

I.3.39 UPPER MESOSPHERE TEMPERATURE CHANGES OBSERVED IN PMSE AND INCOHERENT SCATTER DURING A STRONG POLAR CAP ABSORPTION EVENT, *K. Kubo, J. Röttger and S. Fukao* 222

I.3.30 TURBULENCE STUDIES USING UHF RADAR OBSERVATIONS OVER GADANKI (13.5°N, 79.2°E), *D. Narayana Rao, B. Vasantha, N.V.P. Kiran Kumar and I.V. Subba Reddy* 226

I.3.501 WIND MEASUREMENTS BY THE CHUNG-LI RADAR IN THE PRESENCE OF STRONG CLUTTER AND HARD TARGETS, *E. Praskovskaya, A. Praskovsky, J.-S. Chen and Y.-H. Chu* 230

I.3.504 MU RADAR ESTIMATION OF DOWNWARD TURBULENT OZONE FLUXES NEAR THE TROPOPAUSE, N. M. Gavrilov and S. Fukao 234

I.3.505 LARGE VELOCITIES MEASURED AT MF AND HEIGHTS ABOVE 100KM: REAL OR SPURIOUS?, *C. Meek and A. Manson* 238

I.3.508 LIDAR OBSERVATIONS OF MIDDLE ATMOSPHERIC GRAVITY WAVE ACTIVITY OVER A LOW LATITUDE, *V. Sivakumar and P. B. Rao* 241

I.3.509 APPLICATION OF THE DUAL-BEAMWIDTH METHOD TO A NARROW BEAM MF RADAR FOR ESTIMATION OF TURBULENT SPECTRAL WIDTH, *R. Latteck, W. Singer and N. Engler* 245

I.3.511 MONSOON LOW LEVEL JET OBSERVATIONS OVER GADANKI, *K. Madhu Chandra Reddy, D. Narayana Rao, A. R. Jain and Y. Ohno* 249

SESSION I.4: METEOROLOGICAL PHENOMENA AND APPLICATIONS 253

I.4.3 MESOSCALE ALPINE PROGRAMME (MAP): SYNERGIES BETWEEN WIND PROFILERS AND DOPPLER WEATHER RADARS, *M. Petitdidier, V. Klaus and P. Tabary* ... 254

I.4.4 OBSERVATIONS OF TYPHOON 9426 (ORCHID) WITH THE MU RADAR: MESO-α-SCALE KINEMATIC STRUCTURE AND MESO-β・γ-SCALE PRECIPITATING CLOUDS, *Y. Shibagaki, M. D. Yamanaka, M. Kita-Fukase, H. Hashiguchi, Y. Maekawa and S. Fukao* 258

I.4.6 RANGE, RESOLUTION, AND SAMPLING, *P. Johnston, L. Hartten, D. Carter and K. Gage* 262

I.4.16 AN OBSERVATIONAL STUDY ON INTRASEASONAL VARIATIONS WITH EQUATORIAL ATMOSPHERE RADAR(EAR) IN WEST SUMATERA, INDONESIA, *H. Hashiguchi, T. H. Seto, S. Fukao, M. K. Yamamoto, M. Fujiwara, T. Horinouchi, M. Yamamoto, M. Muzirwan and M. Kartasasmita* 266

I.4.9 A COMPREHENSIVE STUDY ON TROPICAL MESOSCALE CONVECTIVE SYSTEMS USING VHF AND UHF RADARS OVER A TROPICAL STATION, *K. Kishore Kumar and A. R. Jain* 270

I.4.10 VHF RADAR REFLECTIVITY, VERTICAL VELOCITIES AND RAINFALL RATE DURING TYPHOON PASSAGES OVER TAIWAN, *C. J. Pan, M. L. Hsu, L. J. Chung, J. Röttger and J. Wu* 274

I.4.12 DERIVING DROP SIZE DISTRIBUTION FROM VHF AND UHF RADAR SPECTRA, *N. V. P. Kiran Kumar and D. Narayana Rao* 278

I.4.14 DIAGNOSTIC STUDY OF TROPICAL PRECIPITATING CLOUD SYSTEMS USING WIND PROFILERS AT GADANKI, INDIA, *K. Krishna Reddy, T. Kozu, M. Thurai, Y. Ohno, K. Nakamura, A. R. Jain and D. Narayana Rao* 282

I.4.17 TROPOSPHERIC WIND MEASUREMENTS WITH THE PIURA BOUNDARY LAYER RADAR DURING EXTREME RAINFALL EVENTS IN 2002, *K. Takahashi* 286

I.4.18 FOEHN IN THE RHINE VALLEY AS SEEN BY A WIND-PROFILER-RASS SYSTEM AND COMPARISON WITH THE NONHYDROSTATIC MODEL MESO-NH, *S. Vogt and G. Jaubert* 290

I.4.19 STUDY OF A MESOSCALE LAND-TO-SEA LOW-LEVEL JET WITH A NETWORK OF UHF WIND PROFILERS: CASES OF THE MISTRAL WIND, *V. Guénard, J-L. Caccia, B. Bénech, B. Campistron and P. Drobinski* 294

I.4.21 WIND PROFILER AND TOWER OBSERVATIONS OF A GRAVITY CURRENT AND A RELATED SOLITARY WAVE, *A. Adachi, W. Clark, K. Gage and T. Kobayashi* 298

I.4.22 TOWARDS THE ADVANCED MEASUREMENTS OF ATMOSPHERIC TURBULENCE BY SPACED ANTENNA RADARS, *A. Praskovsky and E. Praskovskaya* 302

I.4.23 THE INCLINATION OF REFLECTIVITY STRATIFICATIONS, *J. Röttger* 306

I.4.24 DETERMINATION OF THE TURBULENT FLUXES OF MOMENTUM AND VIRTUAL SENSIBLE HEAT WITH AN UHF RASS PROFILER. COMPARISON WITH IN SITU MEASUREMENTS, *B. Bénech, F Girard-Ardhuin, B. Campistron, F. Saïd, F. Lohou, and V. Puygrenier* 310

I.4.504 RADAR OBSERVATIONS OF TROPICAL PRECIPITATION SYSTEMS AT KOTOTABANG, WEST SUMATERA, *Y. Shibagaki, T. Kozu, T. Shimomai, Y. Fujiyoshi, S. Mori, M. K. Yamamoto, H. Hashiguchi, S. Fukao and M.D. Yamanaka* 314

I.4.506 RAIN DROP SIZE DISTRIBUTION OVER GADANKI, INDIA DURING SOUTHWEST AND NORTHEAST MONSOON, *K.Krishna Reddy, T. Kozu, T.Narayana Rao, K. Nakamura and D.Narayana Rao* 318

I.4.509 WIND PROFILER FOR MONITORING OF MEIYU PRECIPITATION IN THE DOWNSTREAM OF YANGTZE RIVER, *K. Krishna Reddy, B. Geng, H. Yamada and H. Uyeda* 322

I.4.514 TROPOSPHERIC WINDS MEASURED WITH THE PIURA ST RADAR: NORMAL VS. "EL NIÑO 1997-98" CONDITIONS, *L. A. Flores, J. La Madrid and J. L. Chau* 326

I.4.515 AN INVESTIGATION OF OZONE AND PLANETARY BOUNDARY LAYER DYNAMICS OVER GADANKI, INDIA, *K.Krishna Reddy, S. Lal, T. Kozu, K. Nakamura, Y. Ohno, M. Naja and D.Narayana Rao* 330

I.4.519 THE SIGNATURE OF MID-LATITUDE CONVECTION OBSERVED BY MST RADAR, *D. A. Hooper, H. J. Reid and E. Pavelin* 334

I.4.520 PRELIMINARY OBSERVATIONS OF CONVECTIVE BOUNDARY LAYER OVER GADANKI (13.5°N, 79.2°E) USING UHF WIND PROFILER, *K. Kishore Kumar and A. R. Jain* 338

I.4.521 STUDIES ON MOMENTUM FLUXES USING MST RADAR WINDS OBSERVED AT GADANKI (13.5°N, 79.2° E), INDIA, *Narayana Rao, I. V. Subba Reddy, P. Kishore, S. P. Namboothiri, K. Igarashi, K. Krishna Reddy and S. V. Bhaskara Rao* 342

I.4.522 ESTIMATION OF THE TROPOPAUSE HEIGHT USING THE VERTICAL ECHO PEAK AND ASPECT SENSITIVITY CHARACTERISTICS OF A VHF RADAR, *B.-H. Heo, K.-E. Kim, B. Campistron and V. Klaus* 346

SESSION I.5: OPERATIONAL ASPECTS AND RECENT SYSTEM DEVELOPMENTS..... 351

I.5.1 THE WIND PROFILER NETWORK OF THE JAPAN METEOROLOGICAL AGENCY, *M. Ishihara, S. Fukao and H. Hashiguchi* 352

I.5.3 FIRST RESULTS OF THE BOUNDARY LAYER AND TROPOSPHERIC RADAR SYSTEMS FOR ENSO STUDIES IN NORTHERN PERU, *D. Scipión, J. L. Chau and L. A. Flores* 357

I.5.5 MOVEABLE UHF/S-BAND PROFILER/DISDROMETER SYSTEMS AS A CALIBRATION STANDARD IN RAINY PLACES, *W. Clark, K. Gage, C. Williams, P. Johnston and D. Carte*r . 361

I.5.7 TOWARD A MULTISENSOR GROUND BASED REMOTE SENSING STATION, *C. Gaffard, T. Hewison and J. Nash* 365

I.5..506 DEVELOPMENT OF A DIGITAL RECEIVER FOR THE JICAMARCA OBSERVATORY RADARS, *G. Michhue and R. Woodman* 369

I.5.9 ELECTRONIC DIGITAL BEAMFORMING IMPLEMENTATION FOR RADARS, *R. Ney, S. Bonaimé, F. Dolon, J. J. Berthelier, R. Clairquin, D. Nevejans, C. Duvanaud and A. D'Hermies* . 373

I.5.11 ON-LINE ADAPTIVE DC-GROUND-CLUTTER REMOVAL, *J. Röttger* 377

I.5.513 ON THE RADIATION EFFICIENCY OF COCO ANTENNAS, *M. F. Sarango, R. F. Woodman and D. Córdova* 381

I.5.15 A NEW NARROW BEAM MF RADAR AT 3 MHZ FOR STUDIES OF THE HIGH-LATITUDE MIDDLE ATMOSPHERE: SYSTEM DESCRIPTION AND FIRST RESULTS , *W. Singer, R. Latteck, D. A. Holdsworth and T. Kristiansen* 385

I.5.501 ANTENNA BEAM VERIFICATION USING COSMIC NOISE, *T. K. Carey-Smith, A. J. McDonald, W. J. Baggaley, R. G. Bennett, G. J. Fraser and G. E. Plank*..... 391

I.5.502 AN ATTEMPT TO CALIBRATE THE UHF STRATO-TROPOSPHERIC RADAR AT ARECIBO USING NEXRAD AND DISDROMETER DATA, *P. Kafando and M. Petitdidier*..... 395

I.5.516 QUALITY CONTROL FOR DOPPLER WIND PROFILERS USING NIMA, *C. S. Morse, R. K. Goodrich, L. B. Cornman, and S. A. Cohn* 399

I.5.518 SOUSY RADAR AT JICAMARCA: SYSTEM DESCRIPTION, *R. F. Woodman, O. Castillo, G. Michhue, P. Reyes, and S. Villegas* 403

I.5.519 THE EQUATORIAL ATMOSPHERE RADAR: SYSTEM AND NEW RESULTS, *S. Fukao, H. Hashiguchi, and M. K. Yamamoto* 407

I.5.521 VHF ATMOSPHERIC AND METEOR RADAR INSTALLATION AT DAVIS, ANTARCTICA: PRELIMINARY OBSERVATIONS, *R. J. Morris, D. J. Murphy, I. M. Reid, and R. A. Vincent* 411

I.5.522 VORTICAL MOTIONS OBSERVED WITH THE NEW MCGILL VHF RADAR AND ASSOCIATED DYNAMICAL CHARACTERISTICS, *E. F. Campos and W. K. Hocking*..... 415

I.5.523 A NEW MINIRADAR TO INVESTIGATE URBAN CANOPY: CURIE CANOPY URBAN RADAR FOR INVESTIGATION OF EXCHANGES, *A. Weill, C. Legac, R. Ney and L. Chardenal* 419

SESSION PWG 1: SYSTEM CALIBRATIONS AND DEFINITIONS 423

SESSION PWG 2: DATA ANALYSIS, VALIDATION AND PARAMETER DEDUCTION METHODS 425

PWG2 PARAMETRIC ESTIMATION OF SPECTRAL MOMENTS OF OVERLAPPED WEATHER DOPPLER ECHOES BY THE USE OF HIGH-RESOLUTION ALGORITHMS, *E. Boyer, M. Petitdidier and P. Larzabal* 426

SESSION PWG 3: ACCURACIES AND REQUIREMENTS FOR METEOROLOGICAL APPLICATIONS 431

SESSION PWG 4: INTERNATIONAL COLLABORATIONS 433

SESSION II.E: NOVEL PERSPECTIVES AND UNSOLVED ISSUES 435

II.E.1 AN ADAPTIVE CLUTTER REJECTION SCHEME FOR MST RADARS, *T. Sato and K. Kamio* 436

II.E.2 THREE-METRE-SCALE TURBULENCE ANISOTROPY AS A PRECURSOR TO RAIN, *A. Hocking and W. Hocking* 444

II.E.3 WHAT IS THE FUTURE OF THE MULTI-FREQUENCY TECHNIQUES?, *H. Luce* 448

II.E.5 WHAT IS TURBULENCE SEEN BY VHF RADAR?, *J. Röttger* 449

II.E.7 APPLICATIONS OF A WORLD-WIDE NETWORK OF MESOSPHERIC RADARS, WITH SPECIAL EMPHASIS ON THE COLUMBIA SPACE SHUTTLE DISASTER, *W. K. Hocking, S. J. Franke, N. Mitchell, D. Pancheva, P. Batista, B. Clemesha, B. Fuller, B. Vandepeer, T. Nakamura, T. Tsudd and J. MacDougall* 460

II.E.8 THE STRUCTURE FUNCTION-BASED APPROACH TO DATA ANALYSIS FOR SPACED ANTENNA RADARS: A COMPARISON WITH TRADITIONAL TECHNIQUES, *A. Praskovsky and E. Praskovskaya* 461

II.E.9 VHF PARASITIC RADAR INTERFEROMETRY FOR MST ZENITH SOUNDING, *J. Sahr* 471

Participants List..... 481

Authors Index 487

Preface

MST10

The Tenth International Workshop on Technical and Scientific Aspects of MST Radar - MST10 - was held 13-20 May 2003 at the campus of the Universidad de Piura in northern Peru. These international workshops are held every 2-3 years and comprise major events gathering together experts from all over the world, engaged in research and development of radar techniques to study the mesosphere, stratosphere and troposphere (MST). It includes also ionospheric coherent scatter radars and planetary boundary layer radars. It offers excellent opportunities to young scientists, research students and also new entrants to the field for close interactions with the well-known experts on all technical and scientific aspects of MST radar methods.

As a new approach, the workshop consisted of two major parts: (Section I) standard workshop papers presented orally or as posters, and (Section II) a brain-storming session with the aim to highlight open questions and potential solutions, to produce proposals for innovative approaches, define new programs and prepare recommendations and resolutions.

UDEP Campus. MST10 Panel to the left. *(courtesy of F. Lind)*

UDEP's MST Radar. *(courtesy of T. Shimomai)*

The Universidad de Piura (UDEP) is known in radar circles due to its operation of ST and boundary layer radars, which are part of the activities of the Instituto Geofisico del Peru (IGP), operating the Jicamarca Radio Observatory (JRO), in collaboration with institutions like the University of Colorado (via CIRES) and NOAA (via the Aeronomy Laboratory).

Sponsors of MST10 were the Scientific Committee on Solar Terrestrial Physics (SCOSTEP), the International Union of Radio Science (URSI), the National Science Foundation (NSF) of USA, Consejo National de Ciencia y Technología (CONCYTEC) of Peru and various research and development companies.

The International Steering Committee of MST10 consisted of J. Röttger (Chair, Germany), J. Chau (Peru), S. Fukao (Japan), E. Kudeki (USA), and R. Woodman (Peru). Adherent to the International Steering Committee were the Chairpersons of the MST Radar Permanent Working Groups P. Chilson (USA), D. Holdsworth (Australia), G. Nastrom (USA), P.B. Rao (India), and M. Yamamoto (Japan). Honorary Members of the Steering Committee were M.F. Larsen (USA), C.H. Liu (Taiwan), A.P. Mitra (India). The National Organizing Committee of MST10 consisted of: R. Woodman (Chair, IGP), J. Chau (JRO-IGP), Antonio Mabres (UDEP) and M. Sarango (Ciencia Internacional). The Local Organizing Committee consisted of Rodolfo Rodriguez (Chair), William Ipanaque, and Sergio Balarezo. Session conveners and session chair persons were drawn from the international scientific community.

The workshop was opened on Tuesday morning, 13 May 2003, in the presence of the President of the Piura region, Dr. César Trelles, the President of UDEP, Dr. Antonio Abruña, the Dean of the Faculty of Engineering of UDEP, Dr. Sergio Balarezo, the President of the Instituto Geofisico del Perú, Dr. R.F. Woodman and the Chairman of the German Embassy and the Consulate in Piura were represented by R. Niemann and J. M. Irazola.

Opening Ceremony.
From l to r: Ronald Woodman, César Trelles, Antonio Abruña, Juergen Roettger and Sergio Balarezo *(courtesy of G. Hassenpflug)*

Participants were from 17 countries from all continents. A total of 175 abstracts had been submitted, and 109 oral papers (24 thereof invited) and 66 poster papers were presented. A tour of the university institutes and facilities as well as the radar systems took place on Thursday afternoon, which was followed by an outing to a nearby horse farm.

During the get-together on Monday evening and the workshop dinner on Thursday evening the workshop participants enjoyed north Peruvian-style folklore, and an extended tour took place on Sunday to visit the famous historical site of Sipan in the northern Peru region.

Ben Balsley giving his public lecture. *(courtesy of J. Zavala)*

Public lectures at the university were given by R.F. Woodman on "Space exploration from the ground: Peruvian contributions to human knowledge", and by B.B. Balsley on "A half century of cooperation with my Peruvian colleagues". During the workshop dinner D.T. Farley spoke about his long-lasting experience with Jicamarca and corresponding episodes and adventures.

The hotel facilities were excellent, in short-walking distance to the university campus,

and the local organizing committee, supported by Jicamarca personnel and university students, kept track of the very pleasant and highly functional workshop performance.

Session I.1 first speech by David Fritts. *(courtesy of J. Zavala)*

Session I.1 was on radar scattering processes in the neutral atmosphere (convened by H. Luce and A. Muschinski). This session dealt with observational and theoretical investigations (1) on how to separate the effects of different scattering mechanisms in the same data set, and on (2) radar echo characteristics in different radar configurations and their interpretations are presented. Emphasis of the papers was placed on contributions that discuss new observations (e.g., multi-beam, multi-frequency, multi-receiver, and/or multi-regime radar observations, also inter-comparisons with in situ measurements) on the basis of innovative, first-principle theoretical analysis. Invited talks were given by D. Fritts on direct numerical simulations of turbulence and radar backscatter, and by F. Dalaudier on combined radar and balloon observations. B. Balsley's kite observations, which show very thin structures in the lower troposphere point into the direction of understanding the highly specular radar returns as well.

Yen-Hsyang Chu during Session I.2. *(courtesy of J. Zavala)*

Session I.2 was on D-, E-, and F-region coherent scattering (convened by D. Hysell and R.D. Palmer). It was devoted to the theory and observation of coherent scatter from ionospheric irregularities at all latitudes. Papers were presented. pertaining to such mature fields of study as the auroral and equatorial electrojets, PMSE, sporadic E-layers, and equatorial spread-F. Recent and planned campaigns like SEEK II, C/NOFS, and CIELO attest to the fact that numerous problems remain unsolved in these areas. In addition, papers on emerging areas of research were given, including long-lived meteor trails, 150 km echoes, daytime spread-F, and mid-latitude spread-F. Novel experimental techniques such as passive radar, networked radar, radar imaging, and coherent scatter Faraday rotation may promote rapid progress in the areas outlined above. Reports describing new experimental radar techniques were given also in section II. Invited papers were given by E. Kudeki on 150-km echoes, J. Chau on E region studies at low-latitudes,
W. Singer et al. on PMSE, F. Lind on E region irregularities at high latitudes, and S. Fukao on the SEEK-2 campaign. Due to short-notice travel cancellation P. Chilson could not give his invited talk on PMSE.

Session I.3 on winds, waves and turbulence in the lower and middle atmosphere and the lower thermosphere was convened by W.K. Hocking and M.F. Larsen. This session examined recent developments of studies and observations of dynamics in the middle atmosphere and lower thermosphere. Topics of particular interest included wave-wave interaction, wave sources and generation mechanisms, wave deposition processes, non-linear interactions, wave propagation studies, turbulence anisotropy and turbulent transport processes. Correlations of wave events as a function of height, and multi-instrument studies were presented, and inter-comparisons of different techniques were considered to be important. One area of special interest was studies of wave velocity amplitudes and variability in the region above 90 km altitude, with particular interest in determining the frequency of occurrence of large amplitude events and large wind velocities (up to 100 m/s and higher) in this region. D. Fritts gave the invited presentation of P. Franke, who could not attend. This talk expanded the direct numerical simulation of turbulent structures. Investigations on gravity wave break down and the different kinds of instabilities done by G. Klaassen were presented by W. Hocking. The invited review on turbulent diffusivity was presented by R. Wilson, and N. Gavrilov gave an invited talk on gravity wave and turbulence studies and drew attention on the possible relation of middle atmosphere gravity wave activity to El Nino.

Shoichiro Fukao during Session I.3.

K. Krishna Reddy during Session I.4.

K. Gage and D. Riggin convened **Session I.4** on meteorological phenomena and applications.

It was concerned with recent developments in Doppler radar profiling in the lower neutral atmosphere, especially studies of lower atmospheric phenomena made with profilers in combination with other instruments during field campaigns. Topics of interest included the assimilation of profiler data in meteorological models, quality control of profiler data, operational networks of profilers and the impact of profiler data on forecasting. Of special interest were studies that demonstrate the utility of profiling for quantifying the vertical structure of turbulence, humidity, cloud and precipitation fields including drop size distributions and their variability. The invited talks were given by K. Gage (on behalf of S. Koch) on mesoscale analysis and prediction using wind profiler data and by C. Williams and K. Gage on rain drop size distributions deduced from profiler observations.

The operational aspects and recent system developments were handled in **Session I.5**, which was convened by I. Reid and D. Thorsen. The focus was on aspects related to the technical performance of radar systems and multi-instrument measurements. Papers pertaining to all aspects of technical performance of current and/or proposed facilities, including the unique problems associated with operation of remote stations were included. These aspects related as well to pros and cons of system configurations and measurement methods. It was addressed how multi-instruments can be used together to augment scientific research as well as how measurements from diverse instruments (including models) may be appropriately compared.

Short reports and summary presentations on the **Permanent Working Groups (PWGs**) activities were presented at the beginning of the second workshop week. These PWGs deal with (1) system calibration and definitions, (2) data analysis, validation, and parameter reduction methods, (3) accuracies and requirements for meteorological applications, and (4) international collaborations and education.

This was followed by **Section II on "Novel perspectives and unsolved issues".** To stimulate brain storming in this section, several invited talks were presented. T. Sato and K. Kamino introduced an adaptive clutter rejection scheme for MST radars, W. Hocking evaluated diagnostic capabilities of measurements of backscatter anisotropy, H. Luce reviewed the future of the multi-frequency techniques, J. Röttger asked what is turbulence seen by VHF radars, W. Hocking et al. reported about potential applications of a world-wide network of mesospheric radars with special emphasis on the Columbia space shuttle disaster, A. and E. Praskovsky presented a structure-function-based approach to data analysis for spaced antenna radars, and J. Sahr proposed VHF parasitic radar interferometry for MST zenith sounding. These presentations lead to distinct lively discussions. These were summarized in the final plenary session together with reports on the oral poster sessions prepared by the chairpersons.

The **Plenary and Closing Session** was held on Tuesday afternoon and chaired by J. Röttger. It included discussions of the highlights presented in the oral and poster workshop papers of Section I and in particular important issues and questions raised in the presentations of Section II.

Poster Session I. *(courtesy of T. Shimomai)*

The written reports of the session conveners and chairpersons formed a suitable input for the final discussions, which concentrated on topics such as (to mention just a few): Identification of backscattering mechanism by statistical analysis and the Direct Numerical Simulation. Here the questions were how DNS can model turbulence decay and how one can expand the modeling for multiple gravity waves and their breaking. The question on the realistic meaning of the effective diffusivity and turbulence energy dissipation rate remains to be studied. A

dominant item seems to be the contributions of ST radars for the studies of stratosphere-troposphere exchange. Interesting and not yet solved topics are the scattering mechanism of polar mesosphere summer echoes, their structure and inter-hemispheric difference, the creation and propagation of gravity waves from low altitudes to higher altitudes in the mesosphere and lower thermosphere, and their momentum and energy dissipation. Also the E- and F-region irregularities, leading to coherent scatter, are still a relevant item and open questions were summarized, such as their generation mechanisms and their relation to coupling with above (electric fields) and below (gravity waves and tides).

Several approaches are in use to analyze and interpret spaced antenna and interferometer observations and the pros and cons are disputed. Imaging techniques are highlights of the recent developments to understand the structure and dynamics of the atmosphere. A promising idea is to apply the parasitic radar method for lower atmosphere studies. Combination with other techniques, such as the application aspects of the wind profilers, providing data for improving forecasting and modeling, are a most recognized spin-off of the MST radar technique.

The activities of the Permanent Working Groups were evaluated and it was resolved that these groups, which are mostly dormant between workshops, should become part of a discussion group on topical issues, which should be introduced and handled via the internet. The present workshop homepage http://jro.igp.gob.pe/mst10 forms a suitable forum for this purpose.

The normal abstracts of all papers were published by the local organizers in the abstract proceedings. Extended abstracts will be published on CD-ROM and as hardcopy, as usual, in the final workshop proceedings. An editorial team at the Jicamarca Radar Observatory takes care of this duty, supported by the steering committee. Full manuscripts can be submitted for potential publication in a special MST radar issue of the journal Annales Geophysicae. These manuscripts undergo the standard refereeing procedure, where the guest editors are D. Hooper and D.N. Rao. A call for papers has been distributed to all, who had submitted abstracts for MST10.

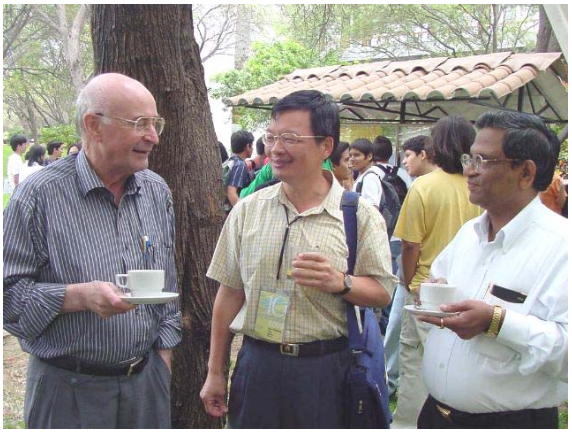

Coffee Break.
From l to r: Jürgen Röttger, Yen-Hsyang Chu and Daggumati Narayana Rao *(courtesy of J. Zavala)*

Several proposals for resolutions were discussed. The one on educational issues aims towards continuing and expanding the international radar schools, such as ISAR, but also supporting the tendencies for establishing regular schools on national levels as well as forming permanent departments on atmospheric radar at universities and other institutions. Concentrated efforts should be undertaken, supported by a resolution, to understand the hemispheric difference and frequency dependence of PMSE using calibrated radar systems.

To improve the understanding of dynamical processes in low latitudes, special campaigns and in particular a tropical network of radars on a global scale was proposed and is laid down in a resolution. In general it was felt that the MST radar technique, although basically mature, still expects further and deeper understanding of the atmosphere by introducing new techniques, establishing new observation sites and upgrading existing facilities. Another resolution covers research requirements to understand mid-latitude E-region irregularities. These resolutions will be published in the final proceedings and submitted to the sponsoring organizations as well as other governing agencies.

The character of the workshop was discussed and it was felt that the addition of a brain storming section to foster new directions has raised the quality of the MST radar workshop. It was decided to continue with these workshops, and also keep the time frame of 8 days, not starting on Monday and including one weekend. Invitations to hold the next workshop - MST11 - were received from Australia, Germany and India. It was noted that Australia had twice been candidate before, but the final decision was postponed to allow more information of the community about the possible venue.

The workshop was closed on Tuesday afternoon leaving in the minds of the participants proper updates on scientific research and technical developments, potential approaches of open questions, views into a promising future and most delightful impressions on the University of Piura and the appreciation of the whole-hearted contributions by the members of the local organizing committee.

Those, who were still present after the workshop had the chance to see the tropical sunset at the nearby ocean front of Colan, - an ultimate finale of a successful workshop on atmospheric research. Our sincere particular thanks for the most efficient performance of MST10 are directed to the sponsors, the University of Piura and the staff of the local organizing committee.

Jürgen Röttger and Jorge Chau

MST10 initialization meeting, May 2002. From l. to r.: Rodolfo Rodriguez, Jürgen Röttger, Erhan Kudeki, Koki Chau and Antonio Mabres. *(courtesy of J. Röttger)*

The beautiful sunset at Colan. *(courtesy of J. Röttger)*

Report on Session I.1 "Radar scattering processes in the neutral atmosphere"

Conveners: H. Luce and A. Muschinski

Abstract of session: Unambiguous retrieval of atmospheric parameters related to turbulence, waves, hydrometeors, etc, from MST radar measurements is still challenging and sometimes impossible. This difficulty is in part due to the nature of the specific inversion problem, in part due to our still insufficient knowledge on the relevant backscattering mechanisms and their relative importance. This session was thus devoted to recent approaches (sophisticated radar observations, intercomparisons with in situ measurements and numerical simulation results) used for improving our understanding on these processes.

Eight papers were presented in the Session I.1 chaired by M. Petitdidier, W. Singer and H. Luce. The two first presentations were invited talks prepared by D. Fritts of Colorado Research Associates (USA) and F. Dalaudier of Service d'Aéronomie (CNRS, France). These talks emphasized the importance of numerical simulations and in situ observations, respectively, for the interpretation of MST radar echoes. D. Fritts presented results of 3D DNS of turbulence generation by KHI and gravity wave breaking. These simulations clearly demonstrate the generation of thin structures at the edges of a mixing layer. These structures are characterized by strong thermal and velocity gradients and are quite similar to those shown by F. Dalaudier observed experimentally in the shear of a jet-stream using high-resolution temperature measurements. The simulation results were strongly debated, in particular, the importance of the initial conditions used (very small Ri number) and of establishing energy budget and the interaction of the mixing layer with other possible processes (such as waves) in its surroundings which could affect the mixing evolution. F. Dalaudier reviewed recent observations by balloon and radar techniques. After a presention of the measurement techniques and results with the CIRES TLS (Tethered Lifting System) and MUTSI experiment, he mainly emphasized the constraints and interpretation difficulties when comparing atmospheric parameters measured by radars and balloons. Finally, these two talks stressed the importance of MST radar experiments coordinated with numerical simulations and in situ observations for a better understanding of the atmospheric dynamics at small scales. More thorough intercomparisons are needed and the creation of a working group on this topic could help to the development of common projects.

D. Hooper (with J. Arvelius, K. Stebel and E. Pavelin) gave two talks showing the possibility to retrieve static stability from MST radar returns and an application of the proposed approach to tropopause erosion by mountain wave breaking. A thorough analysis showed interesting potential of the method based on N^2 estimation from vertical echo power. The observed desagreements mainly resulted from important balloon drifts and horizontal inhomogeneities of the temperature field due to mountain waves. N^2 radar estimates were then used for calculating Ri number from the sole radar measurements and then analysing an event of moutain wave breaking around the tropopause level. The Ri number is an important (but not sufficient) parameter for identifying the nature of the radar echoes. Another approach from MST radar data was presented by A. McDonald by using statistics of the I and Q components of the received signals.

Improving MST radar resolution by using various imaging techniques may be another complementary approach for a better understanding of radar backscattering processes. R. Palmer (with H. Tong, V. Tellabati, B. Cheong and M. Hoffman) presented two talks about radar imaging technique developments on a turbulent eddy 915 MHz profiler. Simulations and applications were discussed. Horizontal maps of the wind field and reflectivity structures obtained with a sophisticated Capon beamforming method applied on data collected from 90 independent receivers were shown. The authors demonstrated the capabilities of the proposed coherent radar imaging, not only for turbulence studies, but also for attenuating airplane interferences. Horizontal maps of echo power using a multi-beam approach are also of great importance for our purpose. Recent papers by R. Worthington et al. were a clear demonstration of their potentials by identifying a systematic skew of the horizontal echo power distribution related to the direction of the wind shear, as recalled by F. Dalaudier. Such a kind of information is crucial for interpreting radar echoes. Unfortunately, a review on the topic was not available because R. Worthington was unable to attend the workshop.

Aspect sensitivity (i.e. the enhancement of echo power in vertical direction with respect to oblique echo power) was discussed by the invited papers and by J. Röttger within the studies of the PMSE layering. PMSE are indeed often aspect sensitive. Double-layer structures are usual but multiple layering structures can also be observed. They may indicate a complex mechanism of interactions between waves and turbulence.

Report on Session I.2 "*D, E* and *F* Region Coherent Scattering"

Conveners: D. Hysell and R. Palmer

Abstract: This session was devoted to theory and observations of coherent scatter from ionospheric irregularities at all latitudes. Reports pertaining to mature fields of study like the auroral and equatorial electrojets, PMSE, sporadic *E* layers, and equatorial spread *F* were solicited. Recent and planned campaigns like SEEK II and EQUIS II attest to the fact that numerous problems remain unsolved in these areas. In addition, reports on emerging areas of research including long-lived meteor trails, 150 km echoes, daytime spread *F*, and midlatitude spread *F* were sought. Also welcome were papers on new radar techniques that can promote rapid progress in these areas such as passive radar, distributed radar, and aperture synthesis imaging.

Despite the breadth of the solicitation, most of the papers submitted to this session fell into one of two categories: low- and mid-latitude *E* region irregularities and PMSE, indicating where community interest is currently focused. The session was accordingly divided into two parts. The main findings of the respective parts are summarized below.

E region irregularities: The first part of Session I.2 was chaired by D. Hysell and T. Ogawa. It opened with an invited presentation by J. Chau, D. Hysell, and M. Mila contrasting the morphology and climatology of *E* region echoes received at equatorial and mid latitude stations: Jicamarca and Piura. Much of the discussion concerned counter electrojet conditions which, although never observed prior to June, 2000 at Jicamarca, have been observed on seven occasions since. The observations revealed that counter electrojet irregularities appear only when large reversed zonal electric fields exist and that their Doppler shifts obey a cosine dependence on zenith angle much like ordinary type 2 echoes. S. Fukao next presented an invited paper by M. Yamamoto and S. Fukao summarizing preliminary results from the SEEK II rocket campaign conducted in Japan in August, 2002. Rockets launched during the campaign encountered multiple, steep, patchy sporadic *E* layers with intense electric fields approaching 10 mV/m and embedded in sheared neutral flow. In a paper by S. Saito, S. Fukao, R. T. Tsunoda, et al., radar interferometry showed that the quasiperiodic (QP) echoes detected during SEEK II arrived from localized, discrete scattering patches drifting southwestward and maintaining altitude as they drifted. This picture was consistent with the one presented by G. C. Hussey, C. Haldoupis, and A. Bourdillon et al. who combined azimuth-time-intensity observations from the Valensole radar in France with soundings from a CADI ionosonde to measure the wind-induced drifts of the sporadic *E* layer patches. In the invited presentation by C. Haldoupis, M. Kelley, G. Hussey, et al. that followed, the current status of mid-latitude sporadic *E* layer irregularities was summarized, and accumulating evidence of a connection to midlatitude spread *F* was emphasized. C. Haldoupis argued that the intense polarization electric fields generated by patchy sporadic *E* layers are, ultimately, the cause of *F* region upwelling and structuring. This novel concept led to a discussion of the roles of the *E* and *F* regions as sources and sinks of ionospheric instability. The subsequent paper by J. Urbina, E. Kudeki, and S. Franke discriminated between unstructured scattering layers and QP echoes at mid

latitudes, arguing that the former can be explained in terms of a secondary wave gradient drift mechanism and, occasionally, by neutral atmospheric turbulence.

The first presentation of the second day of the session was an invited paper by E. Kudeki who addressed the enigmatic echoes detected at equatorial latitudes and ~150 kilometer altitudes during the daytime. These echoes are very aspect sensitive and exhibit virtually no zonal structuring, suggesting a possible role for meridionally propagating gravity waves in forcing their characteristic periodicity. Next, D. Farley presented results from F. Lu, D. Farley, and W. E. Swartz concerning the aspect sensitivity of equatorial electrojet irregularities. In their experiments, type 2 echoes exhibited relatively uniform RMS aspect widths between about 0.2°-0.25° and decreasing with altitude while strong type 1 echoes had considerably smaller widths approaching 0.1°. The type 2 widths were smaller than those reported by *Kudeki and Farley*, [1989], a fact Farley attributed to recent improvements to the experimental apparatus and configuration at Jicamarca. A paper by J. Y. Liu, C. C. Hsiao, S. Fukao, et al. then compared plasma densities measured by the MU radar and with a collocated sounder and endeavored to extract gravity wave parameters from the measurements. The paper by C. L. Chen and C. J. Pan that followed returned the session to the topic of mid-latitude sporadic *E* layers with a discussion of QP echoes observed with the Chung Li radar. Using interferometry, they associated the echoes with drifting quasi-point targets, reverberating the theme from the previous day's session. On the basis of data from the Gadanki radar in India, the next paper by R. K. Choudhary, J. P. St. Maurice, L. Kagan, et al. parsed sporadic *E* layer echoes into two varieties arriving from above and below 110 km altitude, respectively. The dichotomy was reminiscent of the one proposed earlier by J. Urbina et al. However, the assignment of irregularity altitude on the basis of range alone was challenged in the paper by D. L. Hysell, M. F. Larsen, and J. L. Chau which introduced aperture synthesis imaging to the session. Common volume imaging radar experiments with Arecibo again indicated that QP echoes arise from polarized, patchy sporadic *E* layers drifting horizontally and descending slowly. On several occasions, radar imaging also revealed large-scale electrostatic waves propagating to the southwest in the *E* region over Arecibo, further highlighting the importance of *E*/*F* region coupling. The paper by Y. H. Chu and C. Y. Wang that followed analyzed beam broadening effects associated with spectral measurements of sporadic *E* layer echoes using a formalism similar to that applied to MST radar data. Finally, the first portion of session I.2 concluded with an invited presentation by F. D. Lind, J. C. Foster, and P. E. Erickson. This paper described observations of auroral-zone Farley-Buneman waves made through a sidelobe of the Millstone Hill radar as incoherent scatter drifts were measured through the main beam on a common flux tube. Such experiments directly address the saturation mechanism of Farley Buneman waves. The paper concluded with an ambitious proposal to deploy a multi-purpose passive coherent scatter radar network over North America.

PMSE: The last part of Session I.2 was devoted to studies of coherent echoes from the summer mesopause region and was chaired by R. Palmer and M. Sarango. The first paper was an invited contribution by M. Rapp, F. Lübken, and W. Singer. Dr. Singer presented the paper where the underlying cause of Polar Mesosphere Summer Echoes (PMSE) was investigated. In particular, the source of electron density irregularities at scales of $\lambda/2$ was scrutinized. Important characteristics of PMSE were presented including layering and observed differences in upper and lower regions of PMSE. The role of charged ice particles

in the reduction of electron diffusivity and the resulting intense radar echoes was elucidated. The second paper by P. Hoffmann, M. Rapp, R. Lattech, and A. Serafimovich was presented by Dr. Hoffmann and dealt with a thorough statistical study of the multiple layering structure often seen in PMSE. It was shown that approximately 30% of PMSE observations exhibit a double layer structure. An interesting question was raised as to the cause of the multiple layering. Two competing theories are either gravity wave induced layering or layering caused by Kelvin-Helmholtz Instabilities (KHI). An open question is whether KHI can explain layering of more than two layers. The next paper by J. Chen, P. Hoffman, and M. Zecha was presented by Dr. Chen and emphasized the differences between the aspect sensitivity of the upper and lower portions of a PMSE layer. Coherent radar imaging methods were used to investigate this interesting characteristic of PMSE. Dr. Sarango presented the next paper by M. Sarango, R. Woodman, and L. Flores, which outlined differences between southern and northern hemisphere PMSE. Several causes of the observed differences were investigated including instrumental, longitudinal, and possible annual variations. The study emphasized the need for system calibration. T. Ogawa next presented an overview of HF SuperDARN radars and their use for PMSE observations. Scale differences were discussed for the diverse and numerous observations of PMSE. The next paper by J.Röttger, K. Kubo, and S. Fukao was presented by J. Röttger and focused on need for large Schmidt numbers for the existence of turbulence at shorter wavelengths, such as those of the EISCAT radar. After a vigorous discussion, J. Röttger again pointed out the need of calibration for comparison of multiple wavelength observations. His final suggestion was that scientists not use signal-to-noise ratio (SNR) for comparisons. The final paper of the session was by H. Bahcivan and D. Hysell and introduced an intriguing new understanding of coherent scattering from the perspective of phase diffusion.

Report on Session I.3 "Winds, Waves and Turbulence in the Lower and Middle Atmosphere and the Lower Thermosphere"

Conveners: W. Hocking and M.Larsen

Section I.3 was a well attended session, having 26 oral presentations and 7 posters. Topics were diverse and innovative, covering the accuracy and reliability of wind measurements, new radar methods for wind determination, the dynamics of gravity wave propagation and breakdown, and methods for using radar to measure the strength of atmospheric turbulence, among others.

Wind Measurement Techniques.

The first few talks concentrated on the methods of wind measurement Holdsworth and Reid discussed the relationship between true and apparent Full Correlation Analysis wind velocities, relative to the IDI (Imaging Doppler Interferometer) method. Theory predicts that the IDI values should compare best with the apparent velocity, but studies suggest that the IDI method often is similar to the true velocity. The reason for this is still a puzzle. Doviak presented a detailed analysis of the errors implicit in the FCA technique, and advanced the notion that the best FCA methods were often those based on the assumption on Gaussian correlation functions, rather than the more general assumption that the cross-correlation function and auto-correlation functions should have similar forms. Praskovsky et al. presented an alternative form of spaced antenna analysis, based on a structure function approach rather than a correlation function approach. Although both functions contain the same information, it is presented in a different way, and these authors felt that the requisite information for optimal analysis is best presented by the structure function approach. However, the method uses total powers, rather than complex data, and as such is somewhat more susceptible to RF interference. This paper was accompanied by a poster paper (I.3.501) which elaborated on the details of the method. Hassenpflug et al. presented error analyses associated with determination of correlation length scales using spaced antenna techniques. This parameter is important because it relates to the aspect-sensitivity of the scatterers, and therefore to the degree of anisotropy of atmospheric turbulence at the scales of the order of half the radar wavelength.

Experimental Wind Comparisons.

The session then took a more experimental bias, with results of experimental studies of wind motions being presented by Franke et al. (presented by Hocking) and Hoffman et al. The first showed excellent agreement between meteor winds and lidar winds determined at Mauii, and especially noted the frequent existence of wind speeds up to 100 m/s and more at heights above 90 km. The second paper (Hoffman et al.) studied stratospheric-mesospheric interactions using wind data, especially in regard to stratospheric warmings. Longitudinal variations in mean wind characteristics were noted. A related paper, paper I.3.40, which occurred later in the proceedings, also examined meteor wind and spaced antenna MF winds and noted good correlation between the two techniques. Another related

paper was a poster paper, I.3.305, given by Meek, who examined the distribution of large wind speeds measured by FCA methods in the upper atmosphere. Traditionally these winds are rejected in FCA analysis, but Meek wondered about the fact that they could be real, and possibly the radar was able to see through the E-region to higher heights on occasion.

Haldoupis and Pancheva, in a departure from studies exclusively of the neutral atmosphere, examined the impact of neutral winds on determination of sporadic E layers in the ionosphere. Evidence for strong planetary wave modulation was especially noted. Non-linear interactions were also investigated.

Gravity Waves.

The session then turned to discussions about gravity waves. It began with an overview by Gavrilov, who discussed a variety of measurements by both radar and non-radar techniques. A possible correlation between El Nino and gravity wave activity in the upper atmosphere was noted. Pavelin and Whiteway looked at the importance of mountain waves, and how they interact with other waves. One wave could often act to produce a critical layer for another wave. A series of papers then followed relating to gravity wave observations with the Indian MST radar, including papers by Rao, Reddy, Kamala, Kumar and colleagues. Roettger et al. examined relationships between deep convection and wave generation with the Chung-Li radar. A potential relationship with ionospheric spread-F was noted.

One paper also examined lidar observations of gravity waves (I.3.508), and Riggin and Zhou discussed measurements of gravity wave momentum fluxes using a dual beam radar at Arecibo (poster paper I.3.502).

Interaction between Turbulence and Radio Waves.

The topic of discussion then turned to turbulence. To begin, two presentations were given relating directly to the relationship between radio waves and turbulence. David Fritts gave a presentation on behalf of Patricia Franke which showed how a computer model was to be used to simulate radio wave scatter from turbulence. Turbulence would be generated down to scales of about 10 metres or less, and then a realistic radio-wave spectrum was to be "transmitted" into the region, and radio backscatter was to be recorded. Use of a PML (perfectly matched layer) at the top of the model, to produce spurious radiowave reflections, was discussed.

Following this, Kudeki discussed how he had used high resolution radar observations to study fine scale structure of turbulent layers. This was paper I.3.37, which was given out of order, but fitted into the program better at this point. Then Lehmacher et al. (paper I.3.24) presented a follow-up paper which also looked at fine-scale structure in the mesosphere at 150 meter resolution.

Turbulence.

The session then moved into studies of the fundamentals of turbulence. Wilson gave a very thorough review of the various modes of diffusion in the atmosphere, examining items like mixing efficiency, kinetic and potential deposition, and modes of diffusion. He also considered a variety of radar methods for measuring these parameters. Wilson and Dalaudier then demonstrated the information that could be deduced by combining radar and in-situ balloon observations of turbulent layers.

Klaassen had been invited to give a presentation on the modes of breakdown of gravity waves, but could not attend. However, Hocking gave a brief review of his work in a later session, (section II), and we mention it here for completeness. Recent references of Klaassen's, which in turn reference his earlier work, are Sonmor and Klaassen, "Toward a unified theory of gravity wave stability", J. Atmos Sci., p2655, 1997, and Yau, Klaassen and Sonmor, "Principal instabilities of large amplitude inertio-gravity waves", Physics of Fluids, in press.

Several papers discussed the relationship between spectral width and turbulence measurements. Van Zandt and colleagues considered new methods for determining the strength of turbulence by using dual beams with different widths and different azimuth angles, and Nastrom (presented by Van Zandt) discussed use of the Indian MST radar at Gadanki to determine strengths. The meaning of "negative" energy dissipation rates was also a concern to Van Zandt. In a paper somewhat later in the session, Hocking described how current methods for determination of non-turbulent spectral beam-broadening can be improved using full numerical integrals, and showed how these could be performed very quickly on a modern computer, therefore possibly reducing some of the complications which Van Zandt had been concerned about when he introduced the dual beam-width procedure. In a poster paper, Latteck et al. (I.3.509) compared standard and dual beam methods for determination of turbulence strengths made with an MF radar. Melnikov, Fang and Doviak noted that meteorologists rarely use spectral widths from radar data, and suggested that it is a resource which should be better employed in the future. Examples include the observation that the spectral width is often quite wide on the leading edge of squall lines, an observation which could be better employed in forecasting and identification.

Several papers dealt with measurements of vertical diffusion. Hermawan and Tsuda estimated vertical diffusion coefficients with the MU radar and RASS, and particularly noted the effect of variations in the Brunt-Vaisala frequency on estimation of energy dissipation rates and diffusion coefficients. Fukao et al studied cross-tropopause transport by turbulent processes, and Gavrilov and Fukao, in a poster paper (I.3.504) discussed downward turbulent transport of ozone from the stratosphere to the troposphere. Hashiguchi et al., in another poster paper, discussed tropopause processes measured with the EAR radar in Indonesia.

Finally, some papers relating to temperature measurements were presented. Kubo et al. discussed temperature and PMSE changes during a strong polar cap absorption event, Holdsworth et al. discussed comparisons between meteor radar temperatures and winds

with other techniques, and Singer et al., compared meteor temperatures to OH, lidar and rocket measurements of temperature.

Conclusion

In general, the papers were well presented, informative, and challenging. New ideas were suggested, and it is clear that much has been learnt, and yet still much needs to be done, in these various areas.

Report on Session I.4 "Meteorological Phenomena and Applications"

Conveners: K. Gage and D. Riggin

Abstract of Session: This session was concerned with recent developments in Doppler radar profiling in the lower neutral atmosphere, especially studies of lower atmospheric phenomena made with profilers in combination with other instruments during field campaigns. Topics included the assimilation of profiler data in meteorological models, quality control of profiler data, operational networks of profilers and the impact of profiler data on forecasting. Of special interest were studies that demonstrated the utility of profiling for quantifying the vertical structure of turbulence, humidity, cloud and precipitation fields including drop size distributions and their variability.

Five papers were presented in the first part of Session 1.4 which was chaired by Prof. D.N. Rao and Dr. K.S. Gage. The first paper was an invited presentation prepared by Dr. Steve Koch of the NOAA Forecast System Laboratory in Boulder, Colorado, USA. Dr. Koch was unable to attend the meeting but he had prepared a power point presentation which was given by Ken Gage. Ken emphasized the parts of the presentation that documented the value of the NOAA profiler network to forecasters. Ken also showed the results of studies documenting the impact of NPN profiler winds on the NOAA Rapid Update Cycle (RUC) mesoscale model. He noted the results that demonstrated the substantial contribution of profiler winds to the RUC model and the fact that profiler winds complemented ACARS winds. Following the presentation there was considerable discussion about the assimilation of profiler winds into meteorological models. The second paper was presented by Monique Petitdidier with co-authors V. Klaus and P. Tabary. The presentation showed the contribution of profiler wind measurements to the MESOSCALE ALPINE PROGRAM (MAP). Dr. Petitdidier focused on the contribution of profilers to the interpretation of the wind field analyzed from multiple scanning Doppler radars. The third presentation was given by Y. Shibagaki with co-authors M. Yamanaka, M. Fukase et al. Dr. Shibagaki showed observations of winds and precipitating cloud structures observed by the MU radar during Typhoon Orchid. He showed evidence for a field of outward propagating gravity waves. The next paper was presented by Paul Johnston with co-authors L. Hartten, D. Carter and K. Gage. Mr Johnston showed that winds obtained by Pacific wind profilers showed small systematic biases which were attributed to sampling issues related to a non-uniform gradient of reflectivity and different sampling volumes of collocated profilers. Mr. Johnston stressed the importance of using short pulses to resolve lower tropospheric reflectivity structure as much as possible. The final paper of this part of the session was presented by Dr. Hashiguchi with colleagues T. Seto, S. Fukao et al. Dr. Hashiguchi discussed the importance of intraseasonal variability in the context of observations being made with the new EQUATORIAL ATMOSPHERE RADAR (EAR) near Bukkittingi, on the island of Sumatra in Indonesia.

The second part of Session 1.4 was chaired by Dr. Dennis Riggin and Dr. D.N. Rao. Dr. K. Kishore Kumar with co-author A. Jain presented observations made with VHF and UHF

radars at the site of the Indian MST radar at Gadanki. The observation showed precipitation structure seen in both the Indian MST radar and the Lower Atmospheric Wind Profiler (LAWP). Vertical velocity and turbulence structure was shown in addition to reflectivity. J. Röttger made a presentation on behalf of C. Pan, M. Hsu and L. Chung who could not attend the meeting. The observations from the Chung-Li radar on Taiwan showed VHF radar reflectivity and rainfall rate during a Typhoon passage. The third paper was an invited paper by Dr. C. Williams and K. Gage. This work was concerned with profiler retrievals of drop-size distributions. Dr. Gage presented profiler observations that focussed on the vertical structure of convective and stratiform systems. Precipitation parameters such as reflectivity, rain rate and drop diameter have been retrieved using boundary layer radars alone. The drop-size retrieval methodology was applied to observations taken over many months at Kwajalein. The results were summarized statistically and showed a very different behavior for convective precipitation compared to stratiform precipitation. Prof. D. N. Rao with co-authors K. Kumar and V. S. Reddy et al. presented DSD retrievals obtained using the collocated VHF and UHF profilers at Gadanki. Christopher Lukas presented work using an FFT-based deconvolution which seems to have a 10-35% relative error in DSD retrieval with less error on the larger drop end. The methodology uses an exponential distribution and the results are calibrated with rain gages. Dr. Krishna Reddy with co-authors T. Kozu and Y. Ohno presented climatological studies of DSD obtained from several locations. Dr. T. Shimomai with co-authors T. Kozu, H. Hashiguchi, F. Renggonno and S. Fukao presented retrievals of drop-size distributions obtain using the EAR in Indonesia. J. Furomoto with co-authors K. Kurimoto and T. Tsuda presented new results on the retrieval of humidity profiles using MU Radar and RASS. Considerable progress was reported on the ability to retrieve humidity profiles from radar reflectivity and to use GPS precipitable water as a constraint influencing the choice of sign of the gradient of reflectivity.

The third part of Session 1.4 was held on Saturday morning. The session was chaired by Dr. K. Gage. The first presentation was made by K. Takahashi who talked about Piura wind measurements and the relationship between sea breeze circulations and the occurrence of extreme precipitation events. Most heavy rain events are initiated in the afternoon. Dr. S. Vogt with co-author G. Jaubert presented results of the use of a wind profiler-RASS during the MAP campaign. The work concerned the occurrence of Foehn winds and the use of the profiler equipped with RASS to study the Foehn circulation. Dr. J. Caccia with colleagues V. Guenard, B. Benech et al. presented the results of another study related to the MAP campaign. Caccia and colleagues studied the Mistral with a network of UHF wind profilers. The occurrence of the Mistral is related to topography and the presence of an inversion. The authors reported a large diurnal variation in the Mistral. Dr. P. Hoffmann with colleagues D. Peters, A. Serafimovich and Volker Lehmann presented examples of radar observations of inertia-gravity waves observed over northern Germany. The inertia-gravity waves had vertical wavelengths of 2-3 km and horizontal wavelengths on the order of 1000km. The occurrence of these waves was discussed in relation to jet streams.
Mr. Wallace Clark with co-authors A. Adachi and K. Gage et al. presented the results of a study of a gravity current and solitary wave observed at MRI using a wind profiler and a meteorological tower. The gravity current was initiated as part of nocturnal katabatic flow associated with the terrain to the west of the MRI profiler and tower. Dr. A. Praskovsky and E. Praskovskya presented a paper on first results of measurements of atmospheric turbulence with spaced antenna profiling radars. The observations were from the NCAR

Multiple Antenna Profiling Radar (MAPR) and used the novel UCAR-STARS method of retrieving horizontal velocities and turbulence characteristics observed by MAPR. Jürgen Röttger reviewed our current understanding of inclined layers and their implications for vertical velocity measurement. He suggested three scenarios for the tilted layer structure and its relationship to 'horizontal' velocities and isentropic surfaces. He tentatively concluded that it was likely that horizontal motions follow isentropic surfaces while scattering layers are not aligned with the isentropic surfaces. Dr. Röttger stressed, however, that more research is needed to substantiate these tentative conclusions.

Session 1.4 contained a number of novel results and demonstrated the overall progress being made in the meteorological application of profiling radars. In follow-up discussions issues concerned with assimilation of data into models and vertical velocity measurement were extensively discussed. Assimilation of data into models is seen to be a critical issue for the future for radar observations to achieve their full potential utility to the meteorological community. Further research on vertical velocities is needed to understand fully what is being measured especially in complex terrain where isentropic layers can be tilted substantially by mountain lee waves. Furthermore there is a need to assess more completely the precision of measurements of quantities related to turbulence such as eddy dissipation and diffusion.

Report on Session I.5 “Operational aspects and recent system developments”

Conveners: I. Reid and D. Thorsen

A total of eleven oral and fifteen poster presentations were given. A wide range of topics were covered, showing a mature but active area, with the emergence of operational networks being a highlight. New systems continue to be produced, and existing systems to be upgraded. New analysis techniques continue to be applied to existing systems, resulting in access to new parameters. Status reports on the meteorological networks in Japan (WINDAS) and Europe (CWINDE) were provided. It was noted that the future of the US Profiler Network was uncertain. New radars in Indonesia (the EAR VHF Radar), Norway (the SAURA HF Radar), Antarctica (the Davis Station VHF Radar), Canada (the McGill VHF Radar), Peru (the SOUSY VHF Radar at Jicarmarca, and two new VHF BLT systems for ENSO Studies) and France (the CURIE X-Band FMCW Miniradar) were described. New applications of existing radars including the application of the SuperDARN type radar to meteor studies, and of MF radars to meteor work, were outlined by Masaki Tsutsumi. Updates on existing facilities, including a report on the first decade of operation of the Indian MST radar, and a description of the NERC Radar Facility at Aberystwyth, were provided. The reapplication of the DAE technique at MF for estimation of electron densities in the ionospheric D-region was described in a paper by Rupa Vuthaluru. Descriptions of new sub-system developments were provided. These included new digital receivers (Woodman and Michhue), electronic beamforming (Net *et al.*), and on-line adaptive DC-clutter removal (Röttger). Calibration of radar systems using disdrometers was described by Clark *et al.,* and by Petitdidier and Kafando.

Report on Session II “Novel Perspectives and Unsolved Issues”

Conveners: P. Chilson, S. Fukao & J. Röttger

For the first time we had arranged for a special section of the MST radar workshop, which should deal with novel perspectives and unsolved issues, to be discussed in form of a brain storming session. There were seven invited keynote papers, which were arranged to stimulate discussions and conclusions about future research using MST and related radar systems. Unfortunately, not all the invitees could attend MST-10, so we missed some relevant personal input (such as Andreas Muschinski on range imaging), but tried to make up for these by recollecting the work of those not present. Of course, also all the other papers presented in the MST-10 section I in the first week were essential input to this final session of MST10.

Ground-clutter elimination is a very essential requirement for system functionality and reliability. When strong echoes occur from short ranges, these could mask the desired echoes from the atmosphere. Toru Sato, co-authored by Kazunori Kamio, presented a new approach introducing an adaptive system, which makes use of the angle of arrival information and cancels unwanted signals from directions of clutter and interference. This information can be obtained by using an additional small receiving antenna sub-array, set up close to the main antenna array. This method has the further advantage that it does not change the main beam characteristics, which usually occurs in common systems, which use tapering for sidelobe cancellation or suppression, resulting in unwanted gain reduction. Digital receivers allow this new method to be performed on-line and can be added to existing systems. Promising initial test results were presented.

Wayne Hocking, co-authored by Anna Hocking, presented a paper demonstrating that one can use measurements of anisotropy of radar signals to diagnose and forecast the occurrence of precipitation. It was possible to show that this applies for rainfall, by introducing an isotropy index and a precipitation index. They reported that the former is often a precursor of the latter and thus, can frequently be used to forecast rainfall. This novel finding can be essential in meteorological applications and needs further attention.

Hubert Luce critically analysed the commonly applied frequency domain interferometry (FDI) technique, in particular the applications of multi-frequency range imaging. He inquired whether such images can be a signature of the real atmosphere structure and whether one should introduce new filtering and other methods for processing the data. Actually, all the processing methods presented until now are based on methods previously developed in spectral analysis. On the one hand, the non parametric or filter bank methods (such as Fourier's and Capon's methods) do not use a priori information on the vertical distribution of the atmospheric scatterers but in practice do not seem to give much more accurate results than dual FDI processing, at least at VHF. On the other hand, the parametric methods used for spectral line analyses, such as MUSIC or Min-Norm methods, may offer much better resolution than the non parametric methods but only in the case where the data indeed satisfy the hypotheses (i.e., for our application, very thin - almost discrete layers within the radar beam). As input to the brain storming discussions, he

requested more investigations on the properties of the range imaging processing, which are regarded necessary before finally reliable applications can be expected to study atmospheric processes.

Jürgen Röttger asked what is turbulence seen by VHF radar. This paper was regarded as a follow-on of the paper by W. Hocking and J. Röttger during MST-9. It recollected the very early, partially forgotten, work done as early as in the 1960's on scattering and reflection of electro-magnetic waves from rough surfaces. Most of the present VHF radar echoes can be described as resulting from this mechanism. He also introduced a new approach to analyse VHF radar data in combined spatial-domain frequency-domain measurements (SDI-FDI). This approach just analyses raw data without any assumptions for applying mathematical methods and allows most pictorial descriptions the microstructure of VHF radar echoes. There exist limits, though, on the three-dimensional spatial resolution, which are intrinsic to the used instruments and applied methods. This newly presented technique anyhow seems to be a means for improved understanding of the echoing irregularities and discriminating between the two (unnatural) extremes, scattering from pure turbulence and specular-type reflection from stratified refractivity gradients. This means that all observational evidence points to phenomena, which are existing between these extreme limits.

Wayne Hocking, co-authored by S. Franke, N. Mitchell, D. Pancheva, P. Batista, B. Clemesha, B. Fuller, B. Vandepeer, T. Nakamura, T. Tsuda and J. MacDougall, reported about a recent global analysis of the mesospheric wind field observed by radars during the Space Shuttle Columbia accident. He showed that an unusually strong 2-day wave existed which, together with a strong diurnal tide in the mesosphere, created a strong wind shear at 60 to 65 km altitude. Whether such observations can be of use for applications and forecasting middle atmospheric winds was discussed.

A new approach to analyse spaced antenna data was presented by Alexander Praskovsky, co-authored by Eleanor Praskovskaya. Instead using correlation function or spectrum analysis they implemented the structure function alternatively. They claimed the advantage of this method, which can track the diffraction pattern and higher order moments of turbulence parameters by evaluating the rate of pattern changes with a higher temporal resolution than the traditional techniques. They also argue that there would be an advantage to use overlapping receiving antennas, which gains signal-to-noise ratio and thus accuracy. Characteristics of the scattering medium can be obtained with other assumptions than the early standard techniques. It is assumed that this new structure-function based technique can properly complement the commonly used ones.

Basing on the earlier work using existing commercial FM-radio transmitters to do passive radar observations of ionospheric irregularities, John Sahr presented a paper with ideas how to implement this technique for neutral atmosphere studies, which could be a superb alternative to high-power MST radars. Such a system would include a network of distributed receivers separated by some hundred kilometer. Since the cross section of scatterers in the neutral atmosphere is much smaller than of those in the ionosphere, larger receiving antennas have to be used, and higher synchronization accuracy is needed because the scattering is more coherent than that from the ionosphere. There is a requirement to separate ground clutter from the desired forward scatter. The receiving systems,

synchronized by GPS and connected via internet, are inexpensive and can be operated unattended. This visionary system will have that obvious advantage of not needing a transmitter, but John Sahr questioned whether such passive radar systems can offer the same resolution and sensitivity as conventional MST radars. It is regarded most valuable anyhow to follow up this new possibility basing on the experience of running ionospheric passive radars and active MST radars.

These presentations, the corresponding lively discussions and additional issues, which were raised during the workshop, were the basis for the formulation of the following resolutions.

Report on the Third International School on Atmospheric Radar – ISAR-3 – held at the Abdus Salam International Center for Theoretical Physics in Trieste, Italy, 25 November – 13 December 2002

Jürgen Röttger

This school was the third in its role following ISAR-1 in 1988 in Kyoto, Japan, and ISAR-2 in 1995 in Hilton Head, USA. These schools are part of the activities in the scientific and engineering community using radars for studies of the Earth's atmosphere and ionosphere. In particular the mesosphere-stratosphere-troposphere (MST) radars have become major research tools in these applications. A proper knowledge of the basic methods, proper analysis, validation and interpretation of the acquired data, basing on the main theoretical background of atmospheric physics, informatics and technology is demanded for such efficient applications. The school ISAR-3 was particularly held for the purpose of training young researchers and students, who are active in or have proven relations to this area, or could certify a solid interest and a sound perspective on this research and this technique.

The school covered the main subjects of fundamentals of atmospheric radar, hardware and basics of signal acquisition, data analysis and special applications such as interferometry, scattering of radar waves, atmospheric winds waves and turbulence, meteorology of the troposphere and the stratosphere, the mesosphere and the aeronomy of the lower ionosphere. Besides lectures also interactive computer training was applied, intense group and individual discussions were held, and the participants were given opportunity to present short papers on their own research or education.

The school ISAR-3 was held at the excellent premises of the Abdus Salam International Center for Theoretical Physics (ICTP), which also provided the majority of funding for these school activities. Additionally the ISAR-3 was sponsored and funded by the Scientific Committee on Solar Terrestrial Physics (SCOSTEP) and the International Union of Radio Science (URSI). From a total of 140 applicants 28 participants were selected. These were from 17, mostly developing, countries.

The lecturers, well known as researchers in the MST radar field, were Prof. P. Chilson, USA, Prof. S. Fukao, Japan, Prof. W. Hocking, Canada, Prof. R. Palmer, USA, Prof. S. Radicella, Italy, Prof. D.N. Rao, India, and Prof. J. Röttger, Germany. The latter three acted as school directors.

Our thanks are directed to ICTP for providing the funding, facilities, housing, food, administration and school secretariat as well as outstanding computing support and well-equipped lecture and training halls. This helped very impressively to hold the ISAR-3 in a very suitable environment and most pleasant atmosphere.

The highly positive response of the students of ISAR-3 on the performance of this school and the obvious great demand for this kind of education and training let us hope that we may have ISAR-4 at the same place in 2004 or 2005.

10th International Workshop on Technical and Scientific Aspects of MST Radar
MST10
held at the University of Piura in Peru, 13-20 May 2003

Plenary Session MST10:

Resolution

COORDINATED HEMISPERIC AND INTERHEMISPHERIC OBSERVATIONS OF POLAR MESOSPHERE SUMMER ECHOES (PMSE)

Considering:

a) That the geographic distribution of the strength of PMSE is a constraint in any proposed physical model,
b) That some current reported strengths do not conform with their expected behavior,
c) That existing observations have not been made at simultaneous times or equivalent periods,
d) That systems use different antenna sizes, shapes and processing algorithms,

It is resolved:

a) That simultaneous observations be performed with identical (or as similar as possible) antennas, and processing algorithms.

b) When simultaneous observations are not possible, as it is the case when different hemispheres are involved, they should be performed in the same seasonal periods. At least one of the radars should have a long inter-annual record, or be run simultaneously with one that does, to discriminate against inter-annual variations.

c) That standard calibration methods should be developed, adopted and implemented.

10th International Workshop on Technical and Scientific Aspects of MST Radar
MST10
held at the University of Piura in Peru, 13-20 May 2003

Plenary Session MST10:

RESOLUTION ON EDUCATIONAL ISSUES

Considering the facts that:

Meteorological phenomena are paramount to understand climate and weather, and research on these phenomena is growing on a worldwide scale. This includes observations, simulations and models on global, regional and local scales.

Particular research tools in this area are atmospheric radars, such as the mesosphere-stratosphere-troposphere (MST) radars. Scientists from many countries of the world are working in this field and are congregating regularly in international workshops and conferences.

A multitude of master and doctor students have been educated in this field and are now working in high level positions of universities, meteorological agencies and research institutes.

Regular international and national schools on atmospheric radars have been performed, which showed the demand to educate students, newcomers to the field, engineers and young scientists.

Noting that

There is a demand to continue these kind of schools, and also expand them into more permanent educational institutions, which would allow deeper understanding and assuring well trained experts to return to their home country where they can become leaders in research, development and operational meteorology.

It is resolved by the MST radar community that

(1) All efforts should be undertaken that national and international schools should be continued on a regular base at international centers, and where possible expanded.

(2) Wherever possible, regular courses on radar meteorology should be given at universities and research institutes.

(3) Preferably, special departments or sub-divisions should be formed at universities and research institutes with the emphasis on radar meteorology.

Proposals for the implementation of this resolution:

(1) ISAR

The radar schools (International Schools on Atmospheric Radar - ISAR) held at the International Abdus Salam Center for Theoretical Physics in Trieste, Italy, had been very successful and there is a great demand of students and new scientists and engineers applying for participation.

That International Center for Theoretical Physics has excellent facilities to perform schools and attract high-level lecturers and students from all over the world.

It shall be applied that the next International Schools of Atmospheric Radar should preferably be held at this center.

(2) OTCF

There are known plans of the Japanese government to establish a Graduate University in Okinawa (an archipelago located in southern Japan) with international participation.

The Graduate University in Okinawa should host a department on meteorology including a division on atmospheric radar. The region of Okinawa is of particular importance being in the area of passages of heavy typhoons and in the region where the continental climate of Eastern China interacts with maritime climate of the Pacific,

This would allow to establish a center of research and education in this field in the Western Pacific region. Distinguished lecturers can be collected from Japan and from abroad. Students can be attracted in particular from the East Asia and Pacific area.

A kernel to establish such a division is seen to be the already existing Okinawa Typhoon Center Forum (OTCF). This facilitates the establishment of such an educational center.

It is decided that

The permanent MST radar working group on education and training, which was formed by the international community of MST radar research, should take action in order to assure the continuation of the schools in Trieste and the formation of an educational center in Okinawa.

10th International Workshop on Technical and Scientific Aspects of MST Radar
MST10
held at the University of Piura in Peru, 13-20 May 2003

Plenary Session:

RESOLUTION ON A NETWORK ON TROPICAL RADARS

Considering that

It had been very successful to operate the Transpacific Profiler Network for studies of tropical meteorology and ocean-atmosphere interaction.

Studies of the climatology of tropical waves, tropical convection etc. can most effectively be performed by combined observations of the tropical atmosphere along and close to the equator. There is a need to study equatorial atmosphere waves, semi-annual, annual and quasi-biannual oscillations, as well as the Walker circulation and the triggering of equatorial spread-F by gravity waves created by tropical convection, etc.

Several radars exist in the tropics, such as the Equatorial Atmosphere Radar EAR in Indonesia, he Natioal MST Radar Facility NMRF in India, the Jicamarca Radio Observatory in Peru, the Arecibo Observatory in Puerto Rico and others, which can observe wind profiles up to the middle atmosphere.

It is resolved that

Radar facilities should be re-established or upgraded to allow such needed longer-term observations.

Additional radars should be established to fill the gaps along the near-equator region.

Coordination in dedicated campaigns should be arranged such that these radars can be operated in a tropical network, including such radar system in Pohnpei, Biak, Christmas Island, Darwin, Bukittinggi, Gadanki, Jicamarca, Piura, etc.

Corresponding persons should be elected to assure such network establishments and the combination of the collected data for suitable scientific evaluation.

The scientific terms and applicational requirements for these operations should be worked out by the group of these persons in order to prepare proposals to national and international funding agencies.

10th International Workshop on Technical and Scientific Aspects of MST Radar
MST10
held at the University of Piura in Peru, 13-20 May 2003

Plenary Session:

RESOLUTION ON *E*-REGION

Considering that:

a) Theoretical understanding of mid-latitude E region plasma irregularities remains controversial,

b) The phenomenon appears to be an intriguing example of plasma-neutral coupling at multiple scales,

c) Recent radar imaging work shows a great potential for resolving the unsettled questions,

It is resolved that:
1) Further multi-instrument campaigns including multiple-receiver radar radar imaging systems should be organized to study the mid-latitude E-region,

2) Funding agencies and international organizations provide support for such campaigns as well as efforts to develop multiple-receiver capabilities at existing and new radar sites.

Session I.1: Radar scattering processes in the neutral atmosphere

The following three main scattering mechanisms are important for atmospheric radars operating in the UHF/VHF regime: (1) Rayleigh scatter from hydrometeors, insects, etc.; (2) Bragg scatter from turbulent refractive-index fluctuations; (3) Fresnel scatter from refractive-index interfaces that are thin compared to the radar wavelength. Often, more than one of these three scattering mechanisms is relevant to a given observed data set, which may make the unambiguous retrieval of meteorological observables difficult, sometimes impossible. For example, the backscattered power may no longer be interpreted as being related to turbulence characteristics if Rayleigh scatter or Fresnel scatter contributes to, or even dominates the observed backscattered power.

In this session, observational and theoretical investigations (1) on how to separate the effects of different scattering mechanisms in the same data set, and on (2) radar echo characteristics in different radar configurations and their interpretations are presented. Emphasis will be placed on contributions that discuss new observations (e.g., multi-beam, multi-frequency, multi-receiver, and/or multi-regime radar observations, also intercomparisons with in situ measurements) on the basis of innovative, first-principle theoretical analysis.

Conveners:
H. Luce and A. Muschinski

RETRIEVAL OF ATMOSPHERIC STATIC STABILITY FROM MST RADAR RETURN SIGNAL

David A Hooper[1,2], Johan Arvelius[1] and Kerstin Stebel[1,3]

[1]Swedish Institute of Space Physics, Box 812, 981 28, Kiruna, SWEDEN
[2]now at Rutherford Appleton Laboratory, Chilton, Didcot, OX11 0QX, UK
[3]now at Norwegian Institute for Air Research, NO-9296, Tromsø, NORWAY

1. Introduction

The vertical gradient of potential temperature gives a measure of the atmosphere's static stability, i.e. of its resistance to vertical motions. It is conveniently quantified in terms of the square of the Brunt-Väisälä frequency, ω_B^2 (rad^2 s^{-2}):

$$\omega_B^2 = \frac{g}{\theta}\frac{\partial\theta}{\partial z} = g\left(\frac{\partial \ln\theta}{\partial z}\right) \tag{1}$$

where θ (K) is potential temperature [= $T(1000/p)^{2/7}$], T (K) is absolute temperature, p (hPa) is pressure, g (m s^{-2}) is gravitational acceleration and z (m) is altitude. Perturbations of ω_B^2 values are commonly seen in association with a variety of atmospheric phenomena including fronts, gravity waves and turbulence. Moreover, the variations of ω_B^2 as a function of altitude have an effect on both gravity wave propagation and turbulence generation. Routinely derived profiles of this parameter will therefore have a number of uses.

The purpose of this paper is to describe a method of retrieving profiles of ω_B^2 based on the MST radar return signal power, P, for a vertically directed beam. This method has much in common with that described by *Gage and Green* (1982). Data are considered from observations made by the ESRAD MST radar (*Chilson et al.*, 1999), which is located at Esrange, the Swedish Space Corporation's rocket range in northern Sweden (67.9°N, 21.1°E). Comparisons are made between values of ω_B^2 derived from the retrieval method and those derived from measurements made by 221 radiosondes launched from the same site during the winters of 1996/1997 to 1999/2000. In deriving the radiosonde values of ω_B^2 using Equation 1, gradients of potential temperature are evaluated over a vertical interval of 300 m and subsequently transferred to a vertical grid, between 1.0 and 15.7 km altitude at 300 m intervals, so as to correspond to the radar measurements.

2. Method

It has long been appreciated that perturbations of P and ω_B^2 are closely related. The theory of Fresnel scatter (*Gage et al.*, 1981) gives a direct relationship between the two through consideration of the mean vertical gradient of generalised potential refractive index, M (*Ottersten*, 1969). The latter is often conveniently approximated by the dry term, M_D:

$$M_D = -77.6\times10^{-6}\,\frac{p}{T}\frac{\partial \ln\theta}{\partial z} \tag{2}$$

although the full term additionally depends on the both the specific humidity, q (g kg^{-1}), and its vertical gradient:

$$M = M_D \left[1 + \frac{15500q}{T} - \frac{\frac{7800}{T}\frac{\partial q}{\partial z}}{\frac{\partial \ln \theta}{\partial z}} \right] \quad (3)$$

It can be seen that the dry approximation is valid when the second and third terms in the square brackets of Equation 3 are significantly less than 1; this is typically assumed to be the case above the first few kilometres of the atmosphere. This assumption will be examined in greater detail shortly. For the time being the humidity contributions will be ignored entirely.

It will be recognised that the p/T term in Equation 2 is proportional to density, which can be approximated as $\rho_0 \exp(-z/\overline{H})$ where ρ_0 (hPa) is the pressure at mean sea level and $\overline{H}$ (m) is the mean scale height across the considered altitude range. For the data considered in present investigation, the value of H, which is given by RT/g, where R is the gas constant for dry air, is typically around 8 km at an altitude of 1 km and decreases to around 6 km at the tropopause level; it remains approximately constant at this value between the tropopause and an altitude of 15.7 km. A mean value of 6.71 km is calculated over all data points. Assuming $\rho_0 = 1000$ hPa, the observed and assumed values of density are typically within 10% of each other at all altitudes within the range 1.0 - 15.7 km.

Combining the expectation that $P \propto M^2/z^2$ (*Gage et al*., 1981) with Equation 2, and substituting for Equation 1, gives:

$$P \propto \frac{\left[\exp(-z/\overline{H})\omega_B^2\right]^2}{z^2} \quad (4)$$

which can be rearranged in order to define a radar factor r_B^2:

$$r_B^2 = z_{km} \exp(z_{km}/\overline{H}_{km})\sqrt{P} \quad (5)$$

where the altitude above mean sea level, z_{km}, and the mean scale height, $\overline{H}_{km}$, are both given in units of kilometres, such that the following linear relationship is expected:

$$\omega_B^2 = g_0 r_B^2 + y_0 \quad (6)$$

3. Results

Figure 1(left panel) shows the relationship between radar-derived values of r_B^2 and radiosonde-derived values of ω_B^2. The plot area is divided into a 100 by 100 grid, with divisions of 0.1×10^{-4} rad^2 s^{-2} along the y-axis and 0.1×10^3 arbitrary r_B^2 units along the x-axis; the grey scale represents the number of data points falling within each cell. There is clearly a high degree of correlation between the two sets of values and two distinct clusters of data points can be seen; those with small values of ω_B^2 and of r_B^2, which correspond to tropospheric measurements, and those with larger values of both, which correspond to lower stratospheric measurements. There is, nevertheless, considerable scatter around these clusters.

Much of this scatter, for the tropospheric measurements, can be accounted for by the fact that the humidity contributions to M have been ignored in the retrieval model. The values of r_B^2 are, in fact, overestimated by a factor $|M/M_D|$, i.e. by the modulus of the square bracket in

Equation 3. The validity of the retrieval algorithm is therefore limited to those altitudes at which the humidity contributions to M can be ignored. Since the necessary information is available from the radiosonde measurements, humidity-corrected values of radar-derived r_B^2, i.e. $|M/M_D| \times r_B^2$, are shown in Figure 1(right panel). Clearly the oversimplification accounts many of the largest deviations from a linear relationship associated with small values of radiosonde-derived ω_B^2.

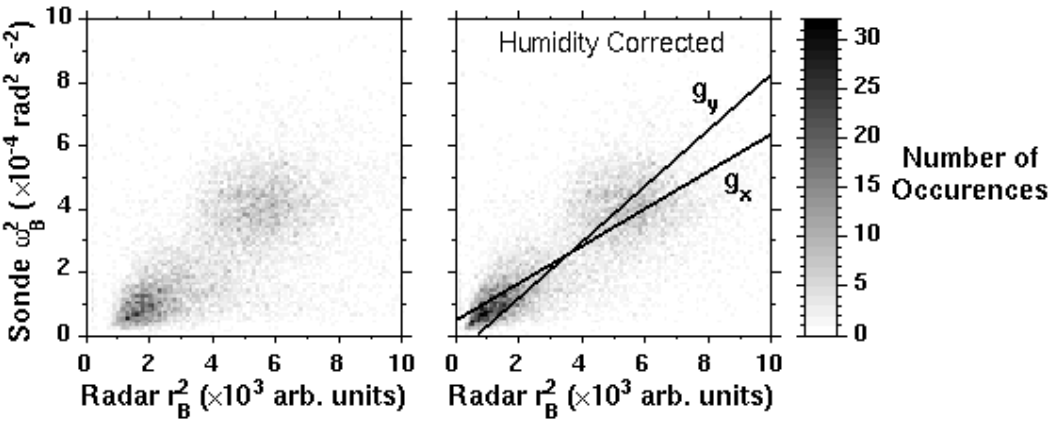

Figure 1: The relationship between radiosonde-derived values of ω_B^2 and radar-derived values of r_B^2 (left panel), and humidity-corrected r_B^2 (right panel).

The best fit between radiosonde-derived values of ω_B^2 and humidity corrected radar-derived values of r_B^2 is found following the method of *Hocking et al*. (2001). The lines with gradients g_x and g_y shown in Figure 1(right panel) represent, respectively, the least squares best fits from the regression of y on x and *vice versa*. These correspond, respectively, to the assumptions that all of the variability is associated with the radiosonde-derived values of ω_B^2,and that there are no errors associated with the humidity corrected radar-derived values of r_B^2,and *vice versa*. In addition to the fact that there are measurement errors associated with both the radar and the radiosondes, each instrument is measuring in different regions of the atmosphere.

Despite the fact that the radiosondes are launched from the radar site, they can drift by up to 100 km downwind by the time that they reach an altitude of 15.7 km. In one extreme case (not shown) the profiles of radiosonde-derived values of ω_B^2 in the lower-stratosphere show large perturbations as a function of altitude whereas the profiles of radar-derived r_B^2 do not. The perturbations of radiosonde-derived ω_B^2 are attributed to mountain wave activity since they are anticorrelated with large perturbations of the balloon ascent rate. The poor correlation between the radar and radiosonde profiles is attributed to the spatially localised nature of mountain wave activity; the radiosonde was 50 km from the radar site by the time that it reached the tropopause level.

Although neither of the lines shown in Figure 1(right panel) represents the best fit between the data, each one represents an extreme of the possible fits. The required best fit lies somewhere between the two. It is speculated that the physical separation between the radar and radiosonde measurements is responsible for a large amount of the scatter seen in Figure 1(right panel). The value of g_0 is therefore selected such that the variability associated with each parameter is equal, i.e. to the condition $\sigma_y = g_0\sigma_x$ (= 7.12×10^{-5} rad^2 s^{-2}) following the nomenclature of *Hocking et al*. (2001).

Figure 2 compares profiles of ω_B^2 derived from radiosonde data (thick grey lines) and radar data (thick black lines) for 5 individual cases. They are clearly quantitatively and qualitatively well matched. The only significant discrepancies occur in the lower troposphere and, as can be seen from the corresponding profiles of humidity corrected radar-derived values (thin black lines), these can be attributed to the over-simplification of assuming $M = M_D$ inherent in the retrieval model. The question remains as to lowest altitude above which the assumption that $M = M_D$ is always valid. The contributions of the humidity terms to M, for specific profiles, can be significant right the way up to the tropopause level. In general, therefore, the retrieval method can only be assumed to be valid at lower-stratospheric altitudes. However, under specific circumstances, the retrieval method can be used at some, or all, altitudes below the tropopause.

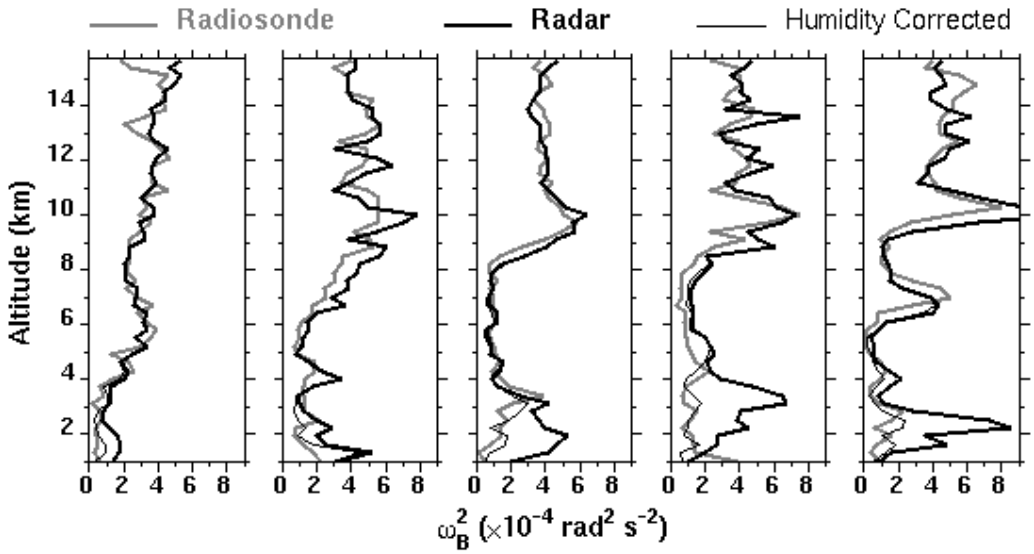

Figure 2: A comparison of profiles of ω_B^2 derived from radiosonde data, radar data and humidity-corrected radar data.

References

Chilson, P. B., S. Kirkwood, and A. Nilsson, The Esrange MST radar: A brief introduction and procedure for range validation using balloons, *Radio Sci., 34*, 427-436, 1999.

Gage, K. S., and J. L. Green, A technique for determining temperature profile from VHF radar observations, *J. Appl. Meteorol., 21*, 1146-1149, 1982.

Gage, K. S., B. B. Balsley, and J. L. Green, Fresnel scattering model for the specular echoes observed by VHF radar, *Radio Sci., 16*, 1447-1453, 1981.

Hocking, W. K., T. Thayaparan, and S. J. Franke, Method for statistical comparison of geophysical data by multiple instruments which have differing accuracies, *Adv. Space Res., 27*, 1089-1098, 2001.

Ottersten, H., Mean vertical gradient of potential refractive index in turbulent mixing and radar detection of CAT, *Radio Sci., 4*, 1247-1249, 1969.

TROPOPAUSE EROSION BY MOUNTAIN WAVE BREAKING

David A Hooper[1] and Ed Pavelin[2]

[1]Rutherford Appleton Laboratory, Chilton, Didcot, OX11 0QX, UK
[2]Department of Meteorology, University of Reading, PO Box 243, Reading. RG6 6BB, UK

Introduction

The tropopause represents a boundary between air masses with distinct chemical and dynamical properties. Traditionally it has been thought of as a discrete level at which these properties change sharply. Although this is often the case, the transition between upper-tropospheric and lower-stratospheric characteristics can also be much more gradual (*Hooper and Arvelius*, 2000). Under such circumstances it is more appropriate to think of the tropopause as a region which can have a vertical extent of up to several kilometres. The current study demonstrates that turbulent mixing, caused by gravity wave breaking, is one of the mechanisms which can lead to a broadening of the tropopause region. A case study is presented for observations made by the UK Natural Environment Research Council MST radar at Aberystwyth.

Case Study of 18th July 2001

MST radar data for the altitude region 8 - 12 km on 18th July 2001 are shown in Figure 1. The crosses superimposed on each panel indicate the altitude of the tropopause derived from the vertical beam signal power (top panel) using an objective algorithm (*Hooper and Arvelius*, 2000); a sharpness value (second panel) of 3 corresponds to a definite tropopause (and a narrow tropopause region), a value of 0 to an indefinite tropopause (and a broad region), and intermediate values to intermediate sharpnesses (and depths of region). As will be shown shortly, the changes in sharpness are more significant than those of altitude. The vertical beam radial velocity fluctuations seen between 0600 and 1500 UT (third panel) are attributed to mountain wave activity corresponding to low-level winds (not shown) from the north-east (*Prichard et al*., 1995). Enhanced values of the beam broadening corrected vertical beam spectral widths (fourth panel) indicate that moderate turbulence coincides with the maximum altitude reached by the mountain wave activity. This is particularly clear at around 9.5 km altitude between 0600 and 1100 UT, but can still be seen, to a lesser extent, as the maximum altitude drops from around 9.5 km, at 1330 UT, to below 8 km, at 1500 UT.

The fact that the mountain wave activity is not able to propagate beyond the tropopause level is attributed to critical level absorption in the upper troposphere (*Worthington and Thomas*, 1996). For a mountain wave, a critical level corresponds to an altitude at which the component of the horizontal wind parallel to the low-level (wave generating) wind has reduced to zero. A mountain wave cannot propagate above a critical level but will dissipate all of its energy at this level through turbulent mixing. It can be seen that the maximum altitude reached by the mountain wave activity corresponds closely to that at which the wind speed (fifth panel) first drops to zero. The existence of a critical level can be demonstrated more explicitly by considering the normalised projected wind (sixth panel). This is the normalised dot product of the wind vector at each level with that at the lowest level observed by the radar (1.7 km), i.e. the cosine of the angle between the wind vectors. The maximum altitude reached by the mountain wave activity corresponds closely to that at which this factor first drops to zero.

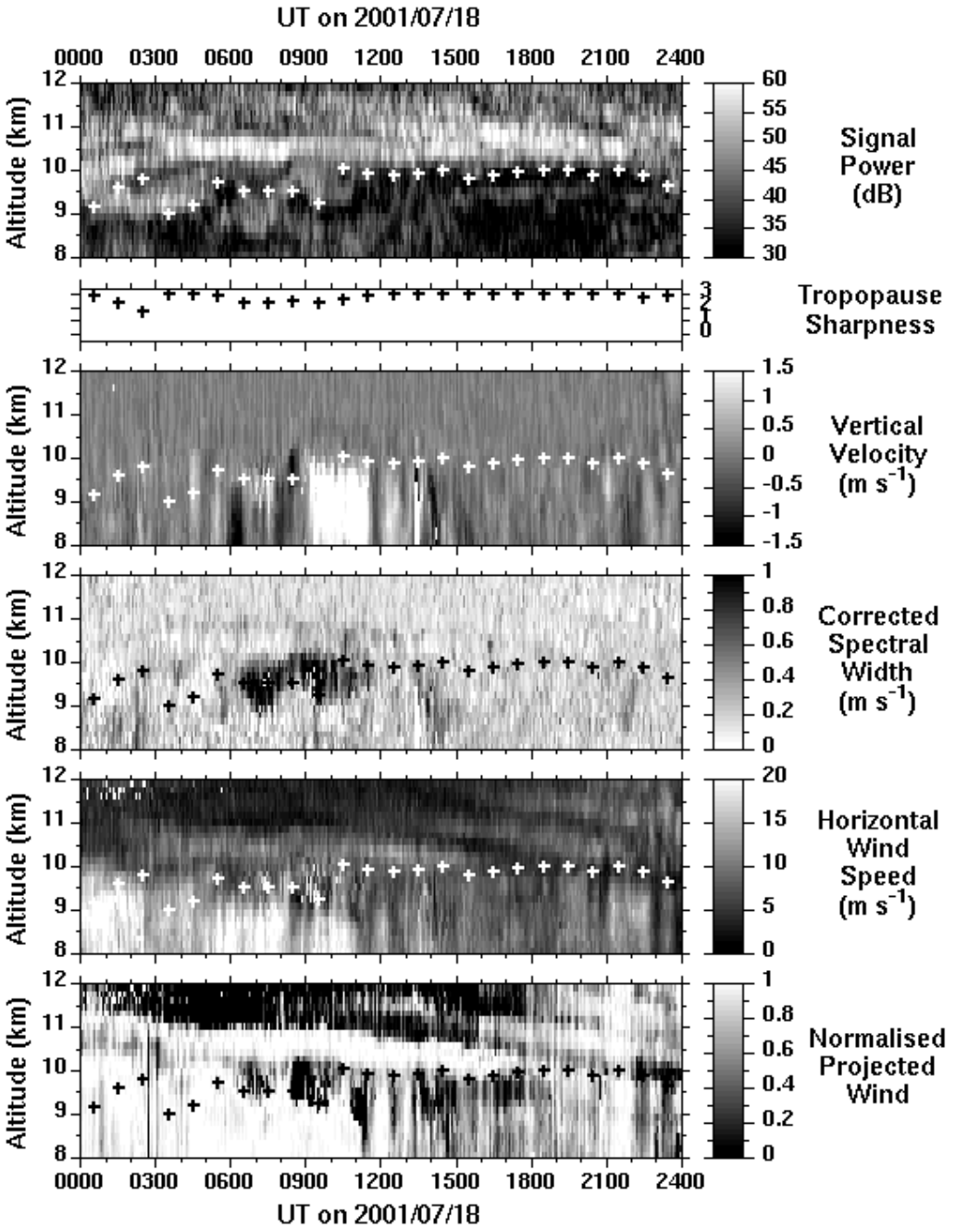

Figure 1: Data from the MST radar at Aberystwyth for 18th July 2001.

Turbulent mixing across a vertical gradient of a conservative passive tracer, such as potential temperature or ozone concentration, will generate irregularities of that tracer over a continuous range of scale sizes. The magnitude of the irregularities will depend on both the initial vertical gradient of the tracer and on the strength of the turbulence (*Ottersten*, 1969). However, if turbulent activity continues for a sufficient length of time, the distribution of the tracer is expected to become more homogeneous across the depth of layer, with sharp tracer gradients occurring at the layer boundaries (*Browning and Watkins,* 1970). As might

therefore be expected, a slight reduction in tropopause sharpness coincides with the period of tropopause level turbulence between 0600 and 1100 UT. The broadening of the tropopause region is apparent from the more gradual overall increase in signal power, with increasing altitude, than occurs either before of after this period. Moreover, careful examination will reveal that the signal power, within the region of enhanced corrected spectral widths, is typically reduced with respect to the layers immediately above and below it; this is particularly clear between 0600 and 1100 UT.

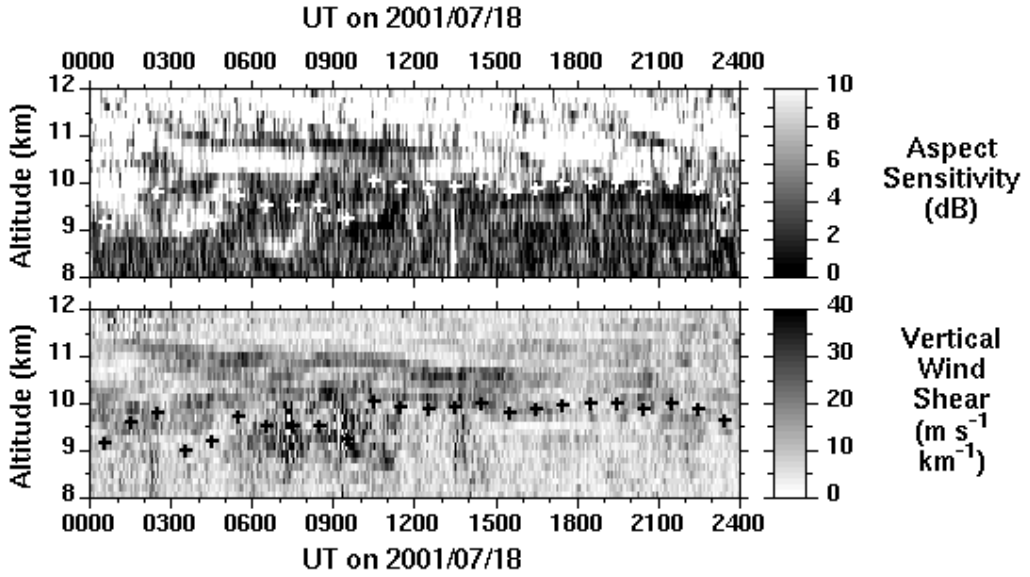

Figure 2: Data from the MST radar at Aberystwyth for 18th July 2001.

The breaking of mountain waves is not the only dynamical feature which is affecting the structure of the tropopause during this time. Careful examination of the plot of corrected spectral widths will reveal the presence of a narrow layer of very mildly enhanced values at around 10.8 km altitude and between 0600 and 1200 UT; the mildly enhanced values spread over a broader region between 0900 and 1200 UT and span the gap between the layer at 10.8 km and the region of significantly enhanced values below 10 km. Although such small values, by themselves, do not give very convincing evidence for the existence of turbulence, attention is drawn to the corresponding plot of aspect sensitivity, i.e. the ratio of the signal power for a vertically directed beam to that for a beam directed 6° off-vertical, shown in Figure 2(top panel). Although the aspect sensitivity is typically large in the lower stratosphere (> 10 dB), *Hooper and Thomas* (1998) showed that it could drop close to zero where turbulence of at least moderate intensity was occurring. The pattern of low aspect sensitivity in the lower stratosphere suggests that mild turbulence is even more widely spread than indicated by the corrected spectral width values. This inference is corroborated by the high degree of correlation between the low values of aspect sensitivity and the high values of vertical wind shear, Figure 2(second panel), the latter indicating the regions which have the highest likelihood of supporting turbulence generation through shear instability. A quantitative measure of this likelihood is given by the gradient Richardson number, *Ri*:

$$Ri = \frac{shear^2}{\omega_B^2} = \frac{\left(\frac{\partial u}{\partial z}\right)^2 + \left(\frac{\partial v}{\partial z}\right)^2}{\frac{g}{\theta}\frac{\partial \theta}{\partial z}}$$

where ω_B (rad s^{-1}) is the Brunt-Väisälä frequency, u and v (m s^{-1}) are, respectively, the zonal and meridional components of the horizontal wind vector, z (m) is the altitude, g (m s^{-2}) is the gravitational acceleration, and θ (K) is the potential temperature. The condition $Ri < 0.25$ must be met in order to generate turbulence, although once turbulence is initiated it is thought that $Ri < 1$ is sufficient for it to be maintained (*Woods,* 1969). Since ω_B^2 can be retrieved from the radar return signal power (*Hooper et al*., 2003), Ri for tropopause altitudes and above can be calculated entirely from MST radar data. Although a full ω_B^2 calibration has not yet been carried out for the Aberystwyth radar, the condition $Ri < 1$ is met for the shear layers (but not shown) using approximate ω_B^2 calibration values.

The shear layers are associated with inertia-gravity wave activity, which is clearly apparent in the plots of wind speed and normalised projected wind shown in Figure 1. The sharpness of the tropopause is therefore eroded by a combination of mountain wave breaking from below and inertia-gravity wave breaking from above. Assuming that the altitudes of the static stability and chemical tropopause levels are coincident prior to the onset of turbulence, the mixing is expected to give rise to exchange of upper tropospheric and lower stratospheric air.

References

Browning, K. A., and C. D. Watkins, Observations of clear air turbulence by high power radar, *Nature, 227*, 260-263, 1970.

Hooper, D. A., and J. Arvelius, Monitoring of the Arctic winter tropopause: A comparison of radiosonde, ozonesonde and MST radar observations, in *Proceedings of the Ninth International Workshop on Technical and Scientific Aspects of MST Radar*, 385-388, Sci. Comm. on Sol.-Terr. Phys. Secr., Boulder, Colorado, 2000.

Hooper, D. A., and L. Thomas, Complementary criteria for identifying regions of intense atmospheric turbulence using lower VHF radar, *J. Atmos. Sol.-Terr. Phys, 60, 59-61*, 1998.

Hooper, D. A., J. Arvelius, and K. Stebel, Retrieval of atmospheric static stability from MST radar return signal power, in *Proceedings of the Tenth International Workshop on Technical and Scientific Aspects of MST Radar*, 2003.

Ottersten, H., Atmospheric structure and radar backscattering in clear air, *Radio Sci., 4*, 1179-1193, 1969.

Prichard, I. T., L. Thomas, and R. M. Worthington, The characteristics of mountain waves observed by radar near the west coast of Wales, *Ann. Geophys., 13*, 757-767, 1995.

Woods, J. D., On Richardson's number as a criterion for laminar-turbulent-laminar transition in the ocean and atmosphere, *Radio Sci., 4*, 1289-1298, 1969.

Worthington, R. M., and L. Thomas, Radar measurements of critical-layer absorption in mountain waves, *Q. J. R. Meteorol. Soc., 122*, 1263-1282, 1996.

COHERENT RADAR IMAGING AND THE EFFECTS OF REFLECTIVITY FIELD VARIATIONS AND BIOLOGICAL CLUTTER

B. L. Cheong[1], M. W. Hoffman[1], R. D. Palmer[1], H. Tong[1], V. Tellabati[1]
S. J. Frasier[2] and F. J. López-Dekker[2]

[1]University of Nebraska-Lincoln, U.S.A. [2]University of Massachusetts, Amherst, U.S.A.

1. INTRODUCTION

This brief article highlights the progress of simulation studies of the Turbulent Eddy Profiler (TEP)[1] using a standard configuration and a new proposed array configuration. Variations on the reflectivity field were found to have systematic bias on the radar imaging process using the traditional Fourier method. By using the adaptive Capon method, the bias from the reflectivity variations were significantly reduced. In addition, a study of the effects of biological clutter in the antenna sidelobes was conducted. Most cases of biological clutter occur from targets in the sidelobes of the antenna.[2] With a subtle change to the TEP array, it is possible to use the Capon beamforming method to virtually eliminate the effects of biological targets in the antenna sidelobes on wind field estimates. It should be noted that the proposed array configuration does not have this beneficial effect using standard Fourier beamforming.

2. EFFECTS OF REFLECTIVITY VARIATIONS ON RADAR IMAGING

One of the main goals of this experiment is to study the variations of the reflectivity distribution on the imaging process. The numerical simulation presented uses a modified version of the method of *Holdsworth and Reid*[3] with a simple reflectivity pattern shown in Figure 1. A

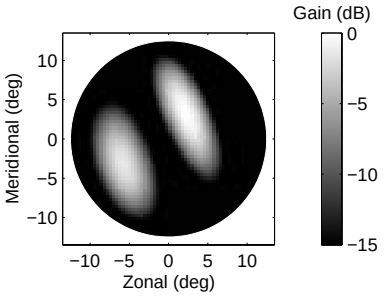

Figure 1. *Model reflectivity used in the simulation is a map with two bivariate Gaussian functions centered at (2°, 4°) and (-6°, -4°). A uniform horizontal wind from* 25° *at 25* ms^{-1} *and a turbulent wind field of* ± 1 ms^{-1} *were used in the simulation.*

uniform horizontal wind (25 ms^{-1} at 45° azimuth) and a turbulent wind field of $\pm$ 1 ms^{-1} across the entire imaging region were used in this simulation. By using radar imaging with TEP, it is possible to reconstruct the reflectivity and wind fields within the beam of the radar.

The left panel of Figure 2 shows two reconstructed images using Fourier and Capon beamforming.[4] An interesting feature is observed near the valley between the two reflectivity peaks. Note the systematic over and under estimation compared to the known actual horizontal velocity indicated by the single arrow in the upper right corner of each frame. Variations in the reflectivity pattern along the direction of the wind are accompanied by either systematic increases, decreases, or rotations in horizontal wind vector estimates. It appears that the variation is more significant in the case of the Fourier estimators than it is for the Capon estimates. The right panel of Figure 2 illustrates the effects of reflectivity variations on the estimates of radial velocity and Figure 3 illustrates the deterministic bias on the radial velocity estimates based on our theoretical argument.

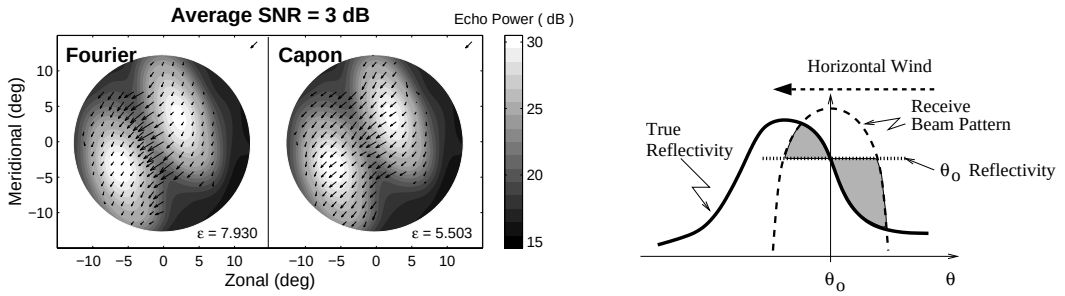

Figure 2. *The left panel shows the images obtained after processing the signals from the simulation. The datasets are processed with both the Fourier and Capon methods. The right panel is a graphical illustration of the effects of reflectivity variation along the wind directions. The shaded regions show the weighting effects of radial velocities. In this example, the radial velocities are under and over weighted on the right and left of θ_o, respectively. This weighting depends on the reflectivity variations, the wind direction and the antenna beam pattern and contritubes a deterministic bias to the radial velocity estimates.*

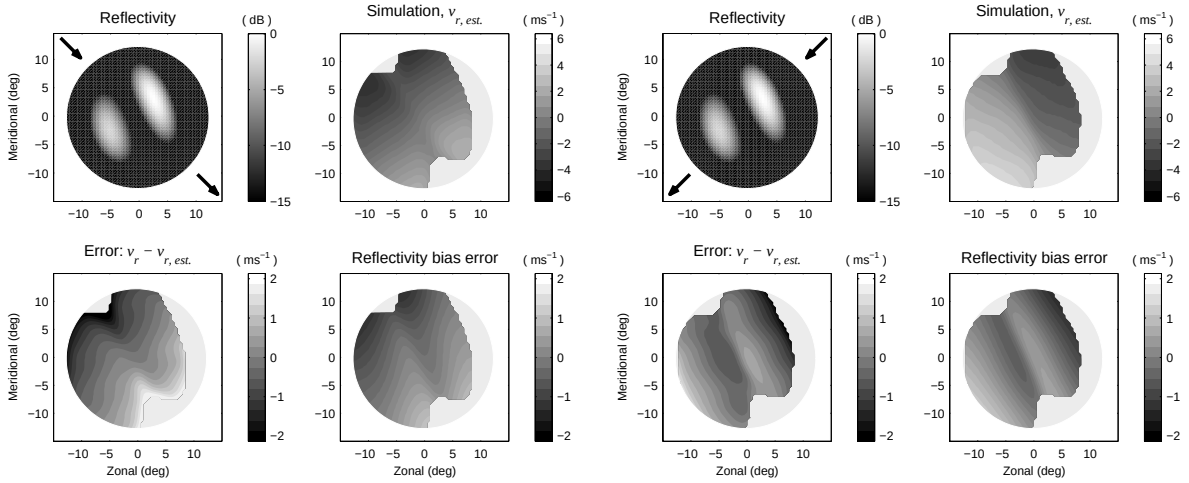

Figure 3. *These plots show the effects of reflectivity variations for two cases with different wind directions. The upper left panel is the true reflectivity with horizontal wind as indicated. The upper right panel is the radial velocity estimate. The lower two panels show the radial velocity estimate error (left) and the predicted bias obtained using the known wind field, the known reflectivity, and the Fourier beampattern.*

3. OPTIMAL SUBARRAY DESIGN

A simple Gaussian reflectivity field pattern is used in this part of the experiment. The main goal of this experiment is to address the bird clutter rejection issue; the model reflectivity is irrelevant. For the first few frames of the simulation, the bird moves through the main lobe of the antenna. Subsequently, the bird moves through a grating lobe. No known method is available to eliminate the bird echo from the main lobe. However, the proposed array configuration shown in Figure 4 (left panel) can significantly reduce the effect of the bird as it progresses through the grating lobes. The quality of the wind field estimates using the original TEP array and proposed array configuration will be compared. Initially, the three subarrays were designed to allow spatial smoothing to mitigate the clutter. However, it was later discovered that imaging using the Capon beamforming method[4] outperformed the spatial averaging method. The results in this report show the performance of the newly configured array using the Capon beamforming method. A statistical search was performed in order to find the optimal array configuration. Figure 4 shows the new array configuration with three hexagonal subarrays and the array response of the system. The right panel shows the total beampattern of the system with nulls in the centers of each grating lobe allowing the mitigation of clutter effects.

One of the main goals of the TEP system is to estimate the three-dimensional wind field with high angular resolution. The proposed array configuration greatly benefits this goal by virtually eliminating the effects of grating lobe echoes in the wind field estimates. Figure 5

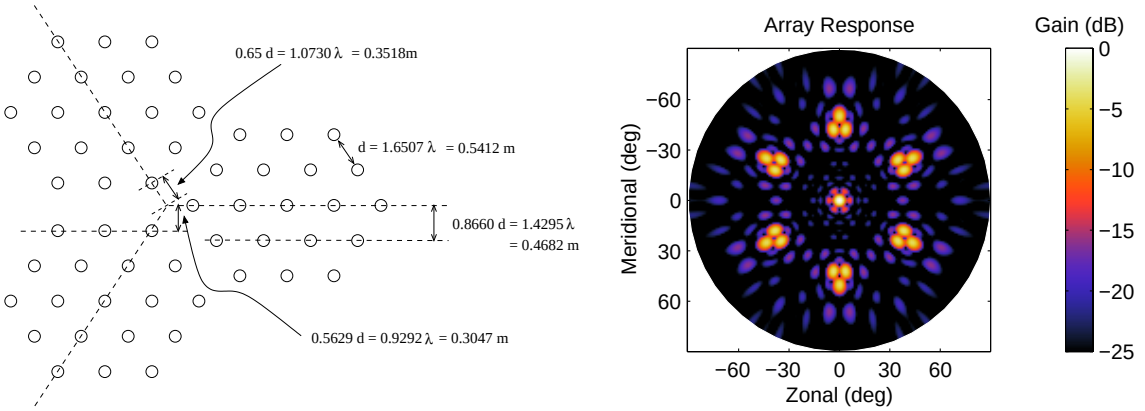

Figure 4. *The proposed TEP subarray array configuration. Subarrays are designed to mimic the original TEP configuration. Note that three subarrays are used which have a slightly different spacing from the original element spacing.*

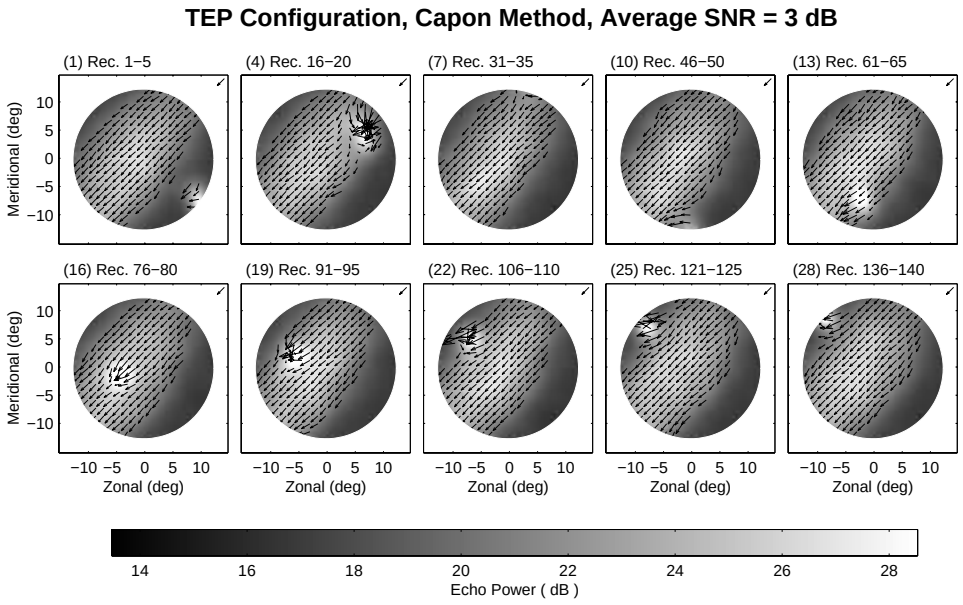

Figure 5. *A uniform wind field is simulated with original TEP array. This series of images show the power distribution obtained using Capon beamforming method with the original TEP array. Using the original TEP configuration, it can be seen that there is a bird flying across the main imaged region in frames 1-7. As the bird continues to fly, it passes through a grating lobe toward the north and is seen as an angularly aliased signal in the maps (frames 10-28).*

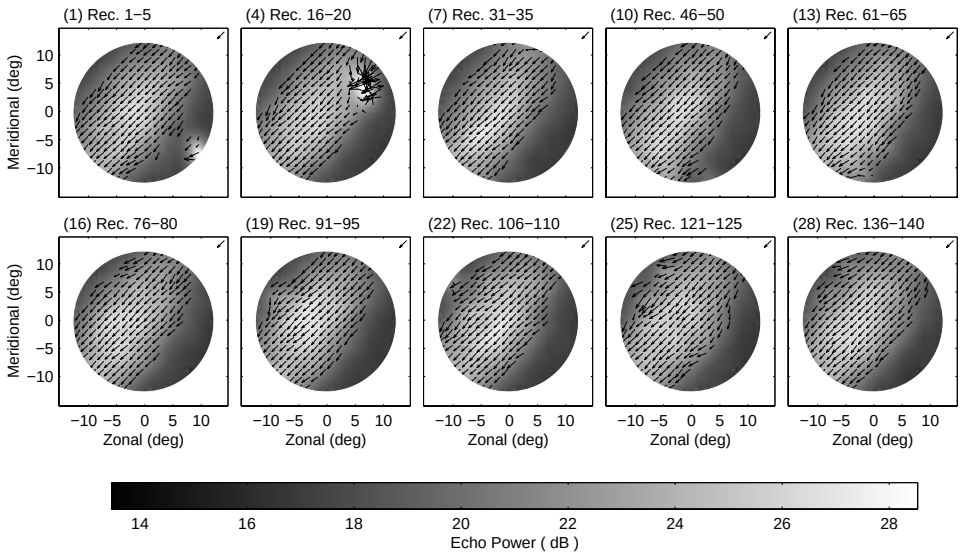

Figure 6. *Same as Figure 5, except using the proposed subarray configuration. As the bird flies through the main beam it is seen in the image (frames 1-7) as in the original TEP array configuration. However, as the bird passes through the grating lobe its returned power is significantly reduced and unique beampattern of the subarray configuration mitigates the interference of the bird clutter in the wind estimation procedure.*

shows a series of images of echo power and wind field estimates for a bird flying across the main imaging region using the original TEP array. As the bird continues, it flies across the grating lobe of the array and is seen as an aliased signal in the images and appears as a moving distortion in the wind field.

For the optimized array configuration, the results are significantly different and are provided in Figure 6. Note that the frame is indicated by the number in parenthesis. During frames 1-7, the bird flies across the main lobe and is seen as an ordinary scatterer with strong reflectivity. However, the grating lobe interference from the bird is significantly reduced in the subarray configuration providing a more accurate wind field map compared to the original TEP configuration. In frames 10-28, however, the bird echo is angularly aliased into the observed image. By using the proposed subarray configuration (refer to Figure 6), a strong returned signal can be seen as the bird moves across the main imaging area. However, during frames 10-28, the bird echo power is greatly reduced and is undetectable. The unique grating lobe structure, caused by the array design, produces significantly higher quality wind field images. Given the fact that a majority of bird echoes occur from sidelobe/grating lobe echoes, the proposed array design warrants further study and experimentation.

REFERENCES

1. J. B. Mead, G. Hopcraft, S. J. Frasier, B. D. Pollard, C. D. Cherry, D. H. Schaubert, and R. E. McIntosh, "A volume-imaging radar wind profiler for atmospheric boundary layer turbulence studies," *J. Atmos. Oceanic Technol.* **15**, pp. 849–859, 1998.
2. J. M. Wilczak, R. G. Strauch, F. M. Ralph, B. L. Weber, D. A. Merritt, J. R. Jordan, D. E. Wolfe, L. K. Lewis, D. B. Wuertz, J. E. Gaynor, S. A. McLaughlin, R. R. Rogers, A. C. Riddle, and T. S. Dye, "Contamination of wind profiler data by migrating birds: Characteristics of corrupted data and potential solutions," *J. Atmos. Oceanic Technol.* **12**, pp. 449–467, 1995.
3. D. A. Holdsworth and I. M. Reid, "A simple model of atmospheric radar backscatter: Description and application to the full correlation analysis of spaced antenna data," *Radio Sci.* **30**, pp. 1263–1280, 1995.
4. R. D. Palmer, S. Gopalam, T. Yu, and S. Fukao, "Coherent radar imaging using capon's method," *Radio Sci.* **33**, pp. 1585–1598, 1998.

ABOUT MULTIPLE LAYERING AND ASPECT SENSITIVITY OF POLAR MESOSPHERE SUMMER ECHOES

J. Röttger
Max-Planck-Institut, 37191 Katlenburg-Lindau, Germany

It is frequently noticed that the Polar Mesosphere Summer Echoes (PMSE) are occurring in a double-layer structure as reported by Röttger (1994), Rüster et al. (2001) and other authors. Although this seems to be dominating on the average if one averages the power profiles, as shown in the upper panel of Fig. 1, we can show that multiple layering is the most common status, but is usually eliminated by averaging over too long time periods. The separation of such persistent sheet-like layers can be as small as one kilometer or less. These thin sheets are explained to occur in regions of lowered temperature due to long-period gravity waves (Röttger, 1994), where heavy ions and ice particle can be formed. These interact with the ionospheric plasma and cause sheet-like PMSE irregularities. Here we show some evident examples and propose how the PMSE irregularities can be created and make a suggestion to explain the PMSE aspect sensitivity, which is observed frequently in the lower PMSE heights.

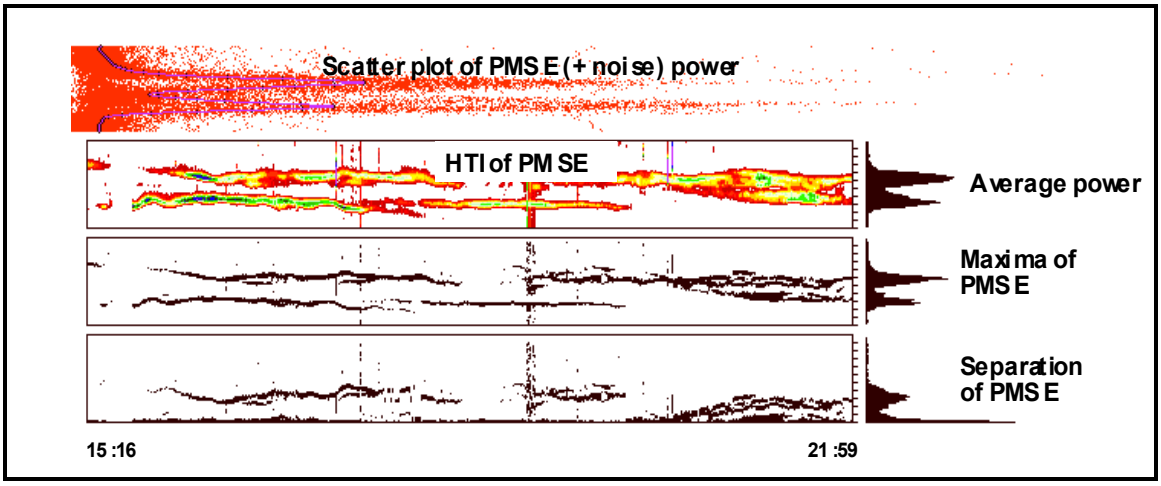

Fig. 1 Typical PMSE plots covering the period of 6.74 hours and altitudes between 80 km and 91 km. These observations were done with the SOUSY Svalbard Radar (Röttger, 2001). on 7 June 2001, 15:16-21:59 UT. The upper panel shows the scatter plot of the signal plus noise power in linear units; the second panel is a common height-time intensity (HTI) plot, the third panel shows the maxima of layers and the lower panel their height-normalized position. The right-hand-side shows the averages over the given period.

To avoid averaging as it is done in the upper panels of Figs. 1 and 2, we have introduced a new method, namely finding the peak (maximum in power) of the thin sheet-like layer. This is plotted in the center panels of Figs. 1 and 2 and we notice that it clearly enhances the sheet-like structure of PMSE. Taking the height of the lowest layer as reference, we have a possibility to measure the distance between the sheet-like layers, namely their separations, shown in the lower panels of Figs. 1 and 2. The right-hand-side plots show the corresponding averages. We recognize that the average power shows the often-referred double peak (Rüster et al., 2001) but tends to smears out the fine structure, which we still recognize when applying the maxima-selection procedures. In particular, Fig. 2 shows that there are more than two layers. This can be shown for almost all observations of PMSE. Although we have analyzed only data from observations with the SOUSY Svalbard Radar, we assume that this multiply layered structure with vertical separations of some kilometer is universal for all PMSE observations.

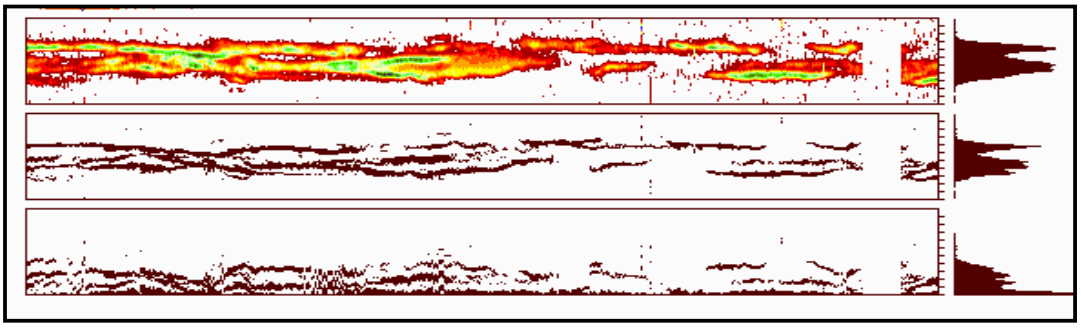

Fig. 2 PMSE plot (SOUSY Svalbard Radar, 17 June, 17:21 UT, to 18 June, 00:04 UT, 2001) showing multiple layering of thin sheets.

Regardless of the scattering mechanism causing the PMSE, there must be a reason why the corresponding irregularities occur in thin sheets. Röttger (1991) had discussed the possibilities and summarized that "the physical mechanisms leading to PMC (Polar Mesospheric Clouds) and NLC (Noctilucent Clouds) on the one hand and PMSE on the other are surely somewhat different, but they must be undoubtedly related". During the past years this has been proved by many experiments and theoretical work (e.g., Rapp et al., 2003), which cannot be summarized in this extended abstract. Röttger (1994) also suggested that cooling in certain phases of gravity waves is a likely mechanism to create heavy ions being responsible for PMSE irregularities. Ice particles and aerosols are now believed to interact with the ionospheric plasma and this results in PMSE as well. Ice particles form when a certain water vapor saturation temperature is reached, and this cooling can be achieved by gravity wave modulation of the mean background temperature profile as sketched in Fig. 3. The cool regions occur quasi-periodically with height. We recognize this in the PMSE plots of Fig. 2.

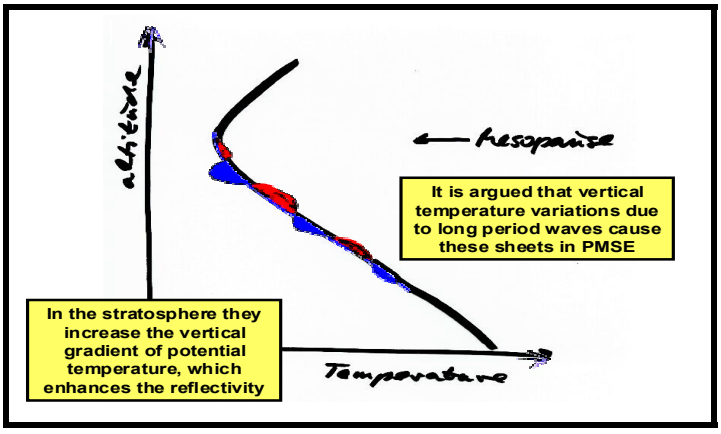

Fig. 3 A simple model how a gravity wave can cause temperature variations of the mean temperature profile of the mesopause region resulting in local regions of cooling where in turn ice particles and PMSE irregularities form.

Gravity waves propagate vertically and horizontally as sketched in Fig. 4. This means that these cool regions (where conditions for PMSE can be formed) move up or down on the mean profile, depending on the gravity wave and background parameters. Longer period waves would remain fairly persistent at certain altitudes, whereas shorter-period waves and interaction of waves which each other would result in quite some variability, as we can see in the plots of Figs. 1 and 2. As Röttger (1994) suggested, there can even be steepening of gravity waves and this in turn could explain the very thin sheets of PMSE, which we often observe.

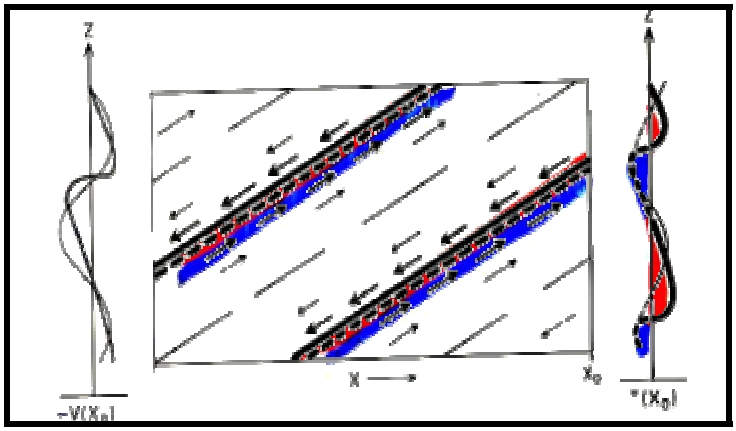

Fig. 4 Schematic drawing of the horizontal and vertical velocity and temperature variations due to gravity waves. Left: vertical velocity; right: temperature profiles at location X_0 of a gravity wave during steepening (dashed are cooled regions). The arrows in the centre panel show the airflow and the inclined lines show the isentropes (from Röttger, 1991).

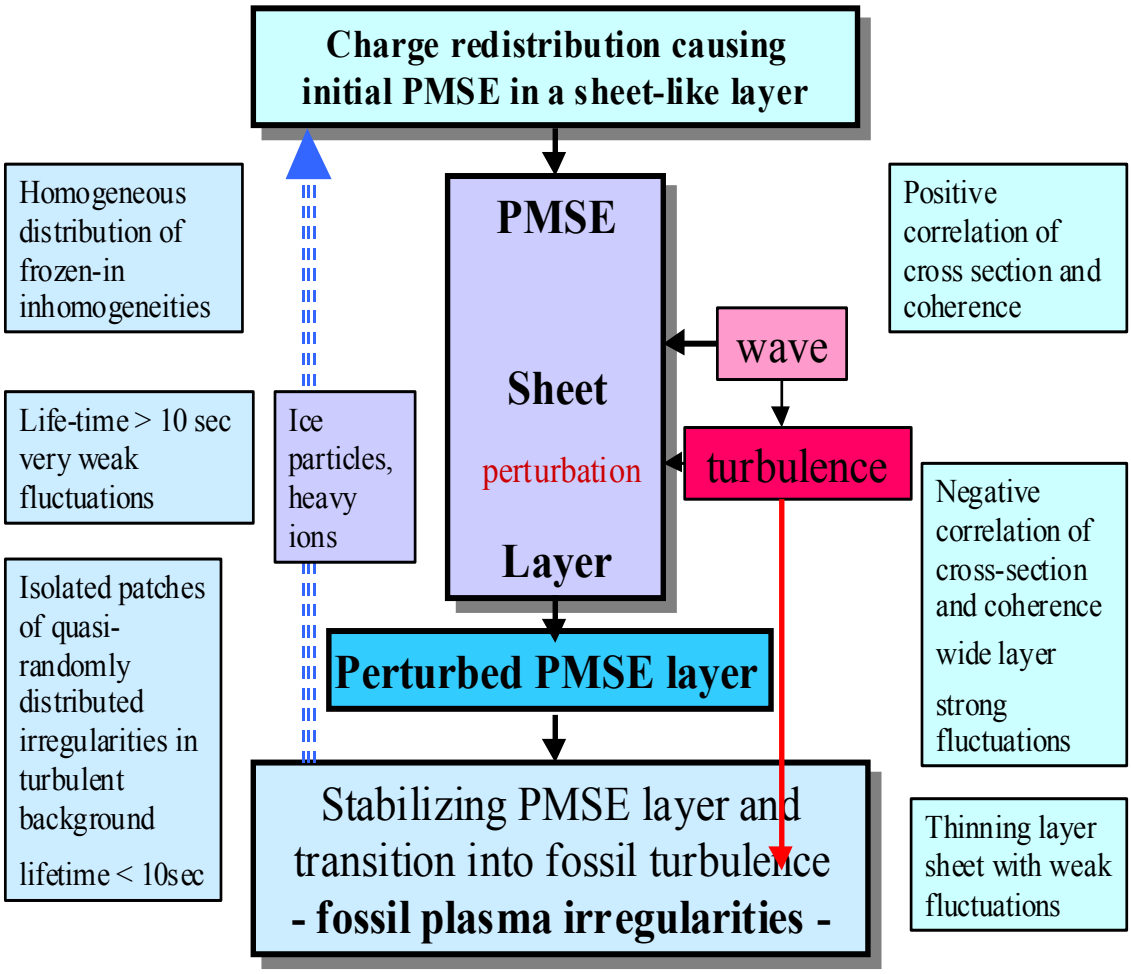

Fig. 5 Block diagram of the life history of Polar Mesosphere Summer Echoes. In the left- and right-hand margin boxes the signal characteristics are summarized, which characterize PMSE in the different development phases shown here.

VHF radar interferometry had shown that PMSE irregularities can be accepted as passive tracers of dynamical processes in the mesopause region. Many observational features cannot prove that these dynamical processes, such as active turbulence, are the immediate cause of PMSE. However, initial, even very weak, disturbances in the neutral atmosphere can translate into disturbances in the ionospheric plasma (Schmidt number effect), and the corresponding charge redistribution strongly increases the radar scatter cross section. The life cycle then could be as shown in Fig. 5. A sheet-like PMSE irregularity structure is disturbed by atmospheric waves and turbulence, which decays into fossil turbulence and fossil plasma irregularities remain. In the presence of ice particles (as described before) or any other particles of larger size than the common molecules in the mesosphere, the scatter cross section of these irregularities is further enhanced, which in turn causes sheet-like PMSE structures. These do not show any signs of active turbulence unless they are disturbed again by waves breaking into active turbulence. This is a repetitive process and can explain the life history of Polar Mesosphere Summer Echoes.

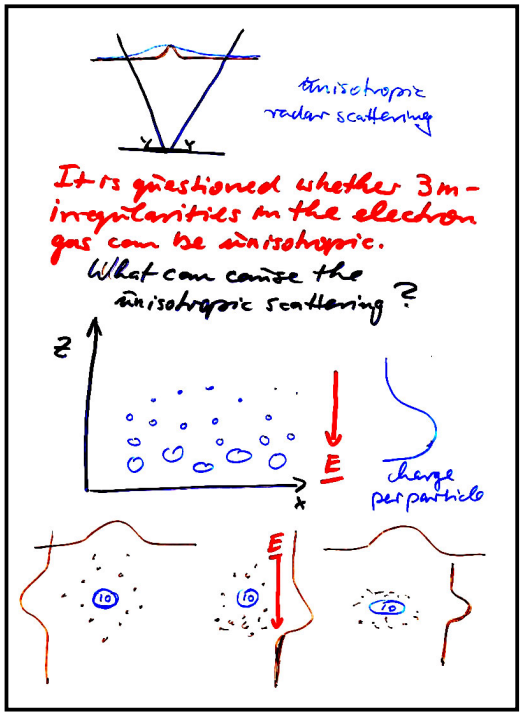

Fig. 6 Sketch showing the vertical distribution of charged particles.

Many observations show that the lower PMSE region is frequently aspect-sensitive. An explanation for this anisotropic scattering is not known yet. It is not immediately conceivable that the scattering structures in the electron gas, which originally result from irregularities in the neutral gas, are horizontally elongated at the short Bragg scale of MST VHF radars, namely a few meters. It is proposed here (sketched in Fig. 6) that some horizontal structuring of the scattering medium at these scales can result from polarization electric fields, which are generated by different charging of heavy ions (NLC ice particles) of different sizes. It is known that the larger ice particles are falling faster than smaller ones, and that these large particles accumulate in the lower heights of PMSE and NLC. Larger particles can attract or carry a larger charge number. Consequently a vertical electric field is established, and the equipotential surfaces are horizontally extended, which in turn would cause aspect sensitive scatter.

In summary we note that the Polar Mesosphere Summer Echoes are resulting from the interplay of neutral dynamical (temperature), aeronomical (chemistry) and electro-dynamical (charge redistribution) processes. The neutral dynamical processes are not dominantly active turbulence resulting from wave breaking.

References:

Rapp, M., F.-J. Lübken, and T. Blix, The role of charged ice particles in the creation of PMSE: A review of recent developments, Adv. Space Res., 31(9), 2033-2043, 2003.

Röttger, J., Middle atmospheric and lower thermosphere processes at high latitudes studied with the EISCAT radars, J. Atmos. Terr. Phys., 56(9), 1173-1195, 1994.

Röttger, J., Observations of the polar D-region and the mesosphere with the EISCAT Svalbard Radar and the SOUSY Svalbard Radar, Mem. Nat. Inst. Pol. Res., 54, 9-20, 2001.

Rüster, R., J. Röttger, G. Schmidt, P. Czechowsky, and J. Klostermeyer, Observations of Mesospheric Summer Echoes at VHF in the Polar Cap Region, Geoph. Res. Lett., 28(8), 1471-1474, 2001.

ASPECT SENSITIVE CHARACTERISTICS OF RADAR BACKSCATTERERS AT VHF: STUDIES USING SIMULTANEOUS OBSERVATIONS OF GADANKI MST RADAR AND GPS SONDE

A.K.Ghosh, Siddarth Shankar Das, A.K.Patra, D.Narayana Rao
V.K.Anandan and A.R.Jain

National MST Radar Facility, P.B.No-123, Tirupati-517502, A.P., India
e-mail: asish_gh@rediffmail.com

Introduction

Study of aspect sensitivity at VHF in the lower atmosphere is of significant interest to the radar community, as it is important to understand the characteristics of the radar backscatterer for better interpretation of the spectral parameters, which represent a number of atmospheric parameters. The shape and the generation mechanisms of scattering refractive irregularities, at various height levels in troposphere and lower stratosphere (up to 25 km) region, are still yet to be fully understood. There are two main causative mechanisms for aspect sensitivity of radar backscattering: (i) specular reflectors and (ii) anisotropic refractive index irregularities (*Gage and Green,* 1978; *Doviak and Zrnic*, 1984; *Hocking and Hamza*, 1997). The contribution of each of these mechanisms at various height levels, however, could not be well determined due to lack of simultaneous high resolution radar and *in-situ* measurements of background atmospheric parameters. In this context, any measurement made simultaneously using radar and high resolution in-situ measurements of the background atmospheric parameters are of significant value. In this paper, an attempt is made to understand the origin of the aspect sensitivity characteristics of the radar backscatterers at VHF using simultaneous MST radar and GPS sonde (Vaisala type) observations carried out from radar site, Gadanki (13.5^{o}N, 79.2^{o}E), during September-October 2002.

Results and Discussion

Figure 1 shows the height profiles of the echo power for the different beam zenith angles (0°, 6°, 9°, 12° and 15°) in E-W and N-S plane for 25 September (top panel) and 8 October (bottom panel) 2002. The vertical and horizontal arrows in each panel represent the noise level of radar observations and the height of the tropical tropopause obtained from GPS sonde respectively. On 25 September there appears to be two distinct regions where the observed radar echoes are aspect sensitive, one in height region of 7-11.5 km and other one above 15 km in both the planes (E-W and N-S). The received echo powers at higher beam angles (>9°) are almost equal. On 8 October, in contrast to that of 25 September, the observed echo powers do not appear to be aspect sensitive anywhere below 18 km. However, above 18 km, the observed echo powers are highly aspect sensitive. The height profiles of echo power on 25 September show a clear wave modulation with vertical wavelength of 1-2 km. Similar signature, however, are not present in the case of 8 October. To understand the difference of the aspect sensitivity as a function of height for the two days, the background atmospheric parameters viz. square of Brunt-Vaisla frequency (N^2) from GPS sonde and square of vertical shears of horizontal wind speed from radar and Richardson number (Ri) from both GPS sonde and radar are plotted in Figure 2. The negative values of N^2 in this figure indicate regions of convective instability, and the values of Ri (0-0.25) indicate the regions of dynamic instability, the conditions that can give rise to

turbulence. From Figures 1 and 2, it can be seen that wherever N^2 is high, wind shear is low, and Ri is high, the power difference between different beam zenith angles is high. This is more specific for lower beam zenith angle, indicating that the aspect sensitivity is caused by the thermal stable structures of the atmosphere (*Luce et al*. [2001] and *Jain et al.* [2001]). From Figures 1 and 2, it can also be observed that wherever N^2 is low or negative in spite of wind shear being either high or low, the echo powers for all the beam zenith angles are the same, indicating that the regions are highly turbulent and atmosphere is well mixed. For understanding the characteristics of the backscatterers the parameter θ_s (aspect angle) profiles are estimated using the observed echo power for beam combinations (0˚, 6˚), (0˚, 9˚) and (0˚, 12˚) and (0˚, 15˚) for both the planes (E-W and N-S) observed on both the days and are presented in Figure 3. The figure shows that in some height regions θ_s could not be computed since Power of smaller beam zenith angle is less than that of higher beam zenith angle. This type of situation could arise due to the passage of atmospheric waves over the radar site, which could cause fluctuations in vertical and oblique beam echo power [*Hobbs and Reid,* 2000]. Figure 3 shows that wherever aspect sensitivity is high (low) θ_s is small (large) indicating that the backscatterers are anisotropic (isotropic) in nature.

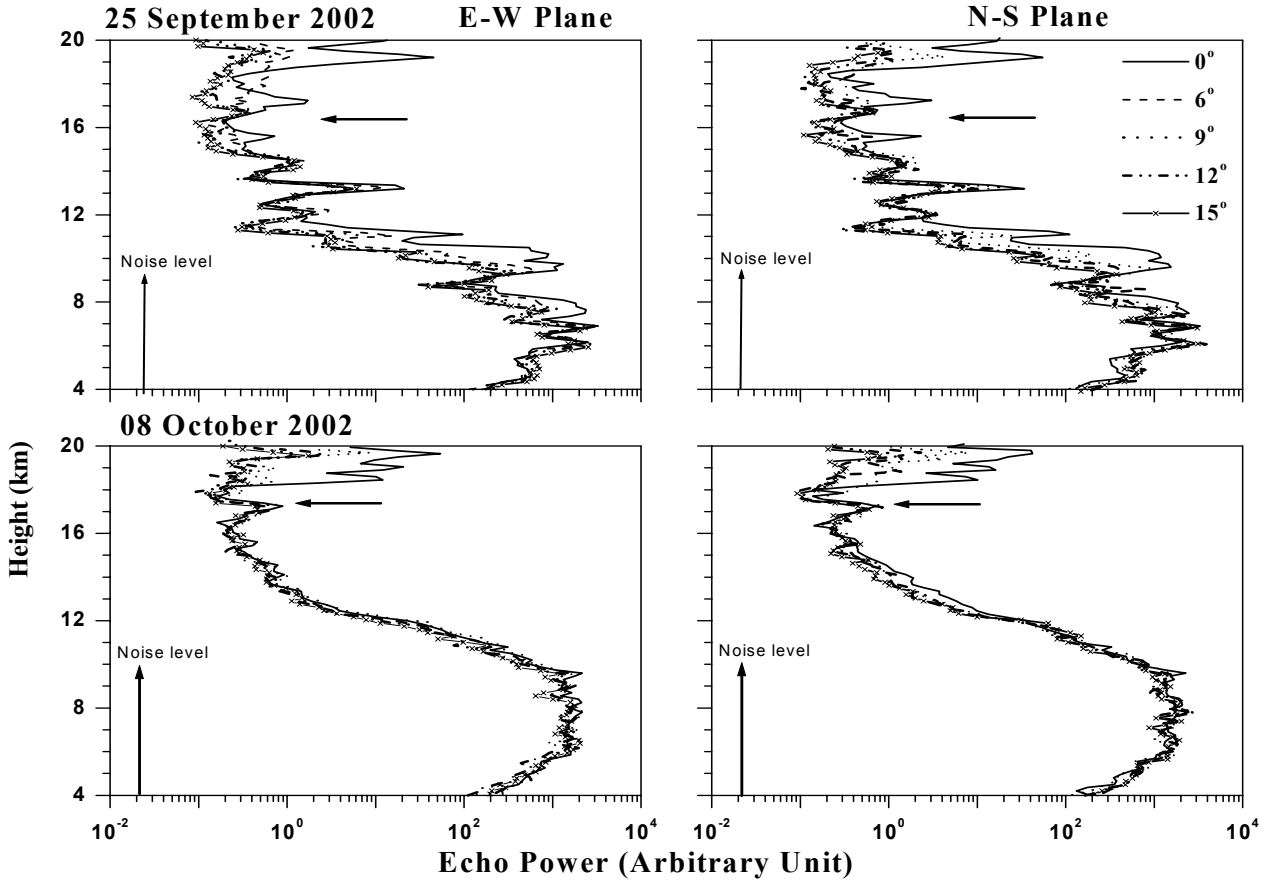

Figure 1: Height profiles of radar echo power for different beam positions in E-W and N-S planes for 25 September and 8 October 2002. The vertical and horizontal arrows in each panel represent the noise level of radar observations and the height of the tropical tropopause reported by GPS sonde observations respectively

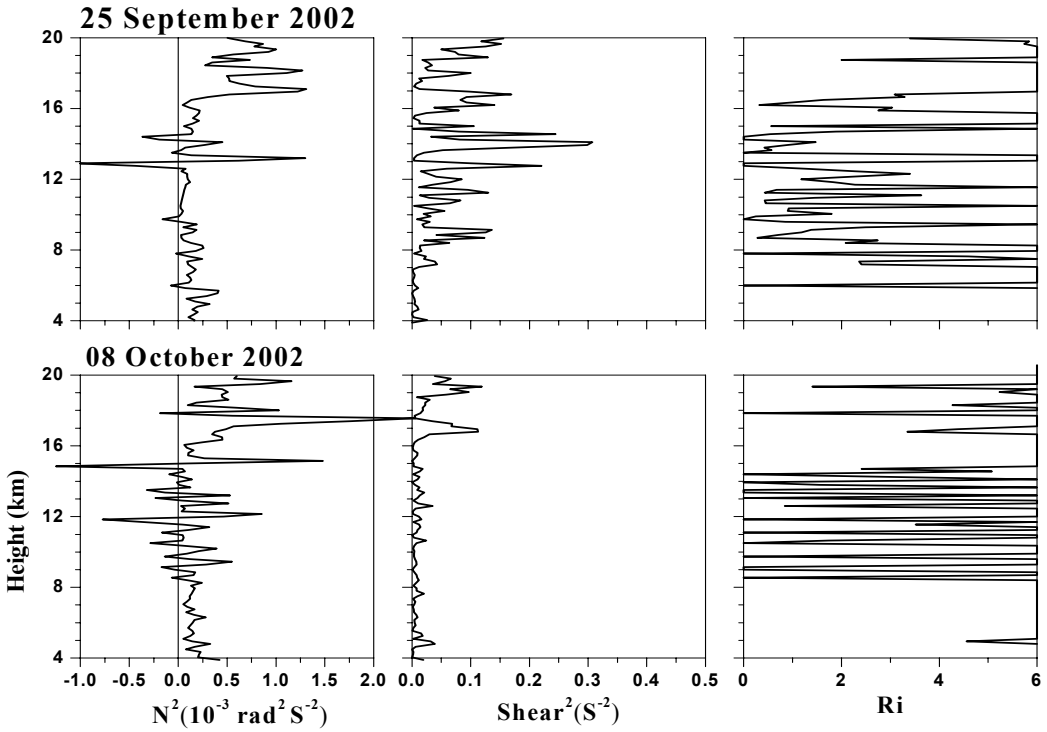

Figure 2: Height profiles of square of Brunt-Vaisala frequency (N^2) from GPS sonde, the square of the vertical shear of horizontal wind speed ($shear^2$) from radar and Richardson number (Ri) using GPS sonde and radar observations.

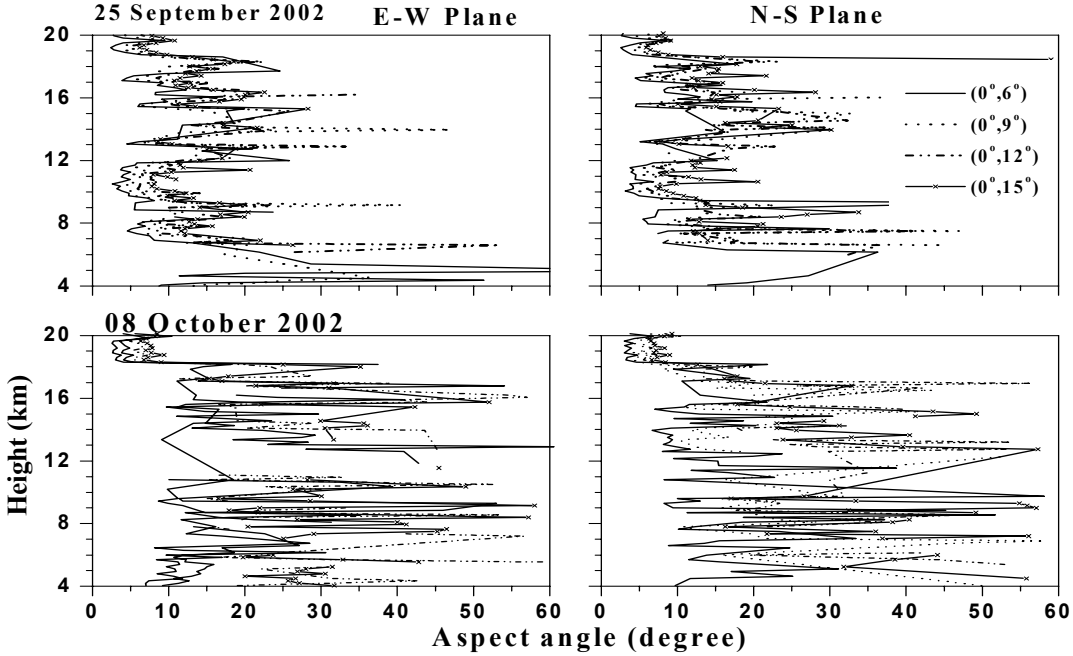

Figure3: Height profiles of θ_s for various beam combinations in E-W and N-S planes for 25 September and 8 October 2002. Each of these beam combinations use zenith beam as reference.

Summary

From the aspect sensitivity measurements presented here the following points can be brought out

(i) While the height region of 16-20 km is in general, aspect sensitive, the aspect sensitivity characteristics of the region below depends on the background atmospheric conditions.

(ii) The height profiles of θ_s reveal that in the regions of high aspect sensitivity the radar backscatterers are highly anisotropic in nature and wherever aspect sensitivity is less the backscatterers are isotropic in nature.

(iii) The layers of enhanced atmospheric stability (N^2) and low wind shear are found to be the cause of enhanced aspect sensitivity especially in the upper troposphere and lower stratospheric regions [*Luce et al,* 2001].

References

Doviak, R.J., and D. Zrinc, Reflection and scatter formula for anisotropically turbulent air, *Radio Sci., 19*, 325-336, 1984.

Gage, K. S., and J. L. Green, Evidence for specular reflection from monostatic VHF radar observations of the stratosphere, *Radio Sci., 13*, 991-1001, 1978.

Hobbs, B.G., and I. M. Reid, Evidence of tilted layers in angle of arrival and Doppler beam steering power measurements, *Radio Sci., 35*, 983-997, 2000.

Hocking, W.K., and A. M. Hamza, A Quantitative measure of the degree of anisotropy of turbulence in terms of atmospheric parameters, with particular relevance to radar studies, *J.Atmos. Solar Terr. Phys., 59,* 1011-1020, 1997.

Jain. A.R., Y.Jaya Rao, and N.S. Mydhili, Height-time-structure of VHF backscatter from stable and turbulently mixed atmosphere layers at tropical latitudes, *J.Atmos. Solar-Terr. Phys., 63*, 1455-1463, 2001.

Luce, H., M. Crochet, and F. Dalaudier, Temperature sheets and aspect sensitive radar echoes, *Ann. Geophysicae., 19*, 899-920, 2001.

HIGH-RESOLUTION ATMOSPHERIC PROFILING USING SIMULTANEOUS MULTIPLE RECEIVERS AND MULTIPLE FREQUENCIES

Tian-You Yu[1] and William O.J. Brown[2]

[1]School of Electrical and Computer Engineering, University of Oklahoma, Norman, Oklahoma 73019, USA
[2]Atmospheric Technology Division, National Center for Atmospheric Research, Boulder, Colorado 80307, USA

1 Introduction

Range imaging (RIM) has been recently developed to improve the range resolution of pulse radar by transmitting a set of slightly shifted frequencies [*Palmer et al.*, 1999]. The capability of RIM for making high resolution observations of the backscatter profile of atmospheric structures have been demonstrated by several authors [e.g., *Palmer et al.*, 1999; *Chilson et al.*, 2003]. However, no Doppler information of these structures was shown. Therefore, one of the goals for this work is to demonstrate application of RIM to obtain high-resolution profile of radial velocity.

Furthermore, measuring horizontal wind at the same resolution as the resolution of echo power and radial velocity in RIM is of primary interest. A new technique, based on a hybrid use of RIM and spaced antenna (RIM-SA), is developed to improve the range resolution of horizontal wind measurements. As a result, RIM-SA has the potential to resolve not only fine reflectivity structures, but also fine-scale wind shears.

2 Theory of RIM-SA

In order to implement RIM-SA technique, a minimum of three spatially separated receivers and two shifted transmitting frequencies are needed. The radar beam points vertically for both transmitting and receiving in a RIM-SA configuration and typically, multiple frequencies are transmitted on a pulse-by-pulse basis. RIM-SA exploits the concept of RIM to generate synthesized time series at several subgates within one range gate for each receiver independently. A high-resolution profile of wind field is estimated using a SA algorithm on synthesized time series data from spaced receivers at every subgate.

In general, signals from M frequencies and N receivers are considered. Let $s_{ij}(t)$ represent the signals from the ith receiver and the jth transmitting frequency at a given gate. In RIM, only signals from M frequencies at a given receiver i are of interest. The synthesized signals $y_i(r_I, t)$ at range r_I and receiver i are defined as a weighted summation of signals from M frequencies and the i receiver [*Palmer et al.*, 1999].

$$y_i(r_I, t) = \mathbf{w}(r_I)^\dagger \mathbf{s}_i(t) \tag{1}$$

where the column vector $\mathbf{s}_i(t)$ consists signals from M frequencies, the dagger is a Hermitian operator, and the column vector $\mathbf{w}(r_I)$ represents a weighting function. The complex weighting function is designed to modulate signals from M different frequencies to create a constructive interference at a given range r_I. In this work, the Capon weighting function was employed because it can provide better resolution than the Fourier weighting function [*Palmer et al.*, 1999].

In previous work, the range brightness was estimated using the correlation matrix made up by $\mathbf{s}_i(t)$ (e.g., (2) in *Palmer et al.* [1999]); Therefore, no synthesized signals (1) were needed. The range brightness represents backscattered power at

a specific range. In this work, synthesized time series are generated by selecting appropriate ranges r_I (subgates) in the weighting function of (1). The synthesized time series inherit the high resolution provided by RIM and therefore, they can be thought of as signals obtained by a conventional single-frequency system operating in a high-resolution mode. A Doppler spectrum can be estimated at each subgate by squaring the time-frequency Fourier transform of $y_i(t)$. Echo power, mean radial velocity, and spectrum width can be obtained by estimating the first three moments of a spectrum [*Woodman*, 1985].

The same procedure (1) is implemented independently for N receivers. Consequently, 'Full Correlation Analysis" (FCA) [*Briggs*, 1984] is applied to synthesized signals at subgates. A range distribution of horizontal wind within the radar volume can be obtained. This hybrid use of RIM and SA, is termed RIM-SA.

3 Experimental Results

An experiment designed to test and verify high-resolution techniques was conducted on April 27, 2002 using multiple antenna profiler radar (MAPR) of National Center for Atmospheric Research (NCAR). The MAPR antenna has an aperture of 2 m by 2 m which is divided into four panels for receiving. MAPR can transmit a maximum of four frequencies generated by independent frequency synthesizers. Detail descriptions of MAPR are provided in *Cohn et al.* [1997] and *Cohn et al.* [2001]. During the experiment, MAPR was located in the compound outside the NCAR Foothills Laboratory in Boulder, Colorado, and operated at two modes from 00 UTC to 03 UTC. In the first mode, a single frequency of 915 MHz and a range resolution of 100 m were used. The data collected in the first mode were processed using a standard FCA to produce profiles of echo power, vertical and horizontal winds. Since MAPR has shown its robust and reliable measurements in this mode [*Cohn et al.*, 1997; *Cohn et al.*, 2001], these 100-m-resolution profiles would be considered as a reference. This mode is termed standard mode. In the second mode, a coarse range resolution of 300 m and four frequencies of 914.667, 915.000, 916.000, and 916.667 MHz were used, and this mode is defined as RIM-SA mode. Signals from four frequencies and four receivers were RIM-SA processed to produce echo power and wind field every 100 m within the 300 m range gate. The two modes were alternated every two minutes throughout the experiment. The profiles obtained using RIM-SA are compared with those profiles obtained in standard mode. 50% oversampling in range was employed in RIM-SA mode in order to mitigate errors toward boundaries of the gate.

Mean profile of echo power and three-dimensional wind over a 3-hour period are presented in Figure 1. Results from standard and Capon RIM-SA modes at 100-m resolution are denoted by the solid line and dashed line with circles, respectively. Note that Capon results were produced from observations made at 300 m resolution. The results suggest that a profile at 100 m resolution can be obtained using a 300 m pulse and multiple frequencies.

Scattering diagrams of results obtained by standard FCA and RIM-SA are shown in Figure 2 for the Capon method. Each data point is an average over 10-min period. Results from standard mode and Capon RIM-FCA analysis are denoted by subscript of S100 and C, respectively. There is a good correlation between standard FCA and RIM-SA results for estimations of echo power (approximately 0.66) and wind field (above 0.7). For three wind components, the results obtained by Capon method are similar and are consistent with results of 100 m standard mode. These results have demonstrated that profiles of echo power and three-dimensional wind fields can be obtained in a spatial scale finer than the range gate using RIM-SA.

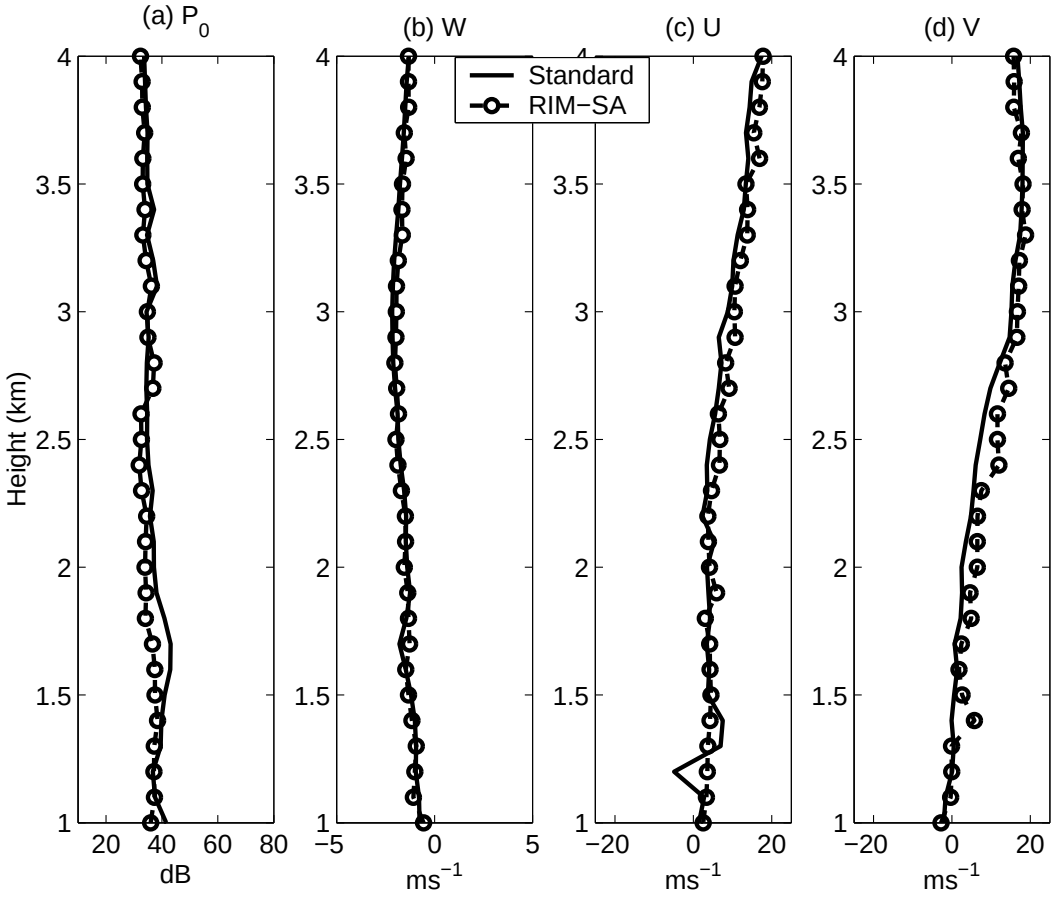

Figure 1: Mean profile of (a) echo power, (b) vertical velocity, (c) zonal velocity, and (d) meridional velocity over a 3-hour period.

4 Conclusions

A novel approach of high-resolution profiling is presented which applies FCA on synthesized time series generated by RIM. The applications of RIM-SA in the boundary layer and lower troposphere are demonstrated using the NCAR MAPR system. A RIM-SA experiment was conducted on April, 27, 2002. High-resolution profiles using RIM-SA are shown to be consistent with profiles measured using a single frequency and short pulse. Furthermore, good agreement between RIM-SA winds and *in situ* winds measured by a radiosonde is shown in *Yu and Brown* [2003].

Acknowledgments
Some work was done when T.-Y. Y was a postdoc at ASP/ATD NCAR. NCAR is sponsored by the National Science Foundation. W.O.J.B. and MAPR received support from the the Environmental Meteorology Program of the Department of Energy under the VTMX (Vertical Transport and MiXing) program.

References

[1] B. Briggs. The analysis of spaced sensor records by correlation techniques. In *MAP Handbook*, volume 13, pages 166–186. SCOSTEP Secretariat, University of Illinois, 1406 W. Green St., Urbana, IL 61801, 1984.

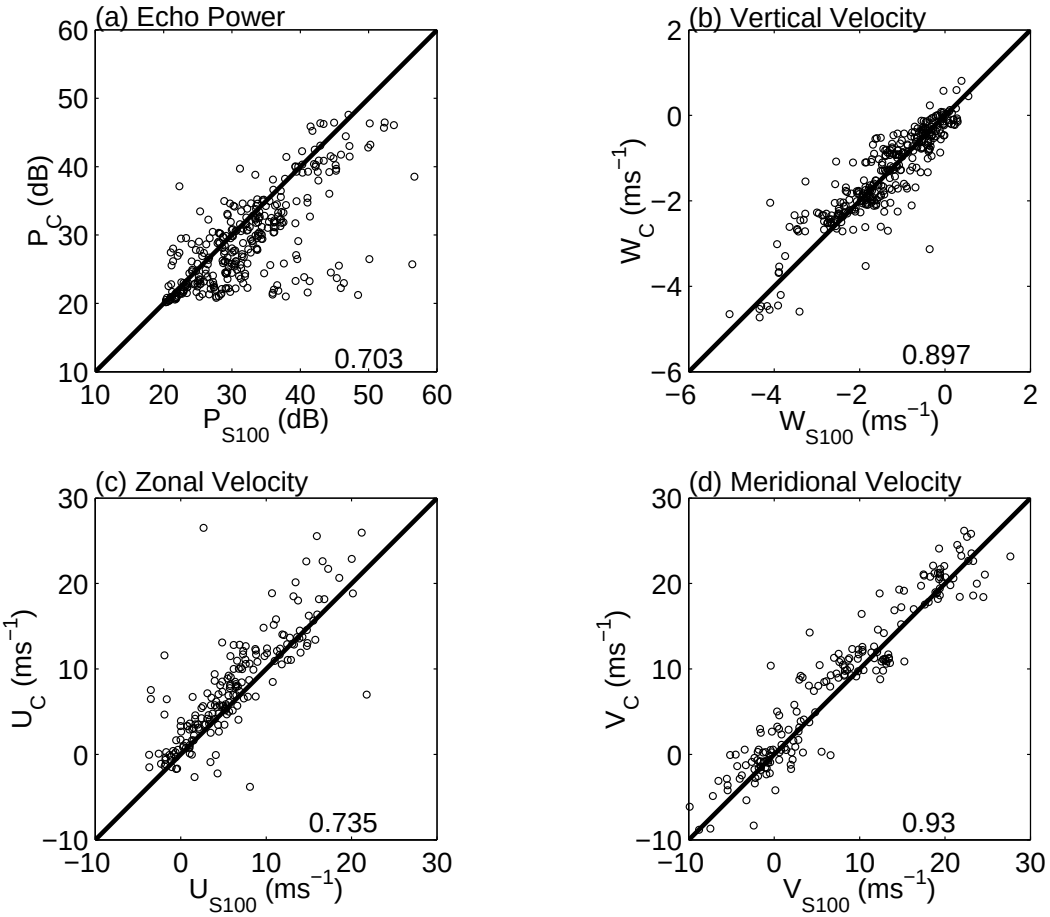

Figure 2: Scatter plots of (a) echo power, (b) vertical velocity, (c) zonal velocity, and (d) meridional velocity for data at altitudes between 0.5 km and 4.0 km over three hours. The x and y axes represent results from 100 m standard mode and Fourier RIM-SA mode, respectively. The correlation coefficient is indicated on the lower right of each plot

[2] P. B. Chilson, T.-Y. Yu, R. G. Strauch, A. Muschinski, and R. D. Palmer. Implementation of range imaging on the platteville 915-MHz tropospheric profiler. *J. Atmos. Oceanic Technol.*, 20:987–996, 2003.

[3] S. A. Cohn, W. O. J. Brown, C. L. Martin, M. S. Susedik, G. Maclean, and D. B. Parson. Clear air boundary layer spaced antenna wind measurement with the multiple antenna profiler (MAPR). *Ann. Geophy.*, 19:845–854, 2001.

[4] S. A. Cohn, C. L. Holloway, S. P. Oncley, R. J. Doviak, and R. J. Lataitis. Validation of a UHF spaced antenna wind profiler for high-resolution boundary layer observations. *Radio Sci.*, 32:1279–1296, 1997.

[5] R. D. Palmer, T.-Y. Yu, and P. B. Chilson. Range imaging using frequency diversity. *Radio Sci.*, 34:1485–1496, 1999.

[6] R. F. Woodman. Spectral moment estimation in MST radars. *Radio Sci.*, 20:1185–1195, 1985.

[7] T.-Y. Yu and W. O. J. Brown. High-resolution atmospheric profiling using combined spaced antenna and range imaging techniques. *Radio Sci.*, submitted, 2003.

ATMOSPHERIC REFRACTIVITY PROFILES OVER PIURA ST RADAR

Rodolfo Rodríguez, Freddy Sosa and Miguel Carrión

Universidad de Piura, Piura - Peru

1. Abstract

The Piura 50-MHz ST radar is part of the Trans-Pacific Profiler Network (TPPN) that monitors the atmospheric dynamics along the Equatorial Pacific Ocean. This system is in operation since 1989 and it is located in the northern coast of Peru, (05˚ S, 80˚ W) one of the continental regions most affected by climatic anomalies due to the El Niño-Southern Oscillation (ENSO) phenomenon. In order to complement the atmospheric observations of wind profiles with this radar, meteorological balloon launchings have been made to gather temperature, humidity and pressure profiles. From these data we have deduced the first atmospheric refractivity profiles that the Piura radar system operates under. Characteristics and variability of these profiles are shown in this work.

2. Introduction

It is well known that the macroscopic changes of radio refractive index (η) in space cause refraction or reflection and that microscopic changes cause scattering (Sato, 1989). Also, it is widely accepted that major contributions to η at frequencies of HF through UHF bands in the troposphere and stratosphere can be expressed approximately as (e.g., Balsley and Gage, 1980):

$$\eta - 1 = \frac{7.76x10^{-5}\,p}{T} + \frac{3.75x10^{-1}\,e}{T^2} \qquad \text{Equation 1}$$

where η is the refraction index, e is the vapor pressure (mB), T is the temperature (K) and p the atmospheric pressure (mB). Since in the atmosphere η is just little greater than 1 and its variations are very small, it is convenient to use the refractivity (N) defined as:

$$N = (\eta - 1)x10^6 = \frac{77.6\,p}{T} + \frac{3.75x10^5\,e}{T^2} \qquad \text{Equation 2}$$

The first term of Equations 1 and 2 is function of p and T and it corresponds to the contribution of the dry air. The second term is function of e and T which corresponds to the contribution of the water vapor in the low and medium atmosphere (Kingsley and Quegan, 1992).
In this work we have applied these formulas to get the first refractivity profiles over the Piura ST radar site.

3. Piura site

The Piura ST radar is located in the oriental end of the Trans-Pacific Profiler Network (TPPN). Like all the radars of this chain, this one is located near the equatorial line, (05˚S, 80˚W), however, unlike the others, it is the only one situated in continental area. Piura is the

most occidental area of South America and very sensible to the El Niño Southern Oscillation (ENSO) phenomenon.

The Piura ST radar operates since 1989 (e.g., Gage et al., 1991). Since then, frequent launches of meteorological balloons have been done from this site to complement the wind profile observations. These soundings were carried out almost daily during the 1997-1998 ENSO phenomenon. The gathered data was used to obtain the refractive properties of the lower atmosphere including the boundary layer.

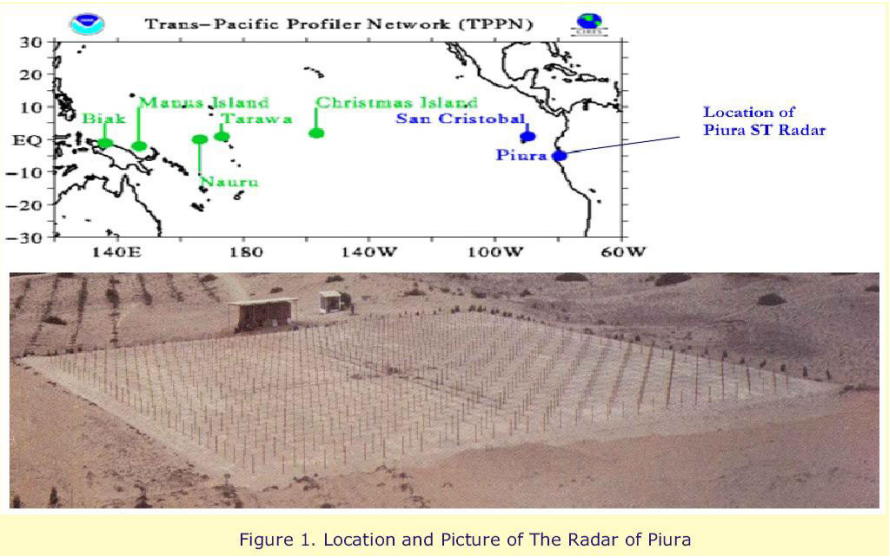

Figure 1. Location and Picture of The Radar of Piura

Figure1. Location and picture of the Piura ST radar

4. Methodology

The meteorological soundings were made using a launch system provided by the NOAA Aeronomy Laboratory in Boulder, CO. This system consists of a radiosonde and a receiver. The transmitter part uses a 403.5 Mhz Vaisala radiosonde which is lifted by a 200 gr. balloon filled with helium gas, while the receiver part uses a 403.5 MHz receiver, an omni-directional antenna and a portable personal computer. The computer is programmed using the PC-TALK software for reception and recording data. The recorded data are: time (t), Temperature (T), humid temperature (T_w) and atmospheric pressure (p).

According to Equations 1 and 2, the necessary data to evaluate the refraction index are temperature (T), vapor pressure (e) and the atmospheric pressure (p). Vapor pressure is deduced based on the data of temperature (T), relative humidity (HR) and humid temperature (T_w). Height (h) is calculated based on the hydrostatic balance equation.

$$h = \frac{R\overline{T}}{g} \ln\left(\frac{p_2}{p_1}\right) \qquad \text{Equation 3}$$

Figure 2 shows the relationship between the recorded data (T, T_w, p) to get the vapor pressure (e) and to use them in the refractivity equation (Equation 2). To read the recorded data and apply this relationship, an IDL (Interactive Dates Language) program was coded.

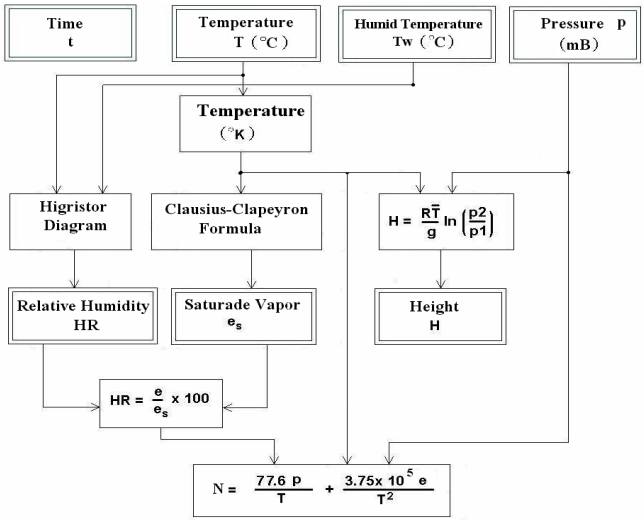

Figure2. Block diagram showing the relationship between root data, vapor pressure and the refractivity equation

5. Results and discussion

Figure 3 shows three examples of the profiles obtained for temperature, relative humidity, atmospheric pressure and refractivity between 0 to about 12 km height.

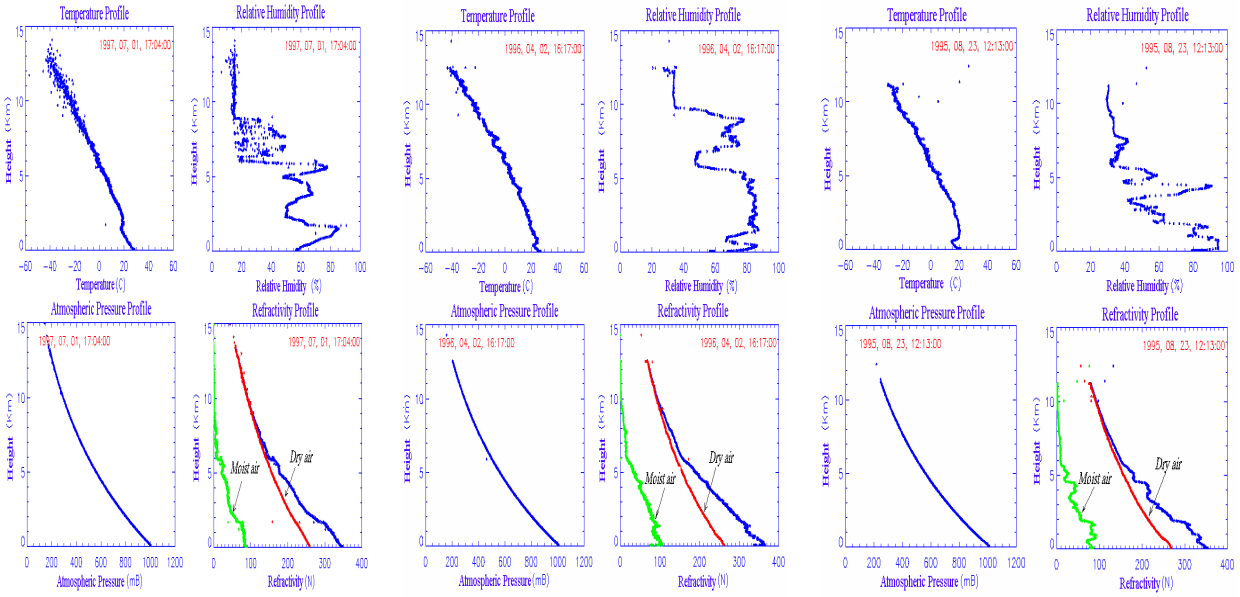

July 01, 1997 April, 02, 1996 August 23, 1995

Figure3. Three profiles of Temperature, Relative Humidity, Atmospheric Pressure and Refractivity. The Refractivity profiles show the contribution of dry air (red line) and humidity (green line)

The profiles of refractivity are the first ones obtained for the Piura area and they agree with the typical variation that has been reported by Sato (1989). Refractivity due to dry air is always bigger than one due to water vapor. The contribution to the profile of refractivity of the dry air has an almost exponential variation while water vapor is only important until a certain height (about 8 km). It seems that water vapor has a higher contribution for refractivity in boundary layer heights (0 to 2 km) and then decays until about 8 km where its contribution is almost neglected.

These results can be used to estimate the change of refractive index with height, known as the refractive gradient dN/dh which causes radio signals bent downwards (Kingsley and

Quegan, 1992). It should be useful to study the radio-propagation in the atmosphere of northern Peru and to simulate the Piura ST radar echoes using the radar equation.

6. Acknowledgements

The authors want to express their gratefulness to National Oceanic and Atmospheric Administration (NOAA) Aeronomy Laboratory and to Cooperative Institute for Research in Environmental Sciences (CIRES) in Boulder, Colorado, USA, which supported the installation and operation of the Piura ST radar and supplied equipment for meteorological sounding.

7. References

Balsley, B. B. and K. S. Gage, The MST radar technique: Potential for middle atmospheric studies, *Pure Appl.. Geophys*., 118, 452-493, 1980.

Gage et al., Wind profiler-related research in the Tropical Pacific, *JGR*, Vol. 96, Supplement, pp 3209-3220, 1991.

Kingsley S. and S. Quegan, Understanding radar systems, *McGraw-Hill Book Company*, 1992

Tapley T. D. and Waylen P. R., Spatial variability of annual precipitation and ENSO events in western Peru, *Hydrological Sciences*, 35, 4, pp 429-446, 1990.

Sato T., Radar principles, *Handbook for MAP*, ICSU-SCOSTEP, Vol.30, 1989.

VHF-RADAR OBSERVATIONS OF TEMPERATURE SHEETS IN THE STRATOSPHERIC-TROPOSPHERIC REGION

Siddarth Shankar Das[1], K. Kishore Kumar[1], A. R. Jain[1],
D. Narayana Rao[1], A.K.Ghosh[1], K. Nakamura[2]

[1]National MST Radar Facility, P.B.123, Tirupati-517502. India.
[2]Nagoya University, Nagoya-464-8601, Japan.
E-mail : dassiddhu@rediffmail.com

1. Introduction:

In past two decades VHF radar observations have contributed much in understanding the various small-scale atmospheric processes. However, knowledge of the VHF radar backscattering plays a vital role in understanding and interpreting these observed atmospheric phenomena. In this regard, several experiments were carried out across the globe to understand the VHF radar backscattering mechanisms. Many of these experiments have reported the multiple layered structures at and around the tropopause regions, especially in the lower stratosphere [e.g. *Jaya Rao et al.,* 1994, *Jain et al*., 1994 and 2001]. It is now well established that these layered structures are due to the presence of strong negative and positive temperature gradients [e.g. *Dalaudier et al*., 1994, *Luce et al*., 2001], commonly known as 'temperature sheets'. VHF radar observations of these temperature sheets in the lower stratosphere are extensively reported by several researchers [*Dalaudier et al.,* 1994], [*Luce et al.,* 2001, *Jayarao, et al*., 1994]. Though, earlier studies have suggested few causative mechanisms for the formation of temperature sheets, they are restricted by means of uncertainty in their proposed mechanism and also due to limited radar resolutions (interms of spatial and temporal). The suggested mechanisms include Kelvin-Helmholtz Instability, (KHI) [*Muschinski* and *Wode*, 1998], viscous or thermal conductive waves [*Hockings et al.* 1991] and gravity waves [*Luce et al.,* 2001]. It has been further showed that the propagation and dissipation of gravity waves, which in turn affected by the KHI [*Frittis* and *Rastog*i, 1985], is responsible for the observed temperature sheets in the lower stratosphere.

In the present study, simultaneous VHF radar located at Gadanki (13.47^o N, 79.18^o E, a tropical site, India) and balloon measurements have been employed to divulge the occurrence of temperature sheets. An attempt has also been made to understand the causative mechanism for the presence of multiple layers structure in terms of gravity waves.

2. Results and Discussions:

The results from concurrent VHF Radar observations at Gadanki and GPS sonde measurements at Tirupati (nearby the radar site) during September 2000 are presented here. GPS sondes provides high-resolutions measurements of temperature, pressure, humidity, wind speed and direction. A temperature profile obtained from GPS sonde, on September 4, 2000, is shown in figure 1(a). This figure displays clearly the existence of inversion layers, by strong positive and negative temperature gradients in the stratospheric-tropospheric height regions. The recorded radar observations interms of range-time signal to noise ratio (SNR) section is shown in figure 1(b). This figure reveals the existence of multiple layered structures in the lower stratosphere and upper troposphere height regions. It further illustrates that the high intensity in SNR is due to the prevailing temperature gradient at the same height region (refer figure 1(a)). Radar measurements at vertical and off-vertical directions provide the measure of aspect sensitivity of the backscatters. The difference in SNR profiles of vertical and off-vertical directions, which gives the first order aspect sensitivity

measurements, is shown in figure 1(c). From this figure high aspect sensitivity can be noticed around the temperature sheets, which in turn confirms the layered structure of the backscatters.

In order to know the vertical wave length of temperature and SNR perturbations, wave analysis have been carried out and is shown in figure 2. As there was no continuous radar observations, the wave anlysis is done in height domain only to find out the vertical wavelenth of the observed perturbations. Both SNR and temperature show a peak in amplitude at the vertical wavelength of 1.6 km. This suggests that the modulation of temperature is due to the propagation of atmospheric waves, which in turn reflects in the SNR observations. As mentioned earlier,due to the lack of continuous observations (both temperature and radar intensity), wave periodicities are not estimated.

Realizing the importance of these studies a comprehensive campaign is carried out to further understand the existence of temperature sheets. During this campaign, we found a similar kind of structure as discussed above on September 25, 2002. On this day, continuous radar observations were taken for a period of 12 hours with time and height resolutions of 7min and 150 m respectively. The radar observations are also supported by the simultaneous GPS measurements at the radar site. Figure 3(a) shows the height profile of temperature, which is revealing the prominent temperature structures in the lower stratosphere.

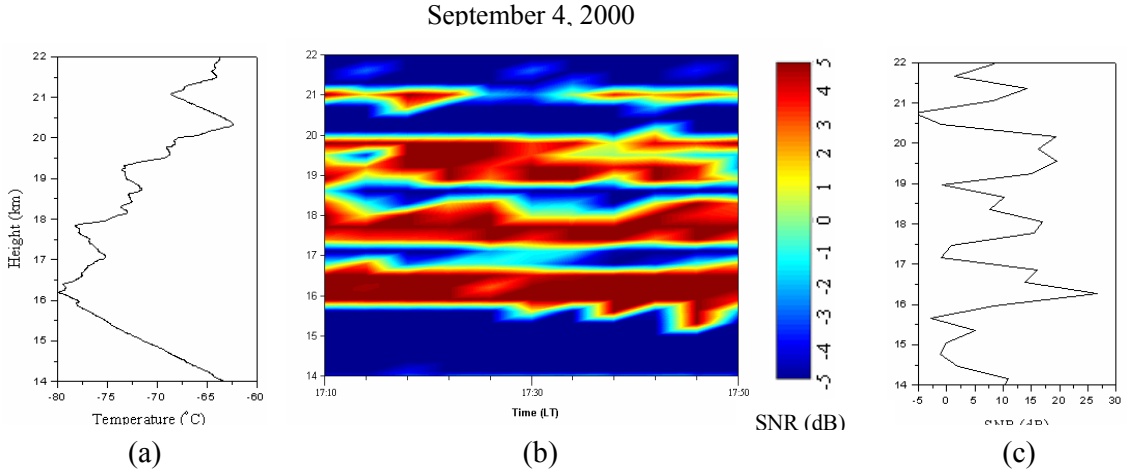

Figure 1. (a) Height profile of temperature derived from GPS-Sonde measurements, (b) Height-Time-SNR section obtained from Gadanki VHF radar and (c) height profile of SNR difference between vertical and off-vertical (10°) beam directions on September 4, 2000.

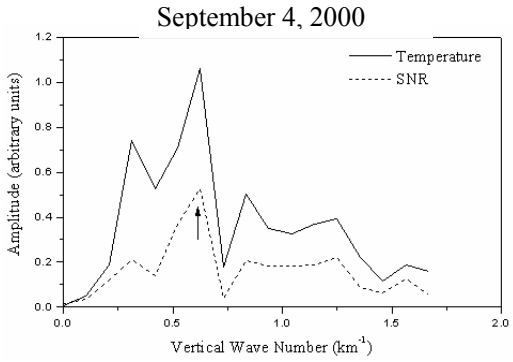

Figure 2. Vertical wave number spectra of temperature and SNR obtained on September 4 2000 (arrow indicates the dominant wave number)

Continuous radar observations have been used to obtain the zonal, meridional and vertical velocities [*Anandan et al*., 1997]. The time series data of zonal, meridional and vertical velocity perturbations are further subjected to Fourier analysis to get the power spectra of the velocity perturbations. Figure 3 (b) shows the power spectra of zonal wind perturbations on September 25, 2002. From this figure it can be noticed that the oscillation with a time period of ~82.4 min is dominant at most of the heights, especially in the lower stratosphere. Moreover, it shows peak amplitudes in the lower stratosphere. But, it has been observed that the wave amplitudes are relatively weaker in the meridional and vertical velocities (figures are not shown). The direction of horizontal propagation of gravity waves in the troposphere are uniform in all directions whereas it will be eastward in the lower stratosphere. This may be the reason for observed enhancement in the zonal wind perturbations in the lower stratosphere [*Tsuda et al*., 1994].

Generally, the gravity waves transport energy and momentum from lower atmosphere to middle atmosphere. Often, these waves break wherever it encounters the dynamic and convective instabilities. When these waves break they deposit the momentum and energy in that region, which are very crucial for understanding the wave interaction with the large-scale environment. In the present study the temperature and wind field observations clearly shows the modulation of respective fields by the gravity waves. A thorough study is underway to reveal the gravity wave breaking and their consequences in the lower stratosphere.

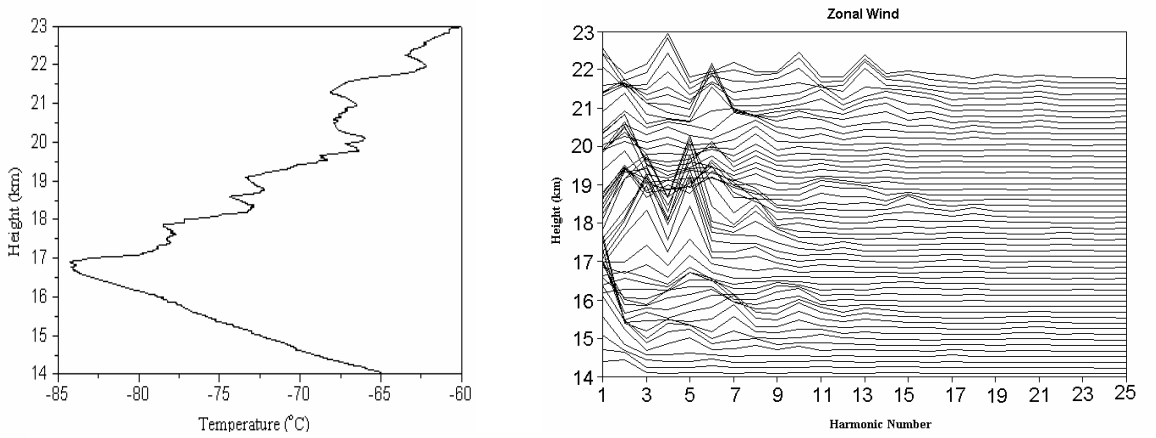

(a) (b)

Figure 3. (a) Height profile of temperature derived from GPS-sonde measurement and (b) the spectra at different height levels for zonal wind perturbations on September 25, 2002 which shows the dominant time period of 82.4 min (period =412/5) corresponding to 5th harmonic number. The total period of observations corresponds to ~412 min.

3. Concluding remarks:

The existence of layered structures in the stratospheric-tropospheric height region using VHF radar observations are presented in this paper. The enhanced radar reflectivity layers associated with high aspect sensitivity are observed in the same height region, which are attributed to the presence of temperature gradients. The spectral analysis revealed the vertical wavelength of ~1.6 km indicating the perturbation of temperature by the propagating gravity waves. For the same kind of structure, on the other day, the periodicity of the propagating waves is found to be 82.4 min. These wave oscillations are more prominently seen in the zonal winds, which have shown the peak amplitudes in the lower stratosphere.

The present observations thus emphasize the gravity waves as an important source for the observed temperature sheets in the lower stratosphere. However, further observations and evidences are required to shed more light on to this aspect.

Acknowledgement:

The authorities of Hydrospheric-Atmospheric Research Center, Nagoya University, Nagoya, Japan and S. V. University, Tirupati, India are acknowledge for their cooperation for launching GPS sondes from Tirupati, India during September 2000. We are also thankful to Prof. G.S. Bhatt (Indian institute of Sciences, Bangalore) for his support in conducting the GPS sonde campaign from NMRF, Gadanki during September-October 2002. One of the authors, SSD, is thankful to Indian Space Research Organisation (ISRO) for proving the fellowship and facility during the study.

References:

Anandan, V.K., P. Balmuralidhar, P.B. Rao and A. R. Jain, A method for adaptive moments estimation technique applied to MST radar echoes, Progress in electromagnetic research symposium, Telecommunication research center, City University of Hongkong, Vol.2, pp. 670, 1997.

Dalaudier, Francis, Claude Sidi, Michel Crochet and Jean Vernin, Direct Evidence of "Sheets" in the Atmosphere Temperature Field, *J. Atmos. Sciences*, 51, 237, 1994.

Fritts,D.C. and P.K.Rastogi, Convection and dynamical instabilities due to gravity waves motions in the lower and middle atmosphere : theory and observations, *Radio Sci.,* 20,1247-1277, 1985.

Hocking, W.K., Fukao, S., M.Yamamoto., T. Tsuda and S. Kato., Viscosity waves and thermal-conduction waves as a cause of "specular" reflectors in radar studies of the atmosphere, *Radio Sci*., 26, 1281-1303, 1991.

Jain, A.R., Jaya Rao Y., P.B.Rao., G. Viswanathan., S.H.Damle., P. Balamuralidharan and Anil Kulakarni, Preliminary observations using ST mode of Indian MST Radar : Detection of the signature of Tropopause, *J. Atoms. and Terr. Phy*, 56, 1157-1162, 1994.

Jain. A.R., Y.Jaya Rao, and N.S. Mydhili, Height-time-structure of VHF backscatter from stable and turbulently mixed atmosphere layers at tropical latitudes, *J.Atmos. Solar-Terr. Phys., 63*,1455-1463, 2001.

Jayarao, Y., A.R.Jain., V.K.Anandan., P.B.Rao., G.Viswanathan and R. Aravindan, Some observations of tropical tropopause using ST mode of the Indian MST radar : Multiple stable layer structure, *Indian J Radio and Space Phy*, 23, 75-85, 1994.

Luce, H., M.Crochet and F. Dalaudier, Temperature sheets and aspect sensitive radar echoes, *Annales Geophysicae*, 19, 899-920, 2001.

Muschinski Andreas and Wode Christian., First In situ evidence for Coexisting Submeter temperature and humidity Sheets in the Lower free Troposphere., *J. Atmos. Sciences*., 55, 2893-2906, 1998.

Tsuda Toshitaka, Yasuhiro Murayama, Harsono Wiryosumarto., Radiosonde observations of equatorial atmosphere dynamics over Indonesia. 2. Characteristics of gravity waves., *J. Geophy. Res*, 99, 10507-10516, 1994.

Session I.2: D, E and F Region Coherent Scattering

This session will be devoted the theory and observation of coherent scatter from ionospheric irregularities at all latitudes. We solicit reports pertaining to such mature fields of study as the auroral and equatorial electrojets, PMSE, sporadic E layers, and equatorial spread F. Recent and planned campaigns like SEEK II, C/NOFS, and CIELO attest to the fact that numerous problems remain unsolved in these areas. In addition, we invite reports on emerging areas of research including long-lived meteor trails, 150 km echoes, daytime spread F, and midlatitude spread F, about which relatively little is known. Novel experimental techniques such as passive radar, networked radar, radar imaging, and coherent scatter Faraday rotation may promote rapid progress in the areas outlined above, and we therefore invite reports describing new experimental radar techniques.

Conveners:
D. Hysell and R. Palmer

RECENT OBSERVATIONS OF *E* REGION FIELD-ALIGNED IRREGULARITIES AT LOW LATITUDES

J. L. Chau[1,2], D. L. Hysell[3], and M. A. Milla[1]
[1] Radio Observatorio de Jicamarca, Instituto Geofisico del Perú, Lima
[2] Laboratorio de Física, Universidad de Piura, Piura, Perú
[3] Department of Earth and Atmospheric Sciences, Cornell University, Ithaca, New York, USA

1. Introduction

In this work we present a summary of recent observations made of *E* region field aligned irregularities at low latitudes, particularly those from the Jicamarca Radio Observatory (~1°N dip latitude) and those from the Piura VHF radar (~7°N dip latitude) both located in Peru. Although the observations at Jicamarca, under the magnetic equator, inside the equatorial electrojet (EEJ) region, started more than 40 years ago, there have been very few of them (few hundred hours a year) until the JULIA (Jicamarca unattended long-term investigations of the atmosphere) system started few years ago. Nowadays we are observing more than 4000 hours per year.

In the case of the Piura radar, which was originally conceived as a wind profiler, we have also started the *E*-region observations on campaign basis [*Woodman et al.*, 1999; *Chau and Woodman*, 1999] by pointing perpendicular to the magnetic field, i.e., 14°N off vertical. Since January 2000, a special observing mode has been added to the normal operations of the Piura radar to get quasi continuous measurements of the *E*-region every 11 minutes [*Chau et al.*, 2002]

It is important to mention that observations of *E*-region irregularities started during the International Geophysical Year (IGY) in 1957. At that time measurements were conducted using bistatic configurations shown in Figure 1. Measurements were conducted at the magnetic equator (over Huancayo), 5° North (over Trujillo), and 5°S (over Arequipa). The main conclusions relevant to this work are (a) *E*-region echoes were stronger during the day at the magnetic Equator and at 5°S; (b) *E*-region scatter signals at 5°N were weaker than those at the magnetic equator and 5°S, independent of season, and absent, most of the time, during the day [*Cohen and Bowles*, 1963]. The locations of the Jicamarca and Piura radars are indicated in the Figure 1 for reference.

First we will describe the different *E* region observing modes currently available at Jicamarca including preliminary statistics based on JULIA observations. Then we describe the observations with the Piura radar along with recent statistics. Finally we summarize the main characteristics of the EEJ and Piura *E* region irregularities, and different parameters that can be derived from those observations at Jicamarca and Piura

2. Jicamarca *E* region modes

The main operating mode at Jicamarca is the Incoherent Scatter Radar (ISR) mode that allows the measurements of densities, temperatures, compositions and drifts of the ionosphere [e.g., *Farley*, 1991; *Kudeki et al.*, 1999]. Due to the presence of strong irregularities at *E* region heights, i.e., EEJ [e.g., *Farley*, 1985], the ISR measurements are not possible at those heights. Given this limitation, in recent years, a number of observing modes has been implemented at Jicamarca to try to derive the state parameters of the ionosphere (e.g., density profiles, electric fields) from observing the *E* region irregularities. These modes can be classified as (a) interferometer, (b) oblique, (c) bistatic, and (d) imaging modes.

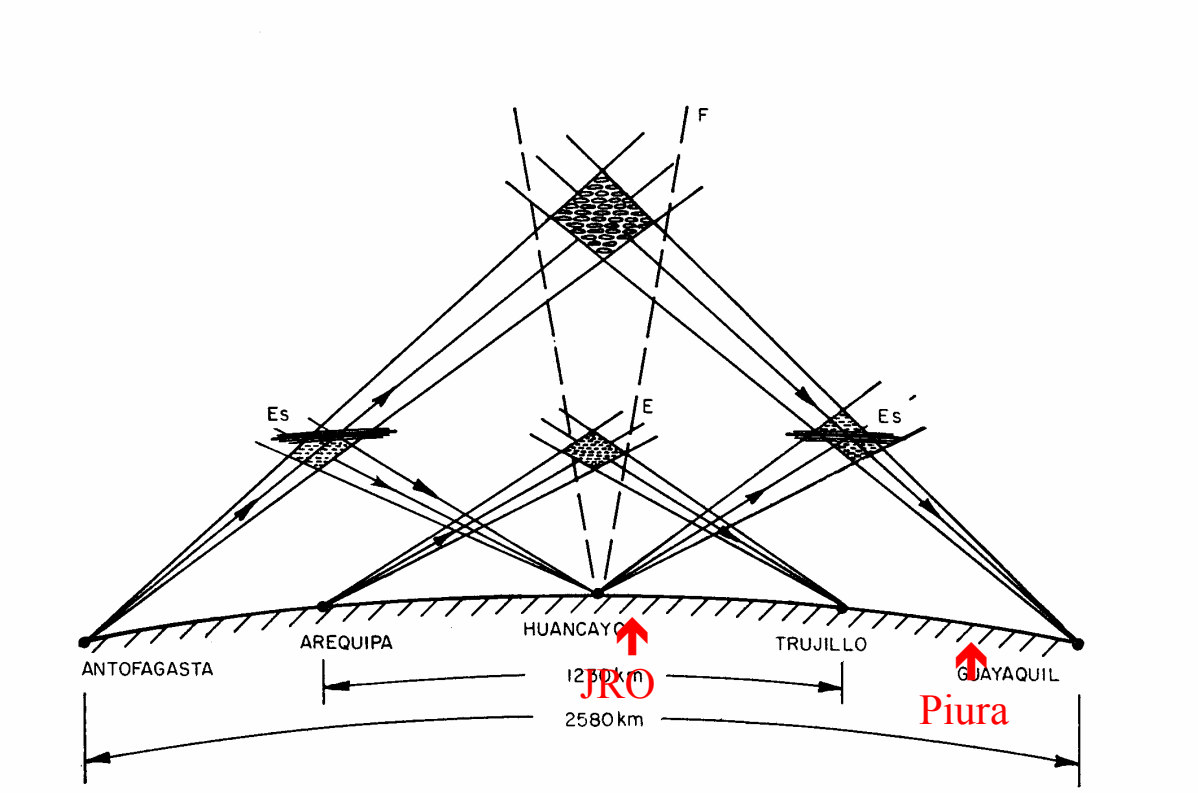

Figure 1. Experimental configurations for *E* and *F* region irregularities during the International Geophysical Year (IGY) in 1957. The Jicamarca and Piura radars are indicated as a reference. Adapted from *Cohen and Bowles* [1963]

2.1 Interferometer mode

Radar interferometry was pioneered by *Farley et al.*, [1981] at Jicamarca and since then it has been applied to study most field-aligned irregularities at different latitudes. At Jicamarca, the north and south quarters are used for transmission while the East and West quarters are both used for reception independently. From the coherence, a measure of the width of irregularities is obtained, while the angle of arrival is obtained from the phase of the cross-correlation between receiving antennas. The main products of this mode are: (a) Signal-to-noise ratio (SNR), (b) Vertical drift (from Doppler velocity), and (c) Zonal drift from tracking the angle of arrival as a function of time [e.g., *Kudeki et al.*, 1982]. In Figure 2, we show a typical example of measurements conducted almost continuously at nighttime. The poor range resolution is because *F* region irregularities are also being observed.

2.2 Oblique mode

The oblique mode observations were introduced by *Balsley* [1969] using the so-called mattress antennas at Jicamarca. The basic idea is to point with small antennas either to the East or West of the Jicamarca and then derived electric fields and neutral winds from the Doppler velocities measured at different ranges [e.g., *Balsley*, 1969; *Balsley et al.*, 1976]. Recently the technique has been improved significantly. Using wide beams with small COCO antennas in addition to proper weighting functions, *Hysell and Burcham* [2000] have been able to obtain reasonable electric fields from the type II Doppler shifts. In addition, by using narrow beams with a relatively long array of Yagi antennas and with the help of a three-dimensional electrostatic model, zonal wind profiles at *E*-region heights could be obtained from the type II Doppler shift profiles [*Hysell et al.*, 2002].

In Figure 3, we show typical spectrograms of oblique observations using wide beams (top row) and narrow beams (bottom row). A two-Gaussian function is fitted to the

measured spectra in order to separate the type I and type II contributions. Type I Doppler shifts are indicated with yellow curves, while type II with black curves.

2.3 Bistatic mode

The bistatic mode was developed by *Hysell and Chau* [2001] using small antenna modules for transmission and reception. The transmitting array was located ~200 km south of Jicamarca (Paracas) while the receiving system was located at Jicamarca. On reception two orthogonal polarizations were used in order to measure the Faraday rotation of the signal due to the changes in density in the connecting path. In this case, we took advantage of the strong EEJ echoes as targets for sampling the *E* region ionosphere. In Figure 4, we show the preliminary density profiles obtained with this technique. For comparison a density profile from a rocket measurement is also shown (left). The first observations were conducted just few days for testing. Continuous measurements are scheduled to start by the end of 2003.

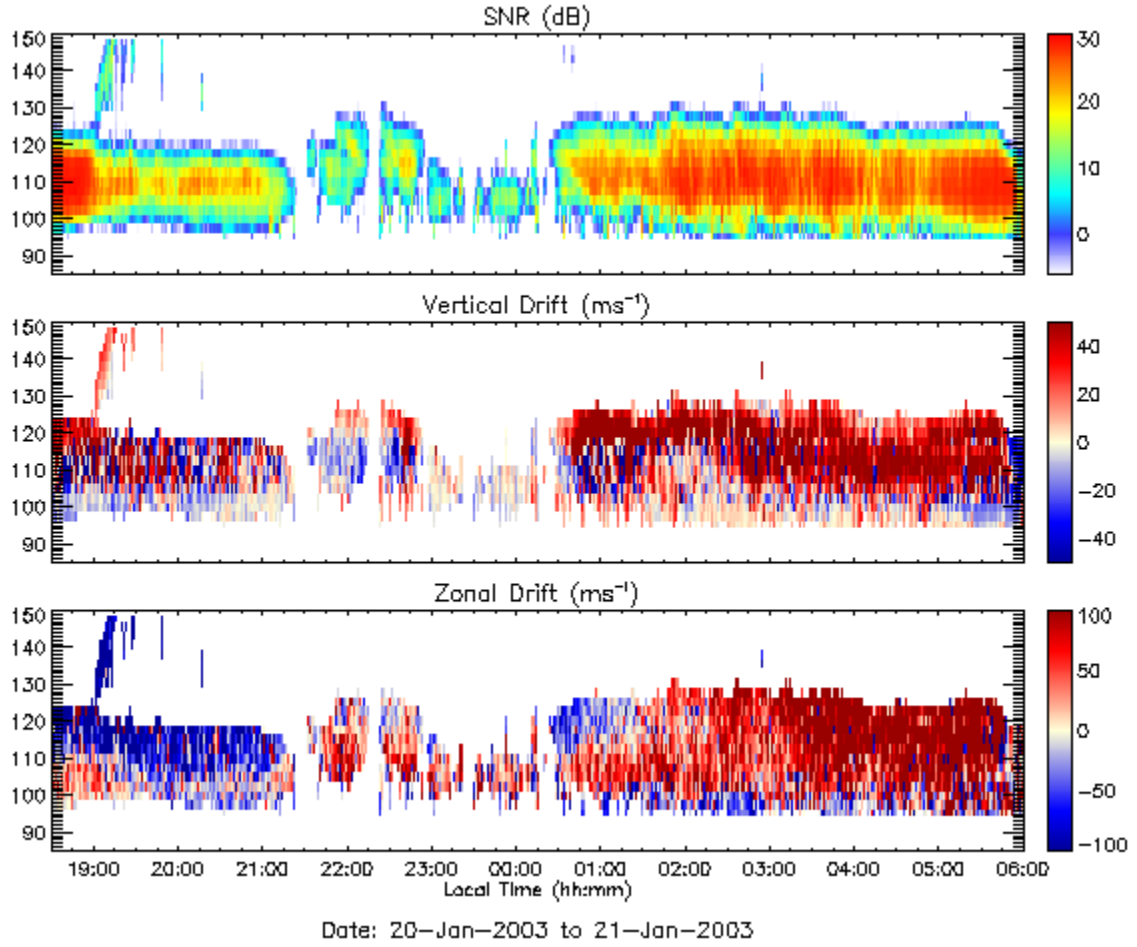

Figure 2. Example of interferometry measurements of nighttime *E*-region irregularities over Jicamarca, SNR, vertical drift, and zonal drift.

2.4 Imaging mode

Radar imaging is an extension of radar interferometry and was first introduced by *Kudeki and Sürücü* [1991] to study the *E* region irregularities. Since then, the technique has been improved significantly and is now being used successfully to study *E* and *F* region irregularities at Jicamarca [e.g., *Hysell and Chau*, 2002; *Hysell and Woodman*, 1997]. The technique makes use of many receiving antennas. At Jicamarca 6 antennas with non-redundant spacing have been used to study the field-aligned irregularities. Since magnetic field is almost horizontal, only a two-dimensional approach is needed (East-West vs.

altitude). In Figure 5 there is an example of the typical range-time intensity (RTI) plot, used by most radars, of nighttime *E* region irregularities (left) and an image for the time indicated by the vertical red line (right). The image shows the structures inside the illuminated beam. Doppler velocity is color coded where pure colors represent very narrow spectral widths (red: away from the radar, green: around zero, blue: towards the radar) while whitish colors represent very wide spectral widths. The intensity is proportional to the SNR. This is a new way of looking at irregularities, so major efforts are being conducted to improve the understanding of the scattering mechanisms and to extract state parameters (e.g., winds, electric fields)

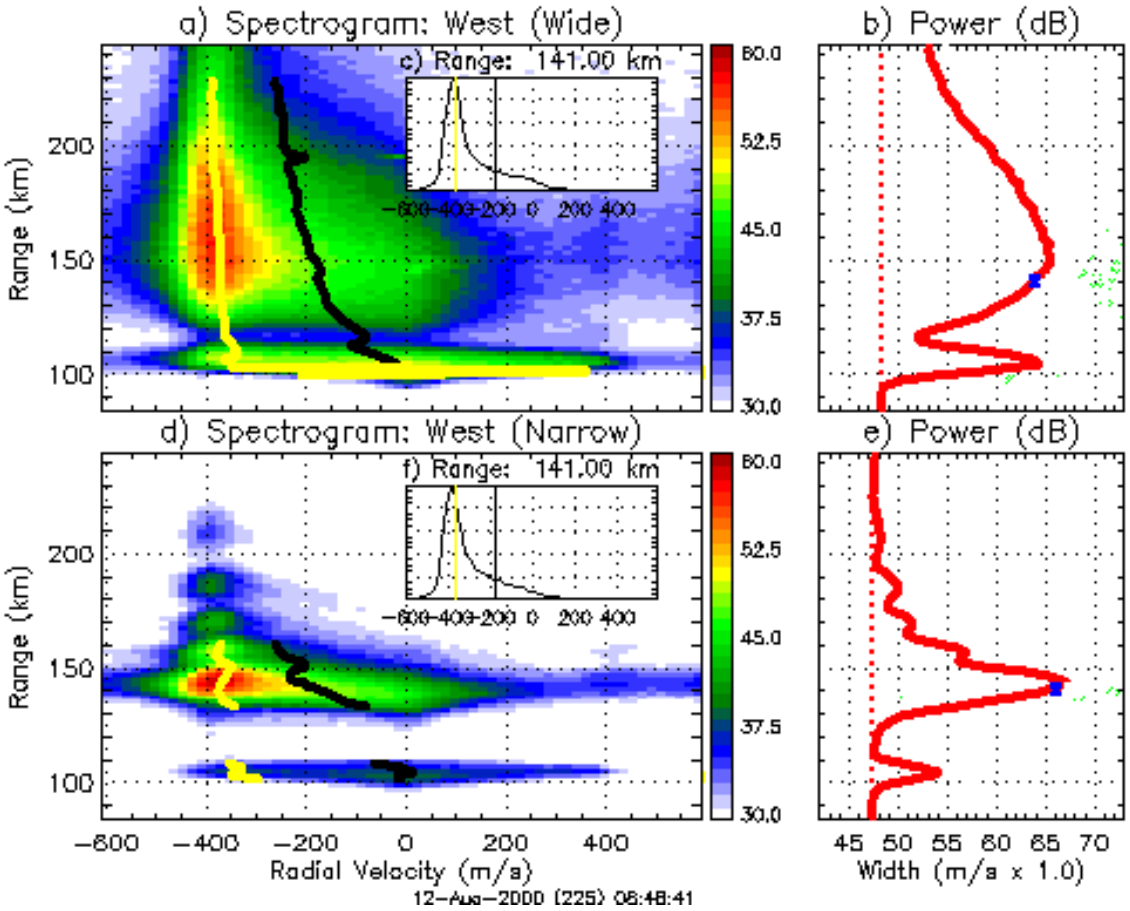

Figure 3. Examples of spectrograms from oblique observations of EEJ using wide beams (top) and narrow beams (bottom). The type I and type II Doppler shifts are indicated with yellow and black curves, respectively.

3. JULIA observations

As we mentioned in the Introduction, the observations of field-aligned irregularities, *E*-region irregularities in particular, are being performed more frequently at Jicamarca by using small transmitter units and small antenna arrays (JULIA concept). Figure 6, shows an example of the latest observing modes using the JULIA system. Between 1830 and 0600 *E* and *F* region irregularities are observed in interferometer mode (range scale on the left). Using the range scale on the right, oblique modes are used between 0600 and 0900 and between 1600 and 1830 using narrow (top) and wide (bottom) beams. Between 0900 and 1600 a narrow oblique beam mode (top) is used for observing the EEJ, while the main Jicamarca antenna is used for observing the 150-km echoes [e.g., *Kudeki and Fawcett*, 1993] (bottom).

Besides getting the day-to-day as well as seasonal variability of these irregularities, the main products of these observations can be summarized a follows: vertical and zonal

drifts at *E* and *F* regions heights between 1830 and 0600 LT, *E*-region zonal wind profiles and electric fields between 0600 and 1830. These observations started in 1996, and since then we have been increasing the number of observing hours every year. In 2002, we have observed close to 5000 hours on these JULIA modes.

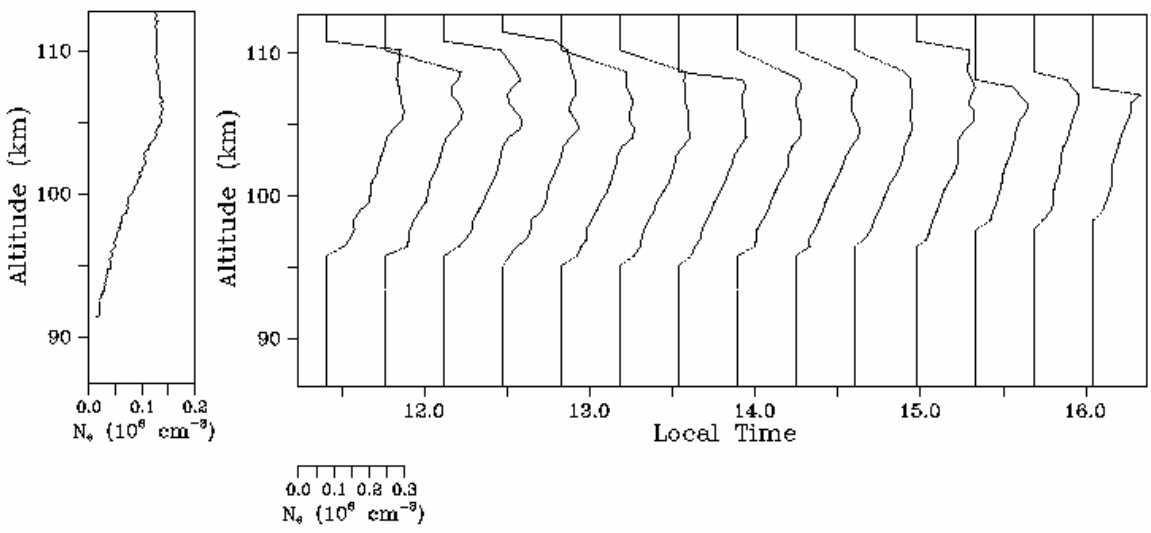

Figure 4. Examples of *E*-region density profiles obtained with a bistatic system (right). The left panel shows one of the few density profiles measured with rockets (from *Pfaff et al.* [1987]).

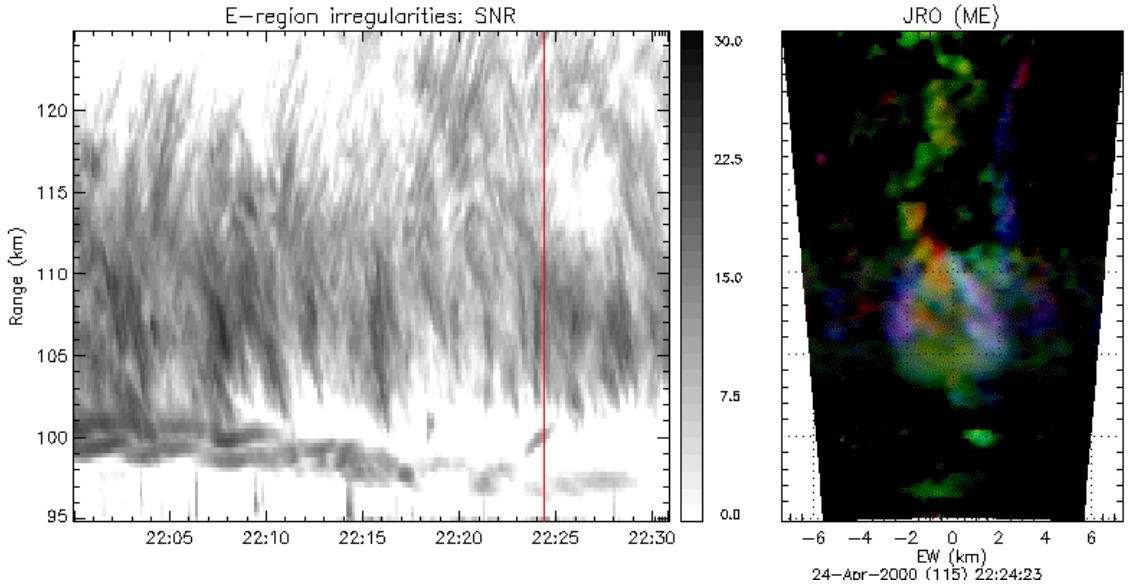

Figure 5. Example of nighttime *E*-region irregularities (a) RTI and (b) Image cut for the time indicated with the vertical red line. The image represents the structures inside the beam where the velocity has been color-coded. The intensity of the colors is proportional to the SNR.

Figure 7 show the occurrence statistics of nighttime *E*-region irregularities for 2002 as function of time of the day, and day of the year. The number of events (days) used to get these statistics are indicated below. Between February and March there were not too many observations. Although we need more years to derive strong conclusions, it appears that the nighttime equatorial *E*-region irregularities occur more frequently during the local summer and before sunrise.

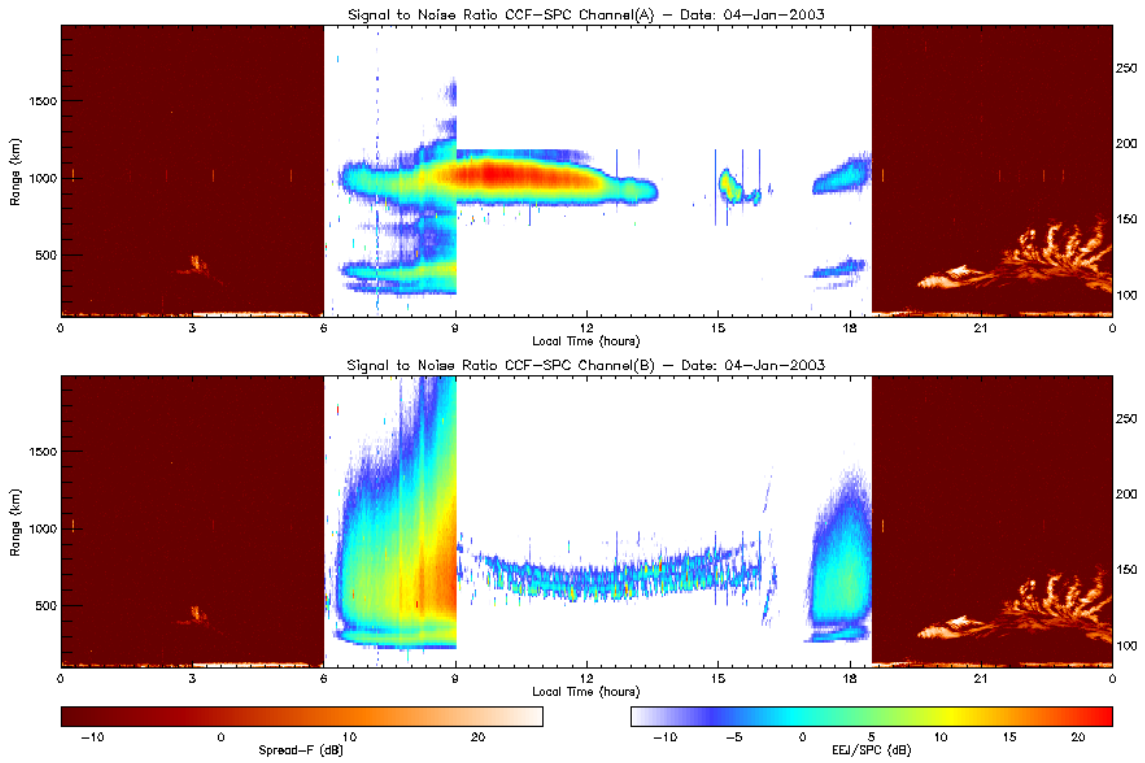

Figure 6. Example of JULIA observing mode (see text for details).

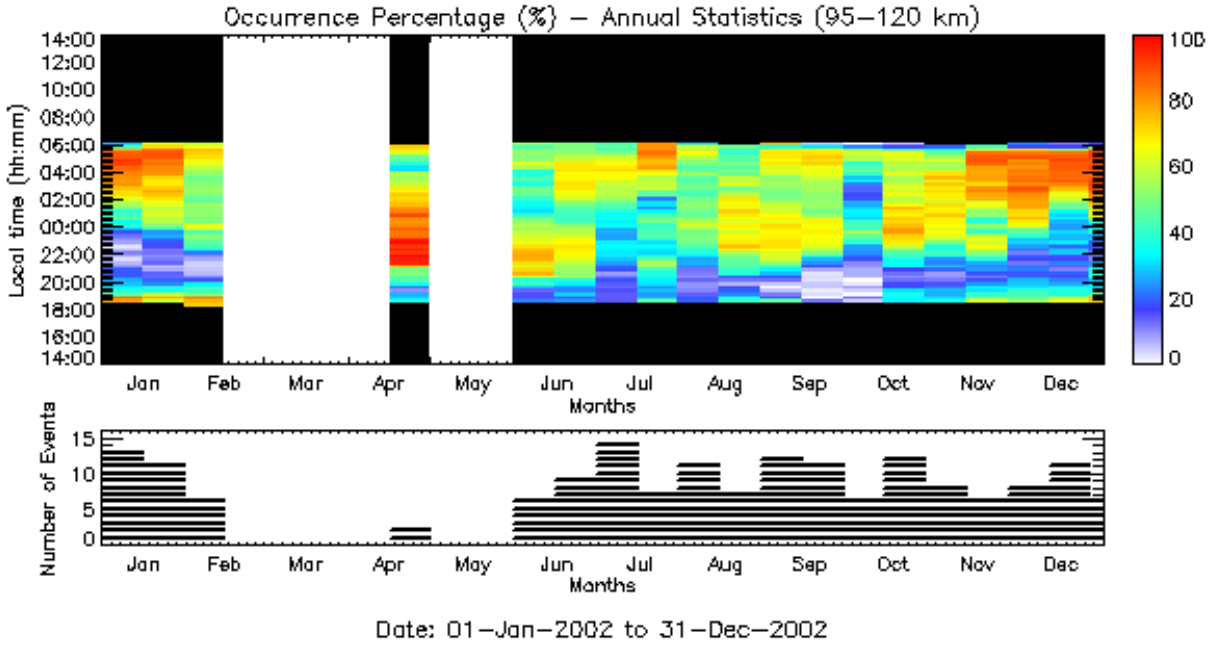

Figure 7. Statistical occurrence of nighttime *E*-region irregularities in 2002 as function of time of the day and day of the year. The number of events used for each period is indicated below.

4. Piura *E* region observations

Piura *E* region observations started in 1991. Since then intermittent measurements have been conducted on campaign basis. Figure 8 shows an example of SNR, Doppler velocity, and spectral width measurements. The main results derived from these intermittent observations are that Piura *E* region irregularities [*Woodman et al*., 1999]:

- Are characterized by type II echoes, i.e., generated by a gradient drift instability.
- Occur mainly at night.
- Occur in two distinct ranges, the upper echoes and lower echoes. Upper echoes present a patchy structure, wide spectral width and positive Doppler shift. Lower echoes are more continuous, have narrow spectral width and their Doppler velocities varies around zero.

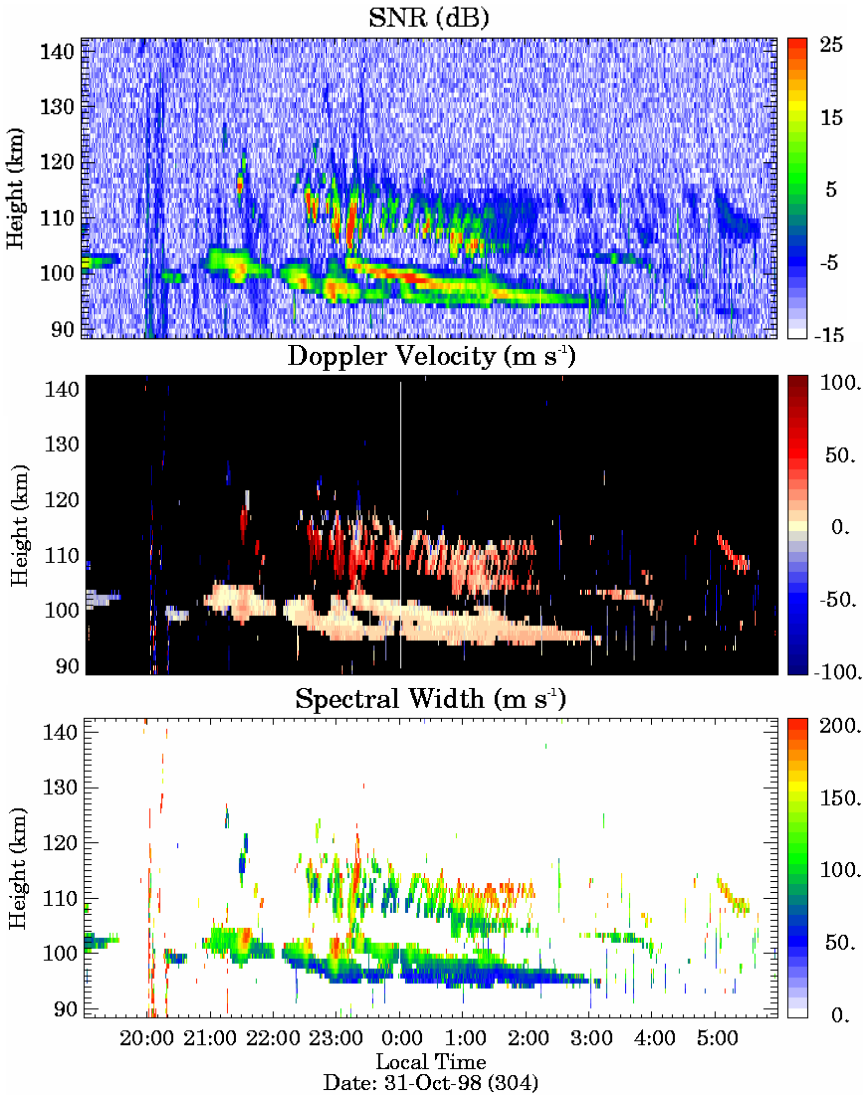

Figure 8. Example of nighttime *E*-region observations over Piura. SNR, Doppler velocity, and spectral width.

From the continuous measurements, we are able to obtain important statistics about these echoes. For example, in Figure 9 we show the percentage of occurrence of these echoes for the last three years for the upper (top) and lower (bottom) echoes as function of season and time of the day. It is clear that these echoes occur mainly at night. Moreover, as in the case of mid-latitude *E*-region echoes, at Piura the occurrence is higher during the summer (southern hemisphere). Note that Piura is located in the northern magnetic hemisphere but in the southern geographic hemisphere.

In addition, we are trying to derive electric fields and meridional winds from the Doppler information. The Doppler is basically a combination of the projected meridional wind and the **ExB** drifts. At lower altitudes where collisions dominate, the Doppler will be

mainly given by the meridional wind. On the other hand, at higher altitudes (above 105 km) the Doppler is given by the **E**x**B** drift. In Figure 10 we show the mean Doppler shifts for the upper and lower region for different seasons. In the upper region, the Doppler velocity is consistently positive (i.e., towards the radar) consistent with the **E**x**B** drifts measured at Jicamarca. The lower region Doppler velocities show a predominant annual variability [*Chau et al.*, 2002]. We expect to improve these crude estimates with proper modeling and compare them to other independent measurements.

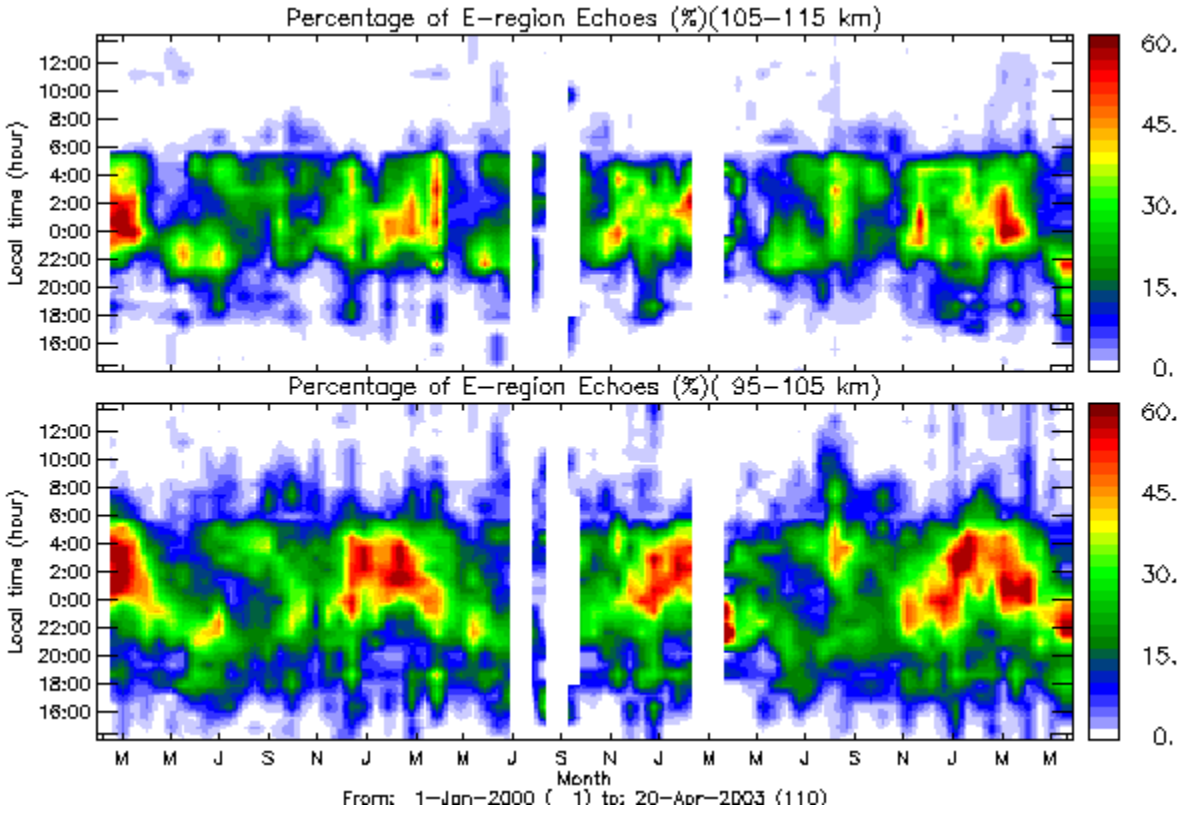

Figure 9. Percentage of occurrence of Piura *E*-region echoes for the upper and lower echoes between January 2000 and May 2003.

5. Summary

Observations are being carried out very frequently of *E* region irregularities under the EEJ region (Jicamarca) and outside the EEJ region (Piura). The main characteristics of the EEJ echoes are:

- They occur during day and night, but are stronger during the day.
- Spectral characteristics are of type I (very narrow spectra and high Doppler velocities) and type II (wide spectra) echoes.
- They are stronger and more frequent during the summer, based on 2002 observations.

Piura echoes are also more frequent and stronger during local summer but they occur mainly at night and present only type 2 echoes.

As we pointed out, a major effort is being placed to deriver ionospheric parameters at *E* region heights from the observations of these irregularities. Among other parameters currently under development, from Jicamarca EEJ echoes it is possible to get (a) zonal wind profiles, (b) electric fields, (c) density profiles, and perhaps (d) temperatures. Moreover, EEj echoes could be used for wireless communications purposes (see *Sarango et al.* this issue)

The main parameters that could be obtained from Piura *E* region measurements are (a) nighttime meridional winds from lower echoes, (b) nighttime electric fields from upper echoes.

Acknowledgements

The Jicamarca Radio Observatory is operated by the Instituto Geofísico del Perú, with support from the NSF Cooperative Agreement ATM-9911209 through Cornell University. The Piura wind profiler is operated by Laboratorio de Física of Universidad de Piura, Perú, with support from NOAA and from the National Science Foundation (NSF) under agreements ATM-9214657, ATM-9614613. The ionospheric observations have been partially supported from NSF agreements ATM-9813910.

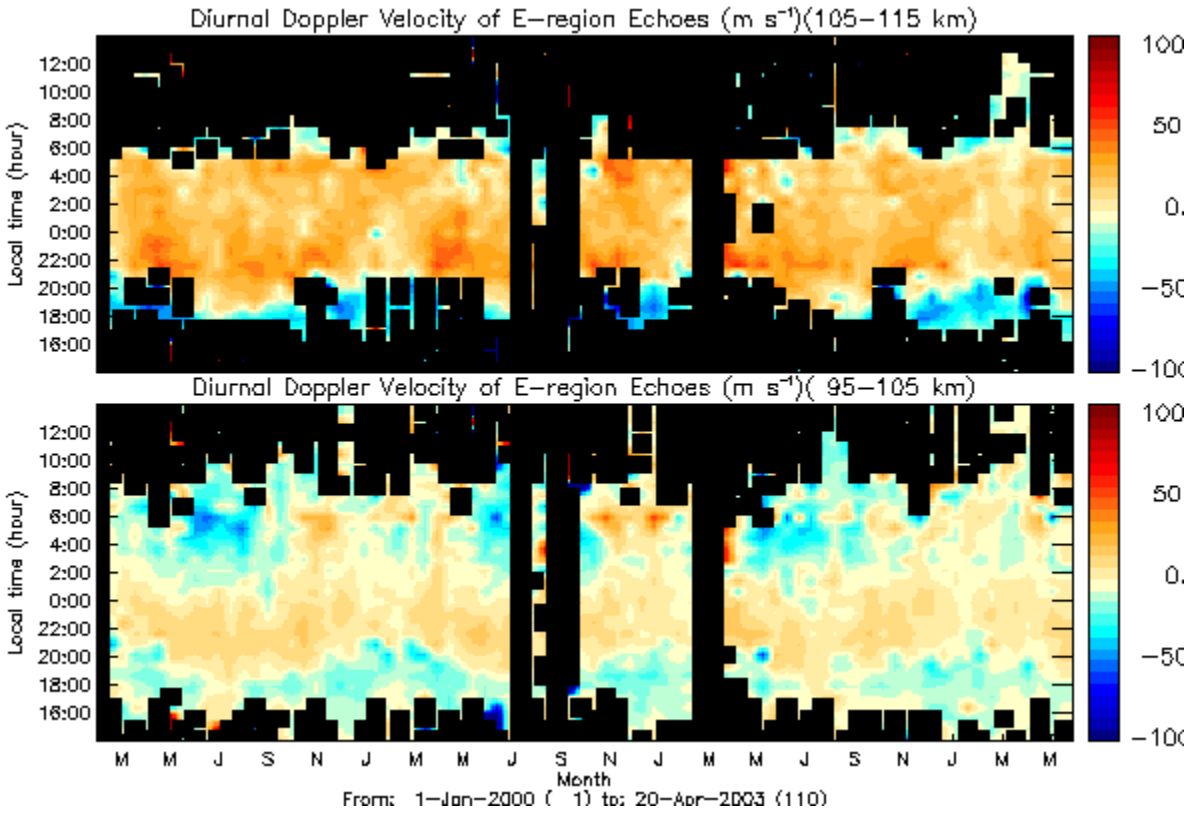

Figure 10. Doppler velocity statistics from Piura *E* region echoes for the upper and lower echoes between January 2000 and May 2003.

Bibliography

Balsley, B. B., Nighttime electric fields and vertical ionospheric drifts near the magnetic Equator, *J. Geophys. Res., 74*, 1213-1217, 1969.

Balsley, B. B., B. G. Fejer, and D. T. Farley, Radar measurements of neutral winds and temperatures in the equatorial *E* region, *J. Geophys. Res., 81*, 1457-1459, 1976.

Chau, J. L. and R. F. Woodman, Low-latitude quasiperiodic echoes observed with the Piura VHF radar in the E-region, *Geophys. Res. Lett., 26*, 2167–2170, 1999.

Chau, J. L., R. F. Woodman, L. A. Flores, Statistical characteristics of low-latitude ionospheric field-aligned irregularities obtained with the Piura VHF radar, *Annales Geophysicae, 20*, 1203-1212, 2002.

Cohen, R. and K. L. Bowles, Ionospheric VHF scattering near the magnetic equator during the International Geophysical Year, *J. Res. Natl. Bur. Stand. U. S., Sect. D, 67*, 459–480, 1963.

Farley, D. T., H. M. Ierkic, and B. G. Fejer, Radar interferometry: A new technique for studying plasma turbulence in the ionosphere, *J. Geophys. Res., 86*, 1467–1472, 1981.

Farley, D. T., Theory of equatorial electrojet plasma waves: New developments and current status, *J. Atmos. Terr. Phys., 47*, 729–744, 1985.

Farley, D.T., Early incoherent scatter observations at Jicamarca, *J. Atmos. Terr. Phys., 53*, 665-675, 1991.

Hysell, D. L. and R. F. Woodman, Imaging coherent backscatter radar observations of topside equatorial spread F, *Radio Sci., 32*, 2309–2320, 1997.

Hysell, D. L., and J. Burcham, Ionospheric electric field estimates from radar observations of the equatorial electrojet, *J. Geophys. Res., 105,* 2443-2460, 2000.

Hysell, D. L. and J. L. Chau, Inferring E-region electron density profiles at Jicamarca from coherent scatter, *J. Geophys. Res., 106*, 30 371–30 380, 2001.

Hysell, D. L., J. L. Chau, and C. G. Fesen, Effects of large horizontal winds on the equatorial electrojet, *J. Geophys. Res., 107*, 10.1029/2001JA000217, 2002.

Kudeki, E., D. T. Farley, and B. G. Fejer, Long wavelength irregularities in the equatorial electrojet, *Geophys. Res. Lett., 9*, 684–687, 1982.

Kudeki, E. and F. Sürücü, Radar interferometric imaging of field aligned plasma irregularities in the equatorial electrojet, *Geophys. Res. Lett., 18*, 41–44, 1991.

Kudeki, E. and C.D Fawcett, High resolution observations of 150 Km echoes at Jicamarca, *Geophys. Res. Lett., 20*, 1987-1990, 1993.

Kudeki, E., S. Bhattacharyya, R. F. Woodman, A new approach in incoherent scatter F-region E x B drift measurements at Jicamarca, *J. Geophys. Res., 104*, 28145-28162,1999.

Pfaff, R. F., M. C. Kelley, E. Kudeki, B. G. Fejer, and K. D. Baker, Electric field and plasma density measurements in the strongly driven daytime equatorial electrojet, 1, The unstable layer and gradient drift waves, *J. Geophys. Res., 92*, 13 578–13 596, 1987.

Sarango, M., J. Chocos, and R. F. Woodman, Point-to-point VHF communications via the equatorial electrojet, *this issue*.

Woodman, R. F., J. L. Chau, F. Aquino, R. R. Rodriguez, and L. A. Flores, Low-latitude field-aligned irregularities observed in the E-region with the Piura VHF radar: First results, *Radio Sci., 34*, 983–990, 1999.

THE ROLE OF UNSTABLE SPORADIC-E LAYERS IN THE GENERATION OF MIDLATITUDE SPREAD-F

C. Haldoupis[1], M. C. Kelley[2], G. C. Hussey[3], and S. Shalimov[4]

1: Physics Department, University of Crete, Iraklion, Crete, Greece
2: School of Electrical and Computer Engineering, Cornell University, Ithaca, NY. USA
3: Institute of Space and Atmospheric Studies, University of Saskatchewan, Saskatoon, Canada
4: The Institute of Physics of the Earth, Moscow, Russia.

1. Introduction

Mid-latitude spread-F is identified in the ionograms by the multiplicity and height spreading of the *F* region trace, caused by strong undulations and irregular plasma structuring in the *F* region electron density. Many of these disturbances are attributed to the passage of large-scale atmospheric gravity waves which can impose a wavelike altitude modulation in the *F* layer [*Bowman*, 1990], but also to electrodynamic forces and large-scale plasma instabilities [*Kelley and Fukao,* 1991]. The latter applies in particular to mesoscale spread-F with scales from a few tens to many tens of kilometres, which occurs overwhelmingly in the summer nighttime. Incoherent scatter radar (ISR) measurements from Arecibo, coherent-backscatter of aspect-sensitive *F* region irregularities, and airglow imaging observations, established a key property of the phenomenon, namely that it relates of plasma regions characterized by rapid turbulent upwelling and abrupt plasma uplifts. An uplift in the *F* region can be caused by upward and northward **E**x**B** plasma drifts driven by an eastward electric field and/or a meridional southward wind. The rapid upwelling of meter-scale irregularities observed by *Fukao et al.* [1991], which can be accounted for only in terms of **E**x**B** plasma motions, and the large electric fields inside spread-F measured by *Behnke* [1979] and inferred by *Swartz et al*. [2002], imply that these uplifts are caused by eastward electric fields rather than southward winds.

In this paper, we postulate that the eastward electric fields required for the *F* region uplifts, and therefore the generation of spread-F, are mapped up along the field lines from within strongly unstable sporadic E layers (E_s). This interpretation emerged from our present understanding of the unstable patchy E_s and from growing evidence for a link between mesoscale spread-F and unstable sporadic E. Here we present a new mechanism for spread-F generation in which the key role is played by polarization electric fields set up within westward-drifting E_s plasma patches and mapping up to *F* region. More details can be found in a paper by *Haldoupis et al* [2003] and a companion one by *Kelley et al.* [2003], both being in press in J.G.R.

2. Unstable Sporadic E Layers and Connection to Spread-F

The term "unstable E_s" refers to the situation when midlatitude sporadic E is destabilised by the gradient-drift and/or the Farley plasma instabilities, which leads to the generation of aspect-sensitive plasma irregularities that can scatter radio waves. The E_s-related echoes are found to possess mostly negative-mean Doppler shifts corresponding to northward and upward (away) velocities with magnitudes usually less than 100 m/s but also at times well above this limit, sometimes even exceeding 300 m/s [e.g., see *Haldoupis et al.,* 1997; *Swartz et al.,* 2002]. Since the echoes are due to **E**x**B** drifting irregularities, the observed velocities are attributable to enhanced eastward electric fields of several mV/m, well above the ambient dynamo fields at midlatitude.

Many radar studies show E_s echoes to associate with unstable plasma regions or structures, presumably patches of sporadic E, which drift across the radar field of view with the neutral wind. The zonal scale lengths of these patches were found to extend from a few km to many

tens of km (mostly between 20 and 100 km) and to drift westward prior to 0200 h local time with the neutral wind and speeds ranging from about 30 to 150 m/s. The inferred large westward winds during unstable E_s can help set up strong eastward polarization fields inside a plasma patch which then can drive the gradient-drift instability, and even the Farley (modified two-stream) instability. The existence of such fields is now understood in terms of a polarization process proposed by *Haldoupis et al.* [1997], which is the same as that at the magnetic equator but with the geometry turned on its side. This requires a sporadic E plasma patch with sharp, horizontal conductivity gradients at its edges that play the same role that vertical gradients play at the magnetic equator. In the presence of an ambient meridional field, a much stronger zonal field will build up inside the patch to maintain divergence-free current flow, just as a vertical polarization field builds up at the equator (which actually drives the equatorial electrojet) so that the vertical Hall and Pedersen currents nearly cancel.

Many studies show that unstable E_s associates with "spread E_s" which refers to patchy and spatially structured sporadic E rather than to continuous blanketing-type layers. This implies an electrodynamic link between unstable E_s and spread-F, given the close relationship between spread E_s and spread-F reported in several ionosonde studies {e.g., see *Bowman,* 1990).

Following suggestions that spread-F occurs in conjunction with unstable Es, we considered testing this theory by revisiting an older data set comprised of common-volume observations of 50-MHz Doppler backscatter and ionosonde recordings carried out over the southern Aegean Sea during summer 1996. The experiment included the Sporadic E SCATter experiment (SESCAT), a 50-MHz continuous-wave Doppler radar located on the northern coastline of Crete that was capable of observing coherent echoes from a fixed E region area about 160 km to the north, and a Canadian Advanced Digital Ionosonde (CADI) that was placed beneath the SESCAT field of view on the island of Milos. For the purposes of this work, we have tried a comparison between CADI spread-F and SESCAT observations. Since midlatitude backscatter is strictly a nighttime phenomenon, we considered only the 10-hour period from 1900 to 0500 LT when vertical incidence ionograms were recorded every 2 minutes. The idea was to inspect the data using quick-look plots and search for a relationship between the two phenomena. Surprisingly, we found a one-to-one relation in the occurrence of strong to moderate SESCAT echoes and CADI spread-F. During nights with a few short lived, low-intensity echoes or no echoes at all, spread-F was absent in the measured ionograms. The inspection of the two data sets indeed suggests a connection between the two phenomena. A quantitative analysis between the occurrence of the two phenomena, that is, the unstable E_s and spread-F, led to a good degree of correlation signified by a linear correlation coefficient near 0.8.

3. A New Mechanism for Generating Mesoscale Spread-F

Based on the SESCAT/CADI comparisons and published results elsewhere, we conclude that there must be a connection between mesoscale spread-F and unstable sporadic E. We postulate that this relation is sustained through electrical coupling of the two ionospheric regions, which allows mapping of electric fields up (down) the Earth's magnetic-field lines. Next, we introduce a new idea which can serve as a mechanism for generating mesoscale spread-F at midlatitude, as illustrated in Figure 1.

The schematic in Figure 1 shows highly conducting sporadic-E patches of metallic-ion plasma with abrupt boundaries drifting with the neutral wind in the nighttime *E* region. In the rectangular coordinate system, x is pointing horizontally to the east, y is perpendicular to the magnetic field pointing southward and downward, and z is along **B**. For simplicity, we ignore any bulk meridional motions and assume that the patches are drifting westward, as suggested by experiment. In accordance with the *Haldoupis et al.* [1997] polarisation mechanism, the total meridional field $E_y = E_y^0 + \mathbf{U}_x x \mathbf{B}$, can drive stronger eastward polarization fields, $E_x^p \cong$

$(\sigma_H / \sigma_P)E_y$ (where σ_H and σ_P are the Hall and Pedersen conductivities inside the Es patch, with a ratio $\sigma_H / \sigma_P \geq 10$). E_x^p in turn can cause strong northward and upward Hall electron drifts which, in conjunction with ambient meridional density gradients, can destabilize the plasma, even at times they might be strong enough to excite the Farley instability. In addition, they may also polarize the patch in the meridional direction, as shown in Figure 1, with a secondary polarization field E_y^p acting to reduce E_x^p. A steady state prevails when divergence-free conditions are established inside the patch through field-aligned current closures. The closure details, which depend upon the ionospheric conductivities and the patch dimensions, are described by *Shalimov et al.* [1998]. Finally, as shown in Figure 1, a westward electric field may also set in inside regions of low electron density as a result of the oppositely charged edges of neighboring E_s patches.

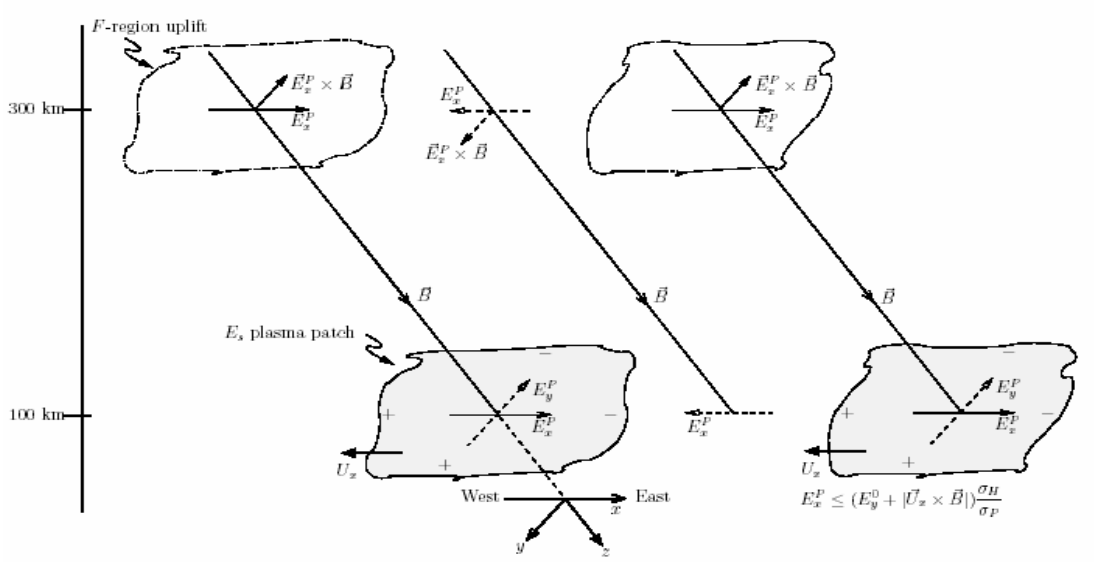

Figure 1. A new mechanism for generation of mesoscale Spread-F at midlatitude

Next, we postulate that the electric fields inside sporadic-E plasma patches map up along the field lines to *F* region altitudes. The effectiveness of mapping depends on the zonal extent of the E_s patch, l_x, and Farley's mapping factor, $(\sigma_0/\sigma_P)^{1/2}$, where σ_0 is the parallel or specific conductivity and σ_P is the Pedersen conductivity. So, the mapping distance along **B** is $l_z = l_x (\sigma_0 / \sigma_P)^{1/2}$. If we adopt a rather conservative value near 10 for $(\sigma_0 / \sigma_P)^{1/2}$, as suggested by *Swartz et al.* [2002], then l_x needs to be greater than about 15 km for the polarization fields, E_x^p, to map to *F* region altitudes higher than 250 km. These scale sizes are below the mean zonal extents measured for unstable E_s layers in various midatitude radar studies, thus we conclude that many of the E_s patches are sufficiently large for their polarization fields to map up to *F* region altitudes. Note that the typical zonal E_s scales measured by the Valensole radar in the south of France range from between 20 and more than 100 km, which seem to compare well with the spread-F azimuthal scales measured, for example, by *Fukao et al.* [1991].

The eastward fields mapped to the *F* region will act upon the magnetized plasma and thus impact upward and northward **E**x**B** drifts, causing *F* region uplifts and, therefore, spread-F. If we take a magnetic dip angle of about 50^0 and consider an eastward E_x^p field of 5 mV/m, this will cause a northward and upward **E**x**B** drift of about 110 m/s to act upon an *F* region volume and thereby produce a vertical plasma uplift of 60 km in about 10 minutes. For a larger eastward electric field of 12 mV/m, the northward and upward drifts will be 250 m/s, and an *F* region uplift of 60 km will form in only 4 minutes. These estimates are in agreement with the measurements of *Behnke* [1979] and *Swartz et al.* [2002], who quoted uplifts of 30 to 100 km, and also with the large negative (away) Doppler velocities measured by *Fukao et al.* [1991].

The remarkable observations of *Fukao et al.* [1991] showed that the spread-F plasma patches, dominated by negative (away) Doppler velocities, often displayed at their edges positive (toward) Doppler velocities, which implies southward and downward **E**x**B** plasma motions there. On rare occasions, the same experiments detected *F* region patches of scatter with negative (away) Doppler motions alternating with patches of backscatter having positive (toward) Doppler velocities. These Doppler-polarity reversals in the spread-F plasma structures may also be understood in terms of the conceptual model shown in Figure 1. The reason might be that the electric fields in the low-conductivity areas between sequential E_s patches reverse polarity and point westward. These fields appear because of opposite-polarity charge buildup at the neighboring edges of sequential E_s patches. If these westward fields also map up the field lines to the *F* region at times, then they can cause southward and downward plasma drifts and thus explain the positive (toward) Doppler motions of *Fukao et al.* [1991] quite nicely.

In summary, the proposed new mechanism seems to be capable of explaining key observational properties of mid-latitude spread-F at the mesoscale and has the advantage of having a simple physical base, in accord with existing experimental evidence and knowledge. On the other hand, we wish to stress that the proposed mechanism may not be capable of explaining all forms of spread-F, and more testing and research is necessary.

4. Acknowledgements

This work was made possible with support from the European Office of Aerospace Research and Development (EOARD), Air Force Office of Scientific Research, Air Force Research Laboratory, under contracts F61775-01-WE004 and FA8655-03-1-3028 to C. Haldoupis.

5. References

Behnke, R. A., F layer height bands in the nocturnal ionosphere over Arecibo, *Geophys. Res., 84,* 974, 1979.

Bowman, G. G., A review of some recent work on mid-latitude spread-F occurrence as detected by ionosondes, *J. Geomag. Geolectr., 42*, 109, 1990.

Fukao, S., M. C. Kelley, T. Shirakawa, T. Takami, M. Yamamoto, T. Tsuda, and S. Kato, Turbulent upwelling of the mid-latitude ionosphere. 1. Observational results by the MU radar, *J. Geophys. Res., 96*, 3725, 1991.

Haldoupis, C., D. T. Farley, and K. Schlegel, Type-1 echoes from the mid-latitude E-region ionosphere, *Ann. Geophys., 15*, 908, 1997.

Kelley, M. C., and S. Fukao, Turbulent upwelling of the midlatitude ionosphere. 2. Theoretical framework, *J. Geophys. Res., 96*, 3747, 1991.

Shalimov, S., C. Haldoupis, and K. Schlegel, Large polarization electric fields associated with midlatitude sporadic E, *J. Geophys. Res., 103*, 11,617, 1998.

Swartz, W. E., S. C. Collins, M. C. Kelley, J. J. Makela, E. Kudeki, S. Franke, J. Urbina, N. Aponte, S. Gonzalez, M. P. Siltzer, and J. S. Friedman, First observations of an *F* region turbulent upwelling coincident with severe *E* region plasma and neutral atmosphere perturbations, *J. Atmos. Solar-Terr. Phys., 64*, 1545, 2002.

STUDY OF A LOW E-REGION QUASI-PERIODIC EVENT FROM CAMP SANTIAGO, PUERTO RICO

Julio Urbina[1], Erhan Kudeki[2], and Steven J. Franke[2]

[1] Donaghey College of Information Science and Systems Engineering, University of Arkansas, USA

[2] Department of Electrical and Computer Engineering, University of Illinois, Urbana, Illinois, USA

1 Introduction

Recent papers by *Patra et al.*[2002], *Pan and Rao*[2002], *Rao et al.*[2000], and *Urbina et al.*[2000]). describe quasi-periodic VHF radar backscatter from lower E-region plasma irregularities detected at a number of low and mid-latitude radar sites. This newly discovered class of VHF radar echoes is observed below 100 km altitude and is referred to as "LQP" to distinguish it from better known QP (quasi-periodic) radar signatures detected at upper E-region heights [e.g., *Yamamoto et al.*[2001]]. At present there is considerable uncertainty about the generation mechanisms of LQP as well as the interpretation of LQP data sets. Uncertainties in data interpretation mostly originate from potential range/height ambiguities and/or the lack of knowledge about the background ionosphere where LQP irregularities grow.

The purpose of this paper is to offer an in depth discussion of a multi-sensor data set collected during an LQP event in an attempt to address some of the difficulties just mentioned. The event, first reported in *Urbina et al.*[2000], was observed with a 50 MHz radar interferometer (RI) operated from Camp Santiago, Puerto Rico, while simultaneous electron density measurements were being conducted nearby in the E-region with the 430 MHz Arecibo incoherent scatter radar (ISR). Figures 1 and 2, discussed in detail in Section 2, show some aspects of the experiment geometry as well as ISR and RI observations. The discussion in Section 2 is focused on the information extracted from different sensors and Section 3 explores the relationship between different sensor outputs. An LQP backscattering scenario compatible with all the observations is constructed and discussed in Section 4. It is shown that the observed event could not have been initiated by a gradient-drift plasma instability process despite the presence of sharp gradients in the background electron distribution.

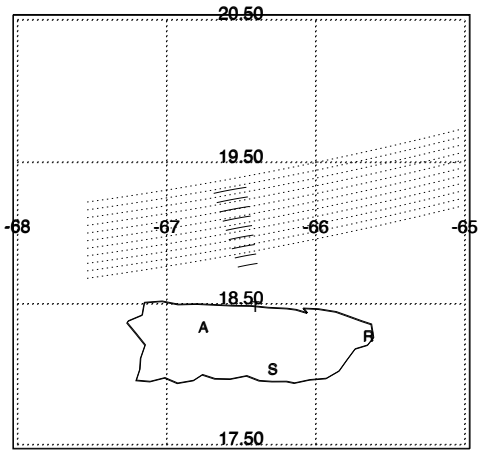

Figure 1: A map showing the Coqui 2 experiment geometry at E-region heights: Solid line segments indicate the geographical coordinates (longitude and latitude) where the viewing directions from the Camp Santiago (S) system cross the Earth's magnetic field at an angle of 90^o at radar ranges 120, 130, 140, ..., 200 km and between the first nulls of the gain patterns of the transmitting antenna. The dashed contours depict the geographical coordinates of perpendicularity at 90, 95, 100, ..., 140 km altitudes.

2 Multi-sensor observations of an LQP event

The location of the 50 MHz Camp Santiago radar interferometer (RI) is marked with an "S" in Figure 1. As discussed in detail in [**?**] the interferometer consisted of two antenna arrays with a 50 m east-west

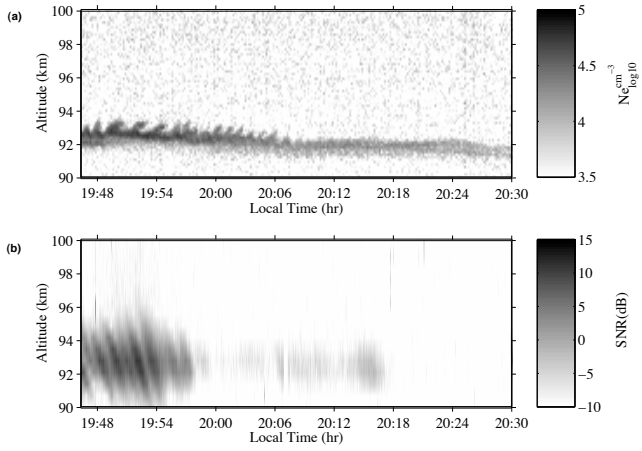

Figure 2: (a) Arecibo electron density collected during the evening of February 25, 1998. (b) Corresponding backscatter map of the low quasi-periodic (LQP) layer observed at Camp Santiago.

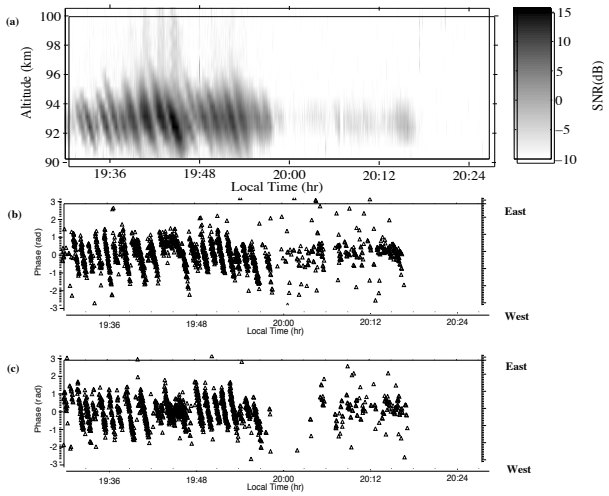

Figure 3: (a) Backscatter map showing the entire duration of the LPQ as observed by the Camp Santiago VHF system. (b) and (c) Phase-streak plots corresponding to scattering layers near 94.5 and 93.1 km, with coherence equal or greater than 0.7. Data shows a westward drift of ∼100 m/s.

separation and overlapping beam patterns pointed with a $\theta = 49^o$ zenith angle in the geomagnetic meridian plane. The radar observation volume along the beam boresight at E-region heights was at a range of approximately 140 km from Camp Santiago and about 65 km northeast of the vertical Arecibo beam within the E-region, marked by an "A" in Figure 1. Solid line contours in Figure 1 highlight the transmission beam of the interferometer antenna between its first nulls at different radar ranges (see the caption for a description of the two sets of contours). In the evening of February 25, 1998, the Arecibo ISR was operated in a high-resolution observation mode and produced the electron density map shown in Figure 2a. The map shows a narrow density layer centered about 92.5 km altitude containing corrugations or filaments on the topside of a few hundred meter heights. The filaments are tilted with positive slopes of $\frac{dz}{dt}$ ∼10 m/s and exhibit quasi-periodicity with mean period of $T \approx 100$ s or less. Figure 2b shows a backscattered power map obtained with the 50 MHz Camp Santiago RI system during the same time interval as that shown in Figure 2a. The backscattered power variation depicted in Figure 2b is also quasi-periodic, with a period of about 100 s, but the altitude extent of the tilted structures seen in Figure 2b is ∼3 km, much larger than seen in Figure 2a. Furthermore, the structures in Figure 2a exhibit a negative slope of $\frac{dz}{dt} \approx -40$ m/s.

The LQP event of Figure 2b started prior to 19:44 LT, which is the start time of the ISR data obtained at Arecibo and shown in Figure 2a. Figure 3a shows the full duration of the LQP event observed from Camp Santiago with the RI system. The event lasted about 30 minutes, and during the event, east and west antenna signals of the RI system were highly correlated and exhibited systematic phase variations corresponding to the drift of localized scattering regions through the system field of view. Figures 3b and c show time and position variations of the differential phase between east and west antennas. In both figures the phase data are organized in well defined streaks with a $T \approx 100$ s periodicity matching the periodicities in Figures 2 and 3a. The streaks indicate that backscattering regions drifted in the westward direction with a speed of about 100 m/s, i.e., $u \approx -100$ m/s using meteorological notation. With $|u| \approx$100 m/s and $T \approx 100$ s it follows that the east-west separation or "wavelength" of backscattering regions or structures is $\lambda_x = |u|T \approx 10$ km. Also, Doppler spectral analysis of VHF radar returns during the event showed a ∼50 m/s Doppler shift in the southward direction. Doppler velocities were steady when the layer was unstructured (before 1930 LT and after 2000 LT), but show some time variability when the layer becomes periodic The spectral widths were ∼30 m/s during the structured phase and less than 10 m/s before and after.

Although the vertical axis of backscattered power

map in Figure 2b (and Figure 3a) is labeled as "altitude", the measurement of backscattered power is in fact performed as a function of radar range, i.e., the radial distance of scattering targets from the radar antenna. The altitudes marked on the vertical axis were derived from radar range assuming that radar targets at 50 MHz are perfectly field aligned 3 m (Bragg scale) density waves propagating perpendicular to the geomagnetic field $\vec{B}$. Since Bragg scale density waves responsible for coherent backscatter at 50 MHz are known to be field aligned [e.g., *Huang et al.*[1995]], the labeling shown in Figure 2b is well justified and facilitates straightforward comparisons of ISR and RI data shown in Figures 2a and 2b. For instance, the mean altitude of the LQP layer in Figure 2b, $z \approx 93$ km, coincides very closely with the altitude of density filaments seen in Figure 2a.

In further comparisons of Figures 2a and b we also need to take into account the height resolutions of ISR and RI data. The ISR data were collected with a range resolution of 150 m which is also the effective height resolution in Figure 2a since the ISR beam was pointed in the vertical direction. RI measurements were conducted using an antenna beam with $\theta = 49^o$ zenith angle and 1.05 km transmitter pulse lengths yielding an effective height resolution of $1.05 \cos 49^o \approx 0.69$ km for Figure 2a. assuming that field aligned target hypothesis is perfectly valid. Notice that the height resolution in Figure 2b, ~ 700 m (or more if waves are not perfectly field aligned), is coarser than few hundred meter vertical extents of the topside density structures seen in Figure 2a. Therefore we cannot expect to see the structures of Figure 2a repeated in Figure 2b. The question is then, what is the cause of the LQP structures seen in Figures 2b and 3a? This will be addressed in the next section.

3 Data interpretation

Rejecting the possibility that quasi-periodic fluctuations portrayed in Figures 2a and b are uncorrelated — i.e., independent phenomena taking place at two different locations — we will describe in this section a radar backscattering scenario that explains the LQP signatures shown in Figure 2b. One reason why we think the structures are correlated is the fact that ISR filaments disappear at a later time than RI structures — that ordering is consistent (causal!) with $\sim$100 m/s westward drift inferred from interferometry data. Furthermore, at the given drift speed the $\sim$65 km distance between the observation volumes is only $\sim$11 minutes apart in time, which is shorter than the overall duration of the LQP event. Most importantly, however, we have seen such a large number of unstructured layers during the measurement campaign described in *Urbina et al.*[2000] that when exceptions occur simultaneously in both ISR and RI data with very closely matching periodicities we can't help but think that the exceptions are not coincidental.

We envision a horizontally extended tidal ion layer [e.g., *Urbina et al.*[2000]] centered about 92.5 km altitude with a rippled topside boundary. The topside ripple is periodic, has a $\sim$7 km periodicity in southwest direction, and travels in the same direction with $\sim$70 m/s speed. As the ripples pass through the vertical pointed Arecibo beam quasi-periodic topside filaments of Figure 2a are measured with $\sim$100 s period. We also envision that the rippled surface "carries" localized regions of enhanced Bragg scale waves in a way that reconciles the common periodicities of Figures 2a and b. In other words a specific phase of the periodic ripple structure is unstable for the Bragg scale density waves observed by the RI system.

The periodic ripple structure described above will have $\sim$100 m/s trace velocity and $\sim$10 km apparent wavelength measured in southward as well as westward directions. These numbers agree with u and λ_x estimates obtained from interferometry data concerning the east-west dynamics of scattering regions. They are also compatible with north-south dynamics of the scattering regions as follows: As the topside ripples travel in the southwest direction through $\sim$northward pointed beam of the RI system (see Figure 1) the radar range to the ripples within the beam will decrease at a rate proportional to the southward trace speed. Using a north-south trace velocity $v = -100$m/s we find that range will change at a rate $\frac{dr}{dt} = v \sin\theta \approx -100 \sin 49^o \approx -75$ m/s. This range rate applies to the ripples as well as any other quantity phase locked to the rippled surface including the localized regions of enhanced Bragg scale waves. Since the vertical axis of the power map in Figure 2b is in effect $z \equiv r \cos\theta$, it follows that $\frac{dz}{dt} = \frac{dr}{dt} \cos\theta \approx -75 \cos 49^o \approx -50$ m/s, which is approximately the observed slope of descending LQP structures shown in Figure 2b (as well as Figure 3a). Likewise, an apparent horizontal wavelength of $\lambda_y \approx 10$ km in north-south direction translates into an equivalent "vertical wavelength" of $\lambda_z = \lambda_y \cos\theta \sin\theta \approx 5$ km which matches quite closely the vertical separations of neighboring structures in Figure 2b. In above calculations $\theta = 49^o$ corresponds to the observation zenith angle of E-region returns as illustrated in Figure 4.

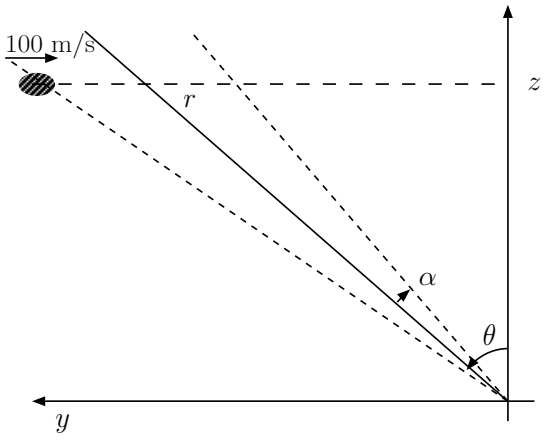

Figure 4: Geometry of the RI system sensitive to Bragg scale irregularities confined to a very narrow layer centered about altitude z.

Figure 4 illustrates the geometry pertinent for the RI system responding to Bragg scale irregularities confined to a very narrow (sub-resolution) altitude layer centered about some z. If Bragg scale irregularities within the layer are strictly field aligned then backscattering will only be possible in direction θ corresponding to a magnetic "aspect angle" of $\alpha = 0^o$ and a unique target range $\frac{z}{\cos\theta}$. Otherwise, i.e., if irregularities with non-zero α can exist within the same layer, backscattered echoes will arrive from ranges between $r_{min} = \frac{z}{\cos(\theta-\alpha)}$ and $r_{max} = \frac{z}{\cos(\theta+\alpha)}$. From earlier studies of magnetic aspect sensitivity of mid-latitude E-region echoes reported in *Huang et al.*[1995] we know that rms spread of aspect angle α can be as large as 0.2^o at about ∼101 km altitude and even larger at lower heights. By using z = 93 km and $\alpha = 0.8^o$, as well as $\theta = 49^o$, we find that $\Delta r \equiv r_{max} - r_{min} \approx 4.5$ km, or, equivalently, $\Delta z = \Delta r \cos\theta \approx 3$ km, which is close to the observed height extent of LQP structures in Figures 2b and 3a. Thus we find ourselves in a position to explain the LQP radar data of Figures 2 and 3 as follows: Due to physical mechanisms to be speculated about in the next section, regions of enhanced and nearly field-aligned Bragg scale (3 m) waves were formed and traveled within a periodic structure with a ∼7 km horizontal wavelength and ∼70 m/s velocity in ∼southwest direction (or more precisely, a 6.25 km wave with 62.5 m/s velocity along a bearing 51^o south of west if we are more careful with the data). Backscattering from these regions was detectible (above the noise floor) up to a magnetic aspect angle of $\pm 0.8^o$ as they transited the north looking radar beam at a fixed altitude of ∼93 km. Westward component of the motion of scattering regions within each gated radar scattering volume accounts for the quasi-periodic phase streaks of Figures 3b and c. Southward displacements of localized scattering regions register as descending power structures of Figures 2b and 3a given the height/range ambiguity inherent in power maps. In summary, some of the outcomes of this explanation are:

1. Velocities and scales inferred from power maps shown in Figures 2b and 3a are related to meridional dynamics of localized scattering regions,
2. Bragg scale irregularities responsible for coherent radar backscatter are observed over a finite range of aspect angles and the aspect sensitivity decreases with decreasing altitude,
3. Large scale density perturbation that organizes the Bragg scale regions is characterized by an aspect angle of about 30^o, indicating that the density filaments of Figure 2a are not at all field aligned.

4 References

Huang, C. M., E. Kudeki, S. J. Franke, C. H. Liu and J. Rottger, Brightness distribution of mid-latitude E-region echoes detected at the Chung-Li VHF radar, *Journ. Geophys. Res.*, *100*, 14,703, 1995.

Larsen, M. F., A shear instability mechanism for quasi-periodic radar echoes, *J. Geophys. Res.*, *11*, 41–44, 1999.

Pan, C. J., and P. B. Rao, Low altitude quasi-periodic radar echoes observed by the Gadanki VHF radar *Geophys. Res. Lett.*, *29*, 25-1, 2002.

Patra, A. K., S. Sripathi, V. S. Kumar, and P. B. Rao, Evidence of kilometer-scale waves in the lower e region from high resolution vhf radar observations over Gadanki, *Geophys. Res. Lett.*, *29*, 13,340, 2002.

Rao, P. B., M. Yamamoto, A. Uchida, I. Hassenpflug, and S. Fukao, Mu radar observations of kilometer-scale waves in the midlatitude lower e-region, *Geophys. Res. Lett.*, *27*, 3667–3670, 2000.

Urbina, J., E. Kudeki, S. J. Franke, S. A. Gonzalez, Q. Zhou, and S. Collins, 50 mhz radar observations of mid-latitude e-region irregularities at camp santiago, puerto rico, *Geophys. Res. Lett.*, *27*, 2853–2856, 2000.

Yamamoto, M., S. Fukao, R. F. Woodman, T. Ogawa, T. Tsuda, and S. Kato, Mid-latitude e region field-aligned irregularities observed with the mu radar, *J. Geophys. Res.*, *96*, 15,943–15,949, 1991.

INTERFEROMETER OBSERVATIONS OF THE BEHAVIOR OF E-REGION IRREGULARITIES IN THE MID-LATITUDE WITH THE CHUNG-LI VHF RADAR

C. L. Chen and C. J. Pan
Institute of Space Science, National Central University, Chung-Li, 32054, Taiwan
Email:s9643001@cc.ncu.edu.tw

Abstract

This paper presents observations of mid-latitude E-region irregularities with the 52-MHz Chung-Li VHF radar. The observations were carried out in interferometer mode to find out the behavior of these irregularities over time and space. The Range-Time-Intensity (RTI) plot obtained through power spectral analysis reveals the quasi-periodic (QP) structure of the backscattered echoes with different striations. Interferometer analysis of the observation for finding three-dimensional structure of the QP echoes shows that the different striations exist almost at same altitudes between 98 and 100 km till the echoes disappear. It is also observed the existence of multiple QP echoes visible at a time and exists at different range gates. The striations presented here show the characteristics of type-II echoes having negative slope. The study also gives a mathematical model for the motion of the echoes in three-dimensional plane.

Introduction

The occurrence of the QP echoes at mid-latitude was first observed with the middle and upper atmosphere (MU) radar in Japan (Yamamoto el al., 1991) and later from other latitudes also. The generation of these echoes explained in terms of atmospheric gravity waves modulating the sporadic E layers in such a way so as to make them non-locally unstable to gradient drift process (Woodman et al., 1991; Tsunoda et al., 1994). Recently Larsen (2000) proposed neutral wind shear instability to explain the spatial and temporal periodicities associated with QP echoes.

There are studies related to E-region echoes using interferometer techniques (Farley and Ierkic, 1981). These techniques extensively used to study the three-dimensional structure and behavior of the echoes. The three dimensional observations with 30 MHz radar (Hysell and Brucham, 2000) shows the QP echoes can be called as quasi-point target scatterers drifting through the radar beam at approximately constant altitude. This paper presents interferometer observation is carried out using 52 MHz Chung-Li VHF radar (24.9°N, 121°E), to understand the characteristics and behavior of the QP echoes.

Observation and Results

The Chung-Li VHF radar consists of three identical antennas, transmitter and receiver modules. We operated the Chung-Li VHF radar in the nighttime between 1800 to 0600 hrs LT from July 3-11 during 2000. The radar is operated with 4 μs pulse width (corresponding to range resolution of 600 m), inter-pulse period (IPP) of 1200 μs, coherent integration of four inter-pulse periods and with an observation window of 120.6 Km to 144 Km. To obtain the RTI map and range rate, 64-point fast Fourier transform (FFT) was utilized to compute the Doppler spectra of the echoes for each range gate of individual channel. Pronounced Es echoes were observed only in the period from 18:00 LT on July 3 to 06:00 LT July 4.

To obtain three-dimensional structure, complex normalized cross-spectral analysis is carried out. Cross spectrum of the echoes received by a pair of antenna modulus 1 and 2 is given by (Farley et al., 1981),

$$S_{12}(\omega) = \frac{\left\langle V_1(\omega) V_2^*(\omega) \right\rangle}{\left\langle \left|V_1(\omega)\right|^2 \right\rangle^{1/2} \left\langle \left|V_2(\omega)\right|^2 \right\rangle^{1/2}} = \left|S_{12}(\omega)\right| e^{i\Delta\phi_{12}(\omega)} \quad , \qquad (1)$$

Where the notations carry same meaning as in Farley et al. (1981). The magnitude or coherence $|S_{12}(\omega)|$ in (1) represents the measure of the localization of the targets in the echoing region, while the phase $\Delta\phi_{12}(\omega)$ of $S_{12}(\omega)$ is the averaged phase difference of the radar echoes received by the separated antenna modulus 1 and 2. In the similar way coherence and phase can be obtained from other module pairs 2 and 3 & 3 and 1 also.

The complex normalized cross spectrum is computed in accordance with (1), is ensemble averaged over 50 times (around 20 sec) to obtain coherence and phase. For the reliability of the estimate, the data were selected if the coherence is greater than 0.8. In order to apply radar interferometry, let z represents local zenith direction with the origin of the reference of coordinate system at the phase center of array 2. With this definition, y is toward 17 degree north by west and x is the axis normal to y and z. From the cross spectra computed from three antenna arrays, we can estimate the azimuth and elevation of the backscatter in each range gate. With the help of observed phase differences $\Delta\phi_{12}(\omega)$ and $\Delta\phi_{23}(\omega)$, the elevation angle $\theta(\omega)$ and azimuth angle $\phi(\omega)$ of target can be derived as following (Wang and Chu, 2001):

$$\phi(\omega) = \tan^{-1}[\tan\beta + \frac{d_{12}}{d_{23}\cos\beta}(\frac{\Delta\phi_{23}(\omega) + 2\pi m + \Delta\Psi_{23}}{\Delta\phi_{12}(\omega) + 2\pi n + \Delta\Psi_{12}})] - \beta\,, \tag{2}$$

$$\theta(\omega) = \cos^{-1}[\frac{\Delta\phi_{23}(\omega) + 2\pi m + \Delta\Psi_{23}}{kd_{23}\sin\phi}]\,, \tag{3}$$

where $k=2\pi/\lambda$ is the wave number, λ is the radar wave length), m and n are, respectively, the interferometry lobe numbers in vertical and azimuth directions resulting from grating lobe effect of interferometer, *and* $\Delta\psi_{12}(\omega)$ *and* $\Delta\psi_{23}(\omega)$ represent the system phase biases for antenna pairs 2-3 and 2-1. β is the angle difference between antenna pairs from right angle triangle. From simple geometry, we have $x = r\cos\theta\sin\phi$, $y = r\cos\theta\cos\phi$, $z = r\sin\theta$, where r indicate range, the elevation angle θ and azimuth angle ϕ that can be obtained from formulas (2) and (3).

Figure 1 shows the RTI plot obtained from backscattered signals detected with array 1. The results presented here are selected from 1820 to 1833 LT. Multiplicity of QP echoes, with up to four echoes being visible with in the scattering volume at a time. The simultaneous presence of multiple of QP echoes up to 8 to 9 striations are also reported else where (Tsunoda et al.,1999; Hysell and Burcham, 2000).

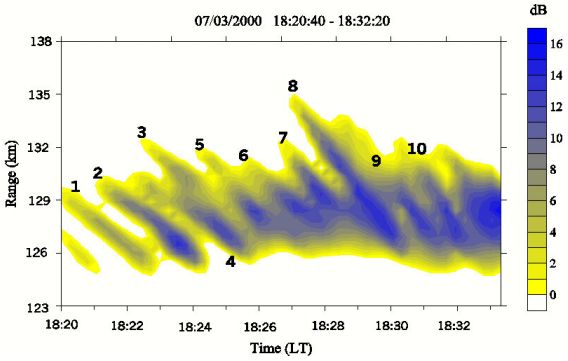

Figure 1. RTI plot at 1820-1833 LT on July, 2000. The numbers indicate QP echoes occur in the 13 minutes.

From the figure 1 it is clear that echoes varying with time for different striations, with negative slope representing the propagation is towards the radar. Interferometry data contains information about the spatial structure of the irregularities underlying the QP echoes. This helps to derive the 3-dimensional information of the backscatter in each range gate and the time history about the spatial variation of the QP echoes.

In Figure 2 we presented the eighth striation such that the conclusive results are the representative case of the observations of Chung-Li VHF radar. The first two panels are range

vs. x and y axes respectively. The third panel displays x-y plane projected motion. The bottom panel is altitude vs. x-axis. Time variation is from left column to right column. Its range distribution shows from 134 down to 126 km (the extent is about 8 or 9 km). Viewing sequences of columns (corresponding to time variation) reveals that the eighth striation drifted southeast and reside at the altitude between 98 and 100 km. Similar characteristics is observed in all striations of QP echoes. In order to show the detailed altitude behavior of the QP echoes more clearly, ten striations were plotted together in Figure 3. When plasma irregularities drifted into the radar scattering volume, they reside in approximately constant altitude between 98 and 100 km. Similar observations were made by Hysell and Burcham (2000) but between altitudes 95 to 120km.

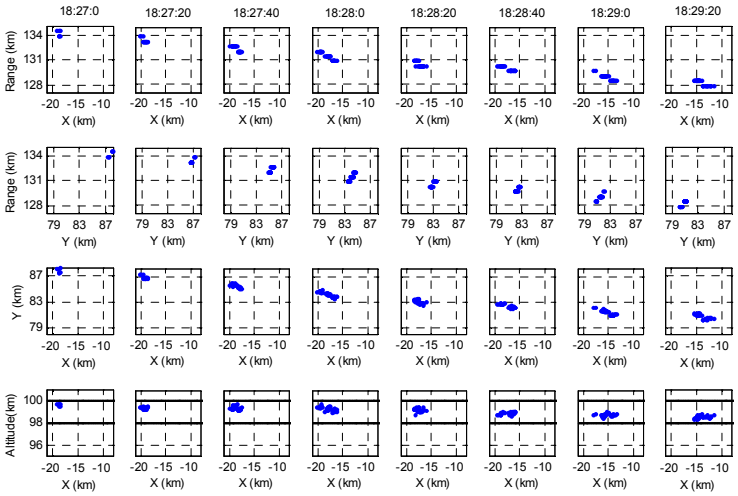

Figure 2. Series of three-dimensional distribution of the eighth striation of QP echoes at 18:27:00-18:29:20.

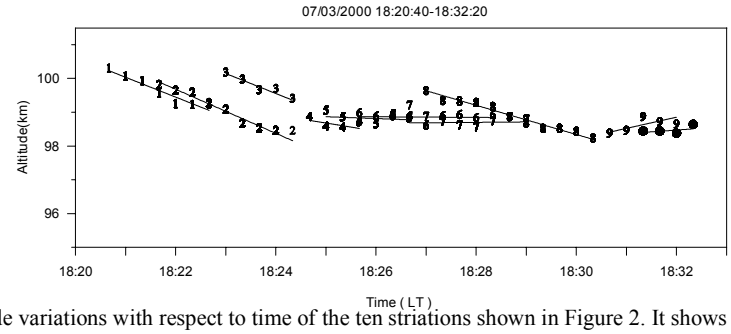

Figure 3. Altitude variations with respect to time of the ten striations shown in Figure 2. It shows average altitudes only.

From the above observations, we propose an interpretation of the striations of the QP echoes as they are the traces of the quasi-point targets drift across the radar scattering volume with constant velocity and altitude, that is to say it moves as a plane motion as displayed in Figure 4.

We propose a mathematical model for obtaining the range rate of the echoes in three-dimensional plane. Suppose the coordinate of the target is P(x, y, z), horizontal velocity $U = (\frac{dx}{dt}, \frac{dy}{dt}, 0)$, $R = \sqrt{x^2 + y^2 + z^2}$.

Where x = Rcosθsinφ, y = Rcosθcosφ, z = Rsinθ, θ and φ are elevation and azimuth angles respectively.

Then we obtain the range rate $$\frac{dR}{dt} = \cos\theta \sin\phi \frac{dx}{dt} + \cos\theta \cos\phi \frac{dy}{dt}. \qquad (4)$$

Where *dx/dt* and *dy/dt* are the velocity projections of the target in the x and y plane respectively. The range of elevations and azimuths for the experiment lies between $48^o \le \theta \le 53^o$, $-15^o \le \phi \le 5$ respectively, or in other words $|\cos\theta \sin\phi| \le 0.18$ and $0.58 \le \cos\theta \cos\phi \le 0.67$. Figure 5 presents the correlation of the estimated range rates from the observation and that of obtained from the model (4). The result shows very good agreement between observation and estimated values with the correlation coefficient near to 0.8.

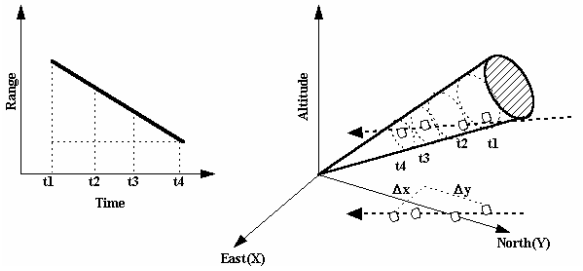

Figure 4. Left plot display range time plot for a striation. Right plot is the counterpart of simple geometry of quasi-point target's plane motion at a constant altitude with a fixed velocity.

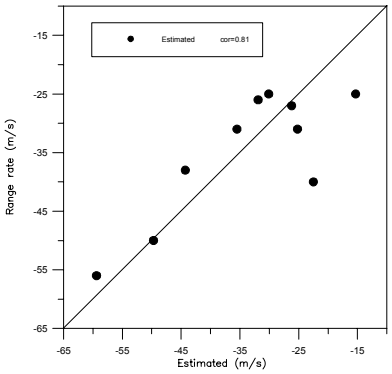

Figure 5. Correlation of the range rates using observation and model based estimation for ten striations.

Conclusion

We now summarize the three dimensional behaviors of the QP echoes revealed by the interferometry observations. The echo patches were localized. These echoes drifting through the radar beam around 98 and 100 km altitudes. Although, there were four striations being observed by the radar at one time, but three-dimensional structures of the QP echoes displayed in different range gate as it is viewed in RTI plot revealed that they resided at approximately constant altitude, and were shown at different region on the horizontal plane. So, the results suggest that the three dimensional behavior of the QP echoes from interferometry data prefer to interpret as quasi-point target scatterers. Range rate estimation through the model also shows good agreement with observation.

References:

Farley, D.T., Ierkic, H.M., Fejer, B.G., Radar Interferometry: a new technique for studying plasma turbulence in the ionosphere, *J. Geophys. Res.,86*, 1467-1472,1981.

Hysell, D.L., and J.D. Burcham, The 30-MHz radar interferometer studies of midlatitude E region irregularities, *J. Geophys. Res.,105*, 12797-12812,2000.

Larsen, M.F., A shear instability seeding mechanism for quasiperiodic radar echoes, *J. Geophys. Res.,105*, 24931-24940,2000.

Tsunoda, R.T., S. Fukao, and M. Yamamoto, On the origin of qsasi-periodic radar backscatter from midlatitude sporadic E, *Radio Sci., 29*, 349-365,1994.

Tsunoda, R.T., J.J. Buoncore, A. Saito, T. Kishimoto, S. Fukao, and M. Yamamoto, First observations of quasiperiodic radar echoes from Standford, California, *Geophys. Res. Lett., 26*, 995-998,1999.

Wang, C.Y. and Y.H. Chu, Interferometry investigations of blob-like sporadic E plasma irregularity using the Chung-Li VHF radar, *J. Atmos. Solar-Terr. Phys*.,63,123-133,2001.

Woodman, R.T., M. Yamamoto, S. Fukao, Gravity wave modulation of gradient drift instabilities in mid-latitude sporadic E irregularities, *Geophys. Res. Lett., 18*, 1197-1200,1991.

Yamamoto, M.,S. Fukao, R.F. Woodman, T. Ogawa, T. Tsuda, and S. Kato, Midlatitude E region field-aligned irregularities observed with the MU radar, *J. Geophys. Res.,96*, 15943-15949,1991.

IN BEAM RADAR IMAGING OF IONOSPHERIC IRREGULARITIES

D. L. Hysell[1], M. F. Larsen[2], and J. L. Chau[3]

(1) Earth and Atmospheric Sciences, Cornell University, Ithaca, New York USA
(2) Department of Physics, Clemson University, Clemson, South Carolina USA
(3) Jicamarca Radio Observatory, Lima, Peru

Synthetic aperture imaging was introduced to the radar community at Jicamarca by *Kudeki and Sürücü* (1991) who used it to observe primary plasma waves in the equatorial electrojet for the first time. In the years since, high-resolution observations of *E* and *F* region plasma irregularities at Jicamarca have been made with a growing number of interferometry baselines (*Hysell*, 2000; *Hysell and Chau*, 2002). Radar imaging has also been implemented at the Piura MST radar and the MU radar in Japan for studies of midlatitude sporadic *E* layers and neutral atmospheric turbulence (*Chau et al.*, 2003; *Hysell et al.*, 2002). Presently, it is being utilized at the High Latitude Monitoring Station (HLMS) in Anchorage to monitor 30 MHz backscatter from the auroral electrojet on a campaign basis. Wherever radar systems with multiple receivers are available, aperture synthesis imaging can be used to produce unambiguous, high-resolution images of the radar backscatter from the illuminated volume with minimal reliance on assumptions about the scatterers present and the data quality.

It is well known that interferometry using a single antenna baseline yields two moments of the radio brightness distribution, the distribution of received power versus bearing (*Farley et al.*, 1981). Interferometry with multiple baselines yields multiple moments, and the totality of these moments can be inverted to reconstruct the brightness distribution versus azimuth and zenith angle. The inversion essentially amounts to performing a Fourier transform of the interferometry cross-spectra or visibility (*Thompson*, 1986). However, since the cross-spectra are inevitably sampled incompletely due to the limited number of interferometry baselines available, and in view of the presence of statistical fluctuations in the data, the inversion is underdetermined and ill-conditioned must be performed using statistical inverse methods to achieve satisfactory results (*Jaynes*, 1982).

For imaging work at Jicamarca, we employed the MAXent algorithm pioneered for applications in radio astronomy and motivated by the "first principle of data reduction" [*Ables*, 1974, p. 383]: "The result of any transformation imposed on the experimental data shall incorporate and be consistent with all relevant data and be maximally noncommittal with regard to unavailable data." The transformation from the visibility to the brightness spectrum that adheres to this philosophy is the one which maximizes the "entropy" of the map in the information theory sense. *Shannon and Weaver* (1949) defined entropy as a measure of the uncertainty associated with a probability distribution function; the greater the entropy of a proposition, the greater the number of questions that must be asked to ascertain if the proposition is true. Choosing a proposition (or an image) with less than the maximum entropy implies that the analyst knows the answers and is therefore only warranted if existing data support the departure. Jaynes' principle then says that maximizing the entropy of an image while maintaining consistency with the measurements in a chi-squared sense is the way to obey Ables' principle.

In the case of aperture synthesis imaging, the image with the highest entropy is the one least committal to unmeasured data. Not only is it the most likely brightness spectrum, it is the one near which most other possible spectra are concentrated in solution space. To choose a spectrum with lower entropy would be to ignore the majority of possible outcomes of the inversion problem and focus on a less likely subclass of solutions, an unwarranted step unless the data support it. By merely formulating the problem in terms of entropy, we exclude from the solution space images with negative components which are obviously unsuitable. The

non-negativity of the image is prior information which, when incorporated into the image inversion along with any other information available, permits finer resolution than the Nyquist sampling theorem would otherwise allow. A compelling discussion of the rationale for the MaxEnt along these lines has been given by *Jaynes* (1982). Other reviews of the MaxEnt principle have been given by *Jaynes* (1985), *Daniell* (1991), and *Skilling* (1991). The computational algorithm we follow in our radar work has been described by *Hysell and Woodman* (1997). It requires the analyst to supply all available radar interferometric cross-spectra along with estimates of the error covariances. Our problem differs from the one in radio astronomy mainly in that radar range gating adds the third dimension to the images. In addition, the time evolution of the scattering medium in the radar case can be evaluated by comparing images from successive data integrations.

What follows are three examples of radar images drawn from low-, middle-, and high-latitude experiments. They illustrate the efficacy of radar imaging in situations where an unambiguous or high-definition determination of the target bearing is essential. At Jicamarca, high-resolution images are necessary for observing the fine structure in equatorial spread *F* flows. In mid-latitude experiments conducted in the Caribbean, radar imaging allowed unambiguous common-volume radar experiments to be performed in conjunction with operations at Arecibo. Radar imagery of auroral zone irregularities can be compared directly with *in situ* measurements made by rockets whose tracks can be followed in the radar images.

At Jicamarca, imaging has become an integral part of research into equatorial spread *F*. In postsunset *F* region imaging experiments, we observe the growth and evolution of large-scale plasma depletions and radar plumes as thin, precursor scattering layers evolve into full-blown ESF events (*Hysell*, 2000). An example of a fully developed radar plume is shown in Figure 1. The brightness of each pixel represents the signal-to-noise ratio on a log scale, the hue represents the first

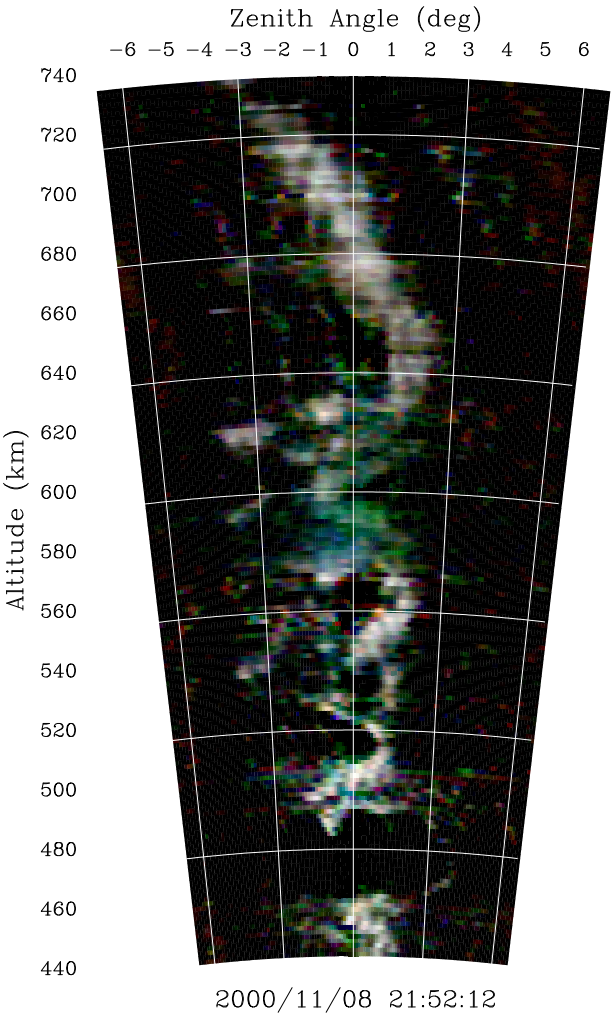

Figure 1: Radar image of plasma irregularities in a radar plume during a fully developed ESF event over Jicamarca.

moment Doppler velocity (red shifted echoes are red, blue shifted are blue), and the saturation represents the spectral half width (pure colors are spectrally narrow, pastel colors are broad.)

Notice the serpentine, branched, fractal quality of the plume in the image. The structuring is mainly due to secondary, wind driven gradient drift instabilities that form once the plume has developed. Animated sequences of images like this one elucidate the evolution of the underlying instability, the background flow surrounding the plume, and the dynamics of the plume once fully evolved. The two-dimensional images are spatially and temporally unambiguous and are directly comparable to numerical simulations.

Figure 2 presents an example of mid-

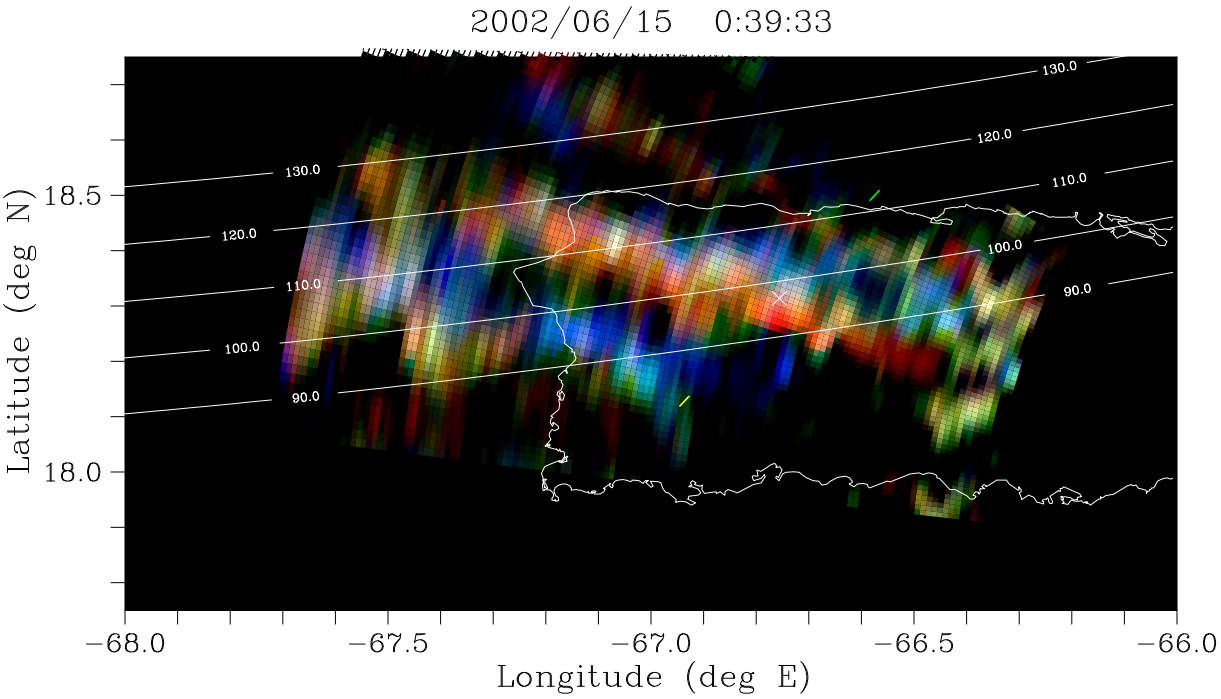

Figure 2: Radar image of coherent *E* region echoes received over Arecibo at 0039 UT by a portable 30 MHz radar imager deployed on St. Croix.

latitude *E* layer quasiperiodic (QP) echoes. While QP echoes mainly arrive from patchy, drifting sporadic *E* layers, they sometimes appear instead to be organized along wavefronts. In Figure 2, a large-scale wave with wavefronts running from northwest to southeast is shown. The wavelength is about 30 km, and the period is about 10 min. Animated sequences of images confirm that the wave propagates to the southwest. Doppler shifts alternate from large positive to negative values. These are the line of sight phase speeds of the small-scale irregularities observed from St. Croix. We expect these phase speeds to be mainly indicative of polarization electric fields in the direction normal to both the radar line of sight and to the geomagnetic field. That is, northeastward and upward or southwestward and downward, approximately normal to the wavefronts in Figure 2. Overall, the images suggest a large-scale electrostatic wave moving through the region.

Finally, Figure 3 shows an image of echoes from the auroral electrojet during a time when rockets launched from the Poker Flat research range were in flight. Each pixel in the image represents a complete Doppler

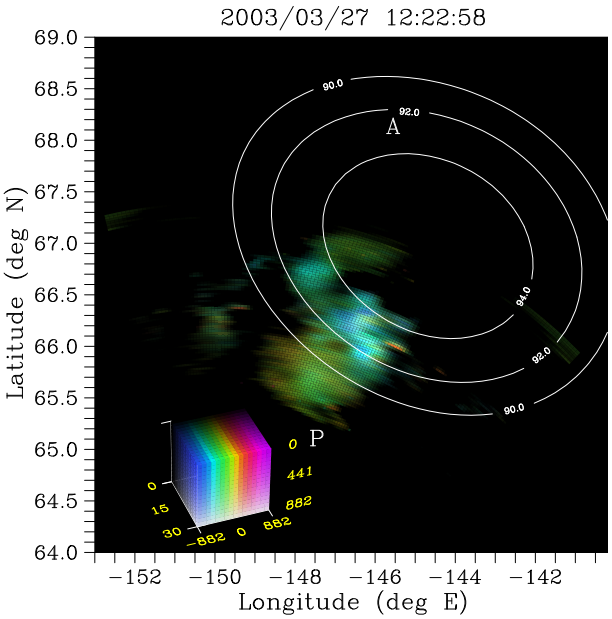

Figure 3: Radar image of auroral *E* region coherent backscatter. The “P” and “A” characters represent Poker Flat and Arctic Village, respectively. Anchorage, the site of the radar, is off the bottom edge of the image. The ovals are the loci of perpendicularity at different *E* region altitudes.

spectrum corresponding to the backscatter from Farley-Buneman waves. Note that the main transmitting antenna beam for the radar was directed toward Arctic Village, explaining why the image peripheries are mainly dark. Backscatter is received from those regions where the threshold condition for instability is satisfied. For the most part, the individual Doppler spectra contain combinations of type 1 and type 2 echoes. Abrupt changes in image brightness, hue and saturation from range to range and azimuth to azimuth signal changes in the convection electric field magnitude and/or direction. The scale sizes of these variations are kilometric and are invisible to other ground-based instruments.

Animated sequences of auroral electrojet images spaced in time by a few seconds convey a sense of the rapid evolution of the radar aurora and the underlying convection pattern at intermediate and small scales. Fine time resolution as well as spatial resolution is evidently necessary to compute accurate convection patterns and derived quantities like Joule heating rates if the results are to remain uncontaminated by coarse averaging.

References

Ables, J. G., Maximum entropy spectral analysis, *Astron. Astrophys. Suppl. Ser., 15*, 383, 1974.

Chau, J. L., D. Scipion, and L. A. Flores, Interferometric observations of *E* region field-aligned irregularities with the Piura VHF radar, paper presented at the IUGG 2003 meeting, June 30 – July 11, Sapporo, Japan, 2003.

Daniell, G. J., Of maps and monkeys. In Buck, B., and V. A. Macaulay, editors, *Maximum Entropy in Action*, chapter 1, pages 1–18. Clarendon, Oxford, 1991.

Farley, D. T., H. M. Ierkic, and B. G. Fejer, Radar interferometry: A new technique for studying plasma turbulence in the ionosphere, *J. Geophys. Res.*, *86*, 1467, 1981.

Hysell, D. L., A review and synthesis of plasma irregularities in equatorial spread *F*, *J. Atmos. Sol. Terr. Phys.*, *62*, 1037, 2000.

Hysell, D. L., and J. L. Chau, Imaging radar observations and nonlocal theory of large-scale waves in the equatorial electrojet, *Ann. Geophys.*, *20*, 1167, 2002.

Hysell, D. L., and R. F. Woodman, Imaging coherent backscatter radar observations of topside equatorial spread *F*, *Radio Sci.*, *32*, 2309, 1997.

Hysell, D. L., M. Yamamoto, and S. Fukao, Imaging radar observations and theory of type I and type II quasiperiodic echoes, *J. Geophys. Res.*, *107*, 1360, 2002.

Jaynes, E. T., On the rationale of maximum-entropy methods, *Proc. IEEE*, *70*, 939, 1982.

Jaynes, E. T., Where do we go from here? In Smith, C. R., and W. T. Grandy, Jr., editors, *Maximum-Entropy and Bayesian Methods in Inverse Problems*, pp. 21-58. D. Reidel, Dordrecht, 1985.

Kudeki, E., and F. Sürücü, Radar interferometric imaging of field-aligned plasma irregularities in the equatorial electrojet, *Geophys. Res. Lett.*, *18*, 41, 1991.

Shannon, C. E., and W. Weaver, *The Mathematical Theory of Communication*, Univ. of Ill. Press, Urbana, 1949.

Skilling, J., Fundamentals of MaxEnt in data analysis. In Buck, B., and V. A. Macaulay, editors, *Maximum Entropy in Action*, chapter 2, pages 19–40. Clarendon, Oxford, 1991.

Thompson, A. R., *Interferometry and Synthesis in Radio Astronomy*, John Wiley, New York, 1986.

FURTHER OBSERVATIONS OF PMSE IN ANTARCTICA

Martin F. Sarango[1], Ronald F. Woodman[1], Luis A. Flores[2] and Santos Villegas[1]

1. Jicamarca Radio Observatory, Apartado 13-0207, Lima 13, Peru
2. Universidad de Piura, Laboratorio de Fisica y Meteorologia, Apartado 353, Piura, Peru

1. Introduction

Here we present and analyze PMSE data from the 2001 Antarctic summer campaign. Observations were performed at the Artigas Uruguayan Station using a 15m x 15m Yagi array. We compare the Artigas results with those obtained in our previous Antarctic summer campaigns (published or reported at MST conferences). Previously we had used the Machu-Picchu Station radar using a 50m x 50m COCO array. Machu-Picchu and Artigas stations are separated 30 Km, both located on King George Is. in Antarctica.

A strong difference in the magnitude of PMSE between the 2001 and the previous campaigns can be observed for the whole season. Furthermore, it is surprising and intriguing that the ~10 dB smaller Yagi array at Artigas (225 m^2) detected stronger echoes than the COCO array at Machu-Picchu (2500 m^2). Although a Yagi array can be more efficient than a COCO array of similar dimensions, we have found from calibration experiments that this is not enough to explain such a discrepancy (see companion paper). After reviewing the alternatives to explain these differences, we conclude that there is evidence that the intensity difference is due to annual variability in the scattering phenomena

2. The Machu-Picchu and Artigas radar facilities

The MST radar facility located at the Machu-Picchu Peruvian Station, in Antarctica (62°06'S, 58°28'W), was used by the Peruvian Atmospheric Research Group in collaboration with the University of Colorado at Boulder, to make the first PMSE measurements in the Southern Hemisphere (1994). Results from the 94-99 PMSE observation campaigns have been published or reported in the literature (Balsley et al., 1995 and Woodman et al., 1999). Among the contributions of Machu-Picchu radar, we can mention the conclusions concerning the existence of an Arctic-Antarctic inter-hemispheric asymmetry in PMSE intensity.

Motivated by these findings, a new VHF radar was installed by the same research group nearby the Artigas Uruguayan site (62°11'S 58°54'W) in December, 2000. This radar was used to perform PMSE observations during the 2000-2001 austral summer.

Figure 1: (left) MST radar antenna (2,500m2 COCO array) located at Machu-Picchu Peruvian Station, Antarctica. **(right)** 4x4 Yagi array (225m2) during the test stage at Jicamarca Radio Observatory in Lima, Peru. It was installed nearby Artigas Station in Antarctica, in December, 2000.

The Artigas and Machu-Picchu Stations are located some 30 Km apart, both on King George Island. The COCO antenna array used at Machu-Picchu (2500m2) and the Yagi array used at Artigas (225m2) are shown in Figure 1.

3. Mesospheric observations at Artigas Station in Antarctica

During the 2000-2001 austral summer, Tropospheric-Stratospheric as well as Mesospheric observations were carried out using a VHF radar installed at Artigas Station in Antarctica. These observations provided 51 days of measurements during the appearance of polar mesospheric summer echoes (PMSE). A typical RTI report from this radar is shown in Figure 2.

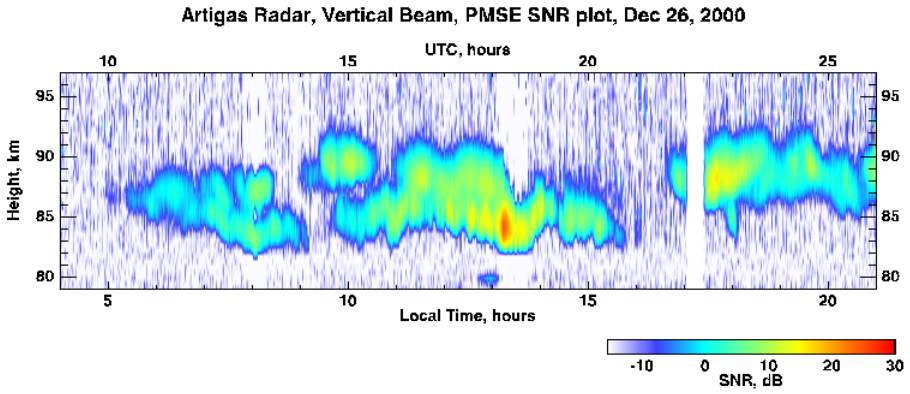

Figure 2: Range-time-intensity plot for the mesospheric region observed by the Artigas radar, December 26, 2000. A typical layered-PMSE event was registered during this day.

4. Comparison of PMSE intensities from Machu-Picchu'98 and Artigas'2001 campaigns

Figure 3 shows the almost-continuous 50-day records of maximum power levels, observed at any PMSE altitude, for the Machu-Picchu'98 (left) and Artigas'2001 (right) campaigns. Evident from this figure is a strong difference in the magnitude of PMSE between the two campaigns; which can be observed for the whole season. What is surprising and intriguing is that the smaller Yagi array used at Artigas (225m2) detected about ~11 dB stronger echoes than the COCO array at Machu-Picchu (2500m2). There are two alternatives to explain the difference between the Machu-Picchu'98 and Artigas'2001 campaigns:

1) unexpected Machu-Picchu poor performance characteristics of the COCO array that have not been accounted for; or
2) an inter-annual variability in the scattering phenomena (i.e., PMSE).

***Arguments against the first alternative*:**

a) we have analyzed Stratosphere-Troposphere power data from Machu-Picchu and Artigas and have found that echo strengths are very similar for the two radars;
b) the results are similar for the four different antenna systems that we have used at Machu-Picchu; i.e., the three original pointing directions installed in 1993 and the new vertical array installed in 1998; and
c) we have found from calibration experiments that a COCO array is ~2.2 dB less efficient than a Yagi array (see companion paper.) However, this is not enough to explain an 11dB discrepancy in the PMSE intensity.

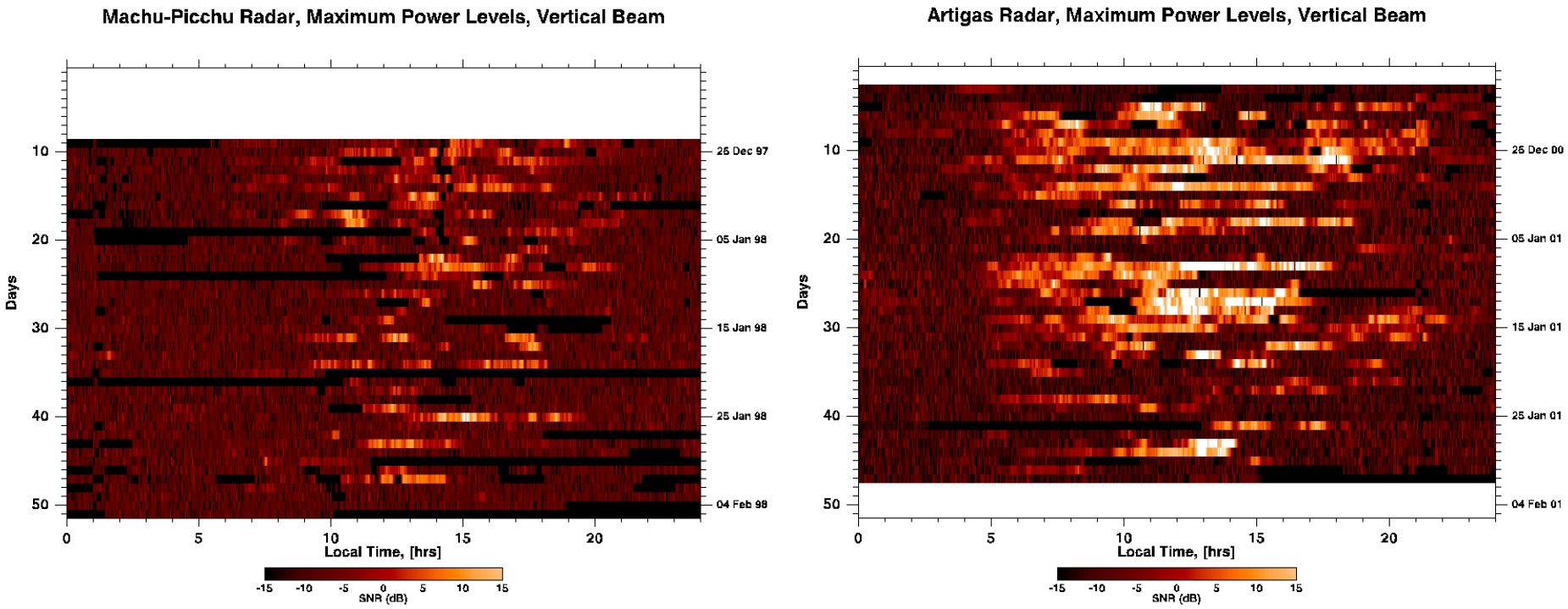

Figure 3: Almost-continuous 50-day records of maximum power levels, observed at any PMSE altitude, for the Machu-Picchu'98 (left) and Artigas'2001 (right) campaigns, both starting a few days before the Summer Solstice. Evident in this picture is a strong difference in the magnitude of PMSE between the two campaigns that can be observed for the whole season. What is surprising and intriguing is that the smaller Yagi array used at Artigas (225m2) detected stronger echoes than the COCO array at Machu-Picchu (2500m2).

Arguments against the second alternative are:

a) Machu-Picchu observations from 1993 to 1999 do not show significant echo strength differences between campaigns; and
b) annual variations in PMSE have not been reported from the Poker Flat data base (B. Balsley personal communications)

Arguments in favor of the annual variability alternative:

a) The results from Svalbard radar in the Northern hemisphere (K. Kubo personal communications, 2002), that report a ~10 dB stronger reflectivity from the 2000 PMSE season with respect to the 1999 and 2001 seasons;
b) Other evidence of long-term variation of mean yearly occurrence of PMSE has been published by Bremer et al., 2003, for the Alomar SOUSY (1994-1997) and ALWIN (1999-2001) radars; and
c) Additional interesting results have been reported by Huaman et al., 2001, from Resolute Bay radar (75N, 95W). Despite its higher latitude, the observed PMSE intensities are weaker than those from Poker Flat. Is this due to annual variability of PMSE?

5. Conclusions

- PMSE have been observed almost every day within a 50-day period, centered on January 5th, 2001, using a small (4x4) yagi array installed at Artigas Station in Antarctica.
- The PMSE observed at Artigas are ~11dB stronger than those from our previous Antarctic campaigns.
- Although there are antenna differences between campaigns, there is evidence that the intensity difference is due to annual variability in the scattering phenomena.
- A 4x4 Yagi array plus a 25 KW transmitter are sufficiently sensitive to obtain PMSE. And since it is an antenna design that many stations already have or could easily implement, it could be used for comparisons of the strength of the PMSE at different latitudes and longitudes.

Acknowledgments: The VHF radar at the Peruvian Antarctic Station "Machu-Picchu" is an important part of the Peruvian research activities in Antarctica. We would like to acknowledge the financial and logistic support received from the Instituto Antartico Peruano (INANPE, ex-CONAAN), the Consejo Nacional de Ciencia y Tecnologia del Peru (CONCYTEC), and the National Science Foundation. Our special thanks to Instituto Antartico Uruguayo and the 2000-2001 crew at Artigas Station.

References

Balsley, B.B., R.F. Woodman, M. Sarango, R. Rodriguez, J. Urbina, E. Ragaini, J. Carey, M. Huaman, and A. Giraldez, On the lack of southern hemisphere polar mesosphere summer echoes, *J. Geophys. Res., 100(D6)*, 11685-11693, 1995

Bremer, J., P. Hoffmann, R. Latteck, and W. Singer, Seasonal and long-term variations of PMSE from VHF radar observations at Andenes, Norway, *J. Geophys. Res., 108(D8)*, 8438, doi:10.1029/2002JD002369, 2003

Huaman, Mercedes M., Michael C. Kelley, Wayne K. Hocking and Ronald F. Woodman, Polar mesosphere summer echo studies at 51.5 MHz at Resolute Bay, Canada: comparison with Poker Flat results, *Radio Sci.*, 36(6), 1823-1837, 2001

Sarango, M.F., R.F. Woodman and D. Cordova, On the radiation efficiency of COCO antennas, *in this volume*, 2004

Woodman, R.F., B.B. Balsley, F. Aquino, L. Flores, E. Vasquez, M. Sarango, M. Huaman, and H. Soldi, First observations of polar mesosphere summer echoes in Antarctica, *J. Geophys. Res., 104(A10)*, 22577-22590, 1999

EISCAT AND SOUSY SVALBARD RADAR OBSERVATIONS OF PMSE – DIFFERENCES AND SIMILARITIES

J. Röttger[1], K. Kubo[2] and S. Fukao[2]
[1] Max-Planck-Institut, 37191 Katlenburg-Lindau, Germany
[2] Radio Science Center for Space and Atmosphere, Uji, Kyoto, Japan

The EISCAT Svalbard Radar (ESR) operates on 500 MHz**;** collocated (at a distance of 1.5 km) with it is the SOUSY Svalbard Radar (SSR), which operates on 53.5 MHz. We have used both radars during PMSE coherent scatter conditions, where the ESR can also detect incoherent scatter and thus allows to estimate the electron density. We describe observations of incoherent and coherent scatter during two observing periods in summer 1999 and 2000.

As described in Röttger (2000) well calibrated signal power was obtained with both radars, from which we deduced the radar reflectivity. Estimating the turbulence dissipation rate from the narrow beam observations of PMSE with the ESR, using the estimate of the electron density and the radar reflectivity on both frequencies we can obtain estimates of the Schmidt number by comparing our observational results with the models. Schmidt numbers of at least 100 are necessary to obtain the measured radar reflectivities, which basically support the models, which claim that the inertial-viscous subrange in the electron gas can extend down to small scales of some ten centimeters (namely, the Bragg scale of the ESR).

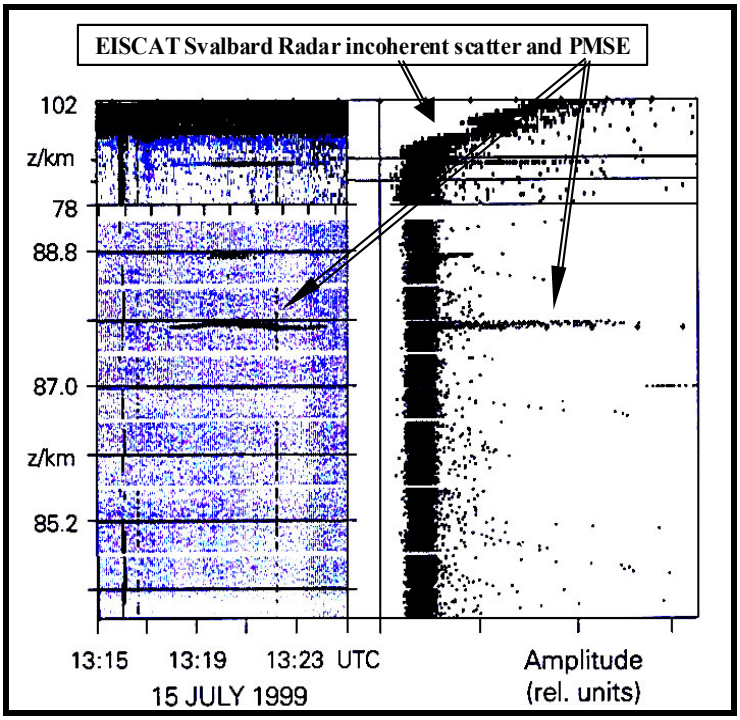

Fig. 1 Incoherent scatter (above 90 km) and coherent scatter (at 87.9 km) from Polar Mesosphere Summer Echoes (PMSE) observed with the 500 MHz EISCAT Svalbard Radar. The upper plots show the height-time intensity (left) and profile of scatter (+ noise) amplitude on the right-hand side. The lower 6 plots show the dynamic spectra (left) and spectra scatter plots (right). See Röttger (2000) for details.

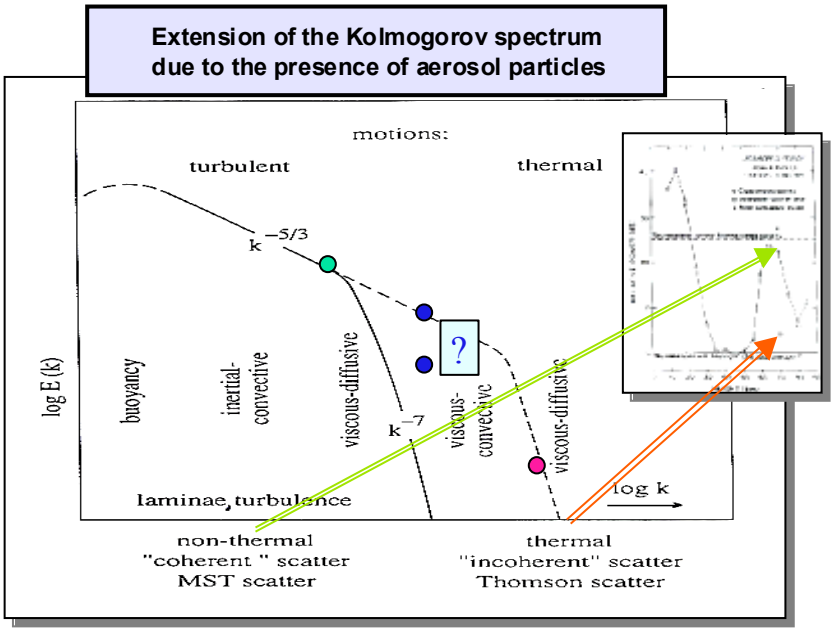

Fig. 2 Schematics of Kolmogorov spectrum showing the transition from turbulent or laminar motions in the inertial-convective subrange into thermal motions at higher spatial wavenumbers k in the viscous-diffusive subrange. Coherent scatter occurs when irregularities of refractive index exist at small wavenumbers in the inertial subrange. Incoherent scatter occurs in the ionosphere when only thermal motions of neutrals, ions and electrons exist far beyond the viscous-diffusive subrange. This subrange can be extended into higher spatial wavenumbers of the electron gas when heavy charged particles exist in the ionospheric plasma, which reduce the diffusivity of the electrons. Then coherent scatter can even occur at high spatial wavenumbers, i.e. at higher radar frequencies. The two arrows point to estimates of radar reflectivity in the D-region for incoherent scatter and coherent scatter (adapted from the Woodman and Guillen paper, 1972), which can merge under such conditions (l.-h. panel).

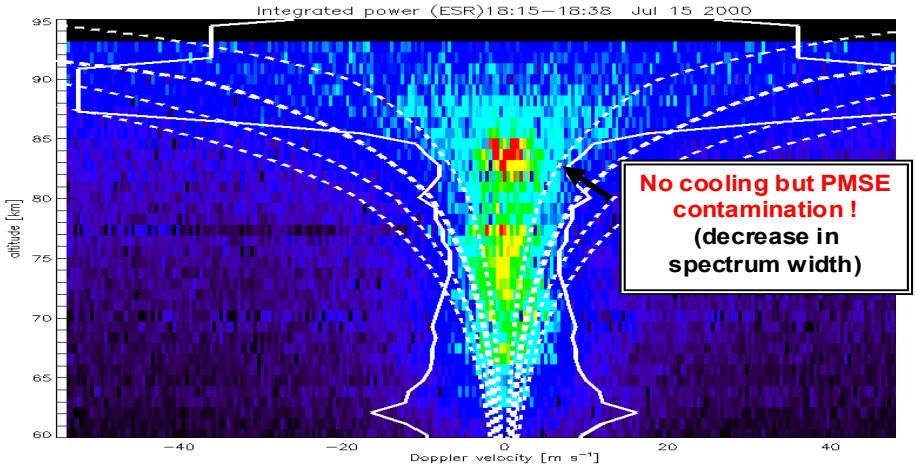

Fig. 3 Spectra of scatter signals observed as function of height in the mesosphere with the ESR on 500 MHz. The enhanced signal around 85 km is caused by coherent scatter from PMSE irregularities which is superimposed on the incoherent scatter, which dominates below and above this altitude. The coherent scatter spectrum is narrower than the incoherent scatter spectrum, which could be interpreted to result from a cooler medium if one would disregard the fact that these are PMSE caused by reduced electron diffusivity.

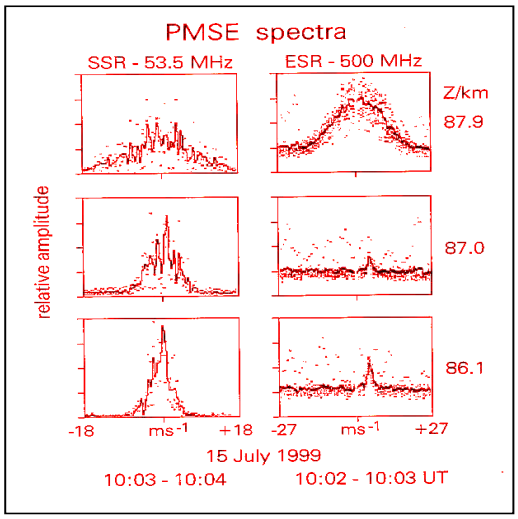

Fig. 4 Spectra of PMSE measured at the almost the same time in the same range gates with the SSR (left side) and the ESR (right side) on 53.5 MHz and 500 MHz, respectively. In the upper range gate the corresponding width in fluctuating velocity units is about equal, whereas this is not the case in the lower range gate 86.1 km. In the lower two range gates spectra on 500 MHz are extremely narrow, and the spectrum on 53.5 MHz show several spikes. This seems to indicate that thescattering medium or the coherent scattering process is different on the two spatial scales of 0.3 cm and 3.8 m, respectively. We also notice that the noise level on 500 MHz is much higher than the one on 53.5 MHz. This provides a gross estimate of the scatter cross section, which is much smaller on 500 MHz than on 53.5 MHz. A quantitative estimate of scatter cross section and Schmidt number was deduced by Röttger et al. (2000). In Fig. 5 we show the results of such deductions which first of all need the radar reflectivity on both frequencies, which is obtained from the signal power, the turbulence energy dissipation from the spectrum width of the narrow-beam ESR spectra (assuming a reasonable BV frequency) and the electron density from the ESR incoherent scatter as well. Schmidt numbers as high as 100 are needed, if we can assume that the scattering mechanism is the same on both radar wavelengths. Recognizing the results shown in Figs. 6 and 7, this may be questioned.

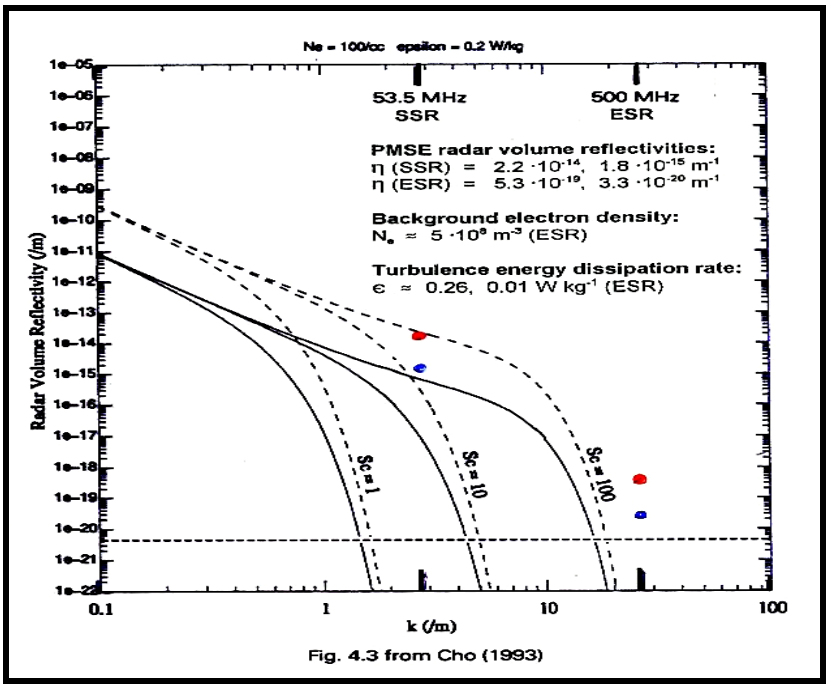

Fig. 5 Models of radar volume reflectivity as function of spatial wavenumber k for different Schmidt numbers, which are determined by the electron diffusivity and reflectivity values measured on 53.5 MHz with the SSR and on 500 MHz with the ESR (see Röttger, 2000, for details and references).

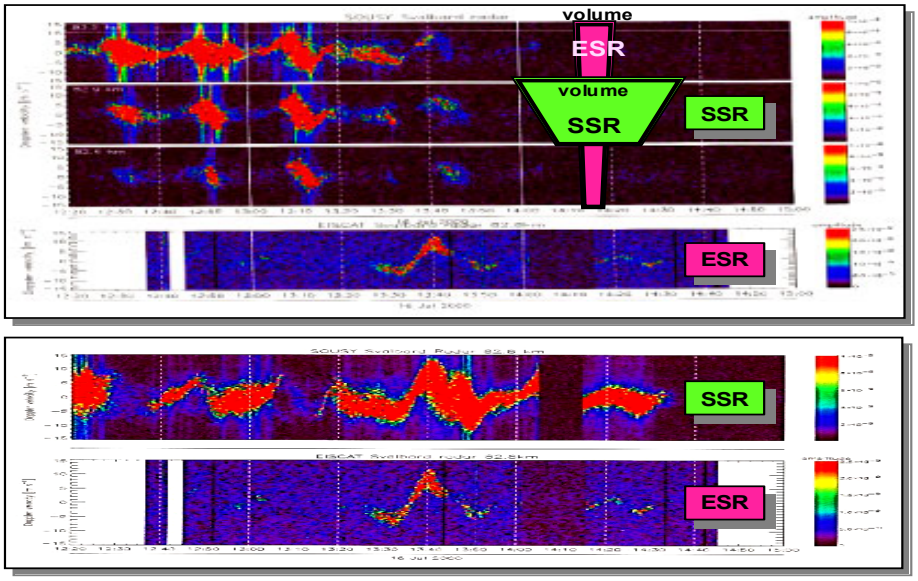

Fig 6 shows dynamic spectra observed on 53.5 MHz with 300 m range resolution (marked SSR) and on 500 MHz with 900 m range resolution (marked ESR). We note first of all that the signals on both frequencies show similar mean Doppler shifts, but different spectrum widths and quite different appearance. The former is caused by beam-broadening of the 53.5 MHz signal (beam widths are 1.6° and 5° respectively as indicated in the upper panel). Both radar volumes are different in width and range, which, however, cannot explain the obvious difference in appearance of the PMSE on both frequencies.

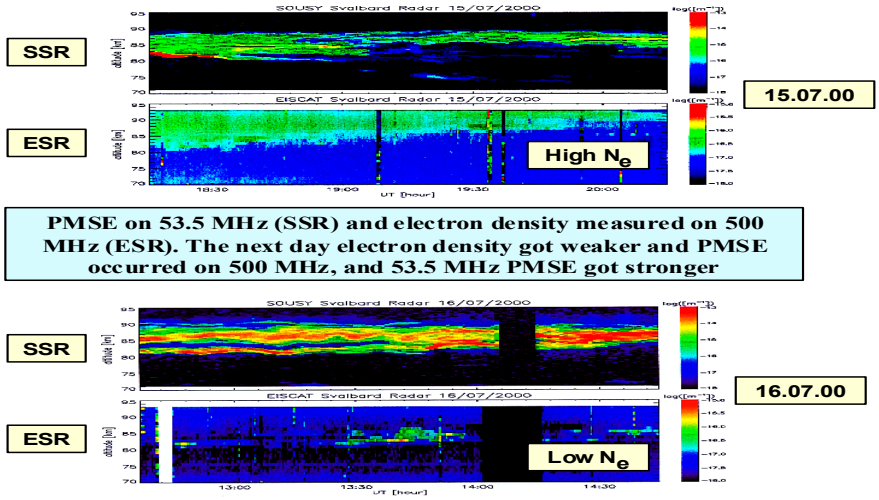

In Fig. 7 the signal power observed on 53.5 MHz (SSR) and on 500 MHz (ESR) are shown as function of height and time. The upper panels observed during high electron density N_e show weak PMSE on 53.5 MHz and no PMSE on 500 MHz, whereas the lower panels show weak electron density, much stronger PMSE on 53.5 MHz and sporadic, but fairly strong PMSE on 500 MHz. An explanation can be given by the theoretical contention that the electron diffusion coefficient is inversely proportional to the electron density (i.e. Schmidt number is small for high electron densities). All this needs further investigations.

Reference: Röttger, J., First D-region incoherent scatter and PMSE observations with the EISCAT Svalbard Radar (500 MHz) and comparison with PMSE observed with the collocated SOUSY Svalbard Radar (53.5 MHz), Proc. 9th Worksh. Techn. Sci. Asp. MST Radar, 129-132, 2000.

PHASE DIFFUSION FORMULATION OF TURBULENT SCATTER SPECTRA

Hasan Bahcivan[1]
David L. Hysell[2]

[1]Department of Electrical and Computer Engineering, Cornell University, Ithaca, NY
[2]Department of Earth and Atmospheric Sciences, Cornell University, Ithaca, NY

Abstract
Coherent radiowave backscattering from plasma irregularities in the ionosphere provides information on the characteristic motion of the scatterers. The average trajectory of a particle in the scattering medium represents diffusion and what a radar at a certain diagnostic wavenumber measures is defined as phase diffusion. While we cannot obtain the extended diffusion observations with a radar, the phase diffusion manifests itself as the relaxation function of the backscattered field. In an attempt to understand the turbulent scattering processes, the characteristic relaxation of the backscattered signal can be understood as the scattered field from a spontaneous fluctuation undergoing turbulent and thermal mixing. In this extended abstract, we suggest a relationship between the decay function in a subsiding turbulence and the backscatter spectral observations from driven steady-state turbulent plasmas. Finally, we provide a range of anomalous spectra based on different diffusion schemes modeled using random walk concepts, which could provide a framework for investigating anomalous scattering processes.

Introduction
Refractive index fluctuations associated with plasma turbulence in the ionosphere gives rise to coherent scattering of radiowaves. Just like density fluctuations in the neutral atmosphere create refractive index fluctuations, electron density fluctuations are the source of the scattered field from the ionosphere. The density fluctuations in a medium are a result of certain characteristic motion of scatterers, where a stochastic model can describe the characteristic motion. The average trajectory of a particle in the scattering medium is termed "diffusion", which reflects, to a certain degree, underlying physical processes.

In the radiowave backscattering, the diffusion quantity we are concerned about is the complex amplitude of the scattered field. This quantity represents the motion of scatterers in a restricted space, called "phase space". Therefore, the diffusional spread of this quantity cannot go on indefinitely. When observed at a fixed wavenumber in k -space, the motion of particles can be visualized as a mixing event. For example, consider inertial range turbulence where energy cascades toward higher wavenumbers. When such system is closed, all the energy will eventually be dissipated due to molecular viscosity or diffusion. The coherent scattered field of a particular wavelength in the inertial range will eventually vanish in the absence of processes creating the density irregularities.

How do the time behavior of the observed complex amplitude of the scatter field, as superposition of the fields from each scatterer, relate to the stochastic motion of

individual particles in a statistical flow? A detailed investigation on the diffusional relaxation of quantities based on several random walk models was made available by Talkner [4]. We think that this diffusional relaxation behavior of characteristic functions will provide an important framework for obtaining a theoretically strong formulation of the backscatter spectra from steady-state turbulent mediums.

In the next section, we start by a definition of the characteristic function and explain the basis how it can be related to the scattered field amplitude. Next, we describe phase relaxation function and how it can be identified as the generalized susceptibility of the fluctuation-dissipation theorem. Then, a simple relation is obtained to connect the spectra of the scattered field from steady-state fluctuations to the phase relaxation function. Finally, we will show several random walk models that may result in anomalous spectra.

Phase diffusion

The characteristic function is defined as the time behavior of phase density for a wavenumber k,

$$\phi(k,t) = \int_{-\infty}^{\infty} dx e^{ikx} \rho(x,t) \qquad (1)$$

where x is the extended space variable along the radar line of sight. If the observation point is far from the whole scattering system the characteristic function yields the complex amplitude of the scattered field for an incident electromagnetic wave with wavenumber k/2 at time t. The halving of the wavenumber comes from the Bragg condition. Hereinafter, we will refer to $\phi(k_B,t)$ as the phase relaxation function, where k_B is the Bragg wavenumber.

Random walk concept comes here in modeling turbulent scattering processes so that the observed backscatter spectra can be related to the phase relaxation function. If a random walk model is successful in modeling a turbulent process, the radar backscatter spectra will have an analytical solution through the corresponding phase relaxation function. One similar study by Balescu [1] shows that the modelling of anomalous diffusion in fluctuating magnetic fields by continuous time random walks is successful to a certain degree. While the physical meaning of a random walk model is beyond the scope of our discussion here, we find it useful here to show that such modeling has significant implication in interpreting coherent radar spectra.

Connection between the phase relaxation function and the steady-state turbulence

We have discussed that the characteristic function at half the electromagnetic wavenumber yields the measured scattered field. Consider for example an inertial range turbulence where energy is cascading from lower wavenumbers to higher wavenumbers and that we are scattering from this turbulent flow at the Bragg wavenumber k_B. We define that in the absence of energy input from scales larger than k_B, the system is in a state of subsiding turbulence. This is the state where the complex amplitude of the scattered field will decay toward zero. Our main assumption will be that this form of the decay curve of the scattered field is the phase relaxation function.

We now consider that the turbulent system is in the steady state and responding an

externally perturbing generalized force of time $f(t)$. In this system, the time correlation of the scattered field of the stationary nature will be,

$$\Phi(t,t') = \Phi(t-t') = \left\langle A(t)A^*(t') \right\rangle \tag{2}$$

where $A(t)$ is the complex amplitude of the scattered field at time t. We now make the assumption that the phase relaxation function can be taken as the generalized susceptibility function, $\alpha(t) = \phi(k_B, t)$, of the fluctuation-dissipation theorem and that the scattered field is the linearized response of the system to the generalized force $f(t)$,

$$A(t) = \int_0^\infty \alpha(\tau) f(t-\tau) \tag{3}$$

The above relation can also be expressed in terms of the Fourier components of the force and the fluctuation,

$$A(\omega) = \alpha(\omega) f(\omega) \tag{4}$$

where the generalized susceptibility is obtained as,

$$\alpha(\omega) = \int_0^\infty \phi(k_B, t) e^{i\omega t} \tag{5}$$

Having specified this function, the behavior of the system under a given perturbation is completely determined [2,3].

What we see in Eq. 2 is the radar backscatter autocorrelation function. The radar backscatter spectra can be obtained by a Fourier Transform operation on the autocorrelation function. From the classical limit of the fluctuation dissipation theorem, the backscatter spectrum $\Phi(\omega)$ can be related to the imaginary part of the generalized susceptibility function as [2],

$$\Phi(\omega) = \frac{2T}{\omega} \alpha''(\omega) \tag{6}$$

where α'' is the imaginary part of the generalized susceptance. T in the above equation can be related to the mean square of the scattered field by,

$$\left\langle |A(t)|^2 \right\rangle = \frac{2T}{\pi} \int_0^\infty \frac{\alpha''(\omega)}{\omega} d\omega \tag{7}$$

These formulae can be viewed as the equation for fluctuations of the scattered field $A(t)$ from a closed system in equilibrium and under the action of a random force. The formulation of the above thermodynamic fluctuation theory is valid for fluctuations of arbitrary size [2,3]. The absence of restrictions on the permissible values of the scattered field amplitude allows us to apply the fluctuation-dissipation theorem to weak incoherent or Thompson scattering as well as strong coherent scattering.

Anomalous spectra

Talkner [4] studied the phase relaxation functions for several random walk models. We list in Table 1, several of those with a range of relaxation from algebraic to faster than exponential. The model parameters associated with each curve can be chosen to fit the corresponding spectra (evaluated analytically or numerically) to the experimental spectra.

Random walk model	$\alpha(t)$	Condition/Form
Processes with independent increments	$e^{-\sigma^2 k_B^2 t^2}$	$\sigma^2 = \gamma + i\beta$
Fractional Brownian motion	$e^{-\sigma^2 k_B^2 t^\gamma}$	$0 < \gamma < 2$
Levy processes	$e^{-(\sigma k)^\gamma t^{\gamma\beta}}$	$0 < \gamma < 2$ $0 < \gamma\beta < 2$
Continuous random walks with long rests and short jumps	$t^{-\alpha}$	
Continuous random walks with short rests and arbitrary jumps	$e^{-f(k_B)t}$	

Conclusion

We have investigated how the stochastic motion of one scatterer can be related to the scattered field spectra. We have shown that if a successful stochastic description of particle movements can be found, the backscatter spectra can be related to the corresponding phase relaxation function of the stochastic or diffusion model. It was shown that such connection could be established by invoking the fluctuation- dissipation theorem and using the phase relaxation function in place of the generalized susceptance. While all these depends on finding a valid random walk model, we believe that once such modeling is successful, corresponding diffusional relaxation functions will have direct and analytical correspondence to the radiowave backscatter spectra from turbulent mediums. We have presented several cases where the spectral density could display a wide range of anomalous behavior from Lorentzian to Gaussian and sometimes slower than Lorentzian. While the rich spectral possibilities one may obtain from different random walk models look promising, the most fundamental question remaining is the validity of the random walk model. It has to physically make sense. Nevertheless, we believe that the theoretical connection between the spectral density of the scattered field from steady-state high-order statistical flows and the phase relaxation function establishes a sound framework for interpreting coherent backscatter spectra from refractive index fluctuations in a scattering medium.

References

[1] R. Balescu, Anomalous transport in turbulent plasmas and continuous time random walks, *Phys. Rev. E* 51, 4807–4822, 1995

[2] Herbert B. Callen and Richard F. Greene, On a theorem of irreversible thermodynamics, Phys. Rev. 86, 702–710, 1952

[3] L. D. Landau, E. M. Lifshitz, Statistical physics 3rd edition Part 1,Nauka, Moskow, 377,1976

[4] P. Talkner, Anomalous diffusion and phase relaxation, *Phys. Rev. E*, 64,061101-1, 2001

MORPHOLOGICAL STUDY OF THE FIELD-ALIGNED E-LAYER IRREGULARITIES OBSERVED BY THE GADANKI VHF RADAR

C. J. Pan[1] and P.B.Rao[2]

1. Institute of Space Science, National Central University, Chung-Li, 32054,Taiwan cjpan@jupiter.ss.ncu.edu.tw
2. National MST Radar Facility, Tirupati-517502, India

Abstract.

We report the Field-aligned irregularities observed at the low latitude Sporadic E layer (Es) with the Indian Gadanki (13.5 deg N, 79.2 deg E ; geomagnetic latitude 6.3 deg N) VHF radar. We operated the radar on the nights (18 to 06 LT) of June 17-20, July 15-18, and August 19-22 during 1998; on the nights of August 5-12 and August 16-19 during 1999. On the other hand, daytime (09 to 18 LT) observations were carried out on June 15-18, July 13-16, and August 17-20 during 1998. The total observation periods are 161 hours for the nighttime and are 68 hours for the daytime observation. The percentage of occurrence of E region echoes during the daytime and nighttime is studies. The histograms of the mean radial velocity and the spectral width of the echoes at three different regions classified according to the occurrence study are shown.

Introduction

Interesting investigation of the FAI in nighttime sporadic-*E* layers reported by *Yamamoto et al*. [1991] with the MU radar (34.9 N, 136.1 E) in Japan has become one of the most important features in the mid-latitude ionosphere. By operating the radar with 600-m range resolution, they found that the FAI displayed different morphologies when viewed in height-time-intensity plots. "Quasi-periodic" (QP) echoes were found to occur during the post-sunset period while "continuous" echoes were found to occur in the post-sunrise period. There are two main explanations so far have been proposed. The first one from *Woodman et al*. [1991] suggested that existing sporadic *E* (Es) layers could be modulated in altitude by a passing atmospheric gravity wave (AGW) through ion drag along geomagnetic field lines. The second was proposed by *Tsunoda et al*. [1994] and relied on the electric field and ionization effects. An intensive effort to obtain more detailed information associated with sporadic E layers and quasi-periodic structures was the Sporadic E Experiment over Kyushu (SEEK) carried out in southern Japan in 1996 [see, *Fukao et al.*, 1998, and other papers in that issue]. The SEEK II campaign is also carried out in the summer of 2002 after the successful SEEK campaign.

We present the FAI radar echoes from the India, which is the most southern station, for the QP studies in the Asian sector updated. Moreover, given the similar dip angles over the Gadanki/India radar and the Piura/Peru radar, it provides a chance for the longitudinal comparison.

Experimental set-up and data processing

The MST radar at Gadanki is a coherent pulse Doppler radar operating at 53 MHz with a peak power aperture product of 3 x 10^{10} Wm^2. The antenna system occupying an area of 130m * 130m is a phased array of 32 * 32 three element Yagi antennas consisting of two orthogonal sets, one for each polarization (magnetic EW and NS). It generates a radiation pattern with a main beam of 2.8 deg (half-power full-width), gain of 36 dB and first sidelobe level of -20 dB. The main beam can be positioned at any look angle within $\pm$ 20 deg off zenith in two principal planes. A detailed description of the Gadanki radar can be found in Rao et al. [1995].

To observe the E region FAI echoes, the antenna beam was positioned at 13 deg due magnetic north from vertical so as to look transverse to the magnetic field in the meridian plane. The observation range was from 84 to 144 km to cover the interesting Low altitude QP (LQP) echoes and the normal QP echoes at higher altitudes. The range resolution is 600 meters; time resolution is 15 seconds (2.5 s for single spectrum including processing time), Doppler velocity window of -354 to 354 m/s and resolution of 5.5 m/s. The spectral moments, providing information on the total signal power, weighted mean Doppler velocity and spectral width, are computed using the expressions given by Woodman [1985].

Data presentation

By summarizing the main results of the early observation we find that: (1) QP echoes appeared during most of the nighttime from the altitudes between 102 and 116 km, (2) the Low-altitude QP (LQP) echoes occurred both during daytime and nighttime and are confined to a slowly descending layer with a thickness of about 2-4 km in the height range of 90-100 km, and (3) two to three layered structures of continuous nature existed during both daytime and nighttime [Choudhary and Mahajan; 1999; Pan and Rao; 2002]

To show the morphological characteristics of the field-aligned E layer irregularities over Gadanki, we present statistical results of the radar echoes obtained with a 15-day data set gathered in 1998 and 1999. Both the daytime (09 to 18 LT) as well as the nighttime (18 to 06 LT) observations has been implemented.

Figure 1 and 2 show the percentage of occurrence of E region echoes during the daytime and nighttime, respectively. The threshold value of the signal-to-noise ratio is –6 dB and the time-range resolution bin is 15 min x 1.2 km. As we can see from the Figure 1, most of the daytime E-region echoes appear at the ranges below 100 km and there is no echo detected above the range of 110 km. Since those irregularities present the QP (which is the so-called LQP echoes) and the continuous features, we further separate them into two categories. For the daytime LQP echoes, the percentage of occurrence is about 69 %. 63% of them occurred at the ranges between 98 and 100 km and 34% of them at 95 to 97 km ranges. The period of the daytime LQP echoes categorize at ~2 minutes (72%), at ~5 minutes (23%) and at 60 to 90 seconds (8%). The layered structures confined QP and continuous echoes are almost horizontally distributed. By examining the Figure 1, we find that the occurrence of the noontime (11 to 14LT) E-region echoes were less than the other periods.

Figure 2 is the percentage of occurrence of E region echoes during the 18 to 08 LT period. We notice that there are two regions with significant occurrence percentage: one below 100km

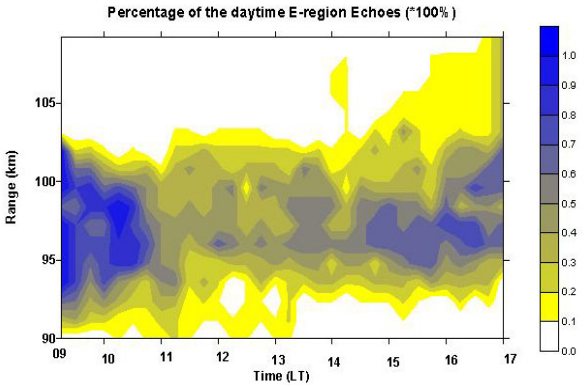

Figure 1. The percentage of the daytime E-region echoes.

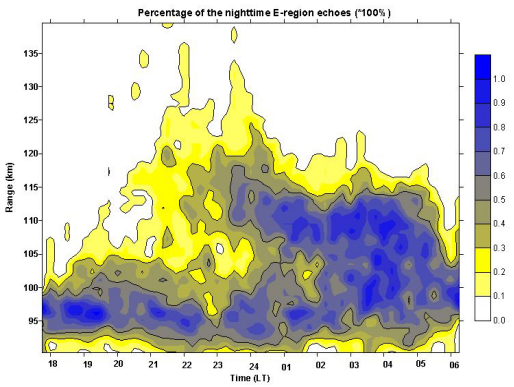

Figure 2. The percentage of the nighttime E-region echoes.

ranges that is similar to the daytime echoes and the other between 105 to 120 km ranges. Usually multi-layers exist at the upper region during the nighttime and get transformed into QP echoes [Choudhary and Mahajan, 1999]. The characteristics of the QP echoes observed at

the upper region are similar to those observed at other radars [Yamamoto et al, 1991; Pan et al., 1998; Tsunoda et al., 1998] and the maximum occurrence period is between 23 and 05 LT.

The lower region echoes consists of QP and continuous features just like those observed in the daytime ones. Again, we find that there is 45 % characterized QP features that is the night LQP echoes [Pan and Rao, 2002]. The occurrence ranges of the night time LQP echoes are slightly lower than the daytime LQP echoes. We note that 57 % of them appeared between 95 to 97 km ranges, 24 % between 92 and 94 km ranges and 13 % of them occurred at other ranges. The periodicity features are similar to those of the daytime LQP echoes that the majority is around 2 minutes period. Unlike the horizontally distributed daytime LQP echoes, most of the nighttime LQP present significant descending rate with about 1.5 km/hour.

Figure 3 presents the histograms of the mean radial velocity of the echoes for three categories: (left) daytime echoes at 90-110 km ranges (central) nighttime echoes at 90 to 105 km ranges, and (right) nighttime echoes at 105 to 140 km ranges. We notice the figure 3 presents wider ranges of value from the left to the right plots. The mean radial velocities at the lower E region vary between –30 and +30 m/s for daytime and –50 to +50 m/s during the nighttime and the values may vary from –100 to +100 m/s during the nighttime upper E region. Furthermore, the mean radial velocities of the lower E region echoes are close to zero for both daytime and nighttime but a downward velocity is noticed at the upper E region.

Figure 4 shows the histograms of the spectral widths of the similar regions as in Figure 3. It is clearly shown in Figure 4 that the daytime and the nighttime (for both upper and lower regions) echo present different distributions. The mean spectral widths in the daytime lower E region present a bell shape distribution with the mean value of about 30 m/s. On the other hand, nighttime echoes are non-symmetric and are wider than those detected in the daytime. The majority of the spectral width in the lower region is narrower (about 50 to 60 m/s) than the one in the upper region (about 70 m/s).

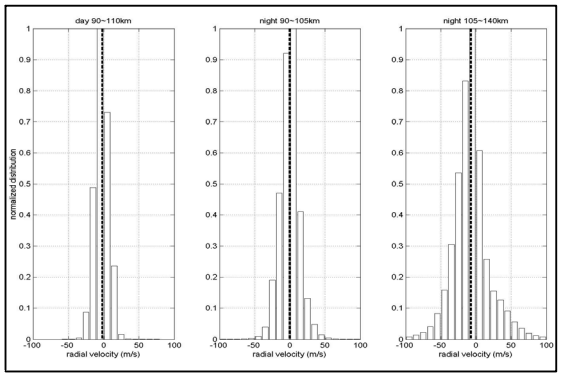

Figure 3. The histograms of the mean radial velocity of the echoes.

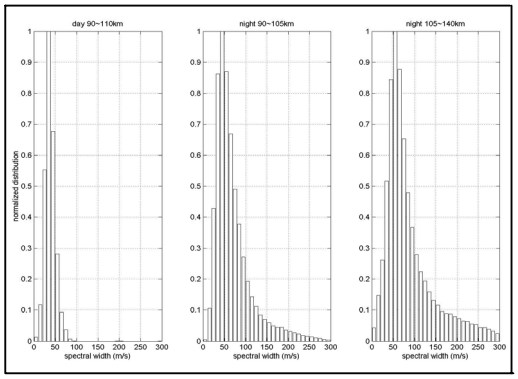

Figure 4. The histograms of the spectral widths of the echoes.

Summary and Discussions

Over all, the following characteristics of the E region FAI observed by the Gadanki radar based on this data set are notified:

(1) There are two echoing regions: the lower region between 90 and 100 km ranges and the upper region between 105 and 120 km ranges.
(2) Echoes observed in both the upper and lower regions are similar to type 2 echoes reported by other radars in the mid-latitudes.
(3) Echoes of the lower region may occur in daytime as well as in nighttime. Although there is an observation break between 06 and 09 LT, noontime (11 to 14 LT) seems to be the minimum period of occurrence. QP echoes are commonly detected at the lower region no

matter daytime or nighttime and are the so-called "LQP echoes".

(4) The spectral characteristics of the lower region echoes differ from daytime and nighttime. The mean Doppler velocities are more variant than those of the daytime and the spectral widths are broader in the nighttime.

(5) The upper region echoes appeared only in the nighttime with a maximum period between 23 and 05 LT. Typical QP echoes detected here are similar to those observed at mid-latitudes.

(6) Unlike the value close to zero of the mean radial velocities of the lower E region echoes, a downward velocity is noticed at the upper E region. Both the mean Doppler velocities and the spectral widths are found larger than those of the lower regions.

Concluding remarks

By examining the 15-day data set gathered in the summer of 1998 and 1999, we present the morphological features of the E region FAI observed by the Gadanki radar. We also compare the features of the FAI echoes between Gadanki and Piura radars since the geomagnetic latitude of these two radars are close. Although the morphological distribution and spectral characteristics are very similar for those FAI echoes, daytime echoes and the LQP echoes are rarely reported by Piura. It is suggested that the neutral winds may play a role in this discrepancy since those echoes usually occur at the altitudes below 100 km. It will be very interesting to study how the neutral winds affect the lower region FAI echoes in the coming communication.

References:

Chau, J.L. and R.F. Woodman, Low-latitude quasiperiodic echoes observed with the Piura VHF radar in the E region, *Geophys. Res. Lett*, *26*, 2167-2170, 1999.

Choudhary,R.K., and K.K.Mahajan, Tropical E region field aligned irregularities: Simultaneous observations of continuous and QP echoes, *J. Geophys. Res., 104*, 2613-2619, 1999.

Fukao, S., M. Yamamoto, R.T.Tsunoda, H. Hayakawa,and T. Mukai, The SEEK (Sporadic E Experiment over Kyushu)campaign, *Geophys. Res. Lett*, *25*, 1761-1764, 1998.

Pan, C.J., and P.B.Rao, Low altitude quasi-periodic radar echoes observed by the Gadanki VHF radar, *Geophys. Res. Lett*, *29*, 25-1, 2002.

Rao P B , A R Jain , P Kishore, P Balamuralidhar, S H Damle and G Viswanathan, Indian MST radar, 1, System description and sample wind measurements in ST mode, *Radio Sci*., 30, 1125, 1995.

Tsunoda, R.T., S. Fukao, and M. Yamamoto, On the origin of quasi-periodic radar backscatter from midlatitude sporadic *E*, *Radio Sci, 29*, 349-365, 1994.

Woodman, R.F., M. Yamamoto, and S. Fukao, Gravity wave modulations of gradient drift instabilities in midlatitude sporadic-*E* irregularities, *Geophys. Res. Lett., 18*, 1197-1200, 1991.

Yamamoto, M., S. Fukao, R.F. Woodman, T. Ogawa, T. Tsuda, and S. Kato, Midlatitude *E*-region field aligned irregularities observed with the MU radar, *J. Geophys. Res., 96*, 15943-15949, 1991

Woodman R F, Spectral moment estimation in MST radars, *Radio Sci.*,20, 1185, 1985.

CONTINUOUS WAVE INTERFEROMETER OBSERVATIONS OF MIDLATITUDE E REGION BACKSCATTER

C. Haldoupis[1], A. Bourdillon[2], A. Kamburelis[1], G. C. Hussey[3], and J. A. Koehler[3]

1: Physics Department, University of Crete, Iraklion, Crete, Greece
2: Institut d'Electronique et de Télécommunications de Rennes, Université de Rennes 1, France
3: Institute of Space and Atmospheric Studies, University of Saskatchewan, Saskatoon, Canada

1. Introduction

Ionospheric radio interferometry was first introduced by *Woodman* [1971] in equatorial electrojet studies in order to determine the magnetic field inclination over Jicamarca, Peru. It was based on cross-correlation interferometry used in radio astronomy to determine the angular position and size of radio noise sources. Ionospheric interferometry was further developed by *Farley et al.* [1981] and applied to studies of equatorial electrojet and spread F irregularities. Since its development, backscatter interferometry has become a powerful tool for studying plasma turbulence and instabilities in the *E* region. First, this technique was applied in studies of the equatorial electrojet, using the capabilities of the large Jicamarca radar array (e.g., *Farley et al.,* 1981; *Kudeki et al*., 1982) and later in radio auroral studies. At midlatitude, where coherent backscatter of radio waves comes from unstable sporadic *E* layers, the technique was applied first by *Riggin et al.* [1986] using the Cornell University Portable Radar Interferometer (CUPRI). Recently multi-line interferometry and in-beam radar imaging techniques has been developed for studying fine structures inside large scale plasma waves in the nighttime equatorial spread *F* and electrojet echoes, and to investigate quasiperiodic (QP) echoes at midlatitude (e.g., see *Hysell et al.,* 2002, and more relevant references therein).

In the following, we first describe a midlatitude *E* region continuous wave (CW) radio interferometer experiment and then present examples of some first results. This work is continuation of research carried out the last decade in Greece, which led to a number of new findings, the most important being the detection at midlatitude of the Farley instability (*Schlegel and Haldoupis,* 1994) and the introduction of a new polarisation mechanism for its explanation (*Haldoupis et al.,* 1997).

2. SESCAT Interferometer

Here we describe in brief the upgrade of SESCAT, the 50 MHz CW *S*poradic *E SCAT*ter experiment located in the island of Crete, Greece, into a single-line azimuthal interferometer. Note that SESCAT is not a pulsed radar, but a continuous wave bistatic Doppler system that observes a fixed scattering volume with excellent temporal and Doppler spectrum resolution. The SESCAT experiment, which is described in detail by *Haldoupis and Schlegel* [1993], had its observing capacity considerably enhanced when operated as an interferometer. As such, it has become very useful for the study of microstructure and short scale dynamics in localised and strongly unstable scattering regions located within sporadic *E* layers.

To upgrade SESCAT into an interferometer a new receiver system was built that consisted of two identical superheterodyne receiver units. In order for the receivers to be phase-coherent, both were driven by a single ultra stable oven-controlled crystal oscillator operating at exactly 1 kHz below the transmitted frequency. This shift relative to the transmitted frequency is necessary for CW radars in order for both positive and negative Doppler shifts to be measured and, as such, for the full Doppler spectrum to be determined. The two antennas required for interferometry were simply provided by splitting the existing receiving array of four Yagis into

two sub-arrays, each sub-array made up from two adjacent single Yagi antennas. In this way an approximately east-west antenna baseline of 16 m was formed that turned SESCAT into an azimuthal interferometer. In this configuration, the beamwidth for each receiving array now becomes about 12 degrees from the 8 degrees it was for the 4 Yagi array, which increased the 3-dB zonal extent of the scattering region to about 40 km at a range of 185 km. The output audio frequency signals of both receivers were digitised and processed on site by using two identical DSP (digital signal processor) units but run by the same clock, housed in a Pentium-class personal computer. Highly efficient software, partly written in assembly language and partly in C++, allowed for fast Fourier transformations and subsequent power spectrum and cross spectrum calculations to be performed in real time. The configuration, in block diagram form, of SESCAT interferometer is summarised in Figure 1.

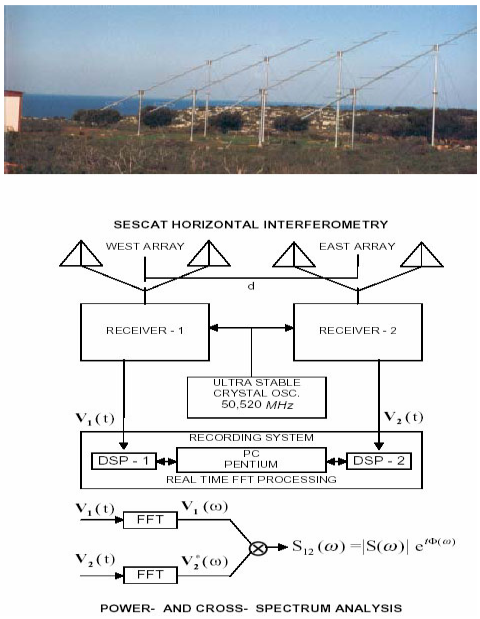

Figure 1. The SESCAT Interferometer

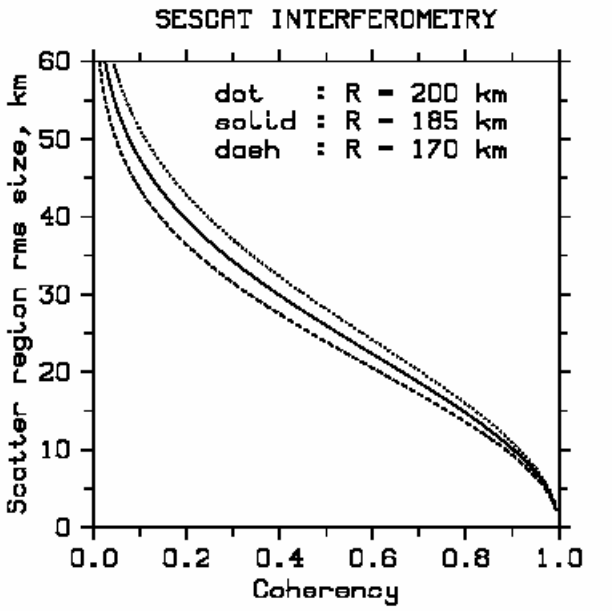

Figure 2. Region mean size for different radar ranges

Figure 2 (above left) shows the scattering source mean sizes as a function of the measured cross spectrum coherencies, in line with the interferometer theory of *Farley et al.* [1981]. The scatter source mean size is computed in Figure 2 for three radar ranges in order to also estimate the anticipated errors due to range uncertainties, which are inherent in a CW bistatic radar. The solid line curve is for the most likely range of 185 km that corresponds to exact perpendicularity at *E* region altitudes near 105 km, the altitude usually assumed to be optimal for plasma instability excitation. In addition, also shown in Figure 2 are the corresponding curves for the ranges of 170 km (dashed curve) and 210 km (dotted curve), which represent the lower and upper range limit, respectively. As seen, the maximum errors anticipated in source mean size because of uncertainties in SESCAT range are not larger 10 %.

3. Examples of Observations

Here we present only a couple of interferometric observations which, although they tend to exemplify somewhat our data base, they are by no means exhaustive. The interferometry records are characterised by a great variety of "signatures" reflecting the complexity of instability mechanisms and dynamics in the scattering medium, and provide information which goes undetected in the Doppler spectrum alone.

Figure 3 shows a rather typical example of SESCAT interferometric observations. The Doppler spectrogram in the upper panel starts with a burst of strong scatter having broad spectra which identify with type 2 echoes. This is followed by some weaker bursts with narrow spectra near zero Doppler shift accompanied by a narrow spectral band of a faint scatter at large negative velocities, presumably of type 1. The latter is depicted much more clearly in the coherency plot which shows the weak type 1 echoes to originate from localised regions at different azimuths relative to the low velocity echoes. The cross phase changes with time, $d\Phi/dt$, show that all regions undergo a bulk motion to the west. A detailed analysis reveals the following: 1) What we identify as type 2 echoes are often structured in Doppler velocity, with positive and negative Doppler bands coming from zonally adjacent echoing regions separated by a few km. Both Doppler bands move as an entity, however across the radar beam with a speed near 50 m/s which means they associate with one and the same scattering region. This picture seems to be in contradiction with the notion of isotropic (Sudan-like) turbulence applying for type 2 echoes. 2) The type 1 echoes, due to Farley's instability, show no structure across their Doppler band and come from the same region, which in this event has a zonal extent of ~10 km and traverses across the radar beam to the west with a speed nearing 120 m/s.

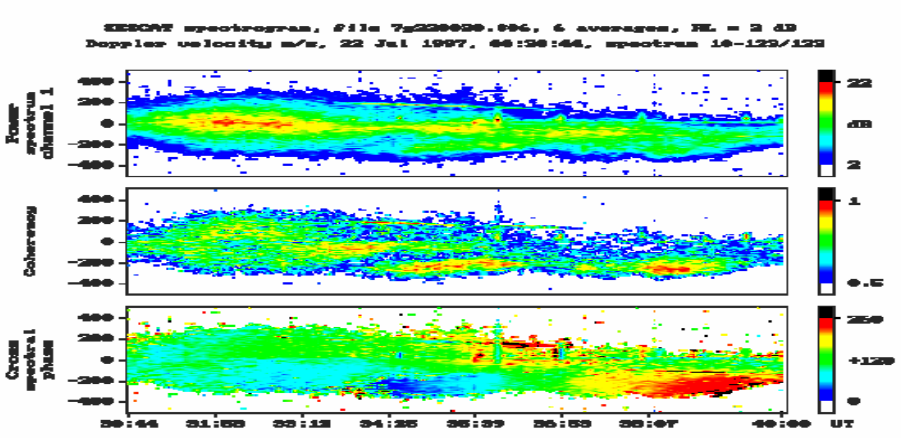

Figure 3. SESCAT Interferometric observations of type 1 and type 2 echoes

Figure 4 shows Doppler spectra and cross-spectral spectrograms for a typical example of quasiperiodic (QP) echoes having on the average a period of about 8 minutes. As seen QP are basically coming from a sequence of unstable plasma patches (or clouds) that move across the radar beam. The systematic phase change for each drifting plasma patch shown in the lower panel, corresponds to a westward near 110 to 120 m/s for the sequential scatter regions traversing across the field of view, apparently, with the neutral wind.

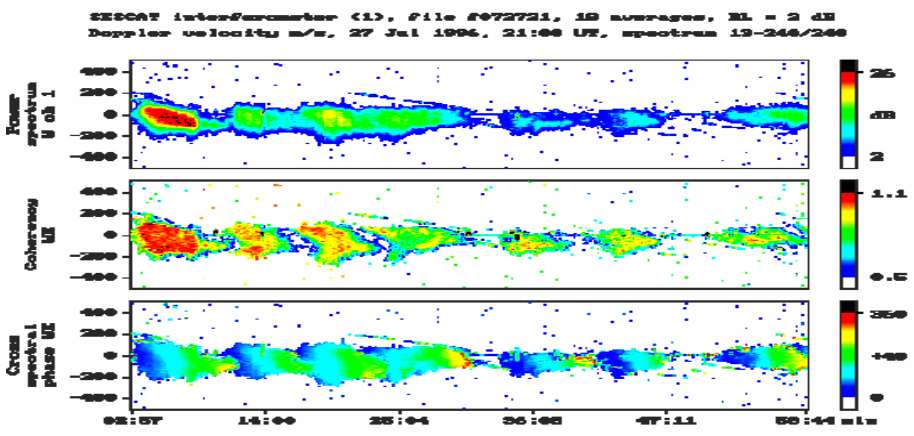

Figure 4. SESCAT interferometer observations of quasiperiodic echoes

4. Summary

Here we describe a radio interferometric experiment and present examples of midlatitude E region backscatter observations. These were obtained with SESCAT (Sporadic E SCATter experiment), a bistatic 50 MHz continuous wave (CW) Doppler radar located on the island of Crete, Greece, which was operated as a single (east-west) baseline interferometer. The interferometric observations reveal that the aspect sensitive area viewed by the radar often contains a few zonally located backscatter regions, presumably blobs or patches of unstable plasma, which drift across the radar field-of-view with the neutral wind. On average, these echoing regions have mean zonal scales ranging from a few kilometers to a few tens of kilometers and drift with westward speeds mostly between 20 and 100 m/s, and occasionally up to 150 m/s. The cross-spectral analysis shows that midlatitude type 1 echoes (Farley waves) occur much more frequently than has been previously assumed and they originate in single and localized areas of elevated electric fields. On the other hand, typical bursts of type 2 echoes are often found to result from two adjacent regions in azimuth undergoing the same bulk motion westwards but producing scatter of opposite Doppler polarity, a fact that contradicts the notion of isotropic turbulence to which type 2 echoes are attributed. Finally, quasiperiodic (QP) echoes are observed simply to be due to sequential unstable plasma patches or blobs which traverse across the radar field-of-view, sometimes in a wave-like fashion. For more on the SESCAT interferometer and its results see recent paper by *Haldoupis et al.* [2003] (*Ann. Geophys.,* 21, 1589, 2003)

5. Acknowledgements

This work was made possible with support from the European Office of Aerospace Research and Development (EOARD), Air Force Office of Scientific Research, Air Force Research Laboratory, under contracts F61775-01-WE004 and FA8655-03-1-3028 to C. Haldoupis.

6. References

Farley, D. T., H. M. Ierkic, and B. G. Fejer, Radar interferometry: A new technique for studying plasma turbulence in the ionosphere, *J. Geophys. Res., 86,* 1467, 1981.

Haldoupis, C., and K. Schlegel, A 50 MHz radio experiment for mid-latitude E-region coherent backscatter studies. System description and first results, *Radio Science, 28,* 959, 1993.

Haldoupis, C., D.T. Farley, and K. Schlegel, Type 1 radar echoes from the midlatitude *E* region, *Ann. Geophys., 28,* 908, 1997.

Hysell, D. L. M. Yamamoto, and S. Fukao, Imaging radar observations and theory of type I and type II quasiperiodic echoes*, J. Geophys. Res., 107*, 1360, 2002.

Kudeki, E., D. T. Farley, and B. G. Fejer, Long wavelength irregularities in the equatorial electrojet, *Geophys. Res. Lett., 9,* 684, 1982.

Riggin, D., W. E. Swartz, J. Providakes, and D. T. Farley, Radar studies of long-wavelength waves associated with mid-latitude sporadic E layers*, J. Geophys. Res., 91*, 8011, 1986.

Schlegel, K. and C. Haldoupis, Observation of the modified two-stream plasma instability in the mid-latitude E-region ionosphere, *J. Geophys. Res., 99,* 6219, 1994.

Woodman, R. F., Inclination of the geomagnetic field measured by incoherent scatter*, J. Geophys. Res.,* 76, 178, 1971.

HF DIGISONDE AND MF RADAR MEASUREMENTS OF E-REGION BRAGG SCATTER DOPPLER SPECTRAL BANDS UNDER THE SOUTHERN POLAR CUSP

R. J. Morris[1], D. P. Monselesan[1,2], D. A. Holdsworth[3], P. L. Dyson[4], M. R. Hyde[1,2], and D. J. Murphy[1]

[1]Australian Antarctic Division, Kingston 7050, Tasmania, Australia
[2]IPS Radio and Space Services, Haymarket, NSW 1240, Australia
[3]Atmospheric Radar Systems, Thebarton 5031, South Australia, Australia
[4]La Trobe University, Bundoora 3083, Victoria, Australia

Introduction

This paper presents new observations of Bragg scatter events in the high-latitude E-region ionosphere using HF digisonde and MF radar. The digisonde transmitted in a swept-frequency mode from 1.2 to 2.7 MHz while the MF radar transmitted at a single frequency at 1.94 MHz. The two independent instruments were programmed to record E-region backscatter. Results from spectral signal analyses show evidence of Doppler spectral bands in the respective HF digisonde and MF radar data. The backscattered signals observed from these different radar techniques at two Antarctic stations appear to originate from the same E-region heights. Moreover there is a remarkable tendency for such spectral bands to occur during intervals of ionosphere slant Es condition (SEC) with lacuna. Independent MF radar observations from Davis (78.0°E, 68.6°S geographic, 74.6°S magnetic) during 2001 and 2003, and HF digisonde observations from Casey (66.3°E, 110.5°S geographic, 80.4°S magnetic) during 1996, are presented. The instrumentation used at the Australian Antarctic stations and in this study is briefly discussed in Morris et al. (1995). The plausibility of these spectral band events being related to E-region ionosphere plasma instability processes will be discussed.

Observations

A comprehensive account of digisonde observations of E-region Bragg scatter spectral signatures observed at Casey during 1996 is in preparation by Monselesan et al. (2003). Observations show that during summer months at solar cycle minimum, F-region lacuna and slant-Es conditions (SEC) are a common feature of daytime ionograms recorded around local magnetic noon at Casey. Digital ionosonde measurements of drift velocity height profiles show that the occurrence of lacuna prevents the determination of F-region drift velocities, and also affects E-region drift velocity measurements. Unique E-region spectral features revealed as intervals of Bragg scatter superimposed on typical background E-region reflection were observed in ionosonde Doppler spectral measurements during intense lacuna conditions. Daytime E-region Doppler spectra recorded at carrier frequencies from 1.6 to 2.7 MHz, below the E-region critical frequency f_oE, have two side-peaks corresponding to Bragg scatter at approximately ±1-2 Hz symmetrically located on each side of a central-peak corresponding to near-zenith total reflections. Both E- and F-region DPS ionospheric drift velocities are usually computed for a refractive index of $n=1$. Monselesan et al. (2003) show that for mean spectral signatures of ±1.0 Hz at 2-MHz and echoes coming from 30° zenith angles ($n=0.5$ at 110-km group range), that $V_i \cong 425$ m/s which corresponds to the side-peaks in the Doppler spectra (as shown in the Figure 1) or possibly equivalent to the irregularity phase velocity, which is near the ion-acoustic speed Cs expected in the polar E-region ionosphere.

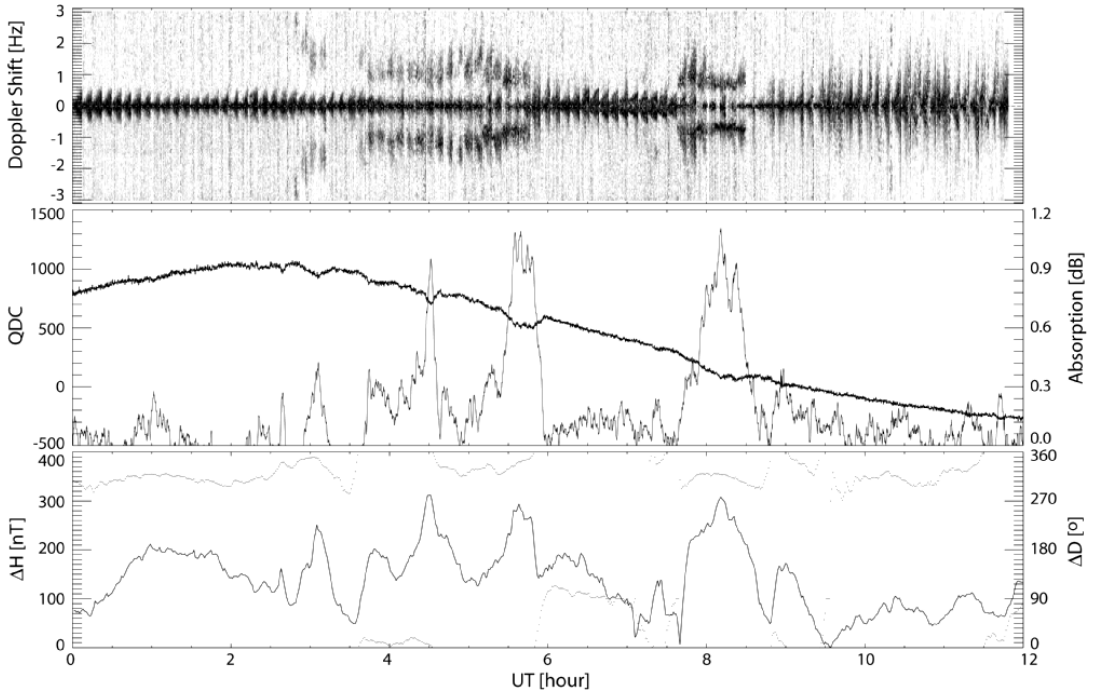

Figure 1. E-region DPS4 spectra, riometer absorption and fluxgate magnetic signatures during three successive SEC/lacuna events on 30 December 1996 at Casey.

Figure 1 illustrates typical DPS4 E-region Bragg spectral signatures during three successive SEC/lacunae events on 30 December 1996 at Casey, starting at 03:00, 03:45 and 07:45 UT respectively. The top window summarizes 12 hours of E-region drift spectra recorded on the central antenna of our four-antenna array interferometer. The middle window displays the corresponding quiet-day curve (QDC) of the co-located 30-MHz riometer (thick line) together with absorption dB values (thin line). The bottom window shows coincident fluxgate magnetometer horizontal ΔH and declination ΔD components. ΔD is measured positive eastwards from geographic north. Geomagnetic perturbations are produced by ionospheric E-region currents mainly driven by omnipresent magnetospheric convection electric fields in the polar cap and modulated by ionospheric conductivities and thermospheric neutral winds. The coincident ionospheric absorption and magnetic deflections with the Doppler spectral side-peaks during SEC/lacuna are suggestive of a relationship with E-region ionospheric irregularities. We also note that Davis and Casey can be located beneath the polar cusp and polar cap during sunspot minimum as a function of dipole tilt and the level of magnetic activity. Thus particles including ionic atoms and molecules (i.e. O^+ and NO^+) can gain direct entry to the E-region that could contribute to the generation mechanism for ionospheric irregularities.

The lacuna phenomenon (Piggott and Rawer, 1978) manifests itself by the partial or total, but sudden, disappearance of normal ionogram traces. The affected portions start at the end of the E-region trace, where retarded echoes are usually missing (E-F lacuna), and can extend to both the F1- and F2 layers (F1 and F2 lacuna). Figure 2 shows the diurnal and seasonal occurrence distributions for SEC/lacuna as scaled from Casey DPS ionogram records for 1996, and clearly illustrates a summer daytime maximum in occurrence consistent with observations from the polar cusp station Dumont d'Urville as reported by Cartron and Vila (1994).

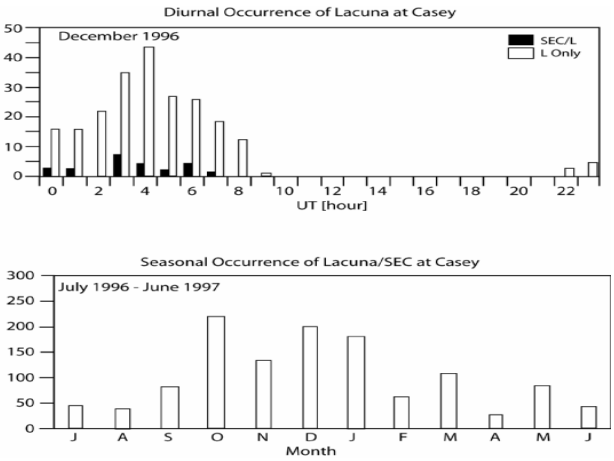

Figure 2. Diurnal occurrence distribution for lacuna and SEC observed at Casey for December 1996 (top). Seasonal occurrence distribution for lacuna observed at Casey between July 1996 and June 1997 (bottom).

Following on from the Casey HF digisonde study by Monselesan et al. (2003) we then conducted high-resolution E-region measurements using the MF radar located at Davis, to see whether these spectral signatures were evident during lacuna conditions (as scaled from the IPS Radio and Space Services 5D ionosonde ionograms). Remarkably we also observed the occurrence of Bragg scatter spectral side-peak events at 1.94 MHz as shown in Figure 3 for 23 February 2001. This event has similar structure and characteristics to the events detected using a digisonde scanning in the 1.6 to 2.7 MHz range at Casey during 1996 as shown in Figure 1.

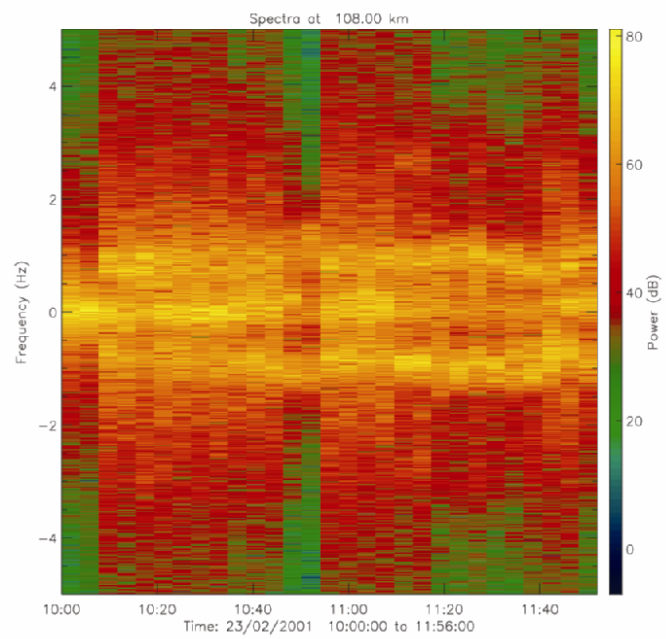

Figure 3. MF radar Bragg spectral signatures during a lacuna event on 23 February 2001 at Davis.

Discussion

It is important to note that erroneous E-region drift velocities result when Doppler sorted interferometry (DSI) techniques are applied to DPS drift data during intervals where Bragg backscatter or spectral bands occur in the high-latitude ionosphere. These events appear to be linked with SEC and lacuna conditions. Thus the velocity contribution derived from the side-peaks or Bragg backscatter echoes must be removed from the data when determining the background E-region drift velocities (see Monselesan et al., 2003).

Tsunoda et al. (1997) recorded similar spectra with the continuous-wave 12.3-MHz radar HF-OSCAR located at Søndre Strømfjord in Greenland. These authors concluded that the spectra were produced by the modified two-stream instability, given their narrow spectral widths and peak Doppler velocities comparable to the ion-acoustic speed at around 95-km altitude. Previous SEC/lacuna studies have been linked to E-region two-stream plasma instability processes (Haldoupis et al., 1993). Ionospheric absorption and associated E-region current studies on events similar to our observations as presented in Figure 1 were also linked to two-stream plasma wave instability processes (i.e. Schlegel and St-Maurice, 1981). We interpret the velocities derived from the side-peaks on the Doppler spectra, as irregularities phase velocities triggered primarily by two-stream instabilities, possibly influenced by gradient drift

effects. It is therefore plausible that the Bragg scatter events reported in this paper might also be linked to the generation of E-region irregularities explained in terms of coherent scatters from electron density irregularities generated by the modified two-stream (Farley, 1963; Buneman, 1963) and the gradient-drift (Maeda et al., 1963) plasma instabilities. However this preliminary interpretation is largely based on previous work discussing SEC/lacuna events, and additional observational parameters (i.e. flow, aspect angle and echo strength) are needed to substantiate this view.

Conclusions

We have shown that interesting E-region Doppler spectral signatures evolve with near symmetrical side-peaks during SEC and lacuna conditions, in the vicinity of the southern dayside polar cusp region, at solar cycle minimum. These Bragg scatter events were observed using both HF and MF radar techniques at two polar stations – although not simultaneously. Our observations are considered in context with independent studies of SEC and lacuna conditions, and studies of Bragg scatter in the E-region. We need to undertake simultaneous HF digisonde and MF radar E-region observations from Davis, Antarctica to confirm that the Bragg scatter spectral signatures reported are related. We suggest that these events may be related to E-region irregularities generated by plasma instability processes. Further research is required to unravel the Bragg scatter source region and generation mechanism in order to develop a theoretical understanding of this interesting high latitude E-region phenomenon.

Acknowledgments

The Australian Research Council and the Australian Antarctic Science Advisory Committee supported the installation and operation of the DPS-4 Digisonde™ at Casey station, Antarctica. We thank Australian National Antarctic Research Expeditions (ANARE) members who contributed to the project, especially Dr. Anthony Breed and Dr. Darryn Schneider who conducted the 1996-1997 summer drift campaign at Casey. We thank Judy Whelan for her assistance with the preparation of the figures.

References

Buneman, O., Excitation of field aligned sound waves by electron streams, *Phys. Rev. Lett., 10*, 285, 1963.

Cartron, S., and Vila, P., Polar lacuna on ionograms. I: Brief morphology, *Ann. Geophys., 12*, 355, 1994.

Farley, D. T., A plasma instability resulting in field-aligned irregularities in the ionosphere*, J. Geophys. Res., 68*, 6083, 1963.

Haldoupis, C., K. Schlegel, and E. Nielsen, Some observations of radio auroral backscatter at 140 MHz during E-region electron gas heating, *Ann. Geophys., 11*, 283, 1993.

Maeda, K., T. Tsuda, and H. Maeda, Theoretical interpretation of the equatorial sporadic E layers, *Phys. Rev. Lett., 11*, 406, 1963.

Monselesan, D. P., R. J. Morris, P. L. Dyson, and M. R. Hyde, Polar cap digital ionosonde observations of E-region Bragg scatter during intense lacuna conditions: implications for drift velocity determination, submitted to *J. Geophys. Res., (2003).*

Morris, R. J., D. P. Monselesan, and A. R. Klekociuk, Australian Antarctic research - A new direction, *Adv. Space, Res., 16(5)*, 151, 1995.

Piggott, W. R., and K. Rawer, U.R.S.I. Handbook of Ionogram Interpretation and Reduction, Revision of Chapters 1 to 4, Report UAG-23A, World Data Center A for Solar-Terrestrial Physics, 1978.

Schlegel, K., and J. P. St.-Maurice, Anomalous heating of the polar E region by unstable plasma waves 1. Observations, *J. Geophys. Res., 86,* 1447, 1981.

Tsunoda, R. T., J. K. Olesen, and P. Stauning, Radar evidence for a new low-frequency crossed-field plasma instability in the polar mesopause region: A case study, *Geophys. Res. Lett., 24*, 1215, 1997.

ROCKET OBSERVATION OF ELECTRIC FIELD CONDUCTED IN THE SEEK-2

T. Yokoyama [1], M. Yamamoto [1], S. Fukao [1], R. F. Pfaff [2]

[1] Radio Science Center for Space and Atmosphere
Kyoto University, Uji, Kyoto, Japan

[2] NASA/Goddard Space Flight Center, Greenbelt, MD, USA

1. INTRODUCTION

Quasi-periodic (QP) echoes associated with a sporadic-E (Es) layer in the midlatitude E-region have been intensively studied since the first discovery with the MU radar [*Yamamoto et al.,* 1991]. In order to investigate the mechanism for the generation of QP echoes, the SEEK (Sporadic-E Experiment over Kyushu) campaign was conducted in 1996 [e.g., *Fukao et al.,* 1998] in which two sounding rockets were launched from Kagoshima Space Center (KSC) in Uchinoura, Japan. A double-probe electric field sensor was loaded on the S-310-25 rocket which was launched at 23:00 LT on August 26, 1996. The detected electric field revealed complex electrodynamics that intense DC electric fields of 20 mV/m associated with narrow plasma density depletions, and a sinusoidal variation of ±3 mV/m between 130-170 km [*Pfaff et al.,* 1998]. The mechanism to generate such a large polarization electric field has been one of the important subjects associated with the QP echoes since the SEEK campaign.

In 2002, the SEEK--2 campaign was conducted as a succeeding project of the SEEK campaign. An electric field detector (EFD) was boarded on the S-310-31 rocket that deploys orthogonal double probes of 4.0 m tip-to-tip length from a rocket body. Four spherical sensors of 44.5 mm in diameter are attached on the tip of each probe to measure potentials with high impedance ($>10^{12}$ Ω) pre-amplifiers. The potential differences along the main diagonal axes were obtained in 1600 Hz sampling with 16-bit onboard A/D converters. The S-310-31 rocket was launched at 23:24 LT on August 3, 2002 from KSC and reached an apogee of 152 km at 194 s after liftoff. All instruments boarded on the rocket worked successfully.

2. OBSERVATIONAL RESULTS

Figure 1 shows the derived electric field during the upleg; the zonal component is shown in panel (a), the meridional component in (b), the magnitude in (c), and the direction of vectors in (d). Below 108 km, electric fields fluctuate strongly with an amplitude of less than 10 mV/m in each component which should be associated with Es layers and plasma irregularities. The fluctuation of electric fields is strongest from 95 to 102 km in which the direction is generally northwestward. The amplitude is relatively small from 102 to 106 km, and the intense peaks appear around 107 km. Above 108 km, on the other hand, such strong fluctuations disappear and 10 km-scale wavelike vertical structure remains up to the apogee with an amplitude of less than 5 mV/m. The direction of electric fields is mainly southward or southwestward but suddenly change to northeastward at 115, 128, and 139 km. They rotate clockwise with altitude from northeast to southwest and change to northeast again. Compared with the electric field measured in SEEK campaign, the major characteristics of strong fluctuations in lower altitudes and large scale structures in higher altitudes are quite similar. However, the magnitude of electric field in SEEK is nearly twice as SEEK-2 and strong fluctuations appeared up to 130 km. One possibility of this difference is solar activity (low in

1996 and high in 2002). The electric field observed during the downleg is shown in Figure 2. The electric field seems to have a offset directed to westward with an amplitude of 2 to 3 mV/m. A similar offset during the downleg is also found in the SEEK observation. The reason of the offset is not clear, but the wake of the rocket may cause this type of offset because the wake is larger during the downleg than the upleg and the nearly eastward rocket trajectory produce the wake at the west side of the rocket. Except the offset, 10 km-scale modulation of electric field was still observed above 110 km, and the peak of the magnitude exists at 103 km. The results below 100 km are not reliable because of the unstable rocket attitude.

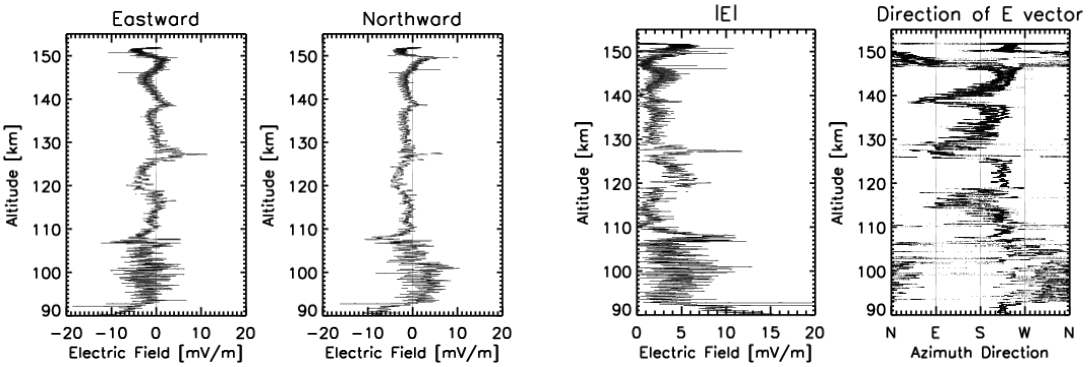

Figure 1. Electric field measured by EFD during the upleg.

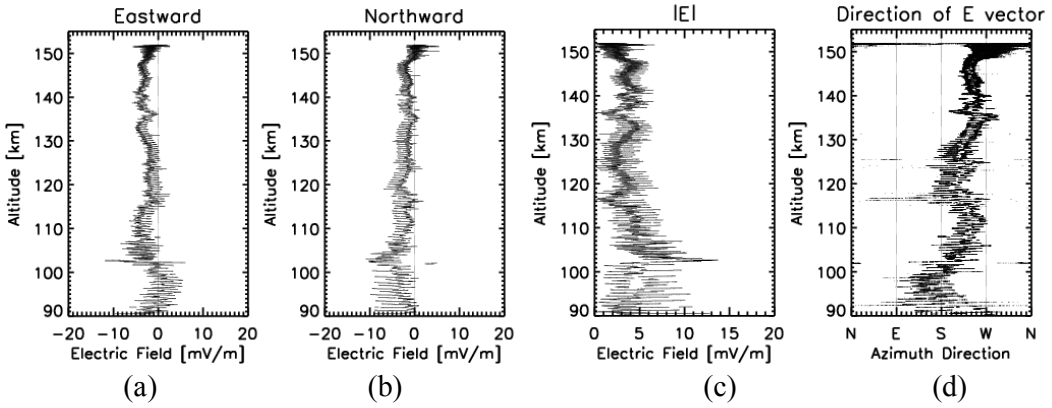

Figure 2. Electric field measured by EFD during the downleg.

3. NUMERICAL SIMULATION

Yokoyama et al. [2003a, b] showed with 2-D and 3-D numerical simulation models that intense polarization electric fields can be generated in association with inhomogeneous Es layer. One of the results is shown in Figure 3. The plasma cloud that has a Gaussian distribution in the meridional plane with a maximum density of 4 x 10^5 cm^{-3} is assumed at 100 km. The half width of the distribution is 3.3 km and the zonal elongation is 15 km. A horizontal Es layer with a maximum density of 1.1 x 10^5 cm^{-3} is assumed at the same altitude. The conductivity integrated over the F-region is added at the top boundary. As an external force, we apply a southward neutral wind which has a Gaussian distribution with the maximum amplitude of 70 m/s at 100 km. In response to the southward neutral wind, polarization electric fields of northward/upward direction are generated to maintain the

current continuity and map along the geomagnetic field. An ambient zonal electric field plays the same role as the meridional neutral wind. The amplitudes are 5.3 and 3.2 mV/m on horizontal and meridional-vertical planes, respectively. The polarization electric fields drive eastward Hall current within the plasma cloud. Since conductivity sharply drops at both edges of the cloud, the eastern edge become positively charged and the western edge negatively. At both edges of the cloud, the current is connected with field-aligned currents that are downward at the western edge and upward at the eastern edge. Around the center of the plasma cloud, the field-aligned current also flows in and out but the amplitude is smaller. As a result, the current circuit is established between the plasma cloud in the lower E-region and the upper boundary, that is, the equivalent F-region. After 60 s, field-aligned plasma structures are formed, especially at the eastern and western edge of the plasma cloud.

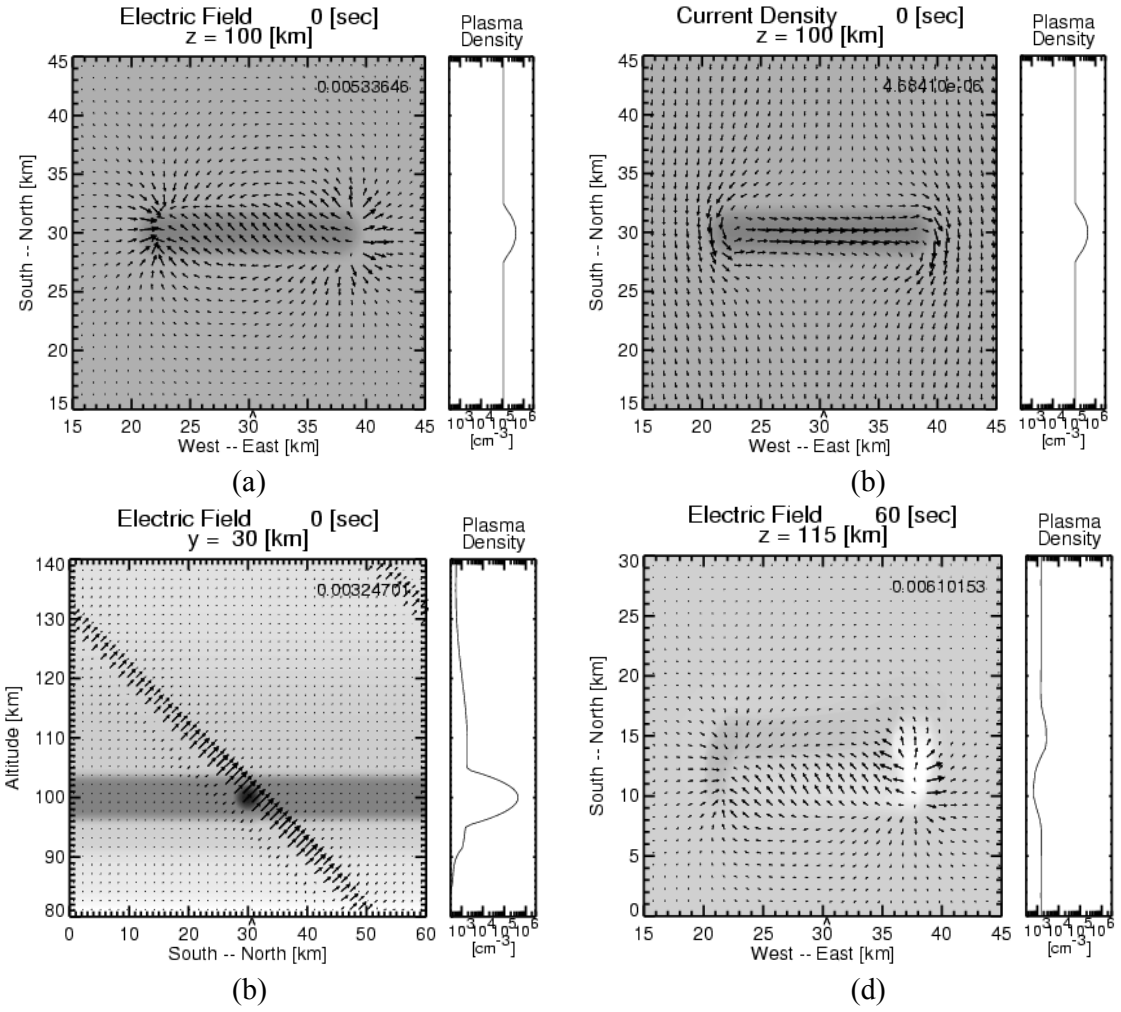

Figure 3. Results of numerical simulation for generation of polarization electric fields.

4. CONCLUSIONS

We have studied electric fields in the ionospheric E-region by the rocket observation and the numerical simulation. When Es layers have inhomogeneous structures, polarization electric fields can be generated by ambient electric fields or neutral winds. The generated polarization

electric fields map along the geomagnetic field and produce field-aligned plasma density structures up to 120 km. 10 km-scale vertical modulation of the electric field observed with the rocket may be due to the horizontal structure of inhomogeneous Es layer. The Hall currents driven by the polarization electric field within the Es layer flow up to the F-region as field-aligned currents which couple both regions. The coupling between the E- and the F-region, and between the ionosphere and the neutral atmosphere will be future works.

REFERENCE

Fukao, S., M. Yamamoto, R. T. Tsunoda, H. Hayakawa, and T. Mukai, The SEEK (Sporadic-E Experiment over Kyushu) campaign, *Geophys. Res. Lett., 25,* 1761-1764, 1998.

Pfaff, R., M. Yamamoto, P. Marionni, H. Mori, and S. Fukao, Electric field measurements above and within a sporadic-E layer, *Geophys. Res. Lett., 25,* 1769-1772, 1998.

Yamamoto, M., S. Fukao, R. F. Woodman, T. Ogawa, T. Tsuda, and S. Kato, Midlatitude E region field-aligned irregularities observed with the MU radar, *J. Geophys. Res., 96,* 15,943-15,949, 1991.

Yokoyama, T., M. Yamamoto, and S. Fukao, Computer simulation of polarization electric fields as a source of midlatitude field-aligned irregularities, *J. Geophys. Res., 108*(A2), 1054, doi:10.1029/2002JA009513, 2003a.

Yokoyama, T., M. Yamamoto, S. Fukao, and R. B. Cosgrove, 3-D simulation on generation of polarization electric field in the midlatitude E-region ionosphere, *J. Geophys. Res.,* in press, 2003b.

MULTITAPER SPECTRAL ANALYSIS OF ATMOSPHERIC RADAR SIGNALS

V.K.Anandan[(1)*], T. Rajalakshmi[(2)], G. Ramachandra Reddy[(2)], C.J.Pan[(1)]

(1) Institute of Space Science, National Central University, Chung-Li, 32054, Taiwan
Email: anandanvk@hotmail.com
*On leave from National MST Radar Facility, Gadanki, India
(2) Department of EEE, SV University, Tirupati, AP, India, 517 502

Abstract

Multitaper spectral analysis using sinusoidal tapers has been carried out on back-scattered signals received from the troposphere and lower stratosphere by the Gadanki mesosphere-stratosphere-troposphere (MST) radar under various conditions. The sine tapers have much narrower main lobe and much higher side lobes. Thus they achieve a smaller bias due to smoothing by the main lobe, but at the expense of side lobe suppression. The analysis is carried out on different data sets. Comparison of study is made with single taper to understand the relative merits of the processing under the scheme. The result shows that multitaper analysis gives better signal to noise ratio or higher detectability. The signals are better identified in the multitaper analysis in both sets of data. The spectral analysis through multitaper and single-taper is subjected to study of consistency in measurements. Result shows that multitaper is having very low variance compared to single taper estimators.

Introduction

Tapering is another name for the data windowing operation in the time domain. Single taper smoothed spectrum estimates are plagued by a trade-off between the variance of the estimate and the bias caused by spectral leakage [Park et al., 1987]. Applying a taper to reduce bias, discards data, increasing the variance of the estimate. Using a taper also unevenly samples the record. Single-taper estimators, which are less affected by leakage, not only have increased variance but also can misrepresent the spectra of non-stationary data. So as long as only a single data taper is used, there will be a trade-off between the resistance to spectral leakage and the variance of a spectral estimate.

Thomson [1982] introduced the multitaper spectral analysis technique and application found in various scientific fields[Park et al., 1987]. First, the data are multiplied by not one, but several leakage-resistant tapers. This yields several tapered time series from one record. Taking the DFTs of each of these time series, several "eigen spectra" are produced which are averaged to form a single spectral estimate. The central premise of this multitaper approach is that if the data tapers are properly designed orthogonal functions, then, under mild conditions, the spectral estimates would be independent of each other at every frequency. Averaging would reduce the variance while proper design of full - length windows would reduce bias and loss of resolution.

Reidel and Siderenko [1995] proposed a set of orthonormal taper, which contain harmonically related sinusoidal tapers. These tapers are called sinusoidal tapers or minimum bias tapers. The discrete analogs of the continuous time minimum bias tapers are called sinusoidal tapers. The n^{th} sinusoidal taper is given by

$$v_k(n) = \sqrt{\frac{2}{N+1}} \sin\left(\frac{\pi k n}{N+1}\right) \quad ; \ n = 1,2,\ldots,N \ ; \quad k=1,2,\ldots,K \qquad (1)$$

Identifying the signal and computing the three low order spectral moments is central to the problem of extracting information from the Doppler spectrum of the Mesosphere-Stratosphere-Troposphere (MST) radar signal. The straightforward method of analyzing the MST radar spectral data is based on identifying the most prominent peak of the Doppler spectrum for each range gate and computing the three low order spectral moments using the expressions given by Woodman [1985]. Since MST radar signals are characterized by rapidly falling signal-to-noise ratio (SNR), the identification of atmospheric signals and in a weak

SNR condition is always difficult and leading to erroneous estimation of moments. To demonstrate the capability and advantageous of this method, analysis is carried out with multitaper spectral estimate on MST radar signals.

Observation and Results

MST radar at Gadanki (13.5°N, 79.2°E) is operated on 11 April and 10 May 2002 with 6 beam directions (Zenith-X, Zenith-Y in vertical and East, West, North, South direction with 10 deg from vertical) in high-resolution mode to receive the atmospheric data. This data is subjected to the analysis based on multitaper and normal windowing (rectangular) spectral estimation. For multitaper spectral estimation 3rd order taper is used, which is found to be optimum in this case. After removing the noise [Hildebrand and Sekhon, 1974], the first three order moments are estimated from the spectrum using the expressions given by Woodman [1985].

Figure 1a1 and 1a2 shows the power spectrum obtained using multi taper and rectangular window on 10 May 2002. This day, the radar echoes were reasonably strong and able to see the data up to 23 km in the case of multi taper spectral estimate and up to 22 Km in the case of rectangular window method. Figure 1b1 and 1b2 shows the data on 11April 2002, analyzed with the multi taper and rectangular window respectively. This day the radar echoes were very weak and trace is visible only up to 20 Km with intermittent breaks. In both cases the multitaper based power spectrum is better visible. In multitaper spectrum the noise fluctuations are very less and the echoes are less compared to that of power spectrum obtained through rectangular window. This shows that multitaper spectral estimation is working in a higher SNR regime and the signal detectability is improved by this method. The method is applied to data obtained through other beam directions also. Similar result is observed in all cases.

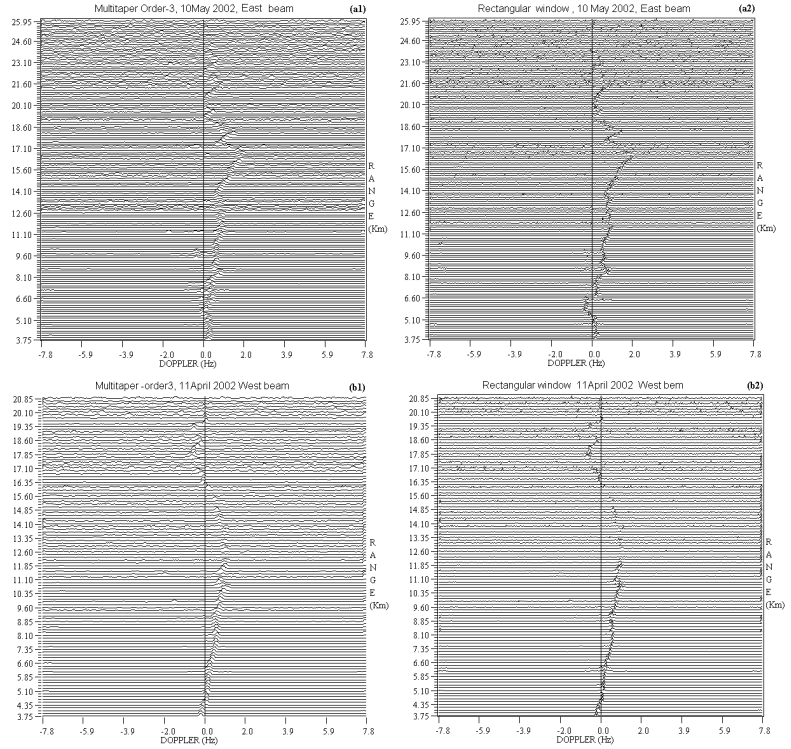

Figure 1 power spectrum obtained through (a1)Multitaper order-3, (a2) rectangular window on 10May 2002, (b1) same as that of (a1) but on 11 April 2002, 9b2) same as that of (a2) but on 11April 2002

The above data further analyzed to estimate the first three order moments such as power (SNR), Doppler and Doppler width. Figure 2a1 and 2a2 shows the mean Doppler obtained from the power spectrum for the west beam on 10 May with Multitaper and rectangular window respectively. The mean Doppler is obtained from 15 minutes observation

(5 frames). The standard deviation is plotted over the mean profile. The result shows that the consistency in estimation and low variance through multitaper spectral estimation than that

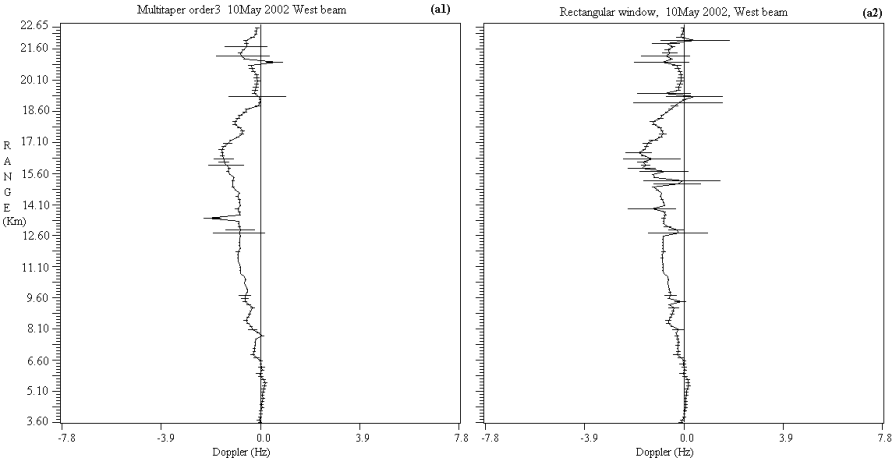

Figure 2 Mean Doppler with standard deviation obtained through (a1) Multitaper order-3 (a2) Rectangular window for west beam on 10May 2002

of conventional method. Figure 3a and 3b shows the SNR plot of Doppler profile with multitaper (solid line) and rectangular window (dot line) for west and Zenith beam respectively. The multitaper based spectral analysis method gives higher SNR of the order of 1- 4dB than that of rectangular window based method. This is due to the fact that in the multitaper spectral analysis noise fluctuation are reduced and there by enhanced SNR.

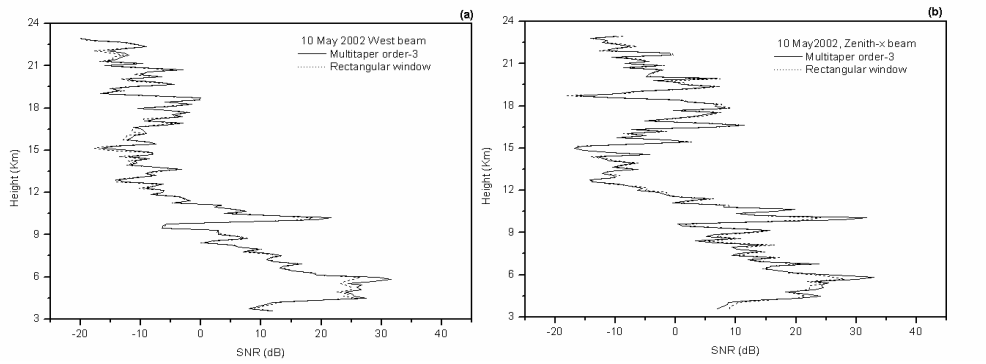

Figure-3 SNR profiles obtained through multitaper and rectangular window on 10 May 2002 (a) West beam (b) Zenith-X beam.

Atmospheric signals are highly contaminated with noise and are often difficult to detect the signal from the background noise. Since multitaper spectral estimation reduces variances of noise the method yield better estimates during such environment. Figure 4a and 4b shows the power spectrum plot of a weak region between 17.55 to 18.30 Km of atmosphere obtained through multitaper and rectangular window method respectively. It is clear from the plots that the echoes are well defined in multitaper spectral estimate than that of other method. The ambiguity in identifying the echoes is very less in the case multitaper method. The result also shows that the spectral peak and the valley point (area under the spectrum) are easy to identify there by better estimation of signals. Due to this obvious reason the spectral width measured by this method is generally higher than that of conventional method. Figure 5a and 5b shows the Doppler width obtained through multitaper and rectangular window for west and Zenith-X beam respectively. Multitaper spectral estimate always shows higher Doppler width in all beams. Since the valley point of signal peaks is able to identify correctly in multitaper spectral estimate this estimation may be more accurate. The Doppler width is one of the important parameter for studying the turbulence and dynamics of the atmosphere, the improvement in measuring the Doppler Width is distinct advantage in this method. The analysis is carried out on all beams and similar result is obtained.

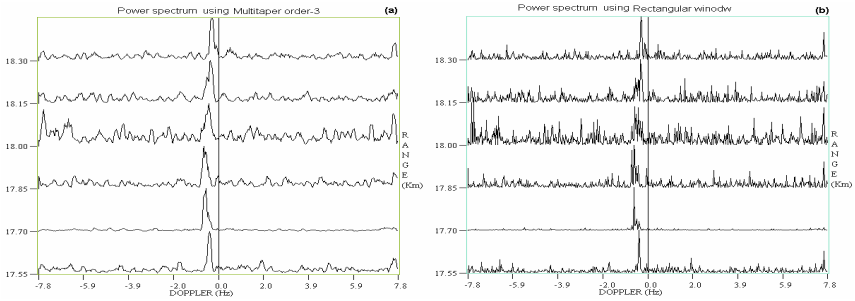

Figure-4 Power spectrum plots of a weak SNR region obtained through (a) multitaper (b) rectangular window

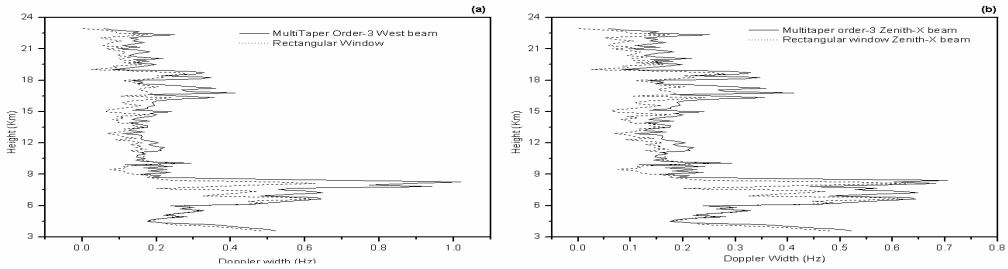

Figure-5 Doppler width profile obtained through multitaper and rectangular window based method for (a) west beam (b) Zenith-X beam

Conclusion

With the above analysis we conclude that multitaper analysis gives a better visible trace and also the tracking of the Doppler echoes up to a height of 23km is achieved where as rectangular analysis could trace up 20 Km with less variance. An improvement of 1-4 dB in the SNR is achieved with multi taper analysis leading to a better detectability. The consistency of the Doppler trace obtained through multi taper analysis is seen to be superior to that of the rectangular analysis. Multitaper analysis is able to produce high-resolution observation points in time. Multitaper analysis generally shows higher Doppler width than that of single taper analysis. Since the signal boundaries are clearly defined in the case of multitaper estimation the Doppler width measured expected to be higher. So, the result shows that multitaper analysis gives distinct advantage over conventional method of spectral analysis.

References:

Hildebrand, P.H., and R.S.Sekhon, Objective determination of the noise level in Doppler spectra, J.Appl.Meterol.,13, 808-811, 1974.

Park Jeffrey, C.R. Lindberg and Frank L. Venron III, Multitaper Spectral Analysis of High Frequency Seismograms, Journal of Geophysical Research, Vol.92, No. B12, November 10,1987.

Reidel Kurt.S., and Alexander Siderenko, Minimum Bias Multiple Taper Spectral Estimation, IEEE Transactions on Signal Processing, Vol.43, No.1, January 1995.

Thomson.D.J., Spectrum estimation and harmonic analysis, IEEE proc., 70, 1055-1096, 1982.

Woodman, R.F., Spectral moments estimation in MST radars, Radio Sci., 20, 1185-1195, 1985.

OBSERVATIONS OF METEOR-HEAD ECHOES USING THE JICAMARCA 50 MHZ RADAR IN INTERFEROMETER MODE

J. L. Chau, R. F. Woodman, and M. A. Milla
Radio Observatorio de Jicamarca, Instituto Geofísico del Perú, Lima

1. Introduction

High-power large-aperture radars frequently detect very fast meteor head echoes with a range-rate velocity which follows the meteoroid as it travels through the upper atmosphere. Although meteor ``head echoes'' were first observed in the late 1940s, this topic has become an area of interest only recently as scientists have focused more intensely on the importance and usefulness of meteors [e.g., *Janches et al.,* 2003, and reference therein]. Head echo measurements accurately give radial velocities (toward the radar) and altitude ranges of deposition. Measurements are also provided for, with varying degrees of accuracy, transverse velocities, deceleration rates, and signal strengths as a function of altitude. The powerful narrow-beam radars which measure head echoes detect far smaller meteors than do classical meteor radars [e.g., *Elford*, 2001]. The use of these radars allows us to study the population of meteors which probably contributes the most material to the Earth's upper atmosphere.

One of the main drivers for the increasing interest on meteor studies has been the presence in recent years of spectacular Leonid meteor showers. At Jicamarca that was not an exception and meteor observations, particularly of head echoes, have been carried out since November 1998.

Meteor studies have been particularly difficult over Jicamarca due to the presence of very strong equatorial electrojet (EEJ) echoes [*Farley*, 1985] and non-specular trail echoes [*Chapin and Kudeki*, 1994]. This geophysical ``clutter'' (for meteor head echo studies) occur at similar altitudes where most head echoes are expected (between 90 and 120 kms). Nonetheless, with the recent improvements of our acquisition systems, we have started the head echo observations around sunrise times when EEJ are expected to be weaker or sporadic.

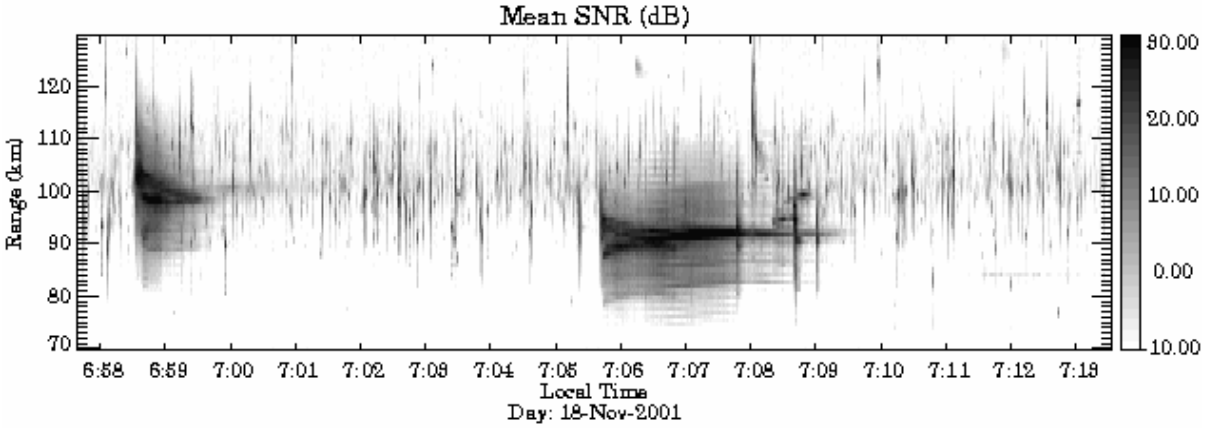

Figure 1. Range-time intensity plot of meteor echoes. The meteor-head are represented by the vertical gray striations (~1 per second). Examples of long-lived meteor trails occur around 0659 and 0706 LT

In Figure 1, we show an example where meteor head echoes are observed at the same time when long-lived meteor trail echoes are present (around 0659 and 0706). All the striations in light gray represent head echoes (~1 head-echo per second). Although in this work we discuss the head echo results, the long-lived [*Chapin and Kudeki*, 1994] and the non-specular [*Dyrud et al.*, 2002] meteor trails are being studied independently (M. Oppenheim personal communication).

As we show below, Jicamarca offers unique observations to the world-wide effort of improving the understanding of meteors. It has the lowest frequency of all the high-power large-aperture radars (50 Mhz), it is located under the magnetic equator and it is able to measure the three dimensional vector of head echoes by operating in the interferometric mode [*Woodman*, 1971]. The MU radar [*Sato et al.*, 2000] and the ALTAIR radar [*Close et al.*, 2002] are also able to determine the three dimensional vector velocity.

2. Experimental Setup

Meteor-head observations have been made using the large Jicamarca array (~300mx300m) for transmission and all four quarter sections for reception (~75mx75m), in both cases using the same linear polarization. The antennas were phased to point on-axis, i.e., -1.46^o off-vertical in the *y* direction (see Figure 2).

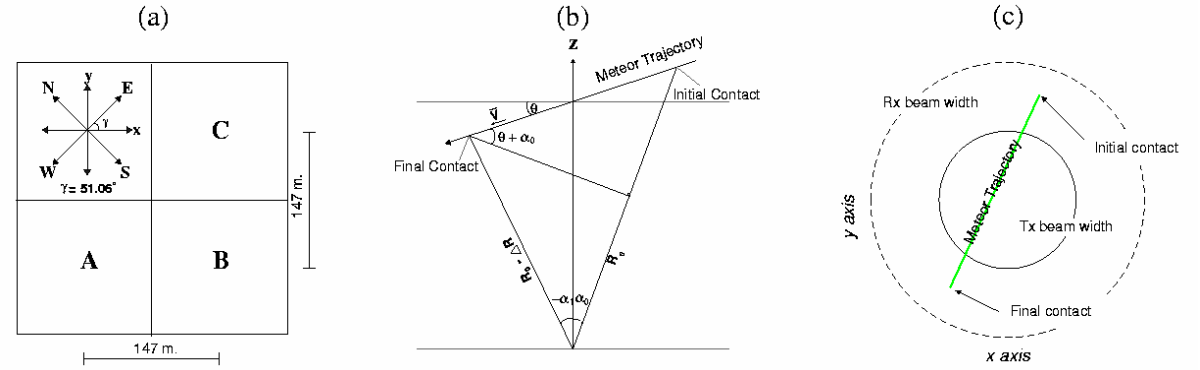

Figure 2. (a) Antenna configuration for interferometric observations of meteors, note that the East-West baseline is rotated ~51.06^o respect to the *x* axes. Simplified geometry of a meteor trajectory respect to the illuminated beam: (b) altitudinal and (c) angular views.

Although complex voltages (raw data) from four quarters were recorded, we only need the information of three non-collinear antennas in order to locate the meteors inside the transmitting beam. For the results we present in this work, we have used quarters A, C, and D to get the direction cosines of meteors respect to the *x* and *y* axis. Note that the East-West baseline is rotated ~51.06^o respect to the *x* axes. Figures 2b and 2c show a simplified diagram of a meteor trajectory inside the illuminated beam as a function of altitude and for an angular view, respectively. The actual transmitting half-power beam width is ~1^o. Although the transmitting beam width is very narrow for most observations at Jicamarca, it is wide enough to detect meteors coming from a wide range of elevation angles.

As it was mentioned in the introduction meteor-head echoes come from altitudes where strong geophysical ``clutter'' due to EEJ and meteor trail echoes occur. Therefore a special observing mode is needed to try to overcome this clutter. The main parameters of this observing mode are IPP of 200 kms, pulse width of 9.75 kms (using 13-bit Barker code), sampling range of 0.75 kms, initial sampling range at 70 kms, and transmitter peak power of 2 MW.

3. Technique Description

Once the raw data has been recorded, we proceed to obtain the parameters of meteor-head echoes. We have divided our processing technique in three different stages: (a) raw data decoding, (b) signal statistics and meteor detection, and (c) meteor characterization. In the case of meteor-head echo observations the decoding is not only use for improving the range resolution but also for estimating the meteor radial velocities. In order to accomplish proper decoding, for each raw-data profile at time *t*, we have iteratively searched for the Doppler velocity that optimizes the decoded power profile. Furthermore, we have used a second filter

on the decoded raw data profiles to decrease further the peak to side-lobe levels (from -22 dB to less than -32 dB) at the expense of spreading the side-lobe contamination into more ranges. This second filter is needed in order improve the discrimination between head and trail echoes.

Once the Doppler velocity for optimum decoding is found, the raw voltages for each of the channels are decoded and signal statistics are recorded. Then we proceed by finding the range where the power is highest for each profile. Working with the ``peak'' signal statistics is much faster, allowing us to test and implement robust algorithms for meteor characterization. We have been able to measure directly, the initial range, the range coverage, signal-to-noise ratio, radial velocities (using three methods), and duration of the meteor, radial decelerations, and azimuth of meteor trajectory. In addition, we are able to derive the absolute velocities and decelerations, and elevation angles.

3. Results

Our observations have been mainly conducted around Leonid meteor showers since 1998. However we have recently started observations at different seasons. Statistically, we are observing similar characteristics during Leonid and non-Leonid events in velocity, deceleration and altitude distributions. In Figure 3, we show examples of where meteors are coming from during a Leonid (left) and non-Leonid (right) event. The sky maps show the projected Ecliptic plane (solid black curve), some constellations for reference, and the Earth's Apex (thick star) for the given time. Each meteor observed around 0700 LT are represented with circles. The absolute velocity is color-coded and the size is proportional to the signal-to-noise ratio (SNR).

4. Summary and Conclusions

As it has been shown in previous sections, we have successfully implemented a technique to observe and characterize meteor head echoes at equatorial latitudes. The use of the large power-aperture capabilities at Jicamarca has allowed us to observe a high rate of meteors (more than 3000 per hour) in the small volume subtended by the 1^o antenna-beam. Moreover, using interferometry, we have been able to characterize the three-dimensional components of meteor velocities in the Earth's frame of reference.

Our results do not show any evidence of the Leonid meteor showers, in agreement to result reported by other large power-aperture radars. We have shown that meteor parameters during both Leonid and non-Leonid events are statistically similar (range of occurrence, velocity distribution, deceleration distribution, origin). Apparently, we detect only the very small sporadic meteors, which are much more abundant than the larger meteors associated to major meteor showers and which seldom cross the 1^o antenna beam.

Besides providing meteor-head observations at a unique frequency (50 MHz) and location (equatorial latitudes), our results are particularly important for the 3D characterization of meteor heads. We have shown, at different seasons that the velocity distribution of meteors respect to the Earth's frame of reference is clustered around the Earth Apex, within $\pm 18^o$ transverse to the Ecliptic and narrow ($\pm 8.5^o$) in heliocentric longitude in the Ecliptic plane. A change to a solar inertial frame of reference, roughly double the widths of these distributions, since most of the meteors have a relative velocity which is about twice the orbital velocity of the Earth. The velocity representation in heliocentric coordinates including the gravitational attraction as well as its orbital distribution will be left for a future effort.

So far, our observations have been concentrated around sunrise time when the EEJ are expected to be weak. In the future, we plan to extend our observations to other times,

particularly during daytime counter electrojet conditions when EEJ are also expected to be weak. Moreover, we plan to continue improving the technique in order to get better time coverage as well as more precise parameters.

More results are presented and discussed in detail by *Chau and Woodman* [2003].

Acknowledgements

The Jicamarca Radio Observatory is operated by the Instituto Geofísico del Perú, with support from the NSF Cooperative Agreement ATM-9911209 through Cornell University.

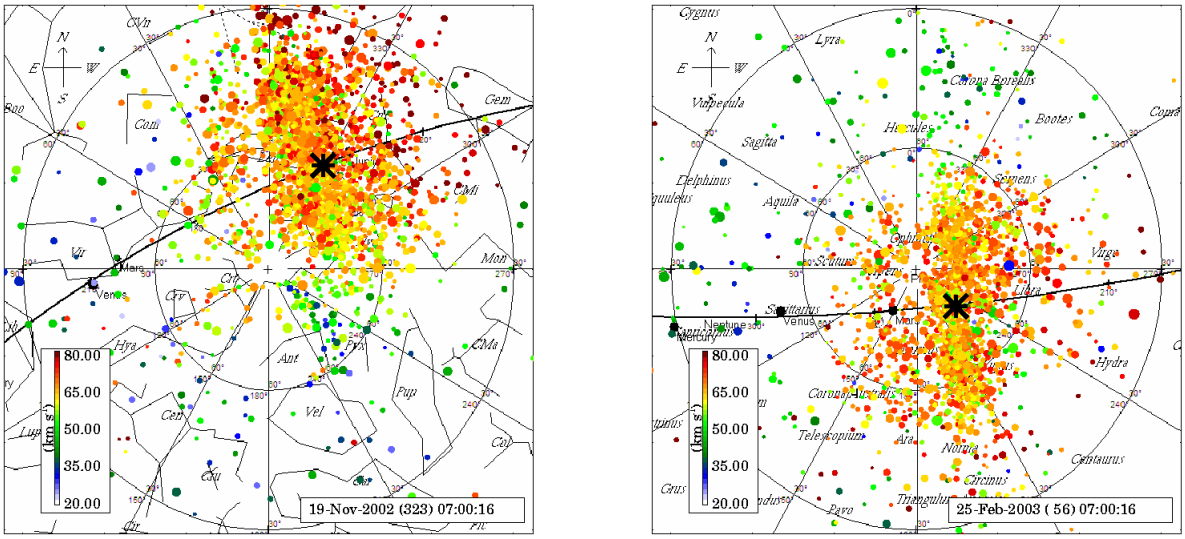

Figure 3. Sky maps representing where meteors are coming from for a Leonid (left) and non-Leonid (right) events, around 0700 LT. Each meteor is represented with circles, the absolute velocity is color-coded and the size is proportional to SNR.

Bibliography

Chau, J. L. and R. F. Woodman, Observations of meteor-head echoes using the Jicamarca VHF radar in interferometer mode, *Atmos. Chem. Phys.*, submitted, 2003.

Chapin, E. and E. Kudeki, Radar interferometric imaging studies of long-duration meteor echoes observed at Jicamarca, *J. Geophys. Res., 99,* 8937-8949, 1994.

Close, S., S. M. Hunt, F. M. McKeen, and M. J. Minardi, Characterization of Leonid meteor head echo data collected using the VHF-UHF advanced research rpjects agency long-range tracking and instrumentation radar (ALTAIR), *Radio Sci., 37,* 10.1029/2000RS002602, 2002.

Dyrud, L. P., M. Oppeneheim, S. Close, and S. Hunt, Interpretation of non-specular radar meteor trails, *Geophys. Res. Lett.*, 10.1029/2002GL015 953, 2002.

Elford, W. G., Novel applications of MST radars in meteor studies, *J. Atmos. Sol. Terr. Phys.*, *63*, 143–153, 2001.

Farley, D. T., Theory of equatorial electrojet plasma waves: New developments and current status, *J. Atmos. Sol. Terr. Phys.*, 729–744, 1985.

Janches, D., M. C. Nolan, D. D. Meisel, J. D. Mathews, Q. H. Zhou, and D. E. Moser, On the geocentric micrometeor velocity distribution, *J. Geophys. Res.*, *108*, 10.1029/2002JA009789, 2003.

Sato, T., T. Nakamura, and K. Nishimura, Orbit determination of meteors using the MU radar, *IEICE Trans. Commun.*, *E83-B*, 1990–1995, 2000.

Woodman, R. F. Inclination of the geomagnetic field measured by an incoherent scatter technique, *J. Geophys. Res., 76,* 178-184, 1971.

RANGE IMAGING OBSERVATIONS OF PMSE USING THE EISCAT VHF RADAR: PHASE CALIBRATION AND FIRST RESULTS

J. R. Fernandez [a], R. D. Palmer [a], P. B. Chilson [b], I. Häggström [c], M. T. Rietveld [d]

[a]Department of Electrical Engineering, University of Nebraska, Lincoln, USA
[b]CIRES–University of Colorado and NOAA Environmental Technology Lab., USA
[c]EISCAT Scientific Association, Box 164, S-98123 Kiruna, Sweden
[d]Max–Planck-Institut fur Aeronomie, 37191 Katlenburg–Lindau, Germany

1 Introduction

In this work, a novel phase calibration technique for use with the multiple-frequency Range IMaging (RIM) technique is introduced based on genetic algorithms. The method is used on data collected with the European Incoherent SCAtter (EISCAT) VHF radar during a 2002 experiment with the goal of characterizing the vertical structure of Polar Mesosphere Summer Echoes (PMSE) over northern Norway. For typical Doppler measurements, the initial phases of the transmitter and receiver are not required to be the same. The EISCAT receiver systems exploit this fact, allowing a multi-static configuration. However, the RIM method relies on the small phase differences between closely spaced frequencies. As a result, the high-resolution images produced by the RIM method can be significantly degraded if not properly calibrated. The novel method is applied to preliminary data from the EISCAT radar providing first results of RIM images of PMSE.

The EISCAT VHF radar has a nominal operating frequency of 224 MHz, but it is capable of operating at frequencies ranging from 222.4–225.4 MHz in steps of 200 kHz. The 16 frequencies are denoted by F0–F15, respectively. Although more frequencies are available, only five receiver boards were available at the time of the experiment. For the preliminary results presented here, the following frequency combination, F7, F9, F11, F13, and F15 were used, providing a 400 kHz frequency separation.

2 Effect of phase errors on range imaging

For notation purposes, the initial phase values for the transmitter and receiver using frequency n will be denoted by δ_T^n and δ_R^n, respectively. Assuming a single layer located at range z_I, the returned, coherently detected signal x_n can be modeled as the following

$$x_n = \tilde{A}_n e^{j[w_d^n t + \delta_n - 2k_n \tilde{z}]} + \epsilon_n \tag{1}$$

where $\tilde{A}_n$ is the returned amplitude and w_d^n represents the Doppler frequency for frequency n. The term $\delta_n = \delta_T^n - \delta_R^n$ is the difference in the phase of the transmitter and receiver, k_n is the corresponding wavenumber for frequency n, and $\tilde{z} = z_I + z_0$ is the sum of the layer range (z_I) and the range shift due to the system delay (z_0). Finally, ϵ_n represents the additive white Gaussian noise in each signal with zero mean and variance σ^2. It should be noted that the phase difference δ_n should remain constant throughout the experiment.

Using the cross-covariance definition between two signals l and m and the Fourier RIM power as defined in *Palmer et al.* [1999], and assuming one layer located at z_I, it can be shown that the Fourier RIM power is given by

$$P_F(r) = \sum_{i=1}^{N} (\tilde{A}_i^2 + \sigma^2) + 2 \sum_{n=1}^{N-1} \sum_{m=n+1}^{N} \tilde{A}_n \tilde{A}_m \cos\left[2(k_n - k_m)(r - z_I) + \hat{\delta}_{nm}\right] \tag{2}$$

where $\hat{\delta}_{nm} = (\delta_l - \delta_m) - 2z_0(k_l - k_m)$ represents the phase errors. As seen, these phase errors introduce a phase shift for each cosine function in the summation of the Fourier power within a given range gate. If no errors are present, the cosine functions will be aligned at the imaged range z_I and will add coherently.

3 Phase calibration using genetic algorithms

The Genetic algorithm (GA) is a robust optimization technique based on natural evolutionary mechanisms. Introduced by *Holland* [1975], the first algorithm was called the simple genetic algorithm (SGA) with the goal of obtaining better estimates in global optimization scenarios. SGA mimics nature's evolutionary characteristics by manipulating a given population of possible solutions (individuals), and searching for the best solution to solve an optimization problem. Basically, SGA operates through the following steps: (1) creation of a population (possible solutions), (2) evaluation of each individual in the population, (3) selection of the best individuals, and (4) genetic manipulation to create a new population. Therefore, after manipulation, a new population is produced with more optimal genetic characteristics. The SGA repeats the cycle until a certain condition is satisfied. This condition could be, for example, a predefined number of generations or some desired fitness level.

The proposed phase calibration algorithm, based on the SGA approach, is devised as follows. First, an image of the total echo power is constructed as a function of time and height. Then a predefined window is chosen as the region surrounding the highest signal-to-noise ratio (SNR) pixel from the image. In the selected window, the SGA algorithm is applied. For our particular application with the EISCAT radar, five frequencies will be used to implement RIM. Therefore, five unknown phase values ϕ_l $(l = 1, \cdots, 5)$ must be estimated. The Fourier RIM power is considered as a fitness function to evaluate new generations of potential solutions. When the fitness function is called for an evaluation, a unique phase calibration matrix denoted by $\mathbf{\Phi}^i$ for a specific individual i is formed with the elements $\Phi^i_{lm} = \langle \phi^i_l {\phi^i_m}^* \rangle = e^{-j\delta^i_{lm}}$ where l and m represent the different frequency combinations $(l, m = 1, \cdots, 5)$. If $\delta^i_{lm} \approx \hat{\delta}^i_{lm}$, the Fourier RIM power will be maximized and the term Φ^i_{lm} is chosen so as to cancel the original phase offsets. Then, the calibration operation is simply performed by an element-by-element multiplication of the contaminated covariance matrix with calibration matrix $\hat{R}_{lm} = R_{lm} \cdot \Phi^i_{lm}$ at every evaluation. The selection algorithm assigns high fitness values to individuals that allow the Fourier RIM power to be maximized. The SGA loop is repeated until a certain number of generations is reached. After the SGA process, the optimal phase calibration matrix $\mathbf{\Phi}$ is formed and used to correct the entire original image.

4 Experimental results

Figure 1 shows a comparison of the corrupted Capon RIM power image with random phase errors and the calibrated RIM image after the application of the proposed GA-based method. The vertical white lines at approximately 10:35 UT emphasize the region to which the calibration procedure was applied. The learning curves from the GA are also provided in the bottom panels of the figure. Given the large vertical extent of the PMSE layers, any enhancement due to the calibration is difficult to observe.

The effect of the GA-based calibration is more easily observed by scrutinizing a smaller region of the data. Figure 2 provides the echo power, original RIM image, and calibrated RIM image for a 10-min period from 1035–1045 UT at an altitude of approximately 85 km. Note the more natural transitions between range gates and finer detail in the calibrated RIM image. Without calibration, the RIM power centers are distorted and unnaturally contained within each gate. Further, range weighting-function effects can be observed similar to those reported by *Chilson et al.* [2003].

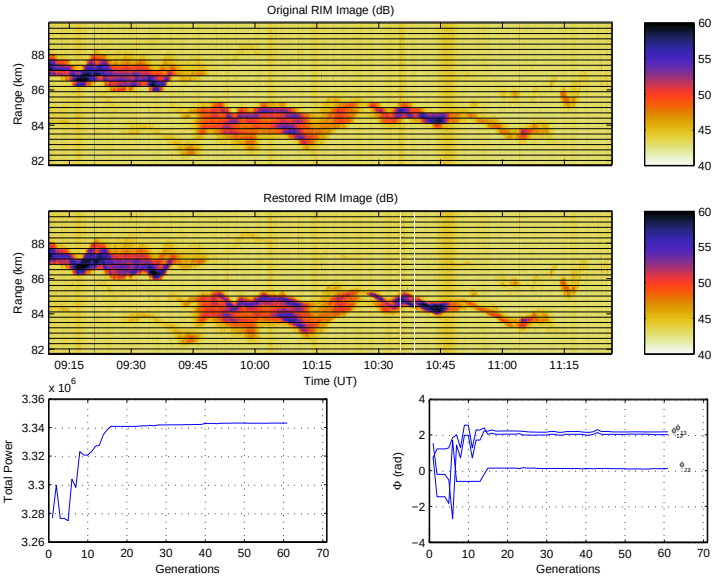

Figure 1: *Comparison of corrupted RIM image and phase-calibrated RIM image.*

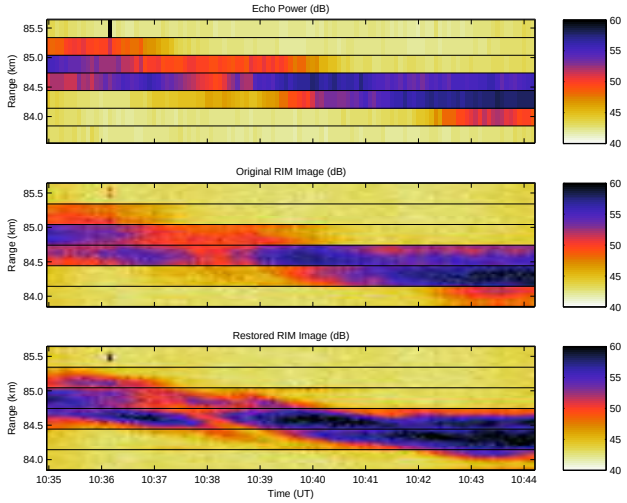

Figure 2: *Smaller region of the overall data set.*

A specific RIM PMSE case study is depicted in Figure 3. This particular data window was chosen since it exhibits significant vertical structure emphasizing the transition between the upper and lower layers. It was taken from the restored RIM image presented in Figure 1. The radial velocity (vertical), spectral width, and calibrated RIM image are shown for a 35-min period and a 7-km region centered at 85 km.

An interesting effect is present in the multiple layers of the overall PMSE structure in that the vertical velocity shows vertical continuity throughout the layers. Therefore, it seems obvious that the multiple layers are dynamically connected, throughout at least the vertical flow, even though the echo power shows a distinct separation between the layers. The spectral width, which is related to aspect sensitivity, exhibits the expected behavior where the lower layer at 84 km shows a significantly smaller spectral width than does the upper layer. More interestingly, the upper layer at 87 km seems to show a similar effect up to about 0934 UT where the bottom side of the layer has smaller spectral width mimicking the behavior of the overall layer. The RIM images can be thought of as high-resolution images of echo power and indicate an almost complete separation between the layers. The small-scale sub-layers possess a natural oscillation and transition between range gates indicative of gravity waves. The period is approximately 5–10 min with direct correlation with the vertical velocity structure. Given the vertical continuity of vertical velocity and the observed gravity wave activity, the multiple layering structure of the

PMSE is more easily interpreted as due to gravity wave modulation of the background temperature profile [*Chilson et al.*, 1997; *Rapp et al.*, 2002]. Generally, we find that the GA-based phase calibration method has allowed the calculation of RIM echo power images with improved resolution and clarity.

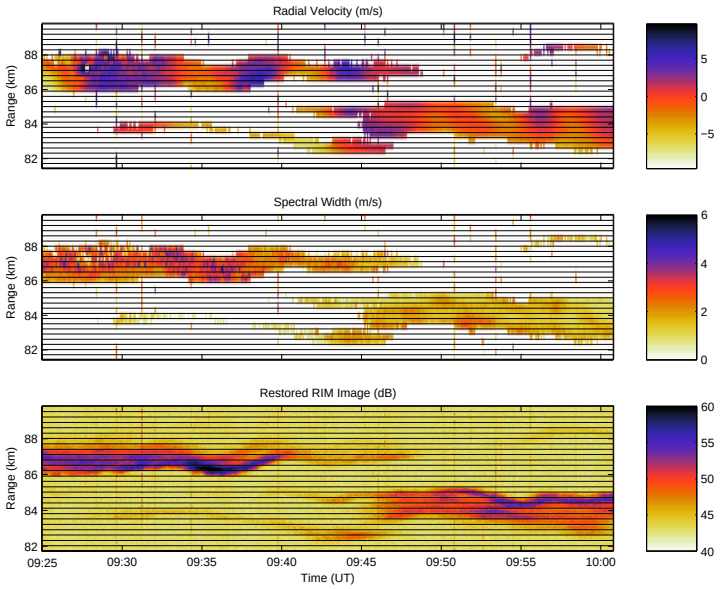

Figure 3: *Radial velocity (vertical), spectral width, and calibrated RIM image.*

5 Conclusions

A novel GA-based phase calibration algorithm for RIM imaging applications has been presented. It was shown that this method provides robust initial phase estimation with fast convergence rates. The total power over a predefined window in the initial RIM image was used as the fitness function. By maximizing this total power as a function of phase error, the GA was able to provide convergent phase estimates within 10–20 generations. After obtaining the phase errors based only on the optimization of the predefined window, these errors could be applied to the entire image, reducing the overall computational burden. Preliminary PMSE images from the application of the RIM technique on the EISCAT radar were presented. Obvious image enhancement was obtained using the GA calibration method to reveal the fine-scale structure in the PMSE.

References

Chilson, P. B., P. Czechowsky, J. Klostermeyer, R. Rüster, and G. Schmidt, An investigation of measured temperature profiles and VHF mesosphere summer echoes at midlatitudes, *J. Geophys. Res.*, *102*(D20), 23,819–23,828, 1997.

Chilson, P. B., T.-Y. Yu, R. G. Strauch, A. Muschinski, and R. D. Palmer, Implementation and validation of range imaging on a UHF radar wind profiler, *J. Atmos. Ocean. Technol.*, *20*(7), 987–996, 2003.

Holland, J. H., *Adaptation in Natural and Artificial Systems*, University of Michigan Press, 1975.

Palmer, R. D., T.-Y. Yu, and P. B. Chilson, Range imaging using frequency diversity, *Radio Sci.*, *34*(6), 1485–1496, 1999.

Rapp, M., F.-J. Lübken, A. Müllemann, G. E. Thomas, and E. J. Jensen, Small-scale temperature variations in the vicinity of NLC: Experimental and model results, *J. Geophys. Res.*, *107*(D19), 4392,doi:10.1029/2001JD001,241, 2002.

PMSE, NLC AND TEMPERATURE OBSERVATION DURING THE ROMA-2001 CAMPAIGN

Marius Zecha[(1)], Jürgen Röttger[(2)], Franz-Josef Lübken[(1)], Josef Höffner[(1)], Cord Fricke-Begemann[(1)], and Arno Müllemann[(1)]

[(1)] Leibniz-Institut für Atmosphärenphysik, Kühlungsborn, Germany
[(2)] Max-Planck-Institut für Aeronomie, Katlenburg-Lindau, Germany

Motivation

Characteristics of the polar summer mesosphere

Temperature

- very low in the upper mesosphere, typically less than 150 K
- cold enough for water ice particles to exist (i.e., the degree of saturation is larger than unity assuming reasonable H_2O-values)

Noctilucent clouds (NLC)

- optical phenomenon in the summer sky at latitudes north of 50°N
- based on scatter of sunlight by small ice particles, which can only exist close to the very cold summer mesopause
- observable by eyes south of the polar circle soon after sunset, and by lidar/satellite continuously and in polar regions too

Polar mesosphere summer echoes (PMSE)

- very intense radar echoes
- occur only during summer a few kilometers below the mesopause
- closely related to charged ice particles which reduce the diffusivity of electrons such that very small spatial scale structures in the electron gas can exist

Goal of the campaign ROMA (Rocket borne Observation in the Middle Atmosphere) in 2001

- simultaneous observation of PMSE by radar, NLC by lidar, and temperature by meteorological rockets
- all instruments were located very close together near Longyearbyen (78N/16E) on the north polar island Spitsbergen
- these are the first combined measurements at these latitudes
- the data should allow a detailed study of creation mechanisms of layers near the summer mesopause, its dependence on the thermal structure and its variation with latitude and season

Instruments

Meteorological rockets

- temperature measurements using the “falling sphere” (FS) technique

Potassium lidar

- NLC obsevation by the mobile lidar of the IAP Kühlungsborn

SOUSY Svalbard Radar

- PMSE observation (*Röttger,* 2001)
- operating frequency 53.5 MHz, peak power 70 kW
- phased antenna array, 356 single Yagis, beam width 4 deg
- standard height resolution 300m

Results

Temperature climatology

- summary of the temperatures from all 25 FS flights (*Lübken and Müllemann,* 2002)
- temperatures are very low (<130 K) from mid July (beginning of FS flights) until approximately end of August
- in comparison to CIRA-86: temperatures are significantly lower by up to 20 K
- in comparison to climatology at 69N (also based on FS flights; *Lübken,* 1999): similar temperatures in 82 km, mesopause altitude (~89 km) approx. 1 km higher

NLC

- from mid June until mid of August
- detection during ~70% of the observation time
- daily occurrence varies from 0% to 100%
- mean peak altitude ~83.5 km
- mean layer thickness ~1.5 km

PMSE

- from mid of May until end of August
- detection nearly permanently until mid of August
- nearly no diurnal variation (note: 24-hours/day daylight during the ROMA-campaign)
- normally between 80 and 92 km with height distribution maximum at 85 km
- multiple layers are a regular feature (*Rüster et al.,* 2001)
- layers are variable in height, time, thickness and intensity

Simultaneous temperature measurements and PMSE observations

- from measured temperatures and model data for water vapor pressure and mixing ratio the saturation values (S) were calculated
- averaged PMSE profiles from one hour before to one hour after the rocket launches were calculated
- between 82 and 88 km all PMSE detections during super-saturation (S>1)
- in the lower and higher altitudes possibly some uncertainty in the model/temperature data
- if saturation S>1 then only in about two-thirds of all cases PMSE detection ⇨ temperatures can be low enough for ice particles but still no PMSE is present because other processes, such as the creation of small scale fluctuations in the plasma, are missing (*Lübken et al.,* 2002)
- there is no apparent correlation between the magnitude of the degree of saturation and the PMSE strength
- in figure 1 an example of simultaneous PMSE observations and temperature measurements on 20 August is shown
- the upper panel displays PMSE (up to 35 dB signal to noise ratio) from one hour before to one hour after a rocket launch (ROFS15) for temperature measurements using "falling spheres"
- Lower panels show the close agreement between the height ranges of averaged PMSE occurrence and super-saturation (left hand panel: profiles of PMSE and S)
- temperature profile T_{ROFS} (violet solid line in the right hand panel) crosses the frostpoint-curve T_{FROST} (blue dashed line) nearly at the boundary of the PMSE layer
- atmospheric temperatures are lower than T_{FROST} (gray shaded band) almost in the entire PMSE height range (colored shaded band)

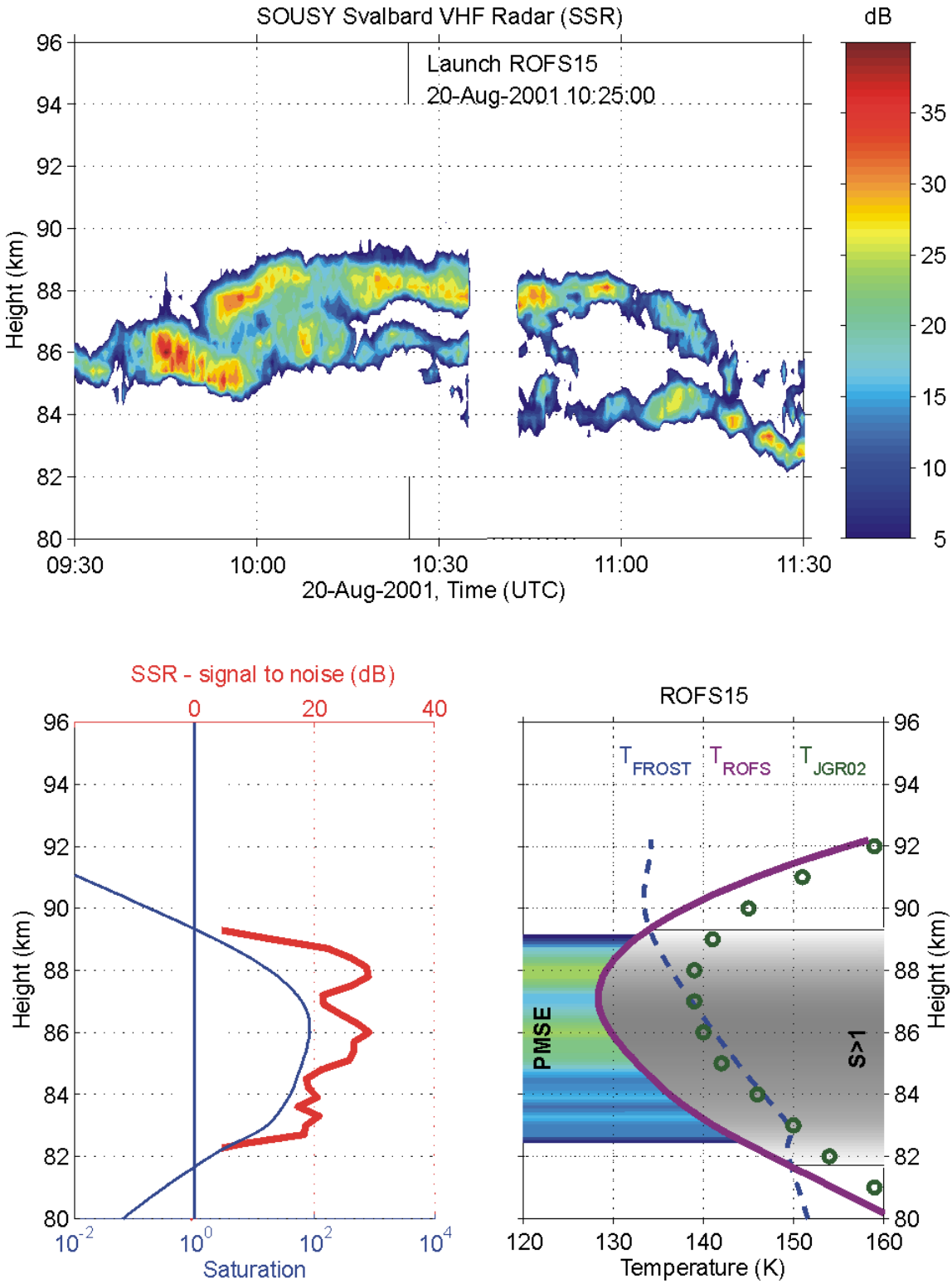

Figure 1: Simultaneous temperature measurements and PMSE observation on 20 August 2001 at Spitsbergen

Simultaneous PMSE and NLC observations

- figure 2 displays an example of simultaneous PMSE/NLC observations on 6 August
- PMSE is shown as color image with signal to noise ratios up to 35 dB, NLC is shown as red contour lines.
- lower ledges of NLC and PMSE coincide nicely ⇨ suggestion: the ice particle population creating NLC and PMSE is identical and the particles affect the plasma and are large enough to be detected by lidar (*von Zahn and Bremer,* 1999)
- PMSE extends above the NLC by several kilometres ⇨ suggestion: there are still enough ice particles to affect the plasma and to reduce the mobility of the free electrons but the particles are too small to be detectable by lidar (smaller than ~20 nm)

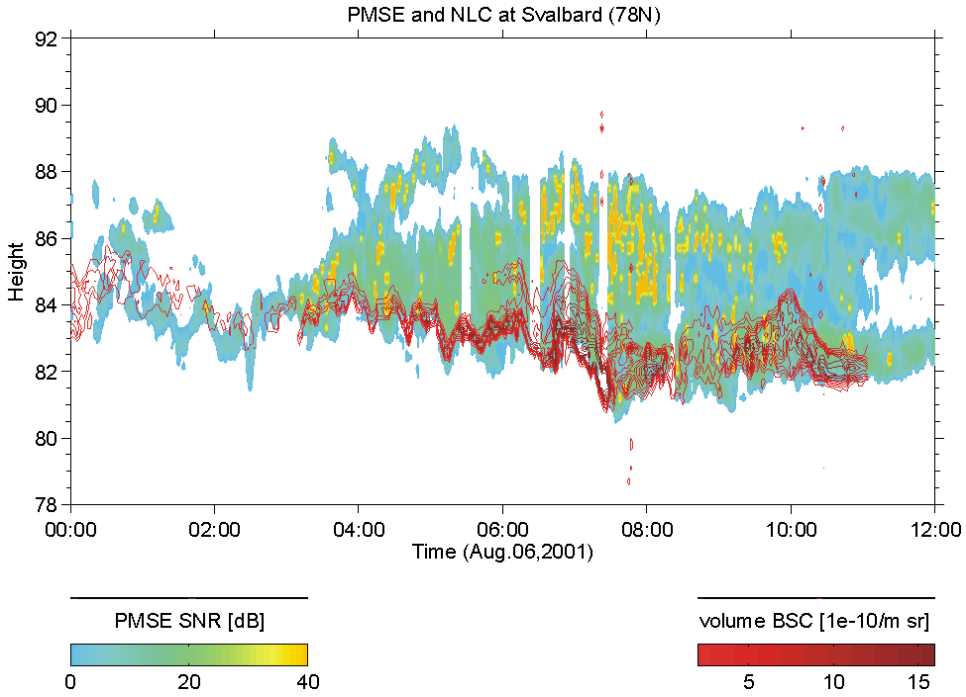

Figure 2: Simultaneous PMSE and NLC observations on 6 August 2001 at Spitsbergen

References

Lübken, F.-J., Thermal structure of the Arctic summer mesosphere, *J. Geophys. Res, 104*, 9135-9149, 1999

Lübken, F.-J., M. Rapp, and P. Hoffmann, Neutral air turbulence and temperatures in the vicinity of polar mesosphere summer echoes, *J. Geophys. Res., 107(D15),* 4273, doi: 10.1029/2001JD000915, 2002

Lübken, F.-J., and A. Müllemann, First in-situ temperature measurements in the summer mesosphere at very high latitudes (78°N), *J. Geophys. Res., 108(D8),* 8448, doi: 10.1029/2002JD002414, 2003

Röttger, J., Observations of the polar D-region and the mesosphere with the EISCAT Svalbard Radar and the SOUSY Svalbard Radar, Mem. Nat. Inst. Polar Res., 54, 9-20, 2001

Rüster, R., J. Röttger, G. Schmidt, P. Czechowsky, and J. Klostermeyer, Observations of mesospheric summer echoes at VHF in the polar cap region, *Geophys. Res. Lett., 28*, 1471-1474, 2001

von Zahn, U., and J. Bremer, Simultaneous and common-volume observations of noctilucent clouds and polar mesosphere summer echoes, *Geophys. Res. Lett., 26,* 1521-1524, 1999

RESULTS OF SEVERAL YEARS MSE OBSERVATION AT KÜHLUNGSBORN (54°N)

Marius Zecha, Jürgen Bremer, and Peter Hoffmann

Leibniz-Institut für Atmosphärenphysik and der Universität Rostock
D-18225 Kühlungsborn, Germany

Introduction

Very strong echoes from upper mesospheric heights in polar regions are observed by VHF radars for several years. The radar waves are backscattered by irregularities of the refraction index of half the radar wavelength mainly caused by electron density fluctuations. Such small irregularities should normally be destroyed at mesospheric heights by viscous forces. Therefore, it is commonly accepted that charged aerosols or ice particles prevent the destruction of these irregularities by an effective reduction of the electron diffusivity (*Cho et al.,* 1992, *Rapp and Lübken,* 2003). The good correlation between PMSE and noctilucent clouds (NLC) as found in simultaneous and common volume observations (*von Zahn and Bremer,* 1999) confirm the existence of ice particles during PMSE.
Mesosphere summer echoes (MSE) at mid-latitudes are a rare phenomenon in contrast to the corresponding polar mesosphere summer echoes (PMSE) at arctic latitudes (*Bremer et al.,* 2003, *Zecha et al.,* 2003). Studies of MSE characteristics are therefore more seldom than studies of PMSE. Nearly continuous measurements at Kühlungsborn during the summers 1998 and 2000 to 2002 gave the chance to study the main properties of MSE on good statistical conditions.

Experiment

The MSE observations were performed with the 53.5 MHz VHF radar system at Kühlungsborn (54.1°N, 11.8°E) near the Baltic Sea.

The essential radar parameters used for mesospheric measurements are listed in the following table:

operating frequency	53.5 MHz
peak power	36 (72) kW
duty cycle	5%
transmitting antenna	144 Yagi array
eff. Antenna area	1900 m2
receiving antenna	array divisible in 6 subarray a 24 Yagi
half-power beam width	6.0°
pulse repetition frequency	1500 Hz
pulse length	2 μs
code (complementary)	16 bit
sampling resolution	300 m
length of time series	~20 sec

Results

Seasonal variation

MSE are normally observed at Kühlungsborn between the beginning of June and the middle of August as tagged by the vertical dashed lines in the upper panel of figure 1a. The mean daily occurrence rates show strong day-to-day variations with values between 0% and 18% (black bars). The blue dashed curve has been estimated by a polynomial fit through the daily values. The mean occurrence rate of noctilucent clouds at mid-latitudes is markedly smaller than the occurrence rate of MSE. No more than three events per year have been observed. Furthermore the NLC period characterized by the green horizontal line is limited to the first half of the MSE period only.
As demonstrated in the lower panel of the figure the degree of saturation S (derived from smoothed and interpolated Kühlungsborn lidar temperature data and a water vapor mixing ratio estimated from model calculations) is in general smaller than 1. Therefore, the condition S>1 as necessary for the existence of ice particles in the mesosphere could only be fulfilled during gravity wave induced temperature minima.

Diurnal variation

In figure 1b the mean diurnal variation of the occurrence rate of MSE is separately shown for the four years of observation (black curves with dots). Normally MSE are observed only during daytime with a maximum near noon. The diurnal variation of electron density is also shown (solid red curves) for an altitude of 85 km at mid-latitudes after the IRI-95 model (http://nssdc.gsfc.nasa.gov/space/model/models/iri.html). The comparison of the MSE occurrence rates with the electron densities leads to the conclusion that MSE can only be observed if the electron density is above about 500 el./cm^3.

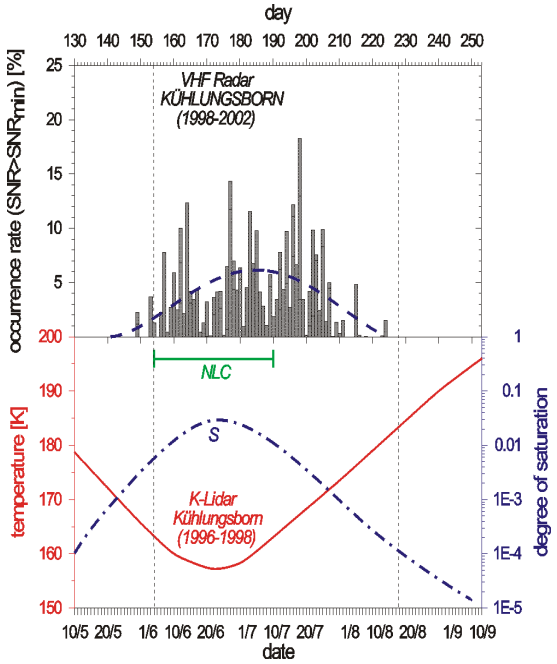

Fig. 1a: Seasonal variation of MSE

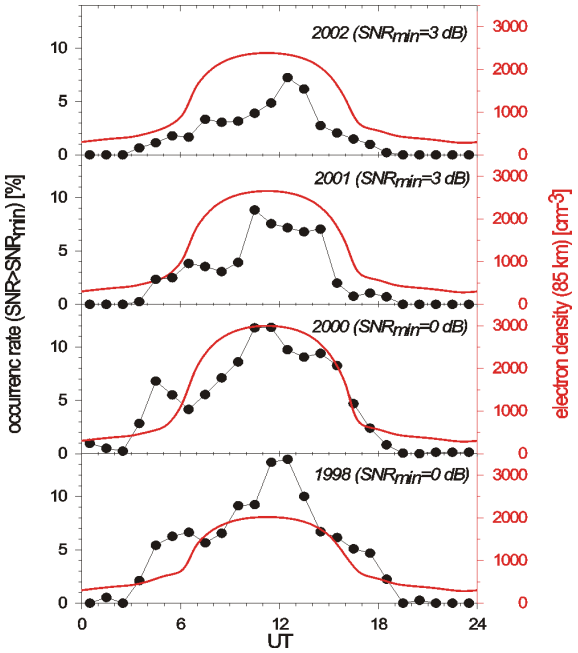

Fig. 1b: Diurnal variation of MSE

Height distribution

MSE are more or less regularly observed in the summer mesosphere, but their occurrence rate depends markedly on altitude. The strongest mesosphere summer echoes during the three years exceeded more than 20 dB signal to noise ratio (SNR).
In figure 2a the height distribution of four-year-mean MSE occurrence is presented for SNR greater than 0 dB. It shows that MSE layers normally occur in an altitude range between 80 km and 90 km with a maximum incidence near 85 km. The average occurrence falls rapidly away the peak. More than 90 % of MSE occur between 82.5 and 87.5 km. The decrease above and below the occurrence maximum is nearly the same.

Scatter characteristics

Received signal power depends linearly on the effective antenna area for a perfect scattering process, and quadratically on the effective antenna area for a plain specular reflection process. If mesosphere echoes were observed at the same location simultaneously with different antenna arrays it can be estimated whether volume scattering or specular partial reflection is responsible for the echoes (*Zecha et al.,* 2001).
The division of the radar array in six subarrays give the feasibility to use the whole antenna with 144 Yagis for transmission and receiption on the one hand, and a subarray of 24 Yagis for simultaneous receiption on the other hand. Both antenna configurations have different effective antenna areas, but the same efficiency otherwise. Thus the ratios of received power hint to plain scattering and reflection processes by values of 3.9 dB and 7.8 dB, respectively.
Normally the values are between these extrema. In figure 2b the solid line connects the median values for each height channel. It is evident that in general the scattering character gain more and more with increasing height.

Aspect sensitivity

Radar backscatter returns are strongest from the vertical direction and show a pronounced dependency on the zenith angle. Mostly a Gaussian function is assumed and the usual parameter to describe this phenomenon is the half-angular width ϑ_s. This so called aspect sensitivity can be estimated also without tilting the radar beam but using the characteristics of the spatial correlation ellipse of the FCA model (*Briggs,* 1984) and the radar beam width.
Similar to PMSE, mid-latitude mesosphere summer echoes are markedly aspect sensitiv. The solid line in figure 2c displays the medians for each height channel. It shows that the aspect sensitivity is very strong especially in the lower part of the MSE layers and becomes smaller with increasing height.

Turbulence parameter

The temporal characteristics of the scatters can be specified by a fading time which is closely related to the total spectral width. This measured total spectral width is determined by turbulent and nonturbulent processes. However, the nonturbulent contribution can be calculated from horizontal wind speed and the half-power beam width of the effective radar beam assuming that beam broadening is in general the dominating nonturbulent process (*Hocking,* 1983). The real values of the resulting spectral width σ_{fluct} due to turbulent processes are shown in figure 2d. The solid line connects the medians for each height channel. In general the turbulent character tends slightly upwards with increasing height.

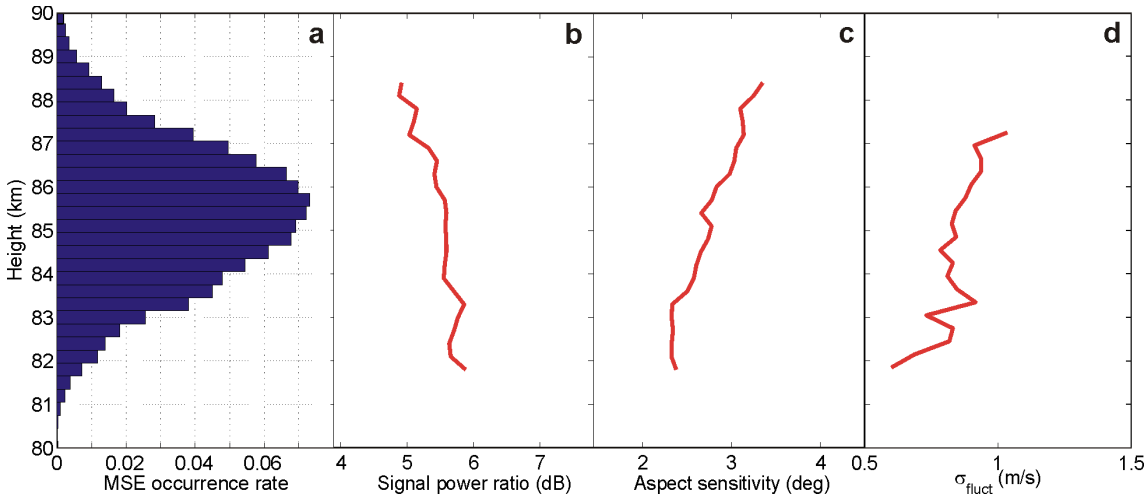

Figure 2: MSE parameters as function of height

All parameters describing the MSE scattering process support an increasing turbulent and isotropic structure at altitude within the interval of 80 to 90 km.

References

Bremer, J., P. Hoffmann, R. Latteck, and W. Singer, Seasonal and long-term variations of PMSE from VHF radar observations at Andenes, Norway, *J. Geophys. Res., 108(D8),* doi:10.1029/2002JD002369, 2003

Briggs, B.B., The analysis of spaced sensor record by correlation techniques, in *Handbook for MAP, Vol. 13,* edited by R. A. Vincent, pp. 166-186, SCOSTEP Secr., Univ. of Ill., Urbana, 1984

Cho, J.Y.N., T.M. Hall, and M.C. Kelley. On the role of charged aerosols in polar mesosphere summer echoes*, J. Geophys. Res., 97,* 875-885, 1992

Hocking, W.K., On the extraction of atmospheric turbulence parameters from backscatter Doppler spectra, I, Theory, *J. Atmos. Terr. Phys., 45,* 89-102, 1983

Rapp, M., and F.-J. Lübken, On the nature of PMSE: Electron diffusion in the vicinity of charged particles revisited, *J. Geophys. Res., 108(D8),* 8437, doi: 10.1029/2002JD002857, 2003

von Zahn, U., and J. Bremer, Simultaneous and common-volume observations of noctilucent clouds and polar mesosphere summer echoes, *Geophys. Res. Lett., 26,* 1521-1524, 1999

Zecha, M. J. Röttger, W. Singer, P. Hoffmann, and D. Keuer, Scattering properties of PMSE irregularities and refinement of velocity estimates, *J. Atmos. Solar-Terr. Phys., 63,* 201-214, 2001

Zecha, M., J. Bremer, R. Latteck, W. Singer, and P. Hoffmann, Properties of midlatitude mesosphere summer echoes after three seasons of VHF radar observations at 54°N, *J. Geophys. Res., 108(D8),* 8439, doi:10.1029/2002JD002442, 2003

Session I.3: Winds, waves and turbulence in the lower and middle atmosphere and the lower thermosphere

This session will examine recent developments in the areas of studies of observations of dynamical motions in the middle atmosphere and lower thermosphere. Topics of particular interest include wave-wave interaction, wave sources and generation mechanisms, wave deposition processes, non-linear interactions, wave propagation studies, turbulence anisotropy and turbulent transport processes, but other papers on related topics will also be considered. Correlations of wave events as a function of height are also of interest. Multi-instrument studies are especially encouraged, and inter-comparisons of different techniques are considered to be important. One area of special interest is studies of wave velocity amplitudes and variability in the region above 90 km altitude, with particular interest in determining the frequency of occurrence of large amplitude events and large wind velocities (up to 100 m/s and higher) in this region.

Conveners:
W. Hocking and M.Larsen

WIND AND TURBULENCE MEASUREMENTS BY THE MIDDLE AND UPPER ATMOSPHERE RADAR USING UCAR-STARS METHOD

Alexander Praskovsky[1], Eleanor Praskovskaya[2],
Gernot Hassenpflug[3], Mamoru Yamamoto[3], and Shoichiro Fukao[3]

[1]National Center for Atmospheric Research, 3450 Mitchell Lane, Boulder, CO 80301, USA
[2]Colorado Research Associates, 3380 Mitchell Lane, Boulder, CO 80301, USA
[3]Radio Science Center for Space and Atmosphere, Kyoto University, Uji, 611-0011, Japan

Spaced antenna (SA) methods for analyzing complex time series of signals from multiple receivers have become commonly used techniques for measuring parameters of the atmosphere from the lower troposphere up into the ionosphere. The most used methods are Full Correlation Analysis in the time domain, and Full Spectral Analysis in the frequency domain (Briggs, 1984; and Briggs and Vincent, 1992). A structure function (SF)-based approach has been developed recently by Praskovsky and Praskovskaya (2003a, b), and the name UCAR-STARS (University Corporation for Atmospheric Research - STructure function Analysis of Received Signals) was coined to describe the data analysis technique based on this approach. The goal of this work is to evaluate the potential of STARS for measuring mean horizontal winds and turbulence characteristics of a scattering medium with SA radars. The Middle and Upper Atmosphere radar (MUR) is one of the most powerful and flexible MST radars in the world, which makes it a natural test-bed for the method. The Holloway and Doviak (HAD) correlation function (CF)-based SA method (Doviak et al., 1996, and Holloway et al., 1997) was chosen from a diversity of existing SA techniques for testing STARS. Comprehensive description of this work including theoretical comparison of STARS and HAD and detailed analysis of experimental results for the MUR is presented in Praskovsky et al. (2003) while only a brief summary is given in this paper.

The MUR is located in Shigaraki, Japan (34.85^o N, 136.10^o E) at approximately 1 km above sea level. It is operated by the Radio Science Center for Space and Atmosphere of Kyoto University. MUR is an MST Doppler research radar with operational frequency 46.5 MHz. It is an active phased array system, the radar's antenna consists of 475 crossed Yagis with the aperture of 8,330 m^2 (103 m in diameter); see Fukao et al. (1985a, b) for details.

The data collection for testing UCAR-STARS was executed on 24 - 25 April 2002. During the experiment, the radar was operated for 6.55 min. in the SA mode, then for 58.4 s in the Doppler Beam Swinging (DBS) mode; the sequence was continuously repeated for several hours for each studied configuration of receiving antennas. Both in DBS and SA modes, a full antenna (475 Yagis) was transmitting at a pulse repetition frequency of 2,500 Hz. The range resolution and the gate separation were 150 m; 64 gates covered a height z_o from 5 km to 15 km above the radar. In DBS mode, the pulses were transmitted in five directions, and the full antenna was used to receive the signals. Different configurations of four receivers each with an aperture of approximately 2,330 m^2 (133 Yagis) were studied in SA mode.

The mean horizontal wind speed components $\langle U \rangle$ (toward east) and $\langle V \rangle$ (toward north) were retrieved from the MUR signals in the SA mode with STARS and HAD methods at the same averaging time T_{av} = 78.6 s, which is close to the DBS T_{av} = 58.4 s. A good agreement of the STARS and HAD-produced mean winds with those produced by DBS was found at heights from 5 km to approximately 11 km where signal-to-noise ratio (SNR) is rather high; typical time series are shown in Fig. 1. Above 11 km, where the SNR is low, the agreement is quite

poor. It was shown that poor performance of SA and DBS methods at low SNR is due to intermittent non-white noise in the MUR signals of yet unknown origin. This problem can be treated, for example by excluding noisy records from data analysis during incoherent averaging of records.

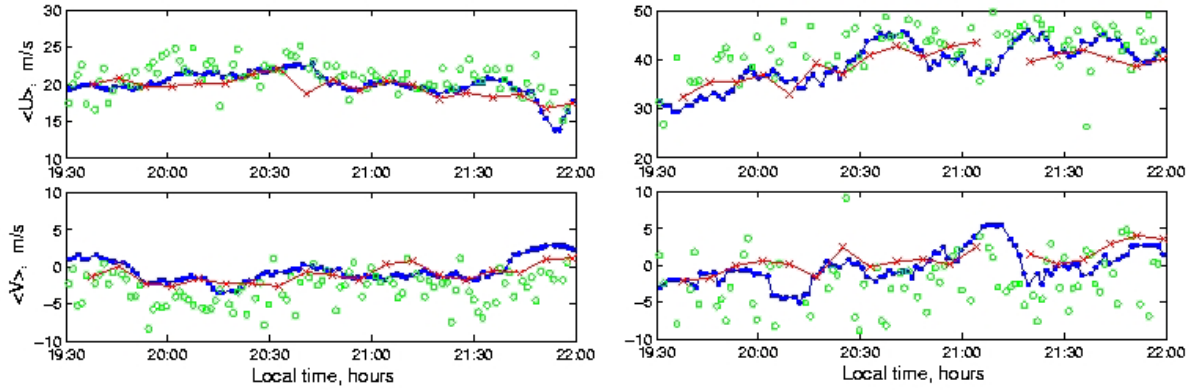

Figure 1. Time series of the easterly $\langle U \rangle$ and northerly $\langle V \rangle$ mean wind speed components on 24 April 2002 at z_o = 5.1 km (left column) and 10.05 km (right column). Red crosses, DBS; blue bullets, STARS; green circles, HAD.

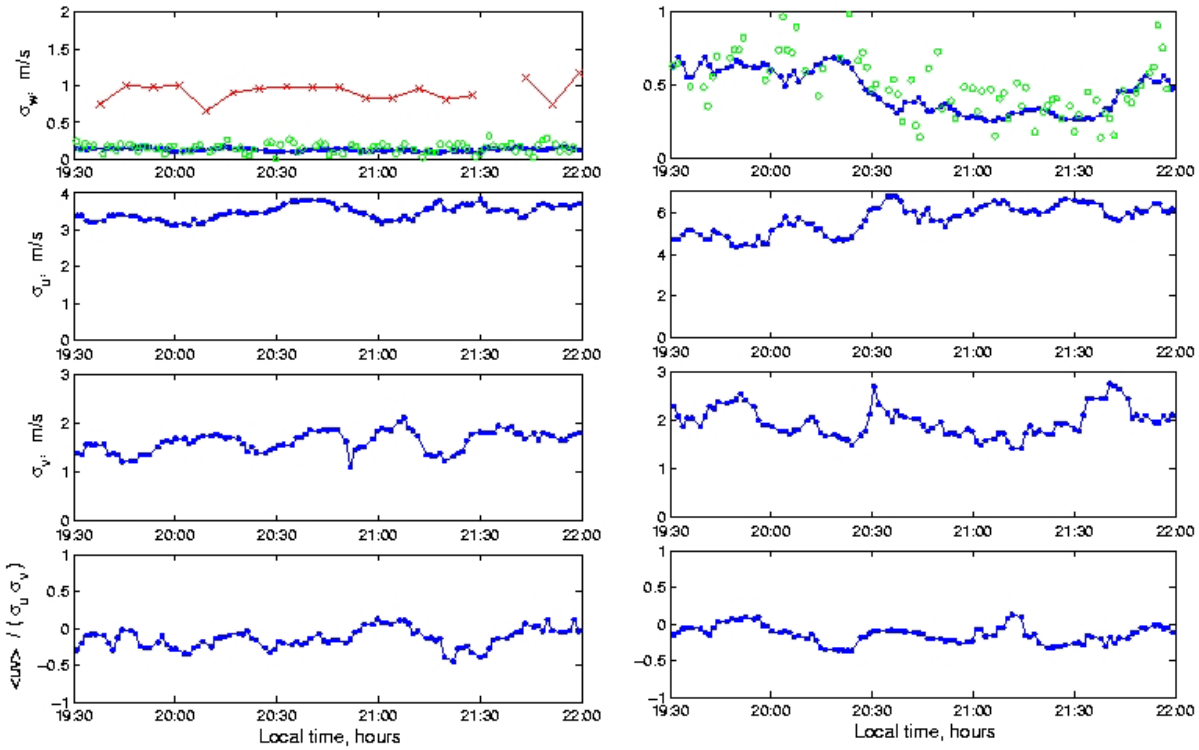

Figure 2. Time series of turbulence characteristics on 24 April 2002 at z_o = 5.4 km (left column) and 10.35 km (right column). See Figure 1 for the legends.

Characteristics of turbulence were retrieved from the MUR signals in SA mode with STARS and HAD techniques at the averaging time T_{av} = 78.6 s, while the spectral width was estimated in DBS mode at T_{av} = 58.4 s. The beam broadening corrections led to numerous negative values of σ_w, and the uncorrected spectral width is presented below. Hereafter u, v, and w denote the turbulent velocity components of a scattering medium in the easterly, northerly, and vertical directions, and the standard deviation of the components are denoted as σ_u, σ_v, and σ_w, respectively. The STARS and HAD-produced values of σ_w are in good agreement although the STARS results are systematically smaller than the HAD results by approximately 20%; typical time series are shown in Fig. 2. The spectral width is much larger

than the SA-produced σ_w; the latter values are unaffected by the beam broadening. The STARS-measured standard deviations σ_u, σ_v, and the horizontal momentum flux $\langle uv \rangle$ are also presented in Fig. 2; these characteristics cannot be measured by other SA techniques. The STARS results show strong anisotropy of turbulence at all studied heights. One should note that, independent of a specific measurement technique, caution is needed in the interpretation of the radar-produced characteristics of turbulence; e.g., Briggs (1980), Hocking et al. (1989), Doviak et al. (1996), Praskovsky and Praskovskaya (2003a, b).

Good agreement between STARS and HAD in measuring the mean winds and intensity of the vertical turbulent velocity seems to be expected because the considered SA techniques are related to each other. Let us consider the standard complex signals from two receivers $E_1(t)$ and $E_2(t)$ where t is time. The second order cross CF and SF, respectively, can be defined in the standard way as follows (Tatarskii, 1971, chap. 1A):

$$C_{12}(\tau) = \left\langle E_1(t)E_2^*(t+\tau)\right\rangle \Big/ \left\langle E_1(t)E_1^*(t)\right\rangle, \quad D_{12}(\tau) = \left\langle \left[S_1(t) - S_2(t+\tau)\right]^2 \right\rangle \Big/ \left\langle \left[S_1(t) - \langle S_1(t)\rangle\right]^2 \right\rangle$$

Here $S(t) = E(t)E^*(t)$ is the instantaneous signal power, τ is the temporal separation, the brackets $\langle\ \rangle$ denote the ensemble averages, and the superscript * denotes the complex conjugation. The auto CF and SF are particular cases of the cross functions at $E_1(t) = E_2(t)$. As shown in Praskovsky et al. (2003), $D_{12}(\tau) = 2 - 2\left|C_{12}(\tau)\right|^2$. However, the CF and SF-based SA techniques are conceptually different in spite of being formally related to each other for a particular case of the second order functions.

CF can be applied to globally statistically stationary random processes while only local stationarity is sufficient for applying SF. Physical processes in the atmosphere are almost never globally statistically stationary while practically any process can be safely considered as locally stationary; e.g., Tatarskii (1971, chap. 1A). Only $\tau \to 0$ is considered in STARS; the small parameter always simplifies a physical task. In particular, STARS requires a smaller number of less restrictive assumptions for deriving operational equations for σ_u, σ_v, σ_w, and $\langle uv \rangle$ than HAD needs for the only characteristic σ_w.

The major difference between CF and SF-based SA techniques is in the physical concept underlying the techniques. As a mathematical tool, the cross-CF describes the similarity between signals from two receivers $E_1(t)$ and $E_2(t+\tau)$ at all temporal separations $-\infty < \tau < \infty$. The physical concept underlying all CF-based techniques is the tracking of the diffraction pattern and its changes, hence the tracking of a scattering medium and its changes in the illuminated volume. The cross-SF as a mathematical tool describes the difference between the signals $S_1(t)$ and $S_2(t+\tau)$ at very small $\tau \to 0$; the SF-based techniques are intrinsically differential. The physical concept underlying the techniques is the evaluation of the rates of spatial and temporal changes in the diffraction pattern, hence evaluation of the rates of spatial and temporal changes in a scattering medium in the illuminated volume. The optimal spatial and temporal increments for CF methods are therefore much larger than those suitable for SF methods, which might lead to the preferential use of one or other method for a given observed diffraction pattern. Due to this difference, the SF-based methods are more strongly affected by noise with small temporal scales than the CF-based techniques, while noise with a large temporal scale, such as ground clutter, affects CF more strongly than SF. The difference also leads to slightly smaller values of σ_w produced by STARS than those produced by HAD.

The use of diffraction pattern similarity in CF methods compared to that of rate of temporal and spatial change by SF methods means that only intensity of vertical turbulent velocity σ_w can be measured with CF-based techniques unless rather restrictive additional assumptions are employed; e.g., Briggs (1980), Hocking et al. (1989), Doviak et al. (1996). SF-based techniques potentially allow the measurement of characteristics of horizontal turbulent velocity components separately such as σ_u , σ_v , $\langle uv \rangle$, and others (Praskovsky and Praskovskaya, 2003a, b).

Therefore, CF and SF-based SA techniques do not compete but rather complement each other. The UCAR-STARS method could become a useful alternative to the traditional CF and spectra-based data analysis techniques for SA radars.

Acknowledgements. NCAR is sponsored by the National Science Foundation (NSF). The first author (AP) was sponsored by the NCAR/RAP Director's fund, and the second author (EP) was sponsored by NSF Grant ATM-0122877. The MU radar belongs to and is operated by the Radio Science Center for Space and Atmosphere (RASC) of Kyoto University. AP and EP were supported by RASC as a visiting professor and a visiting scientist, respectively, during the major part of this research. AP was supported by the International Centre for Theoretical Physics (Trieste, Italy) as a visiting professor during part of his work on this paper.

REFERENCES

Briggs, B. H., Radar observations of atmospheric winds and turbulence: a comparison of techniques, *J. Atmos. And Terr. Phys*., *42*, 823-833, 1980.

Briggs, B. H., The analysis of spaced sensor records by correlation techniques, *MAP Handbook*, *13*, 166-186, 1984.

Briggs, B. H., and R. A. Vincent, Spaced-antenna analysis in the frequency domain, *Radio Sci*., *27*, 117-129, 1992.

Doviak, R. J., R. J. Lataitis, and C. L. Holloway, Cross correlations and cross spectra for spaced antenna wind profilers, 1, Theoretical analysis, *Radio Sci*., *31*, 157-180, 1996.

Fukao, S., T. Sato, T. Tsuda, S. Kato, K. Wakasugi, and T. Makihira, The MU radar with an active phased array, 1, Antenna and power amplifiers, *Radio Sci*., *20*, 1155-1168, 1985a.

Fukao, S., T. Sato, T. Tsuda, S. Kato, K. Wakasugi, and T. Makihira, The MU radar with an active phased array, 2, In-house equipment, *Radio Sci*., *20*, 1169-1176, 1985b.

Hocking, W. K., P. May, and J. Röttger, Interpretation, reliability, and accuracies of parameters deduced by the spaced antenna method in middle atmosphere applications, *PAGEOPH*, *30*, 571-604, 1989.

Holloway, C. L., R. J. Doviak, S. A. Cohn, R. J. Lataitis, and J. S. Van Baelen, Cross correlations and cross spectra for spaced antenna wind profilers, 2, Algorithms to estimate wind and turbulence, *Radio Sci*., *32*, 967-982, 1997.

Praskovsky, A. A., and E. A. Praskovskaya, Structure-function-based approach to analyzing received signals for spaced antenna radars, *Radio Sci*., *38*(4), 7-1 - 7-25, 2003a.

Praskovsky, A. A., and E. A. Praskovskaya, Towards the advanced measurements of atmospheric turbulence by spaced antenna radars, *this volume*, 2003b.

Praskovsky, A. A., E. A. Praskovskaya, G. Hassenpflug, M. Yamamoto, and S. Fukao, Wind and turbulence measurements by the Middle and Upper Atmosphere radar: comparison of techniques, Submitted to *Ann. Geophys*., MST-10 Special issue, 2003.

Tatarskii, V. I., *The Effects of the Turbulent Atmosphere on Wave Propagation*, UDC 551.510, U.S. Dep. of Commerce, Washington, D.C., 1971.

STANDARD DEVIATIONS OF CORRELATION LENGTHS IN SPACED ANTENNA OBSERVATIONS USING THE MU RADAR

G. Hassenpflug† M. Yamamoto S. Fukao

Radio Science Center for Space and Atmosphere, Kyoto University, Gokasho, Uji 611-0011, Japan. †*Mailto:* gernot@kurasc.kyoto-u.ac.jp

Introduction

Expressions for anisotropic correlation scales returned from Bragg scatterers and received by receivers in spaced antenna (SA) configuration are given by *Holloway et al.* [1997a]. We obtain expressions for standard deviation (SD) of correlation lengths of anisotropic correlation ellipses (see Figure 1(a)). Variance of zero-lag cross correlation coefficients is required: we use the expression given in *Awe* [1964], as well as an expressions based on *Zhang et al.* [2003]. Theoretical SD are compared with experimental SD, and show good agreement. Theoretical expressions can be used to predict expected SD, and to design SA configurations for minimum SD within radar limitations.

Theoretical Expressions

Expressions in *Holloway et al.* [1997a] hold for case of receiver antenna phase centers equidistant from transmitter antenna phase center. Using variance of cross correlation coefficients $c_{ij}(\tau)$ in *Awe* [1964], and a new expression for the variance based on *Zhang et al.* [2003],

$$\mathrm{Var}\left[c_{ij}(0)\right] = \frac{1}{2M_I}\left(1 + 2c_{ij}^2(0) - 4c_{ij}^2(0)\exp\left(\tau_p^2/4\tau_c^2\right) + c_{ij}^2(0)c_{ij}^2(\tau_p)\right) \tag{1}$$

we obtain by the standard theory of error propagation SD of the ground diffraction pattern scales ($\xi_{x'}$, $\xi_{y'}$), refractive index perturbation correlation lengths ($\rho_{x'}$, $\rho_{y'}$), and orientation of the correlation ellipse bearing from north ψ_N. Variance given by *Awe* [1964] is slightly greater than that given by Eqn. 1, as seen in Figure 1(b). τ_p is peak cross-correlation lag, τ_c is square root of the second central moment of the correlation function. $M_I = T/(\sqrt{\pi}\tau_c)$ as defined in *Zhang et al.* [2003]. Expressions for variance of $\xi_{x'}$ and $\xi_{y'}$ depend on baseline lengths B_{ij}:

$$\mathrm{Var}\left[\xi_{x'}\right] = \left(\frac{\xi_{x'}^3}{2}\right)^2 \cdot \sum_{i,j=1}^{3(i\neq j)} \left(\frac{1}{B_{ij}^2}\right)^2 F_{ij}^2(\xi_{x'}) \frac{\mathrm{Var}\left[c_{ij}\right]}{c_{ij}^2} \tag{2}$$

$$\mathrm{Var}\left[\xi_{y'}\right] = \left(\frac{\xi_{y'}^3}{2}\right)^2 \cdot \sum_{i,j=1}^{3(i\neq j)} \left(\frac{1}{B_{ij}^2}\right)^2 F_{ij}^2(\xi_{y'}) \frac{\mathrm{Var}\left[c_{ij}\right]}{c_{ij}^2} \tag{3}$$

where F_{12}, F_{13}, F_{23} are parameters related to the SA geometry:

$$F_{12}(\xi_{x'}) = \frac{(1-\cos 2\psi_N)\cot\alpha_{13}\cot\alpha_{23} + (1+\cos 2\psi_N) - \sin 2\psi_N\left(\cot\alpha_{13} + \cot\alpha_{23}\right)}{\sin^2\alpha_{12}\left(\cot\alpha_{13} - \cot\alpha_{12}\right)\left(\cot\alpha_{23} - \cot\alpha_{12}\right)}$$

$$
\begin{aligned}
F_{13}(\xi_{x'}) &= \frac{(1-\cos 2\psi_N)\cot\alpha_{12}\cot\alpha_{23}+(1+\cos 2\psi_N)-\sin 2\psi_N\,(\cot\alpha_{12}+\cot\alpha_{23})}{\sin^2\alpha_{13}\,(\cot\alpha_{12}-\cot\alpha_{13})\,(\cot\alpha_{23}-\cot\alpha_{13})} \\
F_{23}(\xi_{x'}) &= \frac{(1-\cos 2\psi_N)\cot\alpha_{12}\cot\alpha_{13}+(1+\cos 2\psi_N)-\sin 2\psi_N\,(\cot\alpha_{12}+\cot\alpha_{13})}{\sin^2\alpha_{23}\,(\cot\alpha_{12}-\cot\alpha_{23})\,(\cot\alpha_{13}-\cot\alpha_{23})}
\end{aligned}
$$

similarly for $F_{ij}(\xi_{y'})$ where terms in psi_N change sign. Variance of ψ_N is:

$$
\mathrm{Var}\left[\psi_N\right] = \frac{1}{\left(\frac{1}{\xi_{x'}^2}-\frac{1}{\xi_{y'}^2}\right)^2}\sum_{i,j=1}^{3(i\neq j)}\left(\frac{1}{B_{ij}^2}\right)^2 P_{ij}^2\frac{\mathrm{Var}\left[c_{ij}\right]}{c_{ij}^2} \tag{4}
$$

where

$$
\begin{aligned}
P_{12} &= \frac{\sin 2\psi_N\,(\cot\alpha_{13}\cot\alpha_{23}-1)-\cos 2\psi_N\,(\cot\alpha_{13}+\cot\alpha_{23})}{\sin^2\alpha_{12}\,(\cot\alpha_{13}-\cot\alpha_{12})\,(\cot\alpha_{23}-\cot\alpha_{12})} \\
P_{13} &= \frac{\sin 2\psi_N\,(\cot\alpha_{12}\cot\alpha_{23}-1)-\cos 2\psi_N\,(\cot\alpha_{12}+\cot\alpha_{23})}{\sin^2\alpha_{13}\,(\cot\alpha_{12}-\cot\alpha_{13})\,(\cot\alpha_{23}-\cot\alpha_{13})} \\
P_{23} &= \frac{\sin 2\psi_N\,(\cot\alpha_{12}\cot\alpha_{13}-1)-\cos 2\psi_N\,(\cot\alpha_{12}+\cot\alpha_{13})}{\sin^2\alpha_{23}\,(\cot\alpha_{12}-\cot\alpha_{23})\,(\cot\alpha_{13}-\cot\alpha_{23})}
\end{aligned}
$$

Variances of refractive index perturbation horizontal correlation lengths are:

$$
\mathrm{Var}\left[\rho_{x'}\right] = \left(\frac{1}{4}\frac{\xi_{x'}}{\rho_{x'}}\right)^2\mathrm{Var}\left[\xi_{x'}\right] \tag{5}
$$

and similarly for variance of $\rho_{y'}$. Covariance terms $\mathrm{Cov}[c_{ij}, c_{ik}]$ have been neglected, the results in Figure 2 for SA configuration Case 1 [*Hassenpflug et al.*, 2003] show that theoretical estimates using the given expressions agree well with experimental data. $\theta_{x'}$, $\theta_{y'}$ are angular aspect sensitivity of the correlation ellipse.

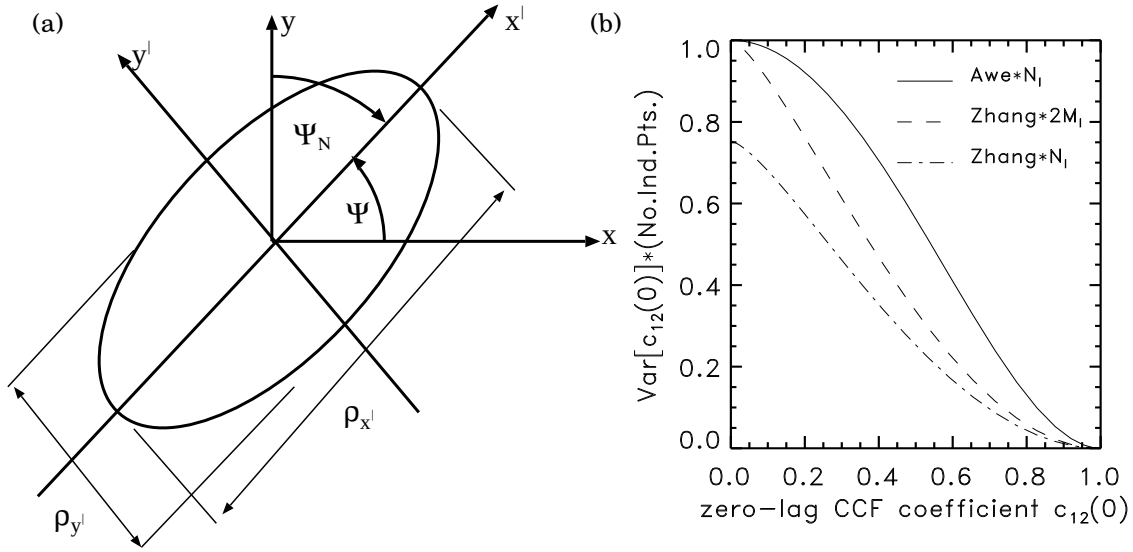

Figure 1: (a) Horizontal correlation ellipse parameters, (b) Zero-lag CCF coefficient variance per Awe, Zhang. Peak CCF coefficient $c_{ij}(\tau_p)$=1, τ_p is varied to change $c_{ij}(0)$.

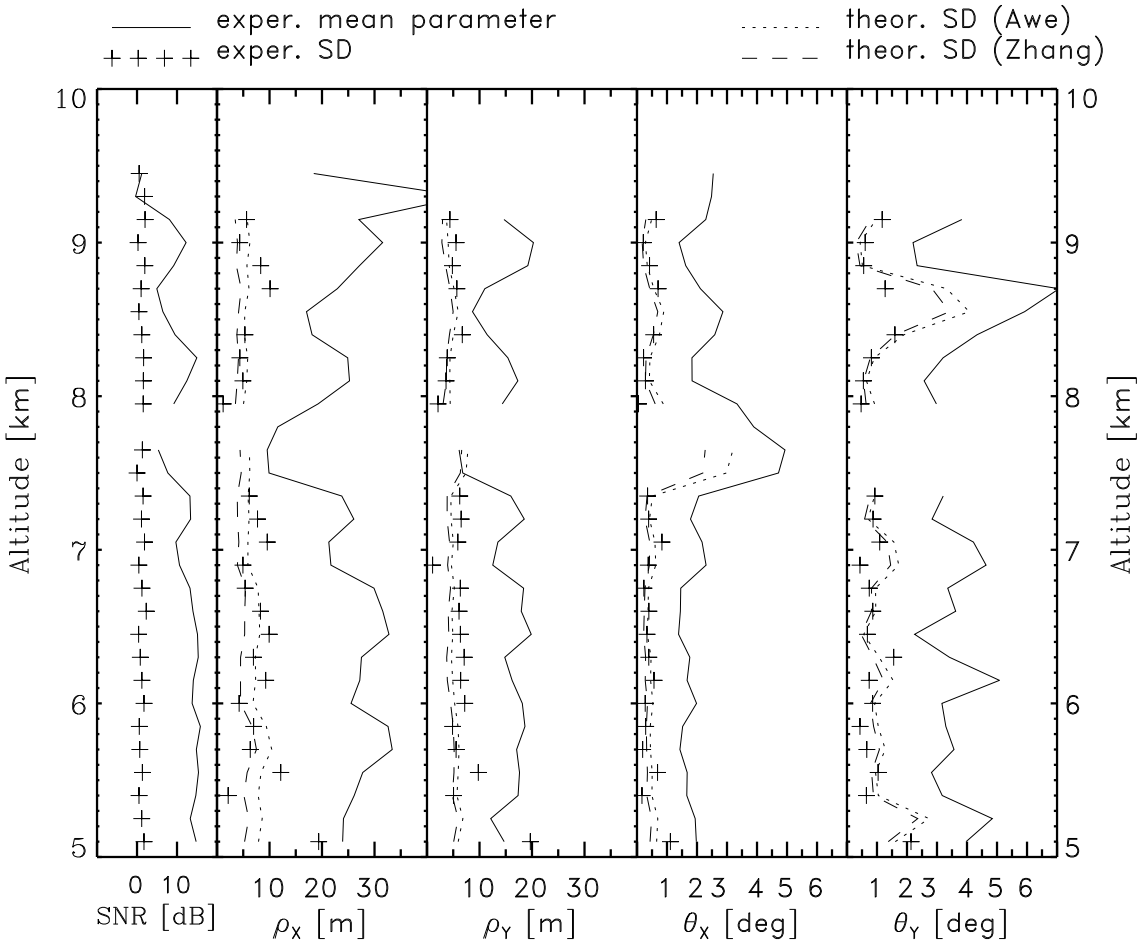

Figure 2: Comparison of experimental SD (+ symbols) with theoretical SD (dotted, and dashed lines) for experiment with MU radar (Feb. 15, 2000). Experimental mean values (over 1 hour) shown with solid lines: $\rho_{x'}$, $\rho_{y'}$ are major and minor correlation ellipse axes, $\theta_{x'}$, $\theta_{y'}$ are the equivalent angular aspect sensitivities.

Application to SA Configuration Design

Dependence of SD $[\rho]$ on baseline length to ξ ratio is shown for an isotropic case in Figure 3(a), and dependence on correlation-ellipse axis bearing relative to baseline orientations in Figure 3(b). Dependencies on τ_c, T and a_h are not shown due to space limitations. From expected theoretical SD of correlation-ellipse parameters, SA configurations can be designed within the limits of the radar's capabilities to reduce the SD. This improves not only the estimation of correlation ellipse parameters, but also wind estimates, since correlation lengths affect the correlation coefficient at the correlation-lag relating auto- and cross-correlation functions (τ_x for Briggs FCA, τ_i for the method in *Holloway et al.* [1997b]).

Conclusions

We used the standard theory of error propagation to derive operational expressions for SD of refractive index perturbation correlation ellipse parameters, using the cross correlation method from *Holloway et al.* [1997a] that yielded results compatible with experimental

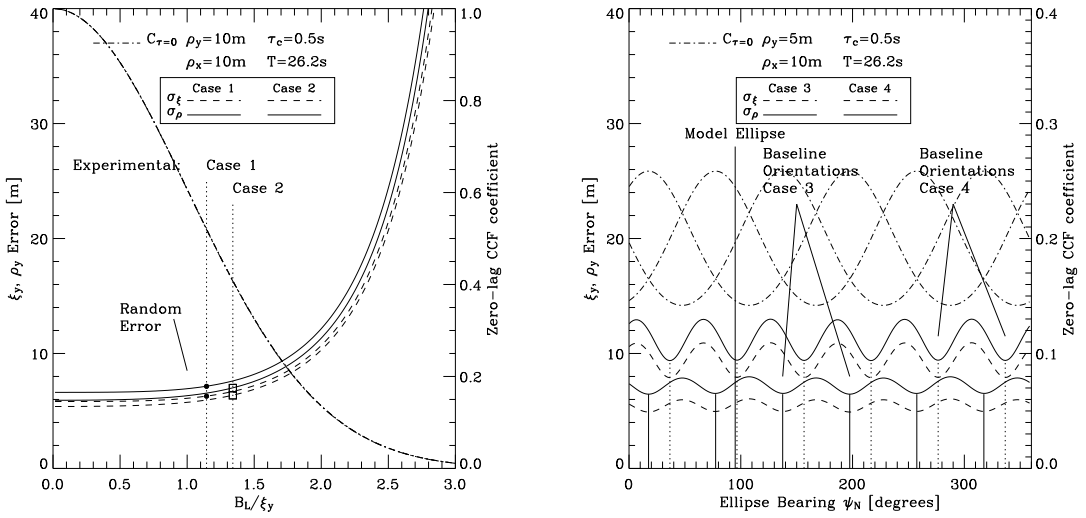

Figure 3: (a) Baseline length dependence of SD $[\rho]$ for isotropic case, (b) dependence on orientation ψ_N for anisotropic case with SD minima when aligned with baselines. SA configuration Cases as per *Hassenpflug et al.* [2003].

SDs. We showed the dependence of the theoretical SD on baseline length, and relative orientation of baselines and correlation ellipse. These dependencies provide a means to optimize spaced antenna configurations for observations of given ranges of correlation lengths. Correlation lengths directly affect wind estimates through steepening of correlation functions as correlation lengths are reduced, hence optimized observations also improve characteristics of wind retrieval by SA methods. SD of wind for anisotropic conditions uses correlation-lags, not only zero-lag coefficients, and is a more complex problem that is currently under investigation.

References

Awe, O., Errors in correlation between time series, *J. Atmos. Terr. Phys.*, *26*, 1239–1255, 1964.

Hassenpflug, G., P. B. Rao, M. Yamamoto, and S. Fukao, MU radar spaced antenna observations with varying apertures : scatterer and antenna contributions to the ground diffraction pattern, *Radio Sci.*, *38*, (9) 1–11, 2003.

Holloway, C. L., R. J. Doviak, and S. A. Cohen, Cross correlations of fields scattered by horizontally anisotropic refractive index irregularities, *Radio Sci.*, *32*, 1911–1920, 1997a.

Holloway, C. L., R. J. Doviak, and S. A. Cohn, Cross correlations and cross spectra for spaced antenna wind profilers 2. Algorithms to estimate wind and turbulence, *Radio Sci.*, *32*, 967–982, 1997b.

Zhang, G., R. J. Doviak, J. Vivekanandan, W. O. J. Brown, and S. A. Cohn, Cross-correlation ratio method to estimate cross-beam wind and comparison with a full correlation analysis, *Radio Sci.*, *38*, (17) 1–14, 2003.

OBSERVATIONS OF THE QUASI 2-DAY WAVES IN THE MESOPAUSE OVER WUHAN, CHINA

J. Xiong*, W. Wei, B. Ning and L. Liu

(Wuhan Institute of Physics and Mathematics, The Chinese Academy of Sciences, Wuhan, China)

1. Introduction

Numerous studies of the mesospheric quasi 2-day wave have been conducted in the last two decades. Most measurements by radars suggest the quasi 2-day wave is predominantly a summertime phenomenon (e.g., Thayaparan et al., 1997; Namboothiri et al., 2002). Many observations by satellite showed strong occurrence of the quasi 2-day waves (Wu et al., 1993). Those preponderance of observational evidence of a recurrent quasi 2-day oscillation in the middle atmosphere led Salby (1981) to suggest that the disturbance was a manifestation of the third Rossby-gravity normal mode of a windless, isothermal atmosphere. However, Meek et al. (1996) examined the Northern Hemisphere zonal wave number and concluded that the wave number of that event may sometimes be 4. Plumb (1983) proposed that 2-day wave observed in summer may be the results of baroclinic instability near the summer stratospheric wind jet. Although the two theories were supported by observations, there is not consistent explanation for the quasi 2-day wave in the mesosphere and lower thermosphere. Since the quasi 2-day wave is important to the global dynamics of the atmosphere, further observations and theoretical study are needed.

We will report the vertical and temporal structure of quasi 2-day wave observed at Wuhan (30.6^{o}N, 114.5^{o}N) by a newly established meter radar.

2. Data

The Wuhan meteor radar is an all-sky interferometric broadband radar system which has almost identical characteristics to the Buckland Park meteor radar in Australia and the SKiYMET radar in Canada (Hocking et al., 2001). The parameters used for routine observations are shown in Table 1.

Table 1 Wuhan Meteor Radar Specifications

Parameter	Value
Peak power	7.5kW
Frequency	38.5MHz
PRF	500Hz (Feb. 2002 to Sep. 2002)
	1980Hz (From Oct. 2002)
Range sampling resolution	2km

The data from Feb 2002 to Oct 2003 have been used in the present study. The zonal and meridional winds for every 2h and 2km step are obtained from the measured radial wind velocity. Generally, we chose a time window of 8-day length for deriving quasi 2-day wave parameters, using the harmonic analysis and Lomb-Scargle periodogram methods.

* Corresponding author. *E-mail address*: xjg@wipm.ac.cn

This work is supported by the National Natural Science Foundation of China (No.40174048 and 40134020).

3. Results

Figure 1 shows the amplitude of quasi 2-day in the zonal and meridional wind, respectively. In the summer of 2002, the 2-day wave is very strong especially in the meridional direction. But in the summer of 2003, the 2-day wave is much weaker than in 2002. A very strong quasi 2-day wave can also be seen during the end of Jan and beginning of Feb 2003. Winter data in 2003 shows stronger 2-day wave than summer data in 2003.

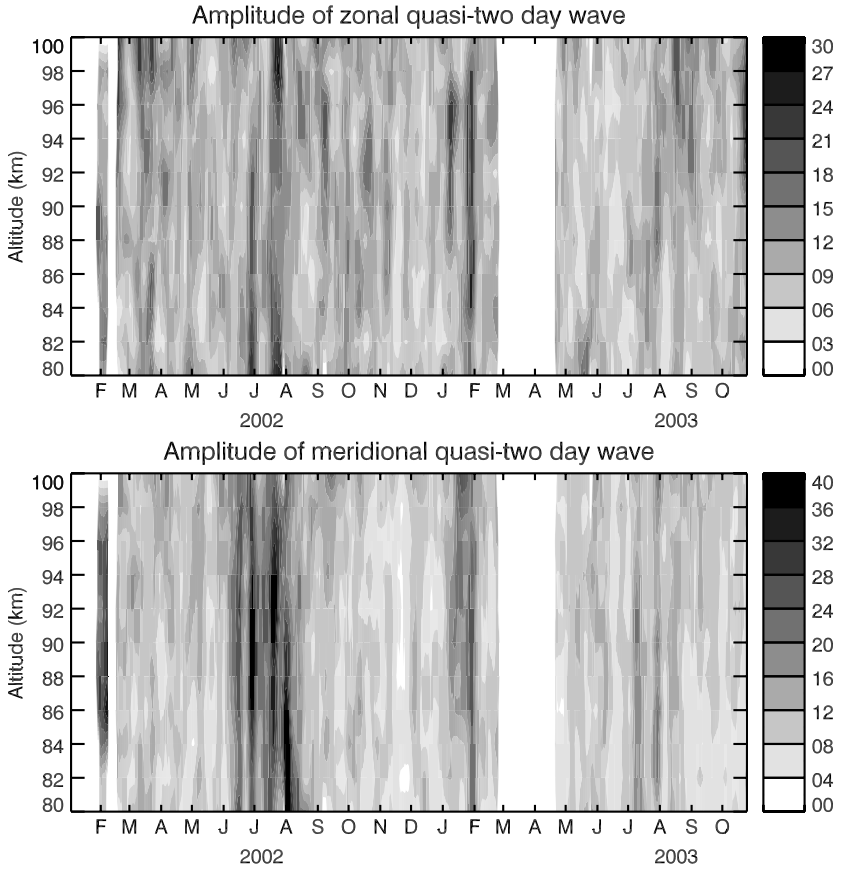

Figure 1 The amplitude of quasi-2-day waves.

Figure 2 is an example of the 2-day wave in winter. The peaks near the frequency 0.5(cycles/day) indicate the occurrence of the quasi 2-day wave. In this example, there are strong 2-day waves in both zonal and meridional directions. The meridional amplitude is a little larger than the zonal amplitude. The periods of quasi 2-day in different height are not same, but the period of zonal component increases with height while that of meridional component decreases. The averaged period for all height exceeds 48 hours. The phase shown here is the phase of wave with maximum amplitude in the period from 42 hours to 54 hours. It is difficult to compare phases of wave component with different periods. If phases of wave with period of 48 hours are computed at different height, we can see the 2-day wave maximize firstly at higher altitude (not shown here). That means the 2-day wave is generated below 80 km. The vertical wave length is estimated to be 106 km and 102 km for the zonal and meridional components, respectively.

Figure 3 is an example in summer. The variations of period and amplitude with height are quite different with those in winter. The periods are below 48 hours at every height. The meridional component is much stronger than the zonal component. The ratio of meridional

amplitude to zonal amplitude exceeds 2. The meridional component observed at Yamagawa is generally 40-60% of the zonal component (Namboothiri, et al., 2002). The difference between our observations and MF observations at Yamagawa may be due to the interannual

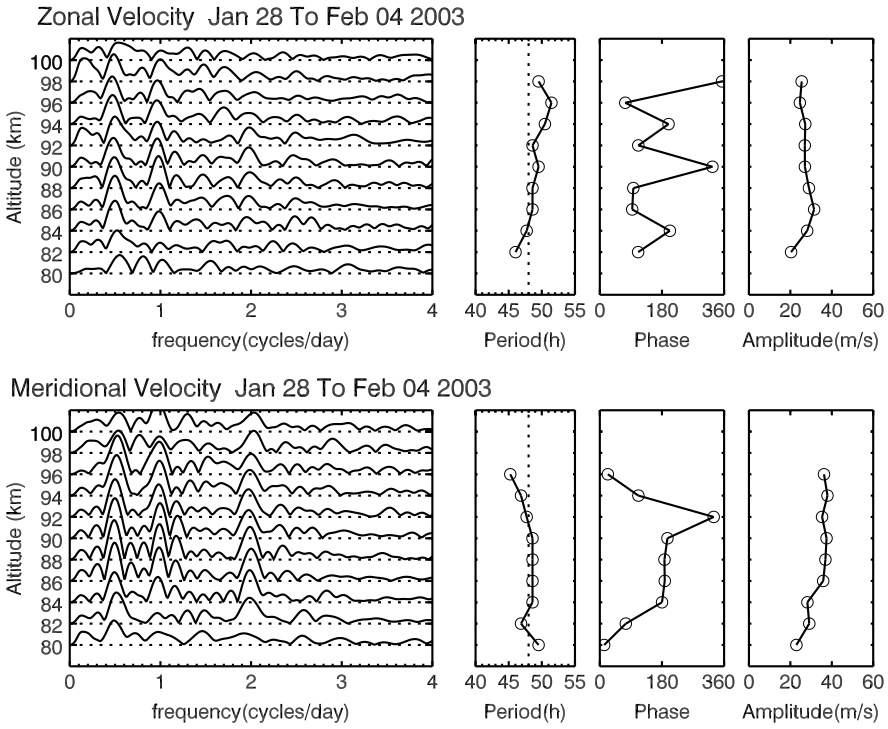

Figure 2 The spectra of wind during Jan 28 and Feb 4 2003 and the periods, phases and amplitudes of quasi-2 day waves.

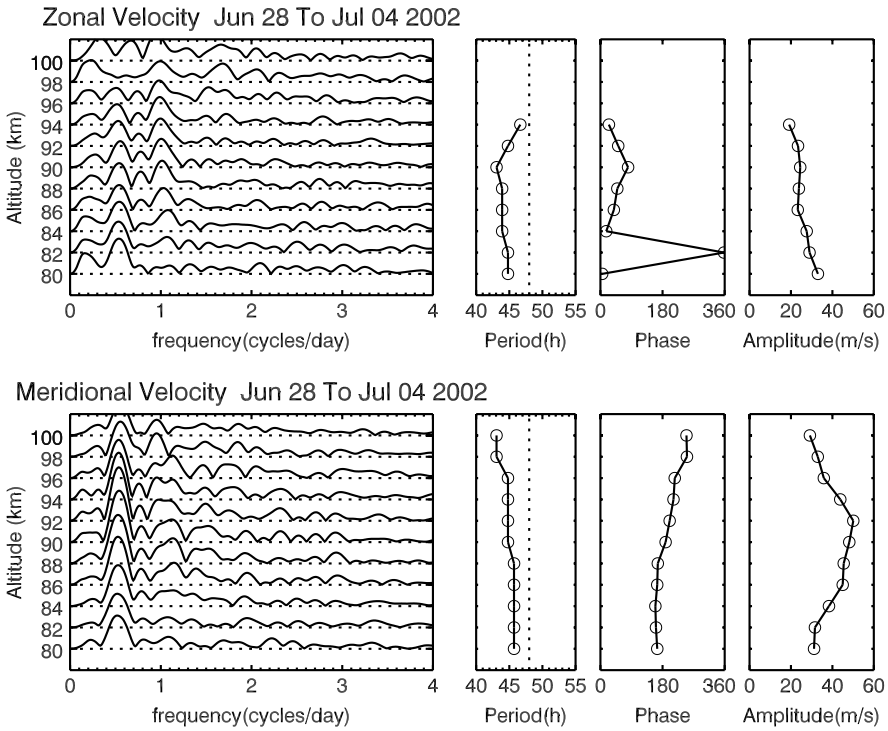

Figure 3 The spectra of wind during Jun 28 to Jul 4 2002 and the periods, phases and amplitudes of quasi-2 day waves.

variability.

Figure 4 shows the averaged height variations of the mean periods and amplitudes of the 2-day wave observed during the summer and the winter. The averaged meridional amplitude in summer is quit larger than that in winter below 95 km. The averaged period in summer is smaller than 48 hours but larger than 48 hours in winter, just as shown in the former examples.

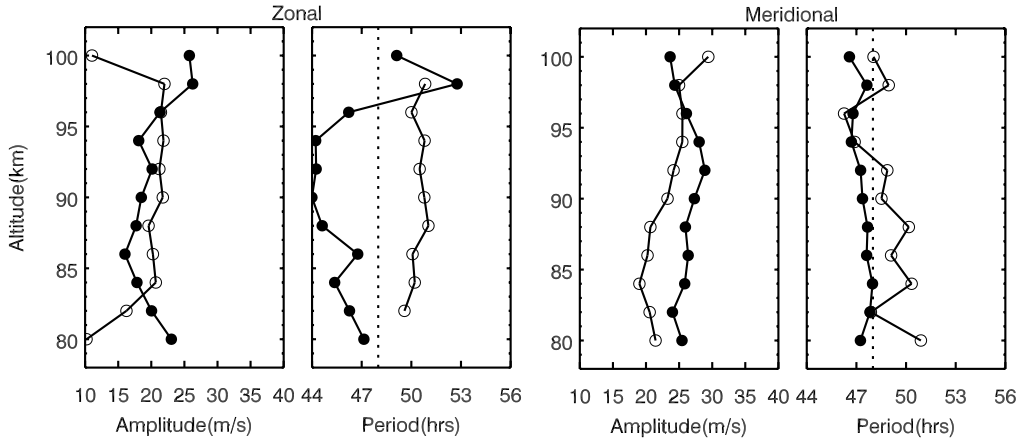

Figure 4 The averaged amplitudes and periods of quasi-2-day waves from Feb 2002 to Oct 2003. Open circles indicate the averaged values in winter and filled circles indicate the averaged values in summer.

4. Conclusion

The present study showed that the quasi 2-day wave is strong in summer and winter 2002, but not strong in summer 2003. The averaged periods in summer is smaller than 48 hours but larger than 48 hours in winter.

References

Hocking, W.K., B. Fuller, and B. Vandepeer, Real-time determination of meteor-related parameters utilizing modern digital technology. J. Atmos. Sol. Terr. Phys., 63, 155-169, 2001.

Meek, C.E., et al., Global study of northern hemisphere quasi-2-day wave events in recent summers near 90 km altitude, J. Atmos. Sol. Terr. Phys., 58, 1401-1411, 1996.

Namboothiri, S.P., P. Kishore, and K. Igarashi., Observations of the quasi-2-day in the mesosphere and lower thermosphere over Yamagawa and Wakkanai, J. Geophys. Res., 107, 10.1029/2001JD00539, 2002.

Plumb, R.A., Baroclinic instability of the summer mesospheric: A mechanism for the quasi-two-day waves?, J. Atmos., Sci., 40, 262-270, 1983.

Sably, M.L., The 2-day wave in the middle atmosphere: Observations and theory, J. Geophys. Res., 86, 9654-9660, 1981.

Thayaparan, T., W. K. Hocking, and J. MacDougall, Amplitude, phase, and period variations of quasi 2-day wave in the mesosphere and lower thermosphere over London, Canada(43^{o}N, 81^{o}W), during 1993 and 1994, J. Geophys. Res., 102, 9461-9478, 1997.

Wu, D.L., P.B. Hays, W.R. Skinner, A.R. Marshall, M.D. Burrage, R.S. Lieberman, and D.A. Ortland, Observations of the quasi-2-day wave from the high resolution Doppler imager on UARS, Geophys. Res. Lett., 20, 2853-2856, 1993.

SPORADIC E LAYER DEPENDENCE ON PLANETARY WAVES. AN EVENT STUDY SHOWING AN INDIRECT RELATIONSHIP TROUGH MODULATED ATMOSPHERIC TIDES

Christos Haldoupis[1] and Dora Pancheva[2]

1: Physics Department, University of Crete, Iraklion, Crete, Greece
2: Department of Electronic and Electrical Engineering, University of Bath, Bath, UK

1. Introduction.

The sporadic *E* layers (E_s), which are thin layers of dense plasma forming in the midlatitude *E* region ionosphere, have been the subject of numerous investigations over many years (e.g., see review by *Mathews*, 1998). Their formation is governed by the complexity of neutral wind dynamics in the mesosphere and lower thermosphere (MLT). In particular, the diurnal and semidiurnal tides, and the vertical wind shears carried by them, are of fundamental importance to E_s, which sometimes are referred to as "tidal ion layers". In addition to the undisputed role of atmospheric tides, recent results suggested that planetary waves (PW) play a role on E_s formation as well, a fact that went unnoticed in the long-going research of sporadic *E*. The first indirect evidence for a link between E_s and PW was provided by field-aligned backscatter observations (obtained with the MU radar in Japan and the SESCAT system in Crete, Greece) that showed PW-period like modulations in the occurrence of magnetic aspect-sensitive *E* region radar echoes which relate with strong sporadic *E* layers.

Here we combine and summarize the results of two recent studies on the PW - E_s relationship published in JGR by *Haldoupis and Pancheva* [2002] (hereafter called *Paper A*), and *Pancheva et al.* [2003] (*Paper B*). *Paper A* provided the first direct evidence in favor of a PW role on E_s generation, whereas Paper B showed that planetary waves can affect E_s formation indirectly through nonlinear interaction and modulation of the semidiurnal and diurnal atmospheric tides. Both of these studies relied on a conspicuous PW event that occurred in August-September 1993 and detected in MLT ground radar and satellite wind measurements (e.g., *Clark et al.*, 2002 and references therein). This large scale atmospheric wave was a westward propagating 7-day PW of zonal number S = 1 that lasted for about 25 days, seen mostly in the meridional wind with peak amplitudes in excess of 15 m/s.

2. Direct Evidence for PW Modulation of Sporadic *E* Layers

Given the dominant 7-day PW event in August-September 1993 and the need to prove (or disprove) the postulated PW- E_s relationship, we obtained from the Colorado World Data Center mean hourly E_s critical frequency (*foEs*) time series for all the northern hemisphere midlatitude stations. In this respect, we found usable data from 8 stations spanning from 58^{o}E to 157^{o}W, that is, covering about 215^o in longitude around the globe. A first look inspection of the hourly mean *foEs* times series has been surprisingly reassuring, as all stations appeared to have recorded a long period modulation in *foEs* during the 7-day PW occurrence.

To investigate the spectral dynamics of all eight time series we applied wavelet transform techniques. The wavelet spectrograms showed a dominant 7-day periodicity to be present, from about middle of August and well into September, in all eight ionosonde stations from the eastmost Ashkhabad to the westmost Maui. This is illustrated in Figure 1 which shows wavelet spectrograms for all eight stations. The *foEs* wavelike modulation maximizes everywhere around end of August, very much in agreement with the maximum of the 7-day PW activity observed in the meridional component of the mesospheric neutral wind, as discussed by *Clark et al.* [2002]. We stress that this 7-day periodicity did not relate to a global geomagnetic activity, as confirmed from similar 3-hourly *Ap* wavelet analysis.

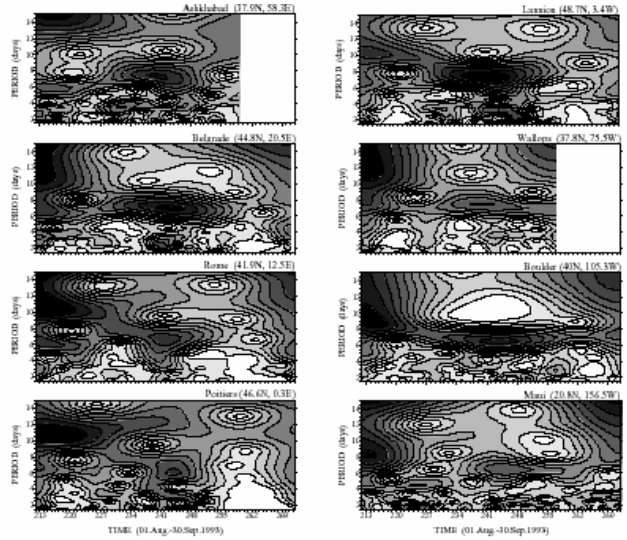

Figure 1. *Period-time amplitude wavelet spectrograms for the mean hourly foEs time series seen simultaneously in all eight ionosonde stations. All stations see a dominant 7-day modulation during the 2nd half of August and into September 1993.*

The observation of the 7-day PW periodicity in *foEs* over a large latitudinal zone, suggested an alternative way for computing PW parameters, like the zonal wavenumber and the propagation properties of the wave. By using 3 independent methods for analysis (for details see *Paper A*) we calculated a 7-day period westward propagating S = 1 wave with a zonal phase velocity near 30 m/s which is in good agreement with the results of MLT neutral wind data analysis published elsewhere. The present findings provided the first direct evidence, proving that PW play an important role in the physics of midlatitude sporadic *E* layers.

3. Planetary Wave Influence on Sporadic E via Modulation of Atmospheric Tides

In *Paper B* the investigation of the PW-E_s relationship was carried one step further by means of correlating concurrent mesospheric neutral winds and *foEs* data from neighboring locations, in order to understand the physical mechanism behind the PW- E_s interaction. The neutral wind data were hourly means of zonal and meridional winds measured by the medium frequency radar in Saskatoon, Canada (52^oN, 107^oW), and the meteor wind radar in Sheffield, UK (52^oN, 2^oW). The wind measurements were compared with available *foEs* observations made with ionosondes located as near to the radars as possible, that is, we used Boulder, Colorado (40^oN, 105^oW) *foEs* data for the American sector (Saskatoon), and Lannion , France (49^oN, 3^oW) data for the West European sector (Sheffield).

For the analysis we have used wavelet transform, digital filtering, and corelloperiodogram power spectral analysis techniques (for details see *Paper B*). The wavelet spectrograms of the wind data verified that a 7-day PW dominated the spectrum from about day 235 to 265, having amplitudes near 16 m/s for UK and 10-12 m/s for Saskatoon. The Saskatoon records show that above 97 km the PW amplitude tends to decrease with altitude. As discussed in the previous section the same 7-day periodicity was also present concurrently in the sporadic *E* critical frequency *foEs* for both stations in Boulder and Lannion.

Next, the 7-day (PW) periodicities seen in the meridional wind were compared directly with those in *foEs* keeping in mind of course that these variations were measured at different altitude. Based on a detailed analysis (see *Paper B*) we concluded that for the strong PW event under consideration there was no convincing evidence in favor of a direct PW role on E_s generation. This pointed to the possibility for an indirect PW role, probably through the modulation of atmospheric tides. We arrived at this option because of the nonlinear

interactions between tides and planetary waves which are known to take place in the middle atmosphere (for relevant references see *Paper B*), and the conviction that PW modulate upward propagating tides and through them mediate their signatures in the ionosphere. Also, the role of atmospheric tides on E_s formation is well established in the physics of midlatitude sporadic *E*. Driven by these ideas, we investigated if there is any PW modulation present in the diurnal and semidiurnal tides measured in Saskatoon and Sheffield and examined if similar effects are concurrently evident in the *foEs* time series. This, if true, would suggest a new mechanism for the observed relationship between PWs and sporadic *E* layers.

The interaction between PW and atmospheric tidal waves is a nonlinear process which resembles, for example, amplitude modulation (AM) in communication systems. Thus, one would expect to find two secondary waves having frequencies respectively equal to the sum and difference of the frequencies of the interacting primary (tidal and planetary) waves. In terms of periods, this means for the 7-day PW that the secondary waves must have periods: (a) for the 12-h tide near 11.1 - 11.2 hours and 12.9 - 13 hours, and (b) for the 24-h tide near 21.0 and 28.0 hours. In the following we search for such secondary waves in both the Saskatoon and Sheffield semidiurnal and diurnal tides.

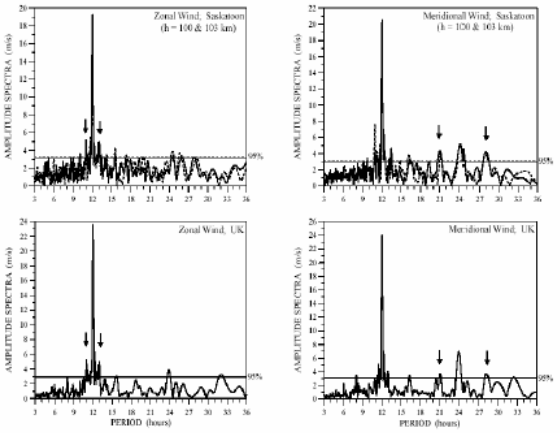

Figure 2. 7-day PW modulation of 24- and 12- hour tides

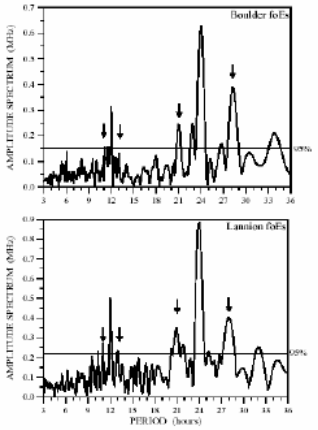

Figure 3. 7-day PW modulation of 24- and 12- hour periodicities in foEs

The analysis (for details see *paper B*) showed clear evidence of 7-day modulation on both the diurnal and semidiurnal tides, and on the 24- and 12- hour periodicities in the *foEs* time series. As shown in Figure 2, the 7-day tidal modulation was found to be present in both amplitude spectra of the zonal (left graphs) and meridional (right graphs) winds measured in Saskatoon (upper panels) and in UK (bottom panels). The two arrow pairs in each plot indicate the position in the spectrum of the secondary peaks discussed previously. As evidenced in Figure 2, in both, the Saskatoon and UK longitudinal sectors the measured tides are 7-day amplitude modulated, with the secondary waves being stronger in the zonal component of the semidiurnal tide and the meridional component of the diurnal tide. To confirm these results and locate in time the tidal modulations, wavelet transform analysis was performed on the time series of the tidal amplitudes, after removing the 7-day PW from the data in order to avoid any artificial coupling between the tidal amplitudes and the mean wind (again for details see *Paper B*). The wavelet spectral analysis confirmed the 7-day PW modulation detected in the correloperiodograms of Figure 2.

The same 7-day PW modulation was also present in the *foEs* 12- and 24-hour periodicities. In search for the 7-day modulation in *foEs* we applied the same methodology used in the wind data, and looked for spectral peak pairs about the 12-hour periodicity near 11 and 13 hours, and about the 24-hour periodicity near 21.0 and 28.0 hours. Figure 3 shows the *foEs* amplitude correloperiodograms for Boulder (top panel) and Lannion (bottom panel). As seen,

the 12-h and 24-h periodicities in *foEs* are present at both stations, with the diurnal periodicity being dominant. Figure 3 shows clearly that the 24- and 12-hour periodicities in *foEs* are both also 7-day amplitude modulated. The presence of the 7-day modulation was also confirmed by wavelet transform analysis (see again for details Paper B).

4. Summary

A large amplitude, 7-day period westward propagating S = 1 planetary wave (PW) has been reported from ground radar and satellite wind measurements in the mesosphere-lower thermosphere (MLT) during the second half of August and well into September, 1993. Following recent suggestions that planetary waves might play a role in the formation of midlatitude sporadic *E* layers , we have analyzed, for the period from August 1 to September 30, 1993, the sporadic *E* critical frequency (*foEs*) time series from 8 midlatitude ionosonde stations covering a longitudinal zone from about 58^0 E to 157^0 W. The analysis revealed that all 8 station *foEs* data showed a strong 7-day periodicity, occurring concurrently with the 7-day planetary wave reported elsewhere. This provided the first direct proof in favor of a PW role on E_s formation. The PW-E_s relationship was investigated further by considering the variations in the mesospheric neutral wind measured with radars in Canada and UK. Our analysis showed clearly that E_s is affected indirectly by the PW through the action of the diurnal and semidiurnal tides which are strongly modulated by the same PW, apparently through a nonlinear interaction process at altitudes below 100 km. This 7-day PW modulation was found to be clearly present simultaneously in the amplitude of the zonal 12-hour tidal wind, the meridional 24-hour tidal wind, and in both, the 12-hour and 24-hour periodicities which existed in the *foEs* time series. These results suggested an explanation for the observed relation between sporadic E layers and planetary waves.

5. Acknowledgements

This work was supported by the Greek Secretariat for Research and Technology and the British Council in Athens through a Greek-British Collaboration Research grant for 2001-2003. Support was also provided by the European Office of Aerospace Research and Development (EOARD), Air Force office of Scientific Research, Air Force Research Laboratory, under contracts F61775-01-WE004 and FA8655-03-1-3028 to C. Haldoupis. We thank H. G. Muller, for providing the Sheffield, and to C. Meek and A. Manson for the Saskatoon, wind data.

6. References

Clark, R. R., M. D. Burrage, S. J. Franke, A. H. Manson, C. E. Meek, N. J. Mitchell, and H. G. Muller, Observations of 7-day planetary waves with MLT radars and UARS/HRDI instrument, *J. Atmos. Sol.-Terr. Phys., 64*, 1217, 2002.

Haldoupis, C., and D. Pancheva, Planetary waves and midlatitude sporadic E layers: Strong experimental evidence for a close relationship, *J. Geophys. Res., 107,* ido10.1029/ 2001JA000212, 2002.

Mathews, J.D. Sporadic *E*: current views and recent progress, *J. Atmos. Sol.-Terr. Phys., 60,* 413, 1998.

Pancheva, D., C. Haldoupis, C. E. Meek, A. H. Manson, and N. Mitchell, Evidence of a role for modulated atmospheric tides in the dependence of sporadic *E* layers on planetary waves, *J. Geophys. Res., 108,* ido10.1029/ 2002JA009788, 2003.

RADAR, OPTICAL AND SATELLITE STUDIES OF CLIMATOLOGY AND EFFECTS OF ATMOSPHERIC GRAVITY WAVES AND TURBULENCE

Nikolai M. Gavrilov

Atmospheric Physics Department, Saint-Petersburg State University, Petrodvorets, St. Petersburg, 198504, Russia, gavrilov@pobox.spbu.ru

Abstract. Some results of studies of climatology of internal gravity waves (IGWs) in the middle and upper atmosphere are presented. MST and MF radars give information about seasonal and interannual changes of the mean winds and IGW variances. Low-orbit satellites receiving GPS signals may give distribution of zones of increased IGW and turbulence intensity and of wave generation. Multi-beam MST radar observations give information about mesoscale nonlinear IGW sources in the tropo-stratosphere. Numerical models allow to study sensitivity of general circulation of the middle atmosphere to global inhomogeneity of IGW sources observed with radars and GPS satellites.

1. Introduction

For better understanding and interpreting, MST radars studies should be completed by other observations with various ground-based and satellite techniques and by theoretical studies. In this paper, we present a short review of some recent studies of climatology of internal gravity waves (IGWs) in Saint-Petersburg University (Russia). These studies include an analysis of seasonal and interannual variations of wind velocity in the middle atmosphere with MST and medium frequency (MF) radars, optical observations of short-period variations of night airglows, analysis of global structure of IGWs and their sources in the lower and middle atmosphere from the data of low-orbit GPS satellites. Numerical modeling of IGW spectrum propagation in the atmosphere and study of sensitivity of a numerical model of general circulation of the middle atmosphere to observed horizontal inhomogeneity of IGW distribution at low boundary are discussed.

2. Analysis of radar data.

In the last years, a considerable progress has been achieved in studies of IGW climatology with radar technique in the atmosphere. A group of Saint-Petersburg University participated in joint analyses of the data from Saskatoon medium frequency (MF) radar [Gavrilov et al., 1995], from Japanese MU radar [Gavrilov et al., 2000], from multi-year D1 observations of ionospheric drifts at Collm Observatory, Germany [Gavrilov et al., 2001], and from other meteor and MF radars. Recently, an analysis of seasonal and interannual variations of IGW characteristics at altitudes of 70 – 90 km over Hawaii (22° N, 159° W) from the data of MF radar was made [Gavrilov et al., 2003a,b].

Hawaii MF radar gives the wind velocity values with time step of about 2 min and height resolution of 2 km. For each altitude, we obtain hourly mean values of zonal and meridional wind velocity components and their hourly variances. The latter give information about wind perturbations with time scales up to 1 hr, which are called as "within hour" (WH) data. Differences of consecutive hourly data give information about perturbations with periods 1 – 5 hr (HD data). Transmission functions of these numerical filters are described by Gavrilov et al. [2003a]. After calculating hourly-mean velocities and WH and HD perturbations, we calculate monthly mean values taking account of numbers, n_i, of good velocity measurements during each hour. Obtained monthly mean winds and variances we use in this paper for the study of seasonal changes of the mean

winds and variances at altitudes 70 - 90 km. To increase statistical reliability, we use only hours with $n_i > N$, where N may vary in different kinds of analysis.

This method is applied for the analysis of measurements with MF radar at Hawaii (22° N, 159° W) during years 1990 - 2000. Figure 1 represents interannual variations of the mean wind components. Below altitudes 82 - 85 km, zonal wind has mainly annual variation with the maxima of eastward wind in winter and of westward wind in summer. Above 82 - 85 km, there is a semiannual variation of the mean zonal wind with additional maximum of eastward wind in summer. Seasonal variations of the mean meridional wind in Figure 1 are more complicated and seem to be a superposition of annual and semiannual harmonics with their phases variable in height.

Figures 2 and 3 show interannual variations of WH and HD wind variances representing, probably, the intensity of IGWs with periods 0.1 - 1 hr and 1 - 5 hr, respectively. One can see clear seasonal variations of the variances with the main maximum in winter and a secondary maximum in summer below altitudes 82 - 85 km, which are more noticeable in Figure 2 for WH component. Above these altitudes, there is a tendency to equinox's maxima of IGW activity in Figures 2 and 3. [see Gavrilov et al., 2003a]. Considering absolute values of WH and HD variances in Figures 2 and 3, one should keep in mind that these values could be overestimated at lower heights, where we have larger numbers of data gaps.

One of possible reasons of wind variations at MLT could be heating and cooling of Pacific surface water known as the El Nino and La Nina events, respectively. An indicator of El Nino effects in the atmosphere is the Southern Oscillation Index (SOI) reflecting the surface pressure difference between tropical observation points Tahiti and Darwin. Positive SOI values correspond to La Nina and negative SOI – to El Nino events.

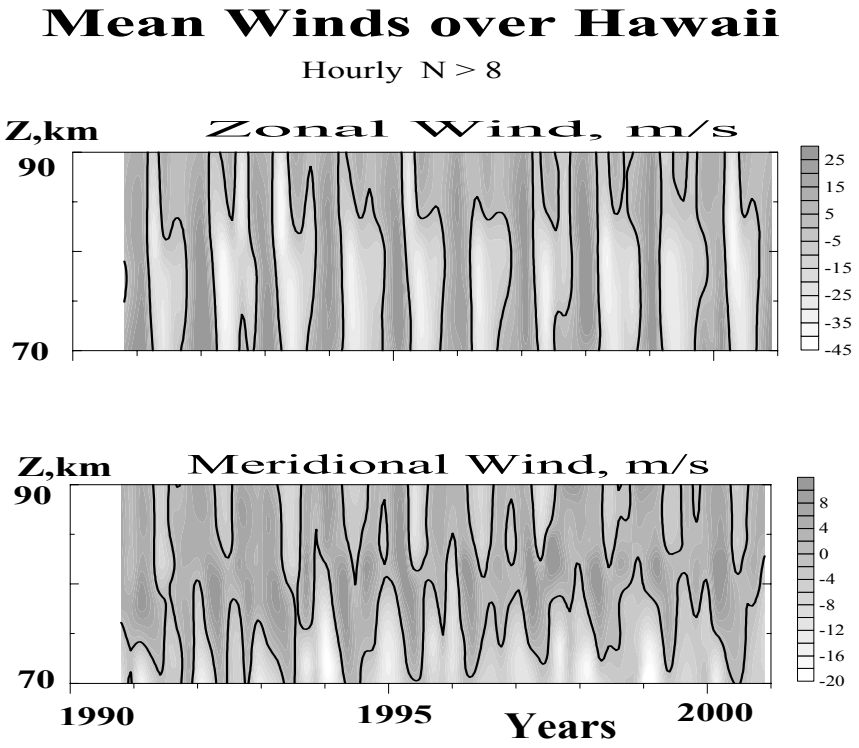

Fig. 1. Height-Interannual variations of the mean wind components over Hawaii.

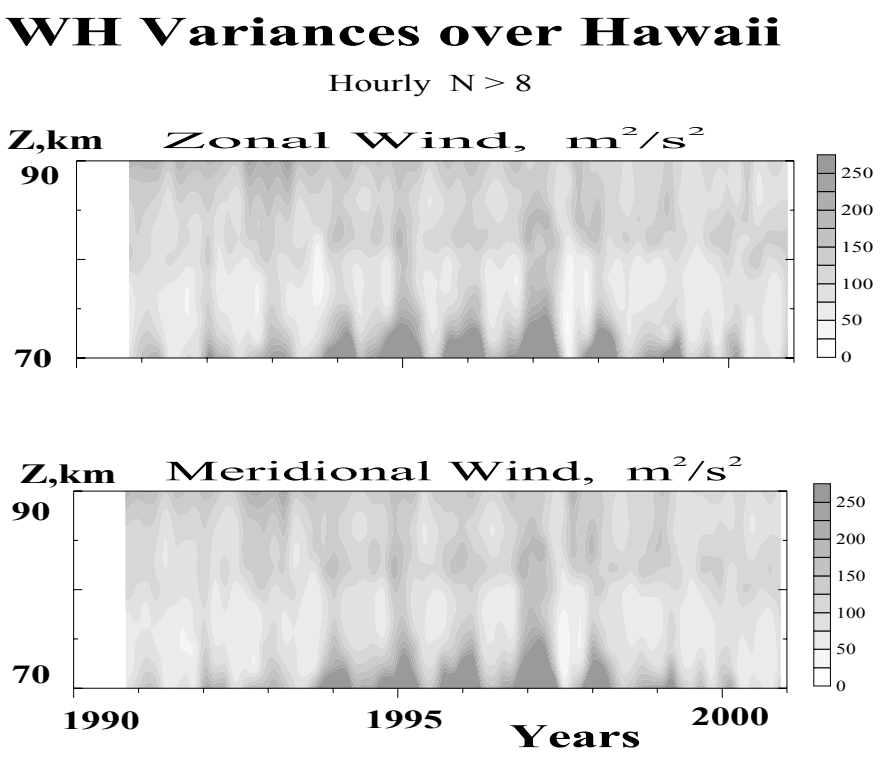

Fig. 2. Height-Interannual variations of WH wind variances with time scales 0.1 – 1 hr.

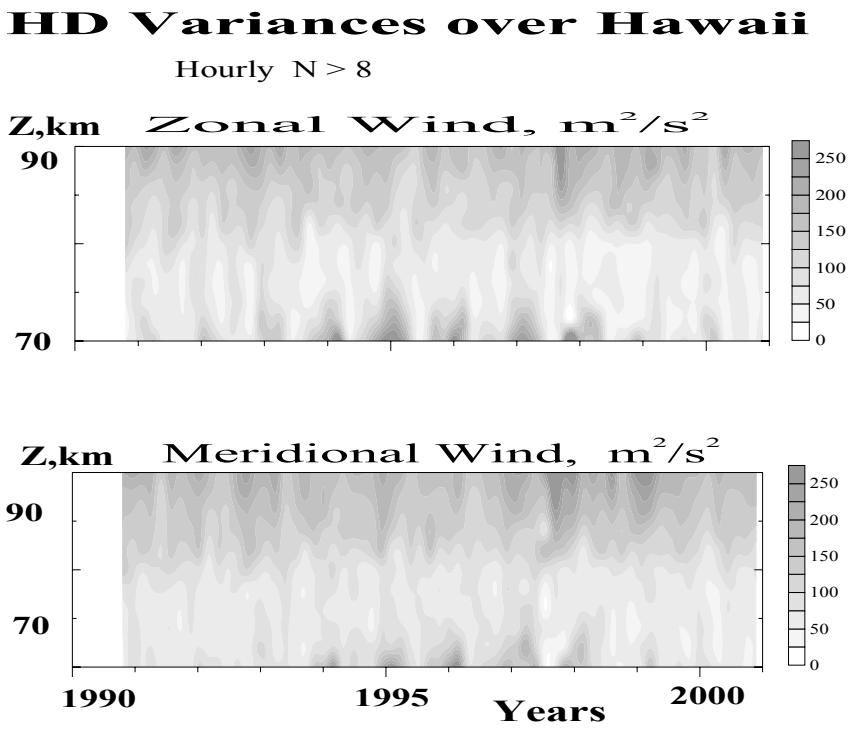

Fig. 3. Height-Interannual variations of HD wind variances with time scales 1 – 5 hr.

Figure 4 shows dependencies of the deviations of monthly mean WH wind variances with periods of 0.2 – 1 hr from the mean seasonal variation on respective monthly SOI values. Figure 4 reveals WH variance correlation with SOI at heights 88 - 92 km, which is better in winter than in summer. El Nino events (negative SOI) correspond to the increase in the wind variances. Larger scale wind variances having time scales 1 - 5 hr show

similar correlation with larger magnitudes at negative SOI above altitude 85 km [see Gavrilov et al., 2003b].

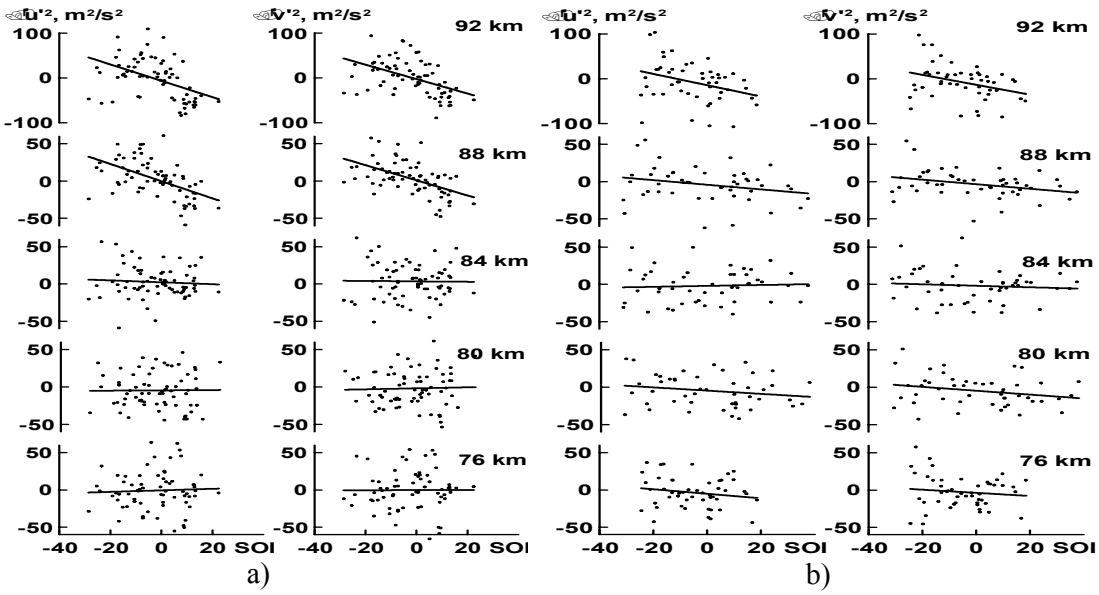

Fig. 4. Dependence of deviations from average monthly values on Southern Oscillation Index for WH variance in winter (a) and summer (b) for zonal (left plots) and meridional (right plots) components .

3. Analysis of nightglow variations.

IGWs in the middle and upper atmosphere may produce variations of intensity and rotation temperature of nigh airglows, which are widely used for studies of waves in the middle and upper atmosphere. A method of the analysis of IGW parameters from observations of variations of night airglows was developed in St. Petersburg University [Gavrilov et al., 2002]. The method is based on the analysis of simultaneous observations of variations of intensity and rotation temperature of night airglows measured by scanning spectral devices simultaneously in several points of the sky. The algorithm includes preliminary quality check of experimental data, low and a high-frequency filtering and spectral analysis of variations of characteristics of night airglows in each point at the sky, and also definition of parameters of spectral components.

This method was applied for the analysis of results of long-term observations of wave variations of night airglows of hydroxyl (OH) and molecular oxygen (O_2) at altitudes around 87 and 94 km, respectively, using optical device SATI, which were carried out in Shigaraki, Japan (35º N, 136º E) since October 1998. Duration of continuous intervals of night measurements varies from 2 up to 12 hours, and the data sampling is about 2 minutes.

For studying seasonal changes of statistical characteristics, all data are divided into four groups: winter (from November to February), summer (May – August), spring and autumn (months between mentioned above). Full numbers of clear moonless nights of observation for these seasons are of 82, 27, 15 and 16, respectively. In Figure 5, polar histograms of azimuths of IGW propagation in layers of OH and O_2 airglows are shown. Some dominance of northwest and southern directions for OH emission, and northwest and southeast sectors for O_2 emission in winter is observed. In summer, IGWs propagate, basically, to northern hemisphere. In spring, distribution of IGW azimuths in Figure 5 is similar to the summer one, and in autumn IGW azimuths have more wide distributions basically into northern hemisphere. Analysis reveals maxima of variations of intensity and rotation temperature of nightglow emissions in November - December and their decreasing in September – October [see Gavrilov et al., 2002].

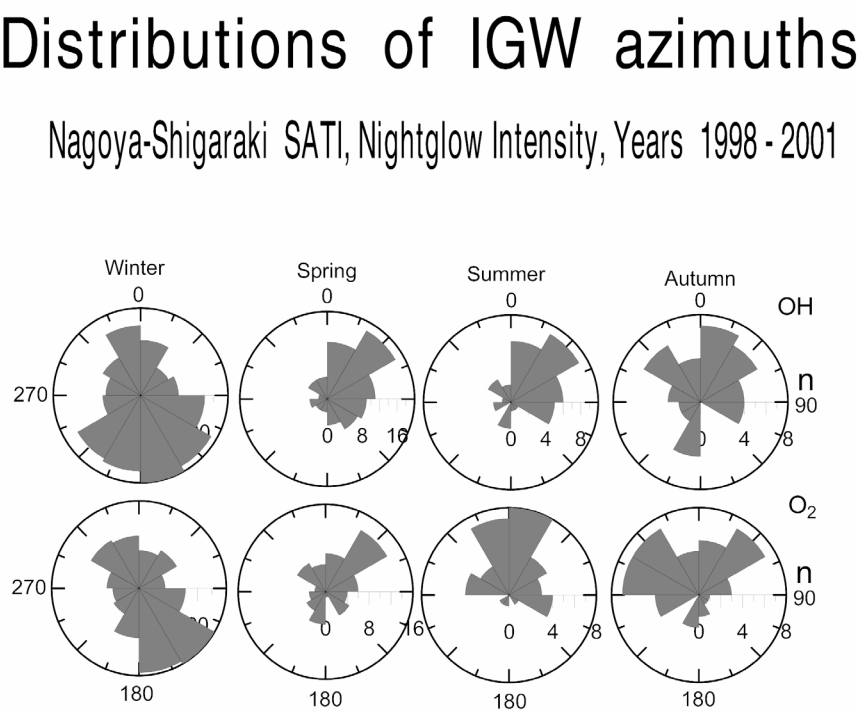

Fig. 5. Azimuths of IGW propagation in Shigaraki from SATI observations.

4. GPS/Microlab satellite data analysis.

Several recent works were devoted to studies of IGW geographical structure in the atmosphere using satellite-borne remote sensing measurements of the background dynamical structure, planetary scale fluctuations, and mesoscale disturbances. Tsuda et al. [2000] made the first analysis of global morphology of IGW activity in the stratosphere from GPS/MET data. Alexander et al. (2002) continued this study and showed that the LEO/GPS occultation technique provides important and unique data for studies of the global distribution of atmospheric IGWs. Tsuda et al. (2000) and Nastrom et al. (2000) showed good agreement between seasonal variations of IGW variances obtained with GPS/MET satellite and with Japanese MU radar and a VHF radar in North America.

Low-orbit GPS satellite usually provides vertical profiles of radio wave refraction index at heights 5 – 60 km with high resolution in altitude. Generally, refractivity $N = (n-1)\times 10^6$ decreases exponentially in altitude. More sensitive to small variations is so called "dry temperature", T_{dry}, given by the expression

$$T_{dry} = 77.6\, p / N, \qquad (1)$$

where p is atmospheric pressure. The dry temperature is a good estimation of atmospheric temperature at altitudes 15 – 30 km. Dynamical variations δp and δT of parameters in (1) for small-scale turbulence and low-frequency short internal gravity waves (IGWs) satisfy to the condition $|\delta p/p| << |\delta T/T|$, and (1) gives

$$\delta N / N \approx -\delta T_{dry} / T_{dry}. \qquad (2)$$

For GPS/MET satellite, height step of the data presentation is $\Delta z = 0.2$ km. For each vertical profile of refraction index measured with GPS/MET satellite, we make quadratic approximation and calculate variances of residual inclinations inside each layer. Then we select groups of these variances for respective months during GPS/MET experiment from 1995 to 1997. At altitudes 15 – 30 km, variances of the refractive index reflect the variances of atmospheric temperature. In the troposphere and at high altitudes variances

of the refraction index are not equal to that of temperature, but may reflect small- and mesoscale dynamical changes in the atmosphere.

Figure 6 reveals zonal mean variances of the refraction index average for entire duration of GPS/MET experiment in 1995 - 1997. At altitudes 15 – 25 km, one can see maxima at latitudes between -20° and 20° in Figure 6. They may be connected with deep convection in equatorial region. At altitudes 20 – 25 km, one can also see the maxima of refraction index variations at high latitudes of northern hemisphere. The variances increase at 35 km, and the maxima near the equator appear. At altitudes near 10 km, maxima of the variances are concentrated between latitudes 20° and 60° in both northern and southern hemispheres. These maxima correlate with locations of tropospheric jet streams having maxima at altitudes 10 - 12 km. An analysis [see Gavrilov et al. 2003c] shows smaller variances in the winter troposphere and larger variances in the winter stratosphere. This may reflect seasonal variations of the intensity of wave sources in the lower atmosphere and of filtering of propagating IGWs by background winds and temperatures in the middle atmosphere.

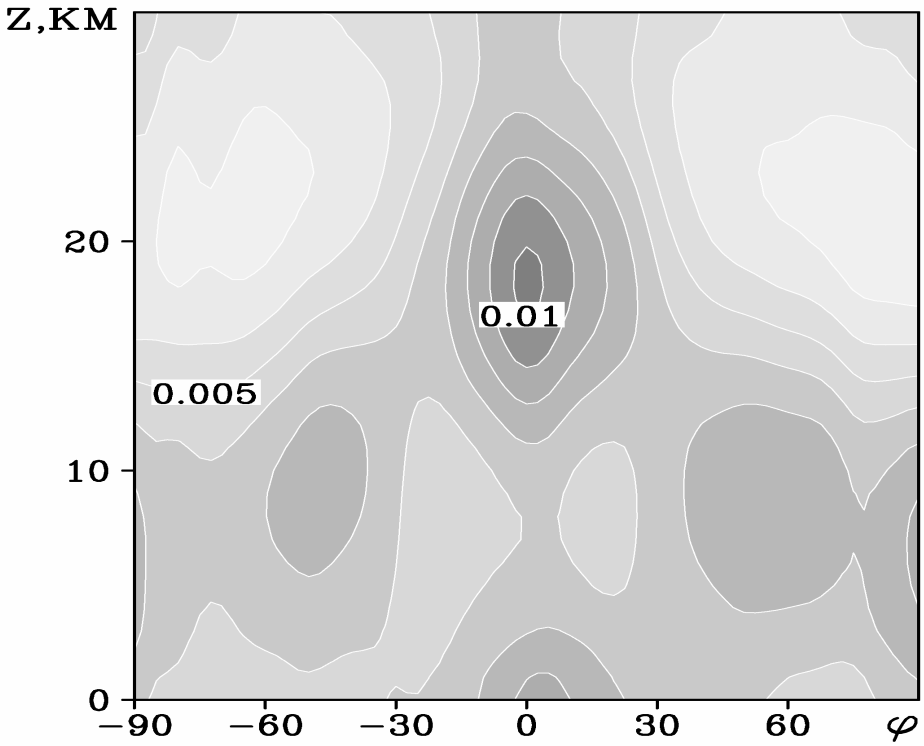

Fig. 6. Zonal mean variances of the refraction index average for entire interval of GPS/MET experiment in years 1995 - 1997.

5. Numerical modeling of atmospheric general circulation.

A simplified mathematical models and parameterization of wave thermal and dynamical effects for the inclusion of IGW effects to the numerical models of atmospheric dynamics were developed. We used a version of COMMA-SPBU model of general circulation of the middle and upper atmosphere, initially developed in Cologne University and then modified in Leipzig University (Germany) [Frohlich et al, 2003] and in Saint-Petersburg State University (Russia). Compared to the other known analogous parameterizations of IGW effects, we took into account horizontal inhomogeneity of gravity wave sources distributions in accordance with GPS satellite observations (see above).

The subroutines for parameterization of accelerations of the mean flow and heating rates due to breaking and dissipating IGWs come from simplifications of a numerical model of IGW generation and propagations, developed in Saint-Petersburg State

University [Gavrilov and Fukao, 1999]. In this study, we developed a modification of Lindzen-type parameterization using 200 IGW harmonics covering the ranges of IGW horizontal phase speeds of 3 - 150 m/s, and eight azimuths of IGW propagation.

An analysis of GPS/MET satellite data (see section 4) shows inhomogeneity of latitude-longitude distributions of IGW intensity, which may be different at different altitudes. To incorporate these realistic distributions of IGW intensities into atmospheric general circulation models, we modified the wave parameterizations to be able to specify boundary conditions for IGW spectrum at any height in the atmosphere. The parameterization was included into the COMMA-SPBU general circulation model.

To study the sensitivity of the general circulation of the middle atmosphere to the latitudinal distribution of lower atmosphere wave sources, we made calculations with the COMMA-SPBU model for constant values of wave velocity variances at altitude 30 km and their latitude distributions shown in Figure 7. These distributions reflect the main structures of tropo-stratospheric jet streams and convective patterns observed with GPS/MET satellite at Figure 6.

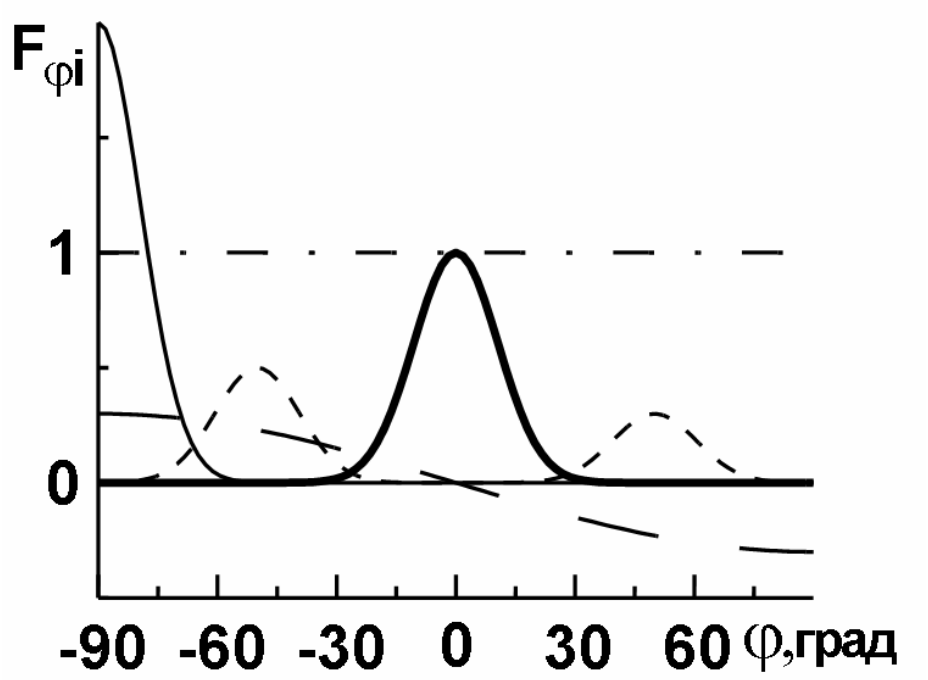

Fig. 7. Model latitude distributions of IGW variances for July at altitude 30 km reflecting constant value (dash-dotted line), seasonal variations (long dashes), winter pole maximum (thin solid line), equatorial maximum (thick solid line) and mid-latitude maxima (short dashes).

Figures 8 and 9 present examples of height-latitude distributions of wind and temperature calculated with COMMA-SPBU numerical general circulation model for July and, respectively, for homogeneous and inhomogeneous (according to the total latitude distribution of the IGW intensity from Figure 7). One can see that taking account of realistic horizontal distribution of IGW activity gives better reversal of general circulation above the mesopause. An analysis by Gavrilov et al. (2003d) shows that structure of general circulation of the middle atmosphere is most sensitive to the wave variances in the middle latitudes.

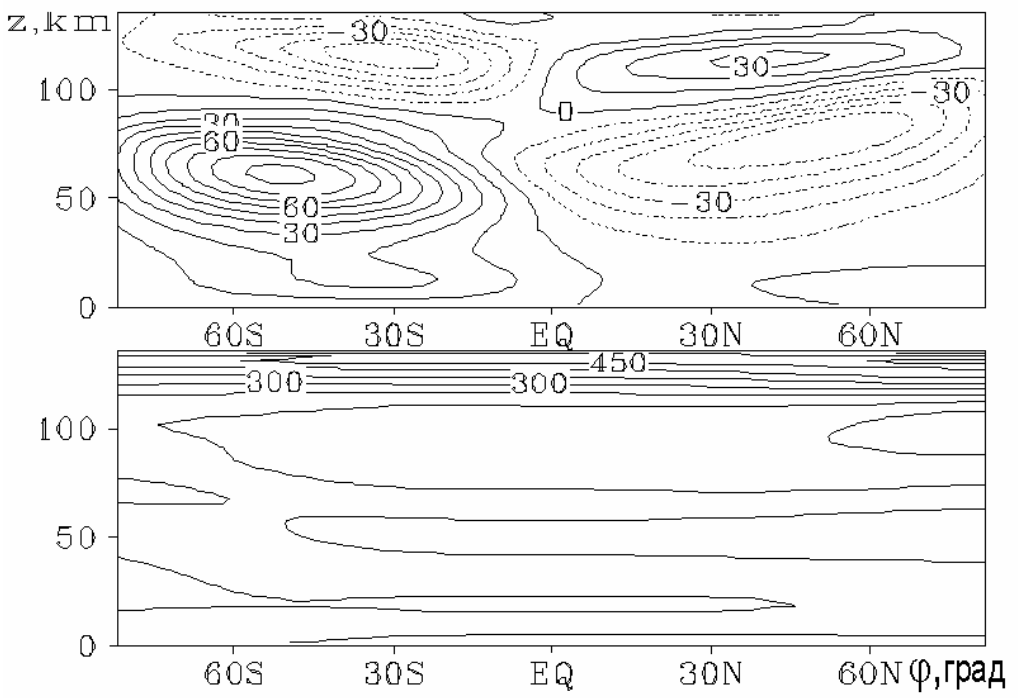

Fig. 8. Zonal wind (top) and temperature (bottom) calculated with COMMA-SPBU general circulation model for horizontally homogeneous distribution of low boundary IGW variance.

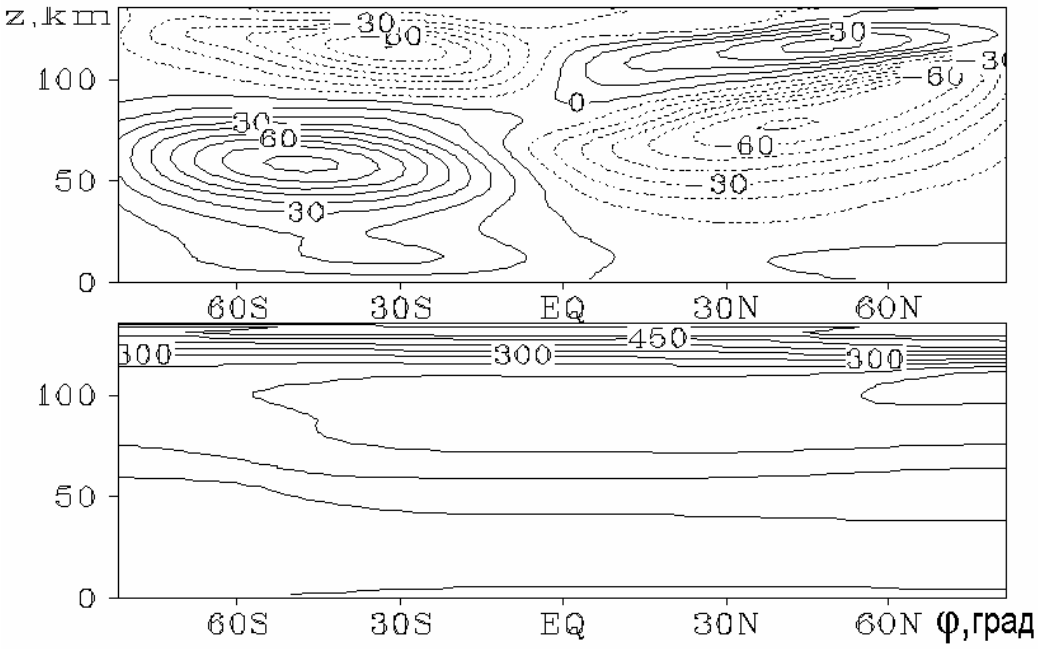

Fig. 9. Same as Figure 8, but for low boundary latitude distribution of wave variance equal to the total of values shown in Figure 7 with correction of the global mean IGW variance to the same value as in Figure 8.

6. Conclusion

In this paper, some results of studies of climatology of internal gravity waves (IGWs) in the middle and upper atmosphere are described. MST and MF radars and ground-based optical observations give information about seasonal and interannual changes of the mean winds and IGW variances. Low-orbit satellites receiving GPS signals may give distribution of zones of increased IGW and turbulence intensity and wave generation. Numerical models allow studying sensitivity of general circulation of the middle atmosphere to global inhomogeneity of IGW sources observed with radars and GPS satellites. Combined radar, optical and satellite measurements are essential for better understanding wave dynamics of the atmosphere.

Acknowledgements. This study was partly supported by Russian Basic Research Foundation. COMMA core version was provided by the Institute of Geophysics and Meteorology, Cologne University. GPS/MET data had been provided by UCAR trough Drs. C. Rocken and S. Sokolovsky.

References.

Alexander, M. J., Tsuda, T., Vincent, R. A., 2002. Latitudinal variations observed in gravity waves with short vertical wavelengths, *J. Atmos. Sci.*, *59*, 1394-1404.

Frohlich K. , A. Pogoreltsev, and Ch. Jacobi, Numerical simulation of tides, Rossby and Kelvin waves with the COMMA-LIM model, *Adv. Space Res.*, in press, 2003

Gavrilov N. M., A. H. Manson, and C. E. Meek, Climatological monthly characteristics of middle atmosphere gravity waves (10 min - 10 hr) during 1979 - 1993 at Saskatoon, *Ann. Geophys., 13*, 285-295, 1995.

Gavrilov, N. M., S. Fukao, and T. Nakamura, Gravity Wave Intensity and Momentum Fluxes in the Mesosphere over Shigaraki, Japan (35° N,136° E) During 1986 - 1997, *Ann. Geophys.*, *18*, 834 – 843, 2000.

Gavrilov, N. M., Ch. Jacobi, and D. Kurschner, Short-period variations of ionospheric drifts at Collm and their connection with the dynamics of the lower and middle atmosphere, *Phys. Chem. Earth, C 26*, 459-464, 2001.

Gavrilov, N. M., K. Shiokawa, and T. Ogawa, Seasonal variations of medium-scale gravity wave parameters in the lower thermosphere obtained from SATI observations at Shigaraki, Japan, *J. Geophys. Res., D107*, 10.1029/2001JD001469, 2002.

Gavrilov, N. M., D. M. Riggin and D. C. Fritts, Medium Frequency Radar Studies of Gravity Wave Seasonal Variations over Hawaii (22 N, 160 W), *J. Geophys. Res., D109*, in press, 2003a.

Gavrilov N. M., D. M. Riggin, and D. C. Fritts. Interannual variations of the mean wind and gravity wave variances in the middle atmosphere over Hawaii, *J. Atmos. Solar-Terr. Phys., 65*, in press, 2003b.

Gavrilov, N. M., N. V. Karpova , and Ch. Jacobi. Morphology of atmospheric refraction index variations at different altitudes from GPS/MET satellite observations, *J. Atmos. Solar-Terr. Phys., 65*, in press, 2003c.

Gavrilov, N. M., A. I. Pogoreltsev, and Ch. Jacobi, Numerical modeling of influence of inhomogeneous gravity waves on general circulation of the middle atmosphere, *Atmos. Oceanic Phys., Izvestia of Russian Acad. Sci., 39*, in press, 2003d.

Nastrom, G. D., Hansen, A. R., Tsuda, T., Nishida, M., Ware, R., A comparison of gravity wave energy observed by VHF radar and GPS/MET over central North America, *J. Geophys. Res., 105*, 4685-4687, 2000.

Tsuda, T., Nishida, M., Rocken, C., Ware, R. H., A global morphology of gravity wave activity in the stratosphere revealed by the GPS occultation data (GPS/MET), *J. Geophys. Res., 105*, 7257-7274, 2000.

STUDIES ON ATMOSPHERIC GRAVITY WAVE ACTIVITY IN THE TROPOSPHERE AND LOWER STRATOSPHERE OVER A TROPICAL STATION AT GADANKI

D. Narayana Rao[1] , I.V. Subba Reddy[2], A. Narendra Babu[2], M. Venkat Ratnam[3] and S. Vijaya Bhaskara Rao[2]

[1]National MST Radar Facility, P.B. No.: 123, Tirupati – 517 502, India
[2]Department of Physics, Sri Venkateswara University, Tirupati - 517 502, India
[3]Institute for Meteorology, University of Leipzig, Leipzig D-04103, Germany

Email: isubbareddy@rediffmail.com,profdnrao2001@yahoo.com, drsvbr@redffmail.com

Abstract

Atmospheric Gravity waves plays a significant role in controlling middle and upper atmospheric dynamics. Till date, frontal systems, convection, wind shear and topography have been thought to be the sources of gravity wave activity in the troposphere. All these studies pointed out that, it is very essential to understand generation, propagation and climatology of gravity waves. In this regard, several campaigns using Indian MST Radar have been carried out to explore the gravity wave activity in the troposphere and the lower stratosphere. The signatures of the gravity waves in the wind fields have been studied in the troposphere and lower stratosphere. The wave activity during pre monsoon, monsoon, post-monsoon and winter seasons have been studied. The large wind fluctuations are more prominent above 10 km during pre monsoon and monsoon seasons. The dominant wave periods and their height profiles of amplitudes are studied. The vertical wavelength and the propagation direction of gravity waves are determined using hodograph analysis and the same are presented.

Introduction

The recent theoretical studies on gravity waves have shown the importance of excitation and vertical propagation of gravity waves and their forcing on the large scale circulation and structure of lower and middle atmosphere. In spite of its importance and significant advancements, very few studies are available in the tropical latitudes. VHF Radar is a promising tool to study such events and their dynamical effects because of its high temporal and spatial resolution capabilities. There have been few important observations on the generation of gravity waves due to convection process using VHF Radar [Fritts and Nastrom, 1992].

Most of the sources for the generation of the gravity waves lie in the troposphere [Fritts and Nastrom, 1992]. Some of the sources have been identified as topography [Nastrom and Fritts, 1992], convective and frontal activity [Fritts and Nastrom, 1992] and wind shear [Fritts, 1984]. Tsuda et al., [1994] also determined that in the equatorial region, gravity wave generation was typically associated with deep convection. Dhaka et al., [2001], [2002] showed the gravity waves activities associated with convection over a tropical region by using Indian MST Radar. The generation of gravity waves has also been attributed to various instability mechanisms occurring in the tropospheric region. Kelvin-Helmholtz instability is one such kind. These unstable wind shears are common sources of vertically propagating gravity waves in the atmosphere. Jet streams are identified as a source of gravity wave generation [Fritts and Luo, 1992]. These waves have typically wave periods of a few tens of minutes with a horizontal wavelength of a few tens to a few hundreds of kilometers. Near the jet stream maximum wind shears are very high providing conditions favoring the occurrences of shear instability and generation of gravity waves. Using radiosonde observations Tsuda et al., [1994] showed that

gravity waves were mostly generated in the middle troposphere and that waves which reached stratosphere were propagating upward.

Data Base

In the present study the VHF Radar at Gadanki (13.48º N, 79.18º E), a tropical station is used to study the gravity wave activity in four typical months representing different seasons namely Pre Monsoon (March - May), Monsoon (June - September), Post Monsoon (October - November) and Winter (December-February) seasons. The observations were taken during 09-12 April 2001(Pre Monsoon), 19-22 July 1999, 16-19 July 2001 (Monsoon), 16-19 October 2000, 26-29 November 2001 (Post Monsoon), 22-25 January 2002 (Winter). Data is collected for three days in each season at 1000 -1600 LT, 2000 – 2030 LT, 0030 – 0100 LT, and 0500 – 0530 LT on each day. The Radar antenna beam was pointed towards 6 beam directions viz., East, West, North, South inclined at an angle of 10º from the Zenith and along two Vertical beams, one in E-W polarization and the other in the North-South polarization. For all the six beam directions, mean radial velocities observed in 3.6 min interval provided the original data. The received echo signals were sampled at height resolution of 150 m during 19-22 July 1999, 16-19 July 2001 and 22-25 January 2002 and 300 m height resolution during 16-19 October 2000 and 09-12 April 2001.

Results and Discussions

Figure 1 shows the background wind information in different seasons on a typical day. In pre monsoon season zonal winds are westward from 2 km to 6 km, eastward from 6-15 km and again westward above 14 km. During Monsoon season because of Jet streams the Zonal winds are maximum ~ -40 m/s around 17 km and these winds are easterlies above 9 km. During post monsoon season the zonal winds are almost westward with less magnitude compared to other seasons. In winter season the zonal winds are westward. In pre monsoon season meridional winds are northward up to 16 km and above that these winds are southward. In Monsoon season up to 6 km southward and above 6 km northward. During Post monsoon and winter seasons meridional winds are towards northward direction. In all the seasons vertical velocities are small with upward and downward oscillations.

Figure 2 represents the time series plot of Zonal velocity in different seasons for one typical day in the troposphere and lower stratosphere during the six-hour period of observation starting at 1000 hrs LT. Above 10 km the wind disturbances are more prominent and while going upward the magnitude of the disturbances are more, this will imply wave motions that are vertically propagating and it is evident from the figure that, wave like structure exists in the time series with a clear phase variation and different characteristic periods and also it is clear that the source mechanisms are originating in the lower atmosphere. In order to calculate the frequency spectra of gravity waves the zonal velocities were taken and they were subjected to the FFT analysis. Figure3 shows frequency spectra for zonal velocity on 18th July 2001 during 1000-1600 hrs observations. From this observations 5 harmonic components were determined and the corresponding time periods are 2 Hr 20 min, 55-46 min, 20-30 min, 20-15 min and 8 min. The maximum amplitude of these waves is 3 m/s. According to Tsuda et al., 1994, the periods ranging from 5 minutes to 2 hours are mainly due to the large wind shears, which are mainly observed during jet streams. The observed periods near the jet streams in the present study (around 16 –17 km) lie within the periods as reported by Tsuda et al., 1994. Previous studies revealed that gravity waves of such wave periods exist over this Radar site [Nagpal et al., 1994; Dutta et al., 1999]. During pre monsoon and monsoon season the wave activity is more dominant.

Figure 4 represents vertical wavelength and propagation direction of gravity waves are obtained using Hodograph analysis. On 18 Jul 2001 Zonal velocity has been taken on X –axis and Meridional velocity has been taken on Y-axis for hodograph analysis from 10.2 -20.1 km during

1100-1200 hours. From this plot 6.3 km vertical wavelength of waves are dominant with clockwise direction. If the rotation of the waves is in clockwise direction it represents that the waves are propagated upward. If it is anticlockwise direction, it represents that the waves are propagated downward. So this plot clearly shows the upward propagating waves means the source region is in the lower atmosphere. The downward zonal momentum flux shows higher values on 18th July 2001. Meridional momentum flux is southward from 7-13.5 km and northward from 13.5-17 km. Zonal and meridional variances are increasing with increasing height and reaching maximum values at higher heights.

Conclusion

The seasonal variation of gravity wave activity in the troposphere and lower stratosphere based on wind velocity observations made with the Indian MST Radar for about 3 days in a each season, continuously for six hours duration April 2001-2002 January have been analyzed. By taking this data we have examined the gravity wave activity in the troposphere and lower Stratosphere. Zonal, Meridional and vertical velocity fields exhibited motions with periods ranging from a few minutes to hours with propagating character.

Acknowledgements

The authors are thankful to the UGC-SVU Center for MST Radar Applications, S.V. University, Tirupati and National MST Radar Facility (NMRF), Gadanki for providing necessary facilities to carry out this work. One of the author s I.V. Subba Reddy is thankful to the Advanced Centre for Atmospheric Sciences, Department of Space, Govt. of India and also to the Council of Scientific and Industrial Research (CSIR) for providing Junior Research Fellowship and Senior Research Fellowship respectively.

References

Dutta G, B.Bapiraju, P.Balasubramanyam, H.Aleem Basha, VHF Radar observations of gravity waves at a low latitude, Ann. Geophysicae., 17, 1012-1019. 1999

Dhaka, S. K, P.K.Devarajan, Y.Shibagaki, R.K.Choudhary, S.Fukao, Indian MST Radar observations of gravity wave activities associated with tropical convection, J. Atmos. Solar-Terr. Phy., 63, 1631-1642, 2001.

Dhaka, S. K, R. K.Choudhary, S. Malik, Y.Shibagaki, M. D. Yamanaka, S. Fukao, Observable signatures of a convectively generated wave field over the tropics using Indian MST radar at Gadanki (13.48º N, 79.18º E), Geophys. Res. Lett., Vol. 29, No.18, 2002.

Fritts, D.C., M.A. Geller, B.B.Balsley, M.L.Chanin, I.Hirota, J.R.Holton, S. Kato, R.S. Lindzen, M.R.Schoebert, R.A.Vincent and R.F.Woodman, Research Status and recommendations from the Alaska Workshop on gravity waves and turbulence in the middle atmosphere, Bull. Am. Meteorol. Soc., 65, 149-159, 1984.

Fritts, D. C., and Z.Luo. Gravity wave excitation by geostrophic adjustment of the jet stream. Part I: Two-dimensional; forcing, J. Atmos. Sci., 49, 861-697, 1992.

Fritts, D. C., and G. D. Nastrom, Sources of mesoscale variability of gravity waves, II, Frontal, Convective and Jet stream excitation, J. Atmos. Sci., 49, 111-127, 1992

Nagpal, O.P., D. Praveen Kumar and S.K. Dhaka., Characteristics of tropospheric gravity waves by the Indian MST Radar: ST mode operation, Indian J. of Radio and Space Physics, 23, 6-11, 1994.

Nastrom, G.D., and D.C.Fritts, Sources of mesoscale variability of gravity waves, I: Topographic excitation, J. Atmos. Sci., 49, 101-110, 1992.

Tsuda, T., Y.Murayama, H.Wiryosumarto, S.B.Harijiono, and S. Kato, Radiosonde observations of equatorial atmosphere dynamics over Indonesia, 2, Characteristics of gravity waves, J. Geophys. Res., 99, 10,507-10,516, 1994

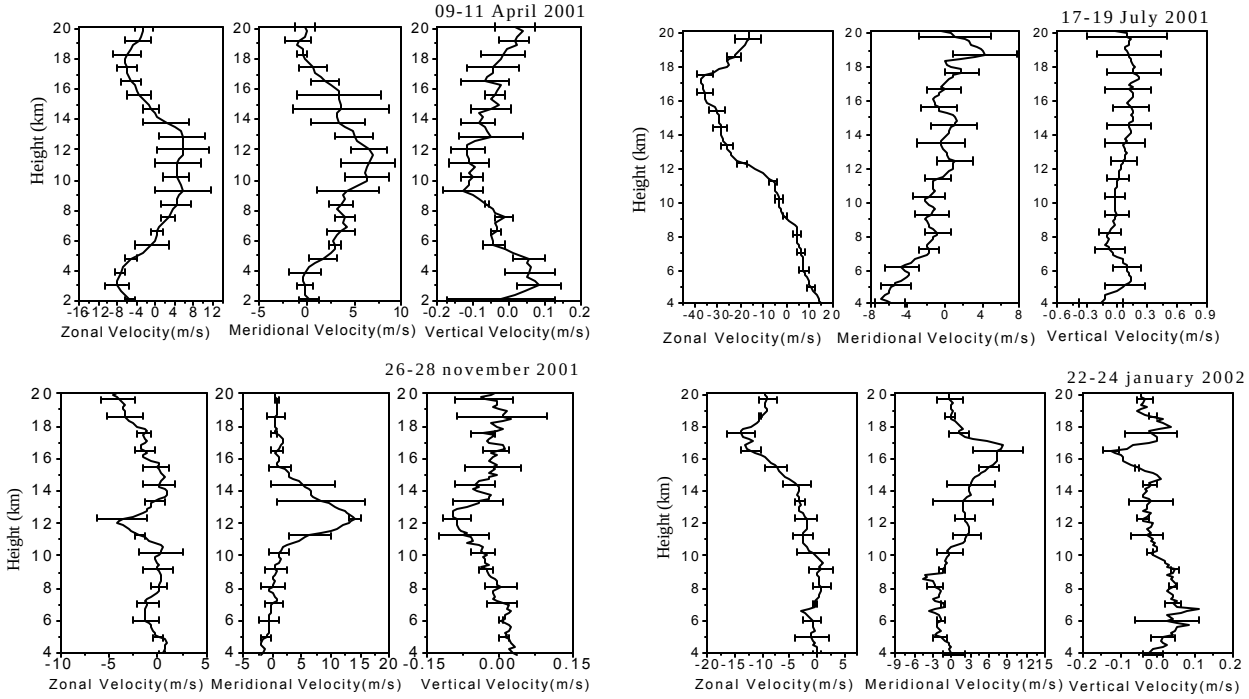

Figure 1. Mean vertical profiles of zonal, meridional and vertical velocities during (a)09-11 April 2001, (b)17-19 July 2001, (c)16-18 October 2001, (d)22-24 January 2002. Average for the entire 03 days time period of observation from 1000-1600 hours(LT) in each day has been taken.

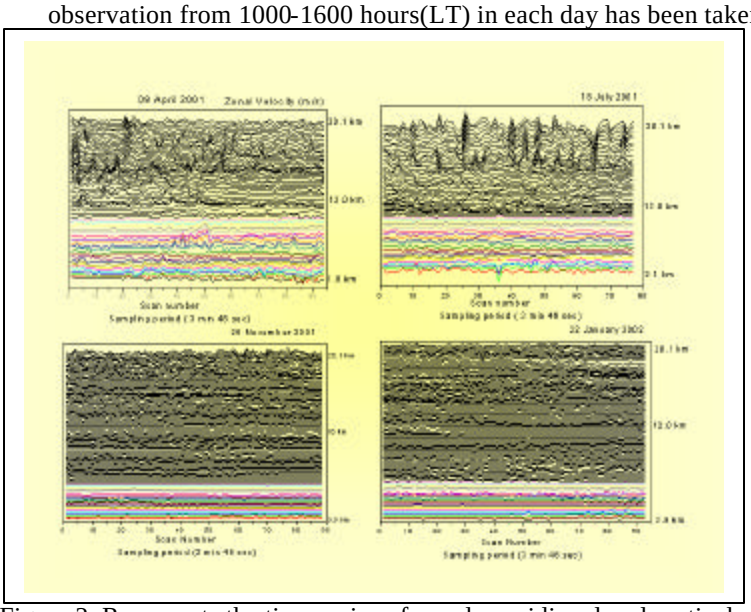

Figure 2. Represents the time series of zonal, meridional and vertical wind components during 06 hour period of observation on a typical day in different seasons starting at 1000-1600 LT (local time).

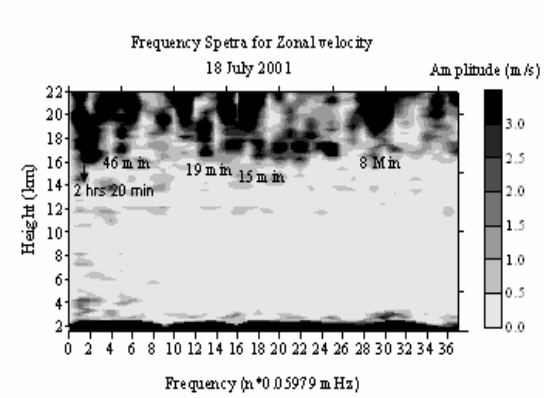

Figure 3. Frequency spectra for zonal velocity on typical day during 18th July 2001

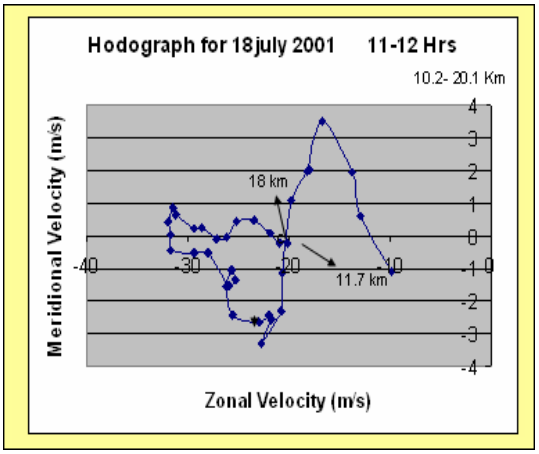

Figure 4. Hodograph for 18th July 2001 from 10.2 -20.1 km at 11-12 hours.

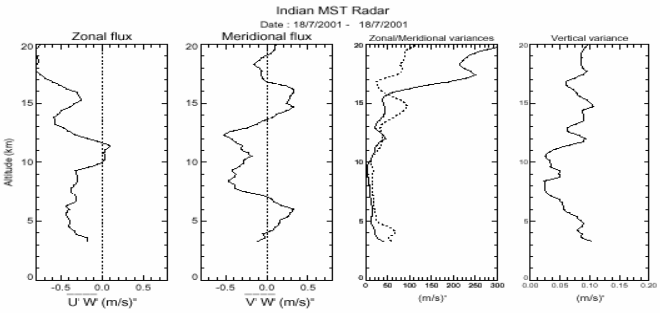

Figure 5. Momentum flux and variance of wind fluctuations determined from the MST radar data during 1000-1600 LT from 18th July 2001. For this total 06 hours of observations were averaged. Dotted line represents meridional variance and solid line represents zonal variance.

STUDIES ON WINDS AND MOMENTUM FLUXES USING UHF RADAR OBSERVATIONS OVER GADANKI (13.5^0 N, 79.2^0 E)

D. Narayana Rao[1] , B. Vasantha[2] , N.V.P. Kiran Kumar[2] and I.V. Subba Reddy[2]
1. National MST Radar Facility, P.B. No.: 123, Tirupati – 517 502, India
2. Department of Physics, Sri Venkateswara University, Tirupati - 517 502, India
Email: profdnrao2001@yahoo.com

ABSTRACT

Wind information obtained from UHF radar observations at Gadanki (13.5^0 N, 79.2^0 E) are utilized for the present study. These studies are related to ten clear air echo days in each month for the observation period of one year i.e. from April 1999 to March 2000. Diurnal, monthly and seasonal variations of horizontal winds and momentum fluxes are studied. Zonal winds are found to be westward in summer, post monsoon and winter seasons, eastward in monsoon season. Meridional winds are found to be northward in summer and southward in post monsoon and monsoon seasons. Zonal and meridional momentum fluxes show upward around noon time in summer and downward in winter seasons.

1. Introduction

These Doppler radar observations have provided detailed three-dimensional wind measurements which have enabled large advancement in the understanding of convective storms, Planetary Boundary Layer (PBL), frontal surfaces and other meteorological phenomena (Kropfli and Hildebrand, 1980).

Several inter comparisons were made between wind profiles of wind profiler and Doppler radar (Weber and Wuertz,1990; Luce et al., 2001; Krishna Reddy et al., 2000) found good agreement. Radar derived three dimensional wind measurements were made in the optically clear planetary boundary layer by Kropfli and Hildebrand, (1980) and concluded that wind fluctuations are in good agreement with anemometric data. Kallistratova et al., (2001) have compared turbulent momentum fluxes derived from Sodar and Sonic anemometer measurements and determined turbulent kinetic energy (TKE) from measurements of three wind components by Doppler radar, momentum flux from the density of turbulent kinetic energy. They showed a good comparison of the results. Peters and Kirtzel, (1994) have measured momentum flux in boundary layer and from radar measurements by Kropfli, (1986).

2 Data base

These studies are related to ten clear air echo days in each month for the observation period of one year. LAWP gives continuous measurement of wind over the entire diurnal cycle (24 hours). The available data in an hour is averaged to represent hourly data. So 24-hourly averages are available on all the days. Seasons are classified as summer (March, April and May), monsoon (June, July, August and September), post- monsoon (October, November and December) and winter (January and February). Diurnal variation of winds and momentum fluxes are represented choosing a typical day in each season. They are 19th April 1999 (summer), 11th July 1999 (Monsoon), 24th November 1999 (Post- monsoon) and 25th January 2000 (Winter). Results and discussion is presented in section 3. Diurnal variation of winds, momentum fluxes in different seasons are presented in section 3.1. Monthly variation of horizontal winds, momentum fluxes, are presented in section 3.2. Summary and results is presented in section 4.

3. Results and discussion

3.1 Diurnal variation of horizontal winds

Figure 1 (a) shows height- time contour of single day observations of zonal winds in different seasons in the altitude region of 0.6 km to 3.3 km. During summer, zonal winds are eastward (westerlies) up to an altitude of 1.0 km and prevail up to 1000 hours LT and then changed to westward (easterlies) over the entire altitude region and then increasing with height. During monsoon season below 2 km altitude, eastward winds of ~ 10 ms^{-1} are found starting from 0100 hours LT and grow towards the day until 1300 hours LT (noon-time). Strong westward winds are found from a lower altitude starting from 0000 hours LT to 1200 hours LT of that day, from then onwards there is a sudden decrease in the magnitude of wind to a value of ~5ms^{-1}. The dominant winds are found to be westward during summer, post- monsoon and winter, whereas eastward in monsoon season.

3.2 Diurnal variation of momentum flux

Vertical flux of horizontal momentum is calculated using the method given by Vincent and Reid, (1983). Figure 2(a) shows diurnal variation of vertical flux of zonal momentum observed on typical days in different seasons. During summer season, downward flux of westward momentum is showing a maximum negative value of ~ 7 m^2s^{-2} at around 1000 hours LT and at 1100 hours LT at an altitude of 0.6 km and 1.2 km. During monsoon season, at an altitude of 0.9 km, a maximum value of downward flux of westward momentum of ~ 22 m^2s^{-2} is observed at around 1200 hours LT and then decreasing. During post-monsoon, downward flux of westward momentum of 5 m^2s^{-2} at around 0300 hours LT and 2000 hours LT at an altitude of 0.6 km and 1.5 km is observed. During winter season, the downward flux of westward momentum of 6 m^2s^{-2} around 1400 hours LT at an altitude of 0.6 km is observed.

Figure 2(b) shows vertical fluxes of meridional momentum in different seasons at four altitude regions. During summer season, vertical fluxes are low at early hours of the day and then increase negatively with a maximum downward flux of southward momentum of 10 m^2 s^{-2} at around 1100 hours LT at an altitude region of 0.6 km and then decreasing towards the night time. Above this altitude a slightly low value of 9m^2 s^{-2} is observed around 1200 hours LT at an altitude of 0.9 km. During monsoon season, vertical fluxes are increasing up to 0.9 km with a maximum downward flux of southward moment um of 13m^2s^{-2} at around 1800 hours LT. During the post- monsoon season fluxes are very much low, slight downward flux of southward momentum of ~1.5 m^2s^{-2} is observed around 1200 hours LT at an altitude of 0.9 km. During winter season, at 0.6 km altitude region, a variation of 7 m^2s^{-2} to 9 m^2s^{-2} in between local time of 0200 hours LT to 1300 hours LT is observed.

3.3 Monthly variation of horizontal winds

Figures 3 (a) and 3 (b) show height-time contour diagram of monthly averaged clear air days of zonal and meridional winds for a period of one year (April 1999 to March 2000). From the figure it is clear that zonal winds are eastward with a maximum of ~10 ms^{-1} in the months of May to September. After September there is a change in the direction from eastward to westward with a maximum of 5 ms^{-1} in the months of October to January. From figure 3 (b) meridional winds are northward up to an altitude of 1.5 km in the month of June. Above this altitude there is a slight change in the direction from northward to southward. Southward winds are observed over the entire altitude region from the months of July to January with a maximum of 6 ms^{-1} in the months of post-monsoon season.

3.4 Monthly variation of momentum flux

Figures 4 (a) and 4 (b) show monthly variation of vertical flux of zonal and meridional momentum averaged over ten days from the afternoon hours (1200-1400LT) in a month for a period of one year. From the month of April, flux is decreasing with time and show maximum downward flux of westward momentum of value ~2.0 m^2s^{-2} at an altitude of 0.6 km in the month of July. From July it increases to August with altitude. From the month of August it increases with altitude, but in the downward direction. Maximum downward flux of westward momentum is observed in the month of July and upward flux of eastward momentum of $0.5m^2s^{-2}$ in the month of April. Figure 4(b) shows maximum downward flux of southward momentum of ~1.0 m^2s^{-2} in the months of July, August and November.

4. Summary and conclusions

Diurnal and seasonal variation of horizontal winds, momentum fluxes are studied in different seasons using typical clear air days. Seasonal variations are studied using ten day clear air day averages in each month for a period of one year. Zonal winds are found to be westward in summer, post- monsoon and winter and eastward in monsoon season. Meridional winds are found to be northward in summer and southward in post- monsoon and winter seasons. Diurnal variation of vertical flux of zonal and meridional momentum indicates maximum downward fluxes in monsoon season. From the monthly mean values, zonal winds show eastward in pre- monsoon and monsoon seasons and westward in post-monsoon and winter seasons. Momentum fluxes around noon time indicate upward fluxes in summer and downward fluxes in winter seasons.

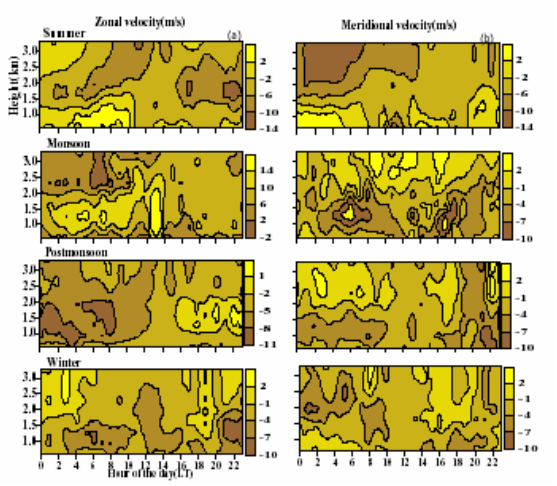

Figure 1. Diurnal variation of height time contour of a) zonal and b) meridional winds observed on typical days: 19mApril 1999 (Summer), 11July 1999 (monsoon) 24 November 1999 (postmonsoon)and 25 January 2000 (winter) in different seasons.

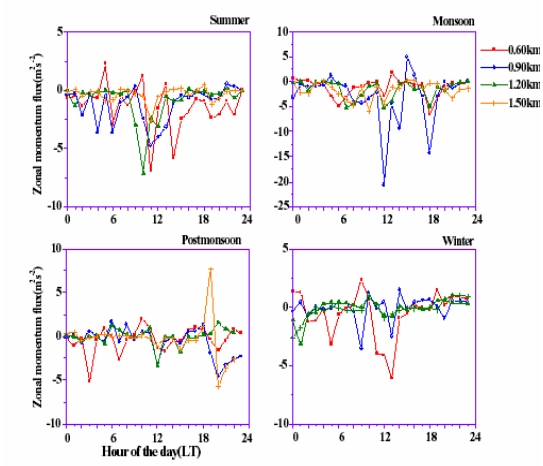

Figure 2(a) Diurnal variation of zonal momentum flux observed on typical days:19 April99 (summer) 11 July99(monsoon),24 November99(post-monsoon) and 25 January 2000(winter)in different seasons)

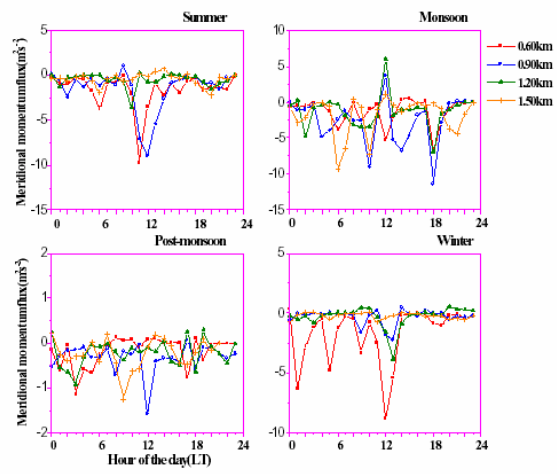

Figure 2 (b) Diurnal variation of meridional momentum flux observed on typical days:19 April99 (summer) 11 July99(monsoon),24 November99(post-monsoon) and 25 January 2000(winter)indifferent seasons)

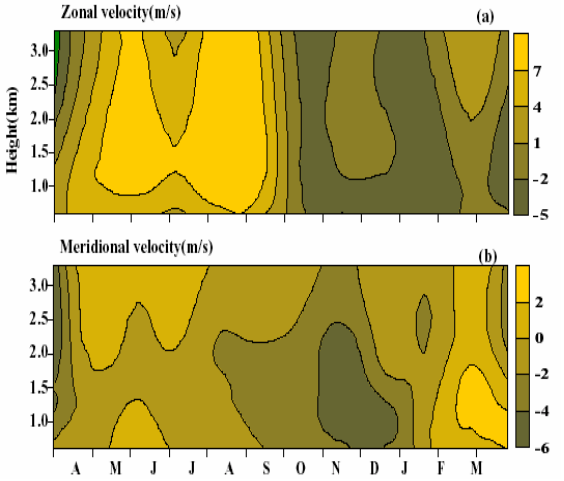

Figure 3. Monthly variation of a) zonal and b) meridional velocities from April 1999 to March 2000 in the altitude range of 0.6 -3.3 km.

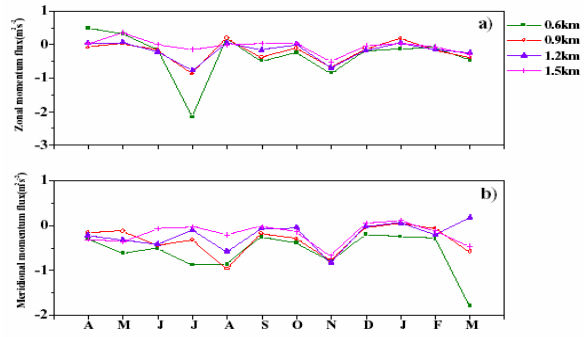

Figure 4. Monthly variation of a) zonal momentum flux and b)meridional momentum flux averaged over 1200-1400 LT of ten clear air days in a month of year (April 1999-March 2000)

DEEP PENETRATIVE CONVECTION AND GENERATION OF WAVE OSCILLATION OBSERVED WITH THE CHUNG-LI VHF RADAR

J. Röttger [2.1], M.L. Hsu[1], W.C. Tsai[1], C.J. Pan[1] and J. Wu[1]
[1] Institute of Space Science, National Central University, Chung-Li, Taiwan
[2] Max-Planck-Institut, 37191 Katlenburg-Lindau, Germany

During September and October 2001 three typhoons passed the island of Taiwan. The Chung-Li VHF radar was operated continuously during most of these events, such as in earlier times (Röttger et al., 1991). We will discuss the radar reflectivity structures of these three typhoons in the companion paper by Pan et al. (this issue), which differ significantly between these typhoons. We often find periodically recurring convection episodes in the meso-beta scale, which reach up to the middle and partially upper troposphere. Additionally the rainfall rate was measured and we compare this in the companion paper with the radar reflectivity and vertical velocity due to convection, measured with the VHF radar.

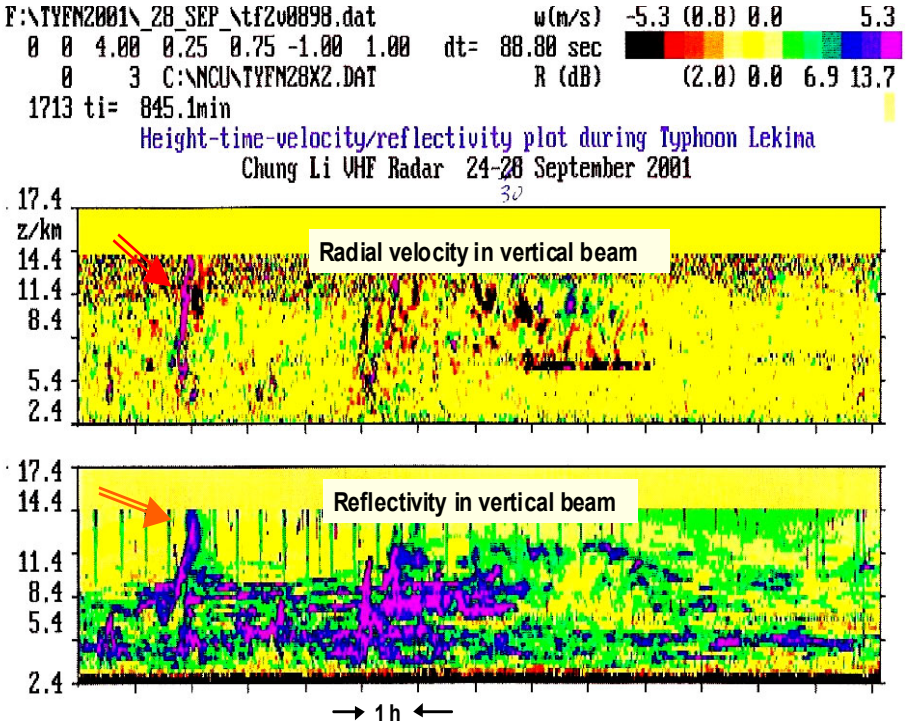

Fig. 1 Height-time-intensity plots of velocity and radar reflectivity (combination of 'clear-air' and precipitation (<6km) echoes) over a 14-h period. The vertical stripes in the reflectivity plot are caused by interference. The high-reaching echo, marked by the arrows, is evaluated in the text.

Here we concentrate on high reaching, deep-convection events. In the period 26-28 September 2001 the typhoon Lekima passed over the southern part of the island of Taiwan. Fig. 1 presents the radar reflectivity and the estimate of vertical velocity (from the radial velocity measured in the vertical beam) over the time period 07:00 to 21:10 LT on 28 September 2001. We have chosen this period, because it shows for the first time a very distinct funnels of radar reflectivity penetrating the usual upper observing height of about 10 km and reaching as high as 14 km. We

attribute this to a strong deep and very localized convection event. It is actually possible to trace this funnel back to its likely origin height around 6 km by inspecting the reflectivity plot. Within about 20 minutes it reached the altitude of 14 km. If this event would have occurred locally over the radar the convection funnel must have moved upward with a velocity of up to 4 m/s. The reflectivity plot shows that the updraft actually accelerated quickly in its lowest altitudes and then moved upward with fairly constant velocity.

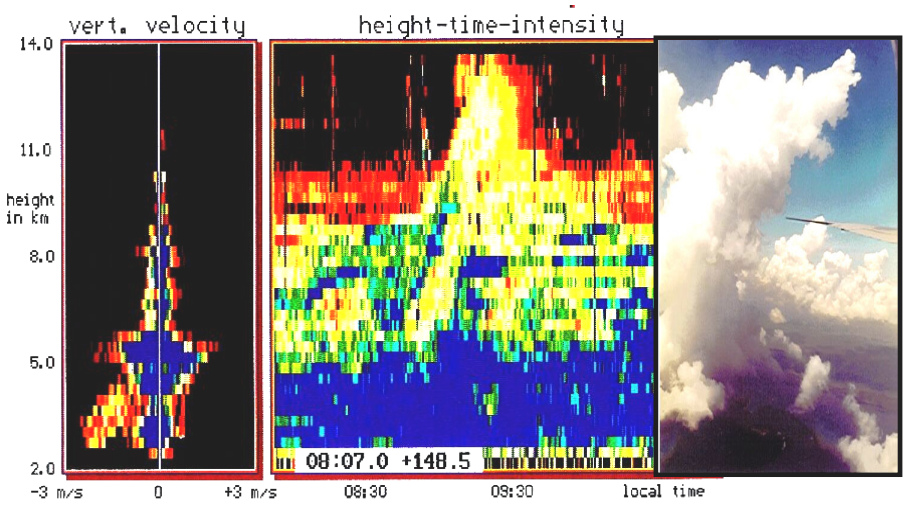

Fig. 2 The funnel event observed with the Chung-Li VHF Radar between 08:07 and 10:35 LT on 28 September 2001. Left-hand panel: spectral plot as function of height at the end of this event (the negative spectra parts below 4 km are due to precipitation; centre panel: radar reflectivity; right-hand panel: a photo of an equivalent deep convection event, taken from aircraft.

The altitudes around 6 km are about the height were precipitation is formed at about 08:30 LT. This can clearly be determined from the spectra (see example in the left-hand panel of Fig. 2). We can assume that the heat released hereby caused the convection to start. From the inspection of Doppler spectra we note that actually the precipitation echo formed and separated clearly from the air echo around these altitudes. This provides further prove that this strong convection event was initiated by heat release during the formation of precipitation. Heated and moist air result in an increase of radar reflectivity, which we observed (see figures).

Looking up the temperature profile, measured with radiosonde, we recognize that the region above about 9 km is getting close to becoming convectively unstable, which must have supported the convective process to grow, accelerate and move up to larger altitudes.

In Fig. 3 we have shown the height-time-intensity plots of reflectivity, vertical velocity and turbulent velocity. We again note the sudden increase in reflectivity above 6 km around 08:40. This is the birth of the convective cell, which then moved upward. quickly. The radial velocity is shown in the centre panel, which is a good estimate of the vertical velocity. Since its magnitude is fairly large we can neglect a significant leakage of a horizontal component. In the origin region of the funnel the vertical velocity is about +1 m/s (upward) and it increases within the funnel to more than +3 m/s. This is consistent with the observed motion of the reflectivity structure (upper panel in Fig. 3). It is well noticeable that around 09:18 at about 11 km the vertical velocity rapid-

ly changes direction with time within the funnel. We regard this as an overshoot of the deep convection into a stable region, which resulted in a following downdraft. This sudden downward velocity is in the same order of magnitude as the upward velocity. Such an event is known as penetrative convection and was observed to create gravity waves. We actually recognize a wave oscillation in this event. To clarify this, we have drawn the vertical velocity in the range gate at 10.8 km along a line indicating that gate. The maximum upward velocity is +3.5 m/s and the maximum downward velocity –2.5 m/s. We recognize that in this altitude three wave periods at about 12 minutes did occur. Following the strong up- and downdraft, two of these periodic oscillations with an amplitude of 0.5 m/s were superimposed on the mean recovery upward flow.

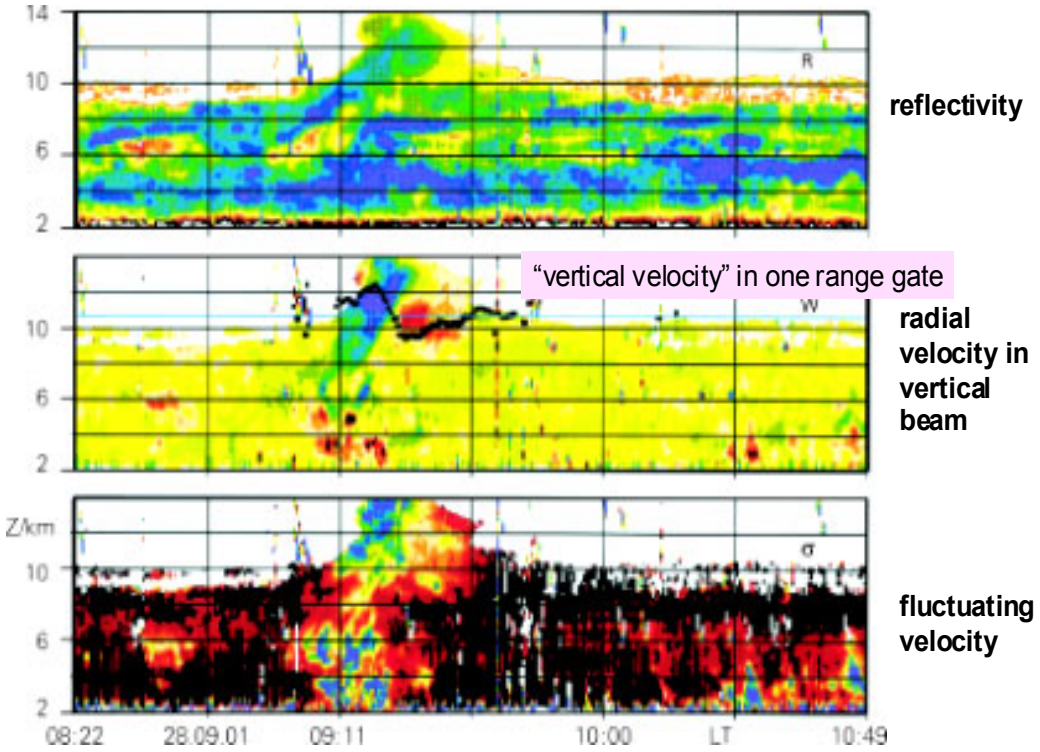

Fig. 3 Height-time-intensity plots of radar reflectivity, radial velocity in vertical beam, and fluctuating/turbulent velocity before, during, and after the deep convection event. The colour scales are yellow (0 dB) to blue (15 dB) for the reflectivity, blue (+3 m/s) to red (-3 m/s) for radial velocity, and black (< 0.5 m/s) over red (1 m/s) to blue (>3 m/s) for the fluctuating/turbulent velocity. The black line in the centre panel shows the vertical velocity in the range gate 10.8 km (max. 3.5 m/s upward).

Fig. 4 shows the principle of penetrative convection. A funnel or pileus (i.e. a localized upward reaching convection cell, such as the one depicted in the photos of Fig. 2 and Fig. 4) of hot and moist air may reach a region of static stability (vertical increase in potential temperature) and, due to its high vertical velocity, penetrate this inversion layer a little until its temperature is equal to its environment. Then the upward motion is reduced and eventually reversed when the air has adiabatically cooled. This is the initialization of a wave propagating along the surface of constant potential temperature. The generated atmospheric gravity waves can also propagate upwards and transport energy and momentum into the middle and upper atmosphere.

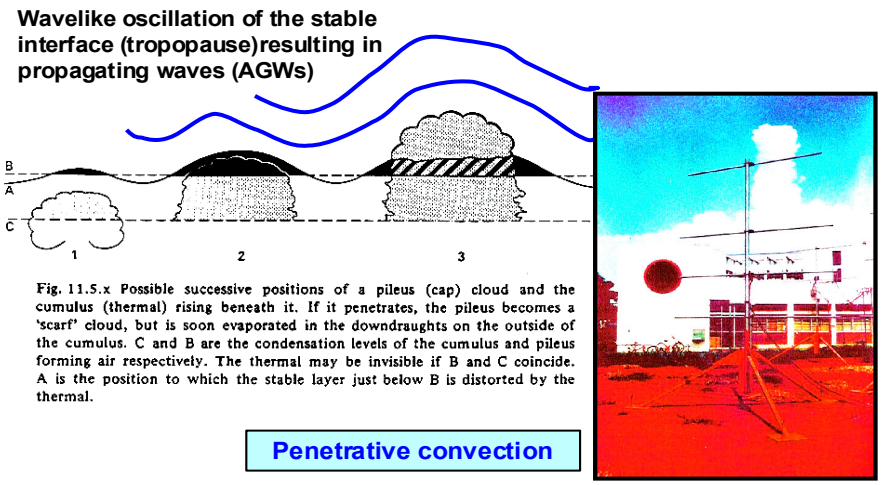

Fig. 4 Schematics of penetration of a pileus (funnel) of hot and moist air through an interface (region of high static stability). This penetration can cause atmospheric gravity waves. The right-hand photo shows such a funnel observed over the Chung-Li VHF Radar.

The upper panel of Fig. 3 shows the turbulent velocity, which was extremely strong at about 3 m/s (with short peaks at 5 m/s) during the updraft of the funnel and slowly decreased thereafter in the downdraft. Because these turbulent velocities are really large and the horizontal wind was small (≈ 10 m/s), we can in a first approach neglect the effect of beam-width broadening. We should also note that the apparently large turbulent velocities in the region below 6 km are due to spectrum widening by precipitation. This had not been eliminated in these analyses, which concentrates on the region above this level. The precipitation also can be noticed in the reflectivity increase in the upper panel, and in the downward velocity bursts in the

Conclusion

The Chung-Li VHF Radar showed its capabilities of long runs to study typhoon passages. For the first time a clear event of very deep convection was observed when the typhoon Lekima passed Taiwan end of September 2001. This penetrative convection event generated a clear gravity wave oscillation. Besides this presented event, several further high reaching convective updrafts were observed during this typhoon passage. We regard these observations as proof that a VHF radar is capable to properly study convection processes, which can create gravity waves.

Reference:

Röttger, J., C.J. Pan, C.H. Liu, and S.Y. Su, Wind field and reflectivity variations investigated with the Chung-Li VHF Radar during typhoon passage, Proc. Int'l. Conf. Mesoscale Meteor., Met. Soc. ROC and AMS, Taipei, 3-6 Dec. 1991, 737-379, 1991.

A BRIEF OVERVIEW OF GRAVITY WAVE BREAKING THEORY

Gary P. Klaassen

Dept. of Earth and Atmospheric Science, York University
4700 Keele St., Toronto ON, Canada M3J 1P3

1. Introduction.

Recent work (Sonmor and Klaassen 1997; Yau, Klaassen and Sonmor 2004) has demonstrated that the periodic temporal and spatial oscillations of internal gravity waves, together with their slantwise parcel motion, play significant roles in their stability properties. This paper briefly reviews this work, contrasting it with the traditional stability theory for parallel flows as applied to gravity waves. Points relevant for the interpretation of observations are highlighted.

2. A Brief History of Gravity Wave Stability Theory.

This paper, being restricted in length, will only provide an much-abbreviated overview of the development of our understanding of gravity-wave breaking. A more extensive review has been given recently by Fritts and Alexander (2003).

The stability of gravity waves was first investigated in the context of oceanographic applications. Phillips (1977) summarizes earlier weakly-nonlinear analyses, which demonstrated that pairs of weak (but finite amplitude) internal waves could interact to produce a third, subject to the resonance constraints

$$\mathbf{k}_1 + \mathbf{k}_2 = \mathbf{k}_3 \qquad \text{and} \qquad \omega_1 + \omega_2 = \omega_3, \tag{1}$$

on the wavevectors $\mathbf{k}_j$ and frequencies ω_j. Holloway (1980) subsequently argued that the observed oceanic gravity wave spectrum is an order of magnitude too large for weakly nonlinear theory to apply. The same conclusion has been generally accepted for the wave spectrum of the middle atmosphere: resonant instabilities are often considered to be insignificant.

A central question in determining the stability properties of any flow is the identification of the threshold amplitude for the onset of instability. One of the earliest attempts to determine such a threshold for gravity waves was made by Hodges (1967). He used an argument based on the Richardson number for horizontally stratified flows to show that gravity wave fields can locally overturn the stable background stratification when their amplitude exceeds a critical threshold A_c. Those regions where the Richardson number becomes negative would clearly be subject to convective instability. Shortly thereafter, Hines (1971) developed a generalized Richardson number criterion to demonstrate that horizontal gradients could, in principle, lead to slantwise instability at amplitudes far below that required to overturn the strong background stratification. A concern remained, however, as to whether the growth of slantwise static instability was sufficiently rapid to overcome the periodic reversal in horizontal gradients associated with basic wave motion (Hines 1988). Fritts and Rastogi (1985) also invoked a Richardson number argument to show that, for low-frequency inertio-gravity waves, the threshold amplitude for vertical dynamic (Kelvin-Helmholtz) instability, A_d, was lower than A_c. This led them to predict that low-frequency waves would break via shear-induced instability before they overturned. The majority of subsequent work, including the well-known gravity-wave drag scheme proposed by Lindzen (1981), has adopted the view that either vertical static or vertical dynamic instabilities represent the dominant mechanism for gravity wave break-

ing, and that any mechanisms operating at amplitudes below the minimum of (A_c, A_d) are negligible.

Fritts and Yuan (1989), Thorpe (1994) and Dunkerton (1997) provided a more rigorous (if still approximate) analysis of the problem by employing a form of the Taylor-Goldstein equation originally developed for analyzing the stability of steady, horizontal, parallel flows. This approach has two fundamental limitations for gravity waves. First, the wave fields are assumed to be "frozen" in time and, second, only the horizontal component of the wave velocity enters into the analysis. These two conditions are consistent with the properties of internal gravity waves possessing sufficiently low frequency. However, the first condition requires the rejection of any mode whose growth rate is not large compared to the basic wave frequency. The second limitation neglects any potential contribution from slantwise instability. Not surprisingly, this technique predicts finite threshold amplitudes for the onset of instability that are consistent with Richardson number arguments.

Klostermeyer (1991) employed a Floquet technique that overcomes the limitations of steady horizontal stability analyses. By transforming coordinates to a frame of reference moving with the oblique wave phase velocity, the method incorporates slantwise parcel oscillations into the analysis and yields exact results for the stability properties of internal waves of any frequency. For a gravity wave of frequency 0.31 times the Brunt-Vaisala frequency, Klostermeyer's calculations revealed three distinct modes of instability. Furthermore, the threshold amplitude for instability of this particular basic wave was zero: the three instabilities he found reduced to various resonant modes in the limit of small basic wave amplitude A. This prompted Klostermeyer to speculate that resonance might be the fundamental mechanism underlying all forms of gravity wave instability.

This earlier work prepared the way for Sonmor and Klaassen (1997) to present a comprehensive theory giving exact stability properties across the full frequency range of monochromatic non-rotating gravity-waves. The technique has recently been extended to rotating inertio-gravity waves by Yau, Klaassen and Sonmor (2004).

3. Unified Theory of Gravity Wave Stability.

In order to introduce notation necessary for interpreting stability results obtained by Sonmor and Klaassen (1997) and Yau, Klaassen and Sonmor (2004), consider the dispersion relation for gravity waves propagating in an incompressible rotating atmosphere:

$$\hat{\omega}^2 = f^2 \left(\frac{m^2}{k^2 + m^2} \right) + N^2 \left(\frac{k^2}{k^2 + m^2} \right) = f^2 \sin^2\theta + N^2 \cos^2\theta \qquad (2)$$

Here, N represents the Brunt-Vaisala frequency and f the Coriolis parameter. The intrinsic wave frequency, $\hat{\omega}$, lies in the range $f \leq \hat{\omega} \leq N$. The horizontal (k) and vertical (m) wavenumbers define the basic wave's propagation angle (θ) with respect to the horizontal, according to $k/m = \cot(\theta)$.

Fig. 1 illustrates the disturbance roll geometry predicted by Floquet stability theory for a monochromatic (rotating) internal gravity wave. For an angle $\gamma = 0$, the disturbance roll axes are aligned in the direction of the basic wave's minor-axis (y) velocity, and maintain the 2D symmetry of the basic wave. For any other value of γ, the rolls introduce 3D structure into the flow. In the case of $\gamma = \pi/2$, the rolls are aligned in the direction of the major-axis (ξ) velocity, an orientation that is referred to as "shear-aligned" in the non-rotating case.

If its fields are normalized by the length and time scales $K = (k^2 + m^2)^{-1/2}$ and N^{-1}, respectively, then the stability properties of a monochromatic gravity wave depend on

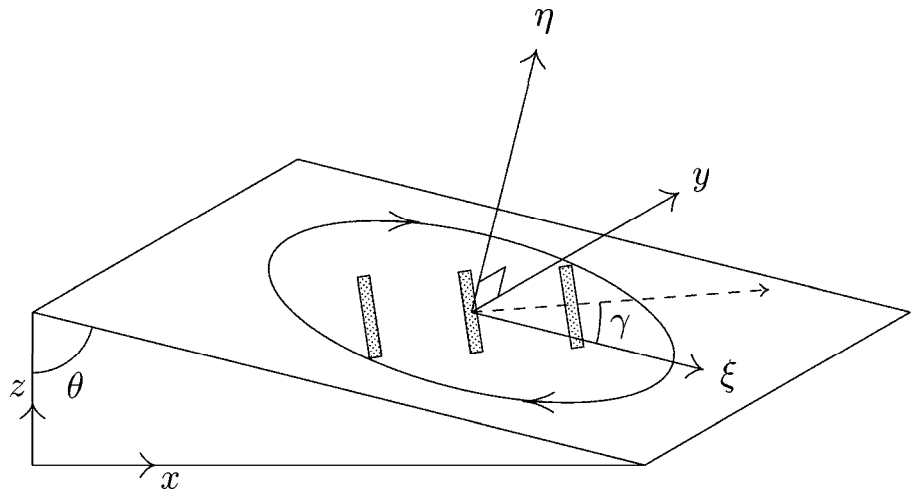

Figure 1: Oblique disturbance rolls (shaded) superimposed on the constant phase plane (ξ, y) of an inertio-gravity wave with wavevector $K\hat{\eta} = k\hat{\mathbf{x}} + m\hat{\mathbf{z}}$. The tip of the basic-wave velocity vector traces out the ellipse shown, with major axis in the ξ direction. In the limit $f \to 0$, the ellipse approaches the straight line characteristic of high-frequency waves. The disturbance spatial structure in the η direction is not shown as it varies from mode to mode. From Yau, Klaassen and Sonmor (2004).

- Intrinsic Frequency $\hat{\omega}$ (or Phase elevation angle θ)
- Richardson number Ri (or Amplitude A).

The absence of wavenumber dependence allowed Sonmor and Klaassen (1997) to present a stability regime diagram for nonrotating gravity waves in the form presented in Fig. 2. It is important to recognize that this regime diagram simply marks the region of basic wave parameters in which a given mode has the fastest growth. Normally, one would expect the disturbance with the largest growth rate to dominate lesser modes. The borders between regions, however, represent parameter values for which the growth rates of the neighbouring instabilities become comparable. Even in regions remote from the borders, the instabilities often remain highly competitive. It is therefore possible for the growing disturbances to be swayed in favour of a particular mode by anisotropies or other biases present in the noise field that induces disturbance growth. In particular, the history of the basic wave amplitude and intrinsic frequency (e.g. if they are changing with height) may also play a role in selecting modes. Finally it should be noted that this treatment is linear and only applies while the disturbances have sufficiently small amplitude; it also does not incorporate the mean background shear.

Fig. 2 shows that slantwise static (SSI) and slantwise dynamic (SDI) instabilities prevail below the overturning threshold amplitude A_c (dash-dot line). These disturbances have an essentially 2-dimensional structure, i.e. the preferred rolls are aligned along the basic gravity wave fronts. Such instabilities will first appear as modulations of the basic wave structure in the direction of the basic wave vector $(K\hat{\eta})$. SSI and SDI are closely related to the branch A and C resonant instabilities, and reduce to those modes in the limit $A \to 0$. Branch A resonance is also known as parametric subharmonic instability (PSI) and is characterized by small spatial scales.

Three-dimensional oblique and shear-aligned (SA) instabilities tend to prevail for most waves just above the overturning threshold. These modes also exist at suboverturning amplitudes, and reduce to higher-order resonances as $A \to 0$. They introduce 3D

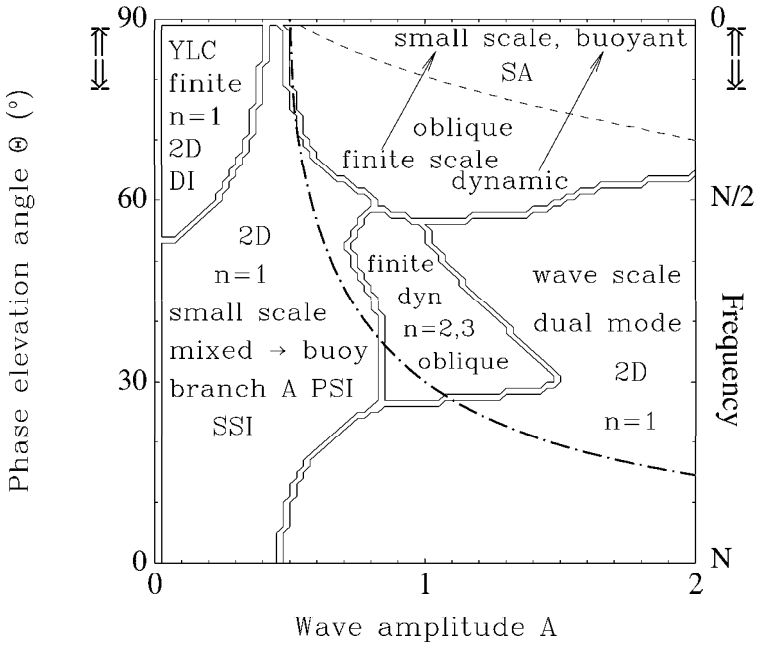

Figure 2: Stability regimes for non-rotating gravity waves in the amplitude-frequency plane, adapted from Sonmor and Klaassen (1997). The phase elevation angle $\theta = 90°$ corresponds to zero intrinsic frequency $\hat{\omega}$, while $\theta = 0°$ corresponds to $\hat{\omega} = N$. The heavy dashed line indicates the critical amplitude for overturning (zero Richardson number). The double arrows indicate the midfrequency range $N/40 < \hat{\omega} < N/5$, which is thought to make the major contribution to the deposition of momentum in the middle atmosphere.

structure into the wave field. It is worth noting that the shear-aligned mode would be expected to arise during critical-level approaches, in which the intrinsic wave frequency decreases.

In terms of its scale preference and its two-dimensional character, the dual mode resembles Kelvin-Helmholtz instability. However, the dual mode is far from being a purely dynamic instability, as it relies heavily on the extraction of basic-wave potential energy. Furthermore, it reduces to branch-A (slantwise static instability). As can be seen from the diagram, the dual mode is the fastest-growing mode only for waves of relatively large-amplitude very high-frequency. It may therefore be difficult to observe in isolation.

It should be noted that over half of Fig. 2 is occupied by very high frequency gravity waves. The midfrequency range, roughly $N/40 < \hat{\omega} < N/5$, is of particular importance, as it is primarily responsible for wave momentum deposition in the middle atmosphere. The sequence of fastest growing modes for the midfrequency range is, in order of increasing wave amplitude, branch C resonance/slantwise-dynamic, slantwise-static, oblique and shear-aligned. Thus the preferred disturbance roll alignment shifts from $\gamma = 0$ (2D symmetry) to $\gamma = \pi/2$ (3D shear-aligned) as the basic wave amplitude increases.

4. Effect of the Earth's Rotation.

Yau, Klaassen and Sonmor (2004) have considered the stability of inertio-gravity waves for $f/N = 0.01$, and found that the Coriolis force strongly affects instabilities of low-frequency waves, in particular those with $\theta \geq 85$. Sonmor and Klaassen (1997) found that overturned, non-rotating gravity waves in this frequency range are subject to oblique instabilities, with orientation shifting toward shear-alignment as the basic wave

frequency decreases. In the rotating case, the shift of disturbance roll-alignment toward major-axis shear gives way to a shift toward alignment with the minor-axis shear as $\hat{\omega}$ decreases. Yau et al. established that differences from the nonrotating case primarily arise due to the minor-axis velocity component of inertio-gravity waves, a component which increases as the wave frequency approaches the inertial limit f. At sufficiently low frequency, the disturbances become isotropic (no preferred orientation), in agreement with the approximate analyses of Dunkerton (1997).

5. Conclusion.

The picture revealed by Floquet stability theory of internal gravity waves is considerably more complex than one might gather from the Richardson number arguments of Hodges(1967) and Fritts and Rastogi (1985). Specifically, no threshold amplitude exists: all instabilities of large amplitude internal gravity waves reduce to resonant triads in the limit of small amplitude. As the basic wave amplitude increases, the triad resonances broaden to include non-wave components, and growth rates increase. In particular, as the overturning threshold is crossed and the potential energy stored in the background stratification becomes available, disturbances tend to gain considerable impetus. The results clearly show that gravity wave breaking depends in a fundamental way on the spatial and temporal oscillations of the basic wave, and reinforce Klostermeyer's conjecture that resonance is the unifying mechanism underlying all gravity wave instabilities.

6. References.

Dunkerton, T.J. Shear instability of internal inertio-gravity waves, *J. Atmos. Sci.* **54** 1628–1641, 1997.

Fritts, D.C. and Alexander, M.J. Gravity wave dynamics and effects in the middle atmosphere, *Rev. Geophys.* **41** 1003, doi:10.1029/2001RG000106, 2003.

Fritts, D.C. and Rastogi, P.K. Convective and dynamical instabilities due to gravity wave motions in the lower and middle atmosphere: Theory and observations, *Radio Sci.* **20** 1247–1277, 1985.

Fritts, D.C. and Yuan, L. Stability analysis of inertio-gravity wave structure in the middle atmosphere, *J. Atmos. Sci.* **46** 1738–1745, 1989.

Hines, C.O. Generalizations of the Richardson criterion for the onset of atmospheric turbulence, *Quart. J. Roy. Met. Soc.* **97** 429–439, 1971.

Hines, C.O. Generation of turbulence by atmospheric gravity waves, *J. Atmos. Sci.* **45** 1269–1278, 1988.

Hodges, R.R. Jr. Generation of Turbulence in the Upper Atmosphere by Internal Gravity Waves, *J. Geophys. Res.* **72**, 3455–3458, 1967.

Holloway, G. Oceanic internal waves are not weak waves, *J. Phys. Ocean.* **12** 293-296, 1980.

Klostermeyer, J. Two- and three-dimensional parametric instabilities in finite-amplitude internal gravity waves, *Geophys. Astrophys. Fluid Dyn.* **61** 1–25, 1991.

Lindzen, R.S. Turbulence and stress owing to gravity wave and tidal breakdown *J. Geophys. Res.* **86** 9707–9714, 1981.

Phillips, O.M., 1977: *The Dynamics of the Upper Ocean.* 2nd ed., Cambridge University Press, 336 pages.

Sonmor L.J. and Klaassen, G.P. Toward a unified theory of gravity-wave stability. *J. Atmos. Sci.* **54**, 2655–2680, 1997.

Thorpe, S.A. The stability of statically unstable layers, *J. Fluid Mech.* **260** 315–331, 1994.

Yau, K.-H., Klaassen, G.P. and Sonmor, L.J. Principal instabilities of large amplitude inertio-gravity waves. *Phys. Fluids*, in press, 2004.

TURBULENT DIFFUSIVITY INFERRED FROM MST RADAR MEASUREMENTS: A REVIEW

Wilson, Richard

Service d'Aéronomie/IPSL, Université P. et M. Curie, Paris, France

1 Introduction

The small scale turbulence in the atmosphere - and ocean - is the sink for mechanical energy, a process inducing irreversible transport of heat, mass and chemical species, as well as the process inducing drag on the large scale flow through the Reynolds stress. Evaluating the actual impact of small scale turbulence in the atmosphere - for instance the diffusive properties - is still a challenging question.

The main goal of this communication is to review and discuss several aspects of radar measurements in turbulence studies, as well as to stress some of the needs for future works.

2 Turbulence in a Stratified Medium

In a stratified medium, turbulent fluctuations of velocity induce fluctuations of temperature, concentration, refractive index... Due to gravity, vertical displacements δz are related to available potential energy (APE). When considering the energetics of stratified turbulence, two quantities have thus to be considered: turbulent Kinetic Energy (KE) and APE.

$$KE = \frac{1}{2}(\overline{u'^2} + \overline{v'^2} + \overline{w'^2}) \qquad \text{and} \qquad APE = \frac{1}{2}N^2\overline{\delta z'^2} = \frac{1}{2}\frac{g^2}{N^2}\frac{\overline{\theta'^2}}{\overline{\theta}} \tag{1}$$

where N is the Brunt-Väisälä frequency, and θ the potential temperature. Therefore, the dissipation rate of temperature variance ϵ_θ, due to thermal conductivity, is related to the the dissipation rate of APE, ϵ_p.

The equations describing the time evolution for turbulent KE and APE reads (Tennekes and Lumley, 1972):

$$\begin{aligned} \frac{d}{dt}KE &= P - B - \epsilon_k + \text{transport terms} \\ \frac{d}{dt}APE &= B - \epsilon_p + \text{transport terms} \end{aligned} \tag{2}$$

where

$$P = -\overline{u'w'}\frac{dU}{dz} \quad \text{and} \quad B = -\frac{g}{T}\overline{w'T'} = -\frac{g}{T}\Phi_T \tag{3}$$

P is the production term through Reynolds stress acting in a shear, the buoyancy flux B expresses a reversible conversion of KE into APE, B being simply related to the heat flux Φ_T. By assuming spatial homogeneity and stationarity, the transport terms and time-derivatives vanish:

$$\begin{aligned} \epsilon_k &= P - B \\ \epsilon_p &= B \end{aligned} \tag{4}$$

These two last relations are the ones widely used for most turbulence studies.

The inertial domain ranges from the viscous scale (10^{-2} – 10 m) to the outer scale L_m (10 – 1000 m). Typically, turbulent energy lies in the range 10^{-2} to 10 J/kg (KE and APE). The dissipation rates of fluctuations variances σ^2 (velocity, temperature ...) scale as $\sigma^2 N$.

Two estimates for the turbulent diffusivity have been proposed, either from the dissipation rate of temperature variance (related to the thermal conductivity), or from the KE dissipation rate, by assuming a given efficiency of mixing.

$$\Phi_T = \overline{w'T'} = K_\theta \frac{d\bar{\theta}}{dz} \quad \begin{cases} K_\theta = \dfrac{\epsilon_\theta}{d\theta/dz} \left(= \dfrac{\epsilon_p}{N^2}\right) & \text{(Osborn and Cox, 1972)} \\ K_\theta = \gamma \dfrac{\epsilon_k}{N^2} & \text{(Lilly et al., 1974)} \end{cases} \tag{5}$$

where the mixing efficiency γ reads:

$$\gamma = \frac{B}{P-B} = \frac{R_f}{1-R_f} = \frac{\epsilon_p}{\epsilon_k} \tag{6}$$

2.1 A turbulent diffusivity estimate ?

An estimation of the mixing properties of turbulence raises several difficulties. The turbulent diffusivity is likely related to the intensity of turbulence (KE or ϵ_k), but not only:

- The diffusivity will depend on that fraction of energy that is **not** dissipated into heat (i.e. ϵ_p rather than ϵ_k). Now, ϵ_k is the commonly evaluated turbulent quantity.
- The turbulence is intermittent in space and time. An effective diffusivity is likely dependent on the space-time distribution of turbulent events, and not only on the turbulence intensity.
- Some assumptions are likely questionable (local homogeneity, stationarity, constant mixing efficiency, ...)

3 Radar measurements of turbulence parameters

Several scattering mechanisms are important for atmospheric radars operating from the MF to the UHF bands: Rayleigh scattering from hydro-meteors, insects, etc... (UHF); Fresnel scattering, from thin refractive-index interfaces (operating frequencies under about 450 MHz) (e.g. Röttger and Liu, 1978; Gage and Green, 1978); and Bragg scattering induced by refractive-index fluctuations at $\lambda_r/2$ (MF to UHF) (Tatarskii, 1961). The Bragg scattering is the relevant process for studies of small scale turbulence in the atmosphere. Actually, VHF measurements have to be obtained from tilted beams, at least 15°from zenith (e.g. Tsuda et al., 1997). UHF measurements are useful if Rayleigh scattering is negligible, i.e. in the UTLS.

MST radar measurements consist of backscattered power, Doppler shift and Doppler width (zeroth, first and second moments of the Doppler spectrum). The radial wind velocity, as well as the velocity variance (provided that the non-fluctuating causes of broadening can be evaluated), are directly estimated, without any calibration. An important point is that these estimates are both range-and-reflectivity weighted averages. On the other hand, the estimation of reflectivity, and related C_n^2, requires a calibrated radar. Furthermore, the reflectivity estimate is a volume average, a uniform fluctuating field being implicitly assumed.

Two methods were proposed for the estimation of turbulence parameters from clear-air radar measurements. Both methods assume that the turbulence is inertial, isotropic, locally homogeneous and quasi-stationary.

- the power method: the two dissipation rates are inferred from the reflectivity, i.e. C_n^2.
- the variance method: the KE dissipation rate is inferred from the turbulent KE.

3.1 The "power" method

The received power is related to the atmospheric reflectivity η (m^2/m^3) [Probert-Jones, (1964), Doviak and Zrnic', (1984)] By assuming that the refractive index irregularities are caused by inertial turbulence (Tatarskii, 1961; Ottersten, 1969b).

$$\eta = 0.38 C_n^2/\lambda^{1/3} \quad \text{where} \quad C_n^2 = a^2 \frac{\epsilon_n}{\epsilon_k^{1/3}} \tag{7}$$

These assumptions were confirmed by direct reconstructions of radar reflectivity profiles from high resolution in-situ measurements (Luce et al., 1996).

Refractive index fluctuations δn are induced by vertical displacements δz, that is $\delta n = M\delta z$, where M is the gradient of generalised potential refractive index (Tatarskii, 1961; Ottersten, 1969b). C_n^2 can therefore be expressed as a function of one or the other dissipation rates:

$$C_n^2 = a^2 \left(\tfrac{M}{N}\right)^2 \frac{\epsilon_p}{\epsilon_k^{1/3}} \quad \begin{cases} C_n^2 = \gamma a^2 \left(\tfrac{M}{N}\right)^2 \epsilon_k^{2/3} \\ \\ C_n^2 = \gamma^{1/3} a^2 \left(\tfrac{M}{N}\right)^2 \epsilon_p^{2/3} \end{cases} \tag{8}$$

The radar estimate of C_n^2 is a volume average, i.e. $\langle C_n^2 \rangle_V = F_T C_n^2$, where F_T is the turbulent fraction within the radar sampling volume. Taking into account the turbulent fraction F_T (VanZandt et al, 1978, Gage et al, 1980):

$$\begin{aligned} \epsilon_k &= \frac{1}{a^3} \left(\frac{N}{M}\right)^3 \frac{1}{\gamma^{3/2}} \left(\frac{< C_n^2 >_R}{F_T}\right)^{3/2} \\ \\ \epsilon_p &= \frac{1}{a^3} \left(\frac{N}{M}\right)^3 \frac{1}{\gamma^{1/2}} \left(\frac{< C_n^2 >_R}{F_T}\right)^{3/2} \end{aligned} \tag{9}$$

3.2 The "spectral width" method

The turbulent velocities induce a spectral broadening of the backscattered echo, (e.g. Frisch and Clifford, 1974; Sato and Woodman, 1982; Hocking, 1983, 1986; Nastrom and Eaton, 1997). Other non-turbulent processes may also contribute to the observed spectral width: (1) beam and shear broadening and (2) wave and 2D turbulence broadening, The causes of spectral broadening being *a priori* independent one from the other:

$$\Delta f^2 = \Delta f_T^2 + \Delta f_{(B+S)}^2 + + \Delta f_W^2 \tag{10}$$

where Δf (Hz) is the half-power half width of the power spectrum, the subscripts indicating the various contributions.

• Beam and shear broadening can be evaluated knowing the beam geometry and the mean wind profile (e.g. Hocking, 1983, 1997). An alternative method for evaluating the (beam + shear) broadening by using two beam-widths was recently proposed by VanZandt et al. (2002).

• The wave contribution can be reduced by short integration time or can be subtracted by using a wave model (e.g. Nastrom and Eaton, 1997).

After corrections, the turbulent velocity variance is simply related to the Doppler width:

$$\overline{v'2} = \left(\frac{\lambda_r}{2}\right)^2 \Delta f_T^2/(2\ln 2) \tag{11}$$

Several others methods exist for estimating the turbulent velocity variance, mostly from MF radars (FCA, IDI).

3.2.1 From $\overline{v'^2}$ to ϵ_k

The question is now to relate the turbulent KE to dissipation rate ϵ_k. Two methods have been proposed (discussed by Hocking (1999)).

• If the radar volume is filled with homogeneous isotropic turbulence: (Frisch and Clifford, 1974; Gossard and Strauch, 1983).

$$\epsilon_k = \frac{1}{\delta}\left[\frac{\overline{v'^2}}{1.35\alpha[1-\beta^2/15]}\right]^{3/2} \tag{12}$$

$$\text{where} \quad \begin{cases} \delta = \sigma_b \quad ; \quad \beta^2 \approx 1-(\sigma_r/\sigma_b)^2 & \text{if} \quad \sigma_r < \sigma_b \\ \delta = \sigma_r \quad ; \quad \beta^2 \approx 4(1-(\sigma_b/\sigma_r)^2) & \text{if} \quad \sigma_b < \sigma_r \end{cases} \tag{13}$$

• If the outer scale of turbulence is much smaller than any scale of the sampled volume : the relations between v'^2 and dissipation rate depends on the outer scale L_m (Sato and Woodman, 1982; Hocking, 1983; Weinstock, 1978, 1981).

$$\epsilon_k \approx 3\left(\overline{v'^2}\right)^{3/2}/L_m \tag{14}$$

Several definition of such an outer scale exist. A commonly used expression, proposed by Weinstock (1978), relates the outer scale to the buoyancy scale L_B: $L_m \approx 1.5L_B \approx 3\pi\left(\epsilon_k/N^3\right)^{1/2}$ The relationship between turbulent KE and dissipation rate reads:

$$\epsilon_k \approx 0.5\overline{v'^2}N \tag{15}$$

• It should be noticed that the hypothesis of a constant ratio L_m/L_B has been questioned by Ivey and Imberger (1991); Weinstock (1992); Smyth and Moum (2000). For instance, Weinstock (1992) suggests that the ratio L_m/L_B varies as a function of Ri: $L_m/L_B \sim (2Ri)^{3/4}$.

3.3 Local Mixing

The heat (or mass) flux can be inferred from the dissipation rates, by assuming homogeneous and steady state turbulence.

$$K_\theta^{\text{local}} = \gamma\frac{\epsilon_k}{N^2} \qquad \text{and} \qquad K_\theta^{\text{local}} = \frac{\epsilon_p}{N^2} \tag{16}$$

As the dissipations rates, these diffusivity estimates are **local quantities**, i.e. within the turbulent patches (or weighted averages of local quantities).

4 Unknown parameters

In order to infer turbulence parameters from radar measurements, additional terms have to be evaluated, M, N, F_T and γ.

The Brunt-Väisälä frequency N, and the gradient of generalised potential index M, are usually evaluated from in-situ routine measurements (non co-located). Various evidences however, suggest that such in-situ estimates of gradients is likely dubious (e.g. Dalaudier et al., 2001) due to the large space and time variability of such gradients. Climatological temperature and pressure can be used if humidity is negligible (e.g. Gage et al., 1980). Co-located measurements of temperature from RASS or lidar, sometimes possible, are anyway preferable.

4.1 The mixing efficiency γ

The mixing efficiency appears when expressing the dissipation rate, ϵ_k, as a function of a quantity related to the turbulent APE, C_n^2 (eq. 8) or heat flux (i.e. K_θ, eq. 5).

• A "canonical" $R_f = 0.25$ gives $\gamma = 1/3$ (e.g. Lilly et al., 1974, based on Thorpe (1973) experiments).

• Numerous evaluations from measurements in the ocean and lakes, or from laboratories experiments, usually from the ratio ϵ_p/ϵ_k, (e.g. Rohr et al., 1984; Imberger and Ivey, 1991; Ruddick et al., 1997; St Laurent and Schmitt, 1999). or DNS as well (Itsweire et al., 1993) indicate $0 \leq \gamma \leq 0.2$

• In situ or radar estimations for the stratosphere give $0.06 \leq \gamma \leq 0.3$ (Alisse and Sidi, 2000; Dole et al., 2001).

• Various expressions for γ can be found in the literature, for instance by writing $R_f = Ri/P_r^T$ (Ri being the gradient Richardson number, P_r^T the turbulent Prandl number), γ reads:

$$\gamma = \frac{1}{P_r^T} \frac{Ri}{P_r^T - Ri} \tag{17}$$

• Several authors suggested however that γ should not be treated as a constant (Weinstock, 1992; Hocking and Mu, 1997; Gossard et al., 1998; Smyth et al., 2001).

4.2 The turbulent fraction

An estimate of the turbulent fraction, F_T, appears necessary when expressing the local C_n^2 from the volume-averaged reflectivity (eq. 9). As will be further discussed, F_T is also a fundamental quantity when expressing an effective diffusivity from local estimates.

• In-situ measurements in the UTLS indicate $0.02 \leq F_T \leq 0.05$ (Lilly et al., 1974)

• Radar measurements in the lower stratosphere show $0.05 \leq F_T \leq 0.2$ (Dole et al., 2001).

• A parameterisation based on a statistical model for the wind shear (VanZandt et al., 1978) gives $0.03 \leq F_T \leq 0.1$.

• A simplified version of this parameterisation suggests $F_T^{1/3} N^2 \sim$ Const. (Gage et al., 1980).

5 Radar observations

5.1 Climatologies of turbulence diffusivity

Several climatologies of turbulence diffusivity inferred from radar measurements are published (Hocking, 1988; Fukao et al., 1994; Kurosaki et al., 1996; Nastrom and Eaton, 1997; Rao et al., 2001). All these climatologies are based on wind variance estimates. The median diffusivity estimates compare very well in the lower stratosphere, $K_\theta^{local} \sim 0.2 - 0.5$ m^{2}s^{-1}. Interesting differences where observed in the upper troposphere, the turbulent diffusivity being increasing with height in one case (Kurosaki et al., 1996), and decreasing for an other case (Nastrom and Eaton, 1997). The annual maximum in the UTLS is observed during winter over Shigaraki, during summer at the WSMR, and during the monsoon and post-monsoon months at Bangalore. In the mesosphere, Hocking (1988) does not observe any clear annual variation. Fukao et al. (1994) and Kurosaki et al. (1996) observe a semi-annual variability with solstice maxima. Rao et al. (2001) found a maximum of diffusivity around about 75 km, the annual maximum being observed during summer.

5.2 Frequency distributions

Several evidences, from radar or in-situ measurements, show that the distribution functions of dissipations rates - as well as the inferred diffusivity - are (approximately) log-normal (Nastrom and Eaton, 1997; Alisse and Sidi, 2000; Dole et al., 2001).

5.3 Persistent layers of enhanced reflectivity

Several authors have reported the existence of persistent layers of enhanced radar reflectivity in the lower stratosphere (Nastrom and Eaton, 2001; Luce et al., 2002). Intense turbulent events in the lower stratosphere were also described from in situ measurements (Pavelin et al., 2002; Luce et al., 2002). Such layers are likely associated with intense mixing ($K_\theta \sim 1$ m^{2}s^{-1} in the lower stratosphere). A climatological study (Nastrom and Eaton, 2001) indicates that these layers are present about $1-2$% of time. The impact on vertical transport has to be evaluated.

6 An effective diffusivity: Theoretical and semi-empirical approaches

The issue of the effective diffusivity of patchy turbulence was addressed by Garrett (1979); Dewan (1981); Woodman and Rastogi (1984); and Vaneste and Haynes (2000) among others.

6.1 Semi-empirical approaches

The question was first to know if intermittent turbulence can be considered as a diffusive process. The response is yes, but in the long-time limit. From a very simple numerical model Dewan (1981) shows that mixing resulting from random layers can be described formally as diffusion by comparing the results of numerical simulations of random mixing layers to the known analytical solutions for different cases (initial conditions):

$$K_\theta^{\text{eff}} = F_T \frac{\overline{d^2}}{8\tau_m} \tag{18}$$

An estimation based on a flux calculation was proposed by Woodman and Rastogi (1984). Considering an arbitrary level z, the flux of a tracer is evaluated across that level by assuming complete mixing. The local diffusivity is a function of the layer thickness d and of the life-time of the patch.

$$K_\theta^{\text{local}} = \frac{< d^2 >}{12T} \tag{19}$$

An extension for sweeping layers is also considered. Woodman and Rastogi (1984) then infer an effective diffusivity profile by combining their flux estimates with high resolution radar observations They obtain $K_\theta^{\text{eff}} \sim 0.2 - 0.3$ m^{2}s^{-1} in the UTLS.

6.2 A Lagrangian approach

A Lagrangian approach was recently proposed by Vaneste and Haynes (2000). They model the diffusion process as a continuous-time random walk. At random time, a fluid particle encounters a turbulent patch, it is then vertically displaced. The variance of the displacement σ_z^2 is related to the local diffusivity (flux per unit gradient):

$$K_\theta^{\text{local}} = \frac{\sigma_z^2}{2\tau_m} \tag{20}$$

where τ_m is the mean waiting time between successive encounters.

The effective diffusivity will depend on three parameters, (i.e. on the P.D.F. of these quantities):

• the height h of the turbulent layers;

• the vertical displacement within a turbulent patch of height h (i.e. turbulence intensity);

• the waiting time τ_m.

In the long time limit, they obtain (for complete mixing within the patches , i.e. the Dewan's hypotheses):

$$K_\theta^{\text{eff}} = \frac{\overline{h^3}}{12 H \tau_m} \tag{21}$$

where H is the height of the considered atmosphere.

6.3 An energetic point of view

It is long time recognised that mixing results in an increase of potential energy (e.g. Thorpe, 1973). Winters et al. (1995) showed how to relate the mixing properties of turbulence to the energy budget. First, following (Lorenz, 1955) they consider the background potential energy of a fixed domain. They show how diapycnal mixing, through destratification, leads to an increase of that background potential energy: the APE (buoyancy flux) is partly irreversibly converted into background potential energy. This is a way to quantify a bulk mixing efficiency of turbulence (already used in laboratory and numerical experiments) for a considered volume. However, this method cannot be applied directly to the atmosphere, as the density in not a conservative quantity.

7 Concluding remarks

Since the early developments of the MST radar technique (Woodman and Guillen, 1974) considerable progresses have been made concerning the physics of measurements (understanding of scattering processes), and signal processing (inference of turbulence parameters). MST radars allow now fairly consistent and reliable estimations of the energetic parameters of small scale turbulence: KE and dissipation rates, even though some assumptions might be questioned. Also, MST radar measurements have learned to us a lot about the morphology of atmospheric turbulence. However, if concerned with the mixing properties of turbulence, several questions remains. In the order:

• What is the correct expression for the effective diffusivity of intermittent turbulence? Theoretical considerations suggest that an estimator of the effective diffusivity depends on parameters describing the space and time characteristics of turbulence events, (i.e. intermittency): height of the layers, waiting-time and turbulence intensity as well.

• How to relate the (measured) energetic parameters of turbulence to a local diffusion coefficient? Several hypotheses seems questionable: $\gamma = \text{Const.}$, or $L_m/L_B = \text{Const.}$.

• What should (can) we measure with MST radars ? It appears that a need exists for high resolution measurements in order to better describe the space and time distribution of turbulent events. Also, it seems that simultaneous KE and C_n^2 estimations are needed as it allows to estimate the mixing efficiency γ.

Finally, an energetic approach, such the one proposed by Winters et al. (1995), is likely promising on the way to estimate the effective diffusivity of small scale turbulence in the atmosphere.

References

Alisse J.-R. and C. Sidi. Experimental probability density functions of small-scale fluctuations in the stably stratified atmosphere. *J. Fluid. Mech.*, 402:137–162, 2000.

Dalaudier F., H. Luce, and M. Crochet. Mutsi: High resolution balloon measurements and mu radar observations. In *Proceedings of the 15th ESA symposium on European Rocket and Balloon Programmes and related research, ESA, SP-471*, pages 127–130, 2001.

Dewan E.M. Turbulent vertical transport due to thin intermittent mixing layers in the stratosphere and other stable fluids. *Science*, 211:1041–1042, 1981.

Dole J., R. Wilson, F. Dalaudier, and C. Sidi. Energetics of small scale turbulence in the lower stratosphere from high resolution radar measurements. *Ann. Geophys.*, 19:945–952, 2001.

Frisch A. S. and S. F. Clifford. A study of convection capped by a stable layer using doppler radar and acoustic echo sounder. *J. Atmos. Sci.*, 31:1622–1428, 1974.

Fukao S., M. Yamanaka, N. Ao, W. Hocking, T. Sato, M. Yamamoto, T. Nakamura, T. Tsuda, and S. Kato. Seasonal variability of vertical diffusivity in the middle atmosphere 1. three-year observations by the middle and upper atmosphere radar. *J. Geophys. Res.*, 99:18,973–18,987, 1994.

Gage K.S. and J.L. Green. Evidence for specular reflection from monostatic vhf radar observations of the stratosphere. *Radio Sci.*, 13:991–1001, 1978.

Gage K.S., J.L. Green, and T.E. VanZandt. Use of doppler radar for the measurement of atmospheric turbulence parameters from the intensity of clear air echo. *Radio Sci.*, 15:407–416, 1980.

Garrett C. Mixing in the ocean interior. *Dyn. Atm. Oceans*, 3:239–265, 1979.

Gossard E. E. and R. G. Strauch. *Doppler radar and weather observations*. Elsevier, 1983.

Gossard E.E., D.E. Wolfe, K.P. Moran, R.A. Paulus, K.D. Anderson, and L.T. Rogers. Measurements of clear-air gradients and turbulence properties with radar wind profilers. *J. Atmos. Ocean. Tech.*, 15:321–342, 1998.

Hocking W. K. On the extraction of atmospheric turbulence parameter from radar backscatter doppler spectra - i. theory. *J. Atmos Terr. Phys.*, 45:89–102, 1983.

Hocking W. K. Observation and measurements of turbulence in the middle atmosphere with a vhf radar. *J. Atmos. Terr. Phys.*, 48:655–670, 1986.

Hocking W. K. Two years of continuous measurements of turbulence parameters in the upper mesosphere and lower thermosphere made with a 2-mhz radar. *J. Geophys. Res.*, 91:2475–2491, 1988.

Hocking W. k. An assessment of the capabilities and limitations of radars in measurements of upper atmosphere turbulence. *Adv. Space Res.*, 17 (11):37–47, 1997.

Hocking W. k. The dynamical parameters of turbulence theory as they apply to middle atmosphere studies. *Earth Planets Space*, 51:525–541, 1999.

Hocking W. k. and K.L. Mu. Upper and middle tropospheric kinetic energy dissipation rates from measurements of c_n^2 - review of theories, in-situ investigations, and experimental studies using the buckland park atmospheric radar in australia. *J. Atmos. Sol. Terr. Phys.*, 59:1779–1803, 1997.

Imberger J. and G. Ivey. On the nature of turbulence in a stratified fluid. part 2: Applications to lakes. *J. Phys. Oceanogr.*, 21:659–680, 1991.

Itsweire E.C., J.R. Koseff, D.A. Briggs, and J.H. Ferziger. Turbulence in stratified shear flows: Implications for interpreting shear-indiced mixing in the ocean. *J. Phys. Oceanogr.*, 23: 1508–1522, 1993.

Ivey G. and J. Imberger. On the nature of turbulence in a stratified fluid. part 1: The energetics of mixing. *J. Phys. Oceanogr.*, 21:650–658, 1991.

Kurosaki S., M. Yamamoto, H. Hashiguchi, T. Sato, and S. Fukao. Vertical eddy diffusivity in the lower and middle atmosphere: a climatology based on the mu radar observations during 1986-1992. *J. Atmos. Sol. Terr. Phys.*, 58:727–734, 1996.

Lilly D.K., D.E. Waco, and S.I. Aldefang. Stratospheric mixing estimated from high altitude turbulence measurements. *J. Appl. Meteorol.*, 13:488–493, 1974.

Lorenz E.N. Available potential energy and the maintenance of the general circulation. *Tellus*, 7:157–167, 1955.

Luce H., F. Dalaudier, M. Crochet, and C. Sidi. Direct comparison between in situ and vhf and oblique radar measurements of refractive index spectra: a new successful atempt. *Radio Sci.*, 31:1487–1500, 1996.

Luce H., S. Fukao, F. Dalaudier, and M. Crochet. Strong mixing events observed near the tropopause with the mu radar and hight-resolution balloon techniques. *J. Atmos. Sci.*, 59: 2885–2896, 2002.

Nastrom G.D. and F.D. Eaton. Tubulence eddy dissipation rates from radar observations at 5-20 km at white sands missile range, new mexico. *J. Geophys. Res*, 102:19,495–19,505, 1997.

Nastrom G.D. and F.D. Eaton. Persistent layers of enhanced c_n^2 in the lower stratosphere from vhf radar observations. *Radio Sci.*, 36:137–149, 2001.

Ottersten H. Radar backscattering from the turbulent clear atmosphere. *Radio Sci.*, 4:1251–1255, 1969b.

Pavelin E., J. Whiteway, R. Busen, and J. Hacker. Airborne observations of turbulence, mixing, and gravity waves in the tropopause region. *J. Geophys. Res.*, 107 (D10):4084, 2002.

Rao D.N., M.V. Ratnam, T.N. Rao, and S.V.B. Rao. Seasonal variation of vertical eddy diffusivity in the troposphere, lower stratosphere and mesosphere over a tropical station. *Ann. Geophys.*, 19:975–984, 2001.

Rohr J.J., E.C. Istweire, and C.W. Van Atta. Mixing efficiency in stably stratified decaying turbulence. *Gephys. Astrophys. Fluid. Dyn.*, 29:221–236, 1984.

Ruddick B., D. Walsh, and N. Oakey. Variations in apparent mixing efficiency in the north atlantic central water. *J. Phys. Oceanogr.*, 27:2589–2605, 1997.

Röttger J. and C.H. Liu. Partial reflection and scattering of vhf radar signals from the clear atmosphere. *Gephys. Res. Lett.*, 5:357–360, 1978.

Sato T. and R. F. Woodman. Fine altitude resolution observations of stratospheric turbulent layers by the arecibo 430 mhz radar. *J. Atmos. Sci.*, 39:2546–2552, 1982.

Smyth W.D. and J.N. Moum. Length scales of turbulence in stably stratified turbulence. *Phys. Fluids*, 12:1327–1342, 2000.

Smyth W.D., J.N. Moum, and D.R. Caldwell. The efficiency of mixing in turbulent patches: Inferences from direct simulations and microstructure observations. *J. Phys. Oceanogr.*, 31: 1969–1992, 2001.

St Laurent L. and R.W. Schmitt. The contribution of salt fingers to vertical mixing in the north atlantic trace release experiment. *J. Phys. Oceanogr.*, 29:1404–1424, 1999.

Tatarskii V.I. Wave propagation in a turbulent medium, 1961.

Tennekes H. and J Lumley. *A first course in Turbulence*. MIT Press, 1972.

Thorpe S.A. Turbulence in stably stratified fluids: a review of laboratory experiments. *Bound.-Layer Meteorol.*, 5:95–119, 1973.

Tsuda T., W.E. Gordon, and H. Saito. Azimuth angle variation of specular reflection echoes in the lower atmosphere observed with the mu radar. *J. Atmos. Solar-Terr.. Phys.*, 59:777–784, 1997.

Vaneste J. and P.H. Haynes. Intermittent mixing in strongly stratified fluids as a random walk. *J. Fluid. Mech.*, 411:165–185, 2000.

VanZandt T.E., W.L. Clarck, K.S. Gage, C.R. Williams, and W.L. Ecklund. A dual-beamwidth radar technique for measuring the turbulent energy dissipation rate ϵ. *Gephys. Res. Lett.*, 29: ??–??, 2002.

VanZandt T.E., J.L. Green, K.S. Gage, and W.L. Clarck. Vertical profiles of refractivity turbulence structure constant: comparison of observations by the sunset radar with a new theoretical model. *Radio Sci.*, 13:819–829, 1978.

Weinstock J. On the theory of turbulence in the buyoancy subrange of stably stratified flows. *J. Atmos. Sci.*, 35:634–649, 1978.

Weinstock J. Using radar to estimate dissipation rate in thin layer of turbulence. *Radio Sci.*, 16:1401–1406, 1981.

Weinstock J. Vertical diffusivity and overturning length in stably stratified turbulence. *J. Geophys. Res.*, 97:12,653–12,658, 1992.

Winters K.B., P.N. Lombard, J.J. Riley, and E.A. d'Assaro. Available potential energy and mixing in density stratified fluid. *J. Fluid. Mech.*, 289:115–128, 1995.

Woodman R. F. and A. Guillen. Radar observations of winds and turbulence in the stratosphere and mesosphere. *J. Atmos. Sci.*, 31:493–505, 1974.

Woodman R. F. and P.K. Rastogi. Evaluation of effective eddy diffusive coefficients using radar observations of turbulence in the stratosphere. *Gephys. Res. Lett.*, 11:243–246, 1984.

SIMULTANEOUS OBSERVATIONS OF ATMOSPHERIC TURBULENCE IN THE LOWER STRATOSPHERE FROM BALLOON SOUNDINGS AND ST RADAR MEASUREMENTS

R. Wilson, F. Dalaudier

Service d'Aéronomie/IPSL

1 Introduction

A field campaign combining in-situ and radar measurements, both with very high resolution, was conducted during April 1998 in St Santin (south of France). The objectives of this campaign were:

- to validate the radar calibration;
- to better understand the "transfer function" of both measurement systems
- to characterise the small scale turbulence from simultaneous and independent in-situ and radar observations.

2 The data set

2.1 The PROUST radar

The PROUST ST radar was a UHF (961 MHz) pulsed Doppler radar allowing very high resolution measurements (Petitdidier et al., 1985; Delage et al., 1996; Dole et al., 2001). The range resolution is 30 m, integration time being reduced to 51 s. The beam width is $\sim 0.3^{\circ}$in the E-W direction and 1.1°in the N-S direction (the stratosphere is in the near field of the antenna). The large Cassegrain antenna (2000 m^2) is pointing in the vertical direction only.

2.2 The SFT measurements

Seven instrumented balloons were launched from a nearby site, about 30 km East of the radar site. Every gondola carried a Väisälä RS80G sonde (including a GPS transponder). Three of the gondolas, referred as SFT ("Structure Fine de Température") carried high resolution temperature and pressure sensors (developed by Service d'Aéronomie). The temperature and pressure profiles have a vertical resolution better than 20 cm. The rms noise of the temperature data is ~ 5 mK rms, slightly varying with height.

2.3 Inference of turbulence parameters

Both instruments provide informations on the small scale temperature fluctuations:

- The radar reflectivity is related to C_n^2, the structure constant of refractive index, by assuming that the fluctuations are induced by inertial turbulence (isotropic and homogeneous).

Specular reflection is negligible for that frequency (961 MHz). Rayleigh scattering from water drop or particles is also negligible in the stratosphere.

• The SFT temperature measurements provide informations for fluctuations larger than about 1 m.

3 Data processing

3.1 Radar data

The PROUST radar is calibrated from the known cosmic noise: (e.g. VanZandt et al., 1978).

$$\langle C_n^2 \rangle = \frac{16\pi^2}{0.38} \frac{k\, T_N\, B_r}{P_t\, \lambda_r^{5/3}\, G_B\, L\, N_{\text{coh}}\, N_{\text{code}}\, H(2l_o/\lambda_r)} \left(\frac{r^2}{\Delta r}\right) \frac{S}{N} \tag{1}$$

Such a radar equation is very usual except for the H and G_B terms. The factor $H(2l_0/\lambda_r)$ takes into account the departure of the temperature spectrum from the $-5/3$ power law for scales close to the dissipation scales. (Hill, 1978; VanZandt et al., 2000). As the range of interest ($11-15$ km) is still within the near field of the antenna, the two way gain, G_B, has to be numerically calculated and tabulated.

3.2 SFT data

The temperature fluctuations were partially denoised by using a wavelet decomposition. The "SFT C_n^2" is then evaluated from the temperature variance for the scale interval ($2-5$ m), assumed to lie within the inertial subrange. If the Kolmogorov hypotheses of an inertial subrange apply, the temperature variance can be expressed as a function of C_n^2:

$$\text{var}(l_1, l_2) = 0.25 C_T^2 \int_{k_2}^{k_1} k^{-5/3} dk \tag{2}$$

The "SFT C_T^2" estimate reads:

$$C_T^2(l_1, l_2) = \frac{8}{3} \frac{(2\pi)^{2/3}}{\left(l_2^{2/3} - l_1^{2/3}\right)} \text{var}(l_1, l_2) \tag{3}$$

For a dry atmosphere, as the lower stratosphere, C_T^2 is simply related to C_n^2:

$$C_n^2 = \left(0.7710^{-6} \frac{P}{T}\right)^2 C_T^2 \tag{4}$$

The temperature variance is smoothed with a 30 m width window (i.e. the radar range resolution) before to be converted into C_n^2. Of course, it should be noticed that C_n^2 is evaluated whatever are the causes of temperature fluctuations (noise, buoyancy range - in which cases C_n^2 does not make any sense - or inertial turbulence).

4 PROUST/SFT comparison

When comparing the processed data sets, we were not abbe to unambiguously identify any turbulent layer simultaneously sampled by the radar and the SFT sondes. We therefore choose to compare the statistical properties of the turbulence field as observed from both instruments.

• There is a detectability threshold for radar estimates of C_n^2, this threshold being altitude dependent. In order to compare the two C_n^2 estimates (radar and SFT), we first apply this radar threshold to the SFT data.

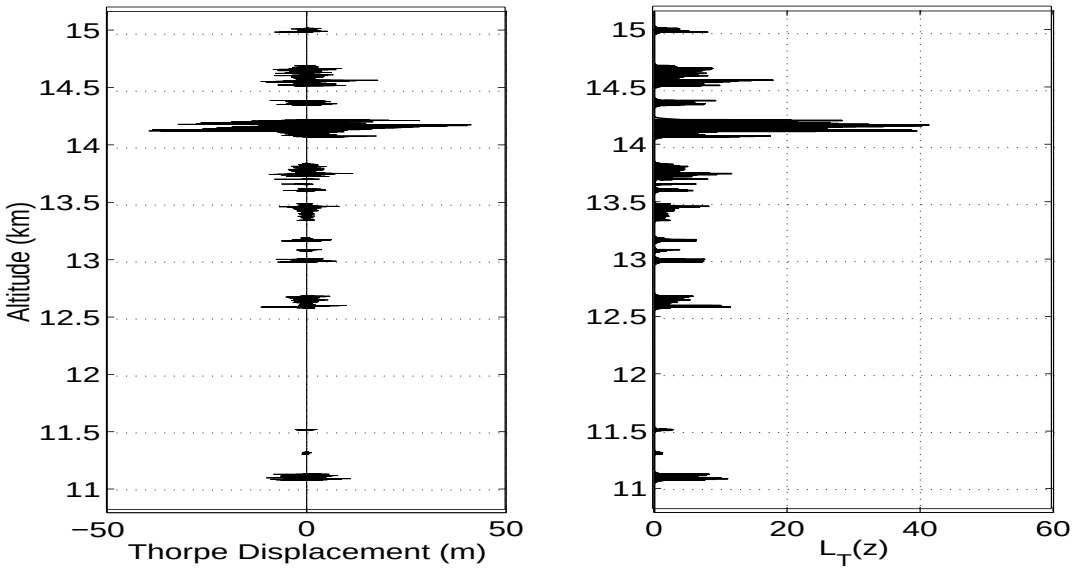

Figure 1: Left: Thorpe displacement for selected patches. Right: Modulus of the Thorpe displacement.

• As previously mentioned, whatever the nature of the fluctuations, a SFT C_n^2 might be evaluated, though not always meaningful. Prior to compare the two data set, one needs to determine if temperature fluctuations are turbulent or not.
• We check for the slope of the spectrum (or the structure function) by comparing the ratio R of two C_n^2 estimates from partially overlapping scale intervals.

$$R = \frac{C_n^2(l_1, l_2)}{C_n^2(l_3, l_4)} \tag{5}$$

If $R < 0.5$ or $R > 2$, the C_n^2 estimates were considered as dubious (i.e. non-turbulent) and eliminated. This criterion was not very selective however (about 20 % of the data were discarded).

• A new method for turbulent patch identification from high resolution temperature profile was recently proposed Piera et al. (2002):

- The method is based an analysis of the Thorpe displacements d_T.
- The Thorpe displacements are compared to their potential error E_{dT}, such an error being evaluated from the temperature noise.
- A data point is classified as signal if $d_T > E_{dT}$ or if $d_T = 0$, and is classified as uncertain otherwise.
- A considered range (30 m depth) is retained if the number of signal points exceed the number of uncertain points.

The Thorpe displacements of the selected turbulent layers are shown in figure (1). The comparison of distributions of the radar and SFT estimates of C_n^2 are shown in figure (2). After patches selection of the in-situ data, the two distributions compare surprisingly well.

5 Conclusions

We have compared very high-resolution radar (30 m) and in-situ (0.2 m) measurements:

- We cannot identify any turbulent layer unambiguously sampled by both instruments.

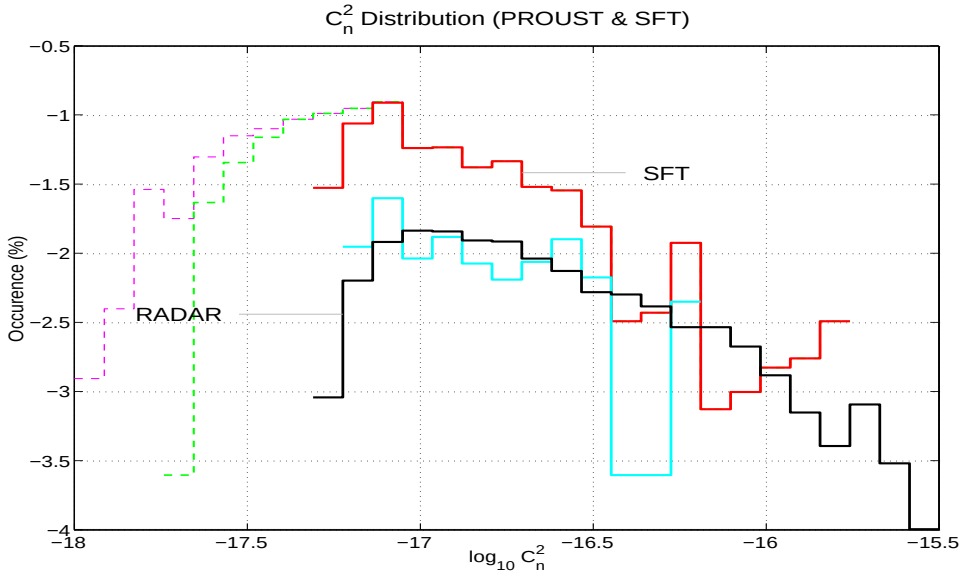

Figure 2: Frequency of occurrence of C_n^2 inferred from the SFT temperature variance (dashed and thin continuous curves) and from the radar data (thick curve). The four curves for the SFT data were obtained after various selection criterion (see text).

- The distributions of the radar and SFT C_n^2 estimates compare well, after thresholding and patches selection of the SFT data.
- Consequently, the radar calibration appears correct.

References

Delage, D., Bertin, F., Crémieu, A., Massebeuf, M., Ney, R., and Desautez, A.: Real time data processing algorithms and first results obtained by the PROUST radar in its final configuration, in 7th workshop on technical and scientific aspects of MST - ST radars, edited by C. SCOSTEP secr., Boulder, pp. 209–212, 1996.

Dole, J., Wilson, R., Dalaudier, F., and Sidi, C.: Energetics of Small Scale Turbulence in the Lower Stratosphere from High Resolution Radar Measurements, Ann. Geophys., 19, 945–952, 2001.

Hill, R. J.: Spectra of fluctuations in refractivity, temperature, humidity, and the temperature-humidity cospectrum in the inertial and dissipation range, *Radio Sci.*, 13, 953–961, 1978.

Petitdidier, M. D. A., M., G., , and Penazzi, G.: A decoder for a 30 m height resolution ST radar, Radio Sci., 20, 1141–1145, 1985.

Piera, J., Roget, E., and Catalan, J.: Turbulent patch identification in microstructure profiles: A method based on wavelet denoising and Thorpe displacement analysis, J. Atmos. Ocean. Tech., 19 (9), 1390–1402, 2002.

VanZandt, T., Green, J., Gage, K., and Clarck, W.: Vertical profiles of refractivity turbulence structure constant: comparison of observations by the Sunset radar with a new theoretical model, Radio Sci., 13, 819–829, 1978.

VanZandt, T., Clarck, W., Gage, K., Williams, C., and Ecklund, W.: A dual-wavelength radar technique for measuring the turbulent energy dissipation rate ϵ, *Gephys. Res. Lett.*, 27, 2537–2540, 2000.

NEW MST RADAR METHODS FOR MEASURING THE TURBULENT KINETIC ENERGY DENSITY

T.E. VanZandt[*], G.D. Nastrom[+], J.-I. Furumoto[#], W. L. Clark[*], and T. Tsuda[#]

[*]Aeronomy Laboratory, NOAA, Boulder, Colorado
[+]St. Cloud State University, St. Cloud, Minnesota
[#]RASC, Kyoto University, Kyoto, Japan

1. Introduction

Clear-air wind profiler Doppler radars offer the capability to estimate the intensity of small-scale turbulent kinetic energy per unit mass (TKE) over a broad range of altitudes in the troposphere and lower stratosphere from the width of the observed Doppler spectrum. The TKE is related to the eddy dissipation rate and the eddy diffusivity. However, the observed spectral widths contain contributions related to the interaction of the radar beam with the large-scale wind which must be removed. These corrections are usually significant, sometimes being larger than the turbulence contribution to the observed spectral width. Much of the theory used to estimate the corrections was developed decades ago. An experiment to test the corrections applied to the spectral width was conducted at the highly versatile MU radar in Japan. Essentially simultaneous observations were made using two different beamwidths and two different zenith angles with oblique beams directed at the four cardinal compass points during a two-day period of relatively strong winds (peak winds over 50 ms^{-1}). Theoretical predictions of changes in spectral width with respect to wind speed, azimuth, and altitude are compared with the observations.

2. The Experiment

- Observations were made at the MU Radar (46.5 MHz, λ=6.45 m) from 1700 JST 15 March to 1900 JST 17 March 2002
- Pulse length: 2 μs (300 m range)
- Zenith angles: 0º, 10º and 20º
- Azimuths: N, E, S, W
- Beamwidths: 3.46º and 1.87º (ratio 1.85)
- Observations at each zenith angle/beamwidth/azimuth took ~55 s, and a full cycle took about 4 minutes
- Altitude range: 5-22 km (5-12 km used in the present study)
- The median peak wind speed was about 55 m/s
- Spectral widths were determined by Gaussian fitting

3. Analysis

The traditional theory of the interaction between the beam shape and the background winds predicts anisotropy between the spectral widths observed on the zonal (U) and meridional (V) beams. The observed spectral widths (σ_U^2 and σ_V^2) are the sums of the atmospheric turbulence and the effects of beam-, shear-, and wave-broadening. As discussed by VanZandt et al. (2002), σ_U^2 and σ_V^2 are given by Eqs. (1) and (2), respectively, where θ is

the beamwidth, α is the zenith angle, u_z=dU/dz, v_z=dV/dz, and R is the range of the sample volume. The difference, $\sigma_U^2 - \sigma_V^2$, is given by Eq. (3).

Because U >V and $|u_z| \sim |v_z|$ for conditions typically found at MU in the upper troposphere and lower stratosphere, Eq. (3) predicts $\sigma_V^2 > \sigma_U^2$ (the final term on the right side is usually negligible). Nastrom and Tsuda (2001) found that $\sigma_V^2 > \sigma_U^2$ at MU and at White Sands, New Mexico, and that the magnitude of the anisotropy was proportional to the magnitude of U for fixed V. Predictions such as this could be inferred from the recent results of Chu (2002), although they did not use observations. Figure 1 shows the results at MU and confirm the anisotropy is related to zenith angle, as predicted by eq. 3.

$$\sigma_U^2 = \sigma_{turb}^2 + \frac{\theta^2}{3}\left[U^2\cos^2\alpha + V^2 - 2U\cos\alpha\sin^2\alpha u_z R + \sin^4\alpha\left(u_z R\right)^2\right] + \sigma_{wave}^2 \quad (1)$$

$$\sigma_V^2 = \sigma_{turb}^2 + \frac{\theta^2}{3}\left[V^2\cos^2\alpha + U^2 - 2V\cos\alpha\sin^2\alpha v_z R + \sin^4\alpha\left(v_z R\right)^2\right] + \sigma_{wave}^2 \quad (2)$$

$$\sigma_V^2 - \sigma_U^2 = \frac{\theta^2\sin^2\alpha}{3}\left[U^2 - V^2 + 2R\cos\alpha\left(Uu_z - Vv_z\right) - \sin^2\alpha R^2\left(u_z^2 - v_z^2\right)\right] \quad (3)$$

4. References

Chu, Y.-H., 2002: Beam broadening effect on oblique MST radar Doppler spectrum. J. Atmos. Oceanic Technol., 19, 1955-1967.

Nastrom, G.D., and T. Tsuda, 2001: Anisotropy of Doppler spectral parameters in the VHF radar observations at MU and White Sands, Ann. Geophys., 19, 883-888.

VanZandt , T.E., G.D. Nastrom, J. Furumoto, T. Tsuda, and W.L.Clark, 2002: A Dual-Beamwidth Method for observing atmospheric turbulence intensity with radar, Geophys. Res. Lettr., 29(12), 10.1029/2001GL014283

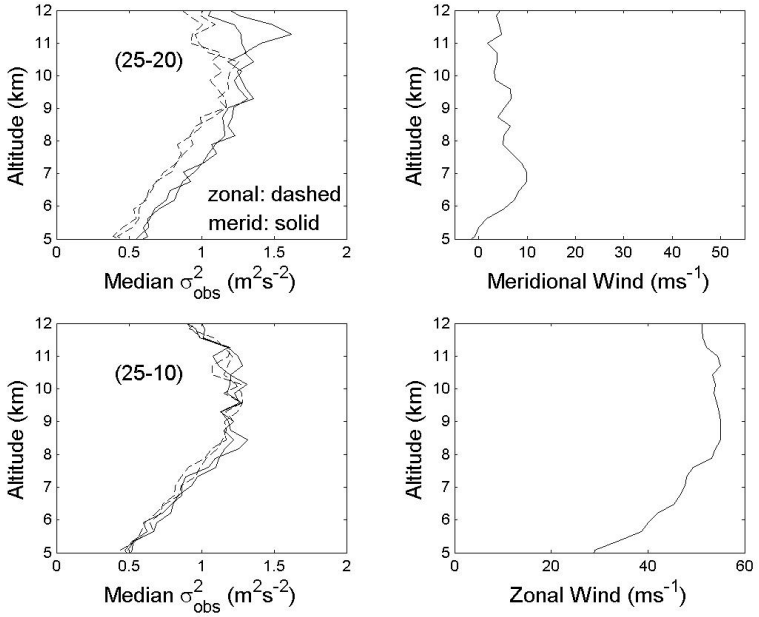

Figure 1. Left: Median TKE for observations using the entire antenna: upper (lower) at 20º (10º) zenith angle. Right: Median wind speeds.

MEASUREMENTS OF ATMOSPHERIC TURBULENCE WITH THE DUAL-BEAMWIDTH METHOD USING THE MST RADAR AT GADANKI, INDIA

G. Nastrom*, P.B. Rao+, V. Sivakumar#

*St. Cloud State University, St. Cloud, Minnesota 56379 USA
+ADCOS-2, National Remote Sensing Agency, Hyderabad 500037 AP India
#Universite de la Reunion, Cassin-97715 St. Denis-C9 France

1. Introduction

A brief experiment was conducted during April and May, 2002, using the MST radar at Gadanki (13.47 ^{o}N, 79.18^{o}E) operating at 53 MHz with average power aperture product of $7x10^{8}$ Wm^{2} to test the dual-beamwidth method of estimating the turbulence kinetic energy (TKE) recently introduced by VanZandt et al. (2002). Because the beamwidth can be modified on only one polarization at a time at Gadanki, an elliptical beam was used with a modified dual-beamwidth analysis. Estimates of the TKE from the dual-beamwidth method and the traditional method using corrections for beam-, shear-, and wave-braodening are very similar in regions of light winds (<~10 ms^{-1}). In regions of stronger wind (>~15 ms^{-1}) the traditional method often gives TKE<0 because the beam-broadening correction is greater than the observed spectral width. In the latter regions the modified dual-beamwidth method gives TKE>0 on the beams parallel to the prevailing wind. It is suggested that the problems with the traditional method are due to uncertainty of the effective width of the radar beam. The data from May extend over a full diurnal period, and the diurnal range of TKE is found to be about 5 dB below about 12 km and near the tropopause, with maximum values during local afternoon.

2. Data

The Gadanki radar antenna array consists of 1024 crossed 3-element Yagi antennas covering 130x130 m. Peak transmitted power is 2.5 MW obtained from 32 transmitters each feeding a sub-array of 32 Yagis. The one-way half-power full beamwidth of the full antenna is about 2.9^{o}.

During this experiment two beamwidths were interleaved each hour. A narrow beamwidth (2.9^{o}) was obtained using the full antenna. By disconnecting 16 subarrays from each polarization of the antenna a second beamwidth was obtained, about 5.8^{o} (i.e., the ratio of the broad and narrow beams is about 2). Because the broad beam could be formed only in one polarization at a time, the resulting beam was elliptical (5.8º by 2.9º degrees) and our application of the dual-beamwidth method accounts for this ellipticity. Our observational strategy included a total of 10 beam positions each hour for each beamwidth: vertical and toward the 4 cardinal directions for 10^{o} and 15^{o} zenith angles. Range-resolution was 150 m from 3.6 to 24.9 km. Data from the vertical beam are not used in this study.

Typically, 6-8 profiles were obtained with each beam direction and beamwidth each hour. Observations were made usually from 1100-1700 local time on 24, 25, 26, 27, and 29 April 2002. Another set of observations were taken over a diurnal cycle from 1500 9 May-1500 10 May 2002. Hourly medians are used for the analyses below.

Local weather conditions during late April and early May 2002 were very hot, with daily maximum temperatures near 40^{o}C every day (the sun is directly overhead at noon at

this latitude in late April). Surface winds were generally light and variable. Scattered cumulus and towering cumulus formed in the afternoon, although no significant precipitation occurred at the radar site.

3. Analysis

The beam of the Gadanki radar is conical when the full antenna is used. When only half of the antenna is used for one polarization the beam is elliptical, resembling a fan beam. Accordingly, an analysis modified from that of VanZandt et al. (2002) must be used as follows (subscript H applies for the half-antenna and F for the full-antenna):

$$\sigma_{obs-H}^2 = \sigma_t^2 + \left[\theta_H^2\left(\cos^2\alpha U^2 + shear\right) + \theta_F^2 V^2\right]/4\ln 2 \qquad (1)$$

$$\sigma_{obs-F}^2 = \sigma_t^2 + \theta_F^2\left(\cos^2\alpha U^2 + shear + V^2\right)/4\ln 2 \qquad (2)$$

where "shear" means the small terms that depend on vertical shear of the horizontal wind.

Solving this pair of simultaneous equations gives

$$\sigma_t^2 = \frac{\left(\theta_H^2/\theta_F^2\right)\sigma_{obs-F}^2 - \sigma_{obs-H}^2}{\left(\theta_H^2/\theta_F^2\right)-1} - \frac{\theta_F^2 V^2}{4\ln 2} \qquad (3)$$

The first term on the right of (3) depends only on the observed spectral widths and the ratio of beamwidths. The second term on the right of (3) requires that we know θ_F as well as V. In principle, the width of the transmitted beam is known and that value of θ_F should be used whenever the sample volume is uniformly filled with turbulence. When the sample volume is not filled, such as when one or more thin horizontal layers of intense turbulence are present, then the appropriate value for θ_F depends on the amount of beamfilling, and perhaps other things, and becomes uncertain (e.g., if only a single intense layer is present in the sample volume then the effective beamwidth is less than θ_F and its value depends on the location of the intense layer within the sample volume). The uncertainty of the value of θ_F may explain why several past studies have obtained results with $\sigma_t^2<0$ using the "traditional method". A major goal of this study will be to compare estimates of σ_t^2 from (3) with those from the "traditional method".

Fig. 1 shows the profiles of median wind speed during the entire period in April (upper left) and in May (upper right) from the 10^o zenith angle observations (results at 15^o are nearly identical and are not shown). Above about 10 km the meridional winds in May are very light while the zonal winds continue to increase with height to a maximum speed near 25 ms^{-1} at 17 km. Above about 20 km winds during the two periods are again very similar. Error bars to show the 95% confidence limits extend one standard error of the mean ($2\sigma/\sqrt{N_o}$ where σ is the standard deviation of the N_o hourly medians used) above and below the curves for E and N beams. The lower panels of Fig. 1 show σ_{obs}^2 during April (lower left) and May (lower right). Except at about 5-7 km and perhaps 17-19 km, where the meridional beams' values are greater than the zonal beams', there is no significant difference among σ_{obs}^2 for the four beams during April. During May the meridional beams' σ_{obs}^2 values slightly exceed the zonal beams' from about 11-17km. The dashed vertical lines show the Doppler resolution for spectral width as used here; in April (May) the values near 14 km and above about 19 km (22 km) are at the resolution limit.

The upper panels of Fig. 2 show σ_t^2 estimated using (3), called σ_t^2-2BW. The lower panels show σ_t^2 estimated using traditional beam-, shear-, and wave-corrections, (Atlas, 1964; Hocking, 1985; Nastrom, 1997) called σ_t^2-Trad. Below about 7 km (8 km) during April (May) results from both methods are relatively large, ranging between about 0.1 and 0.3 m^2s^{-2}, corresponding to the altitudes of active convection. Values for the west beam are consistently smaller than those from the other beams in April below 6 km; from 6 to 7.5 km values for both beams in the zonal plane are smaller than those in the meridional plane. During May there is no apparent anisotropy at the lower altitudes. Above 7 or 8 km all values become less than 0.02 m^2s^{-2} at all altitudes except in the regions of strong winds (discussed below); the σ_t^2-Trad values are slightly smaller than those for σ_t^2-2BW. Note that negative values, where the corrections are larger than σ_{obs}^2, appear in Fig. 2. The May results near 17 km illustrate the differing effects of the correction terms; i.e., for σ_t^2-Trad the beam-broadening corrections due to the large zonal wind speeds cause values for all four beams to be negative while for σ_t^2-2BW only the meridional beams' values are negative. A similar, but smaller, effect is seen near 18 km during April. σ_t^2-2BW may be expected to be more reliable as it is not influenced by thin-layer effects or other beam-filling problems. The curves in Fig. 2 are very similar where the winds are less than about 10 m/s.

4. References

Atlas, D., Advances in radar meteorology, *Adv. Geophys.*, 10, eds. H. Landsberg and J. van Mieghem, Academic, 317-478, 1964.

Hocking, W.K., Measurement of turbulent energy dissipation rates in the middle atmosphere by radar techniques: a review, *Radio Sci.*, 20, 1403-1422, 1985.

Nastrom, G.D., Doppler radar spectral width broadening due to beamwidth and wind shear. Annales Geophysicae, 15, 786-796, 1997.

VanZandt , T.E., G.D. Nastrom, J. Furumoto, T. Tsuda, and W.L.Clark, A Dual-Beamwidth Method for observing atmospheric turbulence intensity with radar, *Geophys. Res. Lettr.*, 29(12), 10.1029/2001GL014283, 2002.

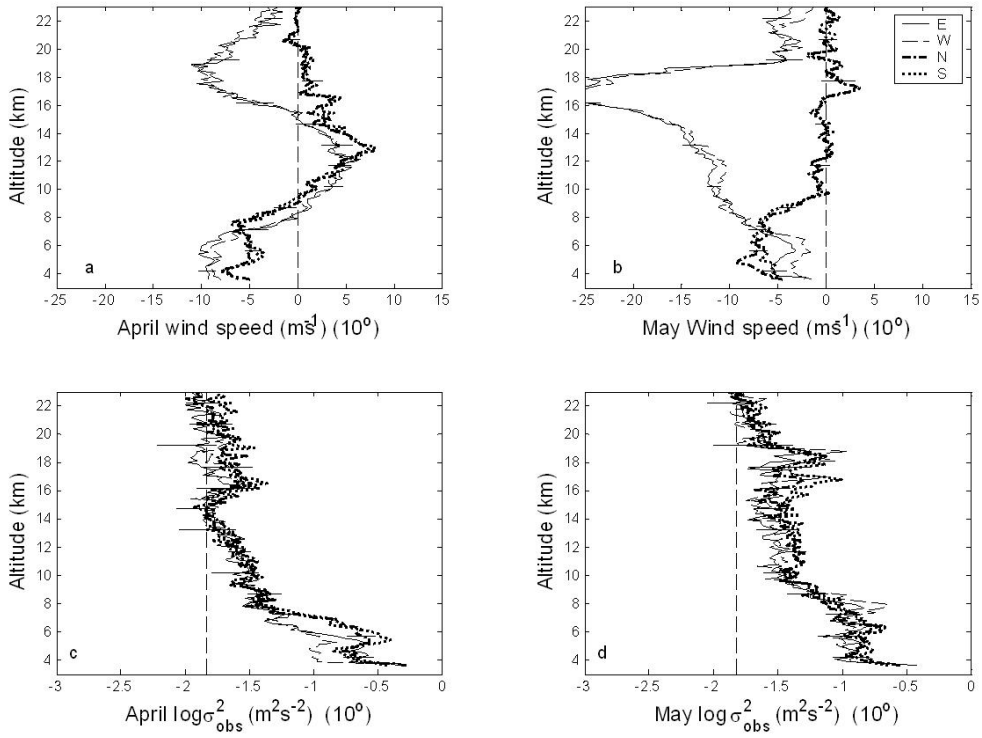

Fig. 1. Median (upper) winds and (lower) observed spectral widths over all observations taken at 10º zenith angle during (left) April and (right) May. Dashed vertical lines in the lower panels show the minimum spectral resolution for Doppler half-width.

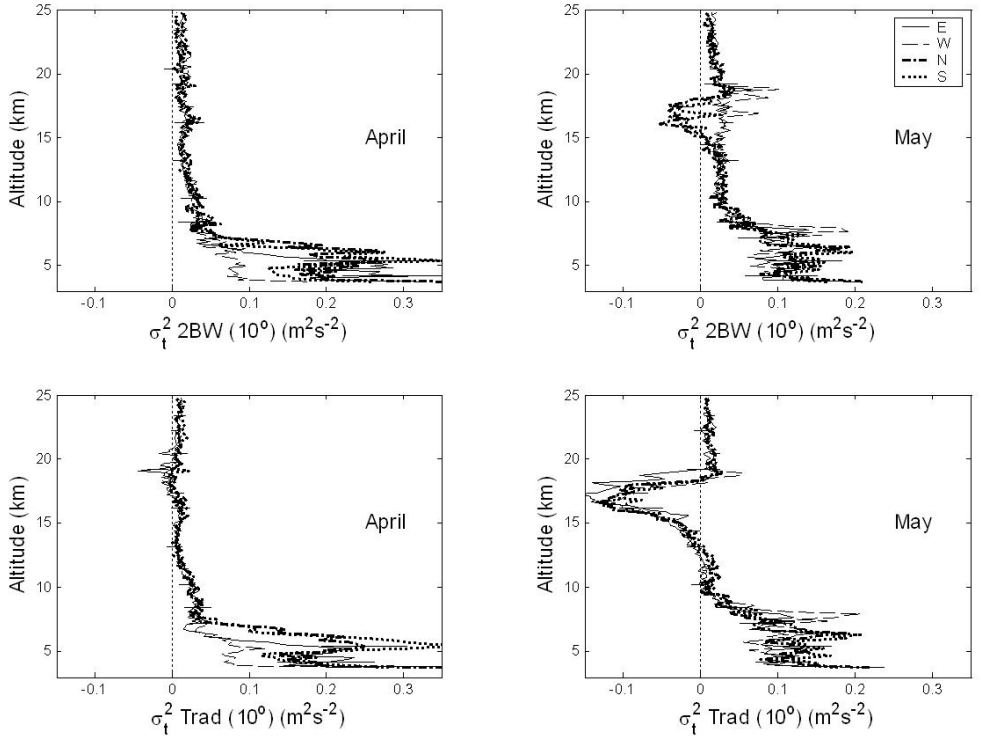

Fig. 2. Median (upper) σ_t^2-2BW and (lower) σ_t^2-Trad over all observations taken at 10º zenith angle during (left) April and (right) May.

FAST AND ACCURATE CALCULATION OF SPECTRAL BEAM-BROADENING FOR TURBULENCE STUDIES

W.K. Hocking

Dept. of Physics and Astronomy, University of Western Ontario, London, Ontario. Canada.

Abstract.
A method is described which allows modern VHF radars to be used to quickly and accurately determine spectral beam-broadening, and hence to determine atmospheric turbulence strengths by spectral width methods. This method is superior to procedures which assume constant winds, or assume constant winds plus a linear wind-shear, and can be carried out quickly and efficiently on modern computers.

Introduction.
For the last 20 years, the techniques for measurement of atmospheric turbulence by spectral width methods using windprofiler radars have been well known. A very general formalism was demonstrated by Hocking (1983), which could be applied even for complicated polar diagrams, variable wind speeds, and different pulse lengths. However, despite the generality of this formula, it has not been properly applied over much of the recent past. Often it is assumed that the wind shows no height variation across the radar pulse, and in other cases it is assumed that the wind varies linearly with height. There are many situations in which neither assumption is valid, and estimates of the broadening due to horizontal motion of the scatterers can be in error. This has been recognized by Nastrom (1997) and VanZandt et al., (2002), and the latter paper has introduced an alternative "dual beam" method which somewhat mitigates inaccuracies in estimates of the beam-broadening effects. However, such procedures are still limited in that they do not properly consider the effects of the radar pulse lengths, layer thickness, and so forth.

Many of problems in estimation of the turbulent energy dissipation rates disappear if the spectral beam-broadening can be properly determined. A very accurate formula which may be used for this calculation was given by Hocking (1983), and we present it again below, with an additional term which we have added to accommodate scatterer anisotropy, viz.

$$\mathcal{P}(f) \propto \int P(\theta,\phi)\, [\sigma/r^2 \otimes g(r)]\, \exp\{-(\sin^2(\theta)/\sin 2(\theta_s)\}\, d\Omega$$

where $\mathcal{P}(f)$ represents the power spectral density as a function of frequency f, $P(\theta,\phi)$ is the radar polar diagram, (θ,ϕ) are the polar coordinates of the scattering point, σ is the backscatter cross-section for isotropic scatter, $g(r)$ describes the pulse as a function of range r, θ_s is the anisotropy parameter, and $d\Omega$ is the solid angle, $= \sin\theta\, d\theta\, d\phi$. The symbol $\otimes$ represents a convolution. In addition we may use the extra relation that $d\Omega = \tan(\theta)\, dV d\phi/\cos(\phi - \phi_0)$, where $V = v_r/V_{mag}$, ϕ_0 is the azimuthal direction of the wind, and V_{mag} is the wind speed. The frequency f is found as $f = 2/\lambda\, v_r$.

The integration actually takes place on contours of constant radial velocity, which are generally hyperbolae, as shown in fig. 1. In the case that vertical velocities become important, these hyperbolae become ellipses at angles close to vertical (e.g., see Chu, 2002) but in the main they are hyperbolae.

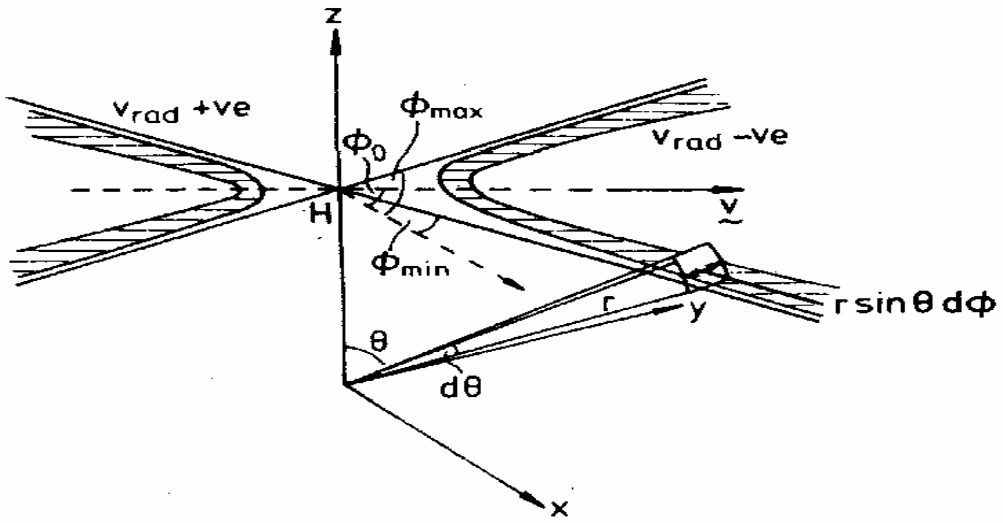

Fig.1. Lines of constant radial velocity at a fixed height H.

This function can be accurately calculated, and this was done by Hocking (1983) for one specific set of polar diagrams. However, the integration is not trivial, requiring (a) an accurate polar diagram determination, (b) a good representation of the transmitted pulse, (c) a convolution and (d) integration over (θ,ϕ) space along the contours shown in fig. 1. The computation can be very time-intensive, and many authors have avoided performing the full integration for real-time applications. This has in turn led to occasional poor representations of the beam-broadened spectral width.

However, it is a relatively simple (although lengthy) task to utilize this equation in its most complete form for real-time applications, and the purpose of this paper is to demonstrate that not only is this feasible, but in fact it has already been done. Examples are discussed.

The Procedure.

Fig. 2 shows a typical (non-linear) wind profile, which has been divided into thin layers. In any realistic situation, the wind is sampled only at discrete range-intervals. Often the wind is sampled at a resolution equal to the pulse length, but it is advantageous to sample at higher resolution. In any case, a good estimate of the true wind profile can be obtained by interpolation using a linear spline in both the north-south and east-west components. Although the optimum interpolation method can be the subject of debate, any reasonable fitting procedure will generally be far superior to assuming a constant wind speed, or using linear interpolation. We use a cubic spline. Sample spectra are shown in fig. 2 for layers A and B. (As a warning, it should be noted that the spectral width does not just depend on the wind speed in the direction of tilt, but rather the total magnitude of the wind speed. Hence although the spectrum for layer B has been drawn as a narrow one, in reality it could be as wide as that for A if the wind perpendicular to the page in layer B were large.)

In order to accurately determine the spectrum, the key spectral parameters are parameterized as functions of various variables. We only need to do this for a thin representative sub-layer, like the one labeled as A in fig. 2. For thin layers, the spectrum can be accurately represented as a Gaussian with spectral offset (f_{off}), peak power (P_0) and spectral width ($f_{1/2}$). In reality we do not determine the frequency spectrum directly, but determine the spectrum of the normalized radial velocity $V = v_r/V_{mag}$, where v_r is the radial velocity seen by the radar and V_{mag} is the speed of the horizontal wind in the layer. Choice of this variable avoids the need

to perform simulations for a wide variety of V_{mag} values. We actually produce parameters V_{off} (offset), P_{V0} (peak power) and $V_{1/2}$ (half-width). Then it is necessary to perform the integral shown above for a wide variety of different wind speed directions, layer ranges (R), range offsets from the pulse-peak (R-R_0), radar pulse lengths, and polar diagram parameters, and produce empirically fitted functions for each of these dependencies. Often polynomial fits, Gaussians and exponentials are suitable fitting-functions. As an example, sample graphs of the dependence of the frequency offset and spectral width as a function of (R-R_0) were shown in the insets of figs. 8 and 9 of Hocking (1983). Due to lack of space, we cannot specify the dependencies determined in detail, but all of the variables V_{off}, P_{V0} and $V_{1/2}$ depend on θ_t (the radar zenithal tilt angle), V_{perp}/V_{mag} *and* V_{par}/V_{mag} *(normalized* components of the wind parallel and perpendicular to the azimuthal direction of beam tilt), R, R-R_0, $\theta_{1/2}$ (the radar beam half-power half-width), the sub-layer depth, and θ_s.

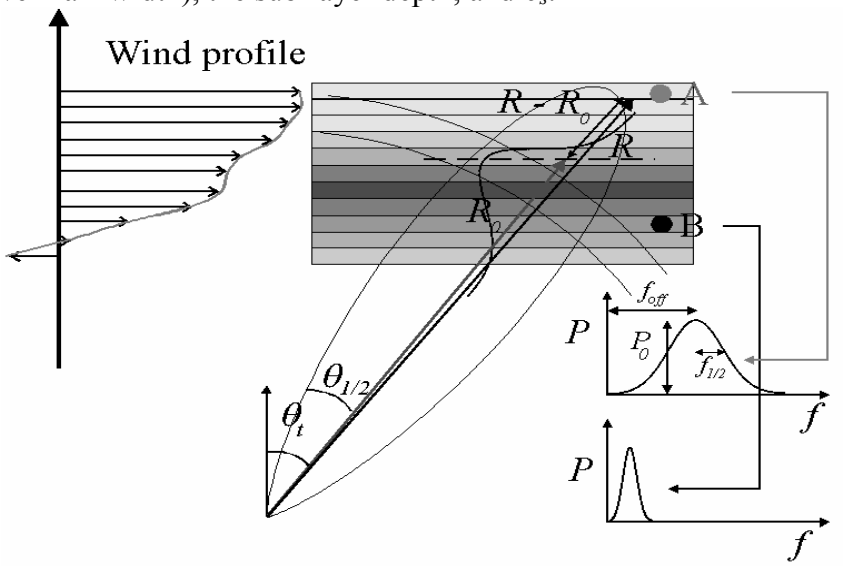

Fig. 2. Diagram showing the dependencies of the spectra produced from thin layers as a function of various atmospheric and radar parameters.

The key parameters V_{off}, $V_{1/2}$ and P_{V0} should be parameterized, and stored as computer subroutines. Sometimes such computer subroutines are called "look-up tables". Then, for any realistic wind profile, the scattering region can be considered to be composed of many sub-layers, each with different wind speeds, as shown in fig. 2. For a VHF radar, a sub-layer depth of 50 m (less than the normal buoyancy scales for turbulence) might be typical. The "look-up tables" described above can be used to determine appropriate values for V_{off}, $V_{1/2}$ and P_{V0} for each sub-layer, and then these can be converted to matching parameters f_{off}, P_0 and $f_{1/2}$. Care is required to ensure that an appropriate Jacobian is used in the conversion. The conversion will be different for each sub-layer, depending on the value of V_{mag} within each sub-layer. The parameters f_{off}, P_0 and $f_{1/2}$ now describe the spectrum as a function of true Doppler frequency for each sub-layer. Once the parameters P_0, f_{off} and $f_{1/2}$ have been deduced for each sub-layer, the spectrum can be explicitly calculated as a function of frequency. Then the spectral values from each sub-layer are added together at user-specified frequencies varying from some reasonable minimum to a reasonable maximum value, to produce the final spectrum. It is quite possible that the resultant spectrum is asymmetric, and large numbers of numerical experiments have demonstrated that this procedure quite closely produces the true spectrum determined from the full integral. Spectral half-power half-width values may now be found by simple search algorithms applied to the final spectrum. The procedure properly considers pulse-length dependencies, and anisotropic scatter – factors

which have not yet been considered in the more simplistic models which have followed the formalism of Hocking (1983). In addition, it is possible to deal with layers that only partially fill the radar volume, or are offset from R_0 (producing artificial wind shears, as discussed by Hocking (1983), and later by May et al., (1988)).

When this "look-up table" is used, computational times decrease by over 100 times and more (relative to performing a full integration). Thus the process, which is fast and accurate, can be used in real-time. The procedure is currently used on-line with the McGill VHF radar (Campos and Hocking, this issue), and the Clovar radar (Hocking 1997). It was also used by Hocking (1988) for MF radar measurements, and also by Hocking et al., (1988). As an example, fig. 4 shows dissipation rates measured during the passage of the remnants of Hurricane Isabel over the McGill radar between 1200 on 19 Sept. and 1200 on 20 Sept., 2003.

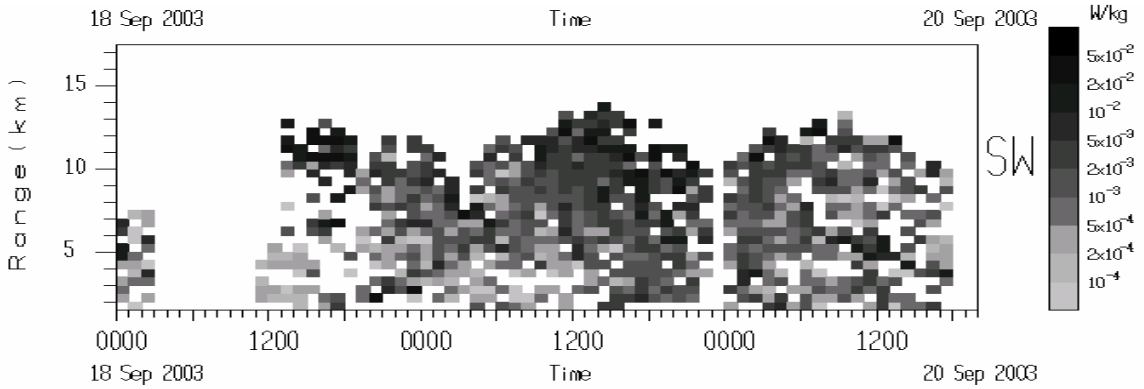

Fig. 4. Sample energy dissipation rates measured with the McGill VHF radar near Montreal, Canada. Times are UT.

References:

Campos, E., and W. Hocking, Vortical Motions observed with the new McGill VHF radar and associated dynamical characteristics, *this issue*.

Chu, Y.-H, Beam broadening effect on oblique MST radar Doppler spectrum*, J. Atmos. Ocean. Tech., 19*, 1955, 2002.

Hocking, W.K. On the extraction of atmospheric turbulence parameters from radar backscatter Doppler spectra -I: theory, *J. Atmos. Terr. Phys.***, *45***, 89-102, 1983.

Hocking, W.K. Two years of continuous measurements of turbulence parameters in the upper mesosphere and ..., *J. Geophys. Res*., **93**, 2475-2491, 1988.

Hocking, W., K. Lawry and D. Neudegg, Radar measurements of atmospheric turbulence..., *MAP (Middle Atmosphere Program) Handbook,Scostep Secretariat, 27*, 443-446, 1989.

Hocking, W.K., System design, signal processing procedures and preliminary results for the Canadian (London, Ontario) VHF Atmospheric Radar, *Radio Sci*., **32**, 687-706, 1997.

May, P.T., S. Fukao, T. Tsuda, T. Sato and S. Kato, The effect of thin scattering layers on the determination of wind by Doppler radars, *Radio Sci., 23*, 83-94, 1988

Nastrom, G.D., Doppler radar spectral width broadening due to beamwidth and wind shear, *Ann. Geophys., 15*, 786, 1997.

VanZandt, T.E., et al., A dual-beamwidth radar method for measuring atmospheric turbulent kinetic energy density, Geophys. Res. Letts., 29, 10.1029/2001GL014283, 2002.

POSSIBLE CROSS-TROPOPAUSE TRANSPORT PROCESSES IN THE TROPICS

Masayuki K. Yamamoto[1], Masatomo Fujiwara[2], and Shoichiro Fukao[1]

1:Radio Science Center for Space and Atmosphere, Kyoto University
2:Graduate School of Environmental Earth Science, Hokkaido University
(e-mail:fukao@kurasc.kyoto-u.ac.jp)

Introduction

Dynamical, chemical, and radiative couplings between the stratosphere and troposphere are the important processes that control the Earth's atmosphere, and the tropical tropopause is the primary region where the tropospheric airmass enters the stratosphere. The VHF radar can directly observe three dimensional winds and turbulent motions with a good height and time resolution in the tropopause region. Some VHF radar observations for this research have been already performed over the tropical Pacific [*Gage et al.*, 1991]. The Equatorial Atmosphere Radar (EAR) is a 47.0 MHz radar with a peak output power of 100 kW and a circular array of approximately 110 m in diameter. It was installed near Bukittinggi, West Sumatra, Indonesia (0.2°S, 100.32°E, 865 m above sea level) in March 2001. The EAR can observe winds and turbulence with a highest vertical and time resolution of 150 m and ∼90 sec in the troposphere and in the lower stratosphere (2–20 km in altitude) [*Fukao et al.*, 2003]. In the present paper, we will show the observational result by the EAR in the tropopause region.

Turbulence at the tropopause due to Kelvin wave

Figure 1 shows the time-altitude plot of the spectral width for the northward beam during the period of 10–30 November 2001. The broadening effects caused by finite width of radar beam and vertical wind shear are removed. On 19–20 November, the tropopause jumped up by ∼2 km, and the enhancement of turbulence suddenly appeared in the 15–17 km region. The enhancement intermittently continued until 23 November. During 12–16 November, the spectral width in the 15.5–17 km region is, on average, 0.46±0.12 m s ^{1}, and during 19–23 November, it is 0.55±0.19 m s ^{1} with seven peaks of 0.8–1.2 m s ^{1}. The peak turbulence intensities are, therefore, a factor of ∼5 larger in kinetic energy in the quiet periods.

Figure 2 shows the time-alitutude plots of potential temperature derived from radiosondes and zonal wind anomaly derived from the EAR. The isentropes near and just above the tropopause move downward before November 19, and their downward motion continued and extended into the region where the turbulence was enhanced. At the same time, significant zonal wind oscillations with the period of ∼13 days are observed in the 15.5–18.5 km region (e.g., at 17 km from 11 to 24 November). There characteristics suggest that the disturbance is induced by an equatorial Kelvin wave.

The turbulence in the tropopause region has merged into the turbulence in the 12–15 km region around 23 November (Figure 1). The turbulence associated with the Kelvin wave may have caused effective and irreversible transport of lower stratospheric airmass deeply into the troposphere.

Kelvin-Helmholtz instability near the tropical tropopause

Figure 3 shows time-altitude cross-sections of vertical wind, zonal echo power imbalance (zonal EPI), zonal wind shear, and Richardson number (Ri). Zonal EPI is defined by the ratio of the echo power in the westward beam to that in the eastward beam. Ri

is calculated from the radiosonde temperature data and the EAR horizontal wind data. A continuous updraft (>0.025 m s ^{1}) is clearly seen in the region 0–1 km above the cold-point tropopause determined by the radiosonde soundings (Figure 3(a)). Temporal variation of the tropopause height is affected by equatorial Kelvin waves [*Fujiwara et al.*, 2003]. The echo power in the westward beam is continuously stronger than that in the eastward beam in the updraft region (Figure 3(b)). A strong eastward wind shear or westward wind which decreases with altitude from the tropopause (10–50 m s ^{1} km ^{1}) is also continuously observed in the same region (Figure 3(c)). *Ri* is almost continuously < 0.5 and sometimes < 0.25. (Figure 3(d)).

KHI is considered to occur frequently, even if observed *Ri* is > 0.25. One reason is that *Ri* is not always < 0.25 in all. Another reason is that occurrence and non-occurrence of KHI recurred, on average, in one hour. The contamination of horizontal wind to vertical wind velocity which is measured in the vertical beam easily occurs, if the echo layer is tilted by billows generated by KHI (KH billows). If the layer is tilted by KH billows, the effective direction of the vertical beam becomes tilted toward the perpendicular axis of the refractivity surface, because the effective direction of the radar beam is determined by the convolution of angle dependence of radar wave scattering with the antenna beam pattern. Under this condition, the horizontal wind component, which is extremely greater than the vertical wind component, contaminates the Doppler shift in the vertical beam. Figure 3(d) shows that *Ri* is almost continuously < 0.5 in the updraft region due to the strong zonal wind shear, and the condition for KHI generation is satisfied. The positive values of zonal EPI in the updraft region (Figure 3(b)) indicate that the echo layer is tilted downward to the west and suggest continuous existence of KH billows under the strong eastward wind shear (Figure 3(c)). Therefore, the updraft in the region 0–1 km above the tropopause is not real nut a spurious one resulting from the contamination of westward winds under the condition of the echo layer tilted downward to the west, which is generated by KH billows. Under this condition, the spurious vertical wind should be upward, which agrees with the observed result. These features consistently suggest that KHI is continuously generated in the TTL.

Conclusion

In this paper, we have shown the enchanced turbulence by the Kelvin wave and the KHI occurence, both of which exist in the tropical tropopause region. Existence of KHI around the tropopause may play a role in tropical stratosphere-troposphere exchange. Further studies on the turbulence in the tropical tropopause layer (TTL) is performed by EAR observations, and will be shown in the near future.

References

Fujiwara, M., M. K. Yamamoto, H. Hashiguchi, T. Horinouchi, and S. Fukao, Turbulence at the tropopause due to breaking Kelvin waves observed by the Equatorial Atmosphere Radar, Geophys. Res. Lett., *30(4)*, 1171, doi:10.1029/2002GL016278, 2003.

Fukao, S., H. Hashiguchi, M. Yamamoto, T. Tsuda, T. Nakamura, M. K. Yamamoto, T. Sato, M. Hagio, and Y. Yabugaki, The Equatorial Atmosphere Radar (EAR): System description and first results, Radio Sci., *38(3)*, 1053, doi:10.1029/2002RS002767, 2003.

Gage, K. S., B. B. Balsley, W. L. Ecklund, D. A. Carter, and J. R. McAfee, Wind profiler-related research in the tropical Pacific, J. Geophys. Res., *96*, 3209-3220, 1991.

Yamamoto, M. K., M. Fujiwara, T. Horinouchi, H. Hashiguchi, and S. Fukao, Kelvin-Helmholtz instability around the tropical tropopause observed with the Equatorial Atmosphere Radar, Geophys. Res. Lett., *30(9)*, 1476, doi:10.1029/2002GL016685, 2003.

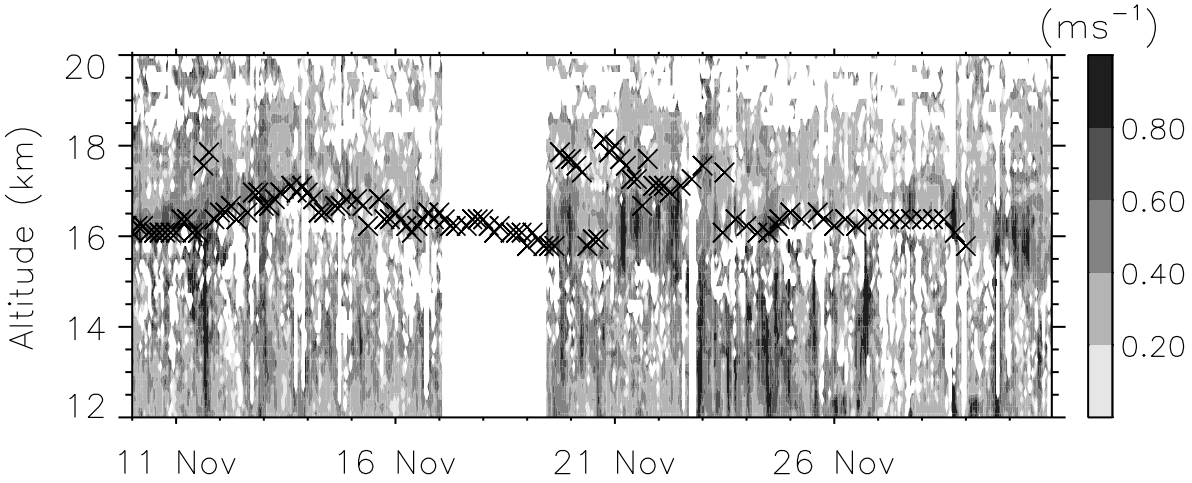

Figure 1: Time-altitude plot of the spectral width for the northward beam from 10–30 November 2001. The location of the tropopause defined by the minimum temperature is indicated by crosses (*Fujiwara et al.*, 2003).

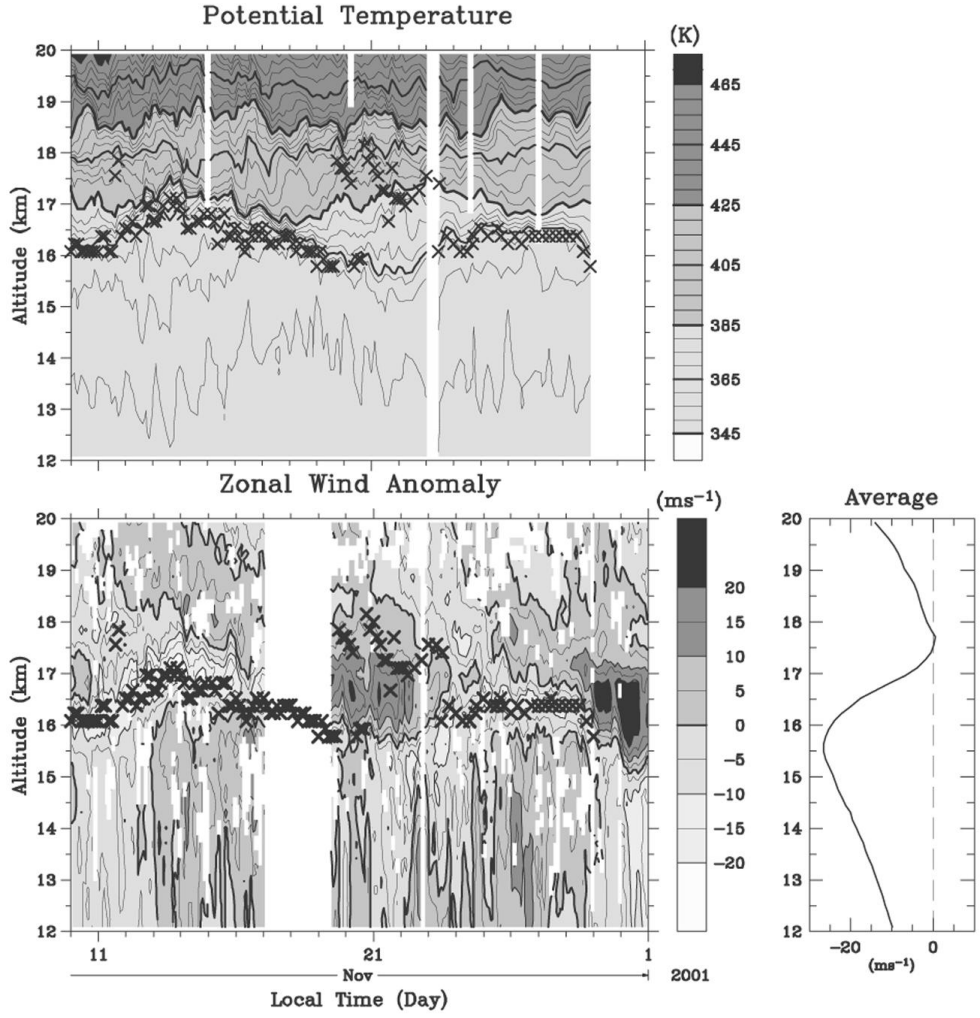

Figure 2: Same as Figure 1, but for potential temperature measured by radiosondes (top) and zonal wind anomaly measured by the EAR (eastward positive; bottom left) with the average profile (bottom right). (*Fujiwara et al.*, 2003).

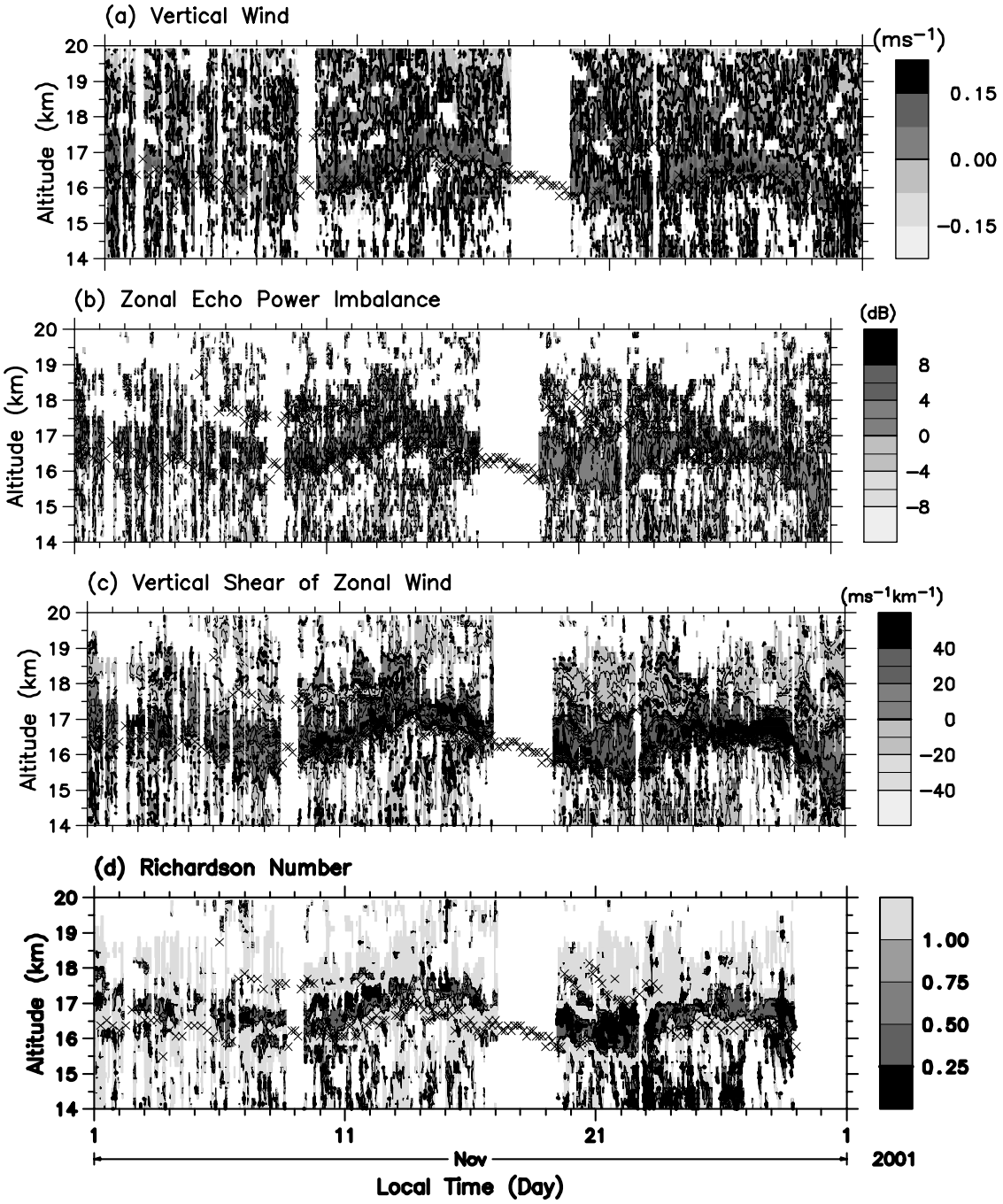

Figure 3: Time-altitude cross-sections of (a) vertical wind, (b) zonal echo power imbalance, (c) zonal wind shear, and (d) Richardson number in November 2001. Positive values in (b) denote that the echo power is stronger in the westward beam than in the eastward beam. Positive values in (c) denote the eastward wind shear. The tropopause defined by the temperature minimum is indicated by crosses (*Yamamoto et al.*, 2003).

UPPER MESOSPHERE TEMPERATURE CHANGES OBSERVED IN PMSE AND INCOHERENT SCATTER DURING A STRONG POLAR CAP ABSORPTION EVENT

K. Kubo[2], J. Röttger[1] and S. Fukao[2]
[1] Max-Planck-Institut, 37191 Katlenburg-Lindau, Germany
[2] Radio Science Center for Space and Atmosphere, Uji, Kyoto, Japan

Middle of July 2000 an extremely strong solar proton event happened (named "Bastille II"), which caused major polar cap absorption (PCA) due to the strong increase of D-region electron density by high energy particle precipitation. The concurrent ionospheric disturbances led to enhanced electric fields, which caused an increase of the ion drift and the neutral wind in the lower thermosphere and possibly the upper mesosphere as well. Through the enhanced ion drag, increases of ion and neutral temperature are usually resulting, which are also known as Joule heating. We tried to recognize this in coherent scatter observations of PMSE with the SOUSY Svalbard Radar (SSR on 53.5 MHz) and observations of incoherent scatter with the EISCAT Svalbard Radar (ESR on 500 MHz). We find two independent observations, which indicate a potential temperature increase of the upper mesopause region due to ion heating.

During the strongest D-region electron density enhancement (i.e. increase of absorption) we recognized a disappearance of PMSE above 86 km lasting over a fraction of a day. This can be seen in Figure 1.

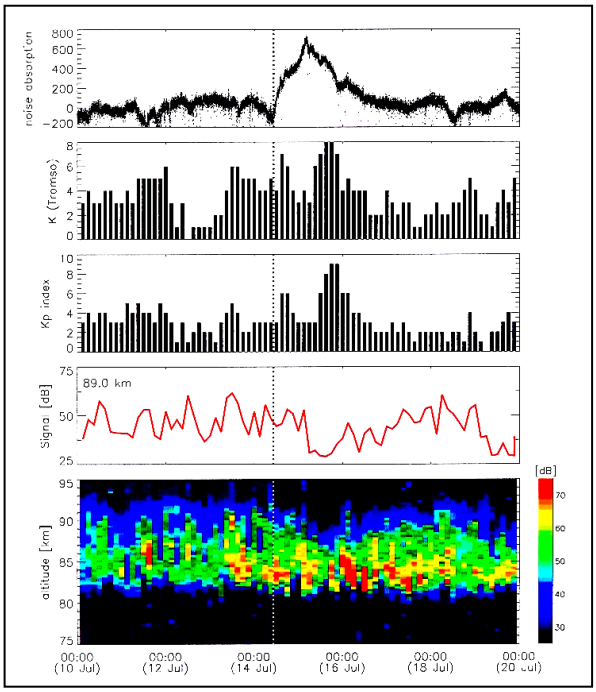

Fig. 1 Five days of observations covering the Bastille II event. In the upper panel the cosmic noise absorption on 53.5 MHz is shown. The two center panels show the K index of Tromsö in northern Norway and the planetary index K_p, respectively. The fourth panel from the top shows the signal strength of PMSE at 89 km, and the lower panel shows the HTI plot of PMSE over the full height range and period. The PMSE were observed with the SSR on 53.5 MHz.

Absorption of cosmic noise is caused by the increase of electron density in mesospheric heights (D-region). The enhancement of electron density is due primarily to the ionizing effects of high-energy solar protons down to even low altitudes of the mesosphere. This is called a Polar Cap Absorption (PCA) event, which spreads out all over the polar cap and can last for many hours and days. We also observed the significant decrease of PMSE intensity during this PCA event, especially at the top of the PMSE layer above 86 km. Figure 1 shows the temporal variations of noise absorption, geomagnetic disturbance, PMSE signal power in the altitude of 89 km and HTI plot of PMSE. The drastic noise absorption, i.e. enhanced D-region electron density, occurred on 14-16 July during the strong geomagnetic/ionospheric disturbance. Despite the increase in electron density, the PMSE signal power around 86-90 km was depleted in comparison with the mean diurnal variation of signal intensity deduced from data sets, recorded before (1-13 July) and after this event (19-31 of July). The lower part of the PMSE layer below 85 km was not affected at all in this event. This is in so far surprising, since we expect a decrease in PMSE signal strength due to the underlying electron density, which causes an absorption of the radar signal as well. When we consider this absorption and correct the measured signal strength of PMSE, we would get an enhancement of the scatter cross section over the whole range. However, the reduction in the upper part still exists, although we cannot fully recover the significant reduction of PMSE signal in the heights above 86 km.

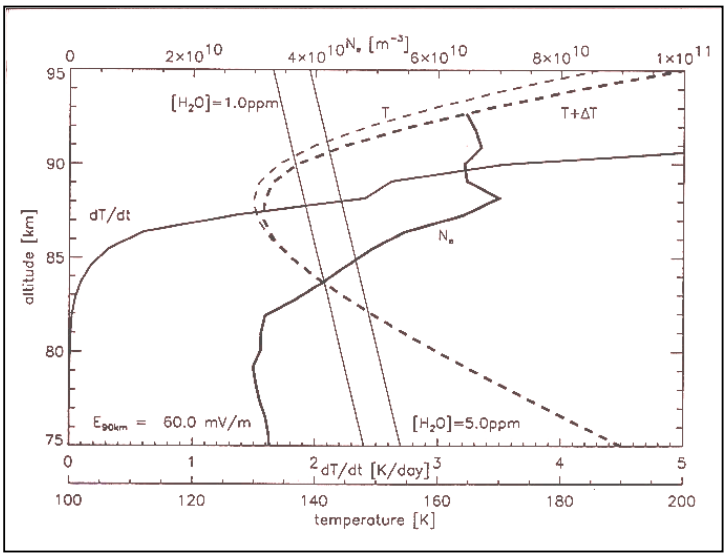

Fig. 2 Height profiles of measured electron density Ne, heating rate dT/dt, neutral temperature T before and after the Joule heating (dashed lines), and the limiting water vapor mixing ratio.

We may assume that the reduction in PMSE signal power above 86 km during this event resulted from a neutral temperature increase by particle heating. To estimate particle heating effect (Banks, 1979), we calculate the Joule dissipation rate, which is deduced from the electron density profile obtained with concurrent incoherent scatter observations with the EISCAT Svalbard Radar. The required profiles of mean background neutral temperature, neutral density, the collision- and gyro-frequencies were obtained from models. The ionospheric electric field measurements, needed to calculate the heating rate, were obtained from complementary incoherent scatter measurements with the collocated EISCAT Svalbard Radar This deduction allowed us to determine the temperature increase (heating rate) with time dT/dt.

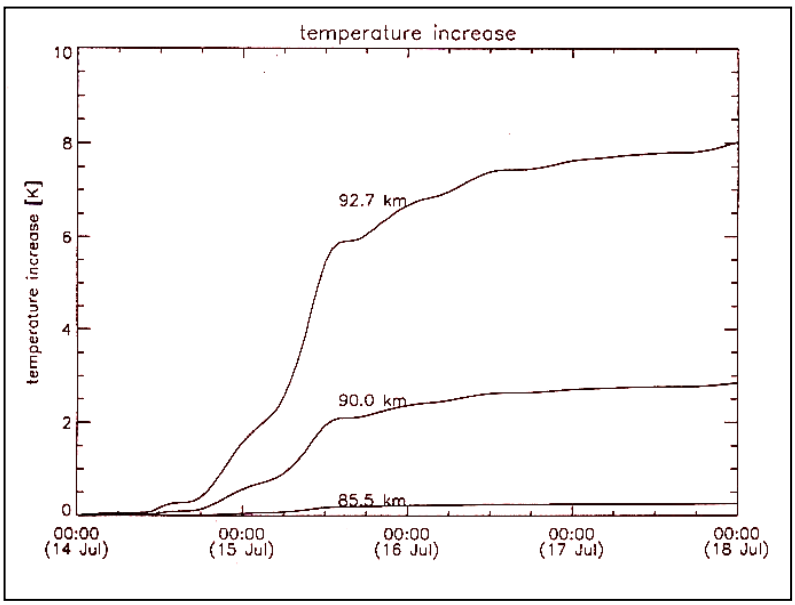

Fig. 3 Cumulative heating rate (temperature increase as function of time) at different altitudes around the mesopause.

Fig. 2 shows the results of our deductions: (a) The electron density profile exhibited an increase around 90 km and significant reduction above 90 km. This result shows a good agreement with the numerical estimation of electron density calculated with the GEOS satellite data of proton precipitation (private communication, Rapp 2001).

Fig 2 also shows (b) the calculated heating rate as function of altitude, and in Fig. 3 we show the accumulated neutral heating rate. i.e the temperature increase over a few days. Of course, this does not include any radiation or heat transport, which likely would reduce the temperature increase. We recognize that there is very little heating of a small fraction of one Kelvin around 80 km but it gets larger with altitude, and it reaches 8 Kelvin at 92.7 km. These calculations are for fairly high D-region electron densities, which are only observed during strong solar proton events. Also the ionospheric electric field of 60 mV/m, which was estimated from the ion drift measurements with the ESR incoherent scatter radar, is fairly high, but representative for this highly disturbed period.

The mean temperature (dashed line in Fig. 2) raised a little due to the heating above 85 km. We have also included in Fig. 2 the limiting curves of water vapor mixing ratio as function of altitude. Only in the regions with temperatures below these curves ice particles can be formed. In the model, which we used in Fig. 2, this means between about 82 and 92 km, where we detect the PMSE. The ice particles interact with the ionospheric plasma, which results in the formation of plasma irregularities raising the radar scatter cross section. When the temperature raises, the ice particles would melt, which in turn will result in a disappearance of the PMSE. At least for this model, the peak temperatures do not change sufficiently strong to cause this melting effect. We, thus, cannot provide full prove from these observations that the disappearance of PMSE in the upper heights can be exclusively explained by a neutral temperature increase due to heating. Rapp et al. (2002) had recalled that the ratio of the product of mean charge and number density of heavy particles to electron density has an influence on electron diffusion and hence a too high electron density would prevent PMSE.

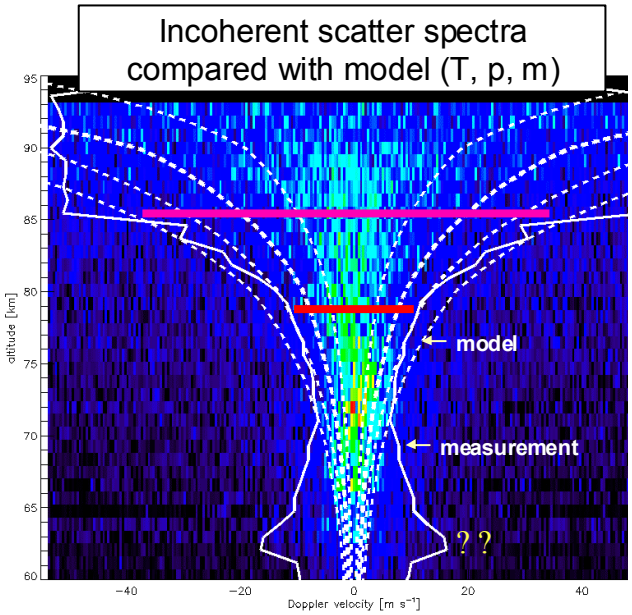

Fig. 4 Plot of incoherent scatter spectra. The solid line gives the half-power width of a fitted Lorentzian, and the dashed lines those from models.

There is another method to deduce the neutral temperatures from incoherent scatter radar observations. The spectrum width depends on the ion-neutral collision frequency (related to pressure p and ion mass m) and the temperature T. Larger temperatures result in a larger spectrum width. In Fig. 4 we show a 4-minutes average of the spectra as function of the altitudes between 60 km and 95 km. The dashed lines are contours for different levels of a model Lorentzian. The lower horizontal bar at 78 km denotes a similarity of model and measurement. The upper horizontal bar at 86 km shows that the measured spectrum is wider than the model. This is an indication of a rise in temperature with height, as we would expect from the Joule heating. Care has to be taken, however, when there are heavy ions or ice particles, which cause PMSE. These have a narrower spectrum than the incoherent scatter spectrum, i.e. could be interpreted as lower temperatures. The observations shown in Fig. 4 are not affected by PMSE. We also have chosen the comparison level at 78 km, where we never detected PMSE. The broad spectra below 65 km, denoted by question-marcs, cannot be investigated here; they may be due to a change of ion mass.
Since we still assume that the observed temperature increases are too small to explain the disappearance of PMSE during this strong ionospheric disturbance, we need to search for another mechanism. Chilson et al. (2000) have observed a significant reduction of scatter cross section of PMSE during artificial electron heating of the PMSE plasma environment. We suspect that natural electron heating, which is quite pronounced during ionospheric disturbances, might have played a role as well. This needs much further investigations.

References:

Banks, P.M., Joule heating in the high-latitude mesosphere, J. Geophys. Res., 6709-6712, 1979.
Chilson, P.B., E. Belova, M.T. Rietveld, S. Kirkwood, and U.P. Hoppe, First artificially induced modulation of PMSE using the EISCAT heating facility, Geophys. Res. Lett., 27 , 3801-3804, 2000.
Rapp.M., J. Gumbel, F.J. Lübken, and R. Latteck, D-region electron number density limits for the existence of polar mesosphere summer echoes, J. Geophys. Res., 107(D15), doi: 10.1029/2001JG000915, 2002.

Turbulence Studies using UHF radar observations over Gadanki (13.5^{0}N, 79.2^{0}E)

D. Narayana Rao[1] , B. Vasantha[2] , N.V.P. Kiran Kumar[2] and I.V. Subba Reddy[2]
1. National MST Radar Facility, P.B. No.: 123, Tirupati – 517 502, India
2. Department of Physics, Sri Venkateswara University, Tirupati - 517 502, India
Email: profdnrao2001@yahoo.com

Abstract

Wind information and Doppler moments obtained from UHF radar observations for a period of one year (April 1999-March 2000) are used to study diurnal, monthly and seasonal variation of turbulence. Turbulence studies are made using Turbulent Kinetic Energy (TKE), spectral widths, Signal to Noise Ratio (SNR) and refractivity structure constant (Cn^2). From the diurnal observations TKE is found to be maximum around noon time and minimum in the night time indicating maximum turbulence in the day time. Spectral widths and SNR observations indicate the intensity of turbulence and mixing depth (height of the boundary layer) in different seasons. Peak SNR indicates the evolution of boundary layer representing mixing level depth or turbulent region. Spectral widths and refractivity structure constant show maximum in summer which show the intensity of turbulence.

Introduction

Boundary Layer is that part of the troposphere that is directly influenced by the presence of earth's surface and responds to surface forcings with a time scale of about an hour or less. These forcings include frictional drag, evaporation and transpiration, heat transfer, pollutant emission and terrain induced flow modification (Stull, 1988). It is also referred to as Atmospheric Boundary Layer (ABL). Atmospheric flows in the PBL are considered to be highly turbulent, mainly generated by buoyant convection or vertical shear in the horizontal fields.

Turbulent Kinetic Energy (TKE) is one of the most important quantities to study the turbulent boundary layer. Kallistratova et al., (2001) have compared turbulent momentum fluxes derived from Sodar and sonic anemometer measurements and determined turbulent kinetic energy (TKE) from measurements of three wind components by Doppler radar, momentum flux from the density of turbulent kinetic energy. They showed a good comparison of the results. Hadi et al., (2000) studied Boundary Layer structure over Gadanki during pre-monsoon period and concluded that PBL height varies with time and local factors, which do not seem to depend on coriolis factor. PBL mixing height is deduced from SNR by Angevine et al., (1998) and from reflectivity by Krishna Reddy et al., (2000) and concluded that strong SNR is induced mainly by the temperature and humidity gradients at the top of PBL rather than by turbulence.

2. Data base

One year Lower Atmospheric Wind Profiler (LAWP) observations at Gadanki from April 1999 to March 2000 are utilized for the present study. These studies are related to ten clear air echo days in each month for the observation period of one year. LAWP gives continuous measurement of wind over the entire diurnal cycle (24 hours).The available data in an hour is averaged to represent hourly data. So 24-hourly averages are available on all the days. Seasons are classified as Summer (March, April and May), Monsoon (June, July, August and September), Post- monsoon (October, November and December) and Winter (January and February). Diurnal variation of studies are represented choosing a typical day in each season. They are 19th April 1999 (summer), 11th July 1999 (Monsoon), 24th November 1999 (Post- monsoon) and 25th January 2000 (Winter). This paper is organized as follows. Database and analysis are presented in section 2. Results and discussion are presented in section 3. Diurnal variation of turbulent kinetic energy, spectral widths, signal to noise ratio and refractivity structure constant in different seasons are presented in section 3.1. Monthly

variations of spectral widths, refractivity structure constant are presented in section.3.2. Summary and results are presented in section 4.

3. Results and discussion

3.1.1 Diurnal variation of Turbulent Kinetic energy

Turbulent Kinetic Energy (TKE) per unit mass is defined as

$$\frac{TKE}{m} = \frac{1}{2}(\overline{u'^2} + \overline{v'^2} + \overline{w'^2})$$

where *u' ,v' and w'* are turbulent portion of the wind in zonal, meridional and vertical directions respectively (Stull,1988)

Figure.1 shows diurnal variation of turbulent kinetic energy per unit mass in different seasons at four different altitudes. During summer season, a large diurnal variation is observed from the early morning hours towards noon time and then decreasing towards night time. Maximum TKE of 60 m 2 s -2 is observed at around 1100 hours LT at an altitude of 0.6 km. Above that altitude TKE is decreasing with altitude, indicating maximum turbulence at lower altitude regions around noon time. During monsoon season, TKE is increasing with altitude and is maximum of 100 m 2 s -2 around 0600 hours LT at an altitude of 1.5 km, 95 m 2 s -2 at 0.90 km around 1500 hours LT , 90 m 2 s -2 at 1.2 km around 1300 hours LT. During post- monsoon season, TKE is increasing with altitude up to 1.2 km and then decreasing slowly with altitude. Maximum TKE of 60 m 2 s -2 is found around 1300 hours LT. In general TKE is maximum around noon time and minimum in the night time indicating maximum turbulence occurrence during the day time.

3.1. 2.Diurnal variation of Spectral widths and Signal to Noise ratio

Figure 2 (a) shows diurnal variation of spectral widths observed on typical days in different seasons. During summer season, spectral widths are low before sunrise and increasing towards noon time and then decreasing till evening and then increase in the night time and remain stable for some time. During monsoon spectral width is maximum in the early morning hours and is decreasing towards night time. During post- monsoon, it is minimum in day time, but maximum in night time. During winter season, spectral widths are minimum compared to all other seasons. Spectral width is maximum in day and night times. From the figure it is observed that spectral widths are maximum around noon time in summer and winter, morning time in monsoon and night time in post-monsoon seasons, indicating maximum turbulence at those timings.

Figure 2(b) shows diurnal variation of SNR observed on typical days. The growth of convective boundary layer, can be identified as strong echo layer rising up quickly in the morning until it reached maximum height around noon. The peak of SNR in summer season reveals boundary layer structure. It also indicates the evolution of boundary layer representing mixing level depth or turbulent region. The peak of SNR is low during early hours after sunrise and goes on increasing with time and attains maximum around noon time and a sudden fall due to dissipation and again increasing due to inversion. A clear diurnal variation of boundary layer structure indicated by the peak SNR in summer season with a maximum height of ~ 2 km around noon time is observed. In general the height of peak SNR, indicating the convective boundary layer height is about 2 km, and low in other seasons i.e. post- monsoon, monsoon and winter. around noon time is observed. Kunhi Krishnan et al., (2001) have observed boundary layer structure as a case study (March 19, 1998) over Gadanki. They reported that ABL depth indicated by the reflectivity goes up to 1.5 km by 12.30 hrs associated with trade wind inversion prevailing over Gadanki and clear evolution of ABL is not observed during August due to intermittency of convective activity.

3.1.3 Diurnal variation of Refractivity Structure constant

A clear air radar such as the boundary- layer profiler receives its return signal primarily from inhomogeneities of the radio refractive index. These inhomogeneities are characterized by the refractivity structure constant Cn^2 . The profiler SNR at a given range is proportional to Cn^2 (Wyngard and LeMone, 1980) and Fairall, (1991) showed that Cn^2 peaks at the inversion atop CBL. Therefore a peak in the range corrected SNR indicates the CBL top and volume reflectivity is given by the relationship

$$SNR = \frac{P_t \alpha_t \alpha_t \tau_e A_e \cos\chi}{8\Pi(\alpha_r T_c + T_r) K B_n r^2 \Delta r} \eta$$

The refractivity structure constant $C_n^2 \approx \frac{\lambda^{1/3}}{0.38}\eta$ indicates the strength of turbulence. Figure 3 shows diurnal variation of refractivity structure constant on typical days. During summer season, turbulence is minimum during early hours. The height up to which turbulent mixing is increasing up to noon time is indicated by an increased structure constant value of -14.2 m -2/3 at 2.2 km at around 1200 hours LT, then it suddenly drops at an hour of 1800 hours LT. This value suddenly attains maximum and remains stable. From the figure it is seen that turbulence is patchy and intermittent. Vigorous mixing is observed during noon time. During monsoon season, Cn^2 is maximum of ~ 15 m-2/3 during early hours of the day i.e. from 0400 hours LT to 1000 hours LT and a sudden drop is observed intermittently. Maximum turbulence is observed at around 2.0 km at 0600 hours LT. After that hour it tends to decrease, indicating less mixing during day time. During post- monsoon season turbulent regions are observed during night time. Low value of Cn^2 of ~ 15.2 m -2/3 are observed during day time. Maximum value of Cn^2 of ~ 13.2 m -2/3 is observed during night time.

3.2 Monthly variation of spectral width and Refractivity Structure Constant

Figures 4(a) and 4(b) show monthly variation of spectral widths and refractivity structure constant averaged over ten days from afternoon hours (1200-1400LT) in a month for a period of one year. From figure (a), it can be seen that the spectral width is maximum in the month of May at an altitude of 0.6 km, indicating strong turbulence. Spectral widths are decreasing from the summer months towards winter. Maximum value of 0.55 ms^{-1} is observed in summer and minimum of 0.2 ms^{-1} in winter season. A similar feature is also evident from the figure (b) of logarithm of refractivity structure constant. It shows a maximum of -14.8 $m^{-2/3}$ in summer at an altitude of 0.6 km and then slightly decreasing in the subsequent seasons and shows a low value of ~-16.25 $m^{-2/3}$ in winter. It is observed that Log Cn^2 value is varying in between the values -14.25 $m^{-2/3}$ and -16.25 $m^{-2/3}$ in the mid afternoon hours over the above period.

4. Summary and conclusions

Diurnal and seasonal variations of refractivity structure constant are studied in different seasons using typical clear air days. Seasonal variation is studied using ten day clear air day averages in each month for a period of one year. Peak SNR represents boundary layer height. A well defined diurnal variation of boundary layer height is observed in summer season. It is maximum around 2 km in summer and minimum in winter season, may not be well defined in monsoon and post- monsoon seasons. From the Turbulent kinetic energy observations, TKE is found to be maximum around noon time in summer and winter seasons, indicating maximum turbulence. Spectral widths and SNR observations indicate the intensity of turbulence and mixing depth in different seasons. Mixing depth indicated by peak SNR is found to be maximum around noon time in summer season. Spectral widths and Refractivity structure constant show maximum in summer and minimum in winter seasons around noon time. Seasonal variation shows similar features of diurnal variations in all the measurements.

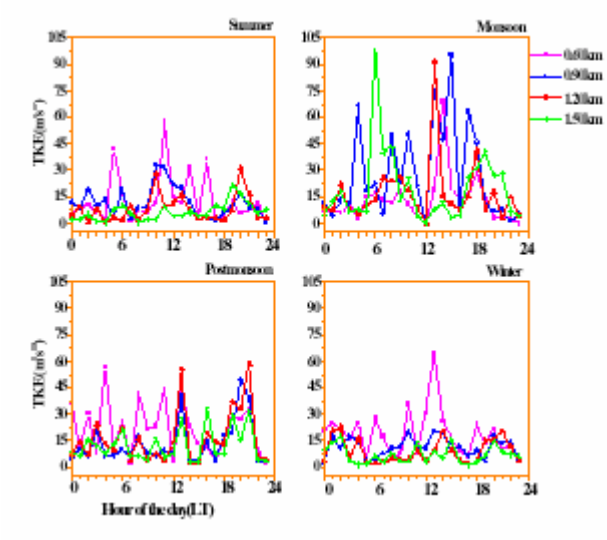

Figure 1. Diurnal variation of Turbulent Kinetic Energy at four different altitudes in four different seasons.

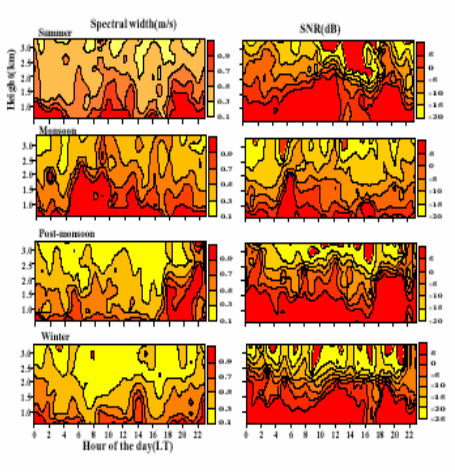

Figure 2. Height –time contour diagram of (a) spectral width (m/s) b) SNR (dB) observed on typical days 19 April 1999 (summer), 11 July 1999 (monsoon), 24 Novenber 1999 (post-monsoon),and 25 January 2000 (winter) in different seasons.

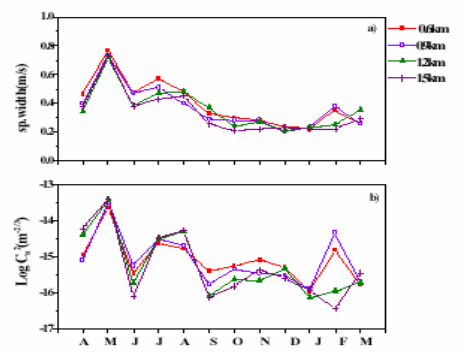

Figure 3. Diurnal variation of refractivity structure constant in four different seasons.

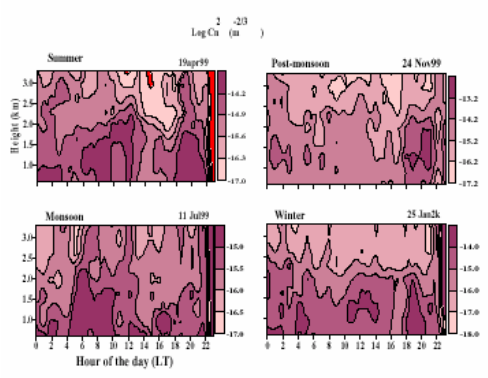

Figure 4. Monthly variation of a) spectral width (m/s) and b) Log Cn2 averaged over 1200-1400 LT of ten clear air days in a month of the year (April 1999-March 2000)

WIND MEASUREMENTS BY THE CHUNG-LI RADAR IN THE PRESENCE OF STRONG CLUTTER AND HARD TARGETS

Eleanor Praskovskaya[1], Alexander Praskovsky[2], Jenn-Shyong Chen[3], and Yen-Hsyang Chu[4]

[1]Colorado Research Associates, 3380 Mitchell Lane, Boulder, CO 80301, USA
[2]National Center for Atmospheric Research, 3450 Mitchell Lane, Boulder, CO 80301, USA
[3]Chien-Kuo Institute of Technology, Chang-Hua, Taiwan 500, R.O.C. (Taiwan)
[4]Institute of Space Science, National Central Univ., Chung-Li, Taiwan 320, R.O.C. (Taiwan)

The received signals from atmospheric spaced antenna (SA) radars might be contaminated by ground clutter and, although less frequently, hard targets. The contamination adversely affects the performance of the correlation function (CF)-based data analysis techniques. Let us consider the standard complex signals from two receivers $E_1(t)$ and $E_2(t)$ where t is time. The second order cross CF is defined as follows (Doviak et al., 1996):

$$C_{12}(\tau) = \left\langle E_1(t) E_2^*(t+\tau) \right\rangle \Big/ \left\langle E_1(t) E_1^*(t) \right\rangle \qquad (1)$$

Hereafter τ is the temporal separation, the brackets $\langle\ \rangle$ denote the ensemble averages, and the superscript * denotes complex conjugation. The auto CF $C_{11}(\tau)$ is a particular case of (1) at $E_1(t) = E_2(t)$. The function $C_{12}(\tau)$ is not affected by white noise with the temporal scale $T_n = 0$, and $C_{11}(\tau)$ is affected by such noise only at $\tau = 0$. For this reason, white noise in the received signals can be easily taken into account in the CF-based techniques such as Full Correlation Analysis (FCA) and the Holloway – Doviak method; see Briggs (1984), Briggs and Vincent (1992); and Doviak et al. (1996), Holloway et al. (1997), respectively. However, no reliable approach to measuring characteristics of a scattering medium with CF-based techniques have been yet developed when noise with a large scale $T_n \geq \tau_p$, such as ground clutter and hard targets, is present; here τ_p is a separation where $\left|C_{12}(\tau_p)\right|$ has the maximum. The major problem is that such noise affects CF at all separations τ and often cannot be distinguished from a signal itself.

A structure function (SF)-based method UCAR-STARS (University Corporation for Atmospheric Research - STructure function Analysis of Received Signals) has been developed recently by Praskovsky and Praskovskaya (2003a, b). The STARS unique feature is a low sensitivity to noise with large temporal scale T_n. This feature was shown theoretically in Praskovsky and Praskovskaya (2003a), and demonstrated experimentally for the case of strong ground clutter in Praskovsky et al. (2003). The STARS low sensitivity to noise with large T_n has simple physical explanation. The second order cross SF is defined as follows (Tatarskii, 1971, chap. 1A):

$$D_{12}(\tau) = \left\langle \left[S_1(t) - S_2(t+\tau)\right]^2 \right\rangle \Big/ \left\langle \left[S_1(t) - \left\langle S_1(t) \right\rangle\right]^2 \right\rangle \qquad (2)$$

where $S(t) = E(t)E^*(t)$ is the instantaneous signal power. The auto SF is a particular case of (2) at $S_1(t) = S_2(t)$. The increment $S_1(t) - S_2(t+\tau)$ is a band-pass filter that extracts fluctuations with temporal scales around $|\tau|$. Only small temporal separations $|\tau| \leq 3\delta t$ are used in STARS, where δt is the radar inter-sample time interval. It is clear that any component in the received signal with a sufficiently large temporal scale $T_n >> 3\delta t$ cannot affect SF because it is merely filtered by the increment. The objective of this paper is a

further experimental test of the STARS low sensitivity to the both ground clutter and hard targets with the Chung-Li radar (CLR).

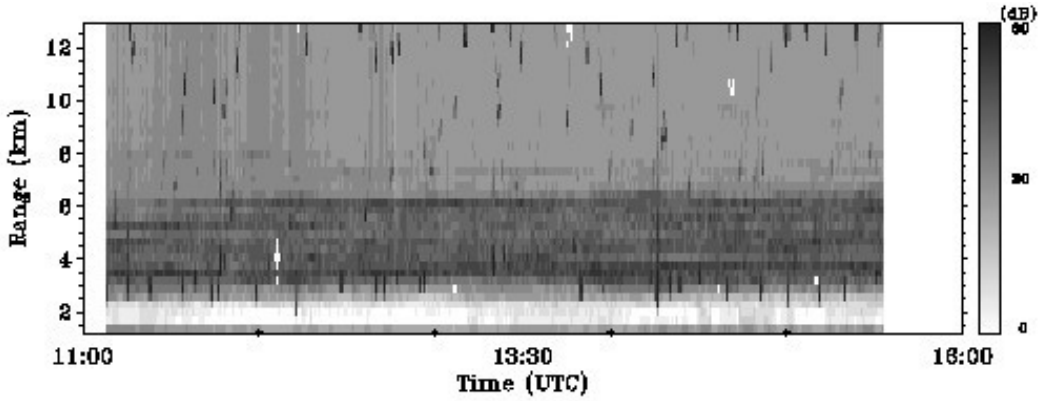

Figure 1. The return signal power during the CLR experiment on 19 June 2002.

The CLR is located at the campus of the National Central University (NCU) of Chung-Li, Taiwan at 24.58°N and 121.0°E and is operated by the Center for Space and Remote Sensing Research and the Department of Atmospheric Physics of the NCU. CLR is a dual-mode radar with the operational frequency 52 MHz; it allows the application of a five-beam Doppler Beam Swinging (DBS) mode as well as a spaced antenna mode with three separate antenna modules. Each of these modules consists of 64 Yagis with the beam width of a single module of 7.5°, and that of the combined three modules of 5°; see Röttger et al. (1990) for details.

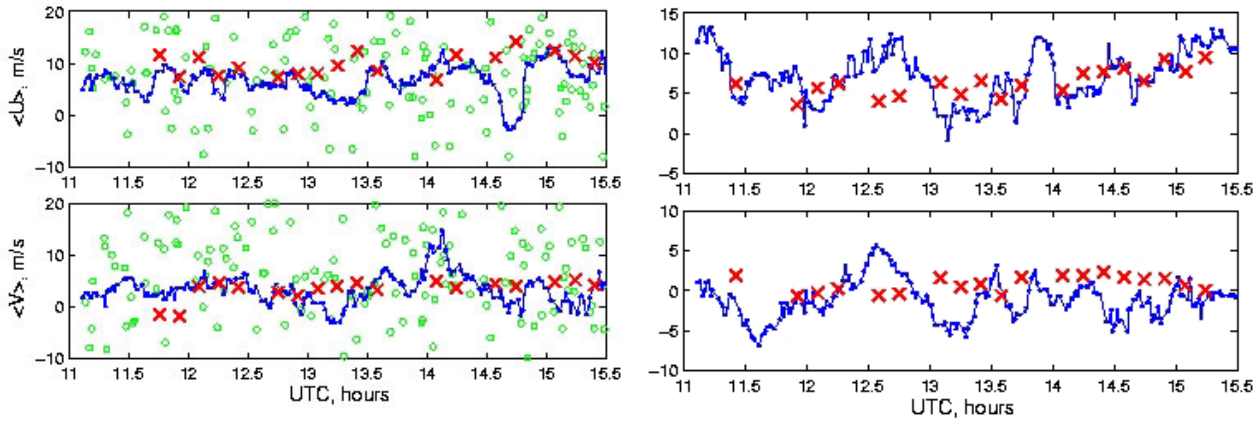

Figure 2. Time series of the easterly $\langle U \rangle$ and northerly $\langle V \rangle$ mean winds on 19 June 2002 at a height above the radar 3.45 km (left column) and 7.05 km (right column). Red crosses, DBS; blue bullets, STARS; green circles, FCA.

The data collection for comparing SA techniques with DBS was executed on 19 June 2002. The radar was operated 8.2 min. in the SA mode with three separate receiving modules, then 1.3 min. in the DBS mode with only one receiving module; the sequence was continuously repeated for approximately 4.5 hours. Both in DBS and SA modes, the radar pulse repetition frequency was 3,333 Hz, and the range resolution and the gate separation were 300 m. At the standard CLR operations, three modules are used for a transmission. Due to temporal defects in the radar hardware, only one module was used in the experiment for the transmission in both DBS and SA modes. The transmitted beam width was about 1.5 times larger, and the side lobes were much wider and stronger than those in the standard operations. Therefore, the received signals were more heavily affected by ground clutter and hard targets such as airplanes. CLR is located quite close to the airplane flight routes in the vicinity of the Chan

Kai Shai airport. The signal power for one receiving module is shown in Fig. 1; the dark vertical strikes at high altitudes are signatures of the airplanes, and those at low altitudes show intensive ground clutter. Although the analyzed data set is untypical for CLR, it is very useful for testing SA data analysis techniques in the adverse measurement conditions.

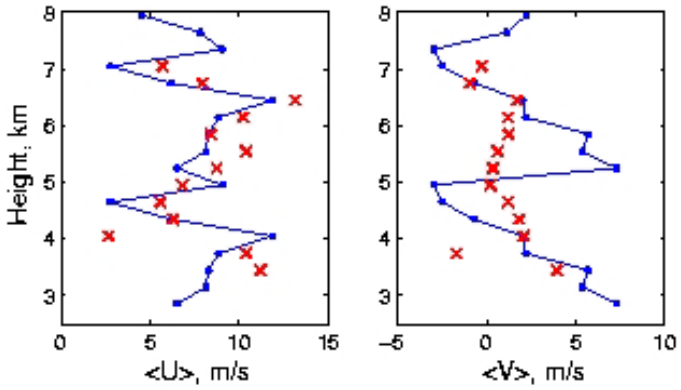

Figure 3. The vertical profiles of the easterly $\langle U \rangle$ and northerly $\langle V \rangle$ mean winds above the CLR on 19 June 2002 at 12:09 UT. Red crosses, DBS; blue bullets, STARS.

The mean horizontal wind speed components $\langle U \rangle$ (toward east) and $\langle V \rangle$ (toward north) were retrieved from the CLR signals in the SA mode with STARS and FCA methods at the same averaging time T_{av} = 61.4 s, which is close to the DBS T_{av} = 76.8 s. Three variants of FCA by Fooks (1965), Meek et al. (1980), and Briggs (1984) were applied to the data. The best FCA results using the Briggs (1984) technique are shown in Fig. 2, left column. The ordinate in this figure is truncated; total scatter of the FCA results exceeds ±100 m/s. The poor FCA performance for the analyzed data set is expected because CF-based techniques are strongly affected by noise with a large scale T_n. The STARS-produced mean winds are in reasonable agreement with those produced by DBS when the latter does not fail. The agreement is illustrated further in Fig. 3; at this time interval DBS retrieved winds at most heights. One can see in Figs. 2 and 3 that the DBS performance is quite poor in spite of sufficiently high signal-to-noise ratio; the latter varied from approximately 0 dB to 15 dB. The poor DBS performance is expected in the presence of hard targets and strong ground clutter.

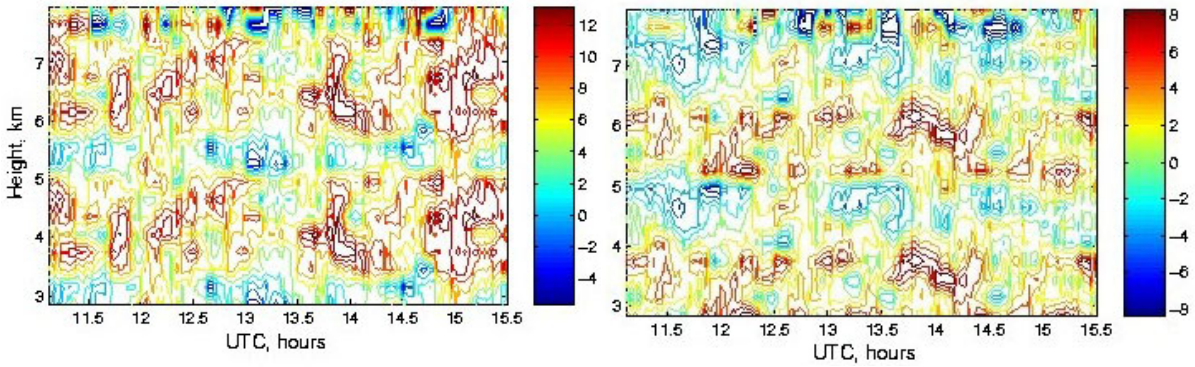

Figure 4. The contour plots of the STARS-produced mean horizontal wind speed components above CLR on 19 June 2003. Left, $\langle U \rangle$; right, $\langle V \rangle$.

At the same time, STARS produced plausible winds and turbulent intensity (not shown in this paper) for all studied heights and times. The contour plots of the mean winds are shown in Fig. 4; one can see propagation of gravity waves in vertical and horizontal directions. The

waves can be observed more clearly in the STARS results than in those produced by DBS; Figs. 2 and 3.

The presented results show that DBS and traditional SA techniques failed most of time in retrieving the mean winds in the presence of strong ground clutter and hard targets while STARS performance was reasonable during the whole data collection period. The results further demonstrate that STARS is not very sensitive to noise with large temporal scale; see also Praskovsky et al. (2003). Therefore, the method could be applied efficiently in quite adverse measurement conditions such as in airports, mountainous areas, and so on. This feature could make the UCAR-STARS technique a useful alternative to the traditional, CF and spectra-based data analysis methods for SA radars.

Acknowledgements. The first author (EP) was sponsored by the National Science Foundation (NSF) Grant ATM-0122877. NCAR is sponsored by the NSF.

REFERENCES

Briggs, B. H., The analysis of spaced sensor records by correlation techniques, *MAP Handbook*, *13*, 166-186, 1984.

Briggs, B. H., and R. A. Vincent, Spaced-antenna analysis in the frequency domain, *Radio Sci*., *27*, 117-129, 1992.

Doviak, R. J., R. J. Lataitis, and C. L. Holloway, Cross correlations and cross spectra for spaced antenna wind profilers, 1, Theoretical analysis, *Radio Sci*., *31*, 157-180, 1996.

Fooks, G.F., Ionospheric drift measurements using correlation analysis: method of computation and interpretation of results, *J. Atmos. Terr. Phys*., *27*, 979-989, 1965.

Holloway, C. L., R. J. Doviak, S. A. Cohn, R. J. Lataitis, and J. S. Van Baelen, Cross correlations and cross spectra for spaced antenna wind profilers, 2, Algorithms to estimate wind and turbulence, *Radio Sci*., *32*, 967-982, 1997.

Meek, C.E., A.H. Manson, and J.B. Gregory, An efficient method for analyzing ionospheric drift data, *J. Atmos. Terr. Phys*., *42*, 835-839, 1980.

Praskovsky, A. A., and E. A. Praskovskaya, Structure-function-based approach to analyzing received signals for spaced antenna radars, *Radio Sci*., *38*(4), 7-1 - 7-25, 2003a.

Praskovsky, A. A., and E. A. Praskovskaya, Towards the advanced measurements of atmospheric turbulence by spaced antenna radars, *this volume*, 2003b.

Praskovsky, A. A., E. A. Praskovskaya, W. O. J. Brown, S. A. Cohn, and S. Oncley, Advanced measurements of atmospheric turbulence with a UHF spaced antenna wind profiler, Submitted to *Ann. Geophys*., MST-10 Special issue, 2003.

Röttger, J., C. H. Liu, J. C. Chao, A. J. Chen, Y. H. Chu, I.-J. Fu, C. M. Huang, Y. W. Kiang, F. S. Kuo, C. H. Lin, and C. J. Pan, The Chung-Li VHF radar: Technical layout and a summary of initial results, *Radio Sci*, *25*, 487-502, 1990.

Tatarskii, V. I., *The Effects of the Turbulent Atmosphere on Wave Propagation*, UDC 551.510, U.S. Dep. of Commerce, Washington, D.C., 1971.

MU RADAR ESTIMATION OF DOWNWARD TURBULENT OZONE FLUXES NEAR THE TROPOPAUSE

Nikolai M. Gavrilov (1) and Shoichiro Fukao (2)

(1) Saint-Petersburg State University, Atmospheric Physics Department, Petrodvorets, St. Petersburg, 198504, Russia, gavrilov@pobox.spbu.ru
(2) Kyoto University, Center for Atmospheric and Space Research, Uji, Kyoto 611, Japan, fukao@kurasc.kyoto-u.ac.jp

1. Introduction

One of the important problems is the role of gravity waves and turbulence in diffusion of ozone and gas species in the tropo-stratosphere. It is supposed recently that the main mechanism of the transport of admixtures influencing the ozone layer between the troposphere and the stratosphere is the general circulation of the atmosphere creating upward motions near equator and downward motions at the middle and high latitudes [Holton, 1990]. Alternatively, a sharp change of vertical temperature gradient near the tropopause can make a sharp increase in the amplitudes of IGWs propagating upwards from the troposphere. It can lead to IGW breaking and to the generation of increased turbulence, which can make the middle latitude tropopause more transparent for the diffusive transport of the admixtures from below. In this paper, we studied this mechanism of IGW and turbulence influence on the atmospheric admixtures transport through the tropopause using a numerical model, which describes IGW propagation and turbulence generation in the non-homogeneous atmosphere.

The numerical model described by Gavrilov and Fukao (1999) is used to study the propagation of IGW harmonics generated by hydrodynamic sources in the atmosphere. It gives the integral energy characteristics of a spectrum of IGW harmonics with various frequencies, horizontal phase speeds and directions of propagation. The model includes IGW generation on the Earth surface and inside the atmosphere, realistic vertical profiles of the mean wind and temperature, IGW dissipation, destruction of waves and generation of turbulence. The results of numerical calculations are compared with the measurements of parameters of IGWs and turbulence in the tropo-stratosphere with Japanese MU radar.

2. Numerical simulation of wave induced turbulent diffusivity near the tropopause.

Sharp increase of vertical temperature gradient at the tropopause may lead to a sharp increase in the amplitudes of IGWs propagating upward from the troposphere. Such IGWs may break and generate increased turbulence, which may make the middle latitude tropopause more transparent for the diffusive admixtures transport. Such diffusive admixtures transport may make an alternative to the traditionally assumed circulation with upward flux of atmospheric mass from the troposphere to the stratosphere in the equatorial region and its downward flux in the middle and high latitudes. In this study, we made evaluations of the relative importance of this mechanism of IGW and turbulence influence on the admixtures transport through the tropopause using a numerical model, which describes the IGW propagation and turbulence generation in the inhomogeneous atmosphere.

The model calculates the integral characteristics of a spectrum of wave harmonics with different frequencies, horizontal phase speeds and directions of propagation. The model is based on the wave action balance equation for every wave harmonic [see Gavrilov, 1997; Gavrilov and Fukao, 1999]. Calculation of the coefficients of turbulent diffusion produced by breaking IGWs is made using the model by Gavrilov and Yudin [1992]. Previously verifications of the model by Gavrilov and Fukao [1999] showed that the model reproduces the seasonal cycles of the amplitudes of IGW zonal wind variations having a maximum in

winter and a minimum in summer near the tropopause. In the mesosphere, the seasonal cycle changes having the maxima in winter and summer, also minima in equinoxes in correspondence with observations [see Gavrilov and Fukao, 1999].

In this study, we calculated vertical profiles of the turbulent diffusion coefficient produced by a spectrum of breaking IGWs. Specifically, we studied the influence of sharp changing of vertical temperature gradient on the changes of the conditions of IGW propagation, increasing their destruction and forming a maximum of the turbulent diffusivity near the tropopause. The mean profiles of wind and temperature are specified using the standard atmospheric models MSIS-90 and HWM-93 for the geographic coordinates of observation site Shigaraki (Japan), from which we have the MU radar data. Below altitude 30 km, we improved the vertical profiles of background wind and temperature from the data of the reanalysis of radiosonde measurements at the National Center for Atmospheric Research of Boulder, USA. Fig. 1 shows the vertical profiles of background temperature and wind for January and July at Shigaraki (Japan).

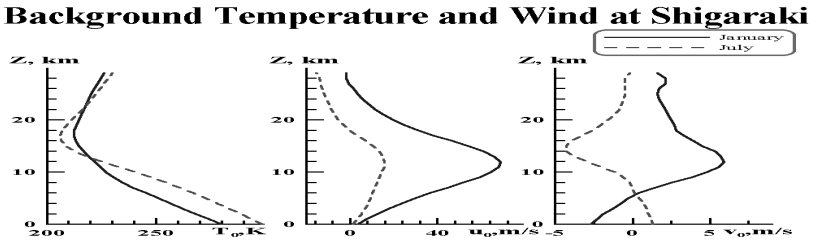

Fig. 1. Vertical profiles of background temperature (left) and zonal (middle) and meridional (right) components of wind velocity at Shigaraki for January (solid lines) and July (dashes).

Fig. 2 represents the corresponding calculated standard deviations of wind velocity produced by a spectrum of IGWs in the ranges of periods 0.3 – 6 hours and horizontal phase speeds 3 – 60 m/s and of the coefficient of turbulent diffusion produced by breaking IGWs. One can see that the IGW intensity and the turbulent diffusivity have maxima at altitudes 15 – 20 km, where the tropopause is located at different seasons. The measurements of turbulent diffusivity with the MU radar at Shigaraki show its maxima near the tropopause [Fukao et al., 1994] and our calculated values well enough correspond to the measured ones.

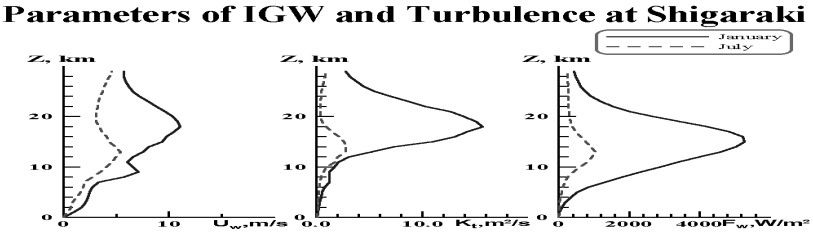

Fig. 2. Calculated standard deviation of horizontal wind velocity (left), turbulent diffusivity (middle) and vertical flux of wave energy (right) produced the IGW spectrum for background fields from Fig. 1 for Shigaraki in January (solid lines) and July (dashes).

In Fig.2, the maxima of IGW amplitudes and turbulence diffusivity in the tropopause region are stronger in winter than in summer.

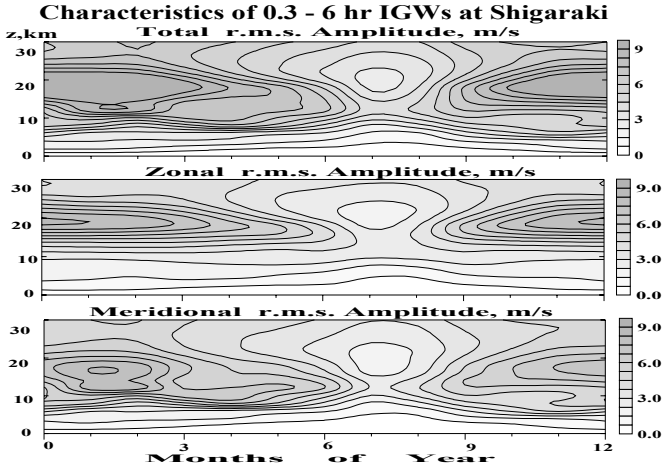

Fig. 3. Calculated standard deviations of horizontal wind (top), zonal (middle) and meridional (bottom) wind components produced by the IGW spectrum and calculated for Shigaraki.

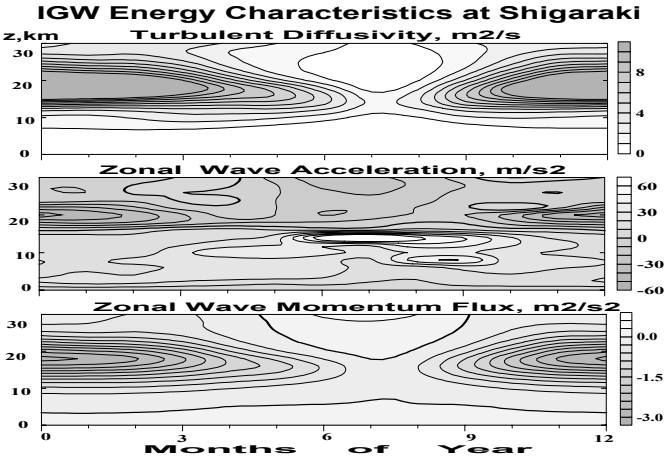

Fig. 4. Coefficient of turbulent diffusion (top), zonal wave acceleration of the mean flow (middle) and the zonal component of vertical wave momentum flux (bottom) produced by the IGW spectrum and calculated for the Issyk-Kul station.

The presence of turbulence in the atmosphere produces the mixing, which leads, in particular, to the fluxes of atmospheric admixtures from the troposphere to the stratosphere or back depending on the vertical distribution of the particular admixture. In particular, turbulence may lead to descend of ozone from the stratosphere to the troposphere. The vertical flux of an admixture can be described by the following formulae:

$$F = -Kncd \ln c / dz , \qquad (1)$$

where K is the turbulent diffusion coefficient; n is the number density of the atmosphere; c is the mixing ratio of the considered admixture. Using the values of c for the altitudes 12 – 17 km from the model of vertical ozone profile [Zuev and Komarov, 1986] for the values of $K \sim$ 1 – 10 m^2/s shown in Figures 2 and 4 we may obtain the estimate $F \sim$ (1–10)×10^{14} m^{-2} s^{-1}. It is comparable with usually assumed downward ozone transport by the general circulation of the atmosphere.

The main recently assumed mechanism of penetration of stratospheric ozone into the troposphere is its transport by the general atmospheric circulation from equatorial latitudes and descending of the air in the middle latitudes [Holton, 1990]. The mean downward ozone flux due to the circulation transport is estimated to be about $F \sim 7\times10^{14}$ м$^{-2}$s^{-1} [Ebel et al., 1993], while the estimations of tropospheric ozone require the fluxes of stratospheric ozone of the order of $(4\text{-}8)\times10^{14}$ м$^{-2}$ s^{-1} [e.g. Crutzen, 1988]. Comparison of these values with the estimations of the ozone diffusion flux obtained above show the comparability of these values. Therefore, the turbulence generation by gravity waves near the tropopause may produce substantial transport of ozone from the stratosphere to the troposphere.

One can estimate the time scale characteristic for the transport into the troposphere of all stratospheric ozone (in the absence of its sources): $\tau \sim N/F$, where N is the total ozone content in the atmospheric column above considered altitude. Described above estimations of K together with the model of vertical ozone distribution [Zuev and Komarov, 1986] lead to the values of $\tau \sim 0{,}3 - 3$ day^{-1}. These values show that the changes of IGW intensity and turbulence near the tropopause may relatively fast lead to the changes of stratospheric ozone concentration and to a shift in the photochemical equilibrium. Therefore, local enhancements of IGW intensity and turbulence at tropospheric altitudes over mountains due to their orographic excitation may lead to the changes in total ozone over mountain regions. This may explain observed TO anomalies over mountain regions [Kazimirovsky and Matafonov, 1998].

3. Conclusion

A numerical simulation was used to verify the hypothesis about the influence of sharp change of vertical temperature gradient at the tropopause on the increase of the amplitudes of IGWs propagating upwards from the troposphere. Estimations of vertical ozone flux from the stratosphere to the troposphere are comparable with usually supposed ozone downward transport with the general atmospheric circulation.

Acknowlegement. This study was partly supported by the Russian Basic Research Foundation and by the International Science and Technology Center.

References.

Crutzen, P. J., Tropospheric ozone: An overview, *In I.S.A Isaken (ed.), Tropospheric Ozone*, D. Reidel Publ. Company, Dordrecht, 3-32, 1988.

Ebel, A., H. Elbern, and A. Oberreuter, Stratosphere-troposphere air mass exchange and cross-tropopause fluxes of ozone. In *Coupling processes in the lower and middle atmosphere*, eds. Thrane, ER. V. et al., Kluner, Dortrecht, pp. 49-65, 1993.

Fukao, S., M. D. Yamanaka, N. Ao, W. K. Hocking, T. Sato, M. Yamamoto, T. Nakamura, T. Tsuda, and S. Kato, Seasonal variability of vertical eddy diffusivity in the middle atmosphere, 1. Tree-year observations by the middle and upper atmosphere radar, *J. Geophys. Res.*, *99*, 18,973-18,987, 1994.

Gavrilov N. M., Parameterization of momentum and energy depositions from gravity waves generated by tropospheric hydrodynamic sources. *Ann. Geophys.*,*15*, 1570-1580, 1997.

Gavrilov N. M., Yudin V.A. Model for Coefficients of Turbulence and Effective Prandtl Number Produced by Breaking Gravity Waves in the upper Atmosphere, *J. Geophys. Res.*, *97*, 7619 -7624, 1992.

Holton, J. R., On the global exchange of mass between the stratoshere and troposphere, *J. Atmos. Sci.*, *47*, 392–395, 1990.

Kazimirovsky, E. S., and G. K. Matafonov, Continental scale and orographic structures in the global distribution of the total ozone, *J. Atmos. Solar-Terr. Phys.*, *60*, 993-996, 1998.

Zuev, V. E., and V. S. Komarov, *Statistical models of temperature and gas components of the atmosphere*, Hydrometeoizdat Press, Leningrad, 1986.

LARGE VELOCITIES MEASURED AT MF AND HEIGHTS ABOVE 100KM: REAL OR SPURIOUS ?

Chris Meek and Alan Manson

Institute of Space and Atmospheric Studies
University of Saskatchewan, Canada

Abstract: The MF data set for Saskatoon has been scanned for large speeds (e.g. greater than 150 m/s). These data are not numerous and usually occur at heights greater than we normally use. They are usually excluded from most analyses by our upper speed selection limit of 170m/s, by rejection of signals above the height of maximum signal (assumed to be obliques), or by our virtual height limit criterion: viz. reject heights greater than 94/105 Km in summer/winter. The latter is necessary in tidal analysis to insure that the daytime and nighttime data refer to the same real height.
Here we look at these large wind values separately, but due to lack of space, we can show only winter data. In winter they tend to occur in the late afternoon, are not spurious, and also contain a tidal signal (in seasonal averages). Data from a separate experiment (a non-coherent system run in winter 1987-88) which looked for signal peaks from 70-355 Km virtual height) are used to argue that we can sometimes see through the daytime E-region.

Discussion:

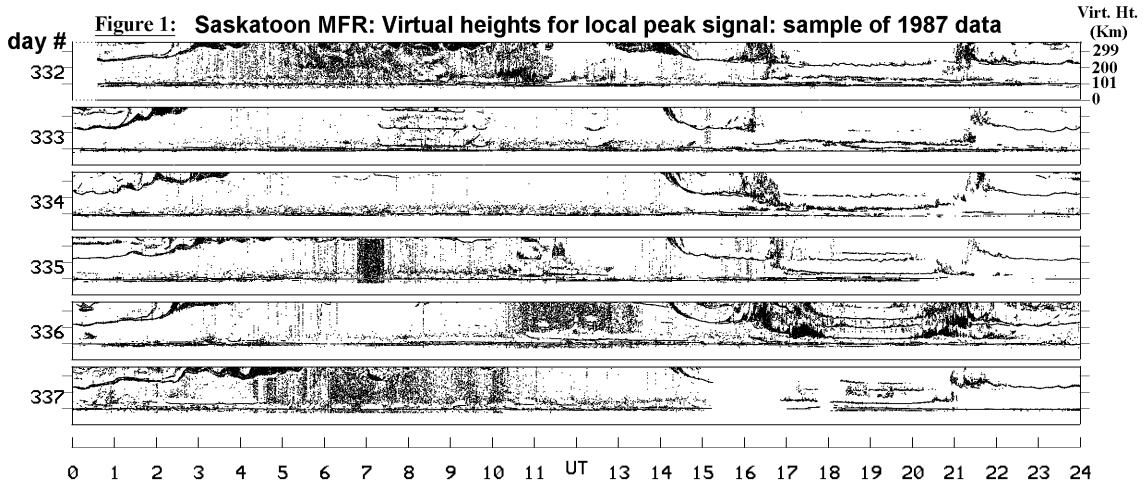

Figure 1. Sample of the 1987 local signal peak data

Figure 1 shows a sample of the 1987 local signal peak data; the time resolution is ~20 sec. Echoes above the E region are most common around 20-22 UT (mid afternoon). These are not multiple hop, since otherwise we would see a lower echo as well. Some F-region splitting (e.g. day 336/01-03 UT) is seen, probably O and X since the experiment used linear polarization.

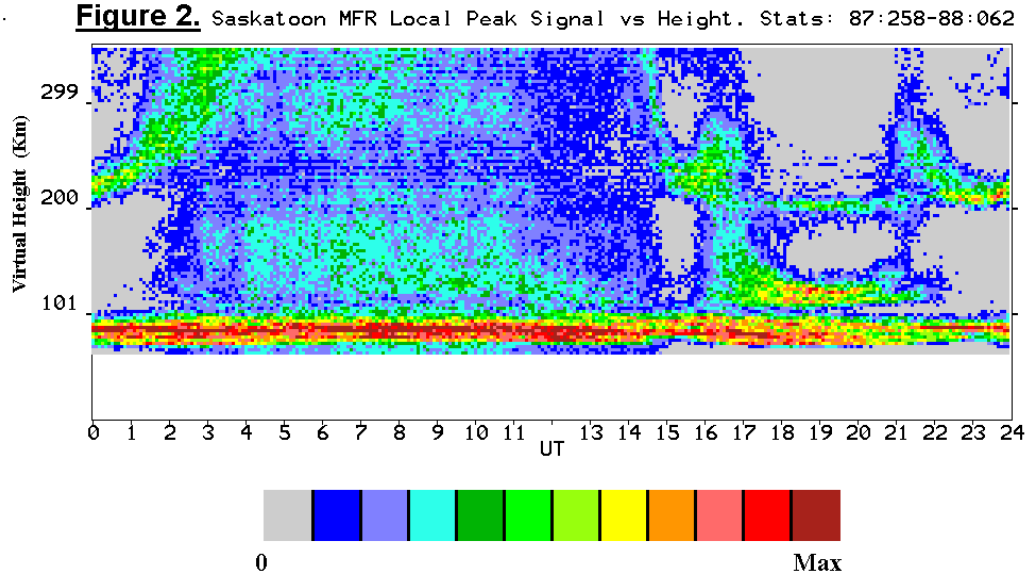

Figure 2. Statistics of numbers of echoes over a whole winter period

Figure 2 shows statistics of numbers of echoes over whole winter period. On the whole, before 21UT, the high echoes are apparently double hop from a lower height – maybe sporadic E. After 21UT the upper echoes do not appear to be double hop. The 'inverted-V' structure in virtual height in early morning and late afternoon is most likely due to the peak E-region plasma frequency, foE, building or decaying respectively past the fixed system frequency (2.219MHz), rather than an ascending or descending layer.

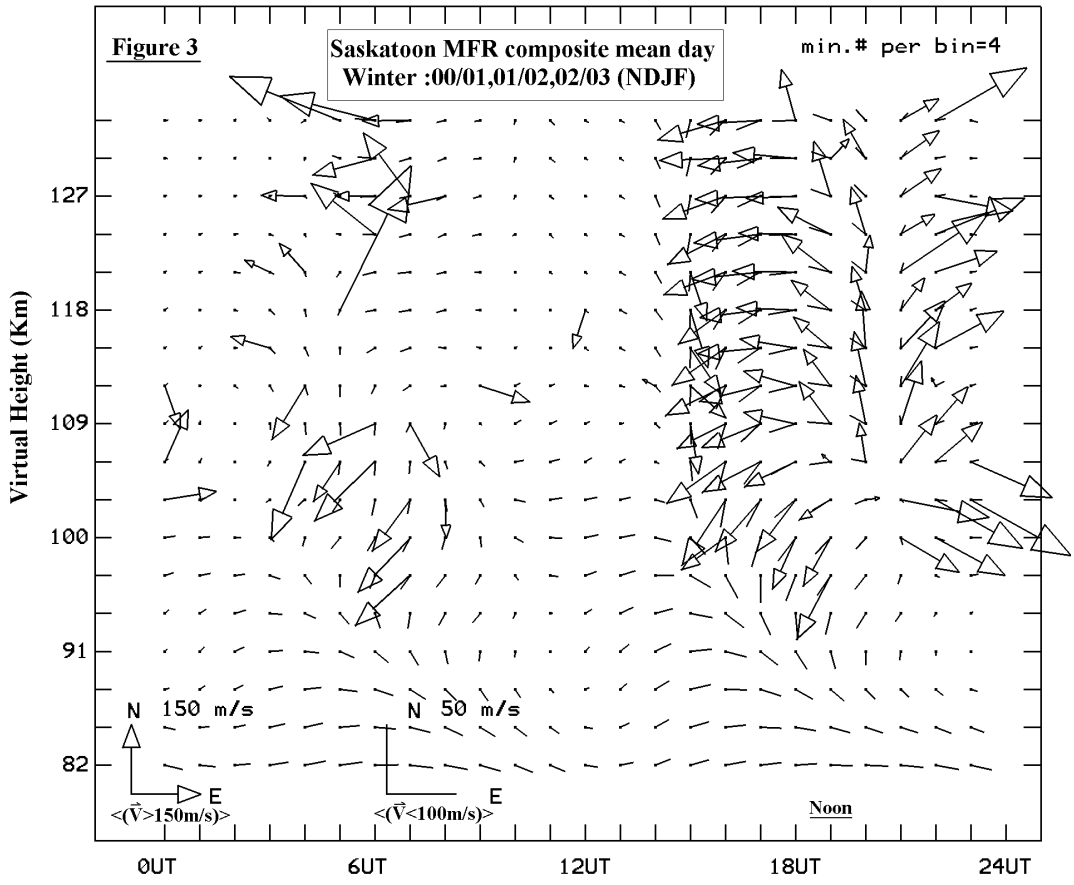

Figure 3. Winds for a composite winter day (Nov. – Feb.)

Figure 3 shows winds for a composite winter day (Nov.-Feb.) – the arrows represent an average of all 5-minute raw wind vectors with speeds greater than 150 m/s and the lines those with speeds less than 100 m/s. The former have numbers in the 10s and 20s, while the latter have numbers in the 100s and 1000s. Individual vectors from the first set often had speeds as high as 400-500 m/s.

Comparison between the two sets of winds in Figure 3 suggest that, while there are some consistent differences in direction, these large speeds merely represent the upper end of the speed distribution, and are not a different phenomenon. The differences in direction could be due the few isolated events of high winds not matching the long term average direction. In both sets there is a significant vector rotation with height around noon, which indicates a real change in height rather than oblique echoes from a total reflection layer. However, the heights still must be assumed to be virtual - i.e. affected by retardation.

The clockwise (CW) rotation in time suggests the presence of a 12 hr tide (because the wind has similar directions 12 hours apart) while the rotation in height, also CW with increasing height, is as expected for downward phase propagation. The majority of high speed cases occur around noon (19 UT).

Conclusion: This shows that the spaced antenna MF experiment can measure large speeds - even larger than would be expected, given the experimental parameters, such as antenna spacing (156m), and sample time (0.5s). In most cases the vectors appear to be consistent in direction with the all-wind average (not shown). On the whole it appears that the large heights, nominally above the E region, are probably virtual, and can be attributed to retardation within the E-region.

LIDAR OBSERVATIONS OF MIDDLE ATMOSPHERIC GRAVITY WAVE ACTIVITY OVER A LOW LATITUDE

V. Sivakumar[1,2] and P.B. Rao[3]

[1]National MST Radar Facility, Post Box. No: 123, Tirupati-517 502, INDIA.
[2]Now at Laboratoire de Physique de l' Atmosphère CNRS -UMR 8105, Université de La Réunion, FRANCE.
[3]National Remote Sensing Agency, Bala Nagar, Hyderabad-500 037, INDIA.
Email: siva@univ-reunion.fr (or) venkatv_siva@rediffmail.com ; rao_pb@nrsa.gov.in

1. Introduction

Gravity waves (GW) play a major role in transporting momentum and energy from lower atmosphere to upper atmosphere. These waves, having their source at lower heights, propagate upwards and deposit energy through wave breaking and dissipation processes in the mesosphere, thereby significantly altering its thermal structure and wind pattern [*Fritts*, 1984; *Fritts and Rastogi*, 1985; *Gavrilov et al.* 2000]. In recent years, the Rayleigh lidar technique has emerged as an effective means to study the GW activity in the middle atmosphere over the height range of 30-70 km. Using the lidar observations made from two stations, Haute Provence (44°N, 6°E) and Biscarrosse (44°N, 1°W), *Chanin and Hauchecorne* [1981] and *Wilson et al*. [1990] have made detailed studies on GW activity in the middle atmosphere over the south of France. They found the GW activity to be maximum during winter and minimum during summer. The dominant wave periods range from 6 to 8 hrs and vertical wavelengths from 5 to 10 km. The lidar observations over Arecibo (18°N, 66°W) reported by *Beatty et al*. [1992] have shown increasing GW amplitude with increasing wave period and vertical wavelength, their results are also consistent to *Gardner et al*., [1989] for Urbana (40°N, 88°W). The wave periods were found to be in the range of 1½ to 15 hrs and vertical wavelengths in the range of 1-17 km.

There have not been any studies similar to the above on gravity waves in the middle atmosphere for low latitudes. The present study aims at delineating the GW characteristics in the middle atmosphere using the Rayleigh lidar observations made at Gadanki (13.5°N, 79.2°E). The results present case studies which include GW characteristics and their seasonal differences during summer and winter.

2. Observations and Data Analysis

The lidar observations presented here were made on 240 nights during the period March 1998 to July 2001. Due to the limitation in time period of observations in most of the cases, we are presenting here only two representative cases during summer and winter. On the selective days, the data were collected continuously for a period of 4 to 6 hrs on clear nights starting around 2000 LT. The recorded raw data is in the form of photon count profiles with a height resolution 300 m and time resolution of 250 s (5000 laser shots were integrated for one profile). The height range considered for the present study extends from 30 to 70 km, although the data were recorded up to 90 km. The large fluctuations resulting from low signal-to-noise ratio at higher heights is the reason for limiting the height coverage for wave studies to 70 km. The method of deriving the temperature profile from the measured photon count profile closely follows the method given by *Hauchecorne and Chanin* [1980].

3. Results and Discussion

A time sequence of 64 temperature profiles at 250 s interval, covering a height range of 30-70 km are presented in figures 1(a) and 1(b) for the nights of 08-09 May 1998 and 27-28 January 1999. These are the running average (4-point in time and 3-point in height) profiles obtained through the analysis. The profiles clearly reveal wave perturbations in temperature in all the four sets. The wave perturbations are characterized by downward phase progression, as expected for upward propagating gravity waves. The rate of progression is

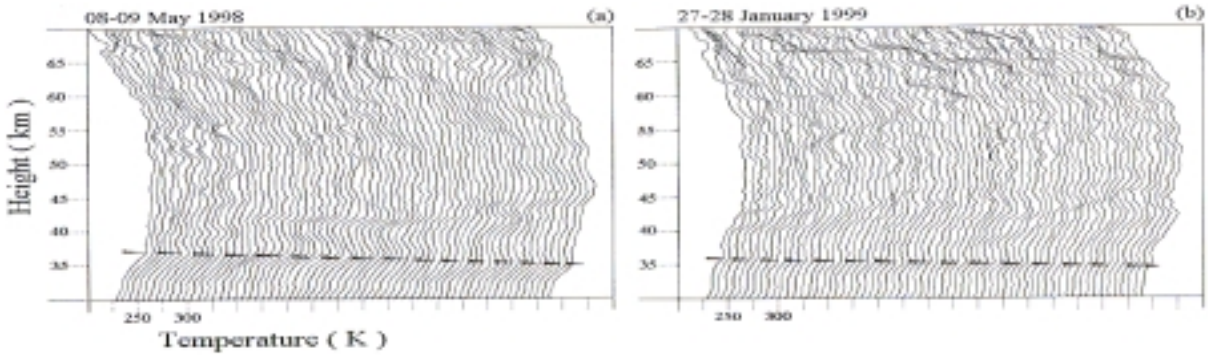

Figure 1. A time sequence of 64 temperature profiles observed on the nights of 08–09 May 1998 and 27– 28 January 1999. The dotted line shows the downward phase propagation in the stratosphere.

clearly seen for lower heights (< 50 km), is found to be in the range of ~0.2-0.4 m/s. On the basis of vertical wavelengths associated with these perturbations, can be inferred that they correspond to wave periods much larger than the observational time period. The obtained height-time variations of the temperature fluctuations, by removing a linear temporal trend at each height, the wave amplitudes associated with the fluctuations are found to increase with height. The perturbation amplitudes are of the order of 10-20 K in the mesosphere and considerably lower (~5-10 K) in the stratosphere. The quasi-periods, seen more clearly in the case of 08-09 May 1998, are found to be of the order of 30-40 min. The vertical wavelengths of these waves are of the order of 5-10 km. For the downward phase progression of 0.2 to 0.4 m/s, the wave period would be of the order of ~7 hrs. The wave amplitudes associated with these waves are of the order of 10-15 K. The perturbations in the mesosphere also are of the same order, but these are due to contributions from shorter period gravity waves. The phase progression at these heights cannot be seen so clearly as at lower heights due to faster changes associated with the shorter period waves.

The frequency and wavenumber power spectra are computed using the time and height series of the detrended relative temperature fluctuations, respectively. The temperature profiles were subjected to four-point running average in time and three-point running average in height before obtaining the time and height series of the relative temperature fluctuations for computing the frequency and wavenumber spectra. Accordingly, the frequency spectra correspond to the periods ranging about 16 min to 4½ hr and the wavenumber spectra to the wavelengths ranging about 900 m to 38.4 km. The obtained frequency-power spectra for 08-09 May 1998 and 27-28 January 1999 are presented in figures 2(a) and 2(b). For both the cases, the wave activity is highest at mesospheric heights with dominant periods covering the range 66 min to 4½ hrs. The GW activity is found to be most intense during summer than winter. It is also noted from the figure that the single dominant components exist for 08-09 May 1998 and multiple components are found for 27-28 January 1999. This seasonal dependence is much different from that of the midlatitudes, where the wave activity was found to be highest during winter [e.g., *Wilson* et al., 1990; *Allen and Vincent*, 1995]. The

latitudinal dependence of the seasonal variation of the wave activity similar to that observed here has been reported earlier [e.g., *Fritts and vanZandt,* 1993].

The wavenumber-power spectra for the same days as of the frequency spectra are presented in figures 3(a) and 3(b). The dominant components have vertical wavelengths in the range of about 5-20 km. The most dominant component with a wavelength of about 20 km is observed during the day of autumn equinox. From the figure (1) and (2), it is

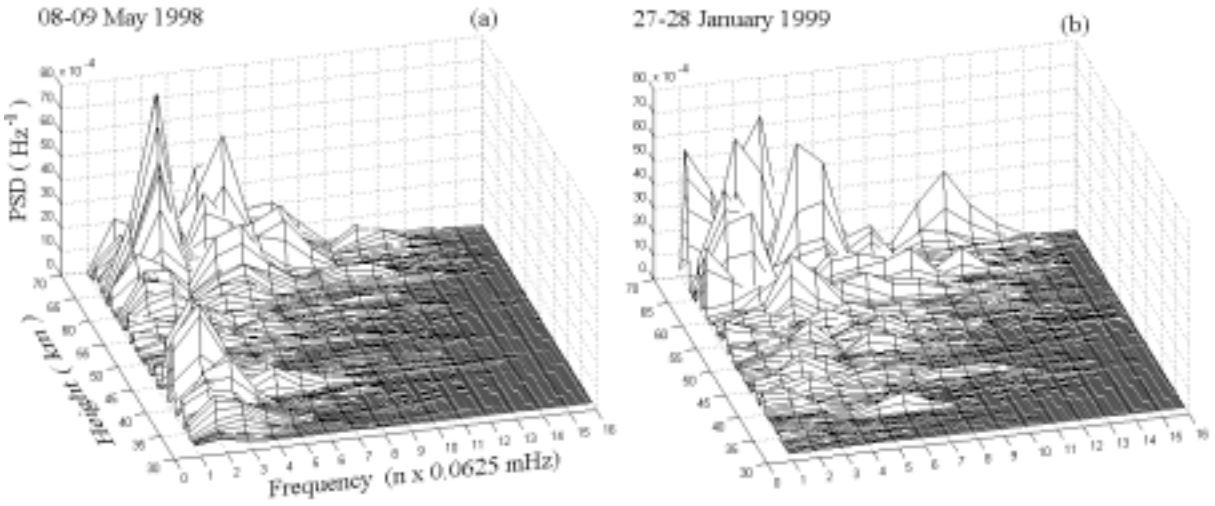

Figure 2. Frequency– Power spectra of relative temperature fluctuation as function of height for the cases shown in figure 1.

evident that the modes with vertical wavelengths greater than 5 km correspond to longer period waves (> 4 ½ hrs). These modes with low rate of vertical phase propagation are seen clearly at stratospheric heights and were referred to as quasi-stationary modes [*Wilson et al.,* 1990]. The basic characteristics of these modes are found to be similar to that observed over midlatitudes [*Gardner et al.,* 1989; *Wilson et al.,* 1990; *Beatty et al.,* 1992]. The difference noted in the seasonal dependence between the larger and shorter period modes need to be confirmed with a larger database than used here.

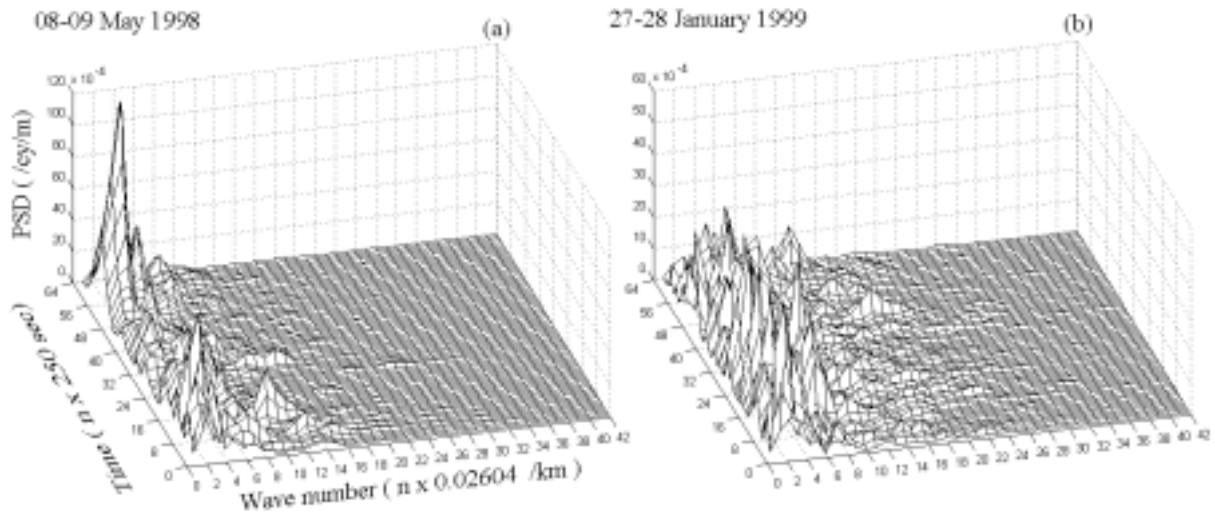

Figure 3. Wavenumber – Power spectra for the 64 vertical profiles of relative temperature fluctuation for the cases shown in figure 1.

4. Summary

The high resolution (250s and 300m in time and height) Rayleigh lidar measurements made on two representative days during summer and wither is presented in this paper. The lidar observations revealed significant gravity wave activity over the entire observed height range of 30-70 km. The wave activity is seen to be distinctly different from stratosphere to mesosphere. From the high-resolution temperature profiles, revealing waves with vertical wavelength of the order of 5 – 10 km and downward phase descent of 0.2 – 0.4 ms^{-1}, it is inferred that long periods (~7 hrs) characterize the wave activity at stratospheric heights. These modes with low rate of vertical phase propagation, referred to as quasi-stationary modes, are found to be similar to that observed over midlatitudes [e.g., *Wilson et al.,* 1990]. In contrast, the wave activity in the mesosphere is dominated by the relatively shorter periods, covering the observed range of ~16 – 270 min. The gravity wave activity is found to be maximum during summer and minimum during winter, a behavior much different from that of mid- and high latitudes where the maximum occurs in winter and minimum in summer.

Acknowledgement

The National MST Radar facility (NMRF) is operated by the Department of Space with partial support from Council of Scientific & Industrial Research, Government of India.

References

Allen, S.J., and R.A.Vincent, Gravity wave activity in the lower atmosphere: Seasonal and latitudinal variations, *J. Geophys. Res.*, 100, 1327-1350, 1995.

Beatty, T.J., C.A. Hostetler, and C.S.Gardner, Lidar observations of gravity waves and their spectra near the Mesopause and Stratopause at Arecibo, *J. Geophys. Res.*, 49, 472-497, 1992.

Chanin, M.L., and A. Hauchecorne, Lidar observation of gravity and tidal waves in the stratosphere and mesosphere, *J. Geophys. Res.*, 86, 9715-9721, 1981.

Fritts, D.C., Gravity wave saturation in the middle atmosphere: A review of theory and observations, *Rev. Geophys. Space Phys*., 22, 275-308, 1984.

Fritts, D.C., and P.K. Rastogi, Convective and dynamical instabilities due to gravity wave motions in the lower and middle atmosphere: Theory and observations, *Radio Sci.*, 20, 1247-1277, 1985.

Fritts, D.C., and T.E. vanZandt, Spectral estimates of gravity wave energy and momentum fluxes, 1. Energy dissipation, acceleration, and constraints, *J. Atmos. Sci*., 50, 3685-3694, 1993.

Gardner, C.S., M.S. Miller, and C.H.Liu, Rayleigh lidar observations of gravity wave activity in the upper stratosphere at Urbana, Illonois, *J. Atmos. Sci.*, 46, 1838-1854, 1989.

Gavrilov, N.M., S. Fukao, T. Nakamura., Gravity wave intensity and momentum fluxes in the mesosphere over Shigaraki, Japan (35°N ; 136°E) during 1987-1997, *Ann. Geophys.*, 18, 834-843, 2000.

Hauchecorne, A., and M.L. Chanin, Density and temperature profiles obtained by lidar between 35 and 70 km, *Geophys. Res. Lett.*, 7, 565-568, 1980.

Wilson, R., A. Hauchecorne and M.L. Chanin, Gravity waves in the middle atmosphere observed by Rayleigh lidar, Part 2: Climatology, *J. Geophys. Res*., 96, 5169-5183, 1990.

APPLICATION OF THE DUAL-BEAMWIDTH METHOD TO A NARROW BEAM MF RADAR FOR ESTIMATION OF TURBULENT SPECTRAL WIDTH

R. Latteck, W. Singer, N. Engler

Leibniz-Institut für Atmosphärenphysik, Schloss-Str. 6
D-18225 Kühlungsborn, Germany

Abstract

Spectral widths observed by narrow beam VHF/UHF Doppler radars can be used to estimate turbulent energy dissipation rates. In case of broader beams, the observed spectral widths have to be corrected for the influence of beam and shear broadening caused by the background wind field. VanZandt et al. (2002) developed a new dual-beamwidth method to estimate the turbulent component of spectral width from MST radar observations without additional knowledge of the wind field and tested it successfully for the troposphere. In summer 2002 a new MF radar was put into operation at Saura on the Andøya island in Norway. The system has high flexibility in antenna beam forming allowing off-zenith beams with different beam widths. Experiments with different beam widths have been carried out with the MF radar to test the dual-beam width method at mesospheric altitudes. We compare spectral width estimates from both the single-beam width and the dual-beam width method on a case study basis.

Introduction

The spectral width σ^2_{obs} of an observed radar Doppler signal is related to the velocity variance due to turbulence σ^2_{turb} what can be used to estimate turbulent energy dissipation rates. If a relative wide radar beam is used σ^2_{obs} is also influenced by variances due to the interaction with the background wind and shear $\sigma^2_{beam+shear}$ and of waves σ^2_{wave} with the radar beam (Hocking, 1983)

$$\sigma^2_{obs} = \sigma^2_{turb} + \sigma^2_{beam+shear} + \sigma^2_{wave} \quad (1)$$

$$\sigma^2_{obs} = \sigma^2_{turb} + \sigma^2_{corr} \quad (2)$$

which have to be removed from the observed spectral width to get σ^2_{turb}. The standard or traditional single-beamwidth method (1BW) consists of estimating σ^2_{wave}, evaluating $\sigma^2_{beam+shear}$ and substracting σ^2_{corr} from σ^2_{obs} (VanZandt et al., 2002). This traditional method works well as long as the horizontal wind is small enough to let the correction term σ^2_{corr} be smaller then the total observed spectral width σ^2_{obs}. The dual-beam-width-method (2BW) considers that the dominant terms in $\sigma^2_{beam+shear}$ are proportional to the beam width θ^2 (**H**alf-**P**ower-**H**alf-**W**idth) what means that σ^2_{corr} is also approximately proportional to θ^2. If σ^2_{obs} is measured simultaneously in nested volumes with radar beams characterized by a narrow beam width θ_n and a wide beam width θ_w two simultaneous equations for $\sigma^2_{obs,n}$ and $\sigma^2_{obs,w}$ can be solved (VanZandt et al., 2002) what results in

$$\sigma^2_{turb} = \frac{\theta^2_w \cdot \sigma^2_{obs,n} - \theta^2_n \cdot \sigma^2_{obs,w}}{\theta^2_w - \theta^2_n} \quad (3)$$

with the advantage, that neither the wind speeds and shears nor the exact pointing angle of the radar beam are required for the correction. The dual-beam width method assumes that for both beam widths the same fraction of the pulse volume is filled with turbulence and require the beam widths only.

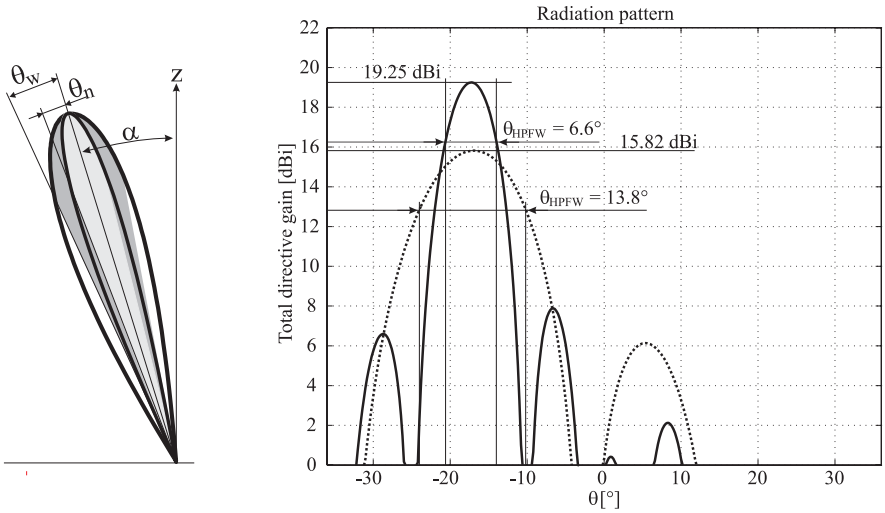

Figure 1: Left: Principle of nested volume measurements with two radar beams characterized by different beam widths. Right: Slice along the NW-SE axis through the the 3D radiation pattern of the Saura MF radar antenna for a narrow (solid line) and wide (dashed line) beam tilted to 17.2°.

System and experiment description

In April 2003 experiments were carried out at the Saura MF radar to test the dual beam widths method in the mesosphere. This new narrow beam MF radar has been installed at Saura on the Andøya island close to the Andøya Rocket Range as part of the ALOMAR observatory to improve the ground based capabilities for studies of the dynamical structure especially small scale features and turbulence of the upper mesosphere (Singer et al., 2003). The main feature of the new radar is the transmitting/receiving antenna which is formed by 29 crossed half-wave dipoles arranged as a *Mills-cross*. The spacing of the crossed dipoles is 0.7 wave lengths resulting in a minimum beam width $\theta = 6.6°$ (**H**alf-**P**ower-**F**ull-**W**idth, one way). Each dipole is fed by its own phase controlled transceiver unit with a peak power of 2 kW what provides a high flexibility in beam forming and pointing. The wide antenna beam with a half-power beam width $\theta_w = 13.8°$ was formed by feeding only half of the crossed dipoles of the *Mills-cross*. The wider antenna beam has nearly twice the beam width of the narrow antenna beam and a reduced antenna gain due to the less number of used antennas (Figure 1).

A sequence of narrow beam and wide beam experiments each pointing interleaved with 17.2° off-zenith towards NW and SE was run on April 24, 2003 to test the dual beam method. Additionally 4 Doppler beam steering (DBS) experiments with narrow beams at 7.3° off-zenith provided the horizontal wind information.

Results

Dual-beams were formed at 17.2° zenith angle with a minimum of the antenna radiation pattern in vertical direction to reduce possible contaminations by specular reflections. Since the narrow and wide beam experiments used opposite azimuth angels alternating in the NE-SW plane, the corresponding radial velocities must have opposite signs and can be used as a quality criterion for the radar meassurements. We chose 3 hours between 10:45 UT and 13:55 UT where the radial velocities had opposite signs in the altitude range between 65 and 84 km (Figure 2) for the comparison of both the single beamwidth and dual beamwidth methods.

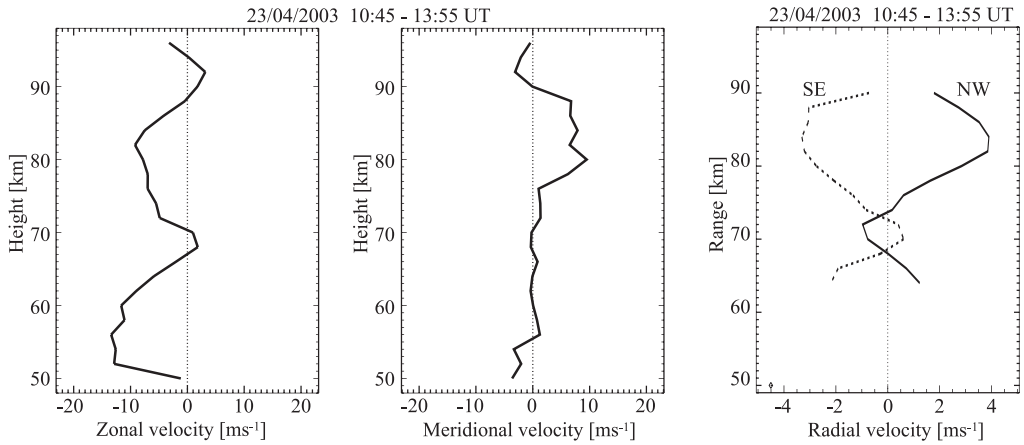

Figure 2: Mean zonal and meridional winds (left and middle) derived from standard DBS experiments and radial velocities (right) obtained with interleaved oblique narrow beams (HPFW=6.6°) at 17.2° off-zenith angle during dual-beamwidth observation.

The mean horizontal winds were less than 10 m/s during the whole experiment period on April 23, 2003 (Figure 2). Since the velocities were very small the correction term for beam and shear broadening used in the single-beamwidth method was negligible (middle panel of Figure 3) and $\sigma^2_{turb} \approx \sigma^2_{obs}$.

The 3-hour mean profile of σ^2_{turb} obtained from the dual-beamwidth method shown in Figure 4 depict velocity variances between 5 and about 15 m^2/s^2 below 78 km where contributions from specular reflections should be small or negligible. With a mean Brunt-Vaisala frequency of 0.018 for the altitude range between 65 and 84 km based on a mean temperature profile for April after falling sphere measurements at Andenes (Lübken, 1999) these turbulent velocity variances can directly be converted into turbulent kinetic energy dissipation rates. These values between 10 and 60 mW/kg (top axis in the right panel of Figure 4) are in reasonable agreement with rocket observations during spring transition (Müllemann et al., 2002). The first results of simultaneous 2BW and 1BW observations during low wind speed conditions are in good agreement. Further tests of

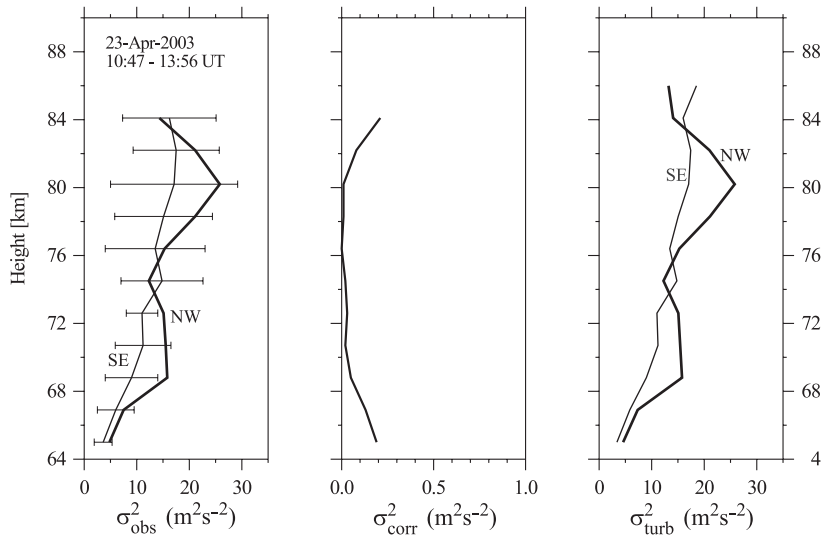

Figure 3: Profiles of the observed spectral widths σ^2_{obs} (left) from the NW and SE narrow beam experiments, the correction term σ^2_{corr} (middle) and the turbulent spectral width σ^2_{turb} (right) obtained with the single beam width method.

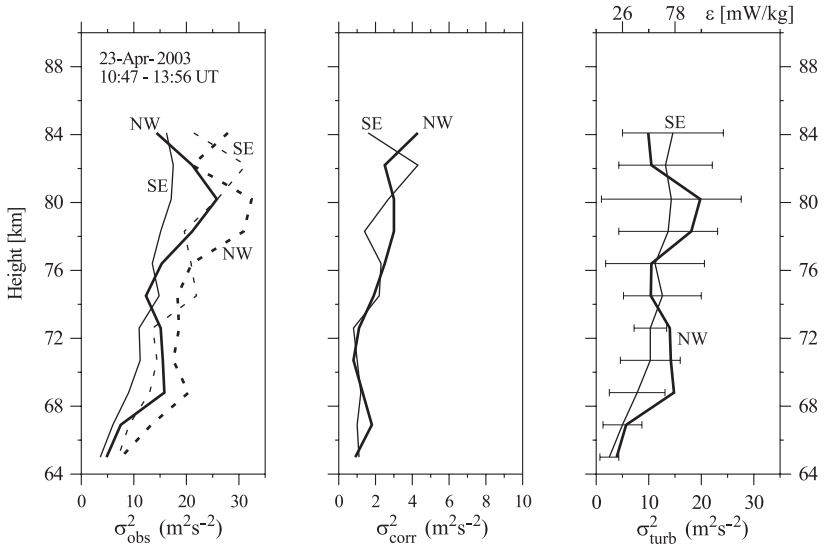

Figure 4: Profiles of the observed spectral widths σ^2_{obs} (left) from NW/SE narrow (solid) and wide (dashed) beam experiments, the correction term σ^2_{corr} (middle) and the turbulent spectral width σ^2_{turb} (right) obtained with the dual beam width method (Note: different abscissa scales are used in the middle panels of Figures 3 and 4).

the dual-beamwidth method will be done in summer during high wind speeds of the summer mesospheric jet.

Acknowledgments

The authors wish to thank the engineers and technicians of the Leibniz-Institut für Atmosphärenphysik and the Andøya Rocket Range for their engagement building up the new antenna system and installing the radar system. Also, the authors express their appreciation to the staff of Atmospheric Radar Systems, Australia for their cooperative support in solving problems connected with remote radar operation and control.

References

Hocking, W. K., On the extraction of atmospheric turbulence parameters from radar backscatter Doppler spectra - I. Theory, *J. Atmos. Solar Terr. Phys.*, Vol. 45, No. 2/3, 89-102, 1983.

Lübken, F.-J., The thermal structure of the Arctic summer mesosphere, *J. Geophys. Res.*, 104, 9135-9149, 1999.

Müllemann, A., M. Rapp, F.-J. Lübken, and P. Hoffmann, In situ measurements of mesospheric turbulence during spring transition of the Arctic mesosphere, *Geophys. Res. Lett.*, Vol. 29, No. 10, 115-1 - 115-4, 2002.

Singer, W., R. Latteck, D. A. Holdsworth, and T. Kristiansen, A new narrow beam MF radar at 3 MHz for studies of the high-latitude middle atmosphere: system description and first results, *in this issue.*

VanZandt, T. E., G. D. Nastrom, J. Furumoto, T. Tsuda, and W. L. Clark, A dual-beamwidth radar method for measuring atmospheric turbulent kinetic energy, *Geophys. Res. Lett.*, Vol. 29, No. 12, 13-1 - 13-3, 2002.

MONSOON LOW-LEVEL JET OBSERVATIONS OVER GADANKI

K. Madhu Chandra Reddy, D. Narayana Rao, A.R Jain and Yuichi Ohno[1],

National MST Radar Facility, Gadanki, India
E-mail: madhucomcom@rediffmail.com
[1]Communications Research Laboratory, Tokyo, Japan.

Abstract

Lower Atmospheric Wind Profiler observations of the Low Level Jet (LLJ) over Gadanki (13.5°N, 79.2°E), a tropical station in India, have been discussed. The present study utilizes vertical profiles of wind parameters, such as 3-D wind vectors (U, V and W), horizontal wind speed, wind direction and wind shear, during the years 1998-2000 in the height range of 0.6 – 4.0 km to explore the LLJ characteristics. The LLJ statistical characteristics and associated probable wave and turbulence effects have been investigated.

Introduction

The Low Level Atmospheric Jet is supposed to be a nocturnal phenomenon (Stull, 1990). It is well established that a strong cross-equatorial westerly Low Level Jet-stream (LLJ) with core around 850 hPa, roughly around 1.5 km above mean sea level (AMSL), exists over the Indian ocean and South Asia during the boreal summer monsoon season, i.e. June to September. Joseph and Raman (1966) established the existence of a westerly low-level jet stream over peninsular India with strong vertical and horizontal wind shears. This LLJ over tropical India could have strong link with Indian monsoon (Sam and Vittal Murty, 2002). This paper concentrates on LLJ observations confined over Gadanki.

System description and Data details

Lower Atmospheric Wind Profiler (LAWP) is a UHF coherent, pulsed doppler, phased array radar with an effective peak power aperture product of about 1.2×10^4 Wm^2. The radar is operated at a frequency of 1357 MHz and the receiver has a maximum gain of 120dB. This radar has been configured to operate in Doppler Beam Swinging (DBS) mode. The antenna beam can be positioned, through electrical phase switching, at three fixed orientations, viz., Zenith, 15°down to East and North. The backscatter echo from three non-coplanar beam beams are utilized to obtained the three-wind vectors, viz., Zonal (U), Meridonal (V) and vertical (W). The wind profiles obtained by this radar are single station observations, i.e. above Gadanki. But, on calm fair-weather day, these wind observations may be representative of a few kilometres over Gadanki. Care has been taken in choosing the calm and fair-weather times wind data for this study. Vertical profiles of 3-D wind components are averaged for every hour, unless otherwise stated, the same is used for this study.

Observations and discussion

In order to understand the overall three-year wind speed information, we have averaged height profiles of wind speeds for every 5 days. The monthly such wind speeds information for the years 1998-2000 is shown in figure 1. It can be seen from this figure that the westerlies prevail during May - September and easterlies during other months.

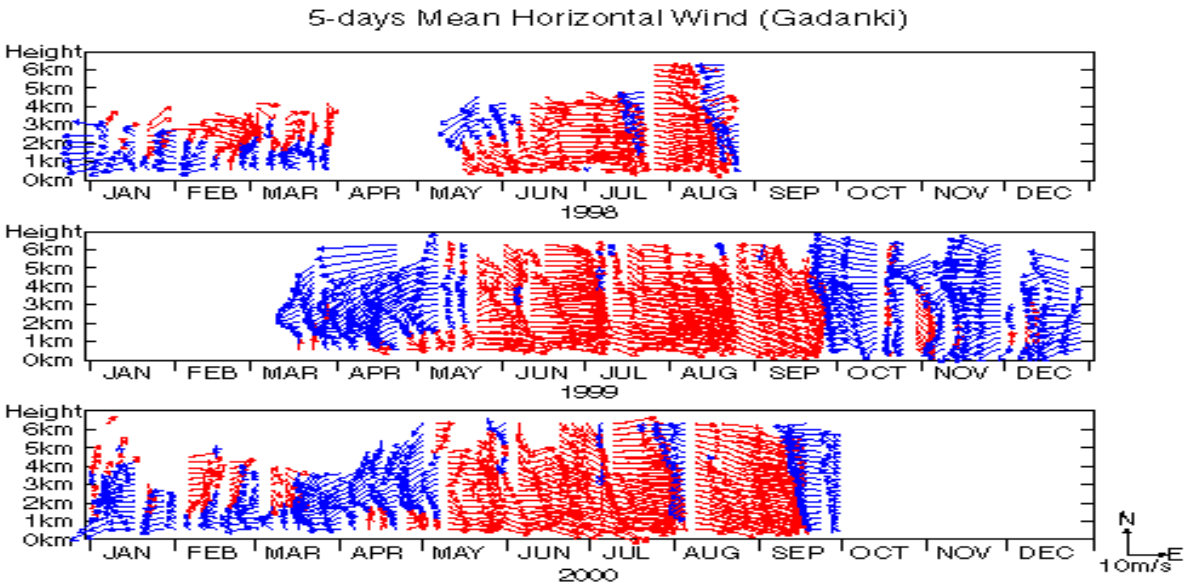

Figure 1. Wind vector diagram for the monthly horizontal wind speed trends for the years 1998-2000.

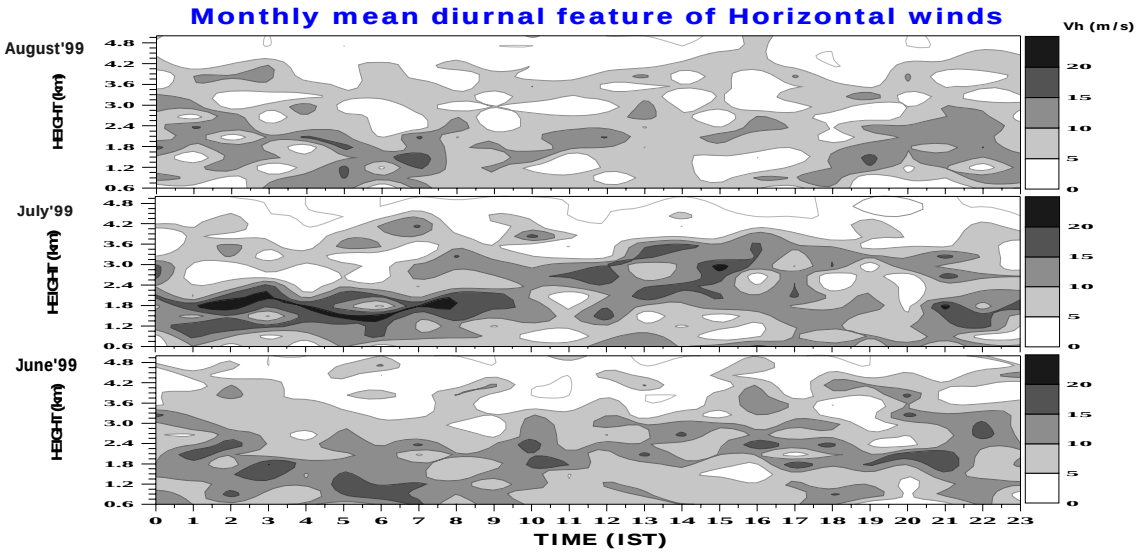

Figure 2. Mean monthly diurnal features of Horizontal wind contours.

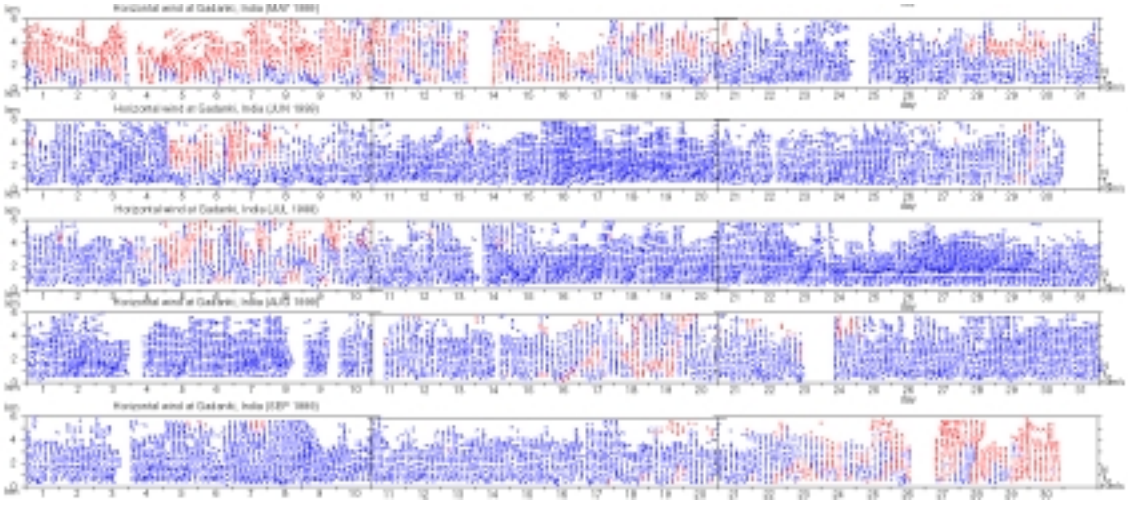

Figure 3. All days Monthly Horizontal wind vector diagram for the year 1999.

The monthly diurnal mean of horizontal wind speeds for the months of June-August is shown as a contour map in figure 2. It can be seen from figure 2 that, in July 1999, the mean wind speeds are high and are in the range of ~ 20 ms^{-1}. Moreover, the jet appears from 2100 – 1000 (LT) around 1.6 ± 0.5 km. During LLJ times, the wind direction is westerly (can be seen from figure 1). LLJ features seem to be diluted in between 1000 and 2200 (LT) and the wind speeds are below 15 ms^{-1} at these times. In the months of June and August LLJ wind speeds are in the range of ~ 10-15 ms^{-1}. The mean strong LLJ feature observed in the month of July is seen to be much more significant than June and August. More or less the same features are observed in 1998 and 2000 as well.

The three-year hourly averaged wind observations on fair-weather days show that horizontal winds are normally below 6-8 ms^{-1} in the height range of 0.6 – 4.0 km. At LLJ times, the maximum wind speed (jet streak) is observed to range from 12 to 30 ms^{-1}. These magnitudes are comparable with Great Plains LLJ observations (Yihua Wu and Sethu Raman, 1998). The LLJ features have observed to be significantly stronger in the monsoon times, especially during the months of June-July. Moreover, during the boreal summer (South-West) monsoon time LLJ intensities are stronger and persist for much longer time in comparison to winter (North-East) monsoon. This can be seen from the figure 3, which is an arrow diagrammatic picture of horizontal wind speeds for each day for the months from May to September 1999. From figure 3, it is clear that the LLJ core seems to appear around 1.5 km. The arrowhead indicated towards east, which confirms that the LLJ direction is mostly westerly during summer monsoon times. In every year, LLJ seems to be stronger and prominent in the Southwest monsoon time over Gadanki, especially in the months of June–August. This can be observed from figure 3.

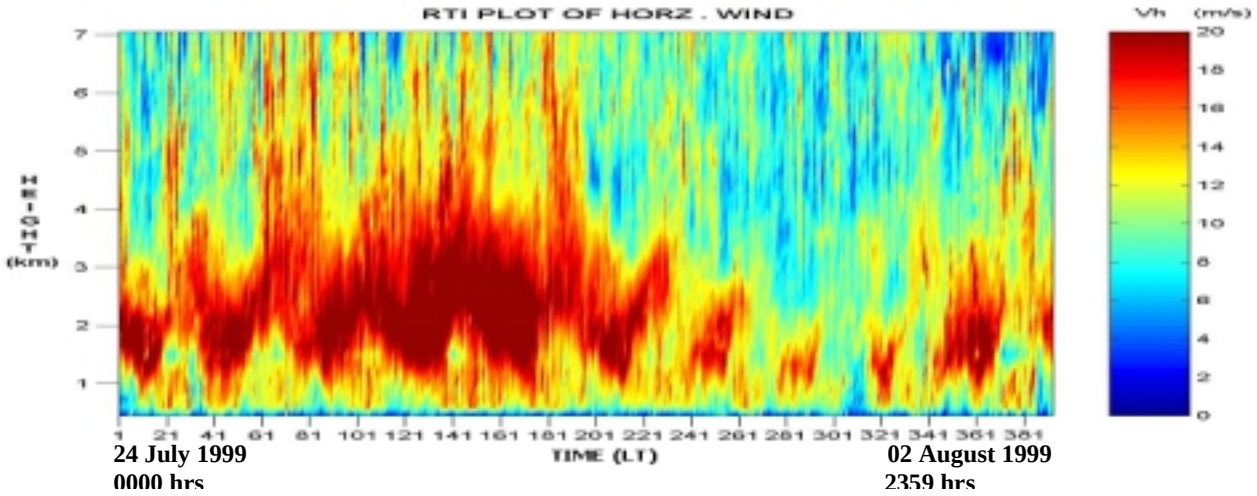

Figure4. Range Time section of Horizontal winds from 24 July – 02 August 1999. Every tick mark on abscissa corresponds to 12 hours.

From figures 2 & 3 it can be understood that the LLJ features are stronger in the month of July. Three years of wind data are also revel that frequent strong LLJ has been observed during day and night continuously for a few days mostly in July. On such occasions Gadanki LLJ seems to be as similar as East-African (Somalia) jet, which lasts day and night for many days (Stull, 1990). So a case study has taken up to understand the wave and turbulence features during the strong LLJ times. For this case study particularly July 1999 is chosen because of availability of simultaneous radiosonde observations at NMRF, Gadanki. Such a typical example can be seen on July 1999 from figure 4. Figure 4 shows the range

time intensity (RTI) of horizontal wind speeds for 10 days i.e. 24 July – 02 August 1999. Abscissa is time in days; every 41 interval represents a day. Here, the height profiles of horizontal winds are averaged for about half an hour to understand the wave and turbulence features at the LLJ times. The vertical extension of LLJ is seen from 0.6 km to even above 4.0 km. From these observations, it is understood that the wind directions are relatively constant in the jet region but not the wind speeds. The maximum wind speed (jet streak) is observed to be 30 ms^{-1} on 27 July 1999. This figure also shows significant information about diurnal variation of LLJ over Gadanki. The axis of the LLJ appears to be shifting up at afternoon times. This may be due the local ground based convective forces. The generation, maintenance and strength of the LLJ are very sensitive to the parameterisation of turbulent mixing in the Boundary layer. Thus, the Turbulent Kinetic Energy (TKE) and the magnitude of the turbulent fluxes associated with LLJ are important and are very interesting to study.

Summary

Single station three-year wind information over Gadanki reveals that the winds are strong and westerly in direction during June–September, boreal summer monsoon period. Low Level Jet features have been most prominently and consistently observed in the months of June to August. The strong LLJ features are most significantly seen in the month of July. The observed average LLJ characteristics are summarised as follows:

Level of jet	1.6 ± 0.5 km
Direction	Westerly, South westerly
Mean wind speeds	20 ms^{-1}
Max. wind speed	30 ms^{-1}
Diurnal features	Maximum during midnight and early morning times and LLJ features has been diluting during the day time.
Persistence	Very steady in direction and variable in speeds.

Most of the times, LLJ observed to be prominent in the early morning times. But it has been observed sometimes, especially in the months of July. The LLJ has been persisting continuously day and night and lasts for a few days similar to Somalia (East Africa) Jet, with varying core height and intensity. Moreover the depth of the Jet (vertical extent) is more than 3 km during on such time. In the afternoon times the axis of the LLJ has shifted to higher altitudes as compared to the early morning observations.

References

Joseph, P. V., and P. L. RamanExistence of low level westerly jet-stream over peninsular India during July. *Ind. J. Met. Geophys.*, **17**, 437-471, 1966.

Sam, N.V., and K.P.R. Vittal Murty Characteristics of monsoon low-level jet (MLLJ) as an index of monsoon activity. *Indian Acad. Sci. (Earth Planet. Sci.)*, **111**, No.4, 453-457., 2002.

Stull, R.B, An introduction to Boundary Layer Meteorology, Kluwer Academic publication, Boston, 500-522, 1990.

Yihua WU, and Sathu Raman, The summertime Great Plains low level jet and the effects of its origin on moisture transport. *Boundary Layer Meteorology*, **88**, 445-466, 1998.

Session I.4: Meteorological Phenomena and Applications

This session is concerned with recent developments in Doppler radar profiling in the lower neutral atmosphere, especially studies of lower atmospheric phenomena made with profilers in combination with other instruments during field campaigns. Topics of interest include the assimilation of profiler data in meteorological models, quality control of profiler data, operational networks of profilers and the impact of profiler data on forecasting. Of special interest are studies that demonstrate the utility of profiling for quantifying the vertical structure of turbulence, humidity, cloud and precipitation fields including drop size distributions and their variability

Conveners:
K. Gage and D. Riggin

MESOSCALE ALPINE PROGRAMME (MAP): SYNERGIES BETWEEN WIND PROFILERS AND DOPPLER WEATHER RADARS

M. Petitdidier[1], V. Klaus[2] and P. Tabary[3]

(1) CETP/CNRS, Vélizy, France, monique.petitdidier@cetp.ipsl.fr
(2) Meteo France, CNRM/GMEI/STM, Toulouse, France, vladislav.Klaus@meteo.fr
(3) Meteo France, DSO/CMR, Trappes, France, pierre.tabary@meteo.fr

Introduction

During the field phase of the Mesoscale Alpine Programme (MAP see Bougeault et al., 2001; Caccia et al., 2001) a number of instruments were deployed in the southern flank of the Alps in the Lago Maggiore area in order to document atmospheric and hydrological processes. In particular the experimental set up included research and operational weather Doppler radars like the French C-band Ronsard, and Swiss C-band Monte Lema Radar(ML) (5.6GHz). This set up provided a coverage of Alpine precipitating systems with a unique spatial and temporal resolution. In order to complement those sets of data, a bifrequency UHF/VHF wind profiler was installed in the area scanned by the weather radars.

The signal of weather Doppler radars(WDR) and VHF wind profilers(WP) are backscattered by different types of targets, hydrometeors and refractive index inhomogeneities respectively, due to their frequency difference. Their running modes are also different. WDR provide a volume observation of the precipitation system at different elevations and azimuths. Vertical profiles of wind speed and direction are deduced by VAD(Volume Azimuth Display) analysis or Velocity Volume Processing(VVP) methods. Over the past decades, many methods have been developed to retrieve the three-dimensional wind field from Multiple Doppler observations, at least 2 radars. The main drawback is that those radars provide no information where there are no hydrometeors. The VHF WPs, whatever the frequency is, operate with antennae oriented in fixed positions, 3 or 5, and provide the wind vector and reflectivity profiles near the vertical direction. One of their drawback is that the observations provide a cut of the cloud or meteorological event passing over the radar. If the system cannot be assumed to be frozen at the observed scale it is difficult to separate spatial and time variations. One interesting point is: the VHF WP provides a description of the air motion inside the cloud and in its environment.

This experiment has been an opportunity to test the complementarity of the two types of data set. First of all, our interest has been focussed on simultaneous wind measurements, then on reflectivity ones.

1-Wind comparison

The VHF wind profiler provides wind vector every 15mn whatever the weather conditions during the MAP experiment. The time resolution of wind profiles deduced from the WDR is the same.

Validation of a new algorithm for WDR

One general problem that occurs in the data processing of WDR observations is the folding of the Doppler spectrum that leads to erroneous wind values. Wind data coming from WP may be used as a reference basis to avoid ambiguity in Doppler radial velocities obtained with WDRs, or to validate new algorithms. Tabary et Petitdidier (2002) validated a Bayesian wind-profile algorithm. This technique applied to WDR data processing does not require any preliminary defolding of the radar data. As a consequence this algorithm is well adapted to operational WDRs. The authors used the wind profiler data to validate this new algorithm.

Integration of the VHF wind profiler data within dual Doppler wind synthesis

From dual Doppler radar observations, 3D wind field may be retrieved in the common observing zone. The retrieving method, used by Petitdidier et al.(2000), was the MANDOP (Multiple ANalytical DOPpler), formerly proposed by Scialom and Lemaître (1990) and adapted to the Alpine case by Tabary and Scialom (2000). This method is based on an analytical expansion of the wind components along each following axis, east, west, north, south and vertical. The expansion coefficients are retrieved in a minimisation process adjusting the analytical wind components to radial velocities and physical constraints, given by the anelastic continuity equation and free-slip boundary condition. This method permits to include other types of measurements like wind profiler data.

Different scenarios were developed to test the impact of the VHF wind components on the retrieved wind fields. The conclusions of this study was the following. The main global impact of the WP was very local due to the volume information provided by the WP relatively to the three-dimensional one observed by the WDR (Fig.1). Nevertheless the impact became significant and helped better conditioning at the upper boundary level of the retrieved wind field and in a region where the radar beams are nearly collinear.

Interpretation of orographic processes

During the MAP experiment there were 13 days of precipitation over the Lago Maggiore area. While the general mesoscale flow in the lower troposphere was approaching the Alpine barrier and rising the foothills, the flow veers and enters in individual river valleys. The locations of the VHF wind profiler and the ML WDR, respectively upstream and upslope, permits to determine a veering mean value. The flow is coming from the SouthWest and veers towards the East by 15°. In the upper level, at 5km the direction of the wind is the same for both radars.

2- Reflectivity

In the ML data reduction, an average reflectivity is computed over the VHF and ML radars locations. Figures 2(a,b,c) present the variation of the radar reflectivites as a function of altitude and time. During this period there was a convective activity in this area. Figure 2a and Figure 2b correspond to the reflectivities observed by the ML WDR, respectively over the ML radar and the WP. The motion of the precipitating system from the WP location to the ML radar one is observed, as it is expected from the results of the wind comparison(Tabary and Petitdidier, 2002). The enhancement of the WP vertical velocity is consistent with the convective activity observed by the ML WDR above the WP. Those simultaneous observations permit to observe the cloud condition above the wind profiler and then interpret the WP observations.

Figure 2c presents in the same range of altitude the relative reflectivity observed by the WP, pointing vertically. The difference of pattern is not so surprising due to the difference of the targets, hydrometeors for the WDR and refractive index perturbations induced by atmospheric turbulence for the WP.

In case of the WDR involved in MAP, the reflectivity is the result of the Rayleigh backscattering by hydrometeors. Those radars carry out observations up to nearly the top of the cloud; at higher altitudes the hydrometeors being too scarce.

In case of VHF wind profiler, the volume reflectivity depends on the refractive index gradient squared (M2), Brunt-Väisälä frequency squared, and the turbulence energy rate ε.

$$M = -7710^{-6}\frac{P}{T}\left(\frac{d\ln\theta}{dz} + \frac{15500q}{T}\frac{d\ln\theta}{dz} - \frac{7800}{T}\frac{dq}{dz}\right)$$

where p, T, q, θ and z are pressure, temperature, specific humidity, potential temperature and height respectively. M is very dependent on the water vapor amount , q, and its gradient in

the lower atmosphere. Worthington and Vaughan (1998) found out that M squared in saturated and dry air is weakest. That can explain a WP reflectivity less important around 6UTC while a cloud is over the WP. The same phenomena occurs at 12UTC while the radiosounding from Milano Linate observed a very large humidity. A first attempt to use the radiosoundings (RS) of Milano Linate, launched every 6hours and around 50km from the WP site, has not been very conclusive due to their time resolution, the lack of wind data at 12UTC, needed to compute C_n^2 and the localization of the cloud system.

3- Conclusion

Different aspects of the synergy between simultaneous measurements of WDR and WP have been investigated. They point out the interest to combine WDR and WP observations. Especially from a wind profiler point of view it is important for cloud physics. A quantitative interpretation of the VHF reflectivity in during the MAP events is ongoing using other sets of data obtained in this area.

References

Bougeault, P., P. Binder, A. Buzzi, R. Dirks, R. Houze, J.P. Kuettner, R.B. Smith, R. Steinacker, H. Volkert, and all the MAP Scientists, The MAP special observing period. *Bull. Meteor. Soc., 82, 433-462,* 2001.

Caccia, JL., J.P. Aubagnac, G. Béthenod, C. Bourdier, E. Bruzzese, B. Campistron, J.-P. Candusso, G. Cherel, J.-P. Claeyman, J.-L. Conrad, R.Cordesses, P. Currier, S. Derrien, G. Despaux, J. Dole, R. Durbe, J. Fournet-Fayard, A. Frappier, F. Ghio, F. Girard-Ardhuin, S. Jacoby-Koaly, V. Klaus, R. Ney, J.-P. Pagès, M. Petitdidier, Y. Pointin, E. Richard, I. Seloyan, L. Smaïni and R. Wilson.The French ST-Radar Network During MAP: Observational and scientific aspects. *Meteorol. Z. , 10, 469-478*, 2001

Petitdidier, M., P. Tabary, J. Bigorgne, G. Scialom, and V. Klaus, Integration of the VHF wind-profiler data within dual Doppler synthesis, *Phys. and Chem. of the Earth, 25, 1195-1199*, 2000.

Scialom, G., and Y. Lemaître, A new analysis for the retrieval of three-dimensional mesoscale wind fields from multiple Doppler radar. *J. Atmos. Oceanic Technol., 7, 640-655*, 1990.

Tabary P. and M. Petitdidier, Application of a Bayesian Wind-Profile Retrieval Technique to Radar data collected in the Alpine Southern upslope region and comparison with upstream wind profiler measurements, *J. Atmos. Oceanic Technol., 19, 875-887*, 2002.

Tabary, P., and Scialom, G., MANDOP analysis over complex orography in the context of the MAP experiment. *J. Atmos. Oceanic Technol., 18, 1293-1314*, 2001.

Worthington, R.M. and G. Vaughan, Effects of humidity, precipitation and severe convection on VHF vertical-beam echoes. *Proceedings of the 8th international workshop on Technical and Scientific aspects of MST/ST radar , pp.69-72,* 1998.

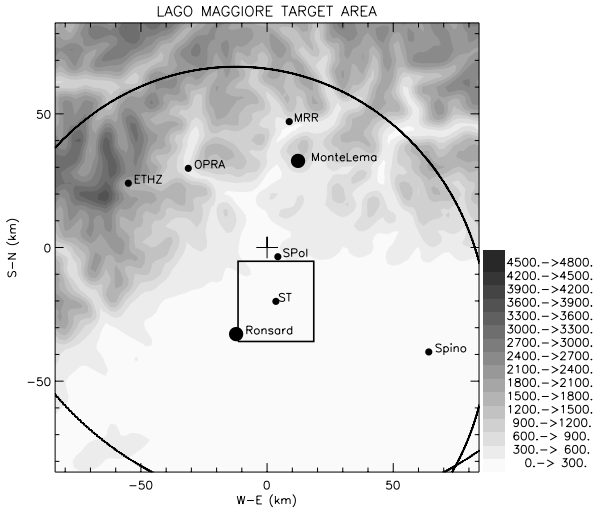

Figure 1 : Map of the Lago Maggiore area : the mountain range is in grey scale according to the altitude ; ST : WP, other symbols : WDRs, the curve line delineates the common area scanned by Ronsard and ML, the square delineates the retrieval domain when WP data included

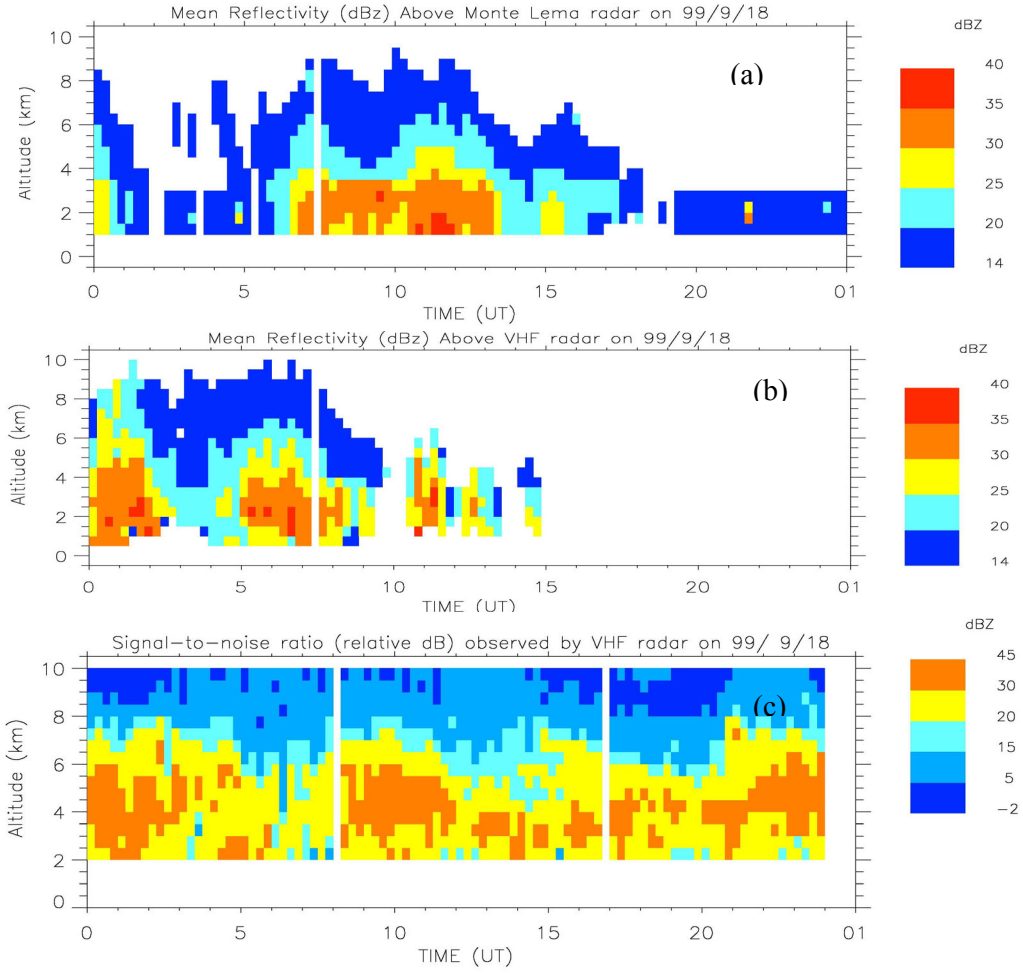

Figure 2 : Reflectivity expressed in logarithm units. (a) and (b) correspond to Monte Lema WDR observations above the ML and WP sites ; (c) corresponds to the signal to noise ratio observations of the WP.

Observations of Typhoon 9426 (Orchid) with the MU radar: Meso-α-scale kinematic structure and meso-β・γ-scale precipitating clouds

Yoshiaki Shibagaki[1], Manabu D. Yamanaka[2], Minori Kita-Fukase[3], Hiroyuki Hashiguchi[4], Yasuyuki Maekawa[1] and Shoichiro Fukao[4]

1: Osaka Electro-Communication University, Osaka 572-8530, Japan

2: Graduate School of Science and Technology Kobe University Kobe 657-8501, Japan

3: Weather News International company, Chiba 261-0023, Japan

4: Radio Science Center for Space and Atmosphere, Kyoto University, Kyoto 611-0011, Japan

1. Introduction

In general, a main precipitation system of a tropical cyclone is of meso-α scale, and it consisted of meso-β-scale precipitation systems (or organized precipitation systems), such as principal band, secondary band, connecting band, and an eyewall. Kinematic structures of the precipitation systems in various scales have been revealed in many observational studies. Since studies covering simultaneously the precipitation systems of different scale were few, however, a general structure of tropical cyclones has not been well understood.

On 29-30 September 1994, we successfully observed Typhoon 9426 (Orchid) by the MU (middle and upper atmosphere) radar of the VHF band at Shigaraki, Shiga, Japan (136.10 ° E, 34.85 ° N), the center of which almost passed over the radar site (Fig. 1). This is the first observation to continuously obtain information up to the lower stratosphere including the inner core region. The typhoon was also observed by an UHF-band radar called the Boundary Layer Radar (BLR) at a distance of 65 km southwest from the MU site. The purpose of the present paper is to demonstrate the meso-α-scale wind and precipitation fields, and to clarify meso-β and -γ-scale features of rainbands and the inner core in the typhoon.

2. Meso-α-scale kinematic structure of the typhoon

In front of the typhoon (Fig. 1), the meso-α-scale wind field is characterized by the low-level cyclonic wind with the maximum and outflow regions tilted outward with height. The tilted outflow regions may be interpreted as internal gravity waves, proposed as a mechanism of the outward-propagating rainband in previous studies. The continuous strong updraft occurs within the stationary precipitating cloud through the orographic effect of the higher mountain region. Meso-β-scale updrafts appear within the inner cloud and band-shaped cloud at upper level. The upper-level clouds seem to contribute to the formation and maintenance of the stratiform precipitation by the seeder-feeder mechanism. In the vicinity of the typhoon center, the tangential wind has the vertical spiral structure for the center, considered as a result from the deformation of the center of the decaying typhoon. In the rear of the typhoon without

precipitating clouds, the cyclonic wind becomes weak, and the outflows and vertical motions seen in the front are not detected.

3. Meso-β and -γ-scale features of rainbands and eyewall

Meso-β and -γ-scale features of the eyewall and wide rainband in the front were examined. In the eyewall, the meso-γ-scale remarkable updraft associated with the outflow region, considered to be a part of the vertical circulation, is found in the upper troposhere. The outflow region tilted outward originates from the area of maximum radial shear of the low-level cyclonic wind. It extends to the updraft region within the upper-level band-shaped cloud. The wide rainband is located at the outer edge of the band-shaped cloud, and it lasts in the development of the cloud. This accompanies the tilted outflow region, the bottom of which is located at the maximum of the cyclonic wind. The narrow rainband, that had a quit short (1.5 hours) lifetime, was also examined based on the BLR observation. It is accompanied by the tilted outflow region in its convective portion, but strong cyclonic wind, as seen in the wide rainband, is not detected in the bottom of the outflow region. These results suggest that the outflow with the wave-like structure, associated with the low-level strong cyclonic wind, contributes to the development and maintenance of the upper-level cloud and rainband.

4. Conclusions

A general structure of Typhoon 9426 (Orchid) up to the lower stratosphere including the inner core region was observed by the MU radar in 29-30 September 1994. The kinematic structure in the front and rear of the typhoon is quite different because of its transition from mature to decaying stages and the asymmetric distribution of cloud and precipitation. A meso-α-scale wind field and meso-β and -γ scale features of precipitating clouds in the typhoon were investigated in this study. In the future, we are expecting to use more transportable wind-profiling radars, and to accumulate observational case studies on typhoons.

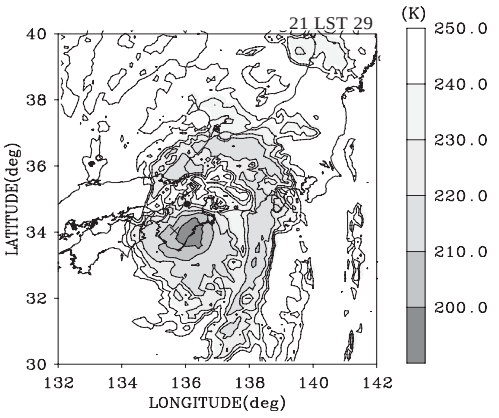

Fig. 1: Horizontal distribution of taller clouds based on TBB of GMS IR at 21 LST 29. Circle and cross marks are locations of the MU site and the typhoon center.

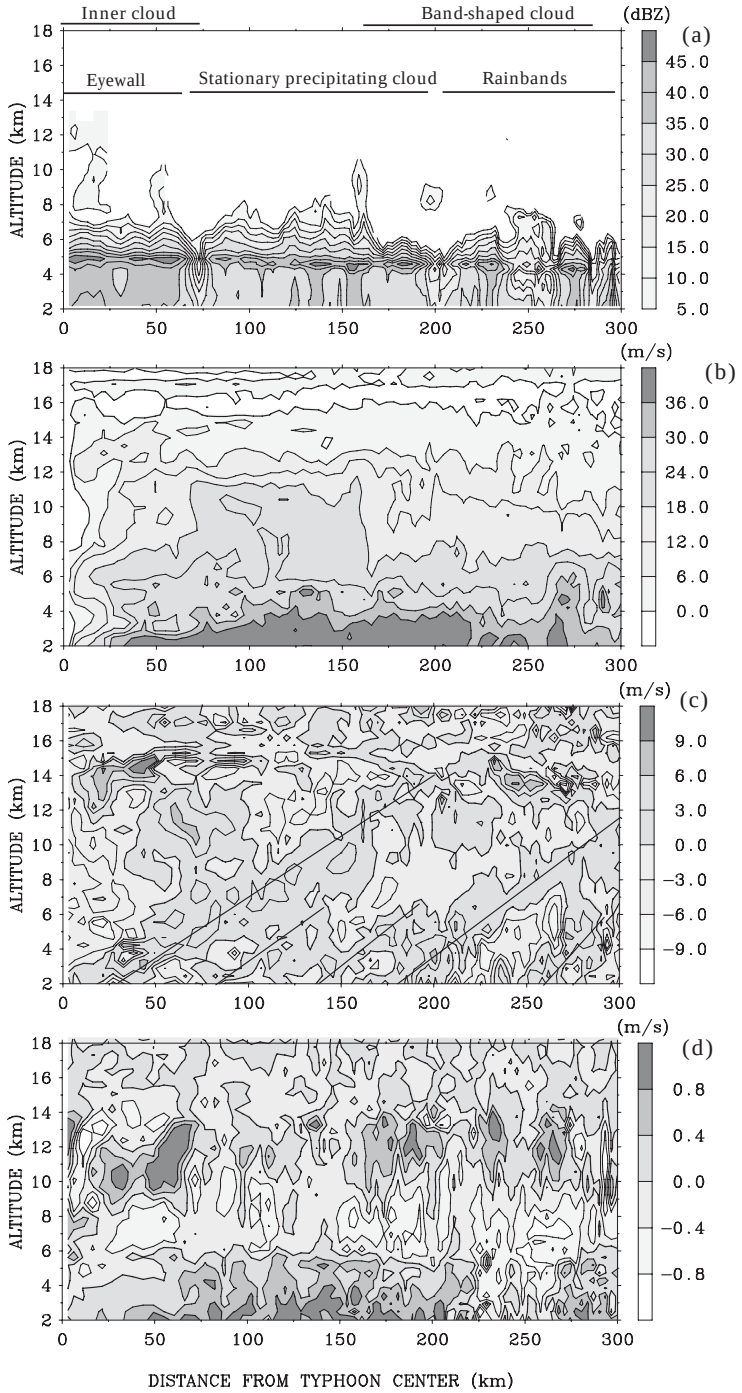

Fig. 2: Radius-height cross-sections of (a) reflectivity observed by the vertical pointing radar, (b) tangential wind and (c) radial wind relative to the environmental wind and (d) vertical velocity obtained by the MU radar in front of the typhoon. In (c), the outflow regions tilted outward with height are shown by solid lines.

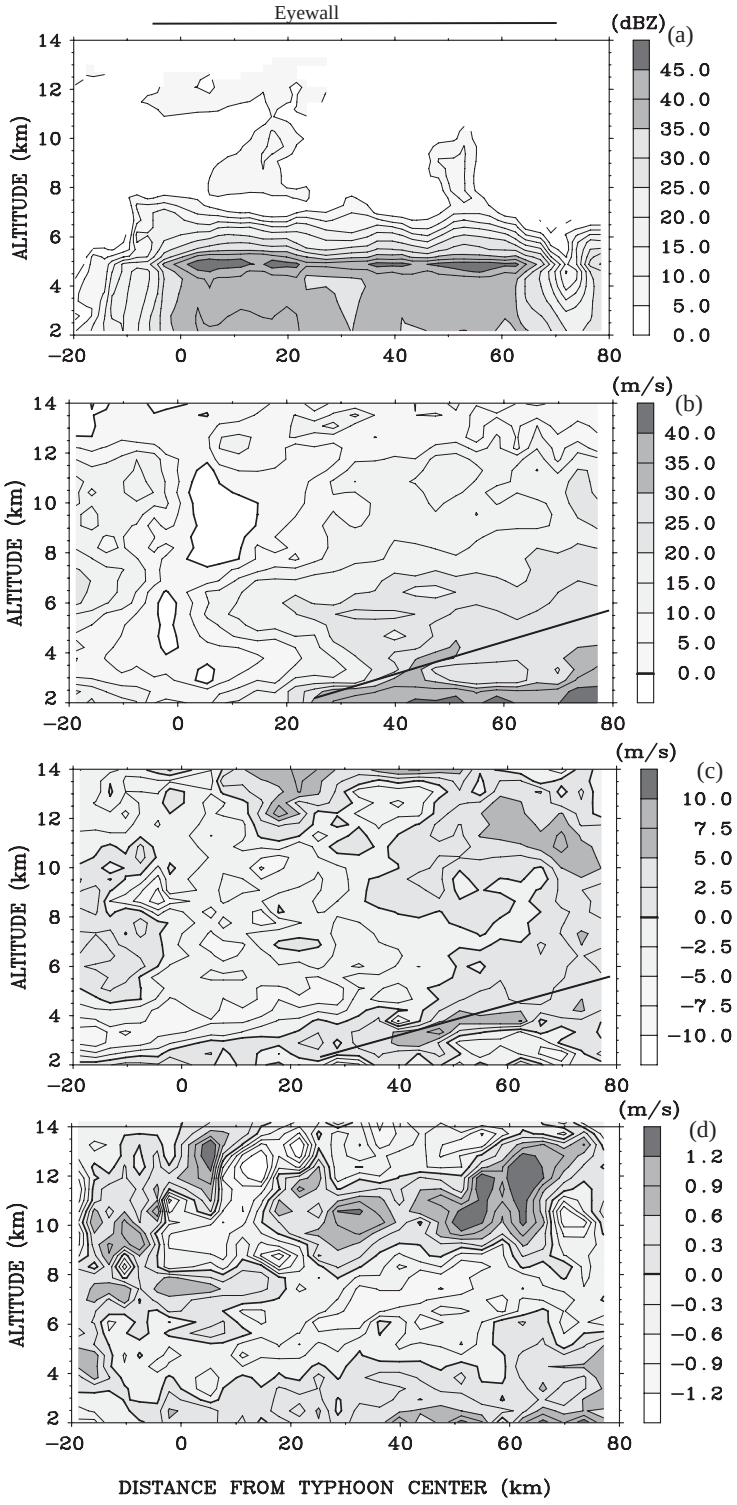

Fig. 3: Radius-height cross-sections of (a) reflectivity, (b) tangential wind and (c) radial wind relative to the environmental wind, and (d) vertical velocity in the eyewall. The outflow region tilted outward with height is shown by a solid line.

RANGE, RESOLUTION, AND SAMPLING

Paul E. Johnston[1,2], Leslie M. Hartten[1,2], David A. Carter[2], and Kenneth S. Gage[2]

1. CIRES/University of Colorado, 216 UCB, Boulder, CO, 80309-0216, USA
2. NOAA Aeronomy Laboratory, 325 Broadway, Boulder, CO, 80305-3328, USA

Figure 1 shows a nagging problem. This plot of wind speed profiles from Christmas Island, Kiribati, shows the results from wind profilers operating with three different pulse lengths. These curves are the average of all available February winds for the years 1994-1996. Two curves are from a 915-MHz radar, using pulse lengths of 100 m and 500 m. The final curve is from a 1000 m long pulse from a 50-MHz radar. There are many measurements represented by these profiles, and the estimated measurement errors in these profiles are very small. However, the low-level jet has a different magnitude and occurs at a different height in each curve.

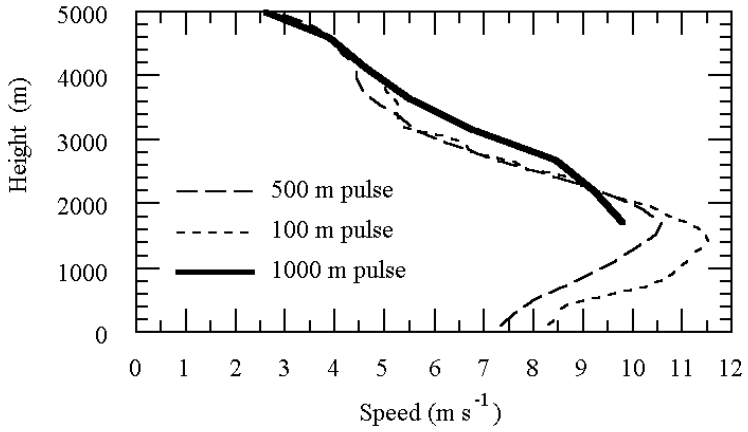

Figure 1. Mean February wind speed for 1994-1996 at Christmas Island, Kiribati. The 1000-m data are from the 50-MHz radar. The 100-m and 500-m data are from the 915-MHz radar. (Adapted from Johnston et al., 2002)

Johnston et al. (2002) discuss why the maxima don't occur at the same heights when observed with different pulse lengths. This paper discusses why different pulse lengths don't observe the same peak velocity. Many in the profiler community would say that the answer is obvious; the longer pulse lengths average over larger volumes and average out peak velocities. This is a true and qualitative explanation of the observations, but some of the details need to be examined to present a more complete picture. This is especially true since the data plotted as continuous curves in Figure 1 are really discrete points, each representing some volume in space.

One classic approach to exploring the range behavior of a radar is to define a range-weighting function, $|W(r)|^2$. This is a description of the ranges that contribute to the observed signal at a given range. It is derived from the time response of the receiver to the transmitted pulse, which is the convolution of the filter response to the transmitted waveform. One common parameterization is to specify the $B_6\tau$ product of the system, where B_6 is the -6 dB (half-voltage) bandwidth of the receiver and τ is the pulse length of the transmitted pulse. For a rectangular transmit pulse and a Gaussian filter response the maximum Signal-to-Noise Ratio, SNR, occurs at $B_6\tau=1.04$, called the matched filter condition (Doviak and Zrnić, 1993). Several factors contribute to the determination of the $B_6\tau$ product in a radar. These include maximizing SNR, setting the range over which the samples are independent, hardware implementation, and data storage and processing limitations. Some Aeronomy Laboratory (AL) radars have $B_6\tau$ products

as low as 0.55. The Piura 50-MHz radar has a $B_6\tau$~0.74 in its current configuration.

A more general form of the radar equation, (1), shows how the range-weighting function affects the data obtained by the radar. In (1), the range-weighting function is shown as a function of the range from the radar, r_0, and the distance around this range, r. The received power comes from the integration of the product of the reflectivity, $\eta(r)$, and the range-weighting function:

$$P_r(r_0) = \int_0^{r_0+\Delta r} \eta(r) \frac{|W(r_0, r)|^2}{r^2} dr \qquad (1)$$

Using numerical methods, the range-weighting function, $|W(r_0,r)|^2$, can be calculated. Figure 2 shows the range-weighting function for a 500 m long transmitted pulse and four values of the $B_6\tau$ product. The range extent of the volume described by the radar output is determined by the range-weighting function. A way to summarize this is to define the range resolution of the radar as the distance between the -6 dB points (0.25 relative power level) of the range-weighting function. Figure 2 shows that when $B_6\tau$ is large, e.g. $B_6\tau$=10.0, the range resolution is 500 m for a 500 m long pulse. The matched-filter case, $B_6\tau$=1.04, gives a resolution of 574 m, $B_6\tau$=0.83 gives a resolution of 648 m, and a small $B_6\tau$ of 0.55 gives a resolution volume that is 877 m between the -6 dB points. In casual discussions, the profiler community describes the range resolution only as the pulse length, $c\tau/2$.

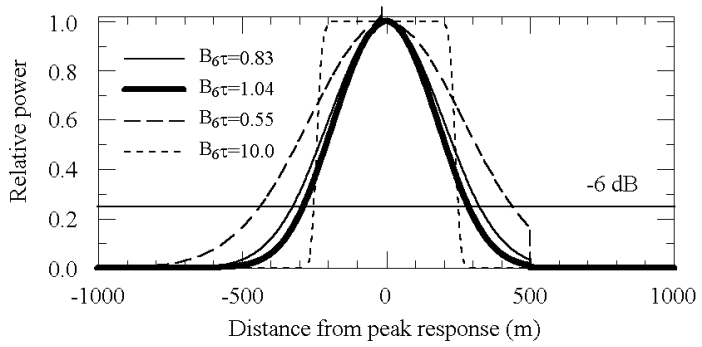

Figure 2. Range weighting functions for a pulse length of 500 m. Four different receiver bandwidths are shown. The horizontal line shows the -6 dB level.

Equation 1 shows that the response of the radar to signals in space is controlled (in range) by the range-weighting function and the reflectivity of the atmosphere. The reflectivity properties of the atmosphere can cause differences in the location of the maximum velocities, as seen in Figure 1 (Johnston et al., 2002). The range-weighting function shown in Figure 2 determines the radial portion of the volume that contributes to the radar data at a given point in space. The antenna response of the radar determines the tangential, or across beam, dimensions of the volume.

When we sample the continuous signal received by the radar at discrete points, the volume represented by each sample is determined by the range-weighting function and the antenna response. This sampling of the radar signals has nothing to do with the range resolution of the radar. Using the example of a 500-m pulse length and a $B_6\tau$ product of 1.04, each data sample will represent data from a volume that is approximately 574 m deep. The sampling of the received signal could be done every 1 m, or every 10 km, and the range represented by each sample would be a radial distance of 574 m centered at the sample range, assuming uniform reflectivity in the volume (c.f. Johnston et al., 2002).

The range-weighting function, which describes the range behavior of a radar, is derived as the convolution of the transmitted pulse and the receiver impulse response. A different way to look at the range behavior is to examine the response in the frequency domain, where the range response can be easily calculated as the product of the transmitted spectrum and the receiver

frequency response. This calculation gives the curves of Figure 3 for two of the $B_6\tau$ values of Figure 2. It shows that higher resolution requires a larger bandwidth. In this case the -6 dB bandwidth for a 500 m pulse ($B_6\tau$=1.04) is 240 kHz, while for the $B_6\tau$=0.55 case, the -6 dB bandwidth is only 152 kHz.

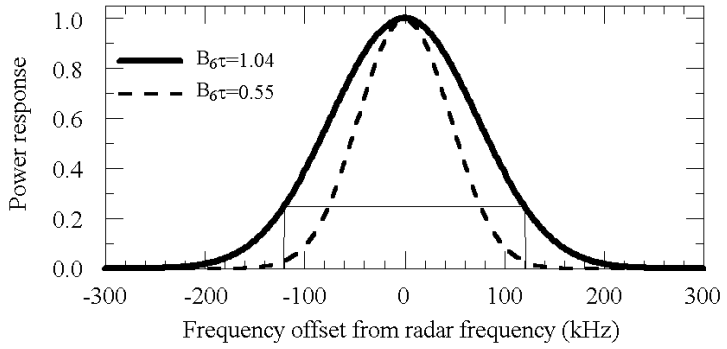

Figure 3. Frequency response of system using 500 m long pulse, with two different B6τ products. The box shows the -6 dB points of the matched filter.

The Nyquist criterion states that if we want to be able to fully reconstruct this signal, we need to sample at a rate at least twice the highest frequency in the signal. The choice of the maximum frequency is arbitrary so if one uses the -6 dB frequencies, then this means that the sampling needs to be done at 2*240 kHz, or 480 kHz, or once every 2.1 μs (312.5 m). Note that many times in the radar community, sampling in range at intervals less than one pulse length is referred to as "over-sampling". Many meteorological radars set the sampling equal to the pulse length so that the samples are independent. However, if one uses a Nyquist criterion to determine sample spacing with the goal of accurately reproducing the signal as a function of time, or the profile as a function of range, then it would not be unreasonable to use 2 or more samples per pulse length.

When looking at time series from a single height, it is useful to examine the Doppler spectrum of the time series. This spectral representation shows how the signal varies as frequency, or the reciprocal of time. This is the method used by the AL to obtain the wind speeds at each height in order to produce the data in Figure 1. Another time series available from the radar is the range series, showing the atmospheric profile of the received signal. We usually convert the time delay from the radar to the echoing volume to distance from the radar, but it is still a time series. In a manner analogous to time series spectra, a spatial frequency could be defined, as the reciprocal of range instead of time. Here we choose not to do this, but to discuss spatial frequencies in units of reciprocal length. For example, the 3.3 μs long pulse requires a 240 kHz bandwidth between the -6 dB points. The reciprocal of 240 kHz is 4.17 μs, which has a reciprocal scale length of 625 m. This means that spatial features of 625 m or shorter (higher frequencies) have been attenuated in the signal by more than 0.25 (-6 dB). If we look at the same atmosphere with a $B_6\tau$=0.55 and a 500 m long pulse, the reciprocal scale length is 987 m, reflecting the fact that the receive bandwidth is narrower.

The time and frequency domains tell us similar information. In the time domain, where the system response is specified by the resolution, we learn about the ranges that contribute to the data in a sample. In the frequency domain, the reciprocal lengths define the size of the structures that contribute to the data at a given range. The frequency domain also gives us information about how we need to sample our data in range in order to accurately reproduce the data.

Why do we want to be able to accurately reconstruct the range profile of the radar signal? The simple answer is to improve the accuracy and precision of the instrument. If we want to

place features in the profile with more precision than ½ of the range resolution we need to be able to reconstruct the profile. If we want to be able to report our data at standard heights, instead of heights determined by the radar hardware, we need to be able to interpolate the data. Interpolation is a reconstruction of the signal followed by re-sampling at the desired ranges. If we want to be able to follow signal attributes in range, we need to make sure we have an accurate range representation of the signal.

In Figure 1, the data were obtained using matched filters ($B_6\tau$=1.04) in all three pulse lengths. The range resolutions of the system bandwidths are 115 m for the 100-m long pulse, 574 m for the 500-m pulse, and 1148 m for the 1000-m pulse. The 1000-m and 500-m data are sampled twice per pulse length, and the 100-m data are sampled once per pulse length. Figure 4 shows part of the data from Figure 1. The range resolution of each mode has been shown as vertical bars at two heights for each profile, so that the volume represented by each sample is clearer. The different attenuation of spatial scales is apparent. The magnitude of the low-level jet is smaller with the longer pulse lengths, as expected, but is not the simple average of the appropriate number of points. For example, the average of the 5 largest, contiguous speeds of the 100-m data is 11.4 ms^{-1}, which is still much larger than the 10.6 ms^{-1} observed by the 500-m pulse. The differences in spatial averaging by the different pulse lengths do not account for all of the observed differences in the profiles. Future work will be directed towards studying the possible interactions between atmospheric reflectivity and velocity structures and the range-resolution characteristics of various profilers.

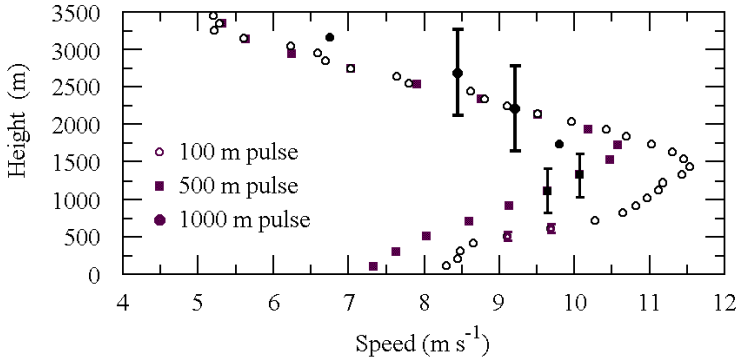

Figure 4. Details of the mean February wind speed for 1994-1996 at Christmas Island, Kiribati. The vertical bars indicate the range resolution of the different pulse lengths.

Range resolution and data sampling are complex issues. The reflectivity of the atmosphere interacts with the radar in a non-linear fashion to produce results that are not straightforward. When we are interesting in the changes of the signal with range, i.e. profiling, special attention needs to be made to the spacing between the samples in range. Careful attention to these issues is important to help produce better interpretations of the data.

REFERENCES:

Doviak, R.J., and D.S. Zrnić, *Doppler Radar and Weather Observations, Second Edition*. Academic Press, 562pp, 1993.

Johnston, P.E., L.M. Hartten, C.H. Love, D.A. Carter, and K.S. Gage, Range errors in wind profiling caused by strong reflectivity gradients, *Journal of Atmospheric and Oceanic Technology, 19*, 934-953, 2002.

AN OBSERVATIONAL STUDY ON INTRASEASONAL VARIATIONS WITH EQUATORIAL ATMOSPHERE RADAR (EAR) IN WEST SUMATERA, INDONESIA

H. Hashiguchi[1], T. H. Seto[1], S. Fukao[1], M. K. Yamamoto[1], M. Fujiwara[2], T. Horinouchi[1], M. Yamamoto[1], M. Muzirwan[3], and M. Kartasasmita[3]

1: Radio Science Center for Space and Atmosphere (RASC), Kyoto University, Uji, Kyoto 611-0011, Japan
2: Graduate School of Environmental Earth Science, Hokkaido University, Sapporo 060-0810, Japan
3: National Institute of Aeronautics and Space (LAPAN), Indonesia

1. Introduction

Intraseasonal variation (ISV) has been extensively studied over the past two decades and is well established as the dominant mode of tropical convective anomalies in the atmosphere. It is characterized by eastward-propagating tropical convection and circulation anomalies with a period of between 30 and 60 days (e.g., Madden and Julian, 1994; Rui and Wang, 1990). Many studies have shown that super cloud clusters (SCCs) correlated with ISV develop over the Indian Ocean, and then propagate eastward (e.g., Matthews, 2000). Convective activities over Sumatera are heavily influenced by ISV, since that place is located at the eastern edge of the Indian Ocean. Hendon and Salby (1994) have shown that convective activities associated with ISV are strongest near 100E. On the other hand, Nitta et al. (1992) showed that eastward propagating SCCs frequently break-off due to the topographic effect of Sumatera when they pass over it. Therefore, convective activities over Sumatera play an important role in ISV behavior over the Indonesian maritime continent.

A VHF radar is an excellent tool to observe three-dimensional winds in the whole troposphere (e.g., Larsen and Roettger, 1982; Gage, 1990; Thomas, 1999). In the tropics, VHF radar observations have been performed over the tropical Pacific (e.g., Gage et al., 1991), and in India (Rao et al., 1995). However, observations through the whole troposphere by a VHF radar have never been performed over Sumatera. The Equatorial Atmosphere Radar (EAR), installed near Bukittinggi, West Sumatera, Indonesia (0.20S, 100.32E), can observe three-dimensional winds in the whole troposphere and the lower stratosphere (2-20 km), with high time and height resolutions of about 90 sec and 150 m, respectively (Fukao et al., 2003). The EAR has been operated continuously since July 2001. In this paper, we focus on an ISV event in June 2002, and study its influence on convective activities over Sumatera.

2. Eastward-propagating convective system

In June 2002, an ISV event was observed over the Indian and western Pacific Ocean. Figure 1 shows the time-longitude plot of T_{BB} averaged over 0.1S-0.3S during June 2002. Eastward-propagating super cloud clusters (SCCs) appear over the Indian Ocean (75-85E) during 1-7 June 2002. Then SCCs move eastward, and pass over the radar site (100.32E) during 11-16 June 2002. After passing over Sumatera, the activities of SCCs became weak around 100-110E, then became active again when they reached the longitude of 135E (during 16-21 June 2002).

Based on the existence of SCCs relative to the radar site, we divide the observational period into 3 periods:

- Period 1 (June 1-10): SCCs exist on the west side of Sumatera,
- Period 2 (June 11-16): SCCs exist over Sumatera,
- Period 3 (June 17-30): SCCs exist on the east side of Sumatera.

During Period 2, two SCCs pass over Sumatera. The first SCC reaches the radar site on 11 June, and the second one exist over the radar site during 14-16 June.

Figure 2 shows the time-altitude plot of the EAR zonal wind in June 2002. Zonal wind is averaged every four hours. Zonal wind at 2-4 km altitude is easterly or weak westerly in Periods 1 and 2. On 17 June 2002, when SCCs passed over Sumatera, a westerly wind burst with amplitude of >10 m s^{-1} is observed in 2-3 km altitude. After that, westerly wind prevails in 2-4 km altitude. The tropopause-level Kelvin waves are seen at 16-20 km altitudes, as was shown in other studies (e.g., Fujiwara and Takahashi, 2001; Fujiwara et al., 2003).

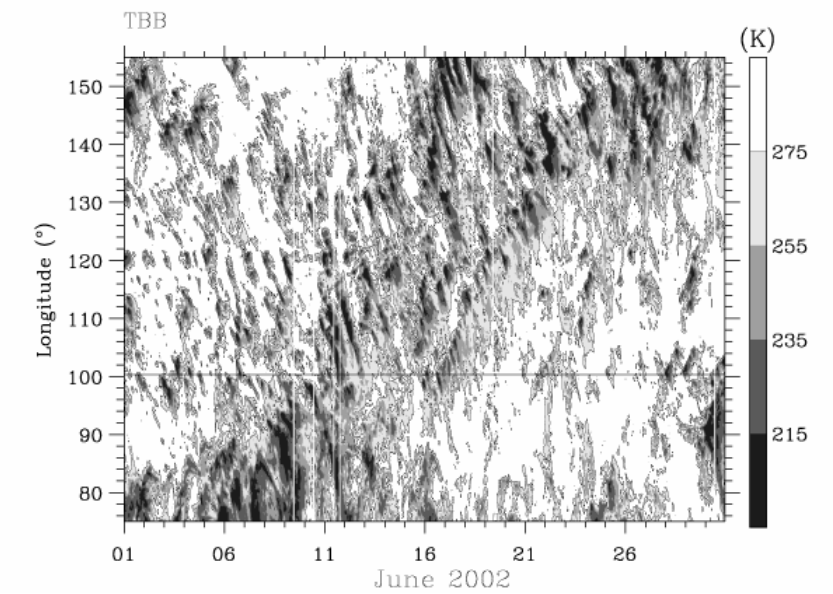

Figure 1: Time-longitude plot of T_{BB} averaged over 0.3S-0.1S in June 2002. Horizontal solid line indicates the longitude of the radar site (100.32E).

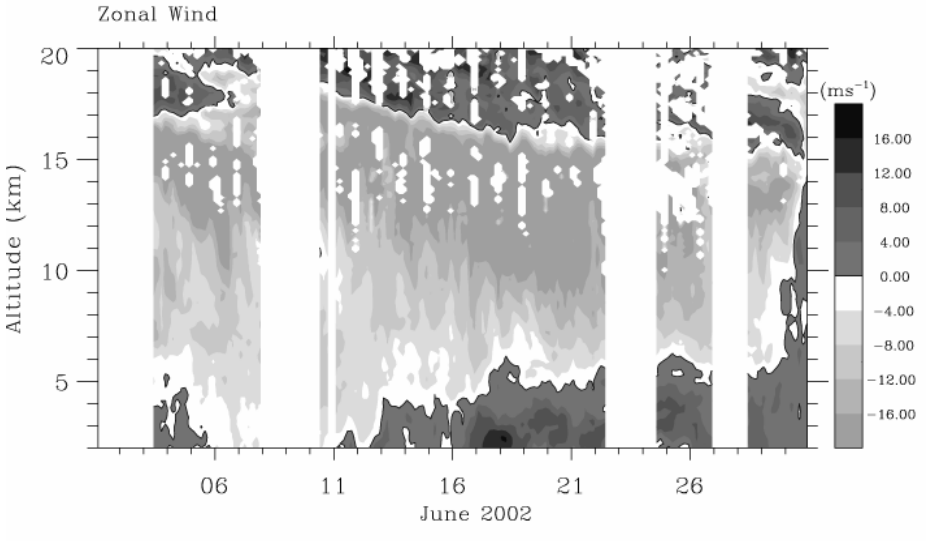

Figure 2: Time-altitude plot of zonal wind observed with the EAR in June 2002.

Low-level zonal wind has a good correlation with eastward-propagating SCCs. Namely, when SCCs exist in the west side of or over the EAR site, easterlies or weak westerlies were observed in 2-4 km altutude, and conversely after SCCs pass over the EAR site, westerlies are observed. Anti-correlation between 2-4 km zonal wind and 10-12 km zonal wind are very clear. Existence of rainfalls in the easterlies and the anti-correlation of zonal winds between in the lower troposphere and upper troposphere agrees well with the structure of the moist Kelvin wave shown by Wang (1988).

3. Variance of vertical wind

As an index of convective activities, we introduce the variance of vertical wind (VVW), which is computed using the vertical wind obtained from the EAR. We confirmed VVW represents convective activities by comparing with K index derived from radiosonde data. Figure 3 shows the time-altitude plot of daily VVW in June 2002. In Period 1, large VVW (>0.07 m^2 s^{-2}) is observed at 2-16 km altitude. On the other hand, large VVW is observed at 7-16 km altitude while small VVW (<0.03 m^2 s^{-2}) is observed at 2-7 km altitude in the beginning of Period 2 (11 June), when the center of first SCC reaches the radar site. At the end of Period 2 (15-16 June), typical VVW (0.03-0.07 m^2 s^{-2}) is observed at 2-16 km altitude. In the beginning of Period 3, typical VVW is observed at 2-4 km altitude, but small VVW is observed above 4 km altitude. This shows that convective activities do not reach the level above 4 km. It is consistent with very little rainfall observed during Period 3. From these results, it can be said that convections are active during Period 1, when low surface pressure and low-level easterlies (or weak westerlies) are observed.

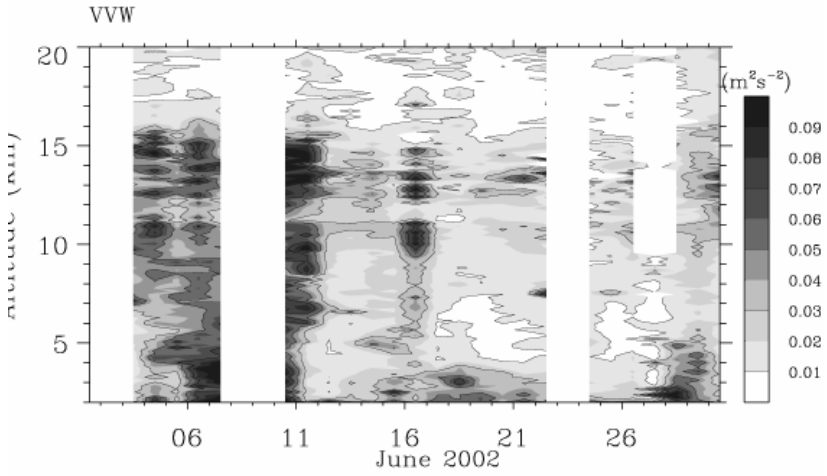

Figure 3: Time-altitude plot of VVW in June 2002.

4. Discussion and conclusion

Following the cloud types defined by Williams et al. (1995), we have classified clouds into four types using BLR observation data. In Period 1, low-level zonal wind is easterly or weak westerly. Low pressure, high humidity, and high solar radiation are observed at the surface. These conditions cause the generation of deep convections over Sumatera. Although high cloud-top clouds are observed over the radar site in Period 2, no significant convective activity exists over Sumatera. Convective clouds develop on the east side of the radar site, propagate westward and are observed as stratiform clouds over the radar site. Rainfall over

Sumatera occurs by stratiform clouds which are dominant in this period. That is why precipitations on 11 June 2002 are dominated by stratiform precipitating clouds. Convections at the end of Period 2 (14-16 June) are shallow because surface convergence moves to the east of Sumatera. In period 3, convections over Sumatera are suppressed by the strong westerly. High surface pressure enlarges surface divergence at the radar site. No cloud activities occur under those conditions.

Acknowledgments

The authors thank Frontier Observation Research System for Global Change (FORSGC), Japan, the Indonesian Agency for the Assessment and Application of Technology (BPPT), Indonesia, and the Indonesian Meteorological and Geophysical Agency (BMG), Indonesia, for providing radiosonde data. The EAR belongs to RASC and is operated by RASC and National Institute of Aeronautics and Space (LAPAN), Indonesia based upon the agreement between RASC and LAPAN signed on September 8, 2000. They also thank all operators who maintain the EAR and BLR. The present study was partially supported by Grant-in-Aid for Scientific Research on Priority Area-764 of the Ministry of Education, Culture, Sports, Science, and Technology (MEXT) of Japan. The first author is financially supported by Loan Japan Bank for International Cooperation (JBIC) - Science, Technology, and Industrial Development (STAID) Program of Indonesian government.

References

Fujiwara, M. and M. Takahashi., Role of the equatorial Kelvin wave in stratosphere-troposphere exchange in a general circulation model, *J. Geophys. Res*., **106**, 22, 763--22, 780, 2001.

Fujiwara, M., M.K. Yamamoto, H. Hashiguchi, T. Horinouchi, and S. Fukao, Turbulence at the tropopause due to breaking Kelvin wave observed by the Equatorial Atmosphere Radar, *Geophys. Res. Lett*., **30**, doi:10.1029/2002GL016278, 2003.

Fukao, S., H. Hashiguchi, M. Yamamoto, T. Tsuda, T. Nakamura, M.K. Yamamoto, T. Sato, M. Hagio, and Y. Yabugaki, The Equatorial Atmosphere Radar (EAR): System description and first results, *Radio Sci*., **38**, 1053, doi: 10.1029/2002RS002767, 2003.

Gage, K, S., The structure and dynamics of the free atmosphere as observed by VHF/UHF radar, in Radar in Meteorology, edited by D. Atlas, pp. 534-565, *American Meteorological Society*, 1990.

Gage, K. S., B.B. Balsley, W.L. Ecklund, D.A. Carter, and J.R. McAfee, Wind profiler-related research in the tropical Pasific, *J. Geophys. Res*., **96**, 3209-3220, 1991.

Hendon, H. H. and M.L. Salby, The life cycle of the Madden-Julian oscillation, *J. Atmos. Sci*., **51**, 2225--2237, 1994.

Larsen, M. F. and J. Roettger, VHF and UHF doppler radars as tool for synoptic research, *Bull. Am. Meteorol. Soc*., **63**, 996--1008, 1982.

Madden, R. A. and P.R. Julian, Observations of the 40-50-day tropical oscillation - A review, *Mon. Wea. Rev*., **122**, 814-837, 1994.

Matthews, A. J., Propagation mechanisms for the Madden-Julian oscillation, *Quart. J. Roy. Meteor. Soc*., **126**, 2637-2652, 2000.

Nitta, Ts., T. Mizuno, and K. Takahashi, Multi-scale convective systems during the initial phase of the 1986/87 El Nino, *J. Meteor. Soc. Japan*, **70**, 447-466, 1992.

Rao, P. B., A.R. Jain, P. Kishore, P. Balamuralidhar, S.H. Damle, and G. Viswanathan, Indian MST radar 1. System description and sample vector wind measurements in ST mode, *Radio Sci*., **30**, 1125-1138, 1995.

Rui, H. and B. Wang, Development characteristics and dynamic structure of tropical intraseasonal convection anomalies, *J. Atmos. Sci*., **47**, 357-379, 1990.

Thomas, L., Aplications of the NERC MST radar facility in mesoscale studies, *Meteorol. Appl*., **6**, 133-142, 1999.

Williams, C.R., W.L. Ecklund, and K.S. Gage, Classification of precipitating clouds in the tropics using 915-MHz wind profilers, *J. Atmos. Oceanic Technol*., **12**, 996-1012, 1995.

Wang, B., Dynamics of tropical low-frequency waves: An analysis of the moist Kelvin wave, *J. Atmos. Sci*., **45**, 2051-2065, 1988.

A COMPREHENSIVE STUDY ON TROPICAL MESOSCALE CONVECTIVE SYSTEMS USING VHF AND UHF RADARS OVER A TROPICAL STATION

K. Kishore Kumar & A.R. Jain

National MST Radar Facility, P.B. 123, Tirupati-517502, India.

1. Introduction

A vast majority of recent observational studies of mesoscale systems have been signifying a renewed interest in tropical mesoscale convective systems (TMCS) and their impact on general atmospheric circulation and hence the global climate. Tropical convection transports and redistributes the large-scale fields of heat, moisture, mass, radiation and momentum throughout the atmosphere. The redistribution of various quantities affects the troposphere composition and its chemistry, especially the tropospheric air quality. They also alter the flow fields and thermodynamic stratification within the atmosphere such that they affect subsequent convective activity.

Several convection campaigns have been carried out since 1996 at this Radar Facility to explore the TMCS. All these campaigns have been carried out in two regimes, one in South – West monsoon (June –September) and another in North – East monsoon (October-November). This article presents a summary on the observations of convective systems carried out during the convection campaigns over Gadanki. VHF and UHF radars observations of TMCS have been studied extensively to understand its various aspects. The Height-time sections of echo power (in terms of signal to noise ratio), turbulence intensity (in terms of spectral width) and vertical velocity of various types of convective systems are discussed. The interesting features like weak echo regions (WER), vertical velocity cores are also discussed. VHF/UHF radar observations have been used to classify the observed system into convective, transition and stratiform regions. The composite height profiles of vertical velocities in these regions are computed from VHF radar observations for the first time at this latitude. The central objective of this paper is to give an idea of various types of convective systems occurring at this latitude and to study their height-time structures.

2. Database

During the campaign periods, all the collocated facilities (VHF radar, UHF radar, Optical Rain Gauge, Disdrometer and Automatic weather Station) available at Gadanki are operated to monitor the passage of convective systems. For the present study, data collected from three instruments *viz.,* VHF radar, UHF radar and disdrometer are used. However, simultaneous VHF and UHF radar observations are available only during August 1997 – September 2001. After this period, due to some technical problems UHF radar is not operated. Disdrometer observations are available from September 1997-June 2002

3. Results and discussion

Figure 1 (a) shows typical VHF radar vertical beam power spectrum obtained during clear-air conditions. This spectrum shows vertical velocities of the order of a few tens of cm/sec. Figures 1(b) and 1(c) show the power spectra obtained during the passage of a deep convective system. The power spectrum shown in the figure 1(b) shows large vertical velocities of the order of several m/s as indicated by the large Doppler shifts. Another substantial difference in clear air and convective system power spectra is the Doppler widths, which are larger for the spectrum obtained in the convective systems as compared to the clear air spectrum. From figure 1 (c), it is

very interesting to note the double traces of the echoes in the height region of 2.4 - 4.5 km. These traces correspond to the clear-air and hydrometeors. The extreme right hand side trace is the hydrometeor fall velocity spectrum due to Rayleigh scattering and the other is the clear-air velocity spectrum due to Bragg scattering. In the present study, only clear-air echoes have been used to explore the structure of the observed convective systems and enough care has been taken to avoid the hydrometeor echoes during the analysis of the present data as suggested by Narayana *Rao et al*. [1999].

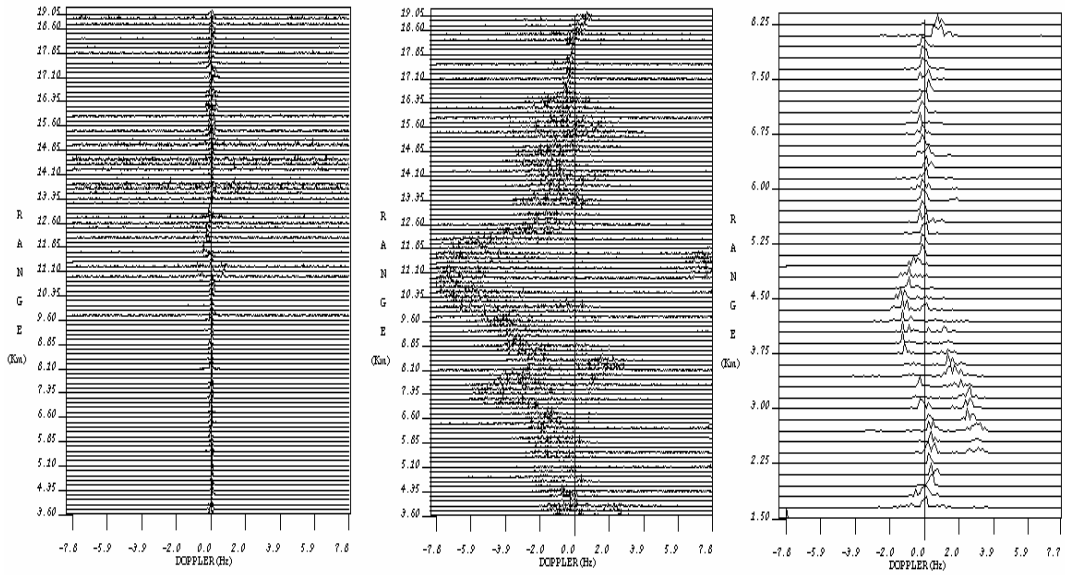

Figure 1: Typical VHF radar power spectra obtained in (a) clear-air, (b) and (c) in convection environments on 25 May 2002.

Deep convection events are classified into single cell, multi cell and super cell events. Out of these, multi cell events are very common at this latitude. Figure 2 shows the typical height-time sections of vertical velocities for the single cell, multi cell and super cell events as observed on 25 May 2002, 15 Sep 2001 and 06 June 1996 respectively. The top panel clearly shows a single vertical velocity core with a maximum velocity of ~15 m/s during 1430-1450 hrs. The vertical extent of this core is of ~ 8km. This plot reveals the structure of a typical single cell convective system occurring at this latitude. The second kind of deep convective system consists of multi cells having more than one vertical velocity core as shown in the middle panel of the figure 2. This panel readily shows three well separated vertical velocity cores with different vertical extents, which make it a multi cell event. It can be noted from this plot that the maximum vertical velocity observed on this day is ~ 10 ms^{-1}.

Most of the height-time sections of vertical velocities of the single/multi cell convective systems observed in the present dataset show one common feature. The vertical velocity cores in these systems are accompanied by downdrafts. These upper level downdrafts (well above the freezing level) adjacent to the updrafts can be attributed to sublimation and condensate loading [*Knupp,* 1987]. Other possibilities for these downdrafts include a blocking effect [*Lemon and Do*swell, 1979], but the downdrafts occur on both sides of the upward cores and other studies show complicated relationship between the upward and downward cores [*Heymsfield and schotz*, 1985]. These studies suggest that the upper-level cores may be driven, at least in part, by pressure perturbations induced by the strong updrafts. The other category of downdraft, which is

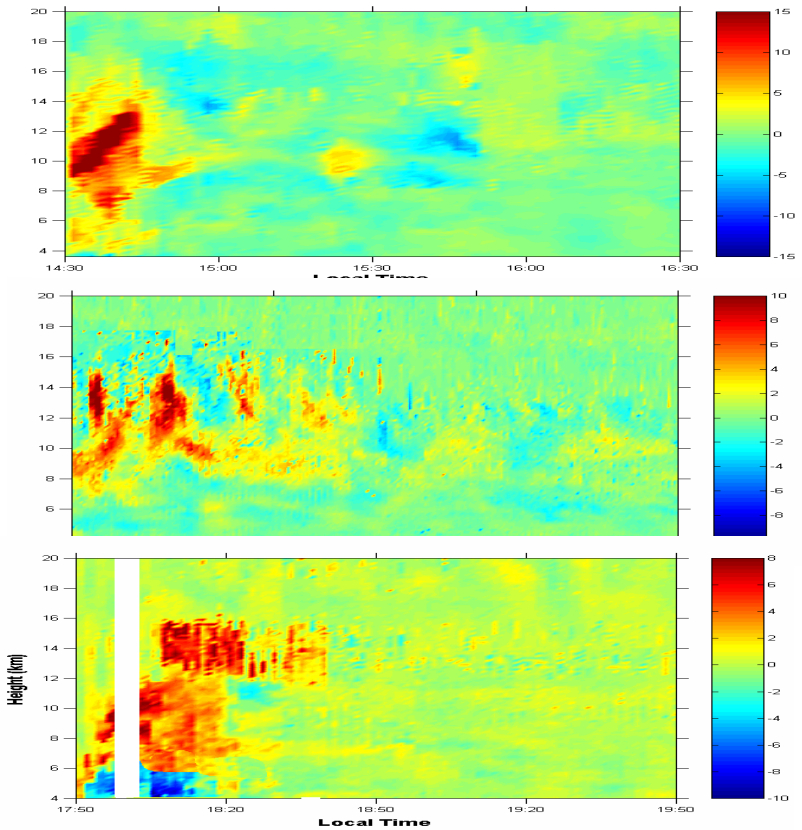

Figure 2: Height time sections of VHF radar observed vertical velocities (m/s) on (a) 25 May 2002 (b) 15 Sep2001 and (c) 06 June 1996.

occurring below the freezing level (low level downdraft), is mainly precipitation/evaporatively driven.

The last category under the deep convective systems is the super cell storms, which are very rare to be observed at this latitude. However, one such system, which closely resembles this type of storm, has been observed in the present dataset. From the bottom panel of vertical velocity plot, it is very exciting to note a single, steady vertical velocity core of ~10 Km vertical dimension with maximum vertical velocity of ~8m/s. This is one of the rare vertical velocity structures to be observed at this latitude. Under very rare circumstances, when there is both large CAPE and large vertical shear of large-scale horizontal wind, moist convection may assume the form of a single, highly organized, quasi-steady circulation, which is widely known as super cell thunderstorm. Another typical character of these storms is the rotating updrafts. Using the present observations, it would not be possible to draw any conclusions on the rotation of the updrafts.

Figure 3 shows the composite height profiles of clear air vertical velocities observed by the VHF radar in convective, transition and stratiform region of the TMCS. Each deep convective system is classified into the above mentioned regions and then the vertical velocities are averaged in the respective regions. These vertical velocity profiles in the three regions are obtained for the 14 deep convective systems and are averaged to get the composite height profiles. In the present study, the composite vertical velocity profile of convective region is showing a peak in the mid troposphere. This represents that the release of latent heat is more at those height regions. These profiles do give an idea of heating within the convective systems. These vertical velocity profiles are very useful in determining the vertical distribution of diabatic heating in the convective and stratiform regions. These composite vertical velocity height profiles of convective, transition regions and stratiform regions, which vary from one geographical location to other, have very special implications in the mesoscale modeling and in the convective system simulation studies.

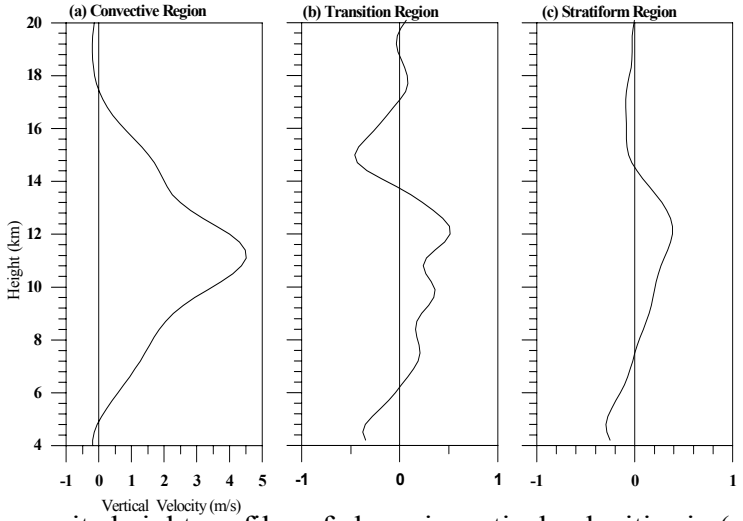

Figure 3: Composite height profiles of clear air vertical velocities in (a) Convective, (b) Transition and (c) Stratiform regions.

4. Summary

The height-time sections of several convective systems are studied to explore their reflectivity, turbulence and vertical velocity structure. The deep convective systems are classified into single, multi and super cell systems and height- time sections of the same are discussed. It is observed that most of the convective systems are multi cell systems at this latitude. Composite height profiles of vertical velocities in convective, transition and stratiform region are obtained and the same are compared with the profiles obtained at other geographical locations. Convective region composite vertical velocity profile of this location is found to have similarities with both middle latitude and other tropical continental MCS. The present stratiform region profile is consistent with other geographical location profiles and the transition region profiles have shown some dissimilarity in the mid troposphere

Acknowledgements

The National MST Radar Facility (NMRF) is operated as an autonomous facility under Department of Space with partial support from Council of Scientific and Industrial Research. The authors are grateful to the NMRF technical staff whose dedicated efforts made possible the observations reported here. UHF radar setup and being operated at NMRF under joint collaborate programme between India and Japan.

References

Heymsfield, G.M., and S. Schotz, Structure and evolution of a sever squall line over Oklahoma, *Mon. Wea. Rev*., 113, 1563-1589, 1985.

Jorgensen, D.P., and M.A. LeMone, Vertical velocity characteristics of oceanic convection, *J. Atmos. Sci*., 46, 621-640, 1989.

Knupp, K.R., Downdrafts within high plains cumulonimbi. Part I: General kinematic structure, *J. Atmos. Sci*., 44, 987-1008, 1987.

Lemon, L.R., and C.a. Doswell III, Sever thunderstorm evolution and mesocyclone structure as related to tornadogenesis, *Mon. Wea. Rev.,* 107, 1184-1197, 1979.

Narayana Rao, T., D. N. Rao and S. Raghavan, Tropical precipitating systems observed with Indian MST Radar, *Radio Sci.,* Vol.34, No: 5, pp.1125-1139, 1999.

VHF RADAR REFLECTIVITY, VERTICAL VELOCITIES AND RAINFALL RATE DURING TYPHOON PASSAGES OVER TAIWAN

C.J. Pan[1], M.L. Hsu[1], L.J. Chung[1], J. Röttger[2,1] and J. Wu[1]
[1] Institute of Space Science, National Central University, Chung-Li, Taiwan
[2] Max-Planck-Institut, 37191 Katlenburg-Lindau, Germany

The Chung-Li VHF radar, located in northern Taiwan, was operated in September and October 2001 to study the radar reflectivity and wind field changes during the approach, passage and departure of typhoons. The reflectivity is given by humidity and temperature changes either caused by turbulence or by stable layering. Additionally the radar observes mean and turbulent velocities. Other than weather radars, the VHF radars obtain the vertical profile of these parameters over a fixed location. Besides measuring the horizontal wind, they are particularly suited to measure the reflectivity and the vertical velocity component. Typhoon studies had also been done earlier with VHF radars (e.g., Röttger et al., 1991; Shibagaki et al., 2003).

The Chung-Li VHF Radar is a stratosphere-troposphere (ST) radar operating on 52 MHz with peak power of 80 kW and an antenna array of 192 Yagis separated into three antenna arrays for receiving in the spaced antenna mode. For the presented typhoon observations the antennas were pointed vertically. The height resolution was 300 m, and 102 ms coherent integration time was applied, which corresponds to a maximum resolvable radial velocity of 14.4 m/s. One record included 256 data points, which were analyzed with the complex auto-covariance method, yielding the radar echo power (from which we deduced the relative reflectivity), the mean radial velocity (which we assumed to represent a reasonable estimate of the vertical velocity) and the turbulent velocity for dwell times of 29 s. This method is very robust with respect to low signal-to-noise ratios, which usually characterize echoes from the upper parts of the observable range up to 10 km. The determination of the horizontal velocity with the spaced antenna method will be performed in a later study. Here we concentrate on reflectivity and vertical velocity and some precipitation observations during passages of three typhoons.

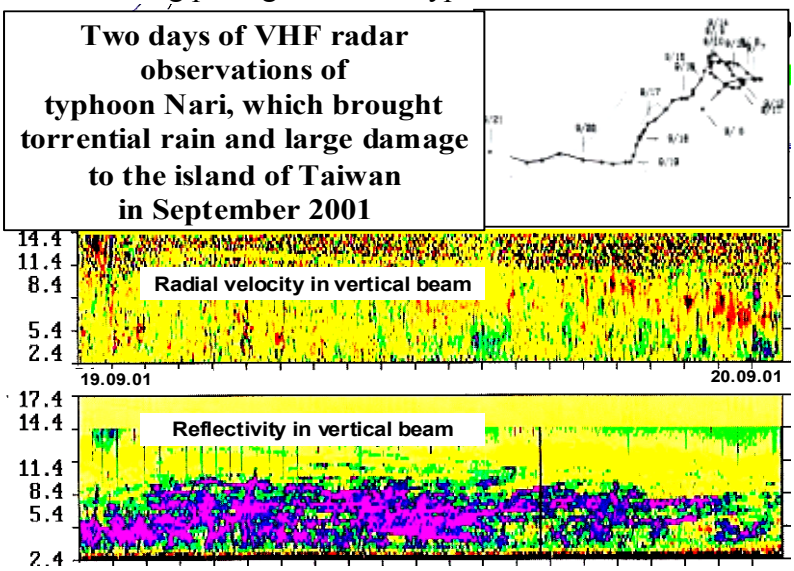

Fig. 1 Typhoon Nari having passed Taiwan on 20 Sep. 2001
VHF radar reflectivity and velocity in vertical beam

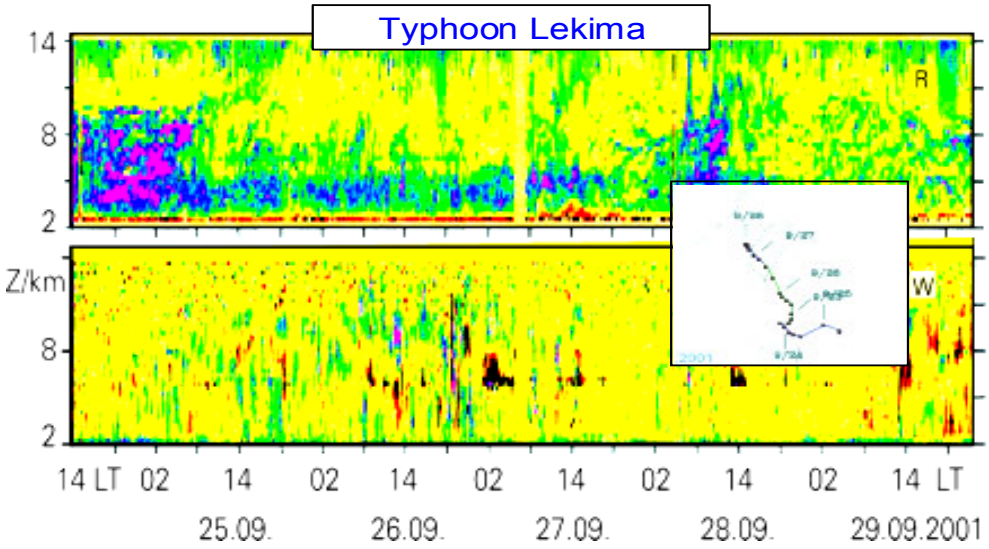

Fig. 2 Typhoon Lekima passing Taiwan on 28 September 2001
VHF radar reflectivity and velocity in vertical beam

After two days of operation during the departure of typhoon Nari (Fig. 1) the Chung-Li VHF radar was operated continuously over about 130 hours between 24 September 2001, 14 LT (UTC+8), and 30 September 2001, 02 LT, with two short interruptions. Fig. 2 shows the radar observations and a map with track of the eye of typhoon Lekima and the location of the Chung-Li VHF Radar. This figure shows the radar reflectivity (lower panel) and mean vertical velocity (upper panel) during this period. On 24 September the eye was about 800 km south of the radar. During this time the troposphere up to about 10 km altitude showed a very enhanced reflectivity, where a separate layer even moved upward to 12 km altitude. The typhoon moved northward the following day and the reflectivity decreased but the convective activity increased. The latter can be seen in the almost vertical streaks of upward motion (green) at time scales of less than a few hours, which are dominating against the downward motions (red). On 25 and 26 September, when the typhoon moved further towards the island several broader layers of reflectivity moved upward to the 10 km level. They comprise boundaries of different air. Since they are separated by some 4 -12 hours, they could be attributed to meso-scale disturbances embedded in the larger-scale typhoon circulation system. Those meso-scale structures can also be seen in the satellite cloud structure records. The reflectivity layer at constant height of about 6-7 km is close to the melting layer where precipitation was formed. We assume that it results from temperature gradients occurring in such conditions. On 26-27 September precipitation can be recognized in the velocity plot as an increase of the downward velocity. Between 6 and 7 km the scatter signal from precipitation dominates the velocity estimate, which therefore is biased downward (due to the falling hydrometeors, which scatter the radar signal). We checked the Doppler spectra carefully and notice that only in the regions of strong downward velocity (red) around 7 km the given estimate is not representing the vertical air velocity. Thus, on 26-27 September the upward streaks above this altitude are clearly showing many events of deep convection. These were reaching altitudes as high as 12 km.

In the second part of 27 September, when the typhoon had its closest distance to the radar location the mean vertical velocity was fairly small without indications of convection and the reflectivity showed mostly short living layers. When the typhoon was departing, strong

reflectivity partially reached up to 14 km altitudes. We have analysed this event in the companion paper by Röttger et al. (2003, this issue), which occurred between 08 and 10 LT on 28 September. Towards the end of the observing period, on the backside of the typhoon, short lived reflectivity layers with upward moving tendencies were observed. This is quite different as compared to the observations 24-26 September on the front-side of the typhoon.

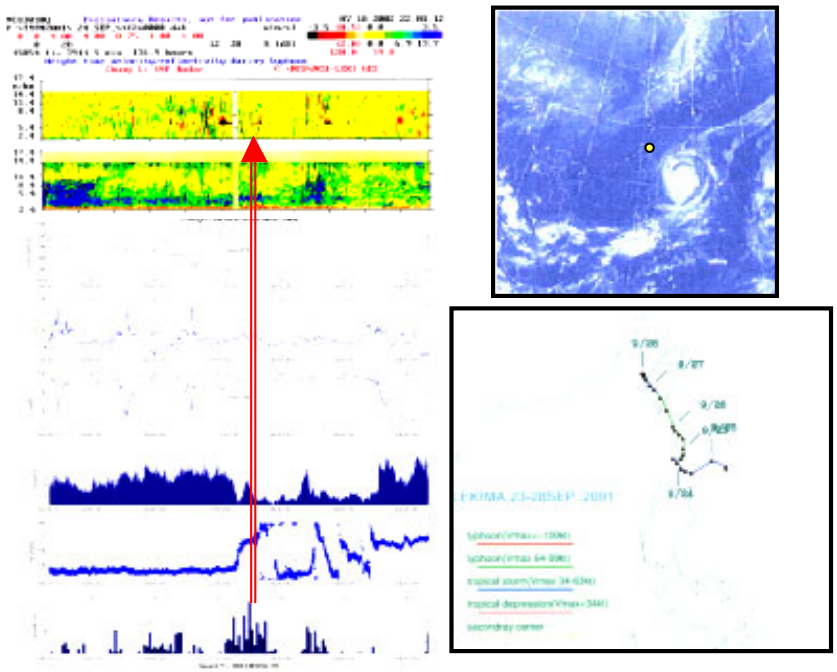

Fig. 3 Radar reflectivity compared with precipitation (lower left-hand panel) during passage of Lekima. The strongest rain fall occurred during the quick change of direction and reduction of wind velocity (second and third left-hand panel from bottom) just after closest approach of the typhoon eye, but there was no particular structure in the reflectivity. The reflectivity was reaching high altitudes of 10 km in the far regions of the typhoon's eye.

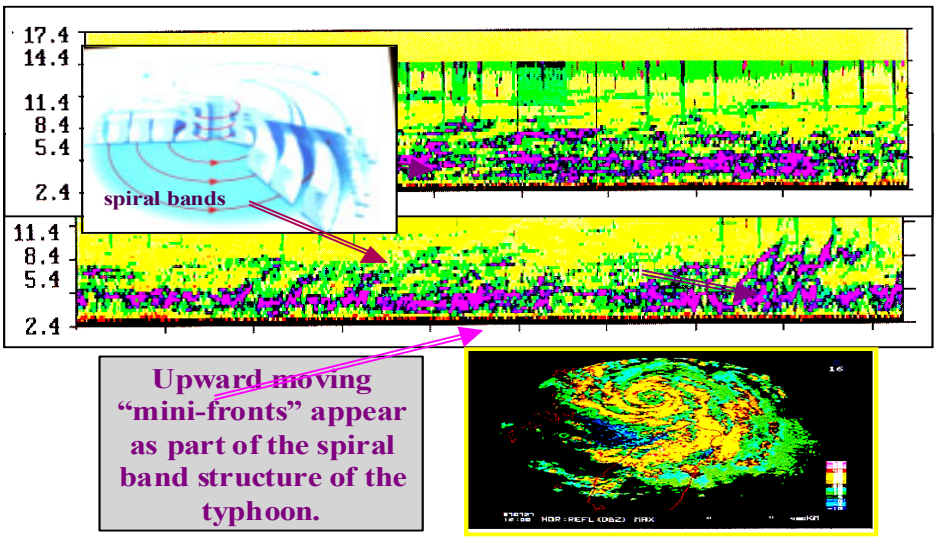

Fig. 4 Zooming in to fine structure in the reflectivity shows mini-structures with periods of less than one hour (each tick-mark in this graph depicts a full hour), which are assumed to be related to the spiral structure of typhoons. Records are over 9.5 hours on 25 September 2001 (Lekima).

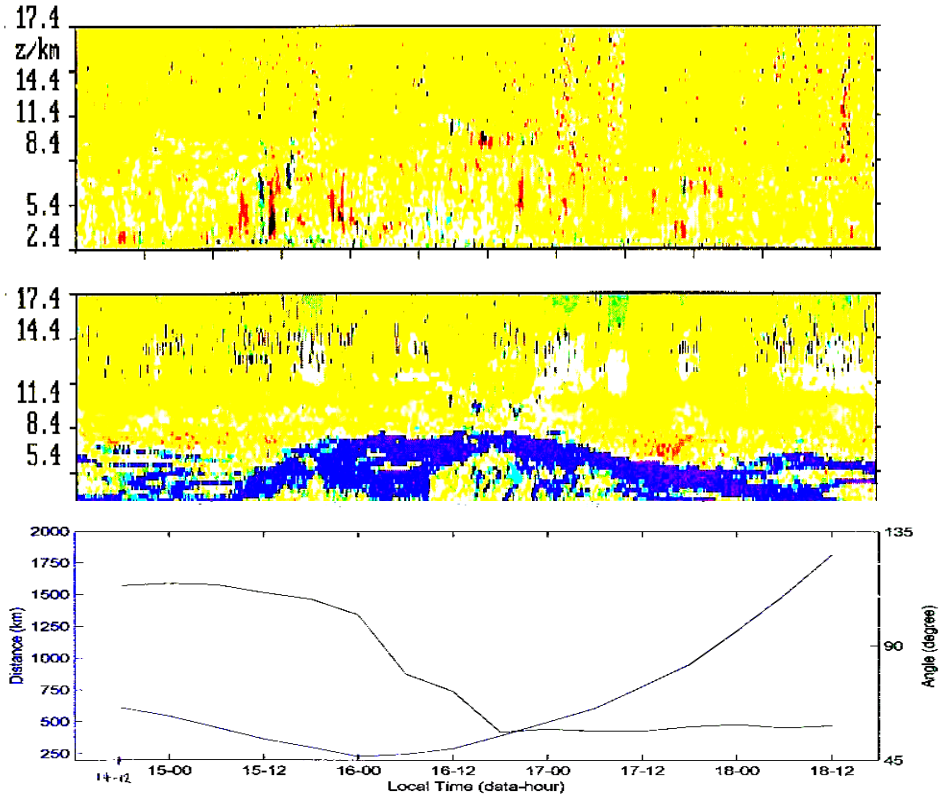

Fig. 5 Passage of typhoon Hayan on 14 – 18 October 2001. The upper panel shows mean vertical velocity, the centre panel reflectivity and the lower panel direction and distance to the typhoon eye. We clearly see that the radar reflectivity is stratified when the typhoon is far away. From the radar. A strong reflectivity band then moves upward to eight kilometres when the typhoon approaches and falls down again when the typhoon departs.

Short conclusions:

(1) Spiral bands in the typhoon circulation pattern are not immediately resulting in strong rainfall, whereas this occurs during time of closest approach of the typhoon. These spiral bands have sub-structures with periods (in the Eulerian frame over the fixed radar location).

(2) Mean potential refractivity gradient does not reflect the region of strong reflectivity as expected from theory. Comparison with radiosonde data indicates that humidity may play a more prominent role in the radar reflectivity than replicated in the standard formalism.

(3) The observed three typhoon show quite some different features in reflectivity, which needs more observations and comparisons with other meteorological observations.

References:

Röttger, J., C.J. Pan, C.H. Liu, and S.Y. Su, Wind field and reflectivity variations investigated with the Chung-Li VHF Radar during typhoon passage, Proc. Int'l. Conf. Mesoscale Meteor., Met. Soc. ROC and AMS, Taipei, 3-6 Dec. 1991, 737-379, 1991.

Shibagaki, Y., M. Yamanaka, M. Kita-Fukase, H. Hashiguchi, Y. Maekawa and S. Fukao, Meso-alpha-scale wind field and precipitating clouds in typhoon 9426 (Orchid) observed by the MU radar, J. Met. Soc. Japan, 81.2, 211-228, 2003.

DERIVING DROP SIZE DISTRIBUTION FROM VHF AND UHF RADAR SPECTRA

N.V.P. Kiran Kumar and D. Narayana Rao

National MST Radar Facility, Gadanki, India

Introduction

Measurements of Raindrop size distributions (DSDs) are very important in the studies of the growth of precipitation, cloud microphysics and for the improvement of radar estimates of rainfall intensities. DSDs describe the number and size of raindrops in precipitation. The vertical distribution and time evolution of the DSD provide information about the dynamical process of precipitating clouds. Vertically pointing Doppler radar profilers operating at very high frequency (VHF) and ultrahigh frequency (UHF) are potential tools for remotely determining DSDs. This is because, with the help of these radars, we can directly determine the fall-velocity spectrum of the hydrometeors. If the velocity can be related to the size of the falling droplets, then the DSDs can be estimated using Doppler radars. And from VHF radars we can determine the ambient air motions in the precipitating clouds that advect overhead.

The ability of wind profilers (UHF or VHF) to estimate DSDs have been demonstrated by several investigators using various techniques (Wakasugi *et al*. 1986; Gossard 1988; Rajopadhyaya *et al.* 1993). Currier *et al.* (1992), Maguire and Avery (1994), and Rajopadhyaya *et al.* (1998) used the vertical air motion information from a VHF profiler to retrieve precipitation characteristics from UHF Doppler spectra. In this present study, we use this approach to evaluate rain-rate estimation in high and low intensity rain regimes of precipitating clouds. The method assumes a DSD shape. A gamma distribution is used in all the results shown in this paper. A theoretical model is fitted to the radar spectrum and is used to estimate the size distribution of raindrops. The derived rain rate and water content are then compared with the collocated surface disdrometer values recorded at the profiler site.

System Description and Method of Data analysis

The Indian MST Radar, Lower Atmospheric Wind Profiler (LAWP) and disdrometer are located at Gadanki (13.5^0N, 79.2^0E), in the southern part of India. The Indian MST Radar operates at a frequency of 53 MHz with a peak power of 2.5 MW. Antenna array consisting of 1024 crossed yagi antennas generates radiation pattern with 3^0 half-power beam width. A complete description of the system is given by Rao *et al.* (1995) and Kishore (1995). For the present study we have used a 2-μs pulsed and only 12 beam positions (four in 10^0 off-vertical directions and 8 in vertical direction) corresponding to a range resolution of 300 m and a time resolution of 58 s.

The operating frequency of the LAWP is 1357.5 MHz. The phased antenna array consists of 24 x 24 elements. It transmits a peak power of 1KW. The receiver has a maximum gain of 120dB. This profiler has been configured to operate in Doppler Beam Swinging (DBS) mode. The antenna beam can be positioned, through electrical phase switching, at three fixed orientations, viz., Zenith, 15°down to East and North. The LAWP is operated in two modes, low and high mode, alternatively. In the low mode, radar samples are taken up to 4.8 km with a range resolution of 150 m, while in the high mode the data are collected up to 12.3 km with a range resolution of 150 m. In the present study we have used only vertical beam. A Joss-Waldvogel disdrometer used for measuring DSDs at the ground continuously and automatically. The surface disdrometer records the number and size of raindrops hitting

the 50 cm^2 sensor head, enabling the direct calculation of reflectivity, rain rate, water content and D_m.

Data observations and discussions

The observations were made on 22-23 June 2000 and during this period a convective precipitating system passed over observation site. Figure 1 shows the first three moments of the Doppler spectra obtained from LAWP during the above period. During 2200-2300 LT the reflectivity (range corrected SNR) exceeds ~80 dB and net upward Doppler velocities indicates the convective rain regime. During 2300-0600 LT a well defined bright band near 5 km is observed. A significant change in Doppler velocity through the bright-band is seen, which indicates the stratiform rain regime [Williams *et al.* (1995), Narayana Rao *et al.* (2001)].

The contour plot of spectral width in fig. 1(c), shows a values of 1-1.5 m/s in the region of high reflectivity, the spectral width of the ice particles above melting level is found to be less than 1m/s which is less than the spectral width of the echoes from water droplets during stratiform rain which is in the range of 1-1.5 m/s.

Figure 1(d) shows time plot of rain rate recorded with a disdrometer and the rain rate reaches a value of ~70 mm/hr during 2200-2300 LT. However, the rain rate reaches a value of 1mm/hr and remains almost constant for about 5hours during 2300 to 0500 hours LT.

Retrieval Methodology:

In this study it is assumed that the DSD can be represented as a gamma function. The radar reflectivity factor for Rayleigh scatter, Z (mm^6m^{-3}) is proportional to the sixth power of the diameter of hydrometers and is expressed as given by (Doviak & Zrnic 1984). Terminal fall velocity of the raindrops is related to its diameter through empirical relation of Beard (1976, 1977). Finally the observed spectrum can be expressed as given by Wakasugi *et al.* (1986). Which consists of vertical air motion spectrum and fall speed spectrum information.

In general it is observed that the observed height and time of the UHF spectrum do not match with the corresponding height and time of VHF spectrum. Therefore we have taken a mean vertical velocity and spectral width. Important point to be noted is that this retrieval process assumes that vertical air motion spectral width of the two profilers will be the same at both frequencies, but errors associated with this assumption are small Rajopadhyaya (1998). Finally precipitation rate R (mm/hr) and water content (kg/m3) are related to the DSD as given by Rajopadhyaya (1998).

Results:

Clear air information is often very difficult to observe with UHF radars and hence for this reason, the mean velocity and spectral width information obtained from the VHF spectrum is used to identify the position of vertical air motion echo in the UHF spectrum. Thus we can isolate precipitation component of the UHF spectrum fro the clear air component.

Inter comparison of rain rate:

Inter comparison of rain rates and water content retrieved from UHF radar and those obtained by surface disdrometer measurements are made. We have considered the UHF data above 1.5 km onwards because the lowest range that can be probed with the VHF (MST) radar is 1.5 km and we have taken the spectrum at 1.8 km. Figure 2 shows a plot between normalised Doppler spectra and vertical velocity. A least squares fit technique is used to obtain the best possible fit values of the parameters N_0, μ and γ. We have obtained a good fit of the derived spectra to that of the observed UHF spectra. Figure 3(a) shows a time series of rainfall rates measured by disdrometer (dashed), rain retrieved (solid) from profiler at 1.8 km. Figure 3(b) is a time series of water content of disdrometer (dashed) rain retrieved (solid) from profiler at 1.8 km. A good comparison is seen between these two. Here we have sampled the disdrometer values according to that of the UHF time resolution. Figures 4 and 5

show comparison of rain rates at high and low rain rates. At high rain rate some discrepancy is observed and this could be due to time lag between the two instruments or due to the high rain rate Rajopadhyaya *et al.* (1998) and at low rain rate a comparison is fairly good. Figure 6 shows time-height cross section of the retrieved rainfall rate of UHF radar in the high and low rain rate conditions.

Conclusions:

Theoretical model spectra of both clear air and precipitation are derived from the observed spectra. Derived precipitation spectra from UHF radar are in agreement with that of the observed spectra. Rain rate and water content estimates from UHF radar spectra and disdrometer are compared. A fairly good comparison is seen between the two and there is a discrepancy between the two at high rain rates.

References:

Beard. K.V., 1976: Terminal velocity and shape of cloud and precipitation drops aloft. *J. Atmos. Sci*., **23**, 851-864.

Beard. K.V., 1977; Terminal velocity adjustment for cloud and precipitation drops aloft. *J. Atmos. Sci*., **34**, 1293-1298.

Currier, P.E., S.K. Avery, B.B. Balsely, K.S. Gage, and W.L. Ecklund, 1992: combined use of 50 MHz and 915 MHz wind profilers in the estimation of raindrop size distributions. *Geo-phys.Res. Lett*., **19**, 1017-1020.

Doviak, R.J., and D.S. Zrnic, 1984: Doppler radar and weather observations. Academic Press, 458 pp.

Gossard, E.E., 1988: Measuring drop-size distributions in cloud with a clear-air-sensing Doppler radar. *J. Atmos. Oceanic Technol*., **5**, 640-649.

Kishore, P., Atmospheric studies using Indian MST radar – winds and turbulence parameters, Ph. D. thesis, Sri Venkateswara Univ. Tirupati, India, 1995.

Maguire, W.B.,II and S.K. Avery, 1994: Retrieval of raindrop size distributions using two Doppler wind profilers: Model sensitivity testing. *J. Appl. Meteor*., **33,** 1623-1635.

Narayana Rao, T., D. Narayana Rao, K. Mohan and S. Raghavan 2001: Classification of tropical precipitating systems and associated Z-R relationships. *J.Geo-phys. Res.*, **106**, 17,699-17,771.

Rajopadhyaya, D.K., P.T. May and R.A. Vincent, 1993: A general approach to the retrieval of rain drop size distributions from wind profiler Doppler spectra: Modelling results. *J. Atmos. Oceanic Technol.*, **10**,710-717.

Rajopadhyaya, D.K., P.T. May, R.C. Cifelli, S.K. Avery, C.R. Williams, W.L. Ecklund, and K.S. Gage1998: The effect of vertical air motions on rain rates and median volume diameter determined from combined UHF and VHF wind profiler measurements and comparisons with rain gauge measurements, *J. Atmos. Oceanic Technol*., **15**, 1306-1319.

Rao, P.B., A.R. Jain, P. Kishore, P. Balamuralidhar, S.H. Damle, and G.Viswanathan, 1995: Indian MST radar, 1, system description and sample vector wind measurements in ST mode, *Radio Sci*.,**30**,1125-1138.

Wakasugi ,K., A. Mizutani, M.Matsuo, S.Fukao, and S. Kato. 1986: A direct method for deriving drop-size distribution and vertical air velocities from VHF Doppler radar spectra. *J. Atmos. Oceanic Technol*., **3**,623-629.

Williams, C.R., W.L. Ecklund, and K.S. Gage, 1995: Classification of precipitating clouds in the tropics using 916-MHz wind profilers, *J. Atmos. Oceanic Technol*., **12,** 996-1012.

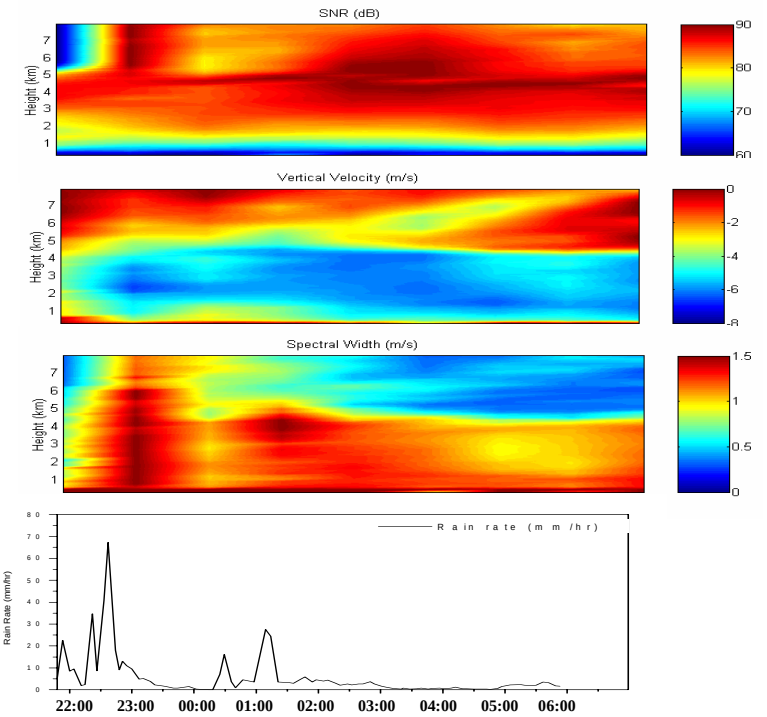

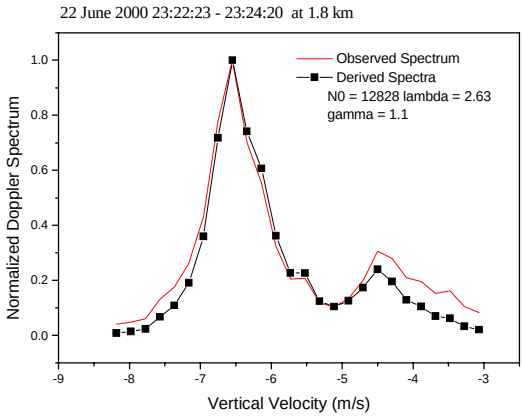

Figure 2: Derived Spectra Versus Observed Spectra

Figure 1: (a) SNR in dB (b) Vertical Velocity (m/s) (c) Spectral width (m/s) Taken from LAWP and (d) Rain rate from Disdrometer

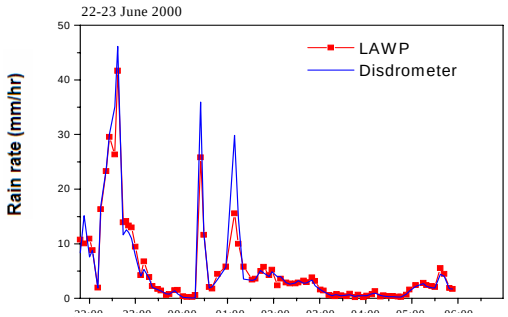

Figure 3a : Comparison plot of time series of retrieved rain rate (mm/hr) from LAWP at 1.8 km and Disdrometer on ground observed on during 22 –23 June 2000

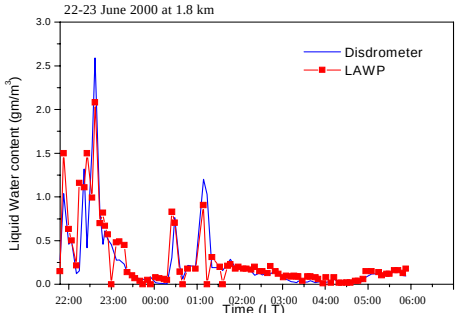

Figure 3a : Comparison plot of time series of retrieved Liquid water content (gm/m^3) from LAWP at 1.8 km and Disdrometer on ground observed on during 22 –23 June 2000

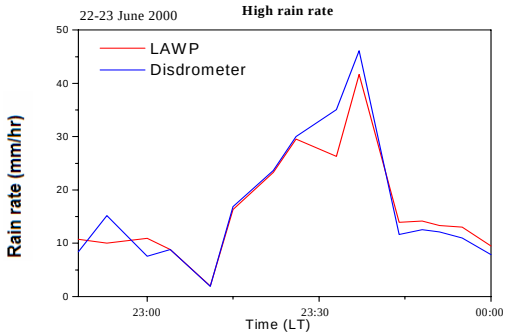

Figure 4: Time series of retrieved rainfall rates from LAWP and in comparison with that of the Disdrometer at the time of high rain rate

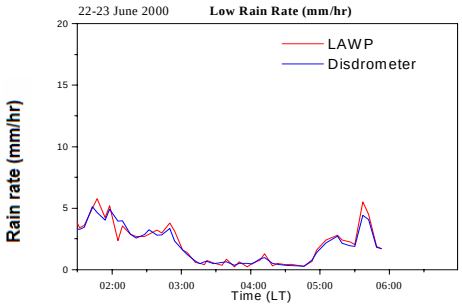

Figure 5: Time series of retrieved rainfall rates from LAWP and in comparison with that of the Disdrometer at the time of low rain rate

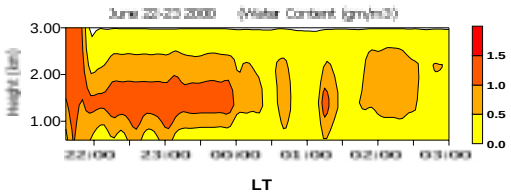

Figure 6: Time series of water content during the period of 22 – 23 june 2000

DIAGNOSTIC STUDY OF TROPICAL PRECIPITATING CLOUD SYSTEMS USING WIND PROFILERS AT GADANKI, INDIA

K.Krishna Reddy[1], Toshiaki Kozu[2], Merhala Thurai[3], Yuichi Ohno[3], Kenji Nakamura[4], A.R.Jain[5] and D.Narayana Rao[6]

[1] Frontier Observational Research System for Global Change, 3173-25 Showa-machi Kanazawa-ku, Yokohama, Kanagawa 236-0001, Japan
[2] Interdisciplinary Faculty of Science and Engineering, Shimane University, 1060 Nishi-kawatsu, Matsue, Shimane 690-8504, Japan
[3] Communications Research Laboratory, Koganei, Tokyo 184-8795, Japan
[4] Hydrospheric-Atmospheric Research Center, Nagoya University, Furocho, Chikusaku, Nagoya 464-8601, Japan
[5] National Physical Laboratory, Dr. K.S.Krishnan Marg, New Delhi 110 012, India
[6] National MST Radar Facility, P.O.Box. 123, Tirupati 517502, India

1. Introduction

The occurrence of deep convection in the tropics plays an important role in the global circulation, since it transports heat, water vapor, and so on, from the PBL to the upper troposphere. The vertical distribution of diabatic heating depends on the vertical structure of the convective system; hence it is important to study the vertical structure of the precipitating clouds occurring in the tropics. An attempt has been made to analyze the measurements made during the two field experiments using multiple radar facility at Gadanki (13.5^{o}N, 79.2^{o}E), tropical India and radiosonde launches to understand the mesoscale convective precipitating cloud systems during South-west (SW: June to September) monsoon and North-east (NE: October to December) monsoon season (October 1997 to 30 September 2000). The first campaign was organized for nearly one-month, extending from 17 July to 14 August 1999. During the second campaign GPS radiosondes were launched from Tirupati (about 40 km to Gadanki) from 28 August to 22 September 2000. The primary scientific objective of both the campaigns was *to understand the organization and evolution of tropical convection at Gadanki, inland region and its role in the atmospheric energy and moisture balance.* Observational periods were organized with three primary goals in mind: 1) examination of the life cycle of convection from the initiation process in the planetary boundary layer (PBL) through mesoscale organization of the deep precipitating cloud systems; 2) classification of vertical structure of precipitating cloud systems; 3) estimation of vertical profiles of raindrop size distribution; 4) melting layer characterization during stratiform precipitation. In this presentation, 2 and 4 are documented.

The melting layer has recently been assessed, as a possible source of uncertainty in microwave rainfall retrievals in stratiform regions (Olson et al. 2001). The characteristics of the melting layer are not only important for understanding the microphysical processes involved in rainfall mechanism but also necessary for rain retrieval algorithms used for the present and future space-borne rain radars such as Tropical Rainfall Measuring Mission (TRMM) precipitating radar (PR) and Global Precipitation Mission (GPM). The current version of the TRMM precipitation radar retrieval algorithm (version 6 of 2A25) uses the Non-coalescence–Non-break up (N-N) model described in Awaka et al. (1985). In order to resolve the uncertainty of the bright band model, it is necessary to go back to experimental data that can provide some physical constraints. For example, using the wind profiler data taken at Gadanki, India during monsoon seasons, it is possible to retrieve the size distribution of rain below the bright band, and, from this, to draw upwardly both the reflectivity and the Doppler velocity profile in the melting particles region.

2. Results and discussions

Observations at Gadanki site with a L-band wind profiler (Reddy., 2003) showed that a profiler is also a useful tool for diagnosing precipitating cloud systems. Figure 1 illustrates

the time-height section of a convective system passing over Gadanki-LAWP on 19 September 2000. Figure 1[(a)] shows the equivalent radar reflectivity factor (dBZ). The raindrop size distribution obtained from the surface-disdrometer is shown in Fig.1(b). The environmental conditions during the second experimental period obtained from Tirupati sounding data are utilized for understanding the local environmental conditions around experimental region. The triangle at the surface in Fig.1(a) indicate the launching time of the radiosonde. The Skew T-log P diagram for sonde launched at 1655 LT is shown in Fig.1(c). The results show a relatively dry surface layer with nearly saturated conditions between 850 and 450 mb. This layer is also characterized by westerly flow extending from 850 mb to 500 mb. Above 500 mb, the flow reverses to easterly/northeasterly. The variability in the flow observed during experimental period is typical for the area and was opportune for studying its effect on precipitating cloud system evolution.

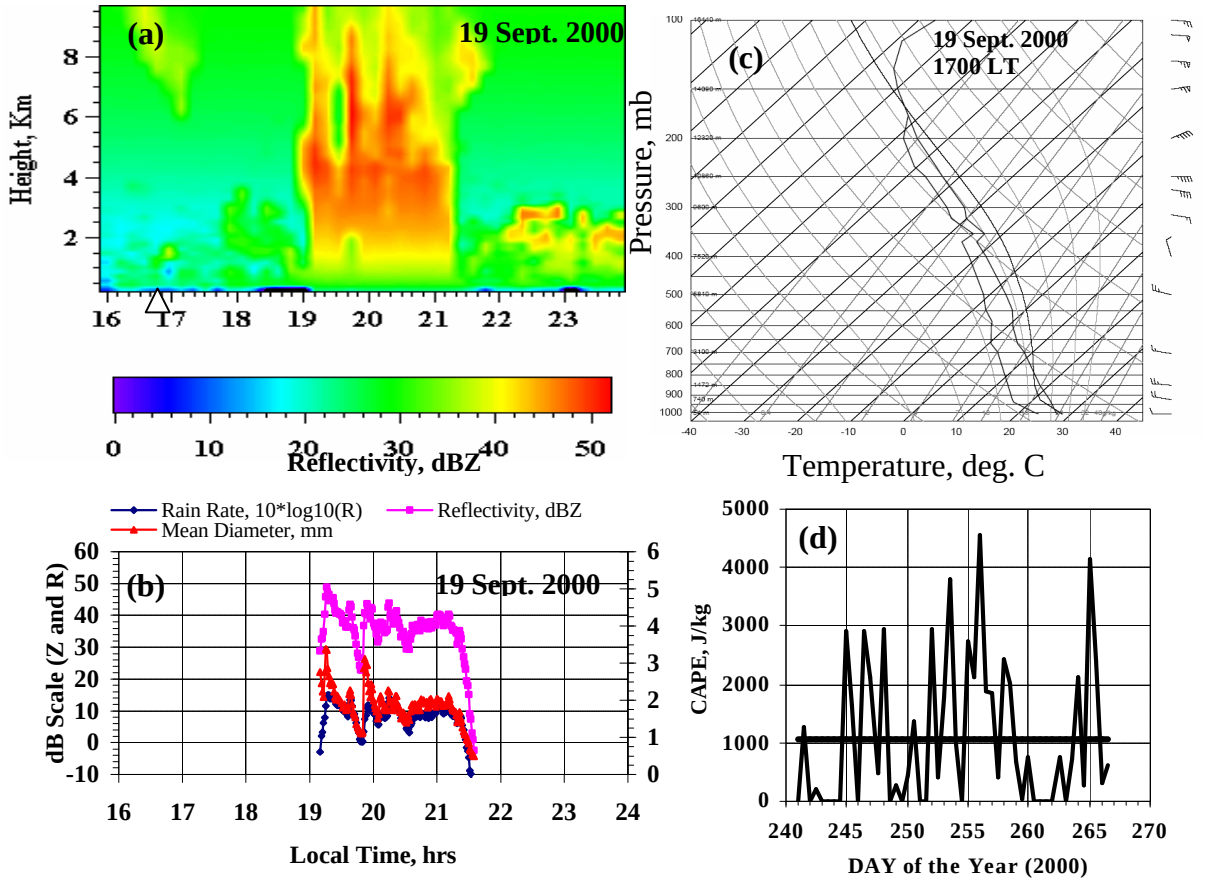

Figure 1. (a) LAWP-measured reflectivity. (b) surface-disdrometer–derived reflectivity, rain rate, and mass-weighted man diameter. (c) Skew T-lop P diagram derived from Tirupati radiosonde observations. (d) Time series of CAPE from 28 Aug. to 22 Sept. 2000.

Convective Available Potential Energy (CAPE) varied considerably during campaign period as shown in Fig. 1(d) and the mean CAPE of 1320 J/kg was observed. There was moderate association between CAPE and environmental flow. Days with a prestorm environment with both low CAPE were evident prior to MCS occurring on 25, 26 November, and 1 December 1995. These days had lower than average total rain volume and associated total rain affected areas. Most days produced a prestorm environment at some time exhibiting a combination of high CAPE (07, 16, 17, 18, and 19 September 2000). Suppression or late development of MCS was sometimes associated with overcast conditions or drier air at low levels. Observations during second experimental period indicated dissipation of initial cumulus

clouds and a failure to develop a significant congests stage until late in the afternoon under the latter conditions. Drying of the internal boundary layer by free tropospheric entrainment was always underway competing with the enhancement occurring at the surface through moisture fluxes. This process is described later. Strong convergence associated with sea breeze "collisions" eventually overcame unfavorable conditions resulting in thunderstorm development on such days.

We have tried to examine the accuracy of the so-called non-coalescence – non-breakup (N-N) melting layer model by fitting the model predictions to the L-band wind profiler data taken in Gadanki. Examples for stratified events are shown in Figures 2. Upper plot [Fig.2 (a)] shows the reflectivity data and the middle plot [Fig.2 (b)] shows the Doppler velocity. In the stratiform region, the 'bright-band' in the radar reflectivity seen between 4 km- 5 km height represents the melting layer and the height of it depends on the zero degree isotherm. Almost of the data taken during stratification, show the melting -layer height to be in this region. The melting process could also be visible in the Doppler velocity (along the vertical), which was characterized by a sharp increase in the mean-fall speed of the hydrometeors during the snow-to-rain - transition process. The surface-disdrometer derived rainfall integral parameters are shown in Fig.2(c). The input to the N-N melting layer model is either the rain rate or the equivalent radar reflectivity in the rain region just below the melting layer. Assuming a Marshall-Palmer drop size distribution, the measured radar reflectivity just below the melting layer was used to derive $N_R(D_R)$ and, using a simple power law formula for the relationship between the velocity and the drop diameter, the model was evaluated in terms of the radar reflectivity and the Doppler mean velocity. Figure 2(d) shows the comparisons for 18 May 1999 (2-hr averaged radar reflectivity profiles are compared in terms of dBZ/10 in order to use the same x-axis scale as the mean velocity). Such averaging was considered to be necessary in order to reduce the effect of vertical wind component on the fall velocity spectra. The spectra so computed are compared with the measurements in Figure 2(e). The same air-density corrections and the same velocity-diameter relationships were applied as before. The comparisons are shown for three cases (i) the top of the melting layer, (ii) the bright-band peak region and (iii) the rain region just below the melting layer. In all three cases, the N-N model derived spectra agree well with the measurements. This indicates that the velocity dependence on the diameter of melting snowflakes as well as the empirical elements of the model, namely the height variations of the form factor and the water content is sufficiently accurate to represent the melting layer characteristics in Gadanki, at least at L-band. A previous study conducted in the tropics used long-term measurements from an S-band vertically pointing Doppler radar to examine the accuracy of the N-N model (Thurai et al 2003). A similar conclusion was drawn from the S-band data taken in Singapore, although the analyses were conducted only in terms of the height profiles of dBZ, Doppler mean and the spectrum width. The current results give further evidence for the validity of the N-N model for retrieval algorithms for climates affected by monsoon seasons, at least at Rayleigh scattering frequencies.

References

Awaka, J., Furuhama,Y., Hoshiyama, M., and Nishitsuji, A., Model calculations of scattering properties of spherical bright-band particles made of composite dielectrics. *J. Radio Res. Lab*., 32, 73-87, 1985.

Olson, W. S., P.Bauer, N.F.Viltard, D.E. Johnson, W.K. Tao, R. Meneghini, and L.Liao, A Melting-Layer Model for Passive/Active Microwave Remote Sensing Applications. Part I: Model Formulation and Comparison with Observations,*J. Appl. Meteor.*,40,1145-1163, 2001.

Reddy, K.K., Diagnostic study on vertical structure of monsoon Precipitating cloud systems, *Indian Journal of Radio & Space Physics* , 32, 198-208, 2003.

Thurai, M., T.Iguchi,T. Kozu, J.D.Eastment, C.L.Wilson and J. T. Ong, Radar observations in Singapore and their implications for the TRMM precipitation radar retrieval algorithms, *Radio Sci.*, 38, 1086, **doi:** 10.1029/2002RS002855, 2003.

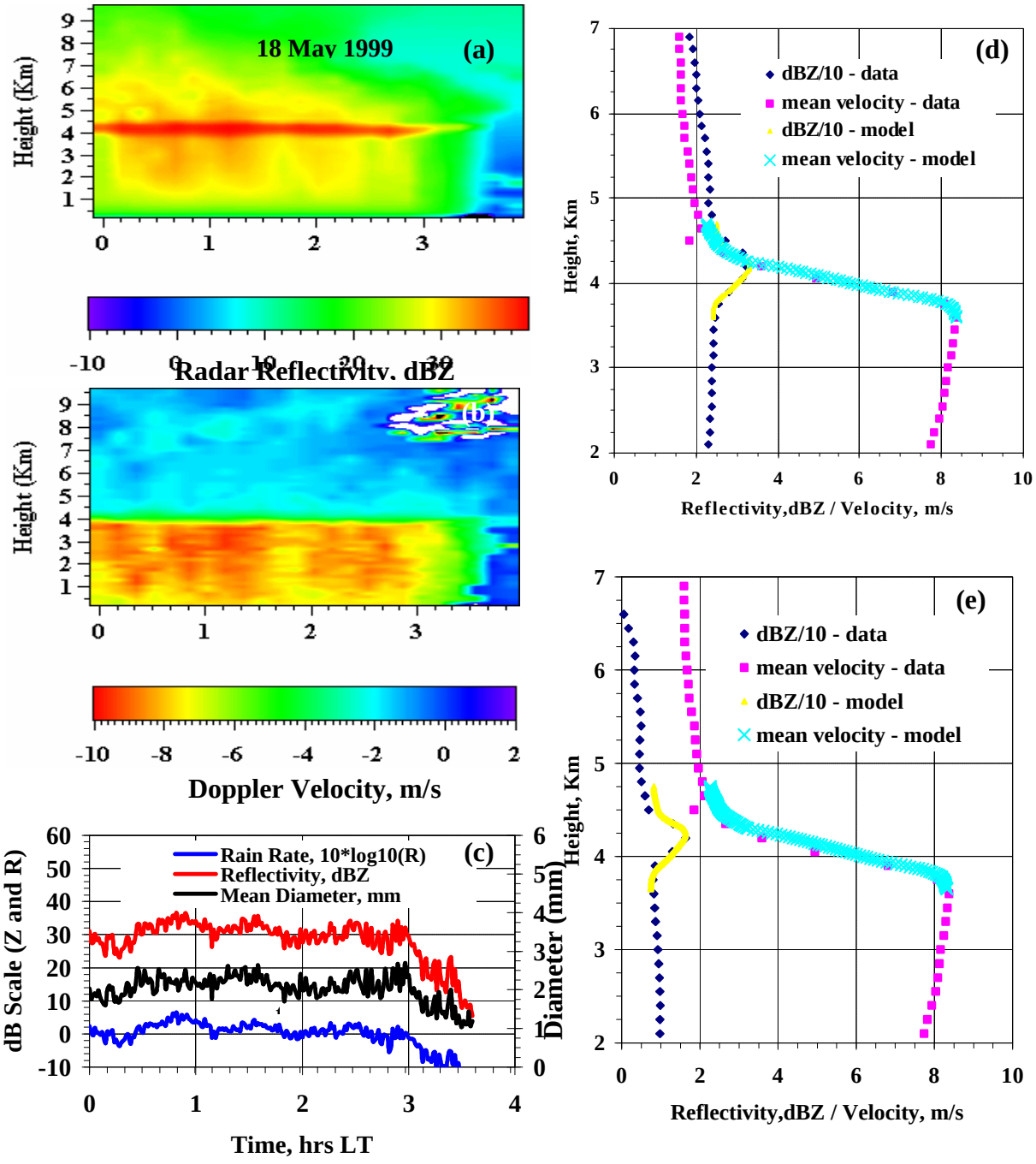

Figure 2. Time-height cross section of (a) Reflectivity (dBZ) and (b) Doppler velocity observed by the vertical beam of the Gadanki LAWP on 17 and 18 May 1999. (c) The 1-min disdrometer-derived rain rate, reflectivity and mean diameter.

TROPOSPHERIC WIND MEASUREMENTS WITH THE PIURA BOUNDARY LAYER RADAR DURING EXTREME RAINFALL EVENTS IN 2002

Ken Takahashi G.

Centro de Predicción Numérica del Tiempo y Clima
Instituto Geofísico del Perú

1. Introduction.

The lowlands of Piura, on the northern coast of Peru, are strongly affected by El Niño events. Heavy rainfall can occur on this normally arid region when the nearby sea surface temperature (SST) is sufficiently high. *Woodman* [1999] has shown that rainfall can be expected when SST exceeds a threshold of around 26°C. However, his analysis was done with monthly rainfall while heavy rainfall tends to occur in intense discrete events. In this work we try to determine which conditions favor some days over others with the occurrence of heavy rainfall given essentially the same SST conditions.

Our study was done for the period of March and April 2002. In this period, SST was favorable for rainfall, exceeding 26°C from the end of February to mid April at a location south of Piura (6.5°S, 82.5°W), which *Woodman* [1999] highlighted as one with good correlation with rainfall. Pluviometric station and river discharge data corroborate that rainfall did occur in this period only.

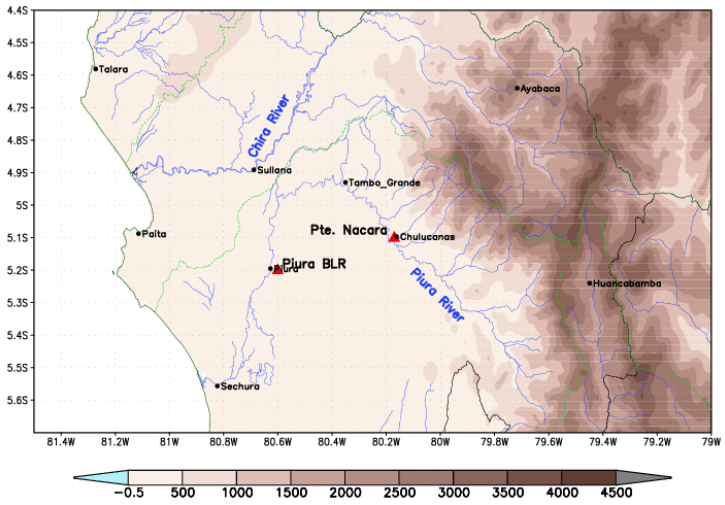

Figure 1: Region of study. Terrain elevation (m) is shown in shading, rivers are indicated in blue and data locations with red triangles. River basin boundaries are indicated in green.

There are two main mechanisms which have been proposed for the genesis of intense convective events in Piura (*Horel and Cornejo Garrido* [1986], *Goldberg et al.* [1987], *Bendix and Bendix* [1998]). One involves the thermally driven sea-breeze circulation which, in the afternoon, would bring low level moist air inland and help it rise up the western slope of the Andes mountains, which is the region of largest anomalous precipitation during El Niño. The other mechanism requires an extended atmospheric instability and is likely to be more important during strong El Niño events.

2. Data and methodology.

We have looked for systematic differences between the circulation in days that had rainfall and days that didn't. The data was composited according to instantaneous river discharge data (Fig. 2) measured at Puente Ñácara, on Piura River (Fig. 1), which served as a good proxy for rainfall (compare to Fig. 3). To do this, we first made a list of days considered rainy and days considered dry. For this classification we used the river discharge data as an indicator of rainfall. Days in which the following morning showed a peak in river discharge were taken as rainy. The magnitude of the peaks had to exceed 500 m^3/s in order to be considered. Conversely, days in which the following morning had discharges below 250 m^3/s and showed no hint of peaks were taken as dry. The consideration of the discharge data of the following morning instead of the same day was done because of the time delay between the signal in river discharge and the signal in rainfall, which can be of several hours.

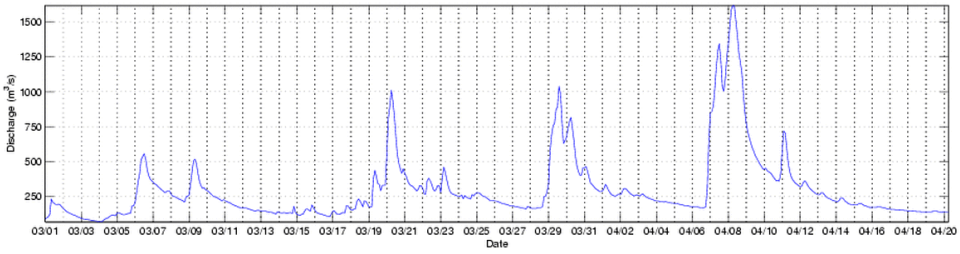

Figure 2: Two-hourly instantaneous discharge of Piura river measured at Puente Ñácara (local time).

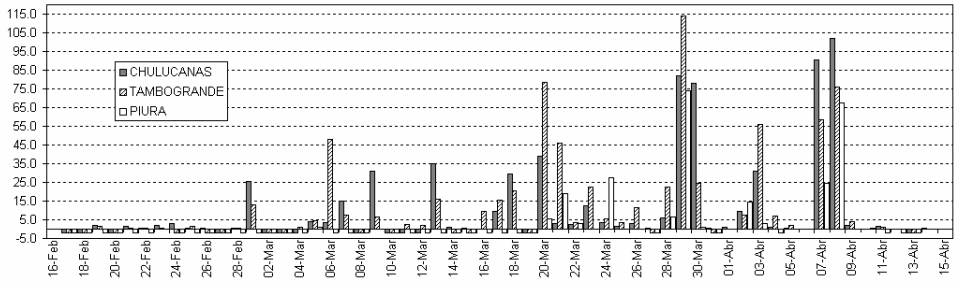

Figure 3: Daily rainfall (mm) measured at three stations. Reports are made at 7 am, negative values indicate missing data.

The composites of the local circulation were made from hourly wind profiles from the Piura BLTR (*Scipión et al.* [this issue]). The synoptic scale circulation composites were made from daily averaged NCEP/NCAR Reanalysis data (*Kalnay et al.* [1996]). The composition of hourly data was justified as long as the assumption that rainfall in this period had a diurnal variation locked to the insolation cycle through the sea-breeze circulation mechanism was dominant. This assumption was supported by the fact that the SST anomalies were moderate in this period and by the observed timing in the river discharge data.

3. Results and discussion.

The results suggest that, given the favorable SST conditions, specific days are favored with rainfall over others through an enhancement of onshore flow near the top of the boundary layer (approximately 1.5 km above the surface) in the morning (Fig. 4, left). A way the enhanced onshore could favor rainfall is through an associated forced lifting of air parcels up the western slope of the Andes, which could trigger convection. This forcing would be more efficient when superimposed on the action of the sea-breeze circulation, which has been invoked previously as an important mechanism for the genesis and timing of the rainfall. It is interesting to note that the meridional wind seems to have little relevance to the occurrence of rainfall. This sheds new light on the statement by *Eguiguren* [1894], who said "...it is a constantly observed fact that it doesn't rain in Piura but when winds blow more or less strongly from the northwest". *Eguiguren* [1894] considered the northerly component of the wind to have the greater relevance to rainfall but in our study we found that the mean wind was essentially from the south and that the westerly component was the most relevant for the rain. It would appear that what is important is that the mean wind blows from the high moisture and heat source, as *Woodman* [1999] suggested, and that it is through enhancement of the westerly flow that rainfall can be triggered. After the convective systems have formed, they will tend to modify the regional circulation. Above 1.5 km the westerly flow was progressively replaced by easterly flow starting near 1.5 km at around noon and extending further up to around 5 km in the evening. We speculate that the progressively higher vertical extension of the westerly wind is due to convective transport of westerly momentum from the boundary layer into the mid-levels.

In the period of study, the rainfall events on Piura tended to be clustered in time and these clusters had a recurrence time of about 10 days. The onshore low-level flow enhancement seems to be related to synoptic scale tropical systems which have similar spatial scales to the 10-day zonal wind oscillations reported in previous works (*Wallace and Chang* [1969]). Our results also show systematic differences in the circulation associated to the subtropical high, with an enhanced equatorward flow off the Peruvian coast in rainy days. The spatial scale of the disturbance allows us to associate it to a planetary wave number 5. Since these waves also have a period on 10 days (*Figueroa* [1999]), it is unclear if their phasing with the circulation changes over Piura is fortuitous or not. Similar studies of other years are needed to address this.

4. References

Bendix, J. and Bendix, A. Climatological aspects of the 1991/1993 El Niño in Ecuador. *Bull. Inst. fr. études andines 27*, 3, 655-666, 1998

Eguiguren, D.V., Las lluvias en Piura. *Bol. de la Soc. Geogr. de Lima*, 1894.

Figueroa, S.N., Estudo dos sistemas de circulação de verão sobre a América do sul e suas simulações com modelos numéricos. Doctoral thesis, INPE, Brasil, 1999.

Goldberg, R.A., Tisnado, G. and Scofield, R.A., Characteristics of extreme rainfall events in north-western Peru during the 1982-1983 El Niño period. *J. Geoph. Res. 92*, C14, 14225-14241, 1987.

Horel, J.D. and Cornejo-Garrido, A.G., Convection along the coast of northern Peru during 1983: Spatial and temporal variation of clouds and rainfall. *Mon. Wea. Rev. 114*, 2091-2105, 1986.
Kalnay and co-authors, The NCEP/NCAR 40-year Reanalysis Project. *Bull. Amer. Meteor. Soc. 77*, 437-471, 1996.
Scipión, D., Chau, J. and Flores, L., First results of the Boundary Layer and Tropospheric Radar System for ENSO. *This issue.*
Wallace, J.M. and Chang, C.P., Spectrum analysis of large-scale wave disturbances in the tropics. *J. Atmos. Sci. 26*, 5, 1010-1025, 1969.
Woodman, R., Modelo estadístico de pronóstico de las precipitaciones en la costa norte del Perú. *El Fenómeno El Niño. Investigación para una prognosis. 1er encuentro de Universidades del Pacífico Sur: Memoria* 93-108. Piura- Perú, 1999.

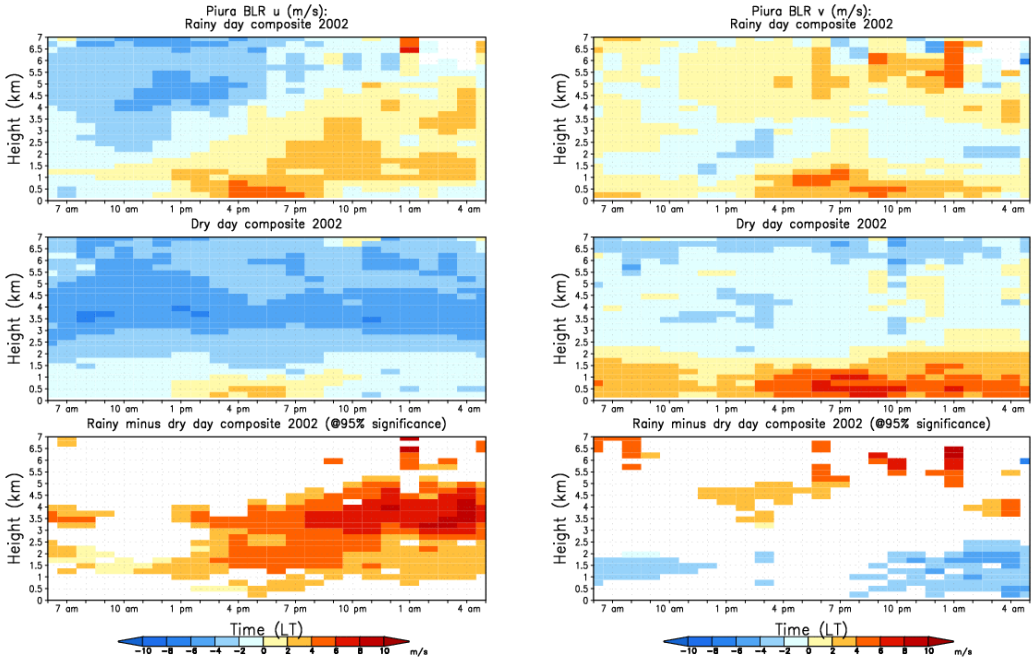

Figure 4: Diurnal evolution of zonal (left) and meridional wind (right) (m/s) in a) rainy days (top) and b) dry days (middle) and c) the difference between the two (bottom). Only differences that pass a Student *t* test at the 95% level are shown. Time is given in UTC (= Local + 5 hours) and height is given in km. Plus and minus signs indicate patches of positive and negative values.

FOEHN IN THE RHINE VALLEY AS SEEN BY A WIND-PROFILER-RASS SYSTEM AND COMPARISON WITH THE NONHYDROSTATIC MODEL MESO-NH.

S. Vogt[1], G. Jaubert[2]

[1] Siegfried Vogt Institut fuer Meteorologie und Klimaforschung, Forschungszentrum
76024 Karlsruhe, Germany
siegfried.vogt@imk.fzk.de
corresponding author

[2] Genevieve Jaubert Centre National de Recherches Meteorologiques
31057 Toulouse, France
genevieve.jaubert@meteo.fr

1. Introduction

Foehn is the generic name for the strong and turbulent wind, which blows from the crests of the mountains towards the lee. This wind brings warm and dry air at the surface. Foehn events are quite common on the northern side of the Alps and represent very important phenomena for the weather forecasting in the Alpine valleys, where a lot of people live.

Different conceptual models have been proposed for the Foehn. However, the lack of data in mountainous regions limits the understanding and the validation of the numerical simulations of the Foehn. The Foehn study in an Alpine valley has been recognized as a major scientific objective of the Mesoscale Alpine Program (MAP), (Binder et al 1996, Bougeault et al 2001).

2. Experimental Design

One of the scientific objectives of MAP addressed the four-dimensional variability of the Foehn flow in the Rhine valley. Of special interest were the investigation of the dynamical processes which determine the spatial extension and the temporal variation of the Foehn. The field experiment FORM (Foehn in the Rhine Valley during MAP), dedicated to this objective, was conducted from September 7th to November 15th 1999, including 10 intensive observing periods (IOP). A unique observing network was deployed, for details see Bourgeault et al., 2001. Fig.1 shows the FORM experimental area.

One of the two wind profilers was the wind-temperature Radar (WTR) of our institute. The WTR is a mobile system, especially designed for probing the lower atmosphere.The WTR works in two modes: the RASS-mode and the clear-air-mode. In the RASS-mode the WTR records the air temperature by detecting the propagation of sound pulses with a RADAR. In the clear-air-mode the WTR observes the electro-magnetic structure parameter of the refractive index $C_n^{2,}$ which in contrast to its acoustic counterpart is mainly dominated by moisture fluctuations but much less by temperature fluctuations.

The WTR has a five-beam geometry with two bistatic radiofrequency (rf) and one acoustic (ac) antenna. The rf antenna emits continuous waves that are frequency shifted with a saw tooth modulation (FM-CW Doppler Radar) in order to provide a fine range gate resolution. The sound source is not only used to measure the vertical sound velocity and hence the temperature, but also to estimate the wind components in the so-called RASS-mode. This is possible because the ac beam is simultaneously shifted in the same four oblique beam directions like the rf beam. The combination of the RASS mode and the clear air mode allows

estimating two independent and redundant wind profiles. A description of the profiler is given in Bauer-Pfundstein, 1999.

3. Model Design

The numerical simulation is performed with the non-hydrostatic model Meso-NH based on the anelastic equation system. Two simulations domains are used with the two-way interactive grid-nesting technique of Stein et al. (2000), the horizontal mesh size being 10 km and 2.5 km. Domains and physical parametrizations are as described in Lafore et al. 1998, except for the use of the most recent radiation scheme of ECMWF (Morcrette et al.2001).
The simulation starts at 12 UTC November 5 th. It is initialized with two mesoscale analyses, performed at the resolution and on the horizontal grid of each of the two nested models, with the CANARI/DIAGPACK assimilation system, developed at Meteo-France and based on optimal interpolation (Calas et al. 2000). Lateral boundary conditions are provided by time-space interpolation between operational analyses of the ARPEGE system of Meteo-France, available every 6 hours.

4. Experimental Data and Model Results

The descending of one strong Foehn in the area of Rankweil from upper layers down to the surface can be seen best by means of time-height cross sections of wind and temperature. Figs. 2 and 3 are showing the virtual potential temperature and the S-N wind component, respectively measured by the WTR. Strong south wind was detected first at an altitude of 1.2 km around midnight November 4th. It lasted more than 19 h until the Foehn penetrates down to the valley floor. The descending was not uniform but with some intermittent periods. Nevertheless an overall descending rate of 33 m/h is estimated. More details of this Foehn event will be found in Jaubert et al. 2003.

Four periods of IOP15 are evident:

1. onset of Foehn, heating and eroding of the stagnant cold pool,
2. break through of Foehn to the surface,
3. intermittence of Foehn,
4. arrival of the perturbation and end of Foehn.

Fig. 4 is showing simulated potential temperature along a S-N transect in the Rhine valley for four selected time periods (16, 19, 23 UTC, Nov. 5th and 6 UTC, Nov. 6th). Left hand side of Fig. 4 is a similar viewgraph of the wind parallel to the cross-section and Fig.5 is the modelled air flow near the surface (90 m level). When comparing the depth of the cold air pool for different time periods measured by WTR to the depth simulated by Meso-NH, the model simulation is very close to the measurements.

6. Conclusion

Thanks to the excellent resolution in time and height of temperature and wind fields measured by the WTR it is possible to get a very detailed picture of the evolution of this Foehn event. The model simulations are in good agreement with the observations. So it will be possible to quantify the physical processes involved in the removal of the cold pool and the instationary nature of the Foehn flow. This will be a significant key to better understanding and, hopefully, to forecast Foehn episodes.

Literature:

Bauer-Pfundstein, M., Bestimmung von Turbulenzparametern und der Schallabsorbtion mit einem Wind-Temperatur-RADAR., *Wissenschaftliche Berichte FZKA **6281,*** 1-152, 1999

Binder, P. and Schär (eds.), C., MAP Design Proposal., *http://www.map.ethz.ch/proposal.htm,* 1996.

Bougeault, P. Binder, P., Buzzi, A., Dirks, R., Houze, R., Kuettner, J., Smith, R.B., Steinacker, R., and Volkert, H., The MAP Special Observing Period., *Bull. Ameri. Meteor. Soc.*, **82**, 433-462, 2001.

Calas, C. Ducrocq, V., and Senesi, S. Mesoscale analyses and diagnostic parameters for deep convection nowcasting. *Meteorol. Appl,* **7,** 145-161. 2000

Jaubert, G., Benech,B., Berger,H., Chimani, B., Flamant, C., Haeberli, C., Nuret, M., and Vogt, S. High resolution simulation of the 4D interaction between the Foehn air and the colder boundary layer: impact of a meso-Beta analysis and validation on a very well documented Foehn event (MAP IOP15). *ICAM/MAP conference Extended abstracts* P.419-422 2003

Lafore, J.P., Stein, J., Asencio, N., Bougeault, P., Ducrocq, V., Duron, J., Fischer, C., Héreil, P., Mascart, P., Redelsperger, J.L., Richard, E., and Vilà-Guerau de Arellano, J., The Meso-NH atmospheric simulation system. Part I: Adiabatic formulation and control simulations., *Annales Geophysicae,* **16**, 90-109, 1998.

Morcrette, J.J. Mlaver, E.J. Iacomo, M.J. and Clough S.A. Impact of the radiation transfer scheme RRTM in the ECMWF forecasting system. *ECMWF Newsletter**,*** **91,** 2-9. 2001

Stein, J., Richard, E., Lafore, J.P., Pinty, J.P., Asencio, N. and Cosma, S., High-resolution non-hydrostatic simulations of flash-flood episodes with grid-nesting and ice-phase parametrization., *Meteor. Atmos. Phys.,* **72**, 203-221, 2000.

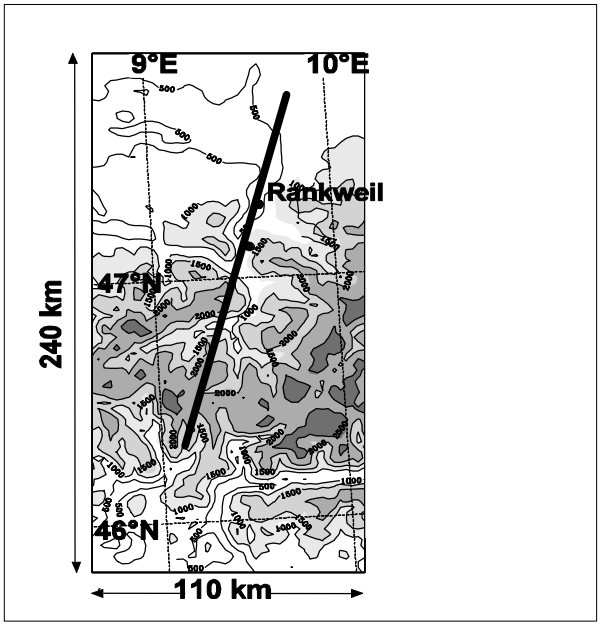

Fig. 1 Topography of the FORM experimental area with S – N transects used in the model simulation., the location of the WTR is near Rankweil

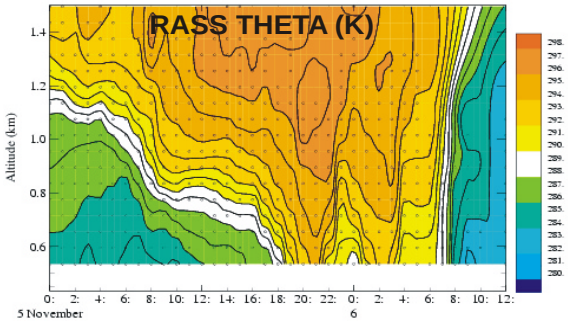

Fig.2 Height-time plot of the virtual potential temperature measured by the WTR.

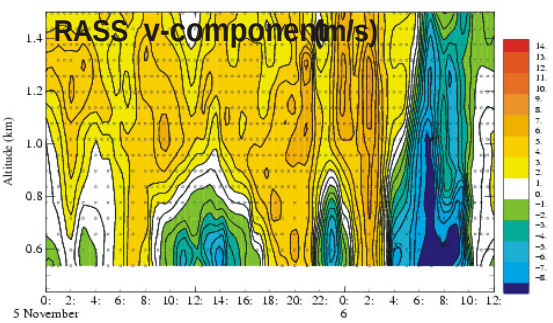

Fig.3 Height-time plot of the S-N wind component measured by the WTR.

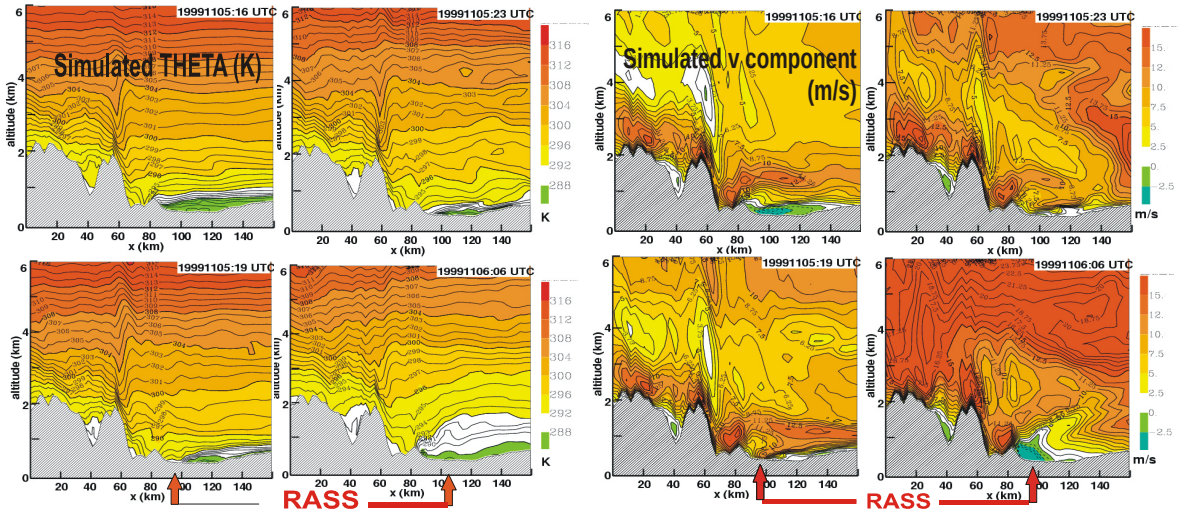

Fig.4 Simulated potential temperature composite (left) and S-N wind component (right) along the cross-section for selected time periods (16, 19, 23 UTC 99/11/05, 06UTC 99/11/06).

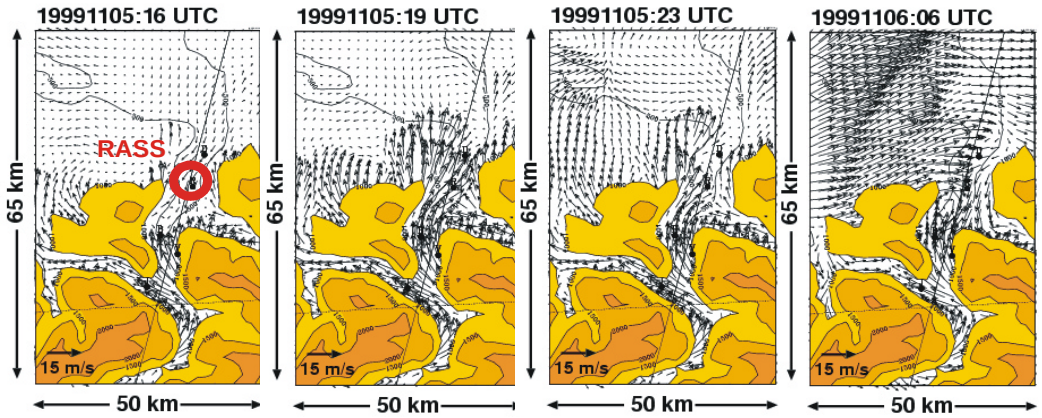

Fig.5 Simulated surface winds (90m level) below 1000m topographic height for selected time periods.

STUDY OF A MESOSCALE LAND-TO-SEA LOW-LEVEL JET WITH A NETWORK OF UHF WIND PROFILERS: CASES OF THE MISTRAL WIND

V. Guénard[1], J-L. Caccia[1], B. Benech[2], B. Campistron[2], and P. Drobinski[3]

[1]LSEET, CNRS/Université de Toulon, BP132, 83957 La Garde, France
[2]CRA/LA, CNRS/Obs. Midi-Pyrénées, Campistrous, 65300 Lannemezan, France
[3]IPSL/SA, CNRS/Université de Paris VI, Jussieu, 75252 Paris Cedex 05, France

Introduction

The Mistral is a northerly low-level, orography-induced, cold-air out-break over the Gulf of Lions blowing offshore the south-eastern region of France at any season. The climate of this area is under the influence of the Mistral which brings clear sky. It is frequently observed to extend as far as a few hundreds of kilometers from the coast and is one of the primary cause of storms over the Mediterranean.

When a westerly to northerly synoptic flow impinges on the Alpine range, it is deflected westward by the Coriolis force as well as the pressure build-up on the upstream edge of the range. As the flow experiences channelling in the Rhône valley separating the French Alps, to the east, from the Massif Central, to the west, by a gap of 200 km long and 40 km width (see Fig. 1), it is substantially accelerated, giving birth to the Mistral (Pettré, 1982).

Although some of the large-scale features of the Mistral are well understood, thus well forecasted, the mesoscale aspects such as the temporal, vertical and horizontal variabilities, the onset and cessation times are still to be investigated. During MAP (Mesoscale Alpine Program, fall 1999, see Bougeault et al, 2001) and ESCOMPTE (Expérience sur Site pour COntraindre les Modèles de Pollution atmosphériques et de Transport d'Emissions, summer 2001, see Cros et al, 2003) field experiments, a UHF-wind profiler network has been deployed in the coastal region of south-eastern France to document the spatial and temporal structure of the tropospheric flow and in particular some Mistral events (e.g. Drobinski et al, 2002). The networking approach combined with the high vertical and time resolutions of the UHF-wind profilers enables the study of the inhomogeneity and unsteadiness aspects of the Mistral as well as its interactions with the ABL (Atmospheric Boundary Layer). In this paper, we have chosen to present and analyse wind and turbulence data obtained by two UHF-wind profilers during the two extreme Mistral cases (the strongest and the weakest ones, in fall and summer, respectively) among the seven cases having occurred during MAP (three cases) and ESCOMPTE (four cases). Those data are used to: (i) evidence and interpret the temporal variability, sometimes very fast, of its vertical structure, (ii) describe the role of the upstream orography, in the fall case, one radar being installed near the Rhône-valley exit and the second one in the lee of the Alps, and (iii) analyse interactions between the Mistral and thermal circulations such as land/sea breezes, in the summer case.

Brief description of the Mistral meteorological aspects

Westerly to northerly upper-level large-scale flow patterns may lead to Mistral events. They must be associated with a Genoa Gulf cyclone in the lee of the Alps that results, at ground level, in a north-south negative pressure gradient component allowing the air masses to be channeled and accelerated along the Rhône valley. The Mistral depth observed near the coast depends on the upstream conditions (wind direction, Froude number, inversion layer height) determining if the flow passes over or is blocked by the mountains along the lateral sides of the valley. In the second case, the air flow comes from the Rhône valley exit only.

Surface winds usually range from 10 to 20 m s^{-1} over land, but situations leading to offshore winds reaching 30-40 m s^{-1} are not seldom. Maximum winds are found between 500 and 1500 m AGL and range from 20 to 50 m s^{-1}. All these values clearly show that the Mistral is a low-level jet which can strongly affect the ABL-dynamics. The duration of the Mistral depends on its synoptic configuration, and ranges from one day to on week or even more in extreme cases.

Experimental set-up

The measurements, made using Degréane UHF-wind profilers (1238 MHz-frequency and 4 kW-peak power), consist of the time evolution of the vertical profiles of the three wind components thanks to one vertical beam and two, or four (depending upon the radar), oblique beams slanted at an off-zenith angle of 17°, the half power beamwidth being 8.5°. The wind velocity is estimated from the frequency corresponding to the mean Doppler shift obtained in the radar echo. The profiles presented here are obtained every 15 min from a height of 100-300 m up to 2500-4000 m with a vertical resolution of 75-150 m. The turbulent dissipation rate, ε, can also be estimated from the width of the Doppler peak in the power spectral density (Jacoby-Koaly et al, 2002). ε-data are usefull to retrieve the ABL structure but can only be correctly derived if the wind speeds are lower than 10-15 m s^{-1} so that ε is only presented for the weak Mistral event.

Two radars are taken into account in our study. During MAP, they were installed at St-Chamas (STC), upstream the Berre pond near Marseilles, and at Toulon (TLN), 90 km to the east (see Fig. 1). During ESCOMPTE, the STC radar was also used whereas the other radar moved to Aix-les-Milles (AIX), 25 km to the east (see Fig. 1).

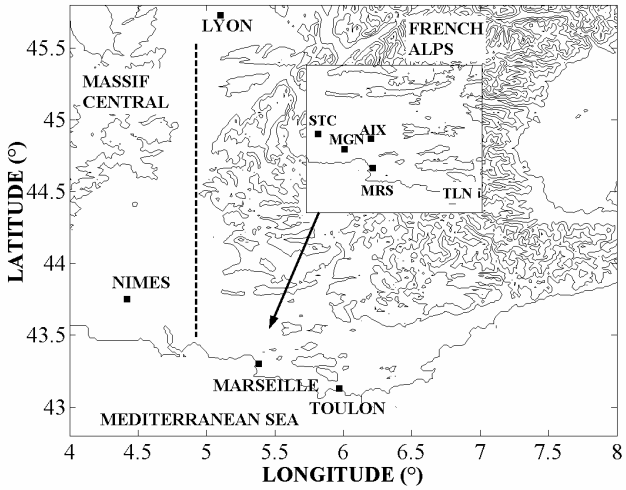

Figure 1: Southern France area concerned by our study. The centered encapsulated map shows the UHF-radar network deployed during ESCOMPTE (STC, MGN, AIX and MRS) and MAP (STC and TLN). The dotted line indicates the Rhône-valley axis. All the contour-lines show mountains of heights above 500 m.

Experimental results and discussions

Fig. 2 shows STC (top panels) and TLN (bottom panels) UHF-profiler observations made during the 6-to-8 November 1999 (MAP). Maximum wind speeds of 35 m s^{-1} at 1300 m, on 6 November 2100 UTC, and 30 m s^{-1} at 1100 m, on 6 November 1900 UTC, are observed above STC and TLN, respectively. The Mistral wind direction is between NW and N during the whole episode, which is a classical feature.

The mechanisms responsible for the temporal evolution of the Mistral vertical structure (see left and middle panels of Fig.2) have already been identified (Guénard et al,

2003). They are related to the evolution of the upstream synoptic wind speed and direction conditions during the event, from west to northwest, in the first part of the event, and north, in the second part. The progressive descent of the upstream inversion layer height (measured by radiosounding at Lyon), associated with the the upstream mountain elevation and the strong acceleration of the air masses along the Rhône-valley axis when the synoptic wind direction is north, are the causes of the passage from a "deep" to "shallow" Mistral situation. Then, the cessation of the Mistral at TLN, several hours before STC, is due to the blocking of this low-level flow by the Alps to the north of TLN (maximum upstream elevation around 3000 m), whereas STC still observed air masses directly exiting from the Rhône valley. This result illustrates the important role played by the upstream orography to determine wether or not a given site is under the influence of the Mistral.

The vertical velocity field is presented here for the first time. Our results are consistent with our basic knowledge of the Mistral, that is, the cold air masses arriving from the north toward the Mediterranean sea are globally subsident. This is particularly true in November where there is no significant ground heating. The right panels of Fig. 2 clearly show such a behaviour, i.e. quasi-systematic negative vertical velocities in the height-time region concerned by the Mistral episode with maximum values between –1 and –1.5 m s^{-1} above STC and between –1.5 and –2 m s^{-1}, above TLN. The values have been temporally smoothed using a 2h-width moving-averaging window in order to remove short period orographically-induced waves

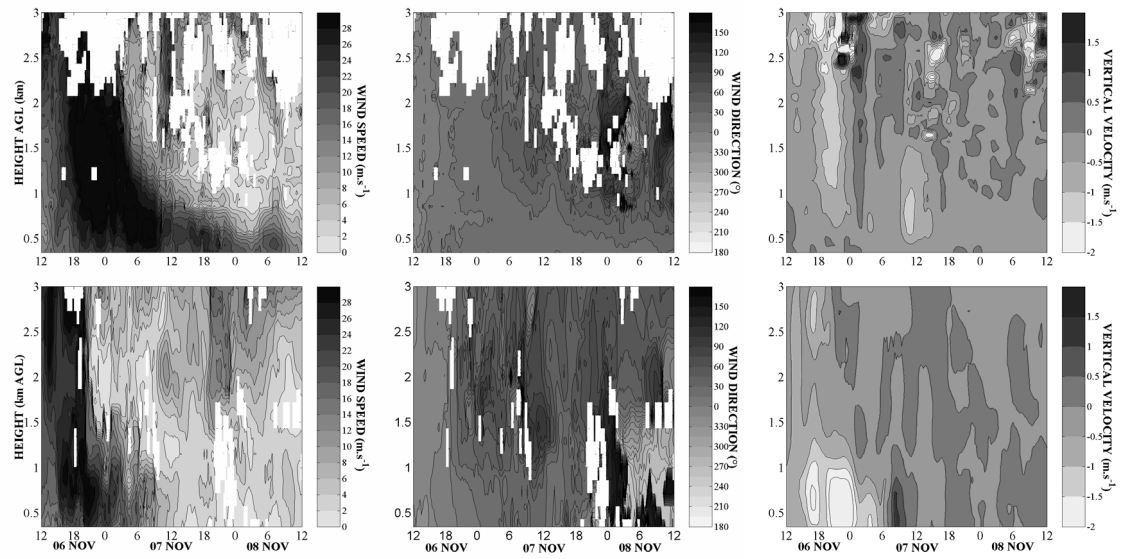

Figure 2: Height-time diagrams of the horizontal wind speed (left panels), wind direction (middle panels) and 2h-averaged vertical velocity (right panels), obtained at STC (upper panels) and TLN (bottom panels), during the 6/8 November Mistral episode.

.

Fig. 3 shows STC (top panels) and AIX (bottom panels) UHF-profiler observations made during the 21-to-23 June 2001 (ESCOMPTE). The maximum wind speed values are between 12 and 15 m s^{-1} below 1500 m.

This event is a typical summer Mistral event, featured by WNW synoptic upstream conditions (quasi-stationary during the whole event), weaker wind speeds and interactions with thermal circulations. The left panels of Fig. 3 clearly show that the Mistral blows at lower levels during the nights and is "lifted up" during daytimes, especially the afternoons where the ground heating is maximum. Right panels of Fig. 3 show the turbulent dissipation rate ε which reveals the installation of the convective boundary layer at the same periods where the Mistral is "lifted up". Moreover, still for the same periods, the near-surface wind is

weak (maximum of 5 m s^{-1}) and the direction reaches WSW (middle panels of Fig. 3). This result is consistent with the presence of sea-breeze circulations.

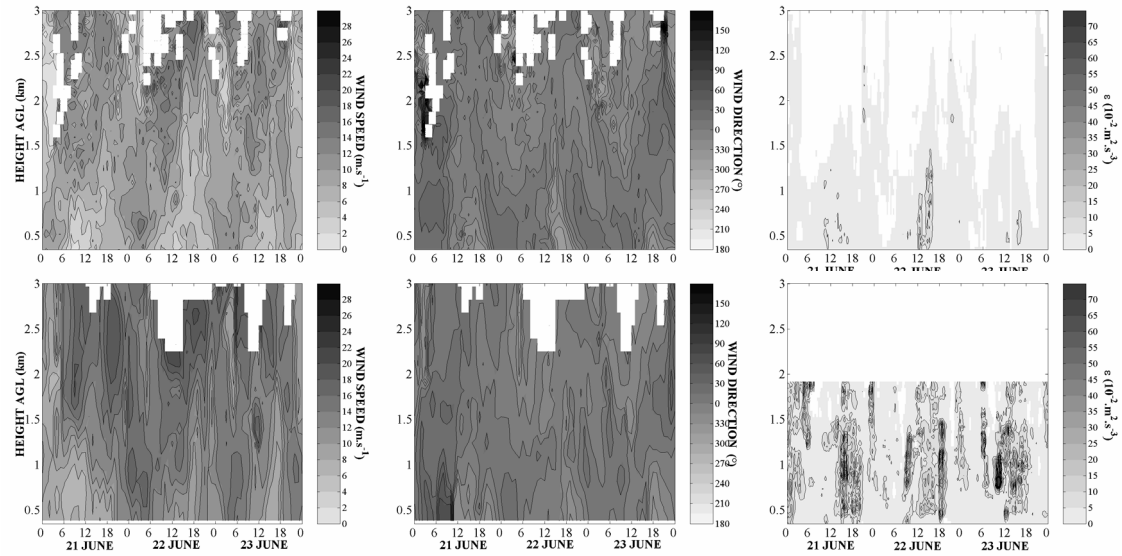

Figure 3 : Height-time diagrams of the horizontal wind speed (left panels), wind direction (middle panels) and turbulent dissipation rate (right panels), obtained at STC (upper panels) and AIX (bottom panels), during the 21/23 June Mistral episode.

Conclusions

Some mesoscale and seasonal aspects of the Mistral in coastal area have been investigated for the first time thanks to UHF profiler data. In fall, when the ground is cool, the Mistral has a synoptically and orographically forced low-level jet structure. The wind speed can be strong, the depth strongly depends on the upstream conditions and on the observation sites (wind fields observed above two places 90 km apart may be very different) and the air masses are globally subsident when approaching the sea. In summer, the Mistral winds are weaker and diurnal variations are observed. During daytimes, the installation of convective boundary layer, revealed by the turbulent dissipation rate, and the sea-breeze circulations tend to weaken and "lift up" the Mistral. During nighttimes, because of the ground cooling, the Mistral recovers its low-level jet structure.

References

Bougeault, P., P. Binder, A. Buzzi, R. Dirks, R. Houze, J. Kuettner, R.B. Smith, R. Steinacker, and H. Volkert, The MAP Special Observing Period, *Bull. Amer. Meteor. Soc., 82*, 433-462, 2001.

Cros, B., P. Durand, H. Cachier, P. Dobrinski, E. Fréjafon, C. Kottmeier, P.E. Perros, V.H. Peuch, J.L. Ponche, D. Robin, F. Saïd, G. Toupance, and H. Wortham, The ESCOMPTE Program: An overview, *Atmos. Res., in press*, 2003.

Drobinski, P., O. Reitebuch, A.M. Dabas, P. Delville, C. Werner, A. Delaval, C. Boitel, H. Hermann, E. Nagel, B. Romand, J. Streicher, S. Bastin, J.L. Caccia, P. Durand, and V. Guénard, Characterization of the 28 June 2001 Mistral event during the ESCOMPTE field experiment, *10th AMS Conf. on Mountain Meteorology, Park City, Utah, USA*, 3-15, 2002..

Guénard V., P. Drobinski, J.L. Caccia, B. Campistron, and B. Benech, Experimental study of the mesoscale dynamics of the Mistral, *Bound.-Layer Meteor., submitted*, 2003.

Jacoby-Koaly S., B. Campistron, S. Bernard, B. Bénech, F. Ardhuin-Girard, J. Dessens, E. Dupont, and B. Carissimo, Turbulent dissipation rate in the boundary layer via UHF wind profiler Doppler spectral width measurements, *Bound.-Layer Meteor., 103*, 361-389, 2002.

Pettré P., On the problem of violent valley wind, *J. Atmos. Sci.*, 39, 542-554, 1982.

WIND PROFILER AND TOWER OBSERVATIONS OF A GRAVITY CURRENT AND A RELATED SOLITARY WAVE

Ahoro Adachi[1,2], Wallace L. Clark[2], Kenneth S. Gage[2] and Takahisa Kobayashi[1]
[1] *Meteorological Research Institute, 1-1 Nagamine Tsukuba, Japan*
[2]*NOAA/Aeronomy Laboratory, 325 Broadway Boulder, Colorado, USA*

1. Introduction

A UHF wind profiler was originally developed at the NOAA Aeronomy Laboratory (Ecklund et al. 1988) to provide continuous, high-resolution wind measurements in the first few kilometers of the atmosphere. The accuracy of profilers in measuring horizontal components of wind has been estimated by the comparison with radio sondes and/or towers. However, there are few studies on estimating the accuracy of profilers in measuring the vertical component, although it has a significant influence on the estimation of horizontal wind (Strauch et al. 1987). One of the reasons is that the vertical airflow is not horizontally homogeneous due to convection and/or plumes, which make the comparison difficult. Moreover, the magnitude of the vertical airflow is usually much smaller than that of horizontal airflow and is easily masked by ground clutter. The measurement of vertical airflow is, however, essential to understand the dynamics of mesoscale phenomena, such as mountain wave, gravity current, bore, and the MCS.

Gossard et al. (1998) proposed the minimizing the variance of the differences (MVD) method to estimate vertical component of wind from four oblique radial velocities, which are less sensitive to ground clutter. They showed that the MVD method can improve the accuracy of RASS. The accuracy of vertical component with this method is, however, still unknown. We, therefore, estimate the accuracy of the MVD method by comparing with a collocated tower at the period when a gravity current passed over our site with strong vertical air motion on Dec. 30, 1997.

2. Method

The meteorological tower at the MRI (Fig. 1) is 213 m in height and equipped with sonic anemometers that measure wind vectors including the vertical components. We used the data recorded at 200 m in height for the comparison. The data were averaged to 2 minutes to match with the profiler observation. Our wind profiler is located about 300 m north of the tower. The profiler was operated in high and low mode. The beam sequence was, Vx, SE, SW, NW, NE, Vy, Vxh, SEh and SWh, where h indicates the high mode. We use only the low mode here. The configuration and operation parameters are summarized in Table 1.

The MVD method determines the vertical air motion that minimizes the variance between the four horizontal velocity components calculated from four oblique radial velocities. One of the advantages of this technique is that it does not rely on vertical beam observation, which is noisy due to clutter. This technique is, however, not available in rain.

Figure 2 shows the time series trace of vertical airflow derived from the tower and the profiler. We plotted the vertical airflow estimated from the vertical beam (hereafter referred as VTB) for a reference. The vertical components whose absolute values are larger than 0.6 m s^{-1} are removed from the VTB measurement. The difference in time that arises from the distance between the tower and profiler is compensated by using the front propagation velocity of the gravity current.

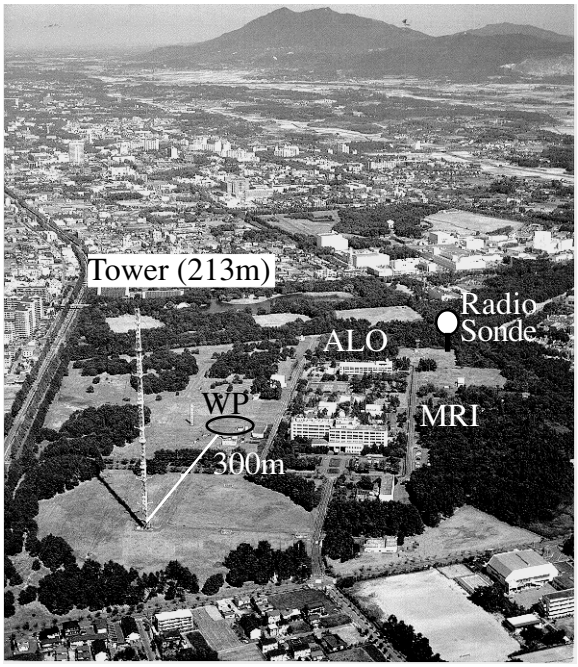

Fig. 1. Picture of Meteorological Research Institute and Aerological Observatory with their observational insturuments. WP indicates the location of the wind profiler.

Frequency	1.3575 GHz
Peak Power	500 W
Beam Width	6°
Beam elevation	90° and 74.5°
Pulth width	400 ns
First Range Gate	150 m
Gate Spacing	60 m
Inter Pulse Period	20000 ns

Table 1. Parameters of the wind profiler.

The vertical component from the VTB has higher time resolution (2.5 min.) than that of the MVD (5 min.). The strong upward airflow seen at 0100 JST in the tower measurement is caused by the passage of the gravity current front. The VTB method could, however, not observe this updraft, because clutter raised noise level around 0 m s^{-1} in the Dopper velocity spectrum. The MVD method, however, could capture this updraft.

The spectrum in high mode shows that there were small droplets above 3 km after 0140 JST. These droplets could be from a cloud which produces rain from about 0300 JST. The second trip echoes from the droplets were observed in the spectrum of the low mode, which masked the echo from clear air as well as the clutter in the vertical beam observation. The bias of the VTB seen after 0140 JST in Fig. 2 could be attributable to the droplets. The MVD has, however, no such bias, because although there were two peaks in the spectrum of oblique beams, one from the atmosphere and the other from droplets, the two peaks were quite different in the Doppler velocity. After 0300 JST when rain was observed at the surface, however, the echo from the rain masked that from clear air even in the oblique beams and made it impossible to use the MVD method.

Figure 3 indicates the vertical airflow measured with the tower versus that from the VTB and the MVD. The data used for the VTB are 0001 – 0137 JST, just before the second trip echo began to contaminate the received signal. The MVD tends to overestimate vertical airflow and the VTB tends to underestimate. The correlation coefficient for the MVD is greater than that of VTB, and bias of the MVD is less than that of the VTB. We concluded that the MVD has a better accuracy than that of the VTB at low altitude. To confirm the reliability of the MVD at high altitude, we analyze the gravity current.

3. Analysis of the gravity current

Wind profiler with RASS is one of the best tools to visualize a gravity current, because it can observe not only wind but also the temperature profile. Figure 4 shows the time-height cross section of horizontal wind and real temperature derived from the tower (below 250 m) and the wind profiler with RASS (above 250 m). Time is right to left so that the gravity current is moving from right to left as it would on a map. The wind directions at low altitude change from NE to NW with temperature decrease at 0100 JST, when the front of the gravity current passed over

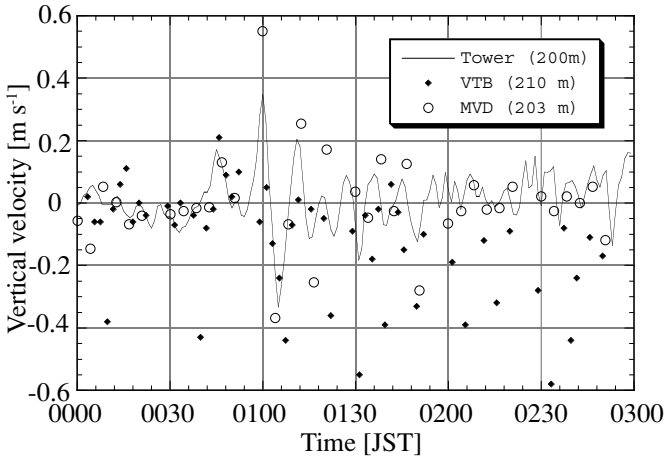

Fig. 2. Time series of vertical air motion derived from the tower and the profiler from 0000-0300 JST on 30 Dec. 1997.

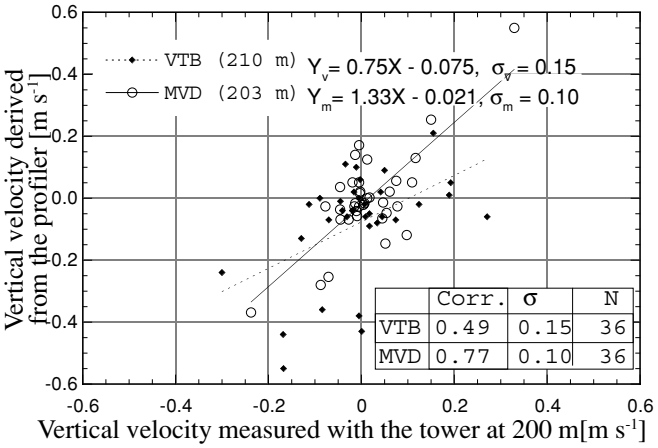

Fig. 3. Scatter diagram of vertical velocity measured with the tower vs that estimated from the wind profiler. The data for the VTB are collected 0001 - 0137 JST and for the MVD are 0000 - 0251 JST.

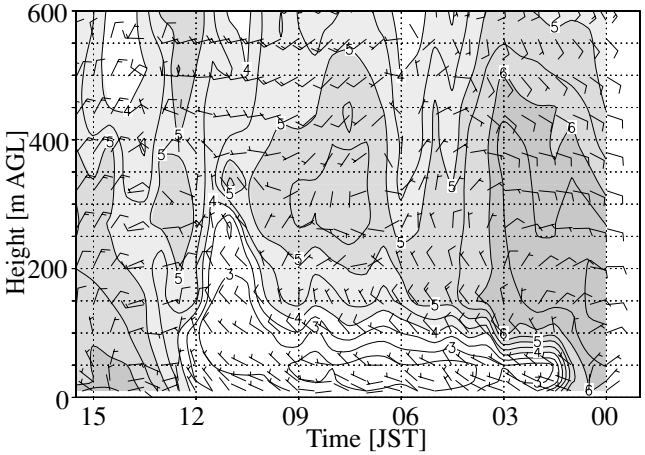

Figure 4: Time-height cross section of wind vectors and temperature derived from the profiler (above 250 m) and the tower. Full barb is 5 m s^{-1}.

the profiler. This figure clearly depicts the gravity current. The depth of the gravity current is 100 m –150 m just behind the front. This gravity current has a "nose", but elevated "head" is obscure. We will refer to this point later. Please note that ahead of the front, there is an inversion layer from the surface whose depth is about the same as the depth of the gravity current.

Figure 5 shows the time-height cross section of two-dimensional flow (u, w), where u is front-normal wind and w is the vertical motion derived from the tower (below 250 m) and the profiler (above 250 m) using the MVD method. There are three regions of waves. The waves seen after 0120 JST are in a region of Kelvin-Helmholtz waves, supported by the layer of instability (Ri < 0.25, not shown). The nose of the gravity current contains two up-down circulation systems that are due to the collision with the environmental wind. This system is similar to simulations (e.g. Jin et al., 1996).This figure also shows that there is a strong upward airflow out ahead of the gravity current. This updraft could be a check for the MVD method.

This updraft is trustable because both the tower and the profiler observed it simultaneously. Moreover, the surface measurement recorded a pressure peak on a pressure trace (Fig. 6). These facts suggest that this updraft is associated with a solitary wave. Indeed, Haase and Smith (1989) theoretically showed that the gravity current head separates from the feeder flow to form a solitary wave if the depth of the inversion layer ahead is almost equal to that of the gravity current. One of the characteristics of this updraft is that the maximum w is observed near the top of this region. This suggests that this wave was not a KdV (Kortweg-de Vries) but a BDO (Benjamin-Davis-Ono) type of solitary wave.

The BDO theory is strictly valid only when the upper layer is neutrally stratified. If the upper layer is weakly stratified, then the waves in the lower layer are no longer truly trapped. Figure 7 shows the profile of virtual potential temperature derived from a radio sonde launched from ALO (Fig. 1) at 2030 JST on 29 Dec. This figure shows that the atmosphere is nearly stratified from 500 m to 2 km in altitude. Rottman and Einaudi (1993) indicated that the solitary wave can propagate in nearly stratified atmosphere if there is a deep enough region of negative K^2 (or even small positive values of K^2) above the wave. They also proposed that a layer of low Brunt Väisälä frequency can act as a reflector of the wave. We, therefore, derive the profile of K^2 and N^2 from profiler and RASS measurements to find such wave guide.

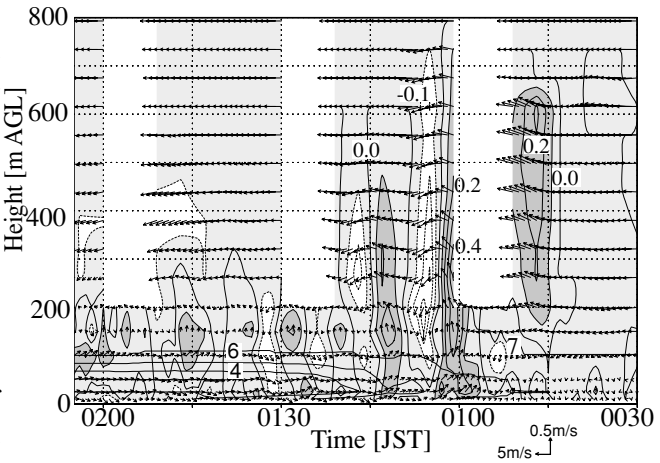

Fig.5. Two-dimentsional flow field deried from the wind profiler and the tower. Vertical components are magnified by 10 times to horizontal component. Contours with gray scale represent vertical airflow. The contours of temperature measured with the tower are also overlaid for help in identifying the gravity current.

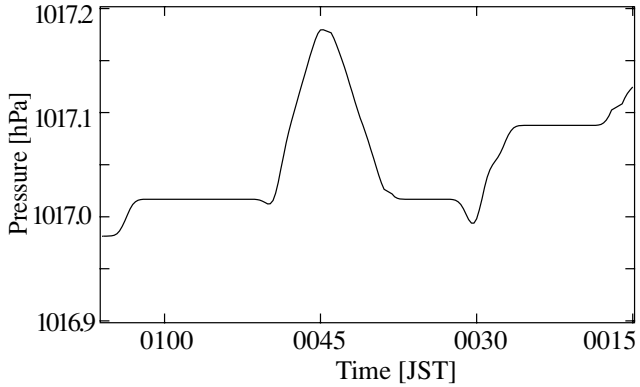

Fig. 6. Time trace of pressure at the surface from 0015 to 0115 JST on 30 Dec. 1997.

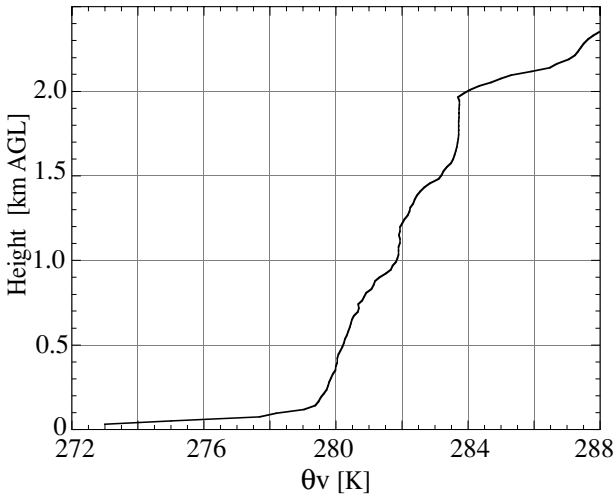

Fig. 7. Profile of virtual potential temperature θv at 2030 JST on 29 Dec. 1997.

Figure 8 shows the profile of virtual temperature (Tv) at 2030 JST on 29 Dec. and at 0030 JST on 30 Dec. derived from the surface measurement, a radio sonde, the tower and RASS. The Tv measured with the radio sonde has a good agreement with RASS at 2030 JST; the Tv from the sonde is almost within the error bar of RASS measurement. The bias of the RASS may be attributable to the increase of Tv with time in the observation. Indeed, the Tv at the surface increased 4 K over four hours. The Tv from RASS at 0030 JST has a good agreement with the tower measurement at altitude of 150 m and 200 m. These results show that the Tv profile measured with RASS is trustable.

Figure 9 indicates the profile of the square of the Scorer parameter derived from the profiler and RASS. The propagation speeds of the solitary wave are assumed to be the same and two times as fast as that of the gravity current in the calculation. This figure shows a region of negative K^2 is just above the solitary wave.

Figure 10 shows the profile of the square of the Brunt Väisälä frequency. This figure also shows a negative region of N^2 just above the solitary wave. These facts show that there are some layers that determine the top of the solitary wave.

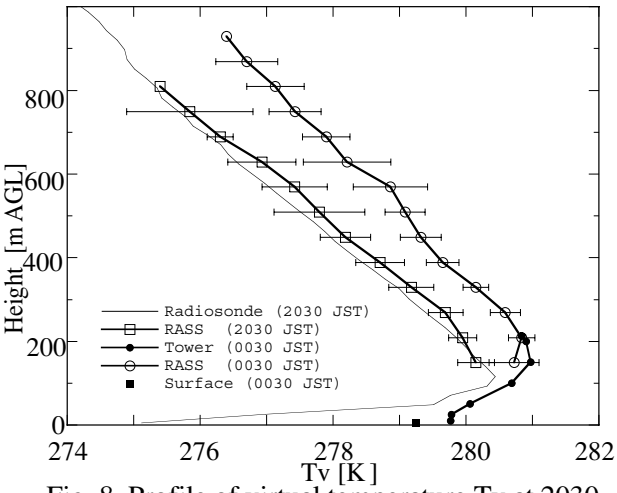

Fig. 8. Profile of virtual temperature Tv at 2030 JST on 29 Dec. and 0030 JST on 30 Dec. The error bars represent 2σ in RASS observation.

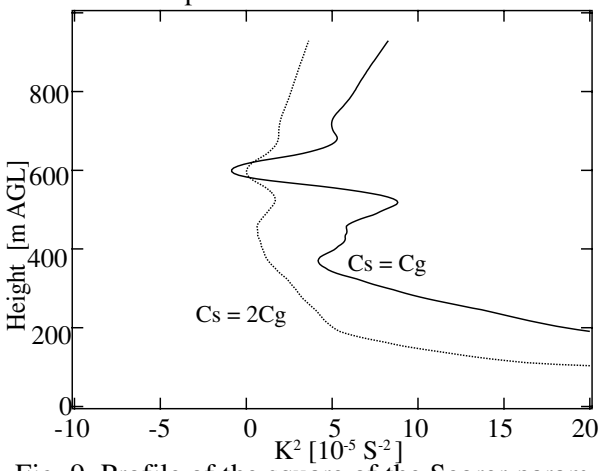

Fig. 9. Profile of the square of the Scorer parameter K^2 at 0030 JST on 30 Dec. derived from the profiler with RASS. The solid line is for the solitary wave propagating at the same speed as the gravity current, while the dashed line is for two times faster than that of the gravity current.

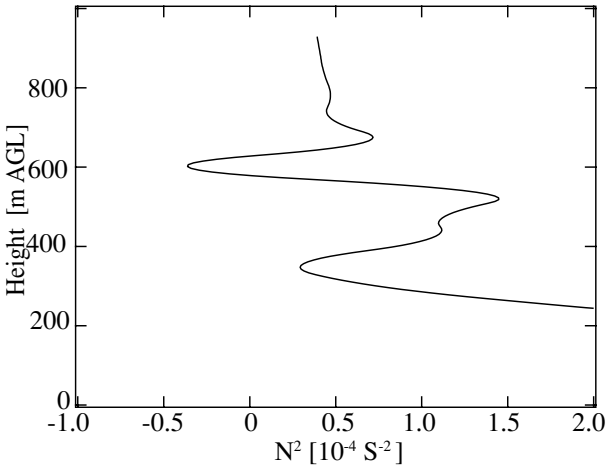

Fig. 10. Profile of the square of the Brunt Väisälä frequency N^2 at 0030 JST on 30 Dec. derived from the profiler with RASS.

4. Conclusion

The MVD method has better accuracy than the VTB method. The MVD is less sensitive to the clutter and to the second trip echo. The maximum w seen at the top of solitary wave is not due to an error of the MVD method but is due to wave duct for a BDO type of solitary wave. The MVD method is shown to be trustable for vertical airflow analysis.

Reference

Ecklund, W. L., D. A. Carter and B. B. Balsley, A UHF wind profiler for the boundary layer: Brief description and initial results, *J. Atmos. Oceanic Technol.*, 5, 432-441,1988.

Gossard, E. E., D. E. Wolfe, K. P. Moran, R. A. Paulus, K. D. Anderson and L. T. Rogers, Measurement of clear-air gradients and turbulence properties with radar wind profilers, *J. Atmos. Oceanic Technol.*, 15, 321-342,1998.

Haase, S. P. and R. K. Smith, The numerical simulation of atmospheric gravity currents. Part II. Environments with stable layers, *Geophys. Astrophys. Fluid Dynamics*, 46, 35-51, 1989.

Jin, Y., S. E. Koch, Y.-L. Lin, F. M. Ralph and C. Chen, Numerical simulations of an observed gravity current and gravity waves in an environment characterized by complex stratification and shear, *J. Atmos. Sci.*, 53, 3570-3588,1996.

Rottman, J. W. and F. Einaudi, Solitary waves in the atmosphere, *J. Atmos. Sci.*, 50, 2116-2136, 1993.

Strauch, R. G., B. L. Weber, A. S. Frisch, C. G. Little, D. A. Merritt, K. P. Moran and D. C. Welsh, The precision and relative accuracy of profiler wind measurements, *J. Atmos. Oceanic Technol.*, 4, 563-571, 1987.

TOWARDS THE ADVANCED MEASUREMENTS OF ATMOSPHERIC TURBULENCE BY SPACED ANTENNA RADARS

Alexander Praskovsky[1] and Eleanor Praskovskaya[2]

[1]National Center for Atmospheric Research, 3450 Mitchell Lane, Boulder, CO 80301, USA
[2]Colorado Research Associates, 3380 Mitchell Lane, Boulder, CO 80301, USA

Remote sensing of turbulence is a task of utmost importance for studying the atmosphere. The existing spaced antenna (SA) methods for atmospheric profiling radars produce directly only the intensity of the vertical turbulent velocity component while other characteristics such as the eddy dissipation rate, turbulent kinetic energy, and others are estimated using the isotropy, the dynamic equilibrium, and other assumptions; e.g., Hocking et al. (1989), Doviak et al. (1996), and references therein. In this paper we consider an application of the structure-function (SF) based method UCAR-STARS (University Corporation for Atmospheric Research - STructure function Analysis of Received Signals) to direct measurements of the intensity of three turbulent velocity components and the horizontal shear stress by SA radars. We present a development of the approach by Praskovsky and Praskovskaya (2003) below referred to as PP. To evaluate the proposed method, results for the NCAR Multiple Antenna Profiler (MAPR) in the atmospheric boundary layer (ABL) at a height of 300 m above the ground are compared with simultaneous measurements by a sonic anemometer located atop a 300-m tower 600 m distant from MAPR.

The transmitter of a SA profiling radar sends pulses of radio waves vertically upwards into the atmosphere and these are scattered by the refractive index irregularities to form a moving and changing diffraction pattern on the ground. Following PP, the irregularities are referred to as scatterers independent of their physical nature. Each scatterer is characterized by its instantaneous location $\vec{x}_i(t)=\{x_i(t),y_i(t),z_i(t)\}$, velocity $\vec{W}_i(t)=\{U_i(t),V_i(t),W_i(t)\}$, and reflectivity $\Delta n_i(t)$. Hereafter t is time, i = 1, 2, ..., M, and M is the number of scatterers in the illuminated volume. The geophysical coordinate system with z axis directed upwards, x axis towards east, and y axis towards north is used hereafter; the values in the brackets {} denote the Cartesian components of a vector. The magnitude and phase of the diffraction pattern is sampled with $N \geq 3$ spatially separated receiving antennas with the phase centers $\vec{x}_{a,k}$ where k = 1, 2, ..., N denotes the receiver number. Each antenna provides a complex received signal $I(\vec{x}_{a,k},t)+\sqrt{-1}Q(\vec{x}_{a,k},t)$ where I and Q are the in-phase and quadrature components of the pure return from the scatterers with no noise or clutter. Equations for SF of pure signals can be used directly in practical measurements while noise can be taken into account while calculating the SF (PP, sec. 4). Consider a pair of receivers with the phase centers $\vec{x}_{a,k}$ and $\vec{x}_{a,m}$, $k \neq m$ = 1, 2, ..., N. The non-dimensional cross SF of order $p \geq 2$ can be defined as:

$$D_p(\Delta\vec{x}_{mk},\tau)=\left\langle\left[S(\vec{x}_{a,k},t)-S(\vec{x}_{a,k}+\Delta\vec{x}_{mk},t+\tau)\right]^p\right\rangle\Big/\left\langle\left[S(\vec{x}_{a,k},t)-\left\langle S(\vec{x}_{a,k},t)\right\rangle\right]^2\right\rangle^{p/2} \qquad (1)$$

where $S(\vec{x}_{a,k},t)=I^2(\vec{x}_{a,k},t)+Q^2(\vec{x}_{a,k},t)$ is the instantaneous power of pure received signals; $\Delta\vec{x}_{mk}=\vec{x}_{a,m}-\vec{x}_{a,k}$ is a spatial separation between the antenna centers, τ is a temporal separation between the signals, and the brackets $\langle\ \rangle$ denote ensemble averages. The auto SF $D_{p,auto}(\vec{x}_{a,k},\tau)$ is a particular case of (1) at $\Delta\vec{x}_{mk}=0$. SF for any atmospheric profiling radar at $\tau \to 0$ and small enough $|\Delta\vec{x}_{mk}|$ can be presented in the following form (PP, sec. 3):

$$D_p(\Delta\vec{x}_{mk},\tau) = a_p(\Delta\vec{x}_{mk}) + b_p(\Delta\vec{x}_{mk})\hat{\tau} + c_p(\Delta\vec{x}_{mk})\hat{\tau}^2 + O(\tau^3)$$
$$D_{p,auto}(\vec{x}_{k,a},\tau) = d_{p,auto}(\vec{x}_{a,k})\hat{\tau}^p + O(\tau^{p+1}) \quad (2)$$

where $\hat{\tau} = \tau/\delta t$, and δt is the inter-sample time interval. Equations for the coefficients a_p, b_p, c_p, and $d_{p,auto}$ at p = 2 and 4 are presented in PP while only those at p = 2 are considered below. The key assumption for deriving Eqs. (2) is the following: the characteristics of each scatterer $x_i(t)$, $y_i(t)$, $z_i(t)$, $U_i(t)$, $V_i(t)$, $W_i(t)$, and $\Delta n_i(t)$, i = 1, 2, ..., M, are locally statistically stationary random processes. Following this assumption, the instantaneous velocity of each scatterer can be presented as a sum of the mean and turbulent components:

$$\{U_i(t), V_i(t), W_i(t)\} = \{\langle U_i\rangle, \langle V_i\rangle, \langle W_i\rangle\} + \{u_i(t), v_i(t), w_i(t)\} \quad (3)$$

It is also assumed that the scatterers have a statistically uniform spatial distribution in the horizontal directions inside the illuminated volume, and that their mean motion is statistically homogeneous, that is: $\langle U_i\rangle = \langle U\rangle$ and $\langle V_i\rangle = \langle V\rangle$ for i = 1, 2, ..., M. These assumptions are sufficient for deriving equations for estimating the mean horizontal velocities $\langle U\rangle$ and $\langle V\rangle$ from coefficients a_p and b_p. To derive equations for estimating turbulence characteristics from coefficients c_p and $d_{p,auto}$, it is further assumed that turbulence is statistically homogeneous $\left(\langle w_i^p\rangle = \langle w^p\rangle, \langle u_i^j v_i^{p-j}\rangle = \langle u^j v^{p-j}\rangle\right.$ for i = 1, 2, ..., M, and $\left.j = 0, 1, ..., p\right)$, and the integral scale of $w_i(t)$ is smaller than σ_r or/and σ_h. Hereafter σ_r and σ_h denote the radar range resolution and the linear width of the transmitted beam. The equation for $c_2(\Delta\vec{x}_{mk})$ was previously presented in a simplified form [PP, Eq. (62)] where intensity of the horizontal turbulent velocity was omitted. The explicit expression for the coefficient is as follows:

$$\frac{c_2(\Delta\vec{x}_{mk})}{1-a_2(\Delta\vec{x}_{mk})/2} = 32\pi^2\delta t^2\left[\frac{\langle w^2\rangle}{\lambda^2} + \frac{\gamma^2\left(\langle U\rangle^2 + \langle V\rangle^2\right)}{\alpha^2 D^2} - \frac{8\pi^2\gamma^4\left|\Delta\vec{x}_{mk}\right|^2\left(\langle U_{mk}\rangle^2 + \langle u_{mk}^2\rangle\right)}{\alpha^4 D^4}\right] \quad (4)$$

where [PP, Eq. (60)]:
$$a_2(\Delta\vec{x}_{mk}) = 2\left[1 - \exp\left(-4\pi^2\gamma^2\left|\Delta\vec{x}_{mk}\right|^2/\alpha^2 D^2\right)\right] \quad (5)$$

Here λ is the radar wavelength; D and γ are the transmitting antenna dimensions and antenna factor; $\alpha^2 = 1 + (\sigma_h/\sigma_a)^2$, and σ_a is the receiver field of view linear width. The values $\langle U_{mk}\rangle$ and $u_{mk}(t)$ are the mean and turbulent components for the projection of the instantaneous horizontal velocity $\{U(t), V(t), 0\}$ of a scattering medium along the baseline $\Delta\vec{x}_{mk}$. To derive Eq. (4), it is further assumed that the integral scale of $u_{mk}(t)$ is approximately equal to, or larger than σ_h. It follows from Eq. (4) that:

$$d_{2,auto}(\vec{x}_{a,k}) = 32\pi^2\delta t^2\left[\langle w^2\rangle/\lambda^2 + \gamma^2\left(\langle U\rangle^2 + \langle V\rangle^2\right)/\alpha^2 D^2\right] \quad (6)$$

This equation relates the intensity of the vertical turbulent velocity $\langle w^2\rangle$ to the ``measurable'' coefficient $d_{2,auto}$ in Eq. (2) for the auto SF. Combining Eqs. (4) - (6) with the standard relation between the instantaneous values $U_{mk}(t)$, $U(t)$, and $V(t)$ for a baseline $\{\Delta x_{mk}, \Delta y_{mk}, 0\}$ (Doviak and Zrnic, 1993, sec. 9.3), one can derive the following expression:

$$\left(\langle u^2\rangle + \langle U\rangle^2\right)\Delta x_{mk}^2 + 2\left(\langle uv\rangle + \langle U\rangle\langle V\rangle\right)\Delta x_{mk}\Delta y_{mk} + \left(\langle v^2\rangle + \langle V\rangle^2\right)\Delta y_{mk}^2$$
$$= \frac{\left(\Delta x_{mk}^2 + \Delta y_{mk}^2\right)^2}{16\ln^2\left[1 - a_2(\Delta\vec{x}_{mk})/2\right]\delta t^2}\left[d_{2,auto}(\vec{x}_{a,k}) - \frac{c_2(\Delta\vec{x}_{mk})}{1-a_2(\Delta\vec{x}_{mk})/2}\right] \quad (7)$$

This linear equation relates the intensities of the horizontal turbulent velocities $\langle u^2 \rangle$, $\langle v^2 \rangle$, and the horizontal momentum flux $\langle uv \rangle$ to "measurable" parameters a_2, c_2, and $d_{2,auto}$ of auto and cross SF for the received signals. The mean velocities $\langle U \rangle$ and $\langle V \rangle$ can be estimated from "measurable" coefficients a_2 and b_2 (PP, sec. 3.4). The characteristics $\langle u^2 \rangle$, $\langle v^2 \rangle$, and $\langle uv \rangle$ can be estimated uniquely by applying Eq. (7) to the coefficients $a_2(\Delta\vec{x}_{mk})$, $c_2(\Delta\vec{x}_{mk})$, and $d_{2,auto}(\vec{x}_{a,k})$ for any three non-parallel baselines $\Delta\vec{x}_{mk}$ at $(m \neq n) = 1, 2, ..., N$.

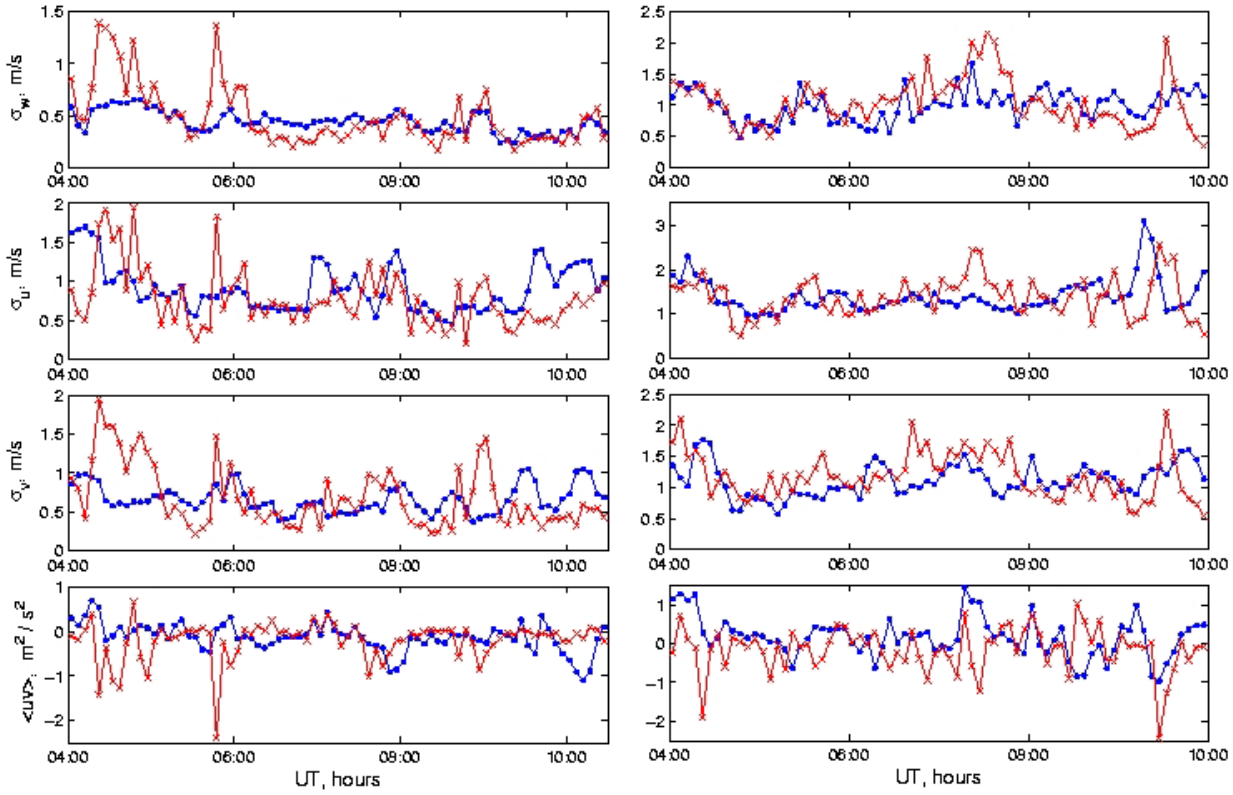

Figure 1. Time series of the turbulence characteristics on 11/16/98 (left column) and 11/23/98 (right column) showing STARS (blue bullets) and sonic (red crosses) results.

The NCAR MAPR is a modified version of the commercially available Radian LAP-3000 915-MHz boundary layer profiler. Modifications allow this radar to be used as a SA system, with the full (four panel) antenna used to transmit and each single antenna panel receiving backscattered energy processed through four independent receiving channels. In November 1998, MAPR was operated at the NOAA Boulder Atmospheric Observatory in Erie, Colorado. The experiment included a sonic anemometer atop a 300-m tower, and MAPR was located approximately 600 m south of the tower; see Cohn et al. (2001) for details of the experiment. MAPR received signals in clear-air conditions were analyzed for two time periods of about six hours each when signal-to-noise ratio (SNR) was sufficiently high. During the selected periods, SNR after 254 coherent and 7 incoherent integrations varied in the range of approximately ± 10 dB. The mean horizontal winds $\langle U \rangle$, $\langle V \rangle$, and characteristics of turbulence $\langle w^2 \rangle$, $\langle u^2 \rangle$, $\langle v^2 \rangle$, and $\langle uv \rangle$ were estimated with STARS at an averaging time of T_{av} = 286 s which is close enough to T_{av} = 5 min. for a sonic anemometer. This paper focuses on turbulence, and the mean winds are not presented. A detailed comparison of the STARS and FCA results for $\langle U \rangle$, $\langle V \rangle$, and $\langle w^2 \rangle$ with those by a sonic anemometer is

presented in Praskovsky et al. (2003). The STARS and sonic anemometer-produced characteristics of turbulence are presented in Fig. 1 where $\sigma_\phi = \sqrt{\langle \phi^2 \rangle}$, $\phi = u$, v, or w, denote the standard deviation of the turbulent velocity components. The reasonable agreement between the anemometer and STARS results indicates a good potential of STARS for measuring $\langle u^2 \rangle$, $\langle v^2 \rangle$, and $\langle uv \rangle$ with SA profiling radars. These turbulence characteristics cannot be measured with existing SA methods; therefore, STARS could become a useful complement to traditional techniques.

Two potential developments of the proposed approach are noteworthy. First, only the second-order turbulence characteristics are presented in this paper. As shown in PP, SF of received signals for any $p \geq 2$ can be derived and used for measurements. For example, one can estimate $\langle u^3 \rangle, \langle v^3 \rangle, \langle w^3 \rangle, \langle uv^2 \rangle, \langle u^2 v \rangle, \langle u^4 \rangle, \langle v^4 \rangle, \langle w^4 \rangle, \langle u^2 v^2 \rangle, \langle u^3 v \rangle$, and $\langle uv^3 \rangle$ with SF at $p = 3$ and 4 while no other radar technique can provide the moments at $p > 2$. To measure the higher-order characteristics, one should derive explicit equations for all coefficients in the decomposition (2) for cross SF up to $\hat{\tau}^p$; the task is conceptually quite straightforward. The second development is the measurement of turbulence above the ABL, and this task is non-trivial. Above the ABL, wave motions (gravity, tidal, and planetary waves) become dominant, and substantial modifications in deriving equations are needed. In particular, Eq. (3) for the instantaneous velocity should include the wave velocity directly; e.g., Holdsworth and Reid (1995). One should replace the pure volume-scattering model by a combination of the volume-scattering and partial-reflection models; e.g., Hocking et al. (1989). Detailed measurements of turbulence characteristics together with simultaneous measurements of wave characteristics in the upper atmosphere by, e.g., MF radars represent the greatest challenge for future developments of the UCAR-STARS method.

Acknowledgements. NCAR is sponsored by the National Science Foundation (NSF). The first author (AP) was sponsored by the NCAR/RAP Director's fund, and the second author (EP) was sponsored by NSF Grant ATM-0122877. The authors are deeply grateful to S.A. Cohn and W.O.J. Brown for the MAPR data and valuable comments on the draft, and to S. Oncley for the anemometer results.

REFERENCES

Cohn, S. A, W. O. J. Brown, C. L. Martin, M. S. Susedik, G. Maclean, and D. B. Parsons, Clear air boundary layer spaced antenna wind measurement with the multiple antenna profiler (MAPR), *Ann. Geophys.*, *19*, 845-854, 2001.

Doviak, R. J., R. J. Lataitis, and C. L. Holloway, Cross correlations and cross spectra for spaced antenna wind profilers, 1, Theoretical analysis, *Radio Sci*., *31*, 157-180, 1996.

Doviak, R. J., and D. S. Zrnic, *Doppler Radar and Weather Observation*, Academic, San Diego, Calif., 1993.

Hocking, W. K., P. May, and J. Röttger, Interpretation, reliability, and accuracies of parameters deduced by the spaced antenna method in middle atmosphere applications, *PAGEOPH*, *30*, 571-604, 1989.

Holdsworth, D. A., and I. M. Reid, A simple model of atmospheric radar backscatter: Description and application to the full correlation analysis of spaced antenna data, *Radio Sci*., *30*, 1263-1280, 1995.

Praskovsky, A. A., and E. A. Praskovskaya, Structure-function-based approach to analyzing received signals for spaced antenna radars, *Radio Sci*., *38*(4), 7-1 - 7-25, 2003.

Praskovsky, A. A., E. A. Praskovskaya, W. O. J. Brown, S. A. Cohn, and S. Oncley, Advanced measurements of atmospheric turbulence with a UHF wind profiler, Submitted to *Ann. Geophys*., MST-10 Special Issue, 2003.

THE INCLINATION OF REFLECTIVITY STRATIFICATIONS

J. Röttger
Max-Planck-Institut, 37191 Katlenburg-Lindau, Germany

It is commonly known that VHF radars observe thin laminae of refractivity structures (reflectivity stratifications). Spatial interferometry shows that these sheets or laminae are frequently not horizontally stratified. This can be particularly pronounced during mountain lee wave events, but also occur very regularly in synoptic-scale disturbances. We will discuss the different scenarios how these stratifications may be related to the atmospheric flow.

In Fig. 1 an example of such a frontal passage, as part of a low pressure region passing Svalbard, is shown, which was described in more detail by Röttger and Trautner (2000). We recognize the reflectivity enhancement near the tropopause and up to four thin multiple stratifications propagating downward, which are explained by meso-scale variations in the passing warmfront. The broad tropopause band in the beginning of the period splits into thin sheets after the warmfront had passed. During warmfront passages the warm air flows over cold air. That flow has an upward component and the isentropes, which might be represented by the thin reflectivity sheets, should be inclined along the frontal surface.

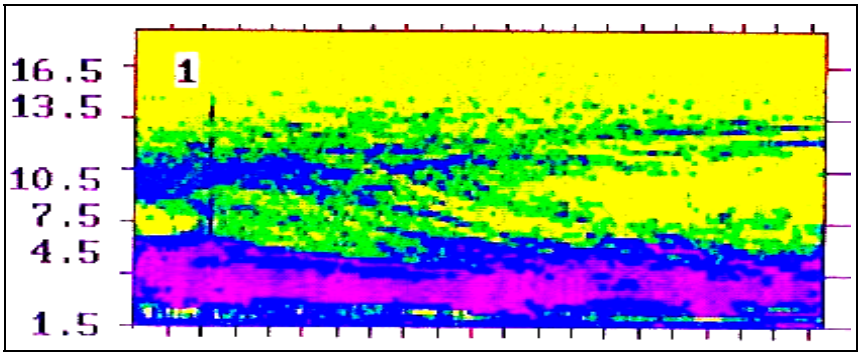

Fig. 1 Radar reflectivity structure observed with the SOUSY Svalbard Radar between 13 Nov., 11:04, and 14 Nov. 1999, 07:28 UT, during a frontal passage. The ordinate is altitude in km.

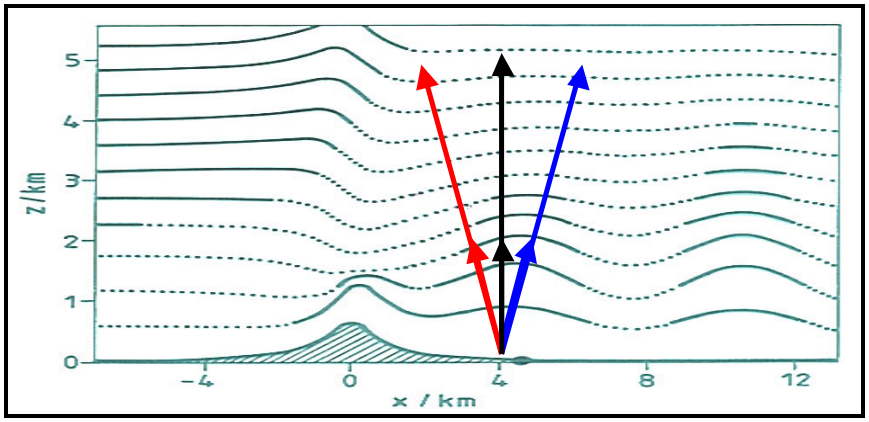

Fig. 2 Air flow (from left to right) over a mountain resulting in mountain waves. A radar located in the vicinity of the mountain looks into different phases of this wave when using the beam swinging method.

In Fig. 2 a sketch of a mountain lee wave is shown. Here we have to consider three properties, which can yield erroneous velocity estimates: (a) The radar beams point into different phases of the wave, which means that the generally applied assumption of a homogeneous wind field is not applicable; (b) the radial velocity is a composite of the mean horizontal wind velocity and the wave induced fluid velocity, which differs at the three beam directions (c) the reflectivity surfaces (sheets and laminae) are inclined at different angles due to the mountain wave, which results in differences of the effective pointing angle (aspect sensitivity).

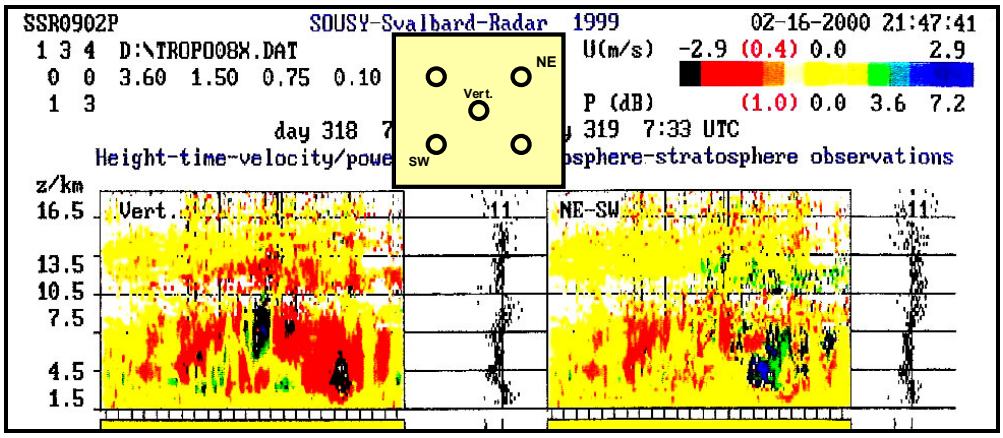

Fig. 3 Height-time-velocity plots measured with vertical beam (left) and with the composition of co-planar NE and SW beam direction (right). The measurements were done over 24 hours with the SOUSY Svalbard Radar 14 Nov., 07:28, to 15 Nov. 1999, 07:33 UT, during strong mountain wave activity.

Fig. 3 shows that these effects have certainly to be taken into account. Whereas in the first half of the observing period the two velocity estimates are about equal, they differ considerably in the second part of this period. At certain times the velocities even have opposite direction. We clearly attribute this discrepancy in velocity estimates due to the effect of mountain waves, resulting from properties (a) and (b). Unless one knows more about the wave parameters, the disentangling of horizontal and vertical velocities will be quite uncertain. That there is also an effect of the inclination of reflectivity surfaces (c) was found by Röttger et al. (1990). As shown in Fig. 4, the radial velocity is correlated with the inclination angle.

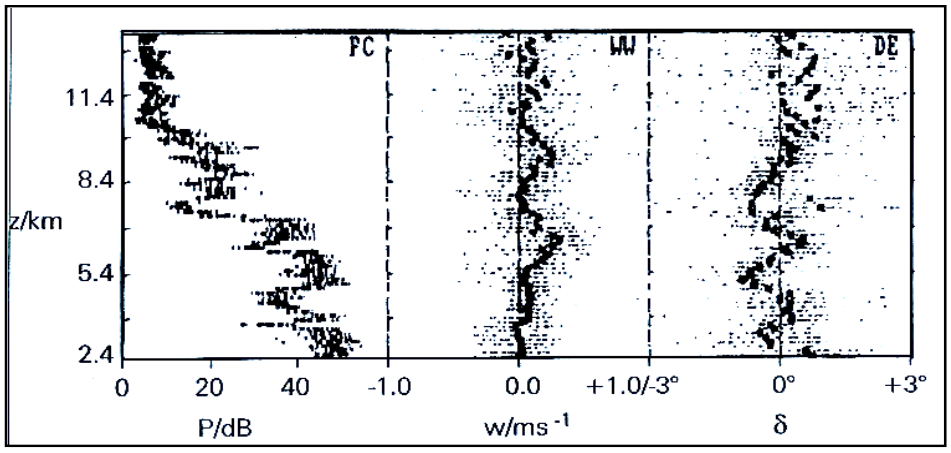

Fig. 4 Radial velocity W measured in the vertical beam and simultaneous estimates of the incidence (inclination) angle δ measured with the Chung-Li VHF Radar

Also Larsen and Röttger (1991) had shown that one needs interferometer measurements to correct the radial velocity for errors arising from tilted reflectivity structures. Incidence angle measurements are needed for this purpose, which can be done by a spaced antenna set up and the analysis of the phase of the cross correlation functions as sketched in Fig. 5.
It was shown that the velocities measured with the vertically pointing beam of 5 degrees width were mostly not the velocities in true vertical direction, since the real incidence of the signal was not from the vertical direction. This was attributed to inclined surfaces of reflectivity. The vertical velocity errors without correcting by the measured incidence angles were between 5% and 200%. This method is not applicable in the Doppler beam swing technique unless the inclinations of the reflectivity structures have a much larger horizontal extent than illuminated by the radar beams. This usually is the case for synoptic-scale disturbances but not for mountain waves, which have much shorter scales.

Fig. 5 Principle of phase measurements with the spaced antenna technique.

In practice, this problem is much more complicated as we will describe in the following by sketching three scenarios considering the inclination of reflectivity structures (so-called reflectivity sheets or laminae), the position of isentropes and the streamlines of the air flow.

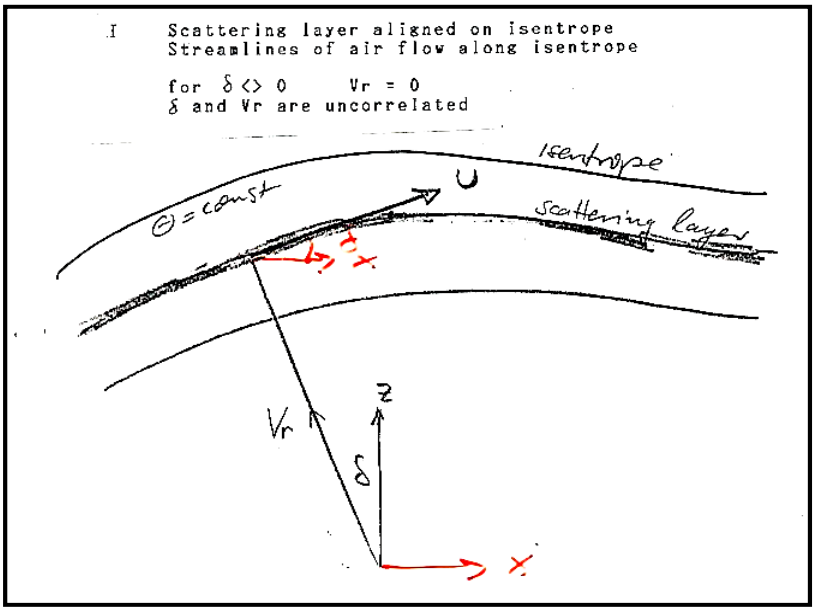

Fig. 6 Sketch showing the main quantities in question:
The incidence angle δ, which is equivalent to the inclination of a thin scattering/reflecting layer (called sheet or laminae, but that also may hold for thicker layers), the measured radial velocity Vr, the air velocity U and the isentrope (surface of constant potential temperature Θ) in the x-z plane.

In Fig. 6 the scattering/reflecting layer, i.e. a lamina of changes in radar refractivity, is aligned on an isentrope (constant level of potential temperature) and the streamline of airflow with velocity U is along the isentrope. For any angle δ, the radial velocity Vr = 0.

In Fig. 7 another scenario is sketched, which assumes that the reflectivity layer is not aligned on an isentrope and the streamline of airflow is in the plane of the isentropic surface. When the angle δ <> 0, the radial velocity Vr <> 0, and the projection U' of U along the measured wave vector direction is the measured radial velocity Vr. The real velocity is U = Vr / sin δ.

In Fig. 8 the lamina is aligned on the isentrope but the streamline is not parallel to the isentrope. In this case U' = U sin δ = Vr, but nothing can be said about the real vertical velocity W.

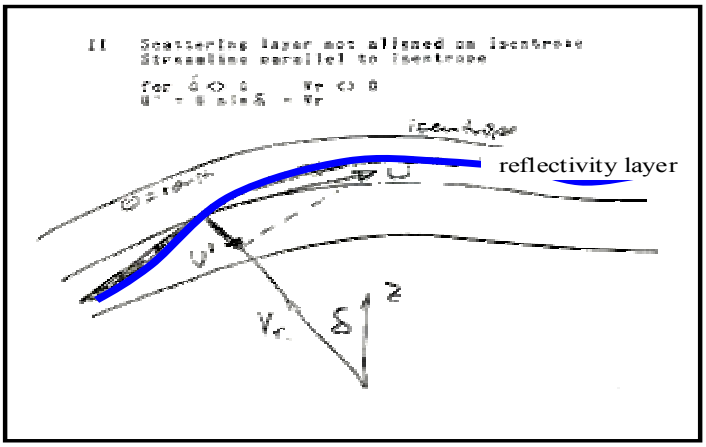

Fig. 7 Reflectivity layer not on an isentrope and not aligned on a streamline, which is on the isentrope.

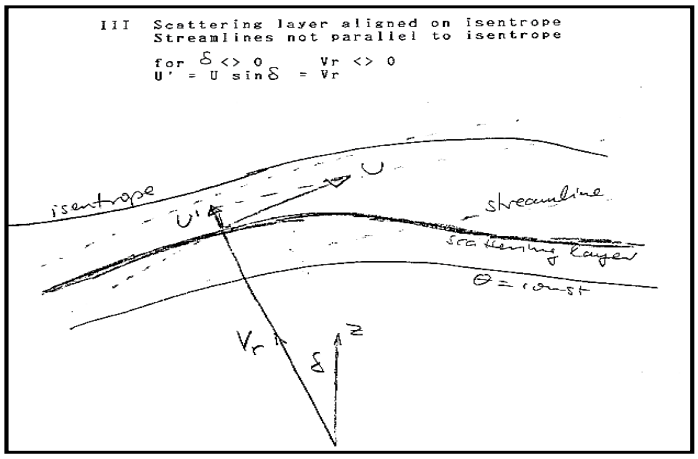

Fig. 8 Reflectivity layer is on isentrope and streamline is not parallel to the isentrope.

Which of these scenarios is occurring in reality determines the accuracy of velocity measurements with MST radar.

New experiments should be performed to discriminate between these possibilities.

References:

Larsen, M.F., and J. Röttger, VHF radar measurements of in-beam incidence angles and associated vertical-beam radial velocity corrections, J. Atm. Ocean. Techn., 8, 477-490, 1991.

Röttger, J., C.H. Liu, J.K. Chao, A.J. Chen, C.J. Pan and I-J. Fu, Spatial interferometer measurements with the Chung-Li VHF radar, Radio Sci., 25, 503-515, 1990.

Röttger, J. and J. Trautner, Synoptic and meso-scale disturbances observed in the Arctic troposphere and lower stratosphere with the SOUSY Svalbard Radar, Proc. 9th Workshop Techn. Scie. Asp. MST Radar, SCOSTEP, 381-384, 2000.

DETERMINATION OF THE TURBULENT FLUXES OF MOMENTUM AND VIRTUAL SENSIBLE HEAT WITH AN UHF RASS PROFILER. COMPARISON WITH IN SITU MEASUREMENTS

B. Bénech, F Girard-Ardhuin, B. Campistron, F. Saïd, F. Lohou, and V. Puygrenier.

Laboratoire d'Aérologie, UMR 5560 CNRS/UPS, Observatoire Midi-Pyrénées, Centre de Recherches Atmosphériques, 65300 Lannemezan, France.

1. Introduction

UHF wind profiler equipped with five antenna has shown to be a very useful tool for the investigation of the convective Atmospheric Boundary Layer (ABL) with a very good temporal and vertical resolution. Previous studies have demonstrated its ability to retrieve the wind velocity field and the mixing height. The Doppler spectral width contains another important information about the fine structure of the atmospheric dynamics, that is the turbulence intensity. For temperature measurements, the UHF profiler is equipped with a RASS system using acoustic sources located nearby the UHF antenna. From the vertical velocity of this 'acoustic echo' measured by the UHF radar, air virtual temperature can be inferred. The spectral width of acoustic echo has been little used as thermal turbulent indicator.

First, we have investigated one method to evaluate the momentum flux based on four beams measurements. The momentum flux is deduced from the combination of the spectral width measurements on two pairs of opposite beams. This estimation has been made in the boundary layer during windy and convective conditions. Some comparisons have been made with aircraft data during two experiments.

Second, we have used two methods to evaluate the vertical virtual sensible heat flux using the height of the boundary layer, the temperature, the spectral width of the vertical velocity. These estimations are compared with in situ measurements made on mast and by aircraft during several field campaigns.

2. UHF characteristics

The Degréane UHF-RASS wind profiler is a 1.238 GHz radar, working with five beams (with 17° off-zenith angle) and four acoustic sources, the beamwidth is 8.5°. It gives wind parameters profiles every 5 minutes with a 75 m height vertical resolution, from 75 m up to 2 to 3 km, depending on atmospheric conditions. In RASS configuration, the radar provides virtual temperature profiles up to 1 km. During the experiment with RASS system, a repetitive sequence made of 5 minutes of RASS mode followed by 10 minutes of wind profiling was used. At each range gate, an online consensus technique on the Doppler spectra selects the atmospheric peak, from which are inferred (for each beam) the radial velocity, reflectivity and spectral width. The virtual temperature is deduced from the measurement of the vertical velocity of the UHF signal backscattered on the acoustic front. The consensus processing works over a 30 minute running period for the dynamic and thermal data.

3. Mean and turbulent parameters deduced from UHF/RASS profiler

The UHF-RASS provides an overview of the diurnal cycle of mean and turbulent characteristics in the ABL through dynamic and thermic measurements. The horizontal wind has been validated on different meteorological conditions by comparison with sodar and mast measurements (for example, see Jacoby-Koaly et al., 2002). UHF negative vertical velocity bias evidenced by Angevine (1987) in the convective boundary layer has been studied by Lothon et al (2002). Figure 1 presents a composite day based on 13 days of measurement of

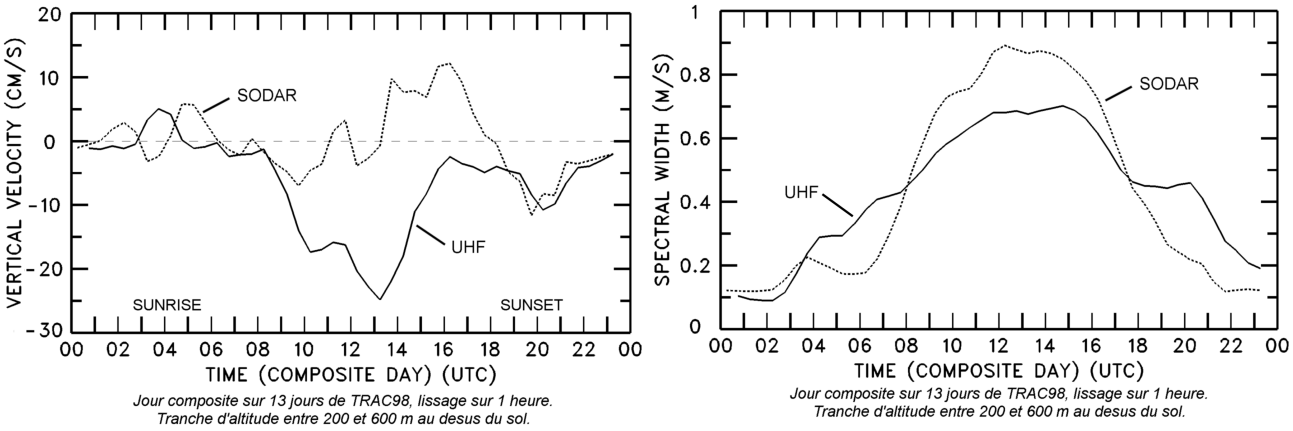

Figure 1*: composite day (13 days) of the vertical velocity (a) and of the Doppler spectral width (b) deduced from the UHF and sodar measurements (200 to 600 m height).*

vertical velocity (a) and spectral width (b) provided by UHF radar and sodar. Compared with sodar data, there is a systematic UHF negative vertical velocity bias during the day time. But the spectral widths of the UHF and sodar present nearly the same time variation.

Girard et al (2003) has shown the possibility of the RASS technique to investigate the dependence of the Doppler spectral width of the sound velocity with the turbulence of the mixed layer. The spectral width of the vertical beams of the sound is related to the variance of radial velocity as: $\overline{V'^2_r} = \overline{(V'_s + W')^2}$. With $\overline{V'^2_s} = \frac{K^4}{4V_s^2}\overline{T'^2_V}$, this expression becomes : $\overline{V'^2_r} = \frac{K^4}{4V_s^2}\overline{T'^2_v} + \overline{W'^2} + 2\frac{K^2}{2V_S}\overline{T'_v W'}$. This expression shows that the variance of the sound spectra is function of the variance of the virtual temperature (Tv), of the variance of the air vertical velocity (W') and of the sensible heat flux ($\overline{TvW'}$). It is necessary to determine two terms by others methods to obtain the third. The contribution of the three terms to the total variance has been estimated to 20 to 30 % for the variance of virtual temperature, to 40 to 60 % for the variance of vertical velocity: and to 30 to 40 % for the virtual sensible heat flux with comparison with data in situ obtained on mast.

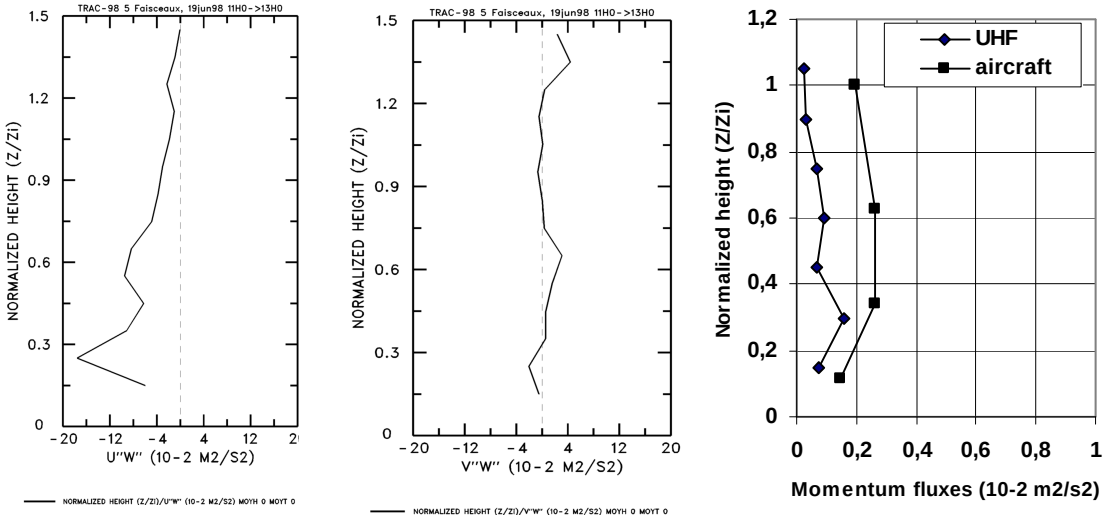

Figure 2: *(a and b)Profiles of the two components of the momentum fluxes deduced from UHF during TRAC experiment (19/06/98). © comparison of the total fluxes with the aircraft data.*

4 Estimation of the momentum fluxes

The momentum fluxes $\overline{u'w'}$ and $\overline{v'w'}$ are deduced from the Doppler spectra width of the four oblique beams of the UHF profiler. Each components of the momentum fluxes is estimated from the difference of the variances of two pairs of opposite oblique beams:

$$\overline{u'w'} = \frac{\left(\overline{v'^2_1} - \overline{v'^2_2}\right)\sin j_1 - \left(\overline{v'^2_3} - \overline{v'^2_4}\right)\sin j_3}{2\sin 2j_s} \quad \textit{and} \quad \overline{v'w'} = \frac{\left(\overline{v'^2_1} - \overline{v'^2_2}\right)\cos j_1 - \left(\overline{v'^2_3} - \overline{v'^2_4}\right)\cos j_3}{2\sin 2j_s}$$

with φ_I the azimuth angle and φ_s the elevation angle of the UHF beam. As an example, the estimation of the momentum fluxes, deduced from the UHF measurements made during TRAC experiment (case of the 19/06/98), is presented in Figure 2 with normalized height. Compared to aircraft measurement, there is an underestimation for the UHF method but the two vertical evolutions are very similar.

5 Estimation of the virtual sensible heat fluxes

The sensible heat fluxes can be deduced from the turbulent kinetic energy equation in using the UHF profiler data. The turbulent kinetic equation given below:

$$\frac{\partial e_{ct}}{\partial t} = -\frac{\partial}{\partial z}\left(\overline{w' e_{ct}'} + \frac{\overline{w'P'}}{?_0} + ?\frac{\partial \overline{e_{ct}}}{\partial z}\right) - \left(\overline{u'w'}\frac{\partial \bar{u}}{\partial z} + \overline{v'w'}\frac{\partial \bar{v}}{\partial z}\right) + ß\overline{w'?_v'} - e,$$

for a stationary and horizontally homogeneous flow, becomes:

$$-\left(\overline{u'w'}\frac{\partial \bar{u}}{\partial z} + \overline{v'w'}\frac{\partial v}{\partial z}\right) + ß\overline{w'?'} - e = 0,$$

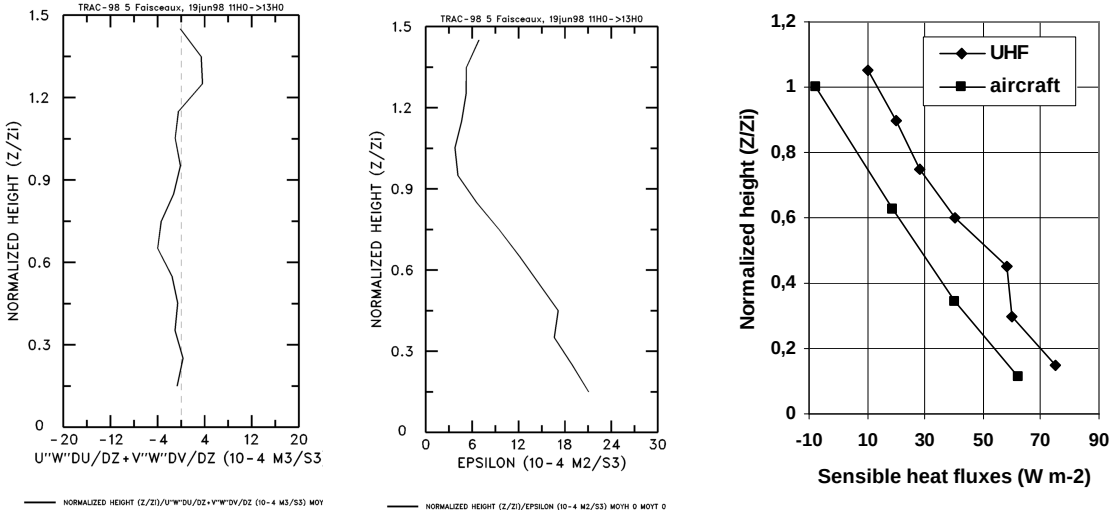

Figure 3*: sensible heat fluxes deduced from the UHF data and compared with the aircraft data: (a) dynamical production term, (b) thermal production term and (c) comparison of the sensible heat fluxes with aircraft measurements.*

The sensible heat flux can be estimated in these cases from the algebric sum (i) of the turbulent dissipation rate deduced from the Doppler spectra of the vertical velocity and (ii) of the dynamical production term including the momentum fluxes and the vertical gradient of the horizontal velocity. Figure 3 presents a vertical profile of the sensible heat fluxes deduced from this method and compared with the aircraft data. The UHF profile overestimates the aircraft data but maintains the same vertical evolution. This overestimation can be due to the underestimation of the momentum fluxes presented above.

The sensible heat fluxes can also be estimated from UHF profiler data in using the heat equation: $\frac{\partial \bar{q}}{\partial t} = -\left(\bar{u}\frac{\partial \bar{q}}{\partial x} + \bar{v}\frac{\partial \bar{q}}{\partial y} \right) - \frac{\partial \overline{w'q'}}{\partial z} \pm Q$. Without advection, the simplified equation becomes: $\frac{\overline{\partial \bar{q}}}{\partial t} = -\frac{\overline{(w'q')_{z_i}} - \overline{(w'q')_0}}{z_i}$ and $\frac{\overline{\partial \bar{q}}}{\partial t} = \frac{1{,}2\overline{(w'q')_0}}{z_i}$ with an entrainment coefficient equal to 0.2 at the ABL top. Then the sensible heat fluxes can be deduced during convective ABL ($d\theta/dt>0$):from the heat rate given by the virtual temperature time evolution deduced from the UHF/RASS measurement and from Z_i deduced from the maximum of reflectivity.

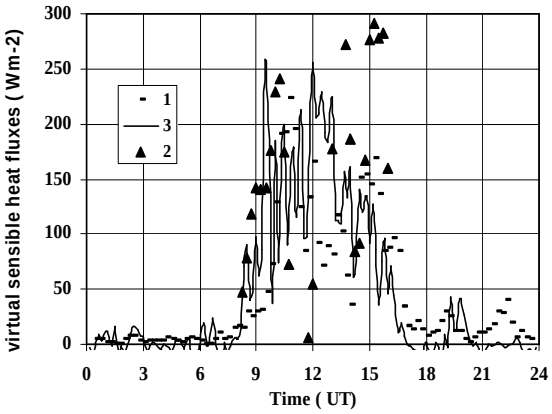

Figure 4: *Time evolution of the virtual sensible heat fluxes deduced from the both methods (1 and 2) compared with the sonic anemometer results (3).*

Figure 4 presents the time evolution of the virtual sensible heat fluxes deduced from the two methods (symbols 1 and 2) with the UHF data taken near 300m height and compared with the sensible heat fluxes measured with sonic anemometer (black line) at 30 m height during a convective day. Compared with the sonic anemometer heat fluxes, a correct time evolution is obtained for the method using the turbulent kinetic equation and more dispersion for the heat equation method.

6 Concluding remarks

This paper has presented some first results about the determination of the turbulent structure of the ABL with a UHF/RASS profiler: (i)-the vertical velocity is found negative during the day in the convective ABL and very different from the sodar vertical velocity. During the night, they have similar variations ; (ii) the spectral width of the velocity from UHF and sodar presents the same diurnal variation; (iii) the spectra width of the UHF vertical velocity of the echo on the acoustic wave is dependant of $\overline{T'^2}$, $\overline{W'^2}$ and $\overline{W'T'}$; (iv) the momentum fluxes deduced from spectra width of the opposite beams are underestimated compared to fluxes measured with an aircraft; (v) the methods of evaluation of the virtual sensible heat fluxes from the turbulent kinetic and virtual heat equations seems promising in a homogeneous, without advection and convective ABL.

References

Angevine, W. M., A. B. White, S. K. Avery, 1994 : Boundary layer depth and entrainment zone characterization with a boundary layer profiler, *Bound.-Layer Meteor.*, **68**, 375-385.

Bok-Haeng Heo et al, 2003: Use of the Doppler Spectral Width to Improve the Estimation of the Convective Boundary Layer Height from UHF wind Profiler Observations, *Journ. Atmos. Ocean Techn.* **20**, *408-424.*

Girard-Ardhuin F. et al, 2003:Remote sensing and surface observations of the response of the atmospheric boundary layer to a solar eclipse. *Boundary-Layer Meteorology*, **l 106**, 93-115.

Jacoby-Koaly S.et al 2002 : Estimation of the turbulent dissipation rate from the Doppler spectral width measured in the Atmospheric Boundary Layer by a UHF wind profiler: comparison with in situ aircraft data *Atmos. Bound. Layer.* **103**, 361-389.

Lothon, M et al, 2002 : Comparison of radar reflectivity and vertical velocity observed with a scannable C-band Doppler radar and two UHF profilers in the lower troposphere. *J. Atmos. Ocean. Technol.,* **19**, *899-910.*

Radar observations of tropical precipitation systems at Kototabang, west Sumatera

Yoshiaki Shibagaki[1], Toshiaki Kozu[2], Toyoshi Shimomai[2], Yasushi Fujiyoshi[3], Shuichi Mori[4], Masayuki Yamamoto[5], Hiroyuki Hashiguchi[5], Shoichiro Fukao[5] and Manabu D. Yamanaka[4]

1: Osaka Electro-Communication University, Osaka 572-8530, Japan

2: Shimane University, Shimane 690-8504, Japan

3: Institute of Low Temperature Science, Hokkaido University, Hokkaido, 060-0808, Japan

4: Frontier Observation Research System for Global Change, Tokyo 105-0013, Japan

5: Radio Science Center for Space and Atmosphere, Kyoto University, Kyoto 611-0011, Japan

1. Introduction

Meteorological satellite observations have revealed the multi-scale structure of synoptic-scale cloud system in relation to intraseasonal oscillation (ISO). The cloud system consists of several meso-scale cloud clusters and the movement of the cloud system is related to the evolution of the meso-scale cloud clusters. However, few observational studies in the evolution of cloud and precipitation system in the ISO have been performed.

In the present study, we investigate the behavior and structure of meso-scale cloud clusters, and the features of precipitation systems in the ISO around Kototabang, west Sumatera Indonesia, using the equatorial atmosphere radar (EAR), boundary layer radar (BLR) and X-band rain radar. We report preliminary results of the radar observation in November 2002.

2. Overview of westward-propagating cloud clusters

In the analysis period, active cloud clusters within a synoptic-scale cloud system are predominant in and around the Indonesia. These cloud clusters indicate the westward propagation about every day. A phase of the synoptic-scale cloud system shifts eastward with time. In the whole troposhere, an easterly wind is predominant in this period. The westward propagation of the cloud clouds corresponds to the environmental wind direction. We study a case on 10 Nov as an example of the westward-propagating cloud clusters.

A meso-scale cloud cluster is traveling from the central Karimantan to west Sumatera on 9-10 Nov (Fig. 1). The evolution of the cloud cluster is related to the diurnal variation of the cloud activity over the both Islands. The cloud cluster passes over the west Sumatra during 16-22 LST. Figure 2 presents time-height cross-section of vertical velocity observed by the EAR in altitude range of 2-13 km. A remarkable updraft, extending over the whole altitude range, is found in the period of 16-19 LST. An updraft and downdraft extending vertically coexist in the period of 19-22 LST.

3. Characteristics of precipitation system within the westward-propagating cloud

Figure 3 presents horizontal distribution of 2-km CAPPI echoes at 10-min intervals in the period of 16-19 LST. A meso-scale precipitation system consists of several smaller convection cells. The lifetime of their cells is 30-40 min. It is evident that they propagate westward according to the environmental wind. While the pre-existing cell in the west part of the convective precipitation decays, new cell forms in the east part of one. As a result, the meso-scale precipitation system propagates eastward. The moving direction is opposite for the cloud system in relation to the environmental wind.

A lower-level wind behavior in relation to the evolution of the precipitation system is examined. Figure 4 presents the time-height cross-section of zonal wind observed by the BLR. When the precipitation system appears around the EAR site, the lower-level zonal wind suddenly changed from easterly to westerly. The westerly wind lasts while the precipitation system is passing over the EAR site. The increase of westerly wind component in the early evening is confirmed in other days. Thus the low-level westerly wind is considered to be a part of a local circulation around the EAR site. It is also suggested that the formation of the new convection cells in the precipitation system results in the convergence of this westerly wind and the environmental wind.

4. Conclusions

Wind field and precipitation associated with westward-propagating cloud clusters in November 2002 is investigated by utilizing the EAR, BLR and rain radar at Kototabang, west Sumatera Indonesia. The moving cloud systems are seen within a synoptic-scale cloud system in relation to the ISO. We mainly study a case on 10 Nov, as an example of the westward-propagating meso-scale cloud cluster. Convective precipitation system appears when the cloud cluster passes around the EAR site. A remarkable updrafts extending vertically are found in the precipitation system. The precipitation system consists of several convection cells. The complicated evolution of the precipitation system is related to the interaction of the westward-propagating cloud cluster and the local circulation occurring around the EAR.

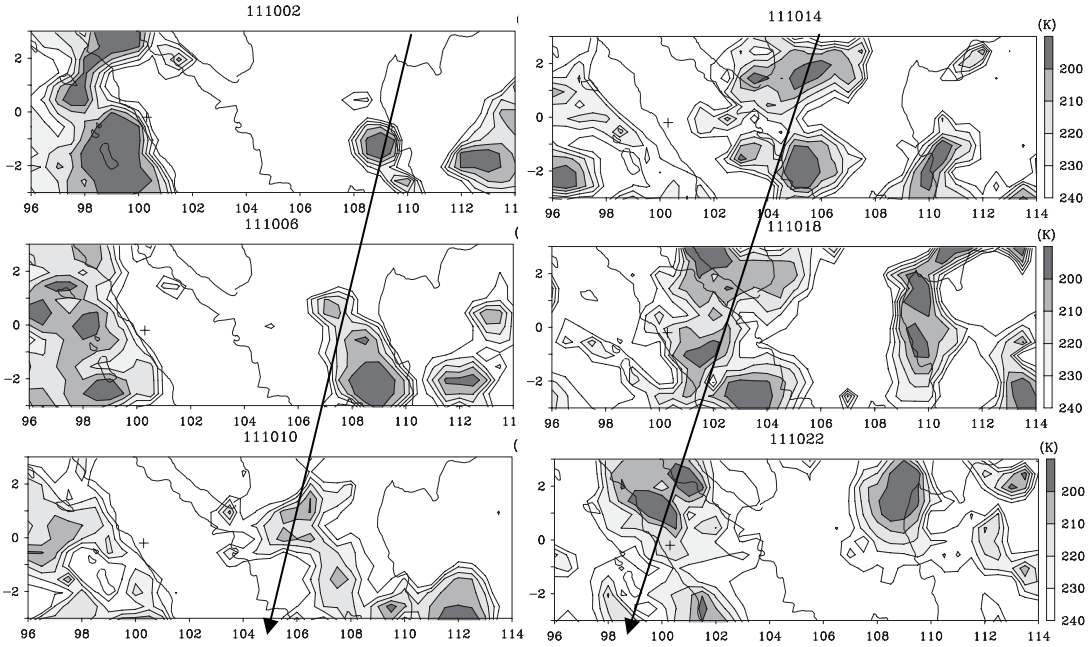

Fig. 1: Movement and structure of meso-scale cloud cluster on 10 Nov 2002. Plus mark is the radar site.

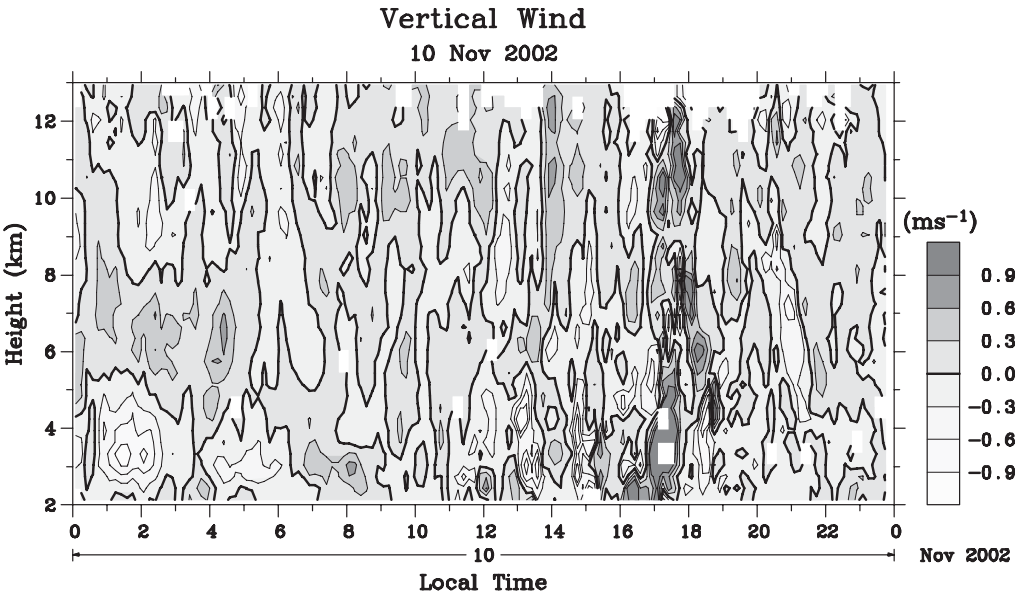

Fig. 2: Vertical velocity observed by the EAR on 10 Nov.

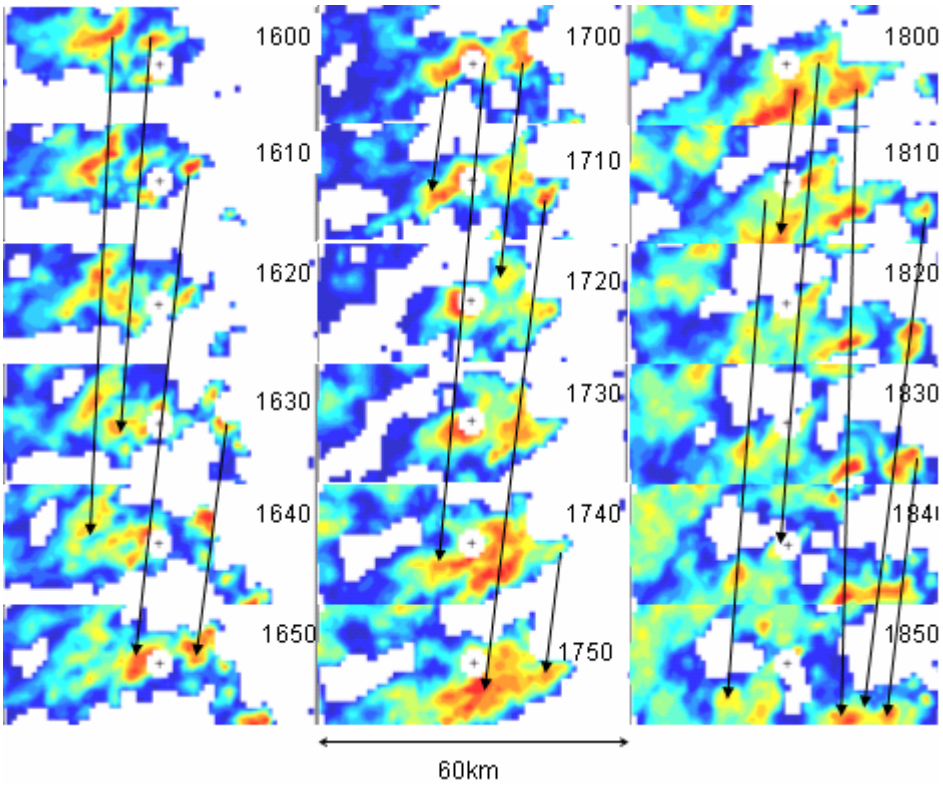

Fig. 3: Horizontal distribution of precipitation system observed by X-band rain radar in the period of 1600-1850 LST 10 Nov.

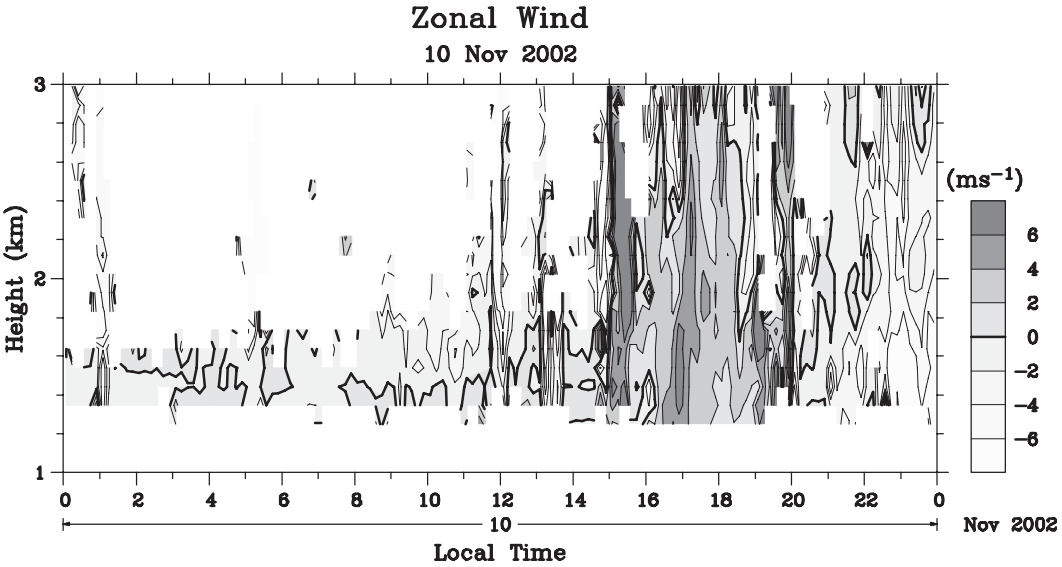

Fig. 4: Lower-level zonal wind observed by the BLR on 10 Nov.

RAIN DROP SIZE DISTRIBUTION OVER GADANKI, INDIA DURING SOUTHWEST AND NORTHEAST MONSOON

K.Krishna Reddy[1], Toshiaki Kozu[2], T.Narayana Rao[3], Kenji Nakamura[3] and D.Narayana Rao[4]

[1] Frontier Observational Research System for Global Change, 3173-25 Showa-machi Kanazawa-ku, Yokohama, Kanagawa 236-0001, Japan

[2] Interdisciplinary Faculty of Science and Engineering, Shimane University, 1060 Nishi-kawatsu, Matsue, Shimane 690-8504, Japan

[3] Hydrospheric-Atmospheric Research Center, Nagoya University, Furocho, Chikusaku, Nagoya 464-8601, Japan

[4] National MST Radar Facility, P.O.Box. 123, Tirupati – 517502, India

1. Introduction

Monsoons are the most complicated yet interesting phenomena as it is associated with rain in large areas and can affect 60% of population leaving under its influence. Further, it plays a significant role in modulating global climate. Among these, Indian summer monsoon (or south-west (SW) monsoon) is the most significant one. Numerous reports are available in literature on the dynamics of the monsoon system (monsoons, 1987 and references therein). Though, the principal rainy season for Indian subcontinent as a whole is the summer monsoon, some parts of India, particularly east coast of south peninsula, gets about 50% or more of the annual rainfall in post monoon season (so called north-east (NE) monsoon). The general features of these monsoon systems, mainly large-scale features, are well known and are well documented (please visit IMD website, www.imd.ernet.in). For instance, the onset of monsoon (1 May for SW monsoon and 20 October for NE monsoon with a deviation of a weak on either side), the seasonal rainfall and the diurnal variation of rainfall. However, much is not known about the differences in the microphysics of cloud systems [for ex, the drop size distribution (DSD)] in these seasons. It is due mainly to lack of suitable measurements at these locations. Recently a UHF wind profiler and disdrometer has been installed at Gadanki (13.5 N, 79.2 E), India under Indo-Japanese colloboration program. It enabled us to study the differences in the microphysics of the cloud systems in SW and NE monsoon seasons. It forms the crux of the present paper.

2. Data and Instrumentation

The Lower Atmospheric Wind Profiler (LAWP) operates at a frequency of 1.3 GHz is located at Gadanki, about 120 km from Chennai and about 80 km from the coast, in southern India. It has been installed in August 1997 and since then operating continuously by providing wind and reflectivity information with a good height and time resolution. The data collected between October 1997 and September 2000 has been used for the present study. Complete description of LAWP and initial results can be found in Reddy et al. (2001). The disdrometer used in the present study is of impact type, originally developed by Joss and Waldvogel (1969). It is located close to LAWP and provides the DSD at 1 min. intervals. Important rain parameters are derived from the available DSD using standard moments method. The present disdrometer data has been successfully evaluated by comparing with the nearby Optical Rain Gauge products (Reddy et al., 2003). Disdrometer has been operating continuously since September 1997, except for few months in 1998 due to malfunctioning of the instrument. For the present study, the data collected between September 1997 and December 2001 are used. Further, seasons are divided as follows with the months May to September comes under southwest monsoon season, while the northeast monsoon comprising October, November and December months.

3. Results and discussion

UHF profiler is an excellent instrumentation system for providing continuous measurements of wind as shown in Figure 1. It shows time series of wind velocity and direction for over one year of observations starting from March 1999 to September 2000. It clearly shows a shift in wind direction from northeasterly to southwesterly in May and again back to northeasterly in late September coinciding with the onset of southwest and northeast monsoon systems. Another noted difference in the wind pattern between these seasons is the magnitude of wind. A strong Low Level Jet (LLJ) apparent at about 2 km with peak magnitude reaching 20 m/s in southwest monsoon season is not seen in northeast monsoon season.

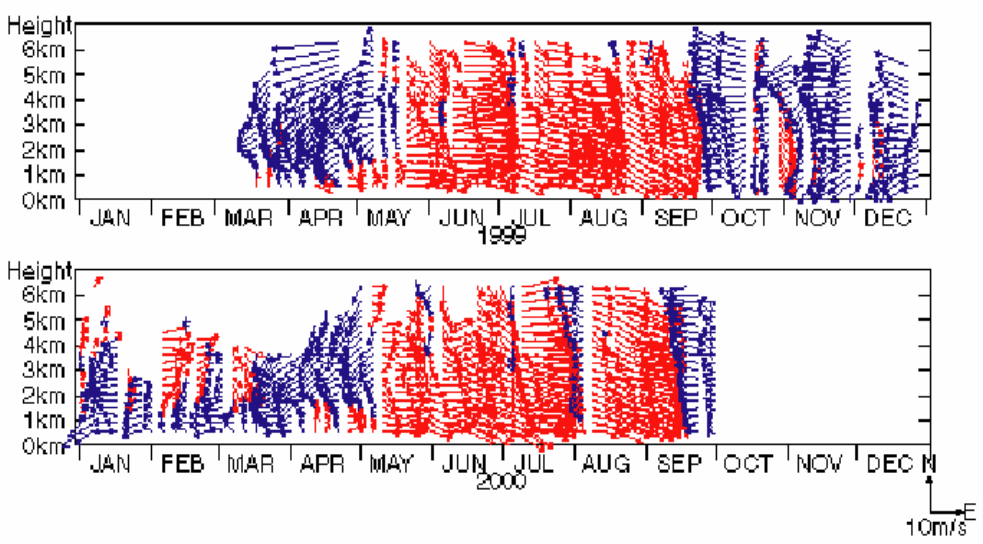

Figure 1. 5 day mean horizontal winds observed from March 1999 to September 2000.

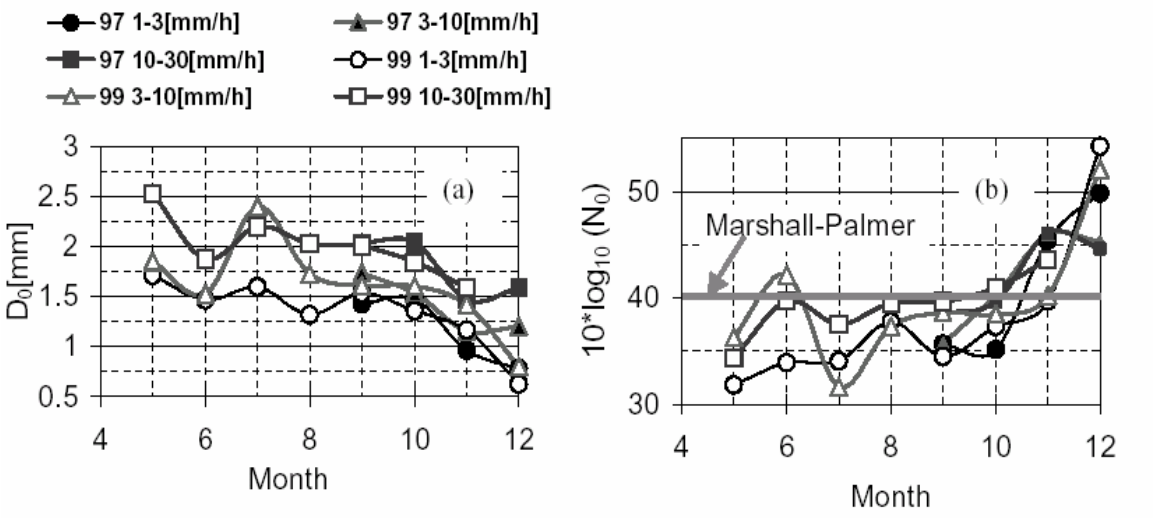

Figure 2. Monthly variation of (a) median volume diameter and (b) N_0.

Disdrometer has collected 5639, 1584, and 9421 minutes of 1 min. samples of DSD during the years 1997, 1998 and 1999 respectively. The rain parameters, median volume diameter (D_0), rainrate (R) and Reflectivity factor (Z) have been estimated from the DSD using the standard method (Rao et al. 2002, Reddy et al., 2003). Further, the gamma parameters (shape, slope and the intercept) are derived using the method proposed by Kozu and Nakamura (1991). The data has been grouped into 3 categories based on the magnitude of R. Monthly variation of D_0 and N_0 has been plotted in Figure 2 (a) and (b), respectively, for all the groups. It is clearly evident from the Figure that D_0 values are higher in SW monsoon season than in NE monsoon season. On the other hand, obviously, the N_0 shows an opposite trend with low values in SW monsoon and high values in NE monsoon. The observed trend is similar for all the groups.

The estimated R and Z are used to derive the Z-R relationships, which is in the form of $Z= 10^a R^b$, where *a* is the intercept and *b* is the slope of the best-fit line on log Z and logR plot. September and December months are chosen to represent SW and NE monsoon seasons. Figure 3(a)-(d) shows the scatter plots of dBR Vs dBZ for all the samples collected in September and December months for 1997, 1999, 2000 and 2001.

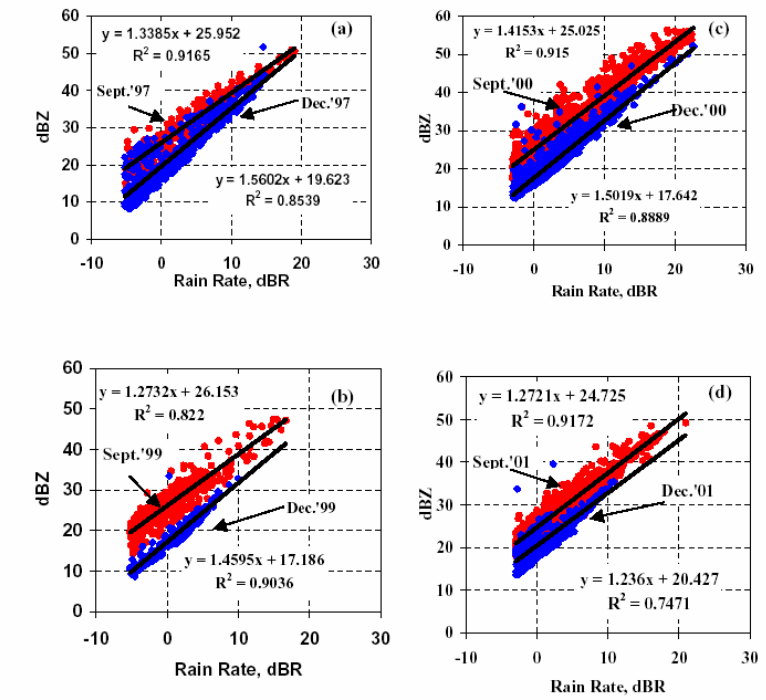

Figure 3. Scatter plots of dBR vs dBZ for samples collected in September and December during (a) 1997, (b) 1999, (c) 2000 and (d) 2001.

It also includes, straight line fitted to the data, the correlation coefficient, the slope and the intercept. Further, it can be noted from the Figure that the intercept and the slopes are different for September and December. The variation of a and b against the month are shown in Figure 4. It can be seen from the figure that, the variation of the intercept is similar to that of D_0 with high values in SW monsoon season and low values in NE monsoon season. On the other hand, the variation of b is not so significant.

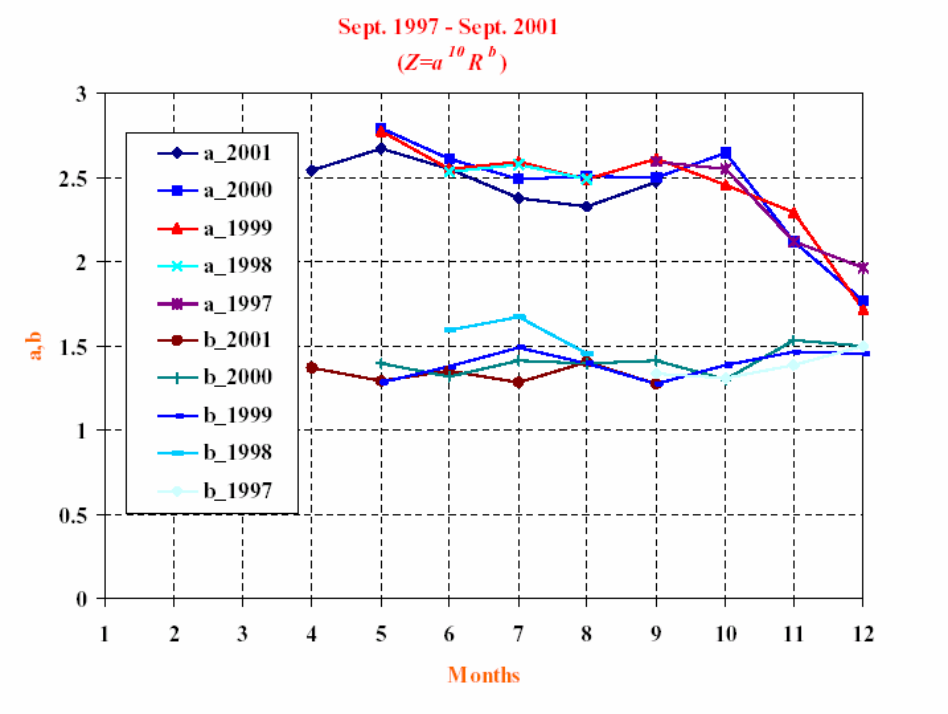

Figure 4. Monthly variation of slope and intercept parameters.

The DSD seems to be distinct in two monsoon seasons. The large median volume diameter (D_0) and the intercept parameter (a) in SW monsoon season clearly suggest that the large drops are more frequent in this season. It can also be seen from the Figure 3, where Z seems be to more in September than in December for any R. It is plausible as the dependence of Z on DSD is high (6^{th} power). The large drops seen in SW monsoon is not unusual as it the season in which updrafts (convection) are strong because of high ground temperatures. These strong updrafts hold the small drops aloft till they grow bigger enough to overcome the upward force by updrafts. The large D_0 is mainly because of these strong updrafts and also evaporation of small drops, which is significant in SW monsoon season.

References

Joss, J., and A. Waldvogel, Raindrop size distribution and sampling size errors , *J. Atmos. Sci.*, 26, 566, 1969.

Kozu, T., and K. Nakamura, Rainfall parameter estimation from dual-radar measurements combining reflectivity profile and path-integrated attenuation, *J.Atmos. Ocean. Tech.*, 8, 260, 1991.

J.S. Fein and P.L. Stephens, Monsoons, Wiley, New York, 1987.

Rao, T.N., D.N. Rao, K. Mohan, S. Raghavan, Classification of tropical precipitating systems and associated Z-R relationships, *J.Geophys. Res.*, 106, 17,699-17,711, 2002.

Reddy,K.K., T.Kozu, Y.Ohno, K.Nakamura, P.Srinivasulu, V.K.Anandan, A.R.Jain, P.B.Rao, R.Ranga Rao, G.Viswanthan and D.N.Rao, Gadanki Lower atmospheric wind profiler at Gadanki, Tropical India: Initial results, *Meteorologische Zeitschrift*, **10**, 457-468, 2001.

Reddy, K.K., and T. Kozu, Measurements of raindrop size distribution over Gadanki during south-west and north-east monsoon, *Ind. J. Rad. Spa. Phy.*, 32, 286-295, 2003.

WIND PROFILER FOR MONITORING OF MEIYU PRECIPITATION IN THE DOWNSTREAM OF YANGTZE RIVER

K.Krishna Reddy[1], Biao Geng[1], Hiroyuki Yamada[1] and Hiroshi Uyeda[1,2]

[1] Frontier Observational Research System for Global Change, 3173-25 Showa-machi Kanazawa-ku, Yokohama, Kanagawa 236-0001, Japan
[2]Hydrospheric-Atmospheric Research Center, Nagoya University, Furocho, Chikusaku, Nagoya 464-8601, Japan

1. Introduction

In the Yangtze River Valley, the rain period from mid-June to mid-July is widely known as Meiyu (or Baiu in Japan, Changma in Korea) or Plum rain (Akiyama, 1989). These heavy rainfall systems play a major role not only in the energy and water cycle of the Asian monsoon regions, but also causes flood disasters in the East Asia region. Elucidating the behavior of the systems is important for understanding and predicting regional climate changes, as well as global climate changes (Ninomiya, 2000). For the first time lower atmospheric wind profiler (LAWP) with radio acoustic sounding system (RASS) was used to study the three-dimensional wind field associated with mesoscale precipitating cloud systems. In particular, LAWP can directly measure the vertical wind component within a convective environment. The objective of this paper is to investigate coherent structures in the boundary layer and interaction between the boundary layer and clouds observed during Meiyu seasons.

2. Experimental location and data collection

A joint field experiment by the Frontier observational Research System for Global Change, Japan and Chinese Academy of Meteorological Sciences (CAMS), China on heavy rainfalls in the downstream of the Yangtze River was conducted during 2001 and 2002.

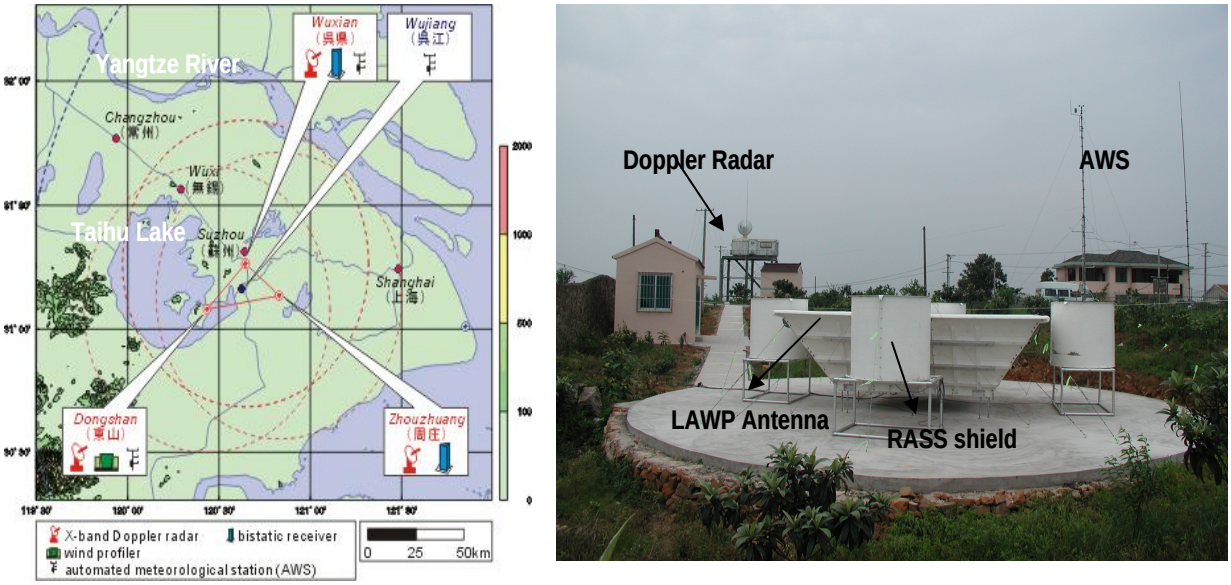

Figure.1 (a) Map showing the topography around experimental site and (b) Lower atmospheric wind profiler with radio acoustic sounding system, X-band Doppler radar and automatic weather station at Dongshan, China

To examine the detailed three-dimensional structure of the mesoscale convective systems (MCS) in the downstream of the Yangtze River [Fig.1 (a)] an observational network of meteorological instruments were deployed. Three X-band Doppler radars, a bistatic radar

system with two receiving antennae, one lower atmospheric profiler with radio acoustic sounding system, and three automatic weather stations (AWS) were deployed for the intensive observational period. However, for the present study, the data collected from LAWP/RASS and AWS were used. The LAWP/RASS was installed [as shown in Figure 1(b)] along with an automatic weather station (AWS), the Institute of Low Temperature Sciences, Hokkaido Universitys' Doppler radar and micro rain radar in the premises of the Dongshan Meteorological Observatory, Jiangsu province, about 80 km west to Shanghai, PR China. Dongshan ($31^{o}4'47''$ N; $120^{o}26'3''$ E) site is ideal because of the surrounding vegetation and some rural houses. The site is in the peninsula of the Taihu Lake, which is the largest in China about 2425 sq km. About 3 km on the west side of the site there are few hills of about 200 m high. Two intensive observational campaigns were conducted during Meiyu period between June and July 2001 and 2002. In this presentation we analysed the LAWP/RASS data from 15 June – 15 July during intensive observation period 2001 (hereafter, IOP-2001) and 2002 (hereafter, IOP-2002).

3. Results and Discussion

The weather map remains one of the key tools for the study of atmospheric processes and the prediction of the weather. Regional objective analyses from JMA on 24 June 2001 at 0020 LST is shown in Figure 2(d). On 24 June 2001, a medium scale disturbance (Meiyu front) was generated near East China Sea and propagated to south of the wind profiler site. Typhoon Chebi (0102), located at South China Sea was traveling towards northward. From Fig.2(d) it could be noticed that the Meiyu front was stationary around the experimental site. The Tropical Cyclone (0102) Chebi was downgraded from Typhoon and became extra-tropical low at 24.8^{o}N 119.4^{o} E at Taiwan Strait, moved northward. A time-height cross-section of reflectivity (SNR) obtained from 23 and 24 June 2001 during Meiyu frontal system and influence of the Typhoon Chebi (0102) are shown in Figure 2(a). Several different types of the vertical structures are evident in this figure during periods of rainfall recorded at the surface [Fig.2(c)] by the influence of Typhoon and Meiyu frontal system. Likewise, the bright-band (layer of enhanced reflectivity) near 4.5 km reveals a time-varying intensity and small fluctuation in height. During the passage of typhoon Chebi, the heavier rain episodes occurred between 15:30 hrs and 22:30 hrs on the 23rd June illustrated a mixture of convection with stratiform rain. The Doppler vertical velocity field W_d [$W_d = w + W_T$, where w is vertical air motion and W_T is the particle terminal fall speed] in Fig. 2(b) reveals a largely stratiform structure, with primarily – 1 to –2 m/s (downward) velocities characteristic of snowfall speeds above the melting region. The LAWP suits for the present study because it can observe the wind profile preceding to the development of Meiyu precipitation. Vectors are directed upward for a northward (southerly) component, and towards the right for an eastward (westerly) component. On 23 and 24 June 2001 a mesoscale convective system (MCS) passed over the lower atmospheric wind profiler (LAWP) site. LAWP revealed an easterly jet stream in the boundary layer bringing a cold air mass from the East China Sea prior to the occurrence of the heavy rainfall about 110 mm within two hours in a limited area. The lifting of the unstable air in the vertical column of the atmosphere by the low-level northerly inflow and horizontal convergence could aid the rapid development of the MCS and the heavy rainfall. Figure 2(e) demonstrates impressively the response of a three-dimensional boundary-layer wind field of the typhoon and Meiyu frontal mesoscale convective system. During the passage of the typhoon (22 and 23 June 2001) the predominant winds were blowing from easterly or southeasterly and above 1 km southerly/southwesterly winds predominant. Another interesting observation was a low-level convergence on 24 June around 0300 LT during the passage of Meiyu precipitating clouds system. Surface (AWS) measurements [Fig.2(f)] also show that the low-level flow changed from northeasterly direction to southwesterly direction.

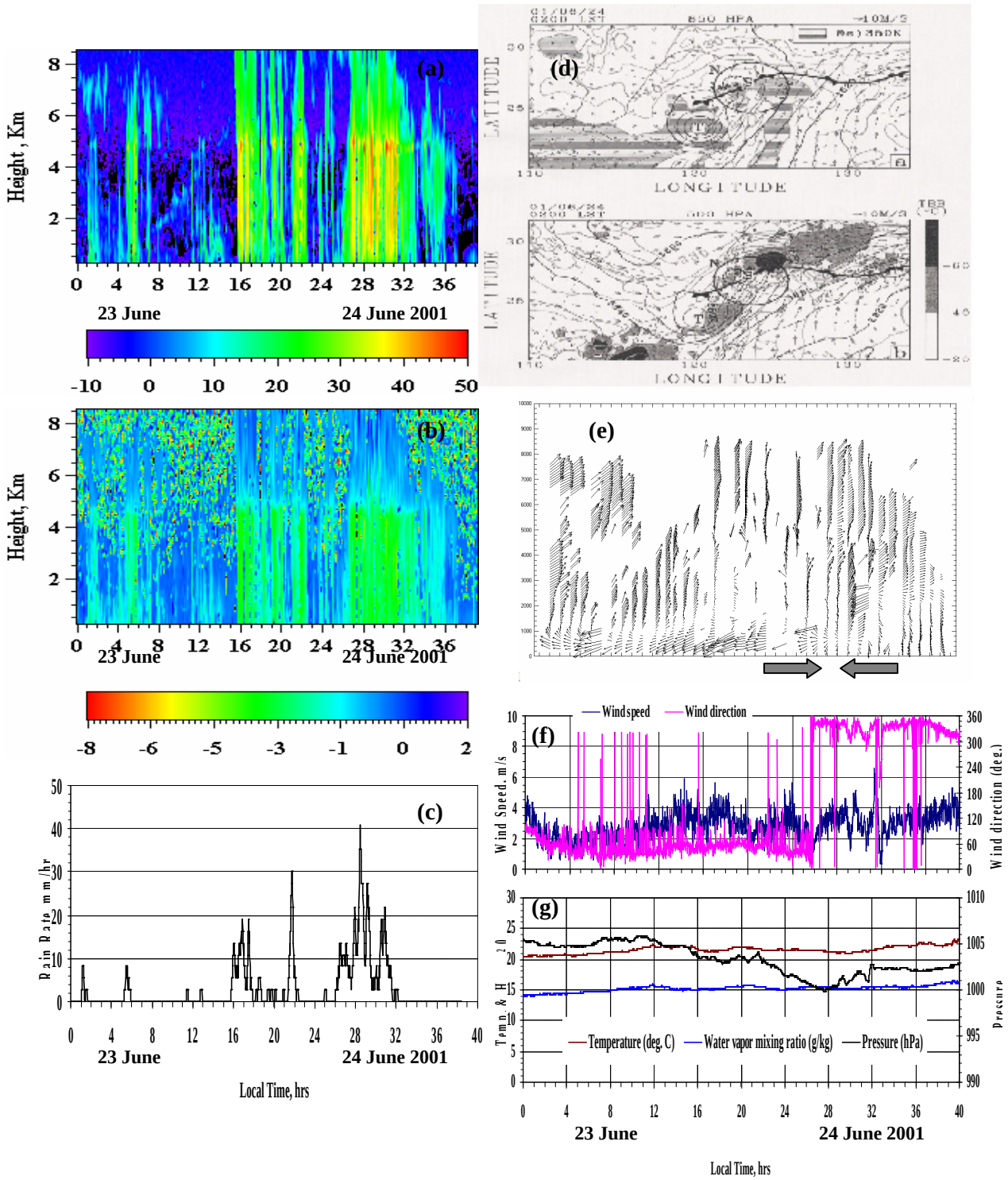

Figure2.Time-height section of (a) return power expressed as a signal to noise ratio (SNR, dB), and (b) Doppler velocity (W_d, m/s during the passage of Meiyu/Baiu frontal precipitating cloud systems between 22, 23 and 24 June 2001. (c) Time series of Rain rate (mm/hr) obtained from AWS. (d) Time-height pattern of horizontal winds (zonal-meridional winds) observed during the passage of Meiyu precipitating cloud systems, and (e) and (f) Surface wind speed, direction (g) temperature, H_2O and Pressure observed from AWS at Dongshan.

From the vertical structure of the precipitating cloud systems, we have classified each profile into convective, transition (mixed convective-stratiform) and stratiform rain based on a modified version of Williams et al. (1995). This algorithm is based on judgment of the presence of a melting layer and the presence of turbulence or hydrometeors above the melting layer. In order to investigate the diurnal variation of occurrence of each precipitating cloud type, the data obtained by Dongshan-wind profiler have been analyzed. Although rainfall could be observed at any time a day, it is noted that there existed distinct diurnal

cycle of precipitation. Figure 3(a) shows the occurrence of diurnal variations of precipitating clouds observed during IOP-2001 and IOP-2002. Diurnal variation of convection seems to occur within 19:00–05:00 LT of next day. The occurrence of stratiform clouds was different from that of Convective clouds. The highest percentage of occurrence appeared in the evening and nighttime. Figure 3(b) shows the mean monthly boundary layer winds observed by the LAWP during 2001. Inspecting Figs. 3(a) and 3(b), it is indicated that occurrence of convective precipitating cloud systems in the late evening and nighttime corresponds to the change of low-level wind direction from easterly to southeasterly. These phenomena suggest that the locally increasing low-level vertical shear and water vapor

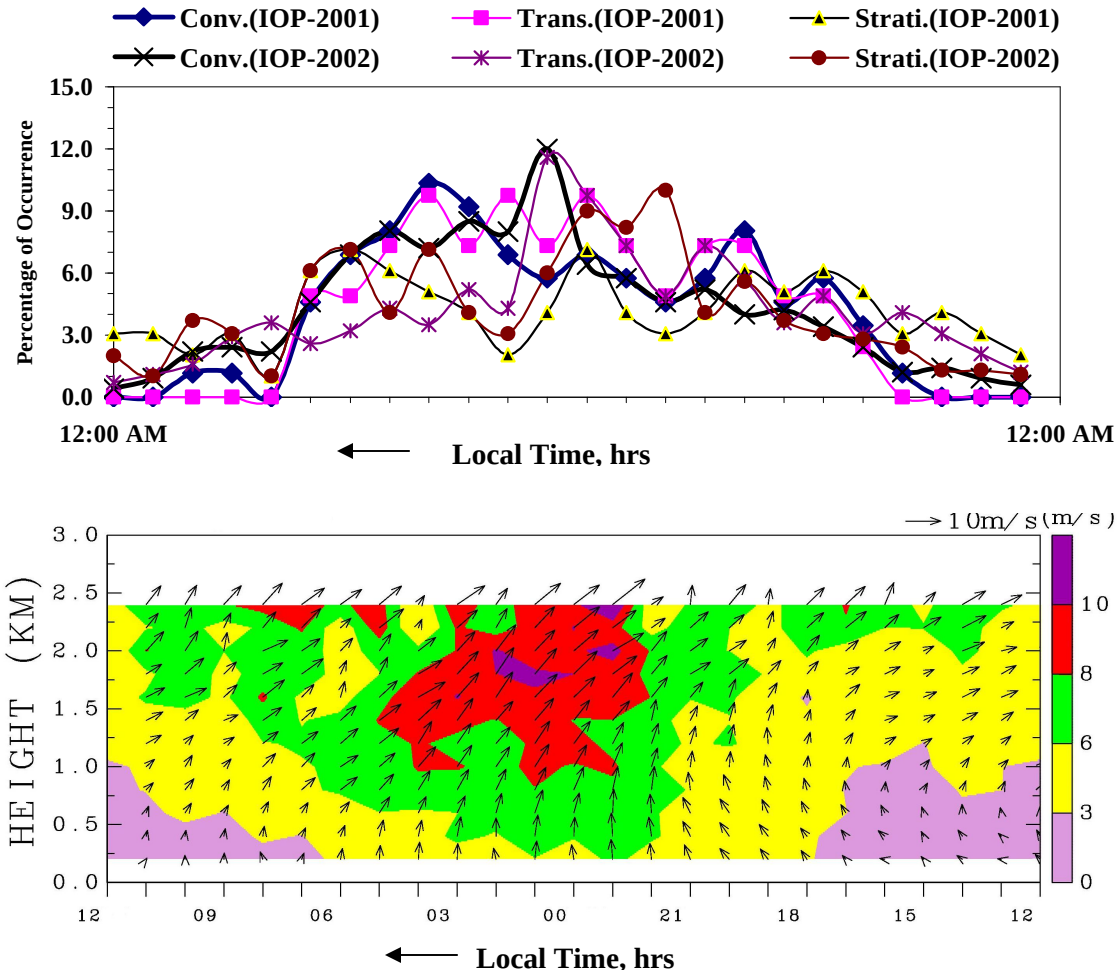

Figure. 3 (a) Diurnal variation and classification of precipitating cloud systems observed during IOP-2001 and IOP-2002. (b) Diurnal variation of mean horizontal wind speed and direction measured by the LAWP. In (a) & (b) Time runs from right to left.

transport would be important for the development of precipitating cloud systems and heavy rainfall in the downstream of the Yangtze River.

4. References

Akiyama, T., Large, synoptic and mesoscale variations of the Baiu front during July 1982. Part 1: Cloud features, *J. Meteorol. Soc. Japan*, 67, 57-81, 1989.

Ninomiya, K., Large- and meso-α-scale characteristics of Meiyu/Baiu front associated with intense rainfalls in 1-10 July 1991, *J. Meteorol. Soc. Japan*, 78, 141-157, 2000.

Williams, C.R., W.L.Ecklund, and K.S.Gage, Classification of precipitating clouds in the tropics using 915 MHz wind profilers, *J. Atmos.Ocean. Tech.*, 12, 996-1012, 1995.

TROPOSPHERIC WINDS MEASURED WITH THE PIURA ST RADAR: NORMAL VS. "EL NIÑO 1997-98" CONDITIONS

Luis A. Flores[1], Jacqueline La Madrid[1], Jorge L. Chau[2]

[1]Laboratorio de Física, Universidad de Piura, Apartado 353, Piura, Peru
[2]Radio Observatorio de Jicamarca, Instituto Geofisico del Perú, Apartado 3747, Lima, Peru

Abstract. The Piura ST (Stratosphere-Troposphere) radar was installed by NOAA Aeronomy Laboratory in 1989 as part of a Trans-Pacific network of wind profilers to study the lower atmospheric dynamics associated with El Niño phenomenon (Gage et al., 1990). In this work we summarize the statistical characteristics of the horizontal winds observed over Piura between 1991 and 2002. The behaviour of the horizontal wind components are shown and discussed as a function of their altitudinal, diurnal and seasonal characteristics. The analysis has been performed for both, normal conditions (periods without El Niño) as well as, for the strong 1997-98 El Niño event. In addition, the horizontal wind characteristics are shown for the two seasons prior to the El Niño 1997-98 event. Our results suggest the existence of two potential precursors in the upper tropospheric horizontal winds when a strong event is involved.

1. Piura VHF Radar.

The Piura VHF radar is located in northern Peru (05°10'S, 80° 38'W) approximately 60 km to west of the Andes. It is a ST (Stratosphere, Troposphere) radar. This radar was installed in 1989 measuring at the beginning just the vertical wind (Ragaini and Rodríguez, 1992). In February of 1991 the radar system was upgraded with oblique rays (14°S and 14°E) allowing the measurement of the horizontal wind components. This radar uses a COCO antenna array of 100m x 100m (Judasz et al., 1987). More details of the system can be found in Gage et al. [1991].

2. Methodology and statistical analysis.

We have analysed wind information from February, 1991 to December, 2002 to obtain the seasonal and diurnal characteristics of the horizontal velocity. The seasons considered are (a) Austral summer (21 Dec-20 Mar), (b) Austral autumn (21 Mar-20 Jun), (c) Austral winter (21 Jun-22 Sep), and (d) Austral spring (23 Sep-20 Dec). The wind convention is as follows: positive to the east and north for the zonal and meridional wind, respectively.

Distribution of frequency We have generated and analysed histograms for the speed corresponding to several years and to several heights. The characteristics and distribution of frequency are studied for annual periods. Thus we have determined the arithmetic mean, mode, variance, standard deviation, coefficient of asymmetry and coefficient of Kurtosis of the horizontal components of wind. Similar analysis we can see in Nastrom et al., 1996.
The data collection of zonal and meridional velocity follow a normal distribution. In figures 1a and 1b we show histograms of zonal and meridional velocities observed in 1993. Similar results were obtained for other periods and altitudes.

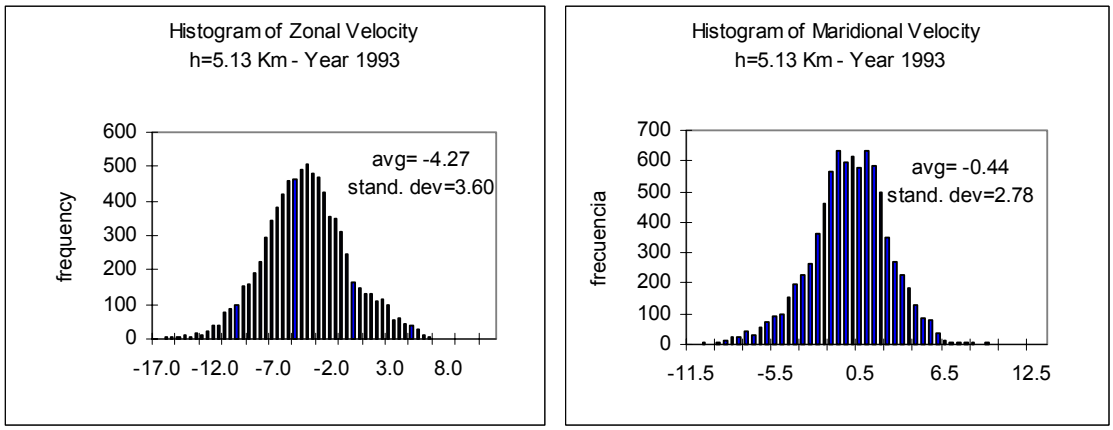

Figure 1. Annual distribution of (a) zonal and (b) meridional velocity, respectively, for 5.13-km altitude.

In the table 1 we present a summary of the arithmetic measurements obtained for 1993. We can see a good agreement between mean arithmetic, median and mode values for the zonal velocities. Also, it is necessary to stand out that the moments of superior order like the asymmetry coefficient and the kurtosis are close to zero. These results suggest that the zonal and meridional winds follow a distribution of normal frequency. Similar behaviour has been observed in other years.

Table 1: Arithmetic measures from 1993

Summay of Arithmetic Measurements Year 1993										
Zonal Velocity										
Height (km)	**1.77**	**2.73**	**3.69**	**4.65**	**5.13**	**5.61**	**6.09**	**6.57**	**7.05**	**7.53**
Arithmetic mean	-1.070	-2.011	-3.893	-4.557	-4.273	-4.089	-4.039	-3.987	-3.861	-3.716
Median	-1.010	-1.970	-3.860	-4.520	-4.360	-4.330	-4.290	-4.130	-4.180	-4.000
Mode	-0.950	-1.770	-4.460	-3.330	-4.790	-5.200	-5.100	-4.340	-4.560	-5.080
Standard Deviation	1.840	2.202	3.205	3.747	3.597	3.479	3.508	3.638	3.958	4.185
Asymmetry coefficent	0.002	-0.139	-0.142	-0.019	0.104	0.350	0.546	0.526	0.499	0.469
Kurtosis	1.814	0.442	0.100	-0.064	0.186	0.576	1.189	1.245	1.402	1.250
Total data	8279	8279	8278	8277	8273	8270	8270	8170	7834	7438
Meridional Velocity										
Height (km)	**1.77**	**2.73**	**3.69**	**4.65**	**5.13**	**5.61**	**6.09**	**6.57**	**7.05**	**7.53**
Arithmetic mean	-0.143	0.168	-0.291	-0.467	-0.444	-0.602	-0.812	-0.880	-0.831	-0.712
Median	-0.060	0.170	-0.380	-0.370	-0.320	-0.560	-0.810	-0.950	-0.990	-0.900
Mode	0.410	-1.740	-0.620	-1.090	0.830	0.760	-0.570	-1.770	-2.360	-1.310
Standard Deviation	3.263	2.975	2.461	2.718	2.779	2.821	2.903	2.992	3.236	3.411
Asymmetry coefficent	-0.088	-0.061	0.118	-0.198	-0.304	-0.261	-0.200	0.024	0.181	0.348
Kurtosis	0.106	0.430	0.827	0.772	0.623	0.550	0.631	0.521	3.730	0.978
Total data	8275	8273	8272	8270	8264	8265	8266	8131	7808	7351

3. Indicators of El Niño and the Southern Oscillation considered

We have obtained the seasonal profiles for El Niño and no Niño conditions. To determine if El Niño events, we have used standard atmospheric and oceanic indicators. The criteria for El Niño events were

i. That the monthly Southern Oscillation Index (SOI) is smaller than –1. According to the CDB No. 00/08 of CPC-NOAA.

ii. That the Superficial Sea Temperature Anomaly (SSTA) is same or bigger than 1 °C in the regions Niño1+2, Niño 3, Niño 4 and Niño 3-4 of the Tropical Pacific. According to the CDB, No. 98/08 of CPC-NOAA based on series 1961-1990 (Smith and Reynolds, 1995).

iii. That the Superficial Sea Temperature Anomaly (SSTA) in front of Paita (in the north coast of Peru) is bigger than 2º C. According to the data of "Instituto del Mar Peruano" (IMARPE).

All of these conditions had to be met at least for three consecutives months.

On the basis of the above criteria, we have considered El Niño events:

* The summer of 1992 (El Niño 1992).
* The period between Winter 1997 and Autumn 1998 (El Niño 1997-98).
* Winter and Spring of 2002 (El Niño 2002)

The present analysis only shows the results for the event 1997-98 because they were more significant. The rest of seasons in the period 1991-2002 were considered as part of the normal conditions.

With regard to the summer and autumn of 1997, in spite of being included in normal periods, they have also been analysed separately in search of possible indicators as precursors of "El Niño" in the high altitude horizontal wind. We have called this period conditions pre-El Niño 1997-98.

4. Validity of the measurements

The dependence of the measurements of vertical and horizontal winds as a function of height with this type of wind profiler has been proven by means of comparisons made by Christmas island (2° N, 157° E) wind profiler, with the analysis of the NMC and the ECMWF interpolated for Christmas island (Gage et al., 1988).

Comparison data from Piura radar ST vs. data of NCEP-NCAR Reanalysis

Maps of zonal, meridional and vertical wind have been made with velocities calculated for Piura according to data of Reanalysis (NCEP_NCAR) and those has been compared to the winds measured by the Piura wind profiler. Both winds are in good agreement, particularly for the high altitudes. The best agreement is observed in the zonal component (results not shown here). However details and figures can be found in Flores et al. [2002]

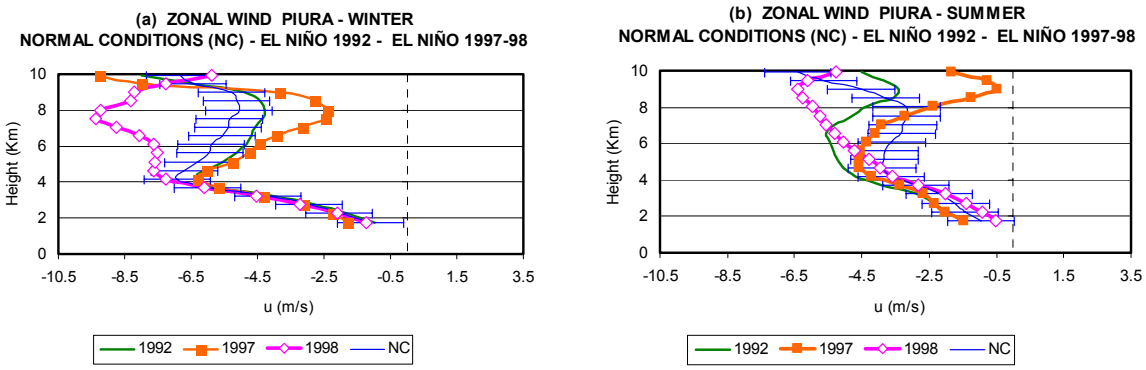

Figure 2. Zonal wind for (a) Winter normal conditions (NC) and "El Niño" conditions, and (b) Summer normal conditions (NC) and "El Niño" conditions. NC are indicated by line with error bars. Values for normal conditions are obtained from the 1991-2000 base period seasonal means.

5. Summary of results and concluding remarks

Based on the diurnal analysis under normal conditions we have found that easterly wind prevails during the whole day at all altitudes. The biggest intensities of wind are given between the 0600 and the 1800 hours. The meridional component, on the other hand, there is southerly wind prevalence between 2 and 5 km during the day, reversing at night. At higher altitudes (5-10 km) we have observed predominant southerly winds as well as a daily variability in the intensity of the wind. This variability can be due to the temperature gradient from north to south and the unequal heating between mountains and the Sechura desert. The specific causes of this effect will be left for future work.

About seasonal analysis in lower troposphere, the meridional wind does not maintain a predominant direction throughout the year. During the winter and the spring the southerly wind dominates all day long. The northerly wind appears only few hours in the afternoon. On the other hand, in the summer and autumn, the northerly wind prevails. In the middle troposphere the northerly winds dominates during all seasons and it is maximum at noon. It is necessary to point out that both the zonal and meridional winds reached their maximum values in the winter

During El Niño 1997-98, in their initial stage we have observed a significant decrease of easterly wind above 4 km compared to normal periods (see Figure 2a). However, in their mature and final phase at the same heights we observe a notable increase of the easterly wind as height increases. On the other hand, there is an increase in the northerly wind above 4 km

During the event 1997-98 in the middle levels the larger differences were observed in intensities of wind along the day, however at lower heights there were significant daily changes: Reinforcement of the east wind around 0200 and 1000 hours during the mature stage of the event and increasing the variability of meridional wind (approximately 1.5 times more) during the initial stage.

We have detected possible precursors of El Niño in the behaviour of the tropospheric wind. In the zonal wind there is a strong decrease of the east wind above 4 km., six months before and during initial stage of "El Niño 1997-98" (Fig. 2b). In addition, there is a significant decrease of the northerly wind in the meridional wind between 2 and 10 km, but only during the previous six months to the event 1997-98.

More details and figures can be found in Flores et al. [2002]

References

Flores L. A., La Madrid J., Chau J. L., Vientos troposféricos observados con el radar VHF en Piura-Perú: condiciones normales versus "El Niño 1997-1998", *Rev. Geof. IPGH, 57*, 81-110, 2002.

Gage K. S., Balsley B. B., Ecklund W.L., Woodman R. F. and Avery S. K. , Wind-Profil-related research in the tropical Pacific, *J.Geophys. Res.,* 96(Suplement), 13209-3220, 1991.

Gage K. S., McAfee J. R., Colins W. G., Soderman D., Bottger H., Radford A. and Balsley B. B., A comparison of winds observed at Christmas Island using a wind-profiler Doppler radars with NMC and ECMWF analyses, *Bull. Am. Meteorol. Soc.,* 69, 1041-1046, 1988.

Judas T. J., Ecklund W. L. And Balsley B. B., The coaxial collinear antenna. Current distribution from the cylindrical antenna equation, *IEEE Trans. Antennas Propag., 35*, 327-331, 1987.

Nastrom G. D., Clarck W. L., Vanzandt T. E. And Warnock J. M., Seasonal and diurnal changes in wind variability from Flatland VHF profiler observations, *Beitr. Phys. Atmosph., 69*(1), 5-12, 1996.

Ragaini E., Rodriguez R., Migioramento del progetto di ricerca sull' indagine troposferica nella regione di Piura, *L'ELETTROTENICA, 79*(9), 863-869, 1992.

Reynolds R. W. and Smith T. S., A high resolution global sea surface temperature climatology, *J. Climate, 8*, 1571-1538, 1995

AN INVESTIGATION OF OZONE AND PLANETARY BOUNDARY LAYER DYNAMICS OVER GADANKI, INDIA

K.Krishna Reddy[1], Shyam Lal[2], Toshiaki Kozu[3], Kenji Nakamura[4], Yuichi Ohno[5], Manish Naja[6] and D.Narayana Rao[7]

[1] Frontier Observational Research System for Global Change, 3173-25 Showa-machi, Kanazawa-ku, Yokohama, Kanagawa 236-0001, Japan
[2]Physical Research Laboratory, Navrangpura, Ahmedabad 380009, India
[3] Interdisciplinary Faculty of Science and Engineering, Shimane University, 1060 Nishi-kawatsu, Matsue, Shimane 690-8504, Japan
[4] Hydrospheric-Atmospheric Research Center, Nagoya University, Furocho, Chikusaku, Nagoya 464-8601, Japan
[5]Communications Research Laboratory, Koganei, Tokyo 184-8795, Japan
[6] Frontier Research System for Global Change, 3173-25 Showa-machi, Kanazawa-ku, Yokohama, Kanagawa 236-0001, Japan
[7]National MST Radar Facility, P.O.Box. 123, Tirupati 517502, India

1. Introduction

It is now widely recognized that the dynamics of convective boundary layer (CBL) in tropics are very important to understand the global climate, and meteorological now–casting, including the prediction of boundary layer evolution and pollution dispersion. The daily cycle of CBL growth and collapse can be seen clearly in time-height displays of the reflectivity profiles of lower atmospheric wind profilers (LAWP). There are usually sharp gradients in aerosol concentration and specific humidity through the entrainment zone at the CBL top as cleaner and dryer air from the free atmosphere is entrained and mixed into the aerosol-laden, moisture boundary layer (Cohn and Angevine, 2000). Although ozone in the CBL exists only in the parts per billion (ppb) range, it is an important gas due to its key role in influencing the oxidation capacity of the lower atmosphere. Several studies have examined the impact of the Asian pollutants on other parts of the world (e.g., Jacob et al., 1999). In spite of the importance of the tropical troposphere, there are no systematic simultaneous measurements of surface ozone and its precursor gases over the Indian region (except those at Ahmedabad, an urban site) until recent years (Naja and Lal, 1996; Lal et al., 2000). The tropospheric ozone problem was once thought to be restricted to urban areas, but now it is recognized that ozone concentrations in rural areas can rival those measured in urban areas. Study of ozone chemistry is important at rural sites because ozone precursors get transported to there from the near–by urban or industrial areas (Angevine et al. 2003). This paper concerns an evaluation about the ozone (O_3) and CBL dynamics over the tropical rural site at Gadanki using UV absorption based analyzer and LAWP for 30 days, during April 1999.

2. Observational Site

The National MST (Mesosphere-Stratosphere Troposphere) Radar Facility (NMRF) at Gadanki (13.5^{o}N, 79.2^{o}E, 375 m above sea level) is situated in a rural area of Chittoor district (Andhra Pradesh state) in the southern part of India [Figure 1 (a)]. The terrain surrounding the radar site is illustrated by the three-dimensional contour map in Figure 1(b). The local and general topography is rather complex with a number of hills and a very irregular mix of agricultural, small-scale industrial and rural population centers. There are hills in the northern and southern sides of the observation site within 1 to 10 km distance. The average height of the hills is about 550 m, with a maximum height of about 1000 m. A major road passes through near the observation site, with the usage of a few thousands of heavy vehicles every day. There is no major industry in the Chittoor district except for few small-scale units at major towns. Tirupati (population about 0.6 million) and Chittoor (population about 0.3 million) are the nearest urban regions about 30 km in Northeast and south/southwest to the experimental site. The observation site is about 120 and 200 km from

the two nearby major cities, Chennai (Madras) to the southeast and Banglore to the Southwest, respectively.

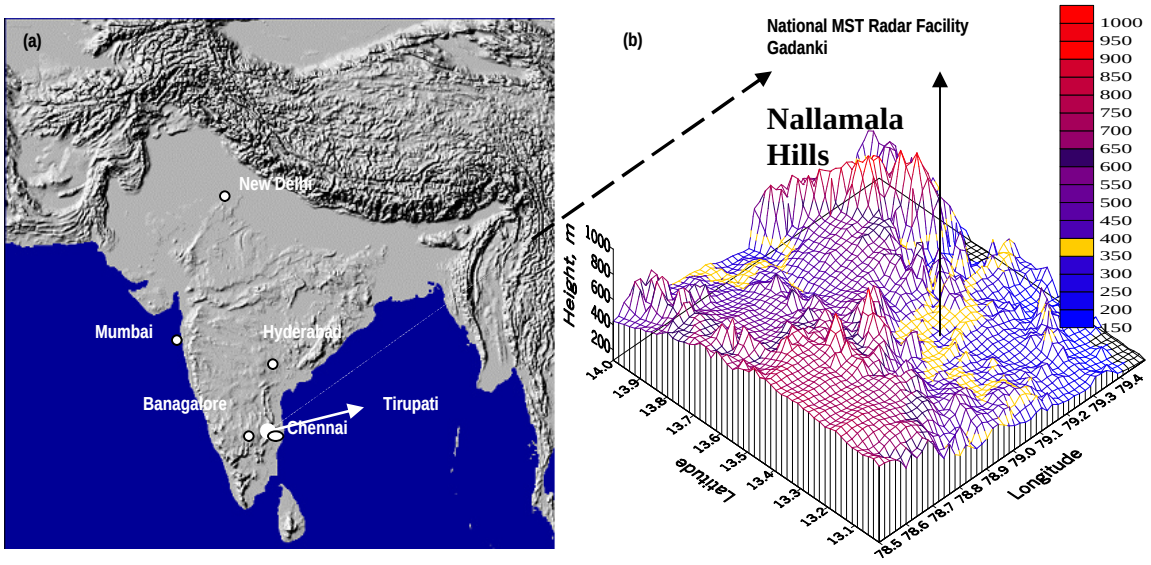

Figure 1.(a) Map showing several cities and major towns near by National MST Radar Facility (NMRF) and (b) Three dimensional view of the main topography around Gadanki (after Reddy et al. 2002).

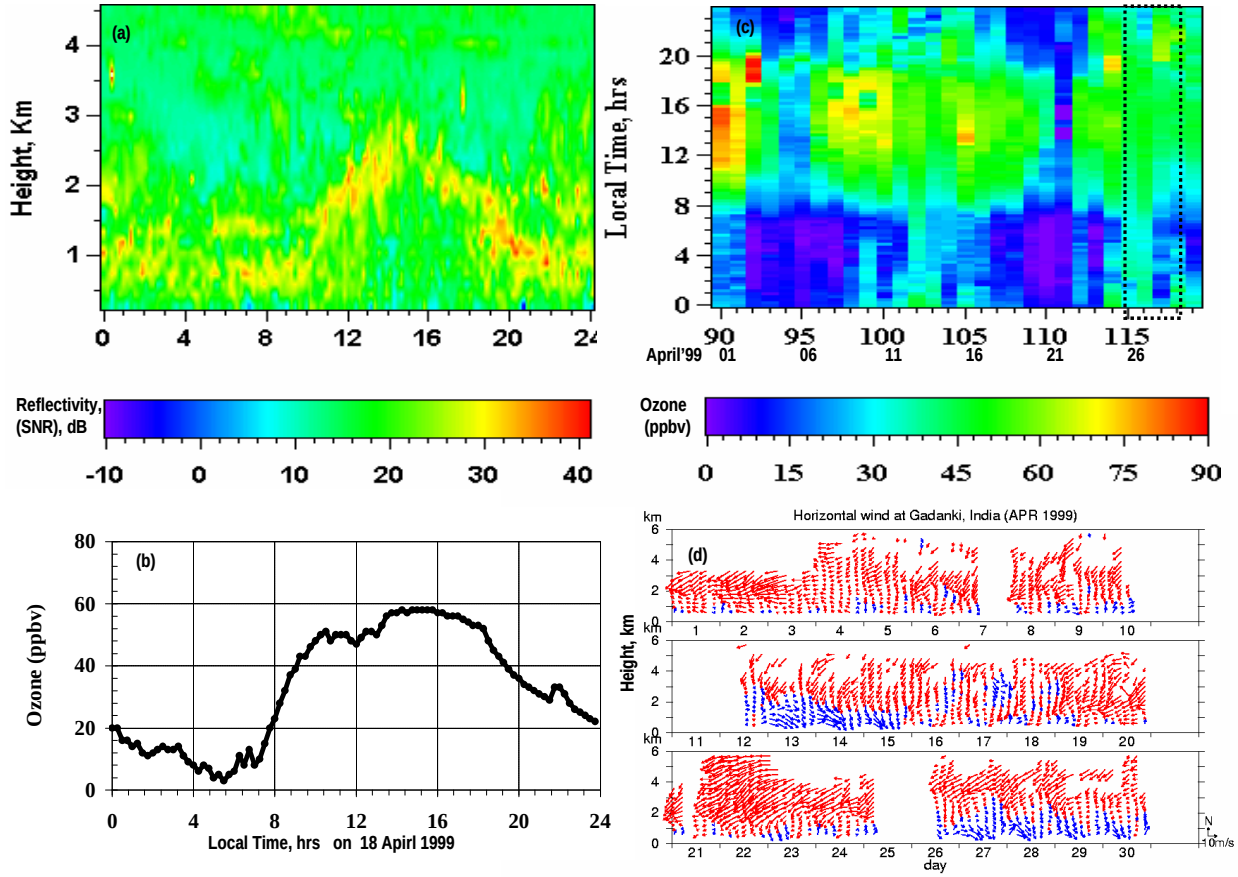

Figure 2. Time-height cross–section of the Gadanki–LAWP Reflectivity (SNR) averaged over 10 min for the vertical beam on clear, sunny day (18 April 1999). Diurnal variation of Ozone distributions at Gadanki on (b) 18 April 1999 and (c) for entire month of April 1999. (d) Zonal-meridional winds averaged every 4-h observed with the Gadanki-LAWP from 01 to 30 April 1999 during dry period.

3. Results and discussion

The LAWP observations [Figure 2(a)] show the top of CBL as a distinctive signature in a time-height plot of reflectivity. Figure 2(b) shows diurnal variations of ozone observed at Gadanki on 18 April 1999. The distribution of ozone in the CBL is irregular due to localized production zones and the dynamic processes of the region. The summer afternoon periods that are most conducive to ozone production and also periods of intense convective mixing in the CBL. Precursor gases are drawn into turbulent eddies from localized sources and from horizontally advected sources located near the top of the boundary layer or folded into the boundary layer by meteorological processes. The irregular nature of the summer afternoon ozone distribution could observed in vertical profiles and time sequences of ozone measurements. At other times of the day, the stable nocturnal boundary layer may exhibit almost constant ozone values. Ozone can be produced during the day by photo oxidation of precursor gases (Crutzen et al., 1999, and references therein). Mixing ratios of ozone start increasing gradually after sunrise, attaining maximum values during near local noontime. Figure 2(c) shows the diurnal variations of ozone observed at Gadanki from 01-30 April 1999 (DOY 90-120). Boundary layer processes and meteorology influences the ozone variability at rural site, Gadanki. Daytime production of ozone is observed throughout the month except during cloudy and rain days. At Gadanki, near to the UV analyzer, LAWP is used to obtain three dimensional wind speed measurements up to about 4000 m with a vertical resolution of 150 m, with a precision of 1 m/s for the wind speed and 10 degree for the wind direction (Reddy et al. 2002). The wind patterns are clearly dominated by the diurnal thermal regime. The daytime winds in the valley were typically from 7 to 10 m/s northeasterly wind regime which developed up to 1800 m between 08:00–09:00 LT (local time) and 19:00–20:00 LT, while the night time winds are rather weak, 1–2 m/s, blowing from the south. A Northeasterly stable wind regime could be noticed [Figure 2(d)] above 1500 m msl during one-month observations. Our results indicate that the diurnal cycle of ozone production is controlled by local thermal winds. In the nighttime, for several days (13-15 & 27-30 April 1999) high Ozone concentrations are noticed when the boundary layer winds are Westerly/northwesterly. Figure 2(c) and (d) show that important aspects of high Ozone concentration patterns are due to the local circulations and sensitive to the interaction of synoptic, regional, and local influences.

The month of April is dry period/pre-monsoon and also the beginning of summer-hot and very humid in southern India. During this period, maturation of the crops and consequent cessation of evapo-transpiration occur. No measurable rain fell during dry season; so soil moisture was probably quite low. It is an ideal situation to form the convective boundary layer at Gadanki region. The depth of the boundary layer is one of the fundamental properties that influences on fluctuating trace gases mixing ratios. The evolution of surface ozone, dynamics and the estimation of the CBL height are shown in Fig.3(a). From the figure it can be inferred that the surface averaged Ozone and CBL height are reasonably in good agreement. Fig.3 (c) and (d) one can notice that the boundary layer winds during 27-29 April 1999 were strong, a shift in wind direction in the middle of the boundary layer, discernable despite in mixing height at Gadanki after 1830 LT. The shift to westerly/southwest winds simply results in the ozone transport from nearby city (Bangalore) that is being advected towards Gadanki region.

The data collected during one-month experiment should prove useful for a wide range of modeling and analytical studies. The data are now being analyzed to obtain a detailed description and understanding of the nighttime ozone transportation from the urban region.

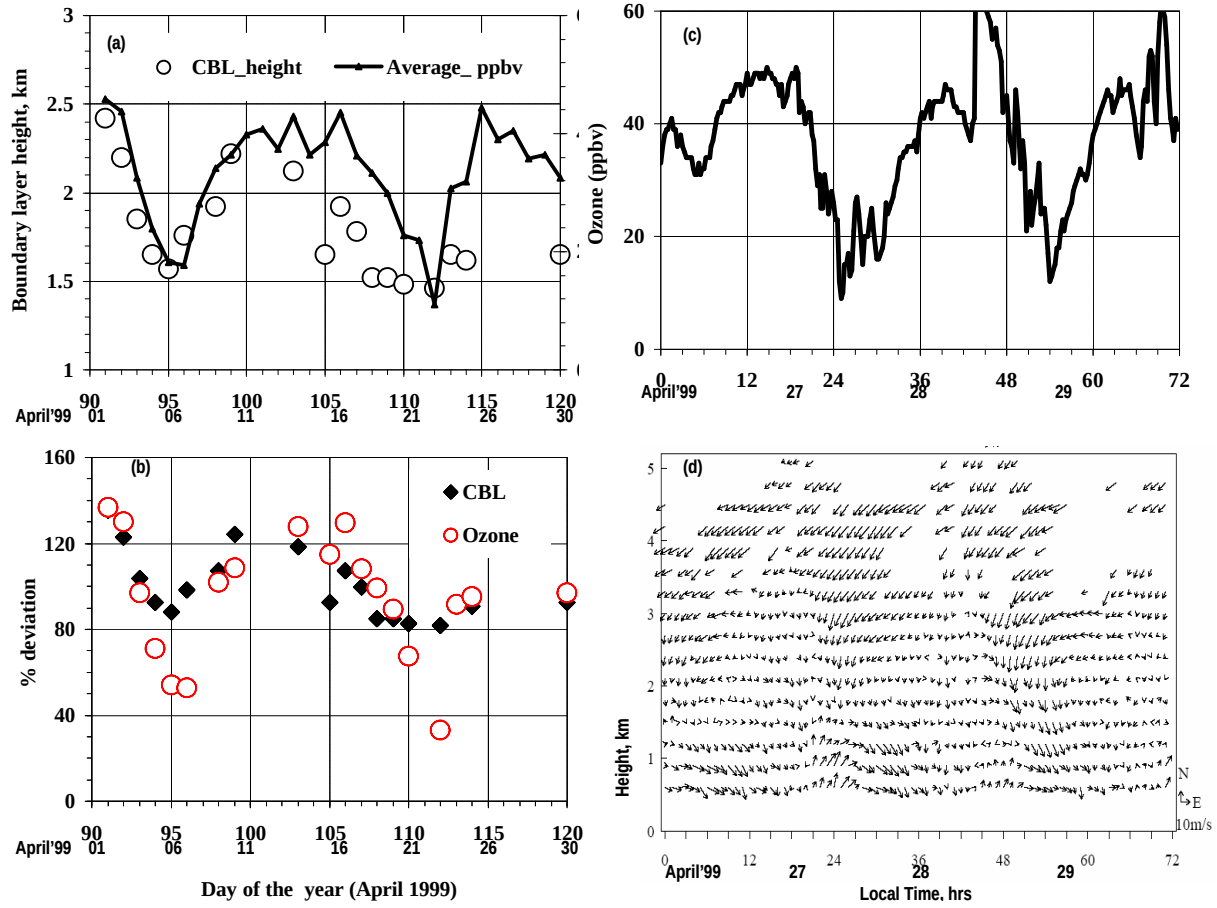

Figure 3. (a) Average convective boundary layer heights and (b) averaged surface Ozone (average over 1200-1500 hrs LT for each day) from 01-30 April 1999. (c) Diurnal variation of suface Ozone and (d) horizonal winds observed from 27-29 April 1999.

Reference

Angevine, W.M., A.B.White, C.j.Senff, M.Trainer, R.M.Banta, and M.A.Ayoub, Urban-rural contrasts in mixing height and cloudiness over Nashville in 1999, *J. Geophy. Res.*, 108, 4092, doi:10.1029/2001JD001061, 2003.

Cohn, S.A., and W.M.Angevine, Boundary layer height entrainment zone thickness measured by Lidars and Wind profiling radars, *J. Appl. Meteorol.*, 39, 1233-1247, 2000.

Crutzen, P. J., M. G. Lawrence and U. Poschl, On the background photochemistry of tropospheric ozone, *Tellus Ser. A*, 51, 123–146, 1999.

Jacob, D. J., Logan, J.A., and Murti, P.P., Effect of rising Asian emissions on surface ozone in the United States, *Geophys. Res. Lett.*, 26, 2175–2178, 1999.

Lal, S., M.Naja and B.H.Subbaraya, Seasonal variations in surface ozone and its precursors over an urban site in India, *Atmos. Environ.*, 34, 2713–2724, 2000.

Naja, M., and S. Lal, Changes in surface ozone amount and its diurnal and seasonal patterns, from 1954– 1955 to 1991– 1993, measured at Ahmedabad (23^{o} N), India, *Geophys. Res. Lett.*, 23, 81– 84, 1996.

Reddy, K.K., T.Kozu, Y.Ohno, K.Nakamura, A.Higuchi, K.M.C.Reddy, P.Srinivasulu, V.K.Anandan, A.R.Jain, P.B.Rao, R.Ranga Rao, G.Viswanthan, and D.N.Rao, Planetary boundary layer and precipitation studies using Lower atmospheric wind profiler over Tropical India, *Radio Sci.*, 37, 14, doi: 10.1029/2000RS002538, 2002.

THE SIGNATURE OF MID-LATITUDE CONVECTION OBSERVED BY MST RADAR

David A Hooper[1], Helen J Reid[2] and Ed Pavelin[3]

[1]Rutherford Appleton Laboratory, Chilton, Didcot, OX11 0QX, UK
[2]Department of Physics, University of Wales Aberystwyth, Ceredigion, SY23 3BZ, UK
[3]Department of Meteorology, University of Reading, PO Box 243, Reading. RG6 6BB, UK

Introduction

For MST radars operating at mid-latitudes, the magnitude of radial velocities observed by a vertically directed beam (henceforth referred to as vertical velocities) is typically no more than the order of 0.1 m s^{-1}. Occasional periods characterised by magnitudes of the order of 1 m s^{-1} are usually associated with mountain wave activity. Convective events are recognised to be a source of even more significant vertical velocity activity at equatorial latitudes, where the magnitudes can be of the order of 10 m s^{-1} (*Jain et al*., 2000). However, mid-latitude convection has received relatively little attention. The aim of the current study is to establish the characteristics of convection as observed by the UK Natural Environment Research Council MST radar at Aberystwyth (52.4°N). It will be shown that these are not just of scientific interest but have consequences for data reliability.

Case study of 1st March 2003

Data from the MST radar at Aberystwyth, and a co-located tipping bucket raingauge, for 1st March 2003 are shown in Figure 1. The crosses superimposed on 4 of the panels indicate the altitude of the tropopause derived from the vertical beam signal power (top panel) using an objective algorithm (*Hooper and Arvelius*, 2000). The time-altitude plot of vertical velocity (second panel) indicates that small magnitude fluctuations (< ±0.5 m s^{-1}) as functions of both time and altitude are present throughout the day; positive vertical velocities correspond to upward movement. These fluctuations are consistent with the expectation that the surface winds (not shown) of between 5 and 10 m s^{-1}, which remain approximately south-westerly throughout the day, will give rise to only weak mountain wave activity (*Prichard et al*., 1995). The fluctuations are easier to discern in the next panel which shows the time series of vertical velocity observed at an altitude of 5.1 km. The vertical velocity behaviour around 0950, 1310 and 1420 UT clearly does not fit the general pattern. It is not just the extra-ordinarily large peak values which distinguish this vertical velocity activity from that associated with mountain waves. It is the fact that the vertical velocities, at any given altitude, change much more rapidly and erratically as a function of time; there is typically little coherence between the profiles of vertical velocity from one cycle to the next (~2.5 minutes).

With respect to the Doppler Beam Swinging (DBS) technique, for a radar beam directed at an angle θ from the vertical (6° in this case) and along an azimuth ϕ, the horizontal component of velocity along the same azimuth, $v_H(\phi)$, is given by:

$$v_H(\phi) = \frac{v_R(\theta,\phi) - w\cos\theta}{\sin\theta} \qquad (1)$$

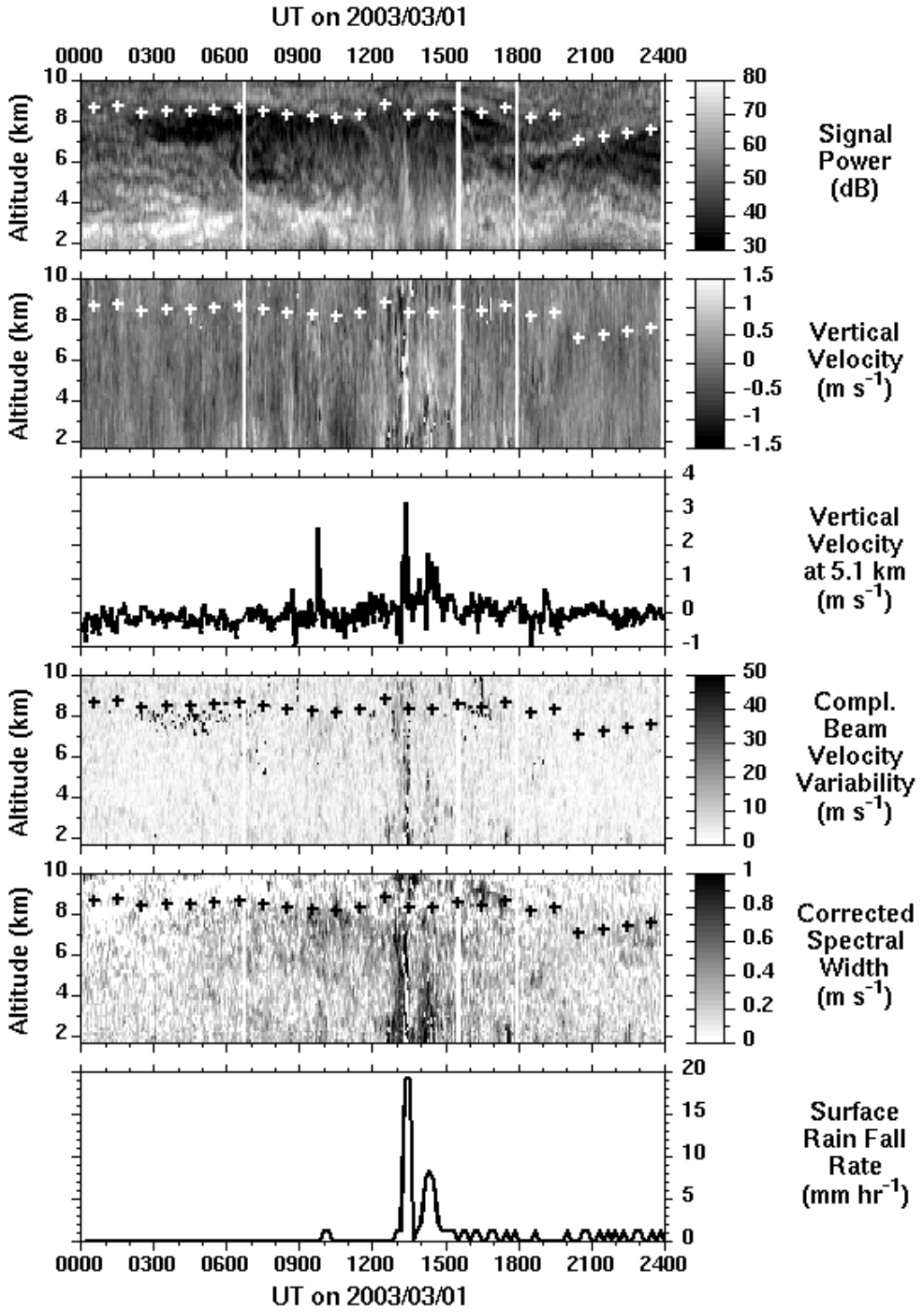

Figure 1:Data from the MST radar at Aberystwyth, and a co-located tipping bucket raingauge, for 1st March 2003.

where $v_R(\theta,\phi)$ is the radial component of velocity and w is the vertical component of velocity, which is taken as the radial velocity observed by a vertically directed beam. The DBS technique implicitly assumes that the wind vector is homogeneous across the spatial scales which separate the radar volumes for the different beam pointing directions and within the time taken to complete a single cycle of observation. The value of $v_H(\phi+180°)$, derived for the complementary off-vertical beam, is therefore expected to be equal in magnitude and opposite in sign to $v_H(\phi)$. This redundancy can be exploited by combing the two values as $0.5\times[v_H(\phi) - v_H(\phi+180°)]$ to give a better estimate of the horizontal component of velocity along ϕ and as $[v_H(\phi) + v_H(\phi+180°)]$ to give a measure of the reliability of this estimate; a small value suggest high reliability whereas a large value suggests poor reliability. The values of the complementary beam velocity variability factor shown in the fourth panel of Figure 1 represent the square root of $[v_H(\phi) + v_H(\phi+180°)]^2 + [v_H(\phi+90°) + v_H(\phi+270°)]^2$.

It can be seen that the value of the complementary beam velocity variability factor is typically small, indicating high reliability of the corresponding horizontal velocity estimates. However, it rises to several 10s of m s^{-1} within specific time-altitude regions, most clearly the one associated with the extra-ordinary vertical velocity activity around 1310 UT. This is attributed primarily to the extremely rapid fluctuations of the vertical velocity which violate the DBS assumption of constancy over the time scale for a single cycle of observation (and which could also broaden the spectral widths). Changes of a few m s^{-1} from one cycle to the next at a particular altitude are not uncommon. As can be see from Equation 1, a change of just 1 m s^{-1} in the vertical velocity has approximately the same effect on $v_R(6°,\phi)$ as a change of 10 m s^{-1} in the component of the horizontal velocity along ϕ. By contrast, the vertical velocities associated with mountain wave activity change much more slowly and they are associated with small values of the complementary beam velocity variability factor.

If attention remains confined to the event around 1310 UT, it can be seen that the extra-ordinary vertical velocity activity is accompanied by enhancements in the radar return signal power and spectral width (corrected for the effects of beam broadening) for the observations made by a vertically directed beam. Both of these signatures are consistent with the effects of moist convection transporting humid air into drier regions of the upper-troposphere and giving rise to turbulent mixing. More will be said about both of these inferences shortly. Finally, it can be seen that this event is accompanied by reasonably heavy rainfall at the surface which is again consistent with the a convective event.

The combination of the above characteristics appears to be a good indicator of the presence of convective activity and a number of events have been identified in this way. The clarity of the enhancement in vertical beam signal power depends largely on the altitude to which the convection reaches. If the maximum altitude is less than 4 km, below which the signal power signature of the humidity field is typically already strong, a convection effect can be hard to discern. In general, both the maximum altitude and the duration of convection events are quite variable; the latter can extend to many hours.

Another common characteristic at the lowest altitudes, albeit one which might not be obvious from the standard data products, is a contribution of Rayleigh scattering from hydrometeors to the radar return signals. Figure 2 shows the normalised power spectra for vertical beam observations made at 1323 UT; these 128 point spectra represent observations made over 22 s. The Power Spectral Densities, PSDs, at each range gate are normalised to the peak PSD for that gate. This is very similar to the pattern seen by *Narayana Rao et al*. (1999) for convective precipitation at a tropical location. The bold lines superimposed on Figure 2 indicate the limits of the spectral regions identified as containing signal using the standard

spectral processing. In this particular case the spectral parameters for altitudes below 4 km relate to the dominant hydrometeor return, which has a increasing downward velocity with decreasing altitude, rather than to the clear air return. Although the clear air return becomes increasingly dominant with increasing altitude in the range 4 - 5 km, the peaks are so narrowly separated that they are both encompassed in the spectral region identified as containing signal. The spectral parameters, under such circumstances, have no simple geophysical interpretation. The spectral width, in particular, will be abnormally enhanced.

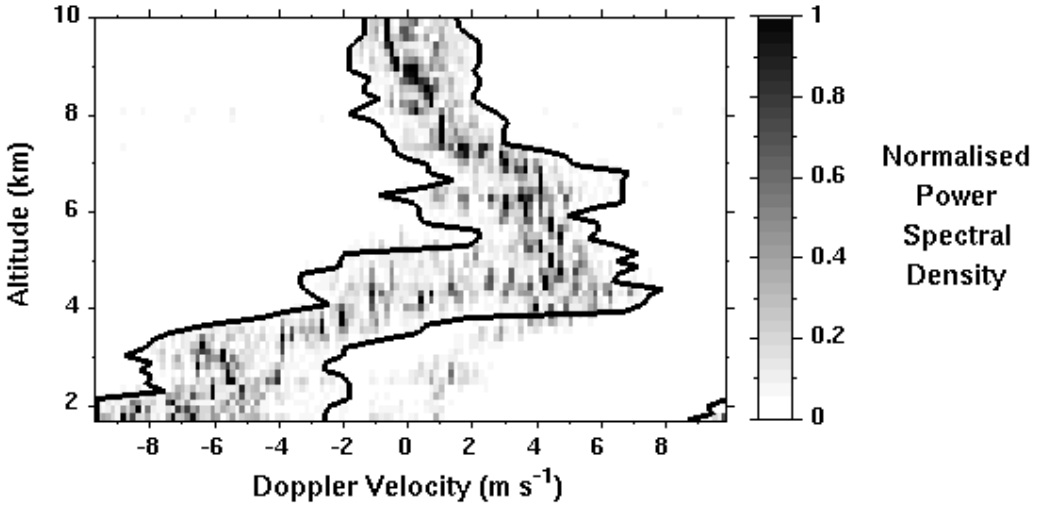

Figure 2: Normalised Doppler power spectra for vertical beam observations made at 1323 UT on 1st March 2003.

References:

Hooper, D. A., and J. Arvelius, Monitoring of the Arctic winter tropopause: A comparison of radiosonde, ozonesonde and MST radar observations, in *Proceedings of the Ninth International Workshop on Technical and Scientific Aspects of MST Radar*, 385-388, Sci. Comm. On Sol.-Terr. Phys. Secr., Boulder, Colorado, 2000.

Jain, A. R., Y. J. Rao, A. K. Patra, P. B. Rao, G. Viswanathan, and K. Subramanian, Observations of tropical convection events using Indian MST radar: first results, *Q. J. R. Meteorol. Soc., 126*, 3097-3115, 2000.

Narayana Rao, T., D. N. Rao, and S. Raghavan, Tropical precipitating systems observed with Indian MST radar, *Radio Sci., 34*, 1125-1139, 1999.

Prichard, I. T., L. Thomas, and R. M. Worthington, The characteristics of mountain waves observed by radar near the west coast of Wales, *Ann. Geophys., 13*, 757-767, 1995

PRELIMINARY OBSERVATIONS OF CONVECTIVE BOUNDARY LAYER OVER GADANKI (13.5^0N, 79.2^0E) USING UHF WIND PROFILER

K. Kishore Kumar & A.R. Jain
National MST Radar Facility, P.O.Box No. 123, Tirupati -517 502, India.

1. Introduction

The development of wind profilers has revolutionized the boundary layer studies with excellent height and temporal resolutions [*Balsley and Gage,* 1982]. Particularly, the clear air radar wind profiling technology field programs are increasingly taking advantage of continuous wind observations available from these systems. Convective Boundary Layer (CBL) height is one of the important parameters, which can be used to characterize the boundary layer. CBL height also serves as basic scaling parameter for fluxes and variances. Therefore, CBL height measurements are a part of the experiments designed to elucidate basic boundary layer structure and its behavior. One of the exciting potentials of the wind profiler is, its ability to infer the CBL height. The CBL height measurements using the wind profilers are pioneered by *white et al.* [1991]. The wind profiler observations of range-corrected signal to noise ratio can be used to infer the CBL height. The height profiles of the range corrected signal to noise ratio show a well-defined sharp peak at the CBL top. The vertical profiles of turbulence refractivity structure parameter (C_n^2) are also used for the determination of CBL height from the wind profilers. It has been proved that the C_n^2 peaks at the inversion top of a CBL [*Wyngaard and LeMone 1980; Fairall, 1991*].

Even though, considerable amount of work has been reported on CBL, so far there is no work relating the evolution of CBL and convection triggering. In this regard, the present study aims to closely monitor the evolution of CBL prior to convection triggering using UHF wind profiler observations during pre-monsoon and monsoon periods. In particular, this study was carried out to understand the pre-convective environments in the boundary layer during the pre-monsoon and monsoon periods to find out whether there is any precursor before the convection triggering.

2. Experimental set up

A convection campaign was carried out during May-August, 1999 employing VHF and UHF radars at National MST radar facility, Gadanki, India to explore the tropical Mesoscale Convective Systems. UHF wind profiler, installed at Gadanki for boundary layer studies [*Krishna Reddy et al.,* 2001], was operated to study the pre-convective environments during the campaign period. UHF wind profiler was operated continuously round the clock to monitor the boundary layer dynamics. For the present study, three dimensional wind fields and CBL heights are estimated from the UHF wind profiler observations. During the campaign, from 19 July 1999 to 14 August 1999, radiosonde observations were carried out along with the wind profiler observations. During this period, everyday, a radiosonde was released from the radar site at 1630 LT (LT=UTC+0530). A ground-based collocated optical rain gauge was also used for the precipitation measurements during the campaign.

3. Results and discussion

In the present study, the CBL height is estimated from the wind profiler observations to monitor the evolution of CBL. For the present study, height profile of C_n^2 has been used to retrieve the CBL height. Figure 1 shows the height–time sections of radar reflectivity (in terms of Signal to Noise Ratio (SNR)) on two typical days. Figure 1 shows the potential of the wind profiler to identify the CBL top. A well distinguishable elevated layer of enhanced reflectivity corresponding to the CBL top can be seen from this figure. However, for the present study, height profiles of C_n^2 are calculated for every 10 minutes and height at which C_n^2 peaks is noted. Median of these heights over one hour period has been taken as CBL height for that hour. Figure 2 shows the height profile of virtual potential temperature derived from the radiosonde observations and corresponding C_n^2 profile from the wind profiler observations. These profiles are obtained from the observations made at 1630 LT on 27th July 1999 during the campaign period. A sharp gradient in the virtual potential temperature at 2.7 km corresponding to CBL top can be seen from this profile. The height profiles of C_n^2 shows a well-defined peak at 2.55 km, which corresponds to the CBL top. Thus, these two independent measurements of CBL top are in reasonable agreement. However, the turbulent fluctuations in the CBL height of the order of ± 200 m is expected as reported by *Davis et al.* [1997] based on lidar observations of CBL. The comparison between the measurements of CBL height made by the wind profiler and from the radiosonde data during the campaign period is shown in figure 3. The good agreement demonstrates that the CBL height can be found accurately from the wind profiler C_n^2 measurements.

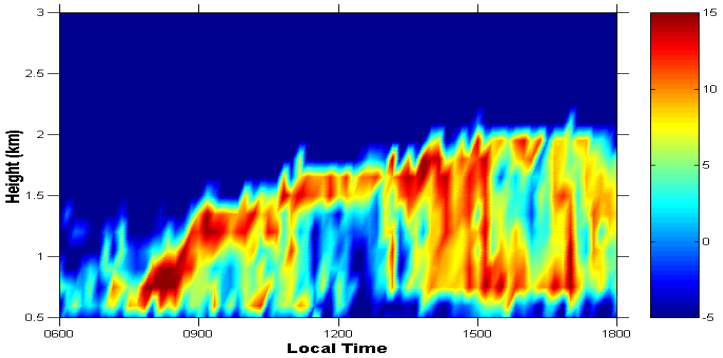

Figure 1: Height-Time section of signal to noise ratio (dB) as observed on 18 March 1999

The present observations are categorized as non-precipitating, pre-monsoon convective and monsoon convective days. Here convective day implies that the precipitation has taken place during that day, which is subjective. Figure 4 (a) shows the evolution of CBL on four non-precipitating days. This plot readily reveals that on all these days a shallow CBL is forming at morning 0800 hrs and afterwards, the CBL grows steadily and reaching its peak at 1200-1300 hrs and coming down thereafter. The interesting feature observed on these days is that the CBL is coming down to the lower heights drastically after 1200-1300 hrs. This happens when buoyancy flux at the surface decreases rapidly which in turn results in poor surface forcing and the shallow CBL. Similar results were reported by *Grimsdell and Angevine* [2002]. Figure 4(b) shows the evolution of CBL on four pre-monsoon convective days. On these days, in the morning hours, the CBL shows more or less similar features like the non-precipitating days.

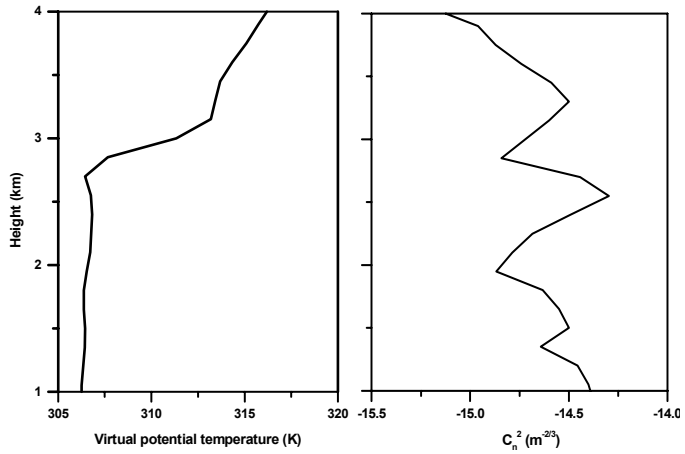

Figure2: Height profiles of Virtual potential temperature and C_n^2 as observed on 27 July1999.

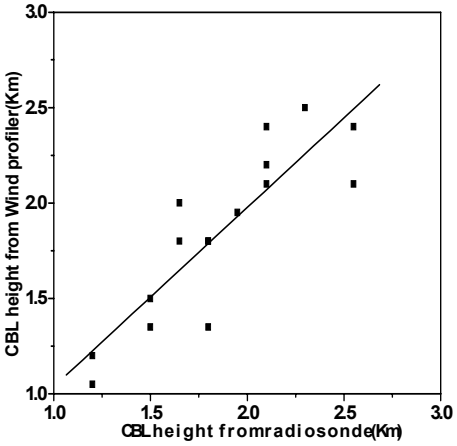

Figure 3: Scatter plot of CBL heights derived from the radiosonde and the wind profiler observations.

The striking feature in the present case is that the CBL is continuously growing after 1200 hrs also. The CBL heights are also very high with an increasing trend up to 1500 hrs, after which precipitation was observed over the wind profiler site. The deepening of the CBL is observed in the late afternoon in the present case, whereas it is observed exactly at the midday on the non-convective days. Figure 4 (c) shows the evolution of CBL on four convective days during the monsoon period. On these days, a different picture has been observed. A shallow CBL confined to ~1.5 km is observed on all the days. It is well known that during the monsoon, boundary layer will be rich in moisture. So, most of the radiation from the surface will be utilized for the evaporation process, which results in a shallow CBL. Enhanced soil moisture probably contributes to increase the latent heat fluxes and thus decreasing the surface sensible flux locally and suppress the CBL growth, as compared to the deeper CBL that develops with reduced soil moisture level on pre-monsoon days. One more cause for the shallow CBLs during the monsoon days may be due to the increased upper level clouds that can reduce the incoming solar radiation. Similar features have been observed on most of the days in each category during the campaign period.

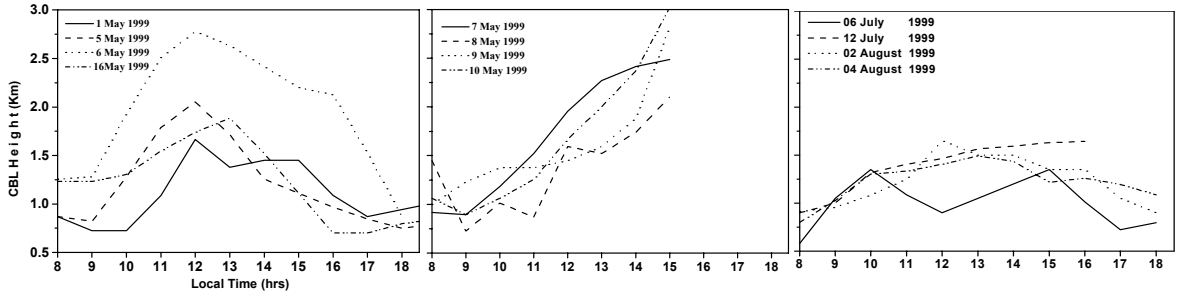

(a) (b) (c)

Figure 4: Evolution of CBL on four (a) non-precipitating days, (b) pre-monsoon convective days and (c) monsoon convective days

4. Summary

An attempt has been made to study the evolution of the CBL in non-precipitating, pre-monsoon and monsoon convective days. A well-distinguishable feature is observed in the pre-convective environments, which can be used as precursor for the convection triggering. In the non-precipitating environments, the CBL has peaked in the mid-day and suddenly descended to lower altitudes and showed decreasing trend thereafter. In the pre-monsoon convective environments, the CBL has continued to grow after mid-day also and shallow CBL has been observed during the monsoon convective days. The intriguing result from these studies is the distinguishable CBL evolution observed in the pre-convective environments of pre-monsoon and monsoon periods. These observations are preliminary in nature and a detailed study using various boundary layer observational facilities like automatic weather station, kytoons and radiation measurements are planed in near future.

Acknowledgements

The National MST Radar Facility (NMRF) is operated as an autonomous facility under Department of Space with partial support from Council of Scientific and Industrial Research. The authors are grateful to the NMRF technical staff whose dedicated efforts made possible the observations reported here. UHF radar setup and being operated at NMRF under joint collaborate programme between India and Japan.

References

Balsley, B.B., and K.S. Gage, on the use of radars for operational wind profiling, *Bull. Amer. Meteorol. Soc.* 63, 1009-1018, 1982.

Davis, K.J., D.H. Lenschow, S.P. Oncley, C. Kiemle, G. Ehret, A. Giez, and J. Mann, Role of entrainment in surface-atmosphere interactions over the boreal forest, *J. Geophys. Res,* 102, 29219–29230, 1997.

Fairall, C.W., The Humidity and Temperature sensitivity of clear-air radars for the cloud free convective boundary layer, *J. Appl. Meteorol*. 8, 1064-1074, 1991.

Grimsdell, A.W., and W.M Angevine, Observations of the afternoon transition of the convective boundary layer, *J. Appl. Meteorol.,* 41, 3-11, 2002.

Krishna Reddy, K., Kozu, T., Ohno, Y., Nakamura, K., Srinivasulu, P., Anandan, V. K., Jain, A.R., Rao, P.B., Ranga Rao, R., Viswanathan, G., and Rao, D.N., Lower atmospheric wind profiler at Gadanki, Tropical India: initial result, Meterologische *Zeitschrift,* 10, 457-466, 2001.

White, A.B., Fairall, C.W., and Thompson, D.W., radar observations of humidity variability in and above the marine atmospheric boundary layer, *J. Atmos. Oceanic. Technol.*, 8, 639-658, 1991a.

Wyngaard, J.C., and M.A. LeMone, Behavior of the refractive index structure parameter in the entraining convective boundary layer, *J. Atmos. Sci*., 37,1573-1585, 1980.

STUDIES ON MOMENTUM FLUXES USING MST RADAR WINDS OBSERVED AT GADANKI (13.5°N, 79.2° E), INDIA

D. Narayana Rao[1], I.V. Subba Reddy[2], P. Kishore[3], S.P. Namboothiri[3], K. Igarashi[3], K. Krishna Reddy[4] and S.V. Bhaskara Rao[3].

[1]National MST Radar Facility, P.B. No.: 123, Tirupati – 517 502, India
[2]Department of Physics, Sri Venkateswara University, Tirupati - 517 502, India
[3]Communications Research Laboratory, 4-2-1 Nukui-kita machi, Kognei-shi Tokyo 184-8795, Japan
[4]Yokohama Institute of Earth Sciences, Frontier Observational Research System for Global Change (FORSGC), 3173-25, Showa-Machi, Kanazawa – KU, Yokohama, Kanagawa – 236-0001, Japan

ABSTRACT

VHF Doppler radars provide a unique database to estimate vertical flux of horizontal momentum in the troposphere and lower stratosphere. Estimation of the oblique momentum flux involves two methods: 1) using three beams – one vertical and two oblique, and 2) using four beams – two pairs of oblique beams systematically offset from the vertical. The rapid steerability of the Indian MST radar allows to make three – and four beam measurements simultaneously. The momentum fluxes measured by the two methods are almost the same for wind fluctuations in a fairly long period range (longer than 5 h). We choose frequency bands corresponding to periods of 30 min-2h, 2-8 h, 2-16h and 2-24 h. Vertical profiles of the zonal and Meridional flux in each frequency band were found to be consistent, in general, with the total flux. Zonal fluxes were small at lower levels and increasingly negative (westward) at higher heights. The dominant contributions to the Meridional flux occur in the lower-frequency band.

Introduction

The importance of gravity wave effects on various dynamical processes has been well documented in the upper and middle atmosphere. However, less is known about these waves in the the lower atmosphere especially in tropics. The upward propagating gravity waves transport energy and momentum in different regions of the atmosphere along with their propagation to produce effects at upper heights [Hines, 1972] indicated that the influence of such waves at upper heights might be significant. Most of the theoretical and modeling studies were primarily concentrated on the effect of gravity waves in the mesosphere and thermosphere, but later it has been found that these effects are also important in the troposphere and stratosphere. In early observations it is identified that for lower heights, the momentum divergence caused by mountain waves [Newton, 1971], and the importance of such divergence in the evolution of the general circulation was emphasized by Lilly [1972]. Furthermore, the lack of height coverage at a given time in aircraft flights is a limitation. Vincent and Reid (1983) presented a technique in which ground-based radars can be used to measure fluxes directly and this technique has been applied to both mesospheric heights [Vincent and Fritts, 1987; Tsuda et al., 1990] and tropospheric and lower stratospheric levels [Fritts et al., 1990; Thomas et al ., 1992]. Because of the continuous operation of multiple instruments, long term studies have been conducted to quantify the variability and latitudinal difference of gravity wave activity [e.g. Vincent and Fritts, 1987; Manson and Meek, 1993; Vincent, 1994]. It has been found that from theoretical and observational studies that the high frequency gravity waves with small horizontal scales are the majority carriers of momentum. ~70 % of the momentum and the associated zonal drag is due to gravity waves with observed periods less than one hour [Fritts and Vincent, 1987]. Chang et al., [1997] used ST radar data from Christmas Island to study tropospheric gravity waves and they found a broad range of frequency associated with gravity wave activity in the troposphere. A method of Vincent and Reid [1983] is used to estimate the vertical flux of zonal and meridional momentum fluxes from the radial velocities in two orthogonal beams measured by the Indian MST Radar at Gadanki (13.48º N, 79.18º E) is presented. These flux values are quite well with the values obtained from previous observations.

The purpose of this study is to examine Zonal and Meridional fluxes and their variation with both height and wave periods, and also to compare fluxes for three and four beam methods.

Data Base

In the present study a VHF Radar at Gadanki (13.48º N, 79.18º E) a tropical station is used to study the gravity wave momentum fluxes in different seasons namely Pre Monsoon (March - May), Monsoon (June - September), Post Monsoon (October - November) and Winter (December-February) seasons. Data is collected continuously for three days in a typical month representing as a season at 1000 -1600 LT, 2000 – 2030 LT, 0030 – 0100 LT, and 0500 – 0530 LT on each day. The observations are taken during 16-19 October 2000, 09-12 April 2001, 16-19 July 2001, 22-25 January 2002.

Results and Discussions

In Figure 1 upper panel shows mean zonal and meridional momentum flux and variance of wind fluctuations around the mean values during post monsoon season using MST Radar. The averaging is made for 3 days i.e.,16- 18 October 2000, for the entire observational period i.e., from 1000-1600 LT in each day. Lower panel is the same as above during 09-11 April 2001 represented as during pre monsoon season. All quantities except vertical wind variance are obtained by the four beam methods. The positive values of Zonal momentum fluxes indicate Eastward transport of momentum and negative values of Zonal momentum fluxes show westward transport of momentum. Zonal momentum flux was eastward from 5.5-12.5 km, westward from 12.5-15.5 km. eastward from 15.5 – 18 km and westward above 18 km. This represents that there is a systematic change in the zonal momentum flux. While going to higher altitudes the magnitude of the zonal momentum flux is increasing either eastward or westward, this represents that the waves are assumed to be generated in the lower part of the atmosphere and upward propagating waves are dominating and westward momentum fluxes are maximum ~ -0.6 m^2/s^2. The positive values of meridional momentum fluxes indicate northward transport of momentum and negative values show southward transport of momentum. During post monsoon season meridional momentum flux is northward from 5 km to 20 km altitude (+0.4 m^2/s^2). The zonal variance is more than the meridional variance in the altitude range of 12-17.5 km. The lower panel in figure 1 (during pre monsoon season) shows east ward momentum flux (+0.6 m^2/s^2) which is dominating rather than the westward momentum flux (-0.45 m^2/s^2). The meridional momentum flux is southward and its value is maximum (-6.5 m^2/s^2) around 11-12 km. In the lower heights up to 10 km the zonal and meridional variances are small and above 10 km the variances are large.

Figure 2 is similar as figure 1 but for monsoon season (upper panel) and winter season (lower panel). In upper panel zonal momentum flux is almost westward, indicating that the west ward fluctuations are more rather than the eastward. The meridional momentum flux is southward up to 7 km, 7- 8.5 km northward, 8.5 - 14.5 km southward and above 14.5 km it is northward. The zonal and meridional variances are small up to 12 km and above 12 km these variances are increasing with increasing height. Lower panel in figure 2 shows east ward momentum flux up to 7 km from 7-11.3 km westward and above 11.3 km it is eastward. The meridional momentum flux is northward up to 11 km, southward 11-13 km, northward from 13 – 17 km and southward from 17-19.5 km. Zonal and meridional variances are high above 13 km indicating that the wave activity is more prominent.

Figure 3 shows zonal and meridional momentum flux, calculated using four beam and three beam method during different seasons. Three and four beam method calculated zonal and meridional momentum fluxes agree within error bars both in magnitude and trend. During monsoon season some discrepancy has been observed above 16 km. This may lead to anisotropy of the backscatters in the atmosphere. During pre monsoon season some discrepancy has been observed below 10 km in meridional momentum flux.

Figure 4 shows vertical profiles of zonal and meridional momentum flux profiles determined by the four- beam method with different frequency bands in different seasons viz., pre-

monsoon, monsoon, post monsoon and winter. The momentum flux for short - period motions during 16-18 October 2000 shows direction towards north for meridional momentum flux and east ward direction for zonal momentum flux. For longer-period motions meridional momentum flux is towards north and zonal momentum flux is towards east except in the altitude range of 11-15 km for all the frequency bands. Especially in the lower stratosphere, both long and short-period motions are towards north and east ward directions. During 09-11 April 2001 zonal momentum flux is towards westward in the troposphere and lower stratosphere except in the altitude range of ~ 15-16.5 km for both short and long-period motions (figure not shown). Meridional momentum flux is towards southward in the troposphere and lower stratosphere for both short and long-period motions. During 17-19 July 2001 zonal momentum flux of short and long-period motions is towards westward, meridional momentum flux is towards northward in the altitude range of ~13-16.7km for both short and long-period motions(figure not shown). During 22-24 January 2002 zonal momentum flux of short and long - period motions are towards east in the altitude range of 11-19 km, meridional momentum fluxes are towards south in the altitude range of ~11-19km for both short and long-period motions (figure not shown).

Conclusions

The excitation source of the short period gravity waves was suggested to be located near the peak of the mean zonal wind. The vertical flux of zonal momentum for waves with periods of 2-24 hours showed westward bias in the 14-17 km. while the zonal flux showed no significant seasonal cycle in the middle troposphere implying that the upward propagating gravity waves in the lower stratosphere mostly travelled westward relative to the background wind. The long period gravity waves which caused these wind fluctuations were generated in the lower troposphere, the observed results suggest that the horizontal propagation of gravity waves is azimuthally isotropic near the wave source and the eastward travelling waves seem to be filtered out during their upward propagation, which might result in the observed westward bias of momentum flux. The overall results suggest that, due to their persistent southward direction of propagation, long-period waves make a contribution to the momentum flux in the lower stratosphere which is comparable to that of short-period waves.

Acknowledgements

The Authors are thankful to National MST Radar Facility (NMRF), Gadanki for providing MST Radar data during the campaign period and UGC-SVU center for MST Radar Applications, S. V. University, Tirupati for providing necessary facilities for carrying out the studies. One of the authors (I. V. Subba Reddy) is thankful to Advanced Centre for Atmospheric Sciences and CSIR for providing Junior Research Fellowship and Senior Research Fellowship respectively.

References

Chang, J.L., S. K. Avery, A. C. Riddle, First results of tropospheric gravity wave momentum flux measurements over Christmas Island, Radio Sci., Vol. 32, No. 2, 727-748, 1997.

Fritts, D. C., T. Tsuda, T. E. Vanzandt, S. A. Smith, T. Sato, S. Fukao, S. Kato, Studies of velocity fluctuations in the lower atmosphere using the MU radar. Part II. Momentum fluxes and energy densities, J. Atmos. Sci., 47, 51-66, 1990.

Fukao, S., T. Sato, T. Tsuda, S. Kato, M. Inaba, I. Kiruna, VHF Doppler radar determination of the momentum flux in the upper troposphere and lower stratosphere: comparison between the three-and four-beam methods, J. Atmos. Oceanic Technol., 5, 57-69, 1988.

Hines, C. O., Momentum deposition by atmospheric waves, and its effects on thermospheric circulation, Space Res., 12, 1157-1161, 1972.

Lilly, D. K., Wave momentum flux- G.A.R.P. problem, Bull. Am. Meteorol. Soc., 53, 17-23,1972.

Manson, A. H., C. E. Meek, Characteristic of gravity waves (10 min-6 hours) at Saskatoon (52^0N,107^0 E): observations by the phase coherent medium frequency radar, J. Geophys. Res., 98, 20,357-20,367, 1993.

Newton, C. W., Mountain torques in the global angular momentum balance, J. Atmos. Sci., 28, 623-628, 1971.

Thomas, I., I. T. Prichard, I. Astin, Radar observations of an inertia-gravity wave in the troposphere and lower stratosphere, Ann. Geophysicae, 10, 690-697, 1992.

Vincent, R. A., D. C. Fritts, A morphology of gravity waves in the mesosphere and lower thermosphere over Adelaide. Australia, J. Atmos. Sci., 44, 748-760, 1987.

Vincent, R. A., I. M. Reid, HF Doppler measurements of mesospheric gravity wave momentum fluxes, J. Atmos. Sci., 40, 1321-1333, 1983.

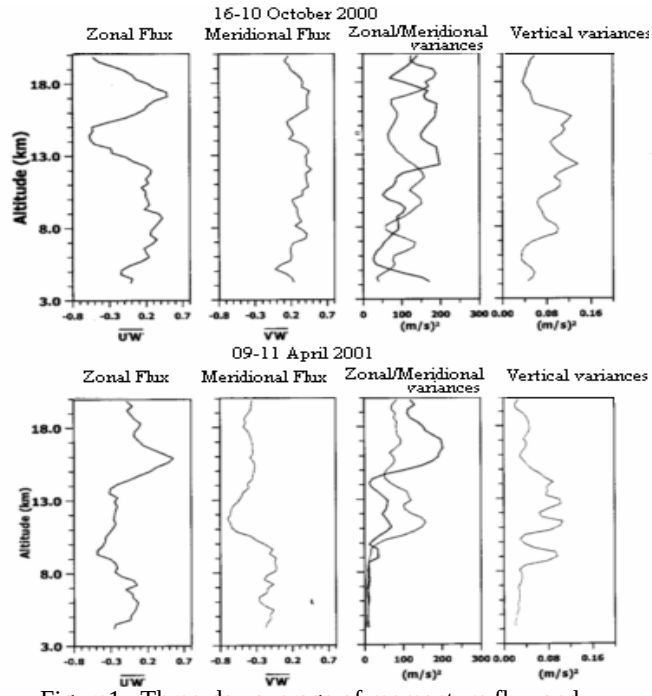

Figure1. Three-day average of momentum flux and variance of wind fluctuations determined from the MST radar data during 1000-1600 LT from 16-18 October 2000 (upper panel), 09-11 April 2001 (Lower panel). Thick and thin solid lines in third panel of both the lower and upper part shows the zonal and meridional variances respectively

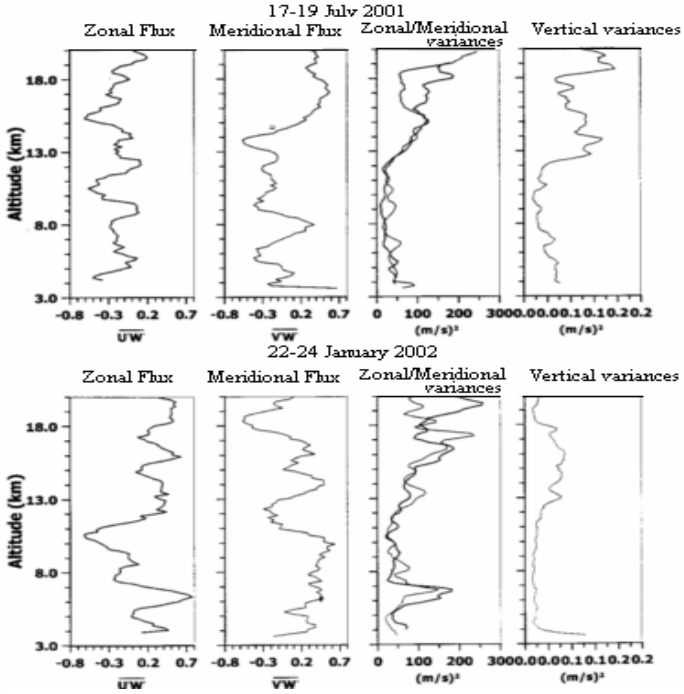

Figure 2. Same as figure 1 but for 17-19 July 2001 (Upper panel) and 22-24 January 2002 (Lower panel)

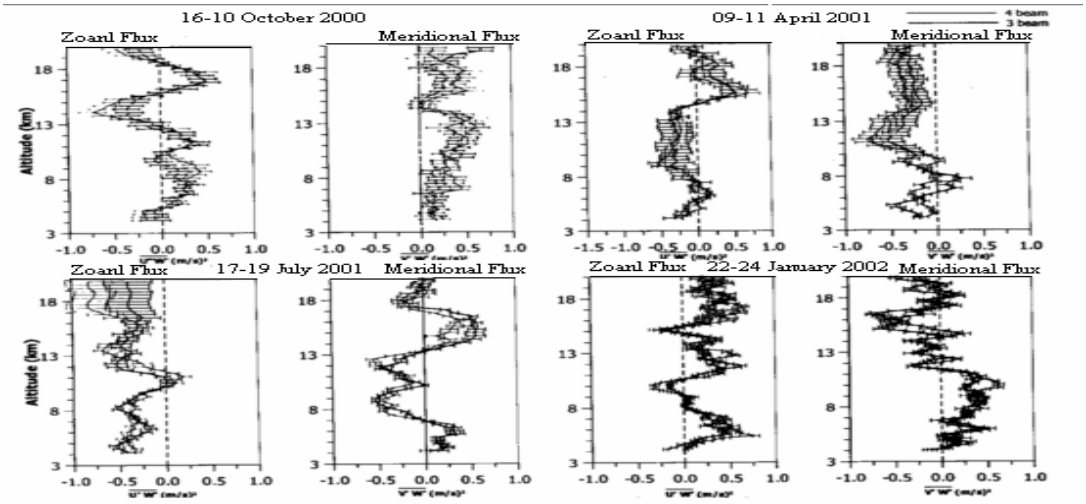

Figure 3. Momentum flux vertical profiles are determined by the four-beam and three-beam method using Indian MST radar winds

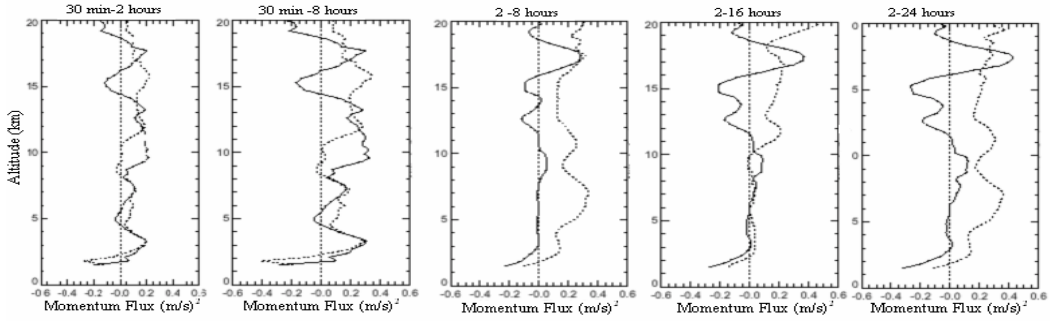

Figure 4. Vertical profiles of zonal and meridional momentum flux determined by the four beam method for different frequency bands during 16-19 October 2000. The solid line represents zonal momentum flux and dotted line represents meridional momentum flux

ESTIMATION OF THE TROPOPAUSE HEIGHT USING THE VERTICAL ECHO PEAK AND ASPECT SENSITIVITY CHARACTERISTICS OF A VHF RADAR

Bok-Haeng Heo[1], Kyung-Eak Kim[2], Bernard Campistron[3] and Vladislav Klaus[4]

[1]Observation Division, Korea Meteorological Administration, Korea
[2]Department of Astronomy and Atmospheric Sciences, Kyungpook National University, Korea
[3]Laboratoire d'Aerologie(CNRS), Observatoire Midi-Pyrenees, Université Paul Sabatier, France
[4]Meteo-France, Laboratoire d'Aerologie (CNRS), France

1. Introduction

Enhancement of the vertical echo power of VHF radars often occurs at or above the tropopause height (Gage and Green, 1978; Röttger and Liu, 1978; Green and Gage, 1980; Balsley and Gage, 1981; Gage *et al*., 1981). The characteristic of vertical echo peaks has been used to estimate the tropopause. The methods used for the tropopause estimation are specular reflection method (Gage and Green, 1978; Röttger and Liu, 1978; Gage and Green, 1979), Zachs method (Westwater *et al*., 1983), maximum echo power method (Vaughan *et al*., 1995) and maximum echo power gradient method (Vaughan *et al*., 1995).

The previous methods require to set up a limit of estimated height interval and are not very efficient in estimating the tropopause height when there were more than two peaks due to cloud layer, precipitation layer, or inversion layer in the profile of vertical echo power (Green and Gage, 1980).

In the present study a new improved method for estimating the tropopause height using VHF radar data was suggested. The method was evaluated by comparing between the tropopause heights determined from rawinsonde data and radar data.

2. Data and instrumentation

The data used in the present study were from two sources: VHF radar observation and rawinsonde data. The VHF radar observation was performed at La Ferté Vidame VHF radar observatory (0.88°E, 48.62°N) during the period from 0000 UTC 6 to 2400 UTC 9 February 1998. The main characteristics of this profiler radar were a 52-MHz transmitted frequency, with a 18-kW peak pulse power, an a 1,000-m pulse length. The profiler used five beam positions - one vertical and four oblique - with a one-way half-power aperture of 6.5°. The oblique beams, with an off-zenith angle of 11.5°, were disposed every 90° in azimuth.

The rawinsonde observations were performed two times a day(0000 and 1200 UTC) at Trappes upper-air observatory (2.02°E, 48.77°N).

3. The improved method to estimate tropopause height from VHF radar data

The proposed method employs aspect sensitivity characteristics to distinguish the reflection echo layer due to the tropopause from other peak echo layers, and estimated the tropopause height without a limit of estimated height interval. The algorithm follows five steps to find a layer of strongest aspect sensitivity from vertical and oblique echo profiles and then to determine the tropopause height using maximum echo power gradient method (Fig. 1).

Step 1: Differences between vertical and oblique echo powers (SNR_V-SNR_O) are calculated every range gate.

Step 2: Positive SNR_V-SNR_O value are integrated and the maximum positive layer is determined as a layer of strongest aspect sensitivity.

Step 3: The height of maximum vertical echo power in the layer is determined as H_{Pmax}.

Step 4: The height of the first minimum value in the vertical echo power profile below H_{Pmax} is denoted H_{Pmin}, provided the power P_{max}-P_{min1} > 6 dB.

Step 5: The height of the maximum vertical echo power gradient between H_{Pmax} and H_{Pmin} is determined as tropopause height TP_{asp}.

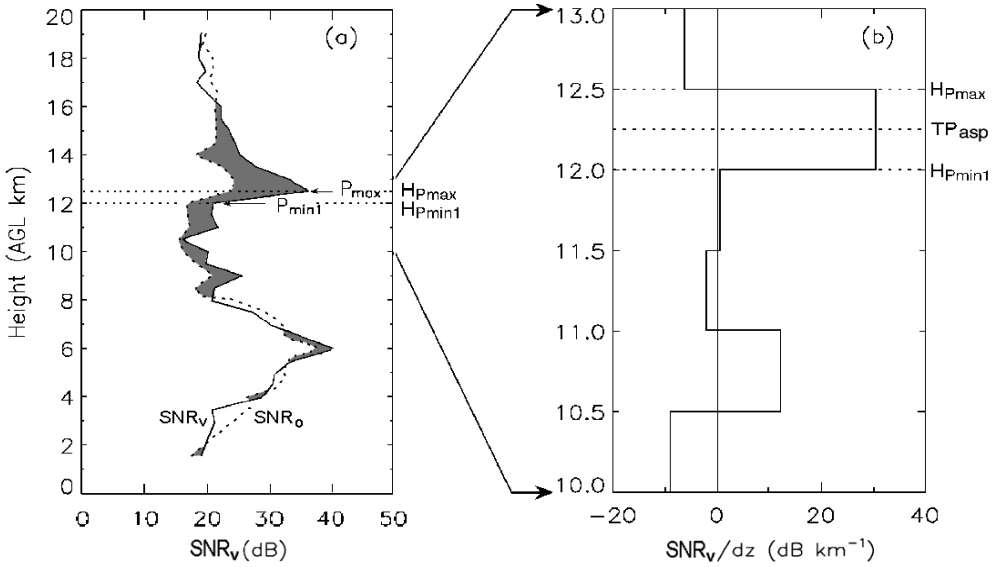

Fig. 1. Schematic depiction of tropopause height estimation from vertical echo profile (SNR_V) of VHF radar by the improved method. (a) Determination of a layer of strongest aspect sensitivity and peak heights H_{Pmax} from vertical echo profile. (b) Determination of TP_{asp} from vertical gradient of vertical echo profile.

4. Comparison between tropopause heights estimated from rawinsonde data and VHF radar data

The tropopause heights estimated by the improved method are shown in Fig. 2a. According to the power ratio of vertical to oblique echo powers (not shown) and rawinsonde data, there were no layers of strong aspect sensitivity due to tropopause until 1800 UTC 6, but appeared at about 10 km and maintained its heights between 10 and 14 km. The tropopause started to descend at

0600 UTC 7 and reached approximately 5 km at 2100 UTC 7. A new tropopause appeared between 11 and 12 km and maintained its height at about 12 to 13 km and until 1800 UTC 7.

The improved method correctly estimated the tropopause heights not only when there were more than two strong inversion layers due to a tropopause folding between 0600 UTC and 1500 UTC 7 but also when there were strong echo peaks due to cloud or precipitation layer below 7 km until 0600 UTC 9. The results of the tropopause height derived from the modified method agreed well with the rawinsonde-estimated tropopause heights and also provide reasonable structure during an event of tropopause folding. This method also gives a good resolution for tropopause height detection.

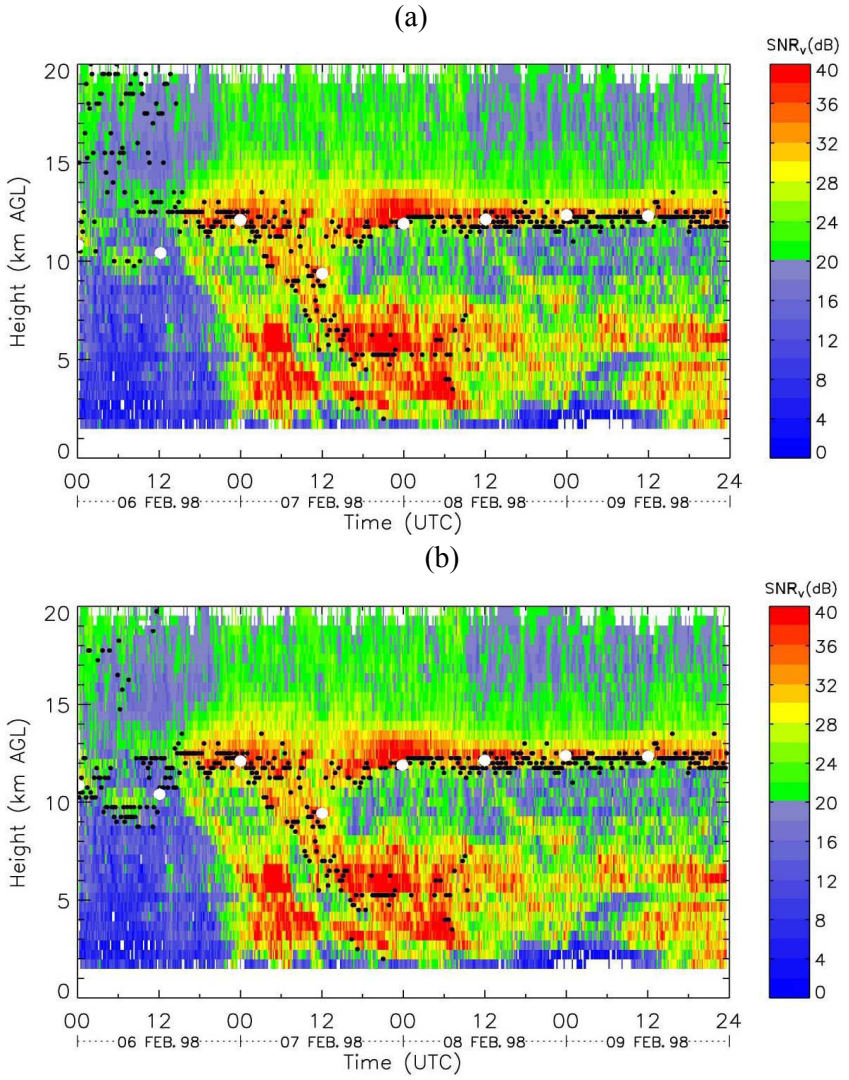

Fig. 2. Time-height cross sections of vertical echo power (SNR_V) and the tropopause heights (black dots) estimated by (a) the improved method and (b) the method combined maximum echo power gradient method and the improved method when there is no limit of estimated height interval. White dots represent tropopause heights determined from rawinsonde observation.

But in case of period until 1800 UTC 6 of Fig. 2a, the method erroneously estimated tropopause heights between approximately 9.5 and 20 km. To improve this disadvantage, the method combined maximum echo power gradient method was introduced. The maximum echo power method without limit of estimated height applied in case that the power ratio of vertical to oblique echo power was less than 6 dB.

The tropopause heights estimated by the method combined maximum echo power gradient method are shown in Fig. 2b. The combined method also correctly estimated the tropopause height not only when there were more than two strong inversion layers due to a tropopause but also when there were more than two strong inversion layers due to a tropopause folding.

5. Conclusions

In the present study, an improved method for estimating the tropopause height using VHF radar data was suggested and evaluated by applying to time series of a VHF radar data.

The proposed method employed aspect sensitivity characteristics to distinguish the reflection echo layer due to the tropopause from other peak echo layers, and estimated the tropopause height without limit of estimated height interval.

The tropopause heights estimated by the method when temperature lapse rate above tropopause height was more than 6 °Ckm^{-1} and the tropopause sharpness was classified into intermediate or definite type. The improved method estimated reliably the tropopause height when there were more than two peaks due to cloud layer, precipitation layer, or inversion layer in the profile of vertical echo power. Therefore, the method is very useful to estimating tropopause height when tropopause breaks and slopes during the stratospheric and tropopause exchange.

References

Balsley, B. B., and K. S. Gage, On the vertical incidence VHF backscattered power profile from the stratosphere, *Geophys. Res. Lett.*, *8*, 1173-1175, 1981.

Gage, K. S., B. B. Balsley, and J. L. Green, A Fresnel scattering model for the specular echoes observed by VHF radar, *Radio Sci*., *16*, 1447-1453, 1981.

Gage, K. S., and J. L. Green, Evidence for specular reflection from monostatic VHF radar observations of the stratosphere, *Radio Sci*., *13*, 991-1001, 1978.

Gage, K. S., and J. L. Green, Tropopause detection by partial specular reflection using VHF radar, *Science*, *203*, 1238-1240. 1979.

Green, J. L., and K. S. Gage, Observations of stable layers in the troposphere and stratosphere using VHF radar, *Radio Sci*., *15*, 395-406, 1980.

Röttger, J., and C. H. Liu, Partial reflection and scattering of VHF radar signals from the clear atmosphere, *Geophys. Res. Lett.*, *5*, 357-360, 1978.

Vaughan, G., A. Howells, and J. D. Price, Use of MST radars to probe the mesoscale structure of the tropopause*, Tellus, 47A*, 759-765, 1995.

Westwater, E. R., M. T. Decker, A. Zachs, and K. S. Gage, Ground-based remote sensing of temperature profiles by a combination of microwave radiometry and radar, *J. Climate Appl. Meteor., 22*, 126-133, 1983

Session I.5: Operational Aspects and Recent System Developments

In this session we seek to focus on aspects related to the technical performance of radar systems and multi-instrument measurements. We solicit papers pertaining to all aspects of technical performance of current and/or proposed facilities, including the unique problems associated with operation of remote stations. These aspects include, but are not limited to, pros and cons of system configurations and measurement methods. We would also like to address how multi-instruments can be used together to augment scientific research as well as how measurements from diverse instruments (including models) may be appropriately compared.

Conveners:
I. Reid and D. Thorsen

THE WIND PROFILER NETWORK OF THE JAPAN METEOROLOGICAL AGENCY

Masahito Ishihara[1], Shoichiro Fukao[2] and Hiroyuki Hashiguchi[2]
[1]Observations Department, Japan Meteorological Agency, Japan
[2]Radio Science Center for Space and Atmosphere, Kyoto University, Japan
E-Mail : ishihara_masahito@met.kishou.go.jp

1. INTRODUCTION

The Japan Meteorological Agency (JMA) established the operational Wind Profiler Network and Data Acquisition System (WINDAS) for the enhancement of capability to watch and predict severe weather in Japan. The network consists of thirty-one 1.3GHz wind profilers which are located across Japan and the Control Center at the JMA headquarters in Tokyo. 25 wind profilers started to be in operation in April 2001 and 6 profilers has been added by June 2003.

Characteristics and performance of the system and effect of the profiler data on numerical weather prediction of heavy rainfall are presented.

2. BACKGROUND AND OBJECTIVES OF WINDAS

Atmospheric radars originally developed in 1970s for the research of the mesosphere and stratosphere have been extensively applied to operational use for observations of the troposphere wind fields since 1990s as demonstrated by the Wind Profiler Demonstration Network (NOAA, 1994) and COST74/76 (Oakley et al, 2000). In Japan, more than ten profilers including the MU (middle and upper atmosphere) radar of Kyoto University are being operated for research use. The Meteorological Research Institute (MRI) of JMA started basic research on wind profilers in 1989. Through the research in MRI and evaluation of profilers data on the numerical weather prediction (NWP) models, JMA decided to install an wind profiler network (Ishihara and Goda, 2000). Considering the cost performance and the allocation condition of radio frequencies in Japan, 1.3GHz wind profilers were selected for the network.

The major aim of WINDAS is to obtain initial wind fields for the operational NWP models. A special role given to WINDAS is to improve the accuracy of the mesoscale model (MSM) for forecasting severe rainfalls, which often cause heavy damages due to floods and landslips in Japan. The horizontal grid size of 10km in MSM allows prediction weather systems organized in meso-beta scale which are responsible for these events. Although wind measurements using 1.3GHz wind profilers are restricted to the middle and lower troposphere, almost all the amount of water vapor is concentrated in the layers and then streams of moist air could be well depicted with the profiler data. WINDAS and MSM are the two major tools in JMA to predict mesoscale severe weather events.

The profiler data have been put onto the Global Telecommunication System(GTS) for global exchange on an operational basis since April 2002 and are also published in CD-ROM for general usage.

3. SYSTEM AND CHARACTERISTICS OF WINDAS

As shown in Figure 1, the locations of 31 profilers were selected giving the high priority on observations in the middle and western Japan where heavy rain storms occur almost every year. The intervals of wind profiler sites are ranged from 67 to 262 km and 120 km on average over the four main islands of Japan.

The profilers of WINDAS were designed based on the technologies developed by the Radio Science Center for Space and Atmosphere(RASC) of the Kyoto University and were produced by the Mitsubishi Electric Corporation. The following points were paid much attention : 1)high transmitting power(1.8kW), 2)high antenna gain(33dB), 3)up-to date pulse compression technique (8-bit coding), 4)intense clutter fences to prevent ground clutter and interference with other radars, 5)semi-globe radomes against heavy snow accumulation, 6) automated data quality control, and 7)full remote operation of the profilers from the headquarters of JMA in Tokyo. Table 1 summarizes main characteristics of WINDAS.

4. SIGNAL/DATA PROCESSINGS AND DATA QUALITY CONTOROL

At each profiler site, vertical profiles of 10-minute averages of spectral moments on the five beams are measured, and U, V, W components of wind are sent every hour to the Control Center via the JMA exclusive telecommunication lines or public digital lines. The computer system of the Control Center makes quality control, and sends the data to the JMA central computer for numerical predictions by 20 minutes after each hour.

Signal processing as well as data quality control are the keys to keep profiler data high quality. The specific processes to WINDAS are the estimation of Doppler spectral moments using the Gaussian function fitting (Hashiguchi et al., 1995) and the quadratic surface check for U and V components (Sakota, 1997). The former has the advantage of obtaining spectral moments under the condition of low S/N ratio. The latter has effectively eliminate erroneous data based on continuity of U or V components on a time-height cross. One to two percents of the total amount of data has been rejected on average at the stage of the data quality control.

At the early stages of the operation of WINDAS, ground clutter disturbed the wind measurement at several profiler sites. Enhancement of the performances of the clutter fences and improvement of the zero-Doppler velocity rejection in Doppler spectra in the data processing have almost solved the problem. Clutters from aircrafts or side robes of the antenna radiation occasionally appear, but they cause little troubles on the wind measurements.

The significant wind measurement error results from migrating birds. The erroneous data appear mostly in the night of spring and autumn under the fair weather conditions as well as in the profiler networks of U.S. and of Europe (Wilczak et al,1995 ; Engerbart and Gorsdorf 1997). The wind measurement deviations due to migrating birds extended to 90 degree in direction and 10 m/s in speed for the most pronounced case. In October 2001 when birds actively migrated over about half of the profiler sites, 12% of the total amount of WINDAS data were contaminated by birds. Echoes from migrating birds had been rejected by monitoring spectrum width during December 2001 to March 2003. The new algorithm, in which Doppler spectra with intense signal power are eliminated before the incoherent integration, has been developed and was introduced in the signal processor of the profilers in March 2003. The algorithm has recovered atmospheric signal from nearly half of birds-contaminated echoes.

5. DATA QUALITY AND IMPACT ON NWP MODELS

The wind profilers of WINDAS have four options in vertical resolutions: 100, 200, 300 and 600m corresponding to four pulse lengths. The longer pulse length has better height coverage, but the less vertical resolution. Data availability for each height resolution examined prior to the operation. Data availabilities of 50% in 100, 200, 300m height

resolution were 3.0 km, 5.4 km and 6.4 km, respectively. Considering these height coverages, we selected the height resolution of 300m as the default operation mode in WINDAS. 300m is a sufficient height resolution for producing initial values of the current NWP models.

Signal power of 1.3GHz wind profilers highly depends on the amount of water vapor in the middle and lower troposphere. Figure 2 shows the monthly total means of height coverage at all the profiler sites from June 2001 to April 2002. The height coverages of WINDAS are 6 to 7 km in summer and at 3 to 4 km in winter and they have reached the original goal of JMA.

The measurement accuracy of WINDAS was evaluated by comparisons with the model forecast winds in June and July 2001. RMSEs of profiler winds from model winds as well as those between rawinsonde winds are shown in Figure 3. There is no significant difference between profiler winds and rawinsonde winds in the RMSEs. This means that the accuracy in the wind measurement of WINDAS is comparable to that in rawinsonde observation.

The data of WINDAS have been used as an initial value in all the NWP models operated in JMA since June 2001. The 4-dimensional variational data assimilation (4D-VAR) started to be in operation in MSM in April 2002. 4D-VAR makes the best use of the potential of profiler data because of the capability of continuous measurement of upper-air winds. Figure 4 illustrates a result of an impact experiment made by MSM using WINDAS data with the 4D-VAR for a severe rain storm occurred in June 2001 (Tada, 2001, private communications) . The profiler data and the 4D-VAR well improved the accuracy of the location of the severe rain storm in MSM.

6. PERFORMANCE IN OPERATION

In order to evaluate the reliability of the operation of WINDAS, the percentage of data received in real-time at the Control Center were examined. The monthly total means over all the sites have been over 98.8% since May 2001. This indicates that stable operation of the system has been accomplished

7. CONCLUSIONS

JMA has operated the wind profiler network for tow years and the profiler data are effectively used in real-time for numerical weather prediction. Issues on ground clutter and migrating birds have been practically solved. Retrieval of vertical water vapor from signal power and spectrum width of profilers will be one of the future plans.

ACKNOWLEDGMENTS

We thank the NOAA Profiler Network staff of the Forecast Systems Laboratory of NOAA for providing useful information on profiler operation. The technical reports published by COST74/76 gave us suggestive information. The impact experiments described in Section 5 was made by the Forecast Prediction division of JMA.

REFERENCES

Engerbart, D and U. Gorsdorf, 1997 : Effects and observation of migrating birds on a boundary-layer wind profiler in a eastern Germany. *Extended Abstract of COST-76 Profiler Workshop*, 227-230.

Hashiguchi, H., S. Fukao, T. Tsuda, M. D. Yamanaka, D. L. Tobing, T. Sribimawati, S. W. B. Harijono and H. Wiryosumarto, 1995 : Observations of the planetary boundary layer over equatorial Indonesia with an L-band clear-air Doppler radar : Initial results. *Radio Sci., 30*, 1043-1054.

Ishihara, M. and H. Goda, 2000 : Operational 1.3GHz wind profiler network of Japan Meteorological Agency. *Proceeding of the MST and COST76 Workshop*. 538-540.

NOAA, 1994 : Wind profiler assessment report and recommendations for future use. National Weather Service and the Office of Oceanic and Atmospheric Research. 141p.

Oakley, T., J. Nash and M. Turp, 2000 : CWINDE project office networking European profilers 1997-2000. *Proceeding of the MST and COST76 Workshop*. 525-528.

Sakota, Y., 1997 : Improvement of the quality control scheme over six-minute-interval wind profiler data. *Extended Abstract of COST-76 Profiler Workshop 1997*, 243-246.

Wilczak J. M., R. G. Strach, F. M. Ralph, B. L. Weber, D. A. Merritt, J. R. Jordan, D. E. Wolfe, L. K. Lewis, D. B. Wuertz, J. E.. Gaynor, S. A. McLaughlin, R. R. Rogers, A. C. Riddle and T. S. Dye,1995 : Contamination of wind profiler data by migrating birds : characteristics of corrupted data and potential solutions. *J. Atmos. Oceanic Tech., 12*, 449-467.

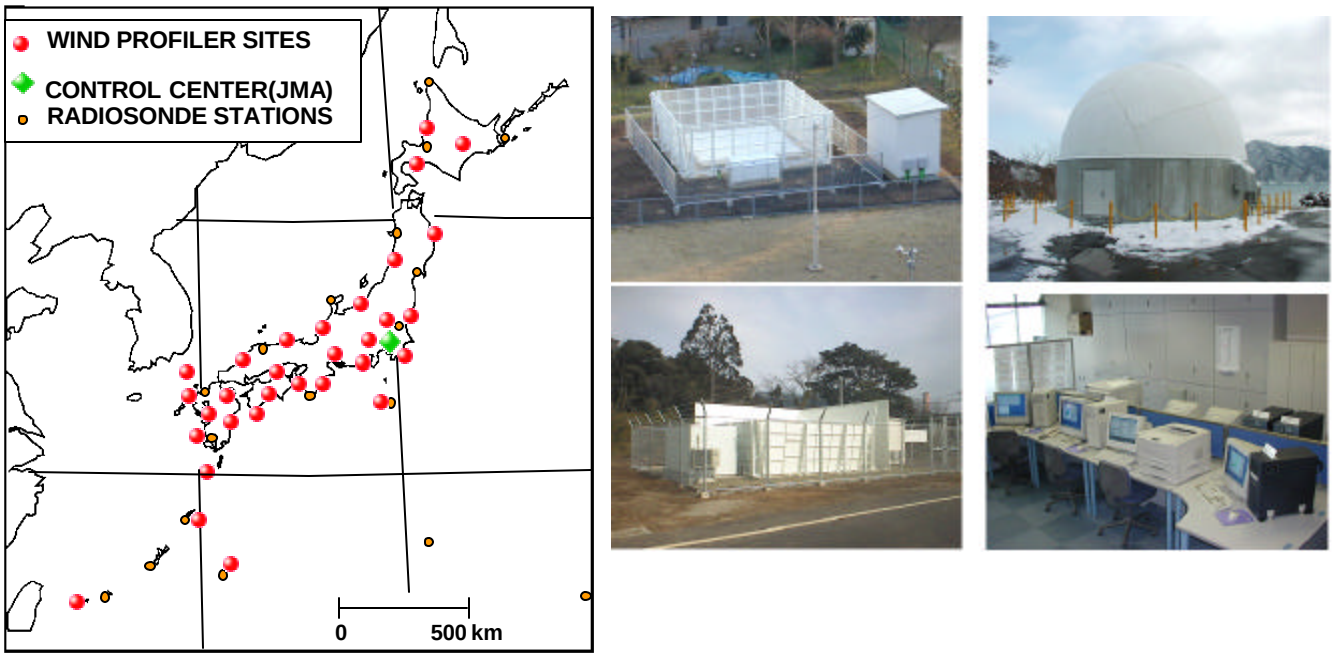

Figure 1. The locations of WINDAS and photos of the wind profiler sites and the Control Center.

Table 1. Characteristcs of wind profilers of WINDAS.

Frequency	1357.5 MHz
Antenna	coaxial colinear arrays with gain of 33dB and size of 4m x 4m
Peak Power	1.8 kW
Beam width	4 deg.
Beam configuration	5 beams
Pulse length	0.67, 1.33, 2.00, 4.00 10^{-6}sec.
PRF	5, 10, 15, 20 kHz
Side robe level	-40dB or -60dB (at elevation angles of 0-10deg)
Basic data	Doppler moments every 1minute
Distributed data	U,V,W-components of wind, S/N ratio & data quality flag every 10 minutes

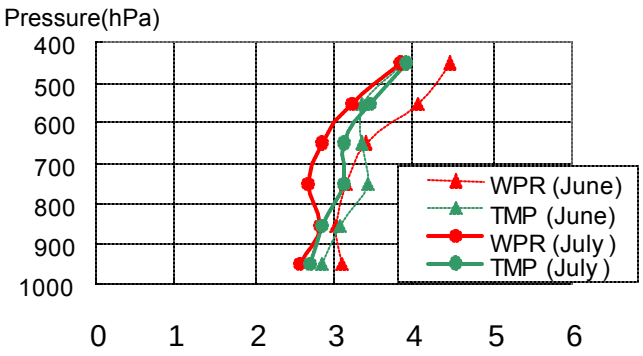

Figure 3. Vertical distributions of RMSEs of profiler winds (WPR) from winds by mesoscale model(MSM) and those of radiosondes winds (TMP). u-components of winds in June and July 2001 are examined.

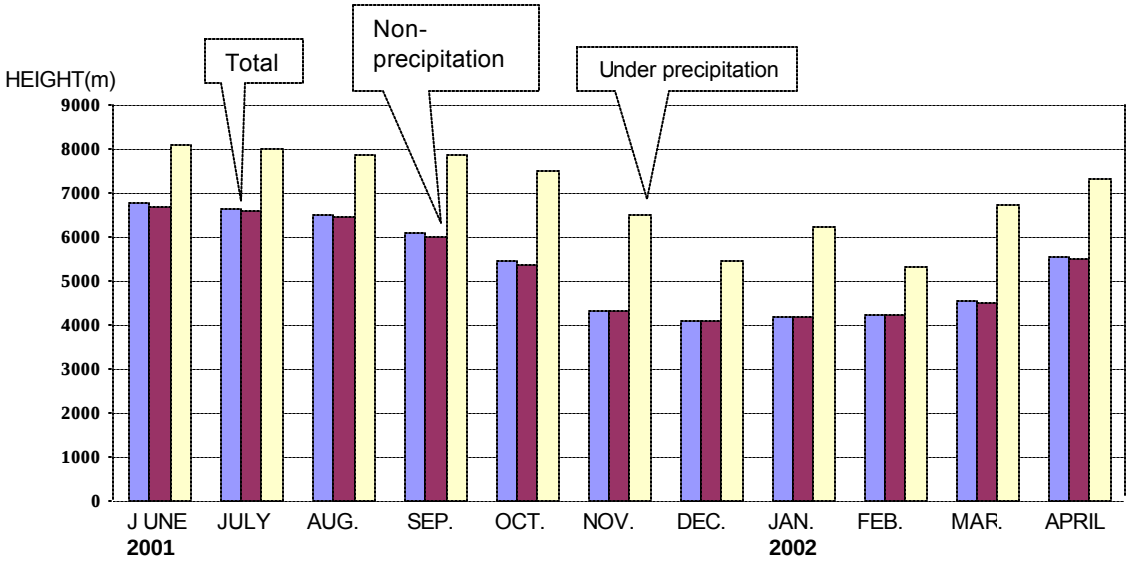

Figure2. Monthly total means of height coverage for 25 wind profilers of WINDAS.

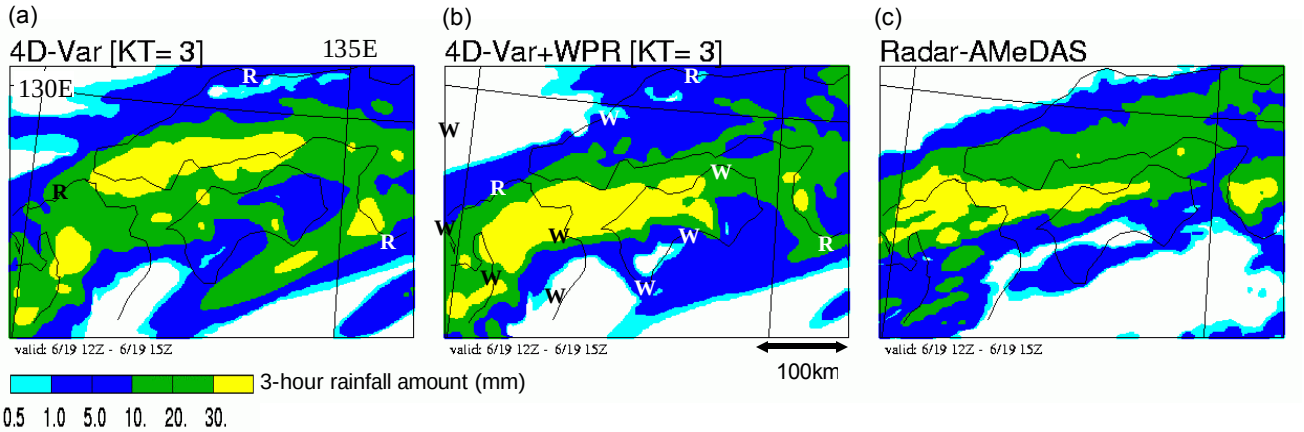

Figure 4. Result of an observing system experiment on comparison between forecasts by the mesoscale model (MSM) and observations for 3-hour rainfall amount. The initial time is 12UTC on 19 June 2001. (a) forecasts from MSM and 4D-VAR without profiler data but radiosonde data, (b) forecasts from MSM and 4D-VAR with both profiler data and radiosonde data, and (c) rainfall amount observed by radars and rain gauges during 12 to 15UTC. 'R's in (a) and (b) indicate the locations of the radiosonde sites and 'W's in (b) the locations of the wind profiler sites.

FIRST RESULTS OF THE BOUNDARY LAYER AND TROPOSPHERIC RADAR SYSTEMS FOR ENSO STUDIES IN NORTHERN PERU

D. Scipión[1], J. Chau[1], and L. Flores[2]
[1]Radio Observatorio de Jicamarca, Instituto Geofísico del Perú, Lima
[2]Laboratorio de Física – Universidad de Piura

1. Introduction.

The Instituto Geofísico del Perú (IGP) has recently bought with the cooperation of the World Bank, two new Boundary Layer & Troposphere Radar (BLTR) systems to improve the capacity for predicting and evaluating the El Niño phenomenon (ENSO) to assist in the prevention and mitigation of disasters in Peru (R. Woodman and P. Lagos, personal communication). Both systems have been installed in northern Peru, because this area is one of the most sensitive to El Niño phenomenon in the World. In particular, Piura which is a desert-like area with an average annual rainfall of 50 mm, in few months of ENSO becomes a tropical area (rainfall of 3000 mm in less than 6 months!). The data from these systems will be incorporated to the regional numerical weather model of IGP.

The first system was installed at Universidad de Piura (UDEP) where it complements the existing Piura ST system [*Gage et al.*, 1991]. As we will show below, the validation of the newly installed BLTR system in Piura has been tested against winds obtained wit the ST radar and also against winds obtained from pilot balloons. The ST and BLTR radars operate at 49.920 MHz, and we avoid possible interference between both of them by operating the BLTR system in slave mode. The second BLTR system was installed ~200 km SE of Piura close to Porcuya. Atmospheric dynamics above this site will be very important because it is located at the lowest part of the Andes in the northern part of Peru and therefore in the border of the Pacific and Atlantic basins.

In this work, we will present first results, comparison and statistical studies between BLTR, ST and Pilot Balloons of instantaneous data, consensus data, and NCEP Reanalysis data over UDEP and Porcuya.

2. Peruvian Profilers

Table 1 shows the different systems operating in Northern Peru. The **ST system** was installed in 1989 as part of the Transpacific Profiler Network [e.g., *Gage et al.*, 1991], it operates at 49.92 MHz and uses the Doppler Beam Swinging (DBS) technique; its range coverage is between 2 – 12kms. with 1km resolution and it takes 12 minutes to cover all the beams (north, south, east, west and vertical).

Table 1 Wind profilers in Northern Peru.

Location	Altitude	Type	Band	Size	Peak Power	Method	Period
Piura	43m.	ST	VHF	100m x 100m	30 kW	DBS	1989 -
Piura	43m.	BLT	VHF	30m x 30m	12 kW	SA	2001 - ?
Porcuya	1163m.	BLT	VHF	30m x 30m	12 kW	SA	2002 -

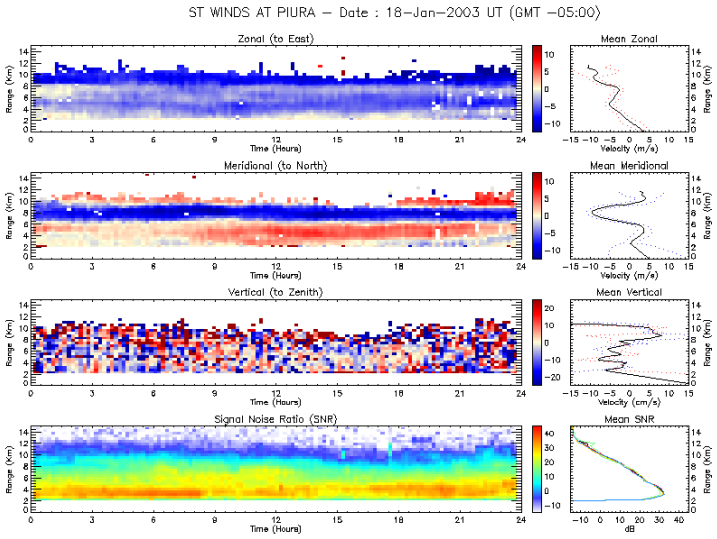

Figure 1. ST Winds at Piura (18th Jan 2003). Height resolution (≈1km), range (2-15km).

The **BLT systems** operate in Piura and Porcuya at 49.920MHz using the Spaced Antenna (SA) Technique (e.g., *Briggs*, 1984), and provide the three components of the wind (zonal, meridional and vertical) every minute. They operate in two modes (low and high mode). In low mode their resolution is 75m., while in high mode is 450m.

The Piura system was installed in May 2001 its range coverage in low mode (Figure 2-left) is between 150 m and 3 km, and in high mode between 800 m and 8 km. The Porcuya system was installed in June 2002, its range coverage in low mode (Figure 2-right) is between 300m up to 4km, and in high mode between 600m to 8km.

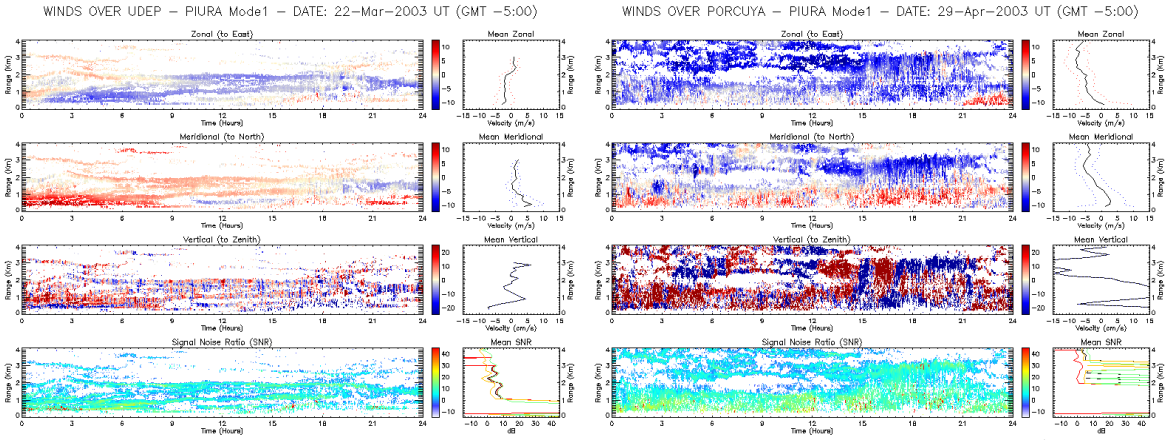

Figure 2. BLT Systems installed in Piura and Porcuya. Left: Low Mode at Piura (22nd March 2003). Right: Low Mode at Porcuya (29th April 2003).

3. Piura Comparison

In Piura we have two systems that help us to validate the information collected by the BLT System, the Pilot Balloons and the ST System. The last system operates at the same frequency as the BLT so we develop a "pulse generator box" to synchronize both systems, the BLT operates in slave mode and reduces its performance because it interferes with *E*-layer observations [e.g., *Chau et al,* 2002] (80-120kms.) using the ST system.

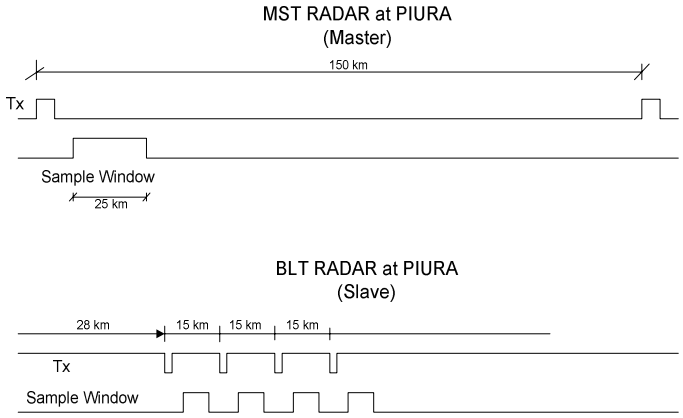

Figure 3. Pulse Design Diagram to synchronize the BLT and ST Systems operating at the same frequency.

For our comparisons we have used hourly averaged data (consensus files) for both systems. We have removed data when the SNR is below a given SNR Threshold (0 dB) and when outliers are present. In order to identify the outliers we calculate the median and standard deviation per each height (continuously) for both modes. Those points that are over 1.5 standard deviations are outliers. A similar approach has been used by *Palo et al.* [1995]. After we obtained the averages for each mode, we combined them to obtain a single file from each site, i.e., in the case of Piura below 1.5 km data from the low mode is used, while above 1.5 km data from the high mode is used. At Porcuya, we have selected 2.5 km to be the border height between the two modes.

Pilot Balloons are launched at Piura almost everyday around 1600 local time, and as we can see in a qualitative form (Figure 4-left), there is a good agreement between pilot balloon winds and BLT winds. There is also very good agreement between the hourly winds obtained with the BLT and the ST system (Figure 4-right). Since the ST system has a poorer range resolution, we have convolved the BLT profiles with a 1-km wide function for the comparison.

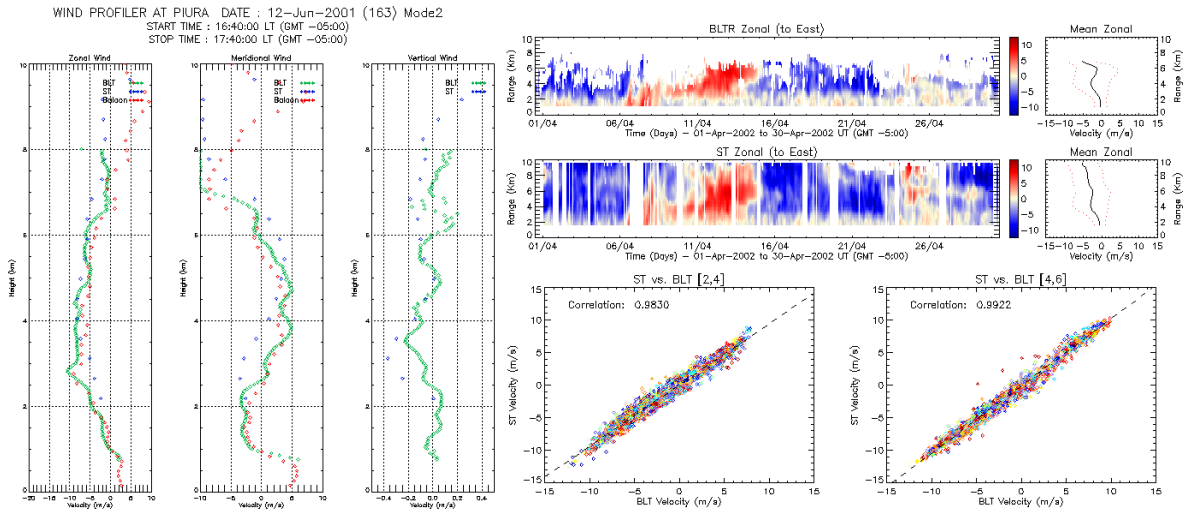

Figure 4. Left: Pilot Balloon, BLT and ST qualitative comparison. Right: BLT vs. ST Comparison. Zonal Winds at Piura (April 2002). Correlation almost 1, between 2-4km and 4-6km data.

In addition, there is an excellent agreement between the radar winds over Piura and winds obtained from the NCEP Reanalysis model [*Kalnat et at*., 1996]. In Figure 5 we show NCEP data for every 6 hours while BLT data are shown for every 1 hour for both Piura (left) and Porcuya (right). At Porcuya the agreement is not as good. We think this is because the model does not have any input data from close by stations and therefore it does not represent well the winds over this part of the Andes. The assimilation of the Porcuya winds will help the model outputs of the NCEP model around these areas.

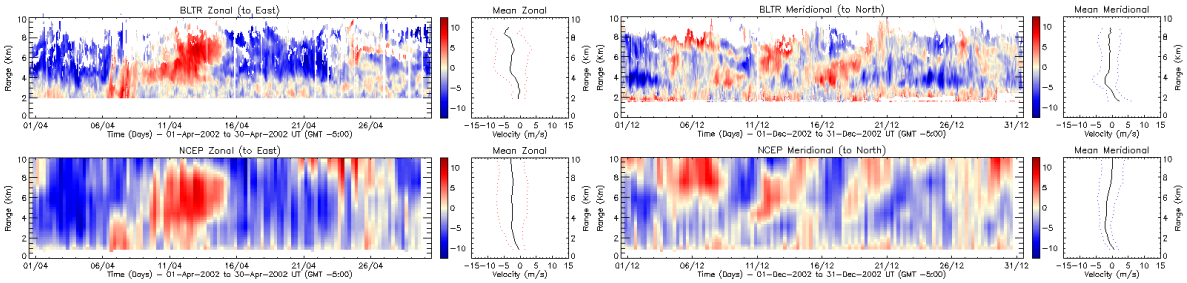

Figure 5. BLT-NCEP Comparison. Left: Piura (Apr, 2002). Right: Porcuya (Dec, 2002)

4. Conclusions

The winds obtained with the newly installed BLT system at Piura are in very good agreement with winds obtained with the collated ST radar and pilot balloon system. In addition, there is excellent agreement with the winds from NCEP Reanalysis model. The discrepancy observed at Porcuya between the BLT and NCEP could be due the poor representation of this part of the Andes by the NCEP model. The assimilation of the Porcuya data will help improve the model outputs.

Currently the BLT winds from Piura are available in real time at the IGP web page and at the NOAA Forecast Laboratory web page. Winds from Porcuya are made available via the same web pages once a month, but we are working on a solution to send them in real time through the GOES system.

5. Bibliography

Briggs, B. H., The analysis of spaced sensor records by correlation techniques, in *Handbook for the Middle Atmospheric Program*, pp. 166-186, SCOSTEP Secr. Univ. of Ill., Urbana, 1984.

Chau, J.L., R.F. Woodman, and L. A. Flores. Statistical characteristics of low-latitude ionospheric field-aligned irregularities obtained with the Piura VHF radar, *Ann Geophysicae*, 20(8), 1203-1212, 2002.

Gage, K. S., B. B. Balsley, W.L. Ecklund, D. A. Carter, and J. R. McAfee, Wind profiler-related research in tropical Pacific*, J. Geophys. Res.,* 96, 3209-3220, 1991.

Kalnay et al., The NCEP/NCAR 40-year Reanalysis Project, *Bull. Amer. Meteor. Soc. 77*, 437-471, 1996

Palo, S.E. , J. L. Chang, S. K. Avery, A. C. Riddle, and K. S. Gage, Detection of Outliers in Stratospheric / Tropospheric Wind Velocity Estimates, *Seventh Workshop on Scientific and Technical Aspects of MST Radar*, 237-240, 1996

IGP Database : http://jro.igp.gob.pe/database/blt_cns/bltrdata.html

NOAA Forecast Lab Database: http://www.profiler.noaa.gov/jsp/profiler.jsp?options=full

MOVEABLE UHF/S-BAND PROFILER/DISDROMETER SYSTEMS AS A CALIBRATION STANDARD IN RAINY PLACES

Wallace L. Clark[1,2], Kenneth S. Gage[2], Christopher R. Williams[1,2], Paul Johnston[1,2], and David Carter[2]

1. CIRES/University of Colorado, Boulder, CO, 80309-0216, USA
2. NOAA Aeronomy Laboratory R/AL3, Boulder, Colorado, 80305-3328, USA

Introduction

A critically important task for many types of radar work is reflectivity calibration. The obvious, and probably most thorough, method of calibrating is to find the radar constant by bringing the reflectivity observed from a standard calibration target into agreement with the value expected. However, the fixed and more or less vertical orientation of profiler/MST radar beams makes the use of such artificial targets quite difficult. Fortunately, in locations where it rains, raindrops can serve as the calibration target. The relation between drop-size distribution (DSD) and reflectivity is well developed and may be measured for any given period of time by a collocated surface disdrometer. The near vertical orientation of profilers and MST radars is nearly optimum for such a comparison, although it is required that a fully recovered range gate in the far field of the antenna be less than a few hundred meters above the surface. Commercial disdrometers are readily available that are rugged, stable over periods of years, and thus suitable as a field reference standard. This technique has been used many times over the years for scanning radar calibration (Joss, J. and Pittini, A., 1991), even though the geometry between scanning radars and a surface disdrometer is generally not so ideal.

Since small profilers (Gage, K. S., Williams, C. R. et al., 2000) such as the AL (NOAA Aeronomy Lab) UHF/disdrometer systems are quite moveable, they can serve as traveling reference standards for larger systems for which the low range gate requirement is not fulfilled. When collocated with such systems, the calibrated profiler becomes a transfer standard to the larger system provided echoes (clear air or rain) can be simultaneously observed in nearly coincident range gates. Differing sizes of range gates, of course, would require some more sophisticated analysis.

Over the last few years the AL has, along with studies of obtaining profiler based DSDs (Williams, C. R., Kruger, A. et al., 2000), been field-testing this disdrometer method of calibrating profilers during the ground validation campaigns of the NASA/NASDA Tropical Rainfall Measuring Mission (TRMM). The results of these campaigns suggest that calibration accuracies within a dBZ or so are obtainable, and the technique has been used for verification, and in at least one case, correction of scanning radar observations. It has also been found easy and beneficial to use this calibration procedure to monitor the health of radar systems, thus allowing timely correction of occasional system component failures.

Calibration Setup

The inset in Figure 1 shows a sketch, more or less to scale, of the geometrical relationship of the disdrometer/profiler combination. The rest of the Figure shows an actual field implementation for calibration of wind-profilers with disdrometers during the TRMM-LBA campaign. In this case there are two profilers of different wavelengths (10.6 and 32.8

cm) positioned side by side to allow study of the effects of clear air scatter on the calibration. The details of the profilers shown are given in Table 1 below.

For pure calibration work, only one profiler, of either wavelength, is necessary. The S-band is less sensitive to the clear-air scatter relative to the precipitation signal, and is therefore a better choice if the system is devoted to hydrometeor work, especially for small drop-size rain. On the other hand, the longer wavelength system allows some clear-air work. However, even this system is limited in clear air as its sensitivity must be limited to avoid saturation in the lower range gates during hard rain. These close in range gates are a must for calibration work in order to ensure that the disdrometer and the radar are observing the same rain and drop-size distribution.

Figure 1: A typical configuration for calibration of a profiler by disdrometer. The sketch in the left panel insert (upper left corner) shows, more or less to scale, the basic calibration geometry. The Ji Parana, Brazil site photograph shows a typical setup, including the clutter shrouds surrounding the antennas for two side-by-side profilers of different wavelength, the control building, and the Joss-Waldvogel Disdrometer (Distromet RD80) located a little over 10 m from the profiler antennas on a 1 m high tripod. Both profilers were calibrated using the disdrometer as a reference standard, though special care had to be taken with the 915 MHz data to ensure clear-air echo was not biasing the results. The right panel shows a close up of the disdrometer.

The right panel of Figure 1 shows a close up of the JWD (i.e., Joss-Waldvogel Disdrometer). Falling raindrops impact the Styrofoam head, and the momentum transfer is converted into drop size. The binning of a 60 second sample of these drop sizes forms a drop size distribution, or DSD. From the definition of the reflectivity factor Z, it is then easy to transform the DSD into the value of Z that a profiler probing the sampling volume of the disdrometer should see.

Statistical Calibration

It cannot be emphasized enough that calibration using DSDs and radar reflectivities is statistical in nature. A single one-minute comparison can be very misleading. This is inherent in the stochastic nature of rainfall (Jameson, A. R. and Kostinski, A. B., 2001), and precise results require the sampling of very large numbers of drops to achieve stability. The nature of this problem and its solution is best shown by example. Figure 2 Left shows the

one-minute Z values determined from two disdrometers located one-meter apart at Wallops Island, Virginia (Dr. Ali Tokay, JCET/ University of Maryland, Baltimore County kindly provided this data set). The data were taken in fairly high winds. Although the superimposed time series from the two disdrometers agree rather well as far as gross trend, the close examination of the differences between the observed Z values shows that one minute values are actually quite noisy, with some simultaneous observations disagreeing by 10 dBZ or so. Nonetheless, the nearly half-day average-difference converges nicely towards zero.

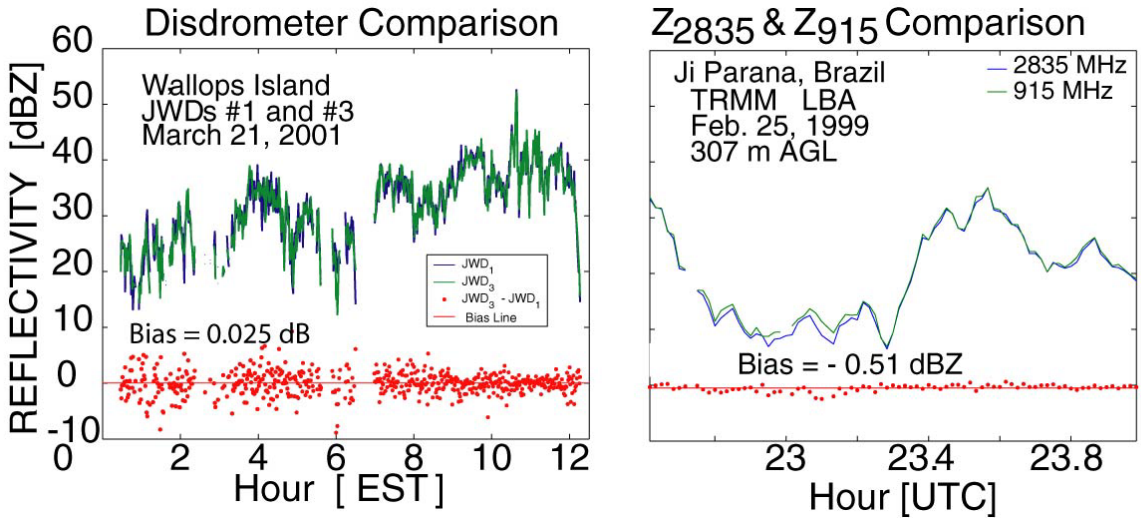

Figure 2 Left: Comparison of 12 hours of Z values from two disdrometers placed 1 meter apart at Wallops Island, Virginia. Right: Comparison of 1 hour of Z values observed from two colocated profilers during LBA. The tick marks are 10 dBZ apart, with the horizontal line at 0 dBZ. The dots around this line represent the difference between the simultaneous observations.

Performing the same exercise, we see in Figure 2 Right that the 915 and 2835 MHz profilers also agree nicely in gross trend. Relative to the disdrometer figure, the smaller scatter shown in the difference plot for the two profilers may be partly due to the larger volumes sampled. However, no firm conclusion should be drawn because the locations and times of the two comparisons are very different. In this case, the statistical fluctuations in the profiler Z difference values are small enough that the enhancing effect of clear-air scatter is easily seen for Z values below, say, 15 dBZ.

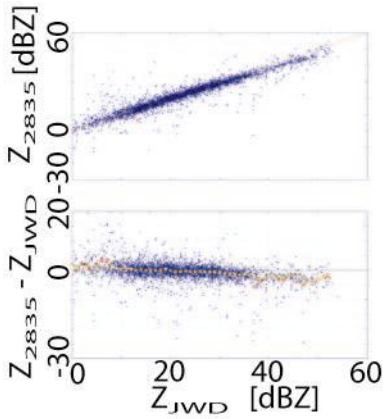

Figure 3: Scatter plots of (top) Z_{2835} vs. Z_{JWD} and (bottom) Z_{2835}-Z_{JWD} vs. Z_{JWD}. Both axes range from 0 to 60 dBZ in 10 dBZ increments. The data represent 39 days of LBA observations.

Finally, in Figure 3 we show an example of scatter plots comparing Z observed by the 2835 MHz profiler versus that from the JWD. These data comprise all the stratiform events observed during the Brazilian TRMM-LBA campaign (about 2 months). Looking at the lower panel, where the difference in observed Z_{2835} - Z_{JWD} is shown, we see that there is apparently still some slight bias from clear-air echo at low Z. More importantly, there is an interesting change in character of the relationship starting about 30 dBZ, wherein Z_{JWD} appears to get progressively larger than Z_{2835} as Z gets larger. This effect remains to be explained, but has caused us to limit the calibration region to Z values between 15 and 30 dBZ. The effect has appeared in all of the profiler systems we have tried, though the same disdrometer, which has been moved from site to site, has been used in all cases.

Table 1.

Tropical Rainfall Measuring Mission (TRMM)
Precipitation Profiler Characteristics

Parameter	S-Band Profiler	UHF Profiler
Frequency	2835 MHz	915 MHz
Wavelength	10.6 cm	32.8 cm
Peak Power	5 Watts	500 Watts
Antenna	1.2 m Shrouded Dish	3 m Shrouded Dish
Beamwidth (two way)	5 degrees	5 degrees
Height Resolution	60 m & 100 m	100 m & 255 m
Pulse Length	60 m & 100 m	100 m & 255 m
Number of Range Gates	100	100
Max. Altitude	6.1 km & 10.7 km	10.7 & 18.5 km
Nyquist Velocity	21 ms^{-1}	21 ms^{-1}
Number of Spectral Points	256	256
Dwell Time	~30 seconds	~30 seconds
Data Recorded	Full Spectra	Full Spectra

Conclusion

Although there was not room to demonstrate them all here, we have the following findings. A collocated disdrometer is an effective way to calibrate and check S-band and UHF profilers. The calibration is statistical and requires at least hours of data to achieve an adequate and reliable precision. This ability to field calibrate small, moveable wind profilers provides the opportunity to use such systems as transfer standards to other types of radar or remote sensors.

References:

Gage, K. S., C. R. Williams, P. E. Johnston, W. L. Ecklund, R. Cifelli, A. Tokay, and D. A. Carter, 2000: Doppler radar profilers as calibration tools for scanning radars. *Journal of Applied Meteorology*, *39*, 2209-2222.

Jameson, A. R. and A. B. Kostinski, 2001: What is a raindrop size distribution? *Bulletin of the American Meteorological Society*, *82*, 1169-1177.

Joss, J. and A. Pittini, 1991: Real-Time Estimation of the Vertical Profile of Radar Reflectivity to Improve the Measurement of Precipitation in an Alpine Region. *Meteorology and Atmospheric Physics*, *47*, 61-72.

Williams, C. R., A. Kruger, K. S. Gage, A. Tokay, R. Cifelli, W. F. Krajewski, and C. Kummerow, 2000: Comparison of simultaneous rain drop size distributions estimated from two surface disdrometers and a UHF profiles. *Geophysical Research Letters*, *27*, 1763-1766.

TOWARD A MULTISENSOR GROUND BASED REMOTE SENSING STATION

Catherine Gaffard[1], Tim Hewison, John Nash
Met Office
Meteorology Building, PO Box 243, Earley Gate, University of Reading, RG6 6BB, UK

1. Introduction

Future UK operations require several sites using ground based remote sensing techniques to provide an upper air network with better spatial and temporal resolution than currently exists. There is currently a network of 5 wind profilers that cover the UK and winds are operationally assimilated in our global and mesoscale model. Our goal is to get a continuous monitoring of the lowest 3-km of the troposphere to improve the humidity field and the boundary layer description for numerical weather prediction (NWP). We investigate how a synergy between different ground based remote sensing instruments, like wind profiler, radiometer cloud radar and lidar ceilometer could meet our user needs. A 12-channel microwave radiometer is being trialed and a low cost cloud radar is under development.

A wind profiler and a ceilometer are operationally operated at Camborne in the southwest of England. At present only the wind and the cloud base information obtained from these instruments are used operationally. As it will be illustrated in this paper more information about the vertical structure of temperature and humidity is available in the return signal of the wind profiler and of the ceilometer. The main cause of wind profiler radar returns is due to a Bragg scattering by turbulent inhomogeneities in the refractive index. Therefore there is a close link between the return signal and the gradient of the temperature and the humidity profile. Some studies (Stankov, 2003,1998) have shown that a wind profiler can be used in association with other instruments as RASS, radiometer, GPS, humidity profiles could be retrieved at the vertical resolution of the radar.

Three intensive observation periods have been conducted, when radiosondes were launched hourly. These cover three different situations: development of the convective boundary layer, cloud evolution and clear air situation.

2. Development of the Convective Boundary Layer Case Study

Figure 1 shows the time-height evolution of the wind profiler signal to noise ratio (SNR). Superimposed in white circles are the cloud bases detected by the ceilometer, which show a lot of broken cloud. The cloud base is in the middle of a wide layer of high wind profiler signal to noise ratio, except for a couple of clouds which are just at the edge of the wind profiler signal. For these clouds, the cloud base appears to be more steady. The altitude range covered by the wind profiler with a high SNR increases from 1000 m at 08:00 to its maximum (2150 m) at around 11:30. During this period, the vertical distribution of the strong wind profiler SNR's and cloud bases become more spread. This is likely to be due to

[1] Corresponding Author:
Catherine Gaffard, catherine.gaffard@metoffice.com, phone: +44 118 937831, fax: +44 118 3788791

development of convection in air which is nearly saturated as suggested by the radiosonde profiles.

Above what appears to be the signature of the convective boundary layer, another zone of enhanced signal is highlighted in red. This line nearly coincides with a strong discontinuity in the refractive index (transition from a humid layer to a dry one associated with a temperature inversion). The time height evolution of the square of the gradient of the potential refractive index (Gossard 1998) $(dn/dz)^2$ in Figure 2 shows this discontinuity clearly. $(dn/dz)^2$ can't reproduce the signature of the convective boundary layer because turbulence is not taken into account. The turbulence contributes to the width of the Doppler spectra and may be retrieved from it, but more signal processing has to be done to make this information accurate (Cornman 1998**)**. It is also possible that microstructures in the temperature and the humidity that might be associated with the cloud exist. These structures are not well represented by radiosonde profiles.

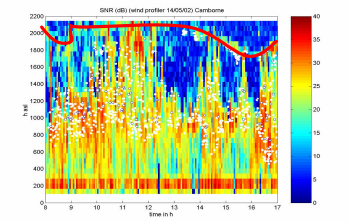

Figure 1- signal to noise ratio of wind profiler (dB scale) on 14/5/02 at Camborne. White and blue circles show cloud base reported by ceilometer

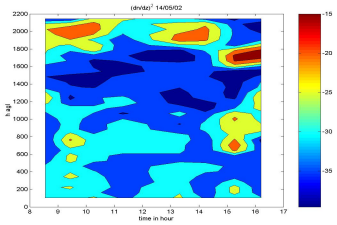

Figure 2 - Time-height series of square gradient of the refractive index (dB scale) computed from hourly radiosonde on 14/5/02

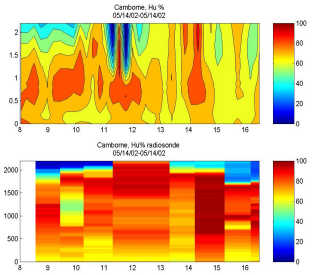

Figure 3 - Time-height series of humidity profile from radiometer (upper panel) and radiosonde (lower panel), Camborne 14/5/02.

With a very coarse vertical resolution, the radiometer (Figure 3) indicates a humid layer with clouds. The general evolution of the temperature is also reproduced (Figure 4). A couple of unrealistic measurements occurred between 10:30 and 12:30. These are likely to be the result of water deposit on the radiometer window.

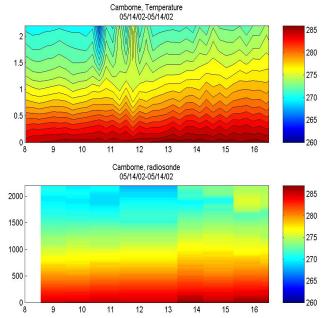

Figure 4 - Time-height series of temperature profile from radiometer (upper panel) and radiosonde (lower panel), Camborne 14/5/02.

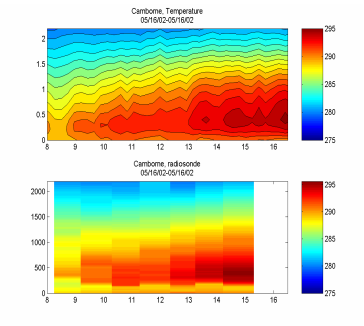

Figure 5 - Same as figure 4 but for 16/05/03**.**

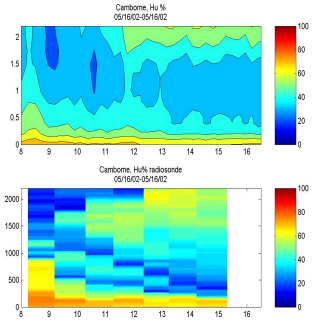

Figure- 6 Same as figure 3 but for 16/05/03.

3. Cloud Evolution Case Study

On the 2nd example of wind profiler data (Figure 7), there is a layer of strong signal between 200 m and 600 m, with variable structure above. There are two types of cloud base: from 08:00 to 11:00 the cloud base is very variable and coincides with strong signal, and from 12:30 to 15:00 the cloud base is more stable and is located below the enhanced wind profiler signal. During the morning low stratus broke up into convective cumulus of moderate extent. By the afternoon, an extensive sheet of less convective stratocumulus appears at 1000 m.

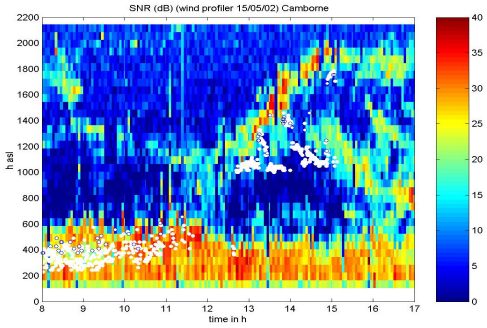

Figure 7 - Same as figure 1 but for 15/5/02

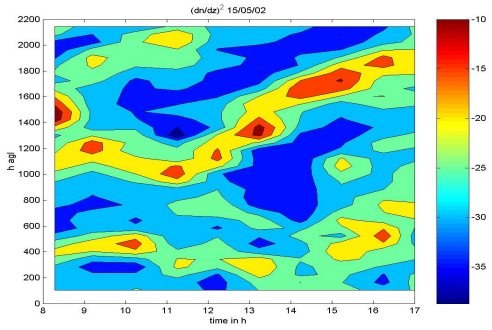

Figure 8- Same as figure 2 but for 15/5/02

The evolution of $(dn/dz)^2$ shown in Figure 8 is in good agreement the signal to noise ratio evolution above the first layer of strong signal. This seems to suggest that the structures seen by the wind profiler above 600 m are not dominated by convective turbulence. As in the previous example, the radiometer reproduces the general tendency for the temperature and the humidity but could not resolve the temperature inversion.

4. Clear air situation

In the third case (Figure 9), there is no low-level cloud. Nevertheless the ceilometer indicates a double layer (Figure 10). The top of the 1st layer corresponds to a large temperature inversion. The top of the 2nd layer just fits underneath the local maximum of the wind profiler and corresponds to a strong decrease in the humidity and a weak temperature inversion. These 2 layers also reproduce some of the oscillations seen in the wind profiler signal. Aerosols trapped underneath the temperature inversion backscatter the ceilometer signal. The evolution of $(dn/dz)^2$ shown of Figure 11 reproduces the signal to noise ratio. In this case, the radiometer retrieved the temperature inversion correctly and reproduced the oscillation in the humidity field as shown respectively on Figure 5 and 6.

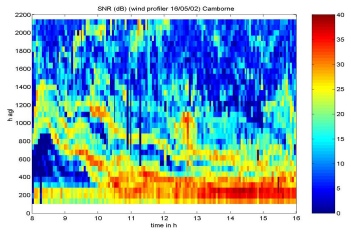

Figure 9 - Same as figure 1 but for 16/5/02

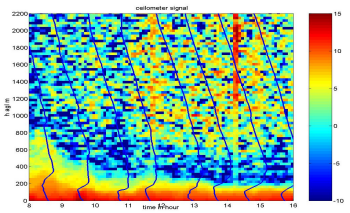

Figure 10 - Ceilometer signal averaged over 5 mn for 16/5/02. Blue curves are temperature profiles.

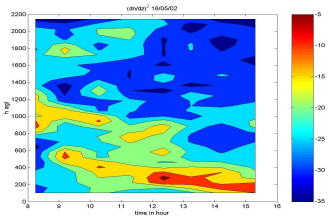

Figure 11 - Same as figure 2 but for 16/5/02.

5. Conclusion

The agreement between the gradient of the potential refractive index and the signal to noise is rather good despite no correction being applied for turbulence. Collocation with the ceilometer has allowed us to identify two strengths of convection and confirmed the presence of a temperature inversion. A collocated cloud radar would allow complete discrimination between clear air echo and cloud echo.

In the future, we hope to enhance the vertical resolution of the retrievals from ground-based microwave radiometers with collocated active instruments, such as wind profilers by using an estimation of the gradient of the refractive index with the radiometer assimilation.

Bibliography

Cornman L. B., R.K.Goodrich, C.S.Morse, and W.L Ecklund,: Fuzzy logic method for improved moment estimation from Doppler spectra. *J. Atmos. Oceanic Technology*,15, 1287-1305. 1998

Gossard, E. E, D. E. Wolfe, K. P. Moran,R. A. Paulus, K. D. Anderson, and L. T. Rogers: Measurements of clear_air gradients, fluxes and stucture paramaters in elevated layers. *J.Appl. Meteor.*, 21, 211-226 1998.

Stankov, B. B., E.E Gossard, B. .l. Weber, R.J. Lataitis, A. B. White, D. E. Wolfe, D. C. Welsh, R. G. Strauch,: Humidity Gradient Profiles from Wind Profiling Radars Using the NOAA/ETL Advanced Signal Processing System (SPS), *J. Atmos. Oceanic Technology*.,20. 2003

Stankov B. B.,:Multisensor Retrieval of Atmospheric Properties. *Bull. Amer. Meteor. Soc*. 79, 1835-1854. 1998.

Cornman L. B., R.K.Goodrich, C.S.Morse, and W.L Ecklund,: Fuzzy logic method for improved moment estimation from Doppler spectra. *J. Atmos. Oceanic Technology*,15, 1287-1305. 1998

DEVELOPMENT OF A DIGITAL RECEIVER FOR THE JICAMARCA OBSERVATORY RADARS

Gabriel Michhue and Ronald F. Woodman
Jicamarca Radio Observatory, Instituto Geofísico del Perú, Lima, Peru

The large proliferation of cellular telephones and services has made available very powerful digital receivers at a very economical price. This has open the possibility to modernize the receivers used at the Jicamarca Observatory, using this technique, for all of the radars currently in use at the observatory, including the IS radar, JULIA, the Antarctic MST and the SOUSY radar. The receivers are flexible enough and they could be used for other radio experiments with a simple change of front end and/or receiver local oscillator.

The approach taken was to develop our own, but rather than building the receiver using our own integration of commercially available chips, we have taken advantage of the existence of compatible evaluation boards for the 12-bit ADC, sampling at RF frequency speeds, and an evaluation board for the digital receiver proper. This may had not been the proper economical approach if we were to produce a large number of units, but for a limited production, it has allowed us to reduce the development time and engineering effort. Our development effort has been limited to the development of the receivers interface to a National Instruments PCI PC digital interface and the associated data acquisition software.

On figure 1 we show a schematic diagram of the receiving system. In this case we show version 1, for two receivers; the minimum required for most of the IS experiments. We use an Analog Devices AD6620 Digital receiver evaluation board. This board uses the PC parallel port for receiver configuration setup and for data taking. The low speed of the parallel port is not a limitation for the configuration function but it is too slow for data taking. Fortunately, the board has a direct access to the parallel data output of the digital receiver chip which is connected directly to the PCI interface. Independent configuration of the two receivers is performed through the parallel port. This port also allows us to use the manufacturer's software for receiver evaluation tasks that do not require high speed. In this version the two 16-bit data outputs of the two receivers are concatenated to produce 32-bit output, which is connected to a National Instruments PCI board through a 64KWord FIFO, which is part of our interface board. We can achieve in this way a maximum throughput of 80 Mega samples/sec, much higher than required by the maximum bandwidth (BW) of the transmitter/antenna and analog receiving front end.

The antenna signals are passed through a 25dB gain analog front end with a BW of 4MHz. The analog filter has a sharp cut-off and is used to reject any RF interference before the sampling and digital filtering operations. Sampling is performed at 64MHz, which effectively beats the 50MHZ signal to an aliased –32 to +32 MHz window with a center frequency of 14Mhz. Sampling is performed in an AD6640 12-bit analog to digital converter. The AD6620 digital receiver schematic is shown in figure 2. The 14 MHz is converted there to base band, it is then filtered and decimated by the three internal filters of the AD6620 unit. The first two cascaded integrated comb (CIC) filters are used to reject further undesired frequencies and reduced the sampling rate to a convenient rate (~4MHz). Final hardware filtering is performed in the third unit ram coefficient finite impulse response (RCF) filter, a programmable 256 register FIR filter which as such has a large flexibility to produce almost any desired BW shape, including exact matched-filters matched to the "square" transmitter waveform. The 16-bit output of the receiver gives us approximately 90 dB of dynamic range, before incoherent integration, when the receiver scaling is adjusted to give 2 bit RMS noise

samples. We normally use the three filter stages as fix filters matched to the widest analog system BW and perform further filtering in the PC for software convenience, but other configurations are available if desired. When further filtering is performed in the PC, the dynamic range is further enhanced.

We use a single 64 MHz local oscillator to generate the ADC, digital filter and radar controller clock as well as the transmitter excitation frequency. This guarantees the coherence of the receiver and transmitter frequencies.

Following we summarize the digital receiver advantages:

- Dynamic range greater than 85dB.
- No cross talk.
- Perfect coherent quadrature detector.
- Exact control of BW shape.
    - Same in multiple receivers.
    - Same for I and Q.
- Programmable filter and perfect match filter.

On version 2 we plan to implement 4 digital receivers with a single control card. In this version the configuration of the receivers is performed using the same PCI card it is used for data taking. More receivers can be easily implemented by duplicating the system with additional interface cards.

Illustrative results

On figure 3 we show a range time intensity plot showing signals from the equatorial Electrojet, Spread-F and Incoherent-Scatter signals from the F region. On figure 4 we show the same signals for two different times, this time showing the signal power profile and spectrum for the two receivers (left and right). On figure 5 we show power profiles and spectrum of Electrojet echoes as well as echoes from the 150-km irregularities. Note the large dynamic range for all, although we are still not exercising the full dynamic range of the system. The radar parameters for the two experiments shown are displayed in Table 1.

	Experiment 1	Experiment 2
IPP	999Km	199.8Km
TX	40.5Km	9Km
N samples	177	200
DH	4.5Km	2.25
H0	76Km	76Km
Antenna setup	CP2	CP2
Code	1,1,1,1,1,1,-1,-1,1	1

Table 1 Experiment parameters.

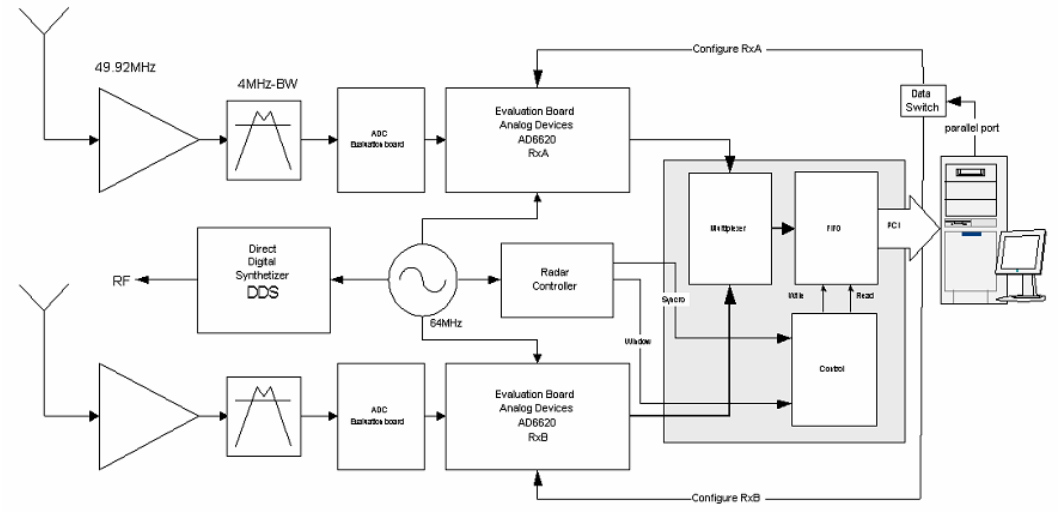

Figure 1 Schematic diagram of the Jicamarca digital receiver system version 1.

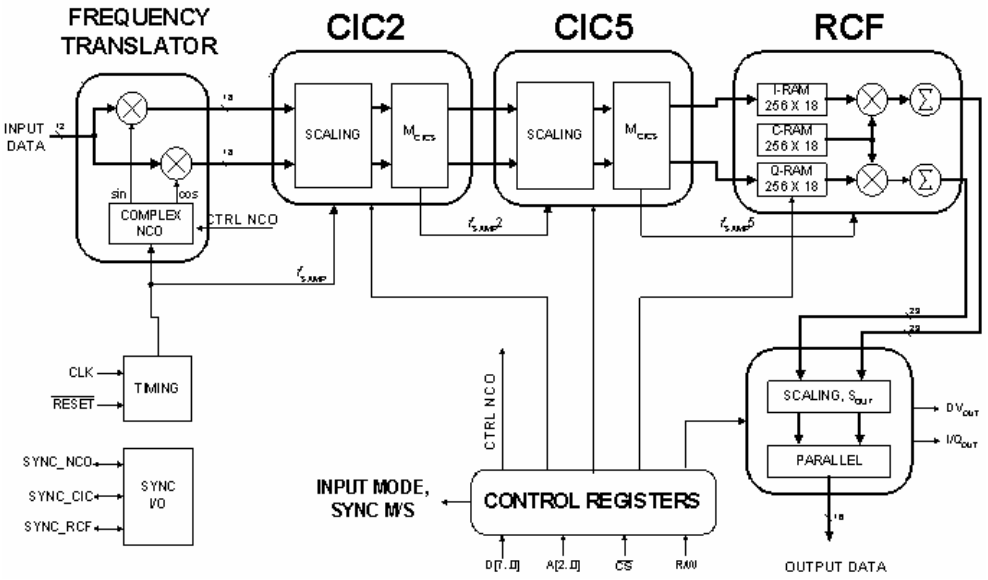

Figure 2 Block diagram of the Analog Devices AD6620 digital receiver

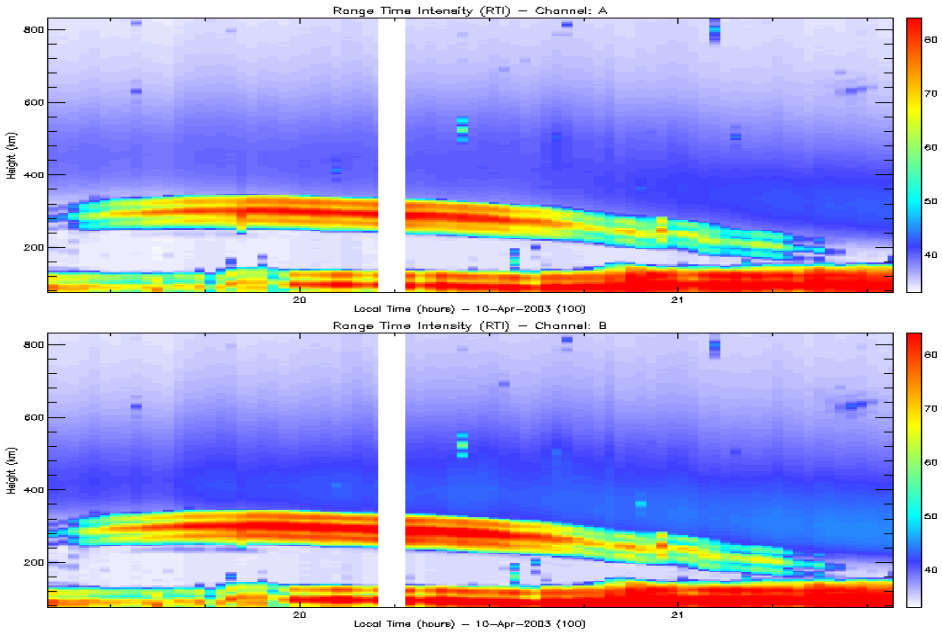

Figure 3 RTI Experiment 1

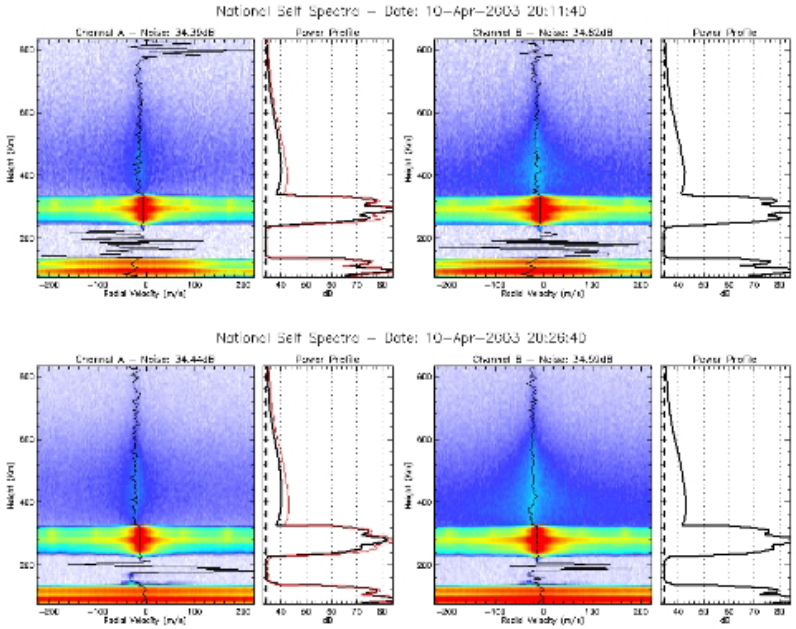

Figure 4 Power spectrum Experiment 1

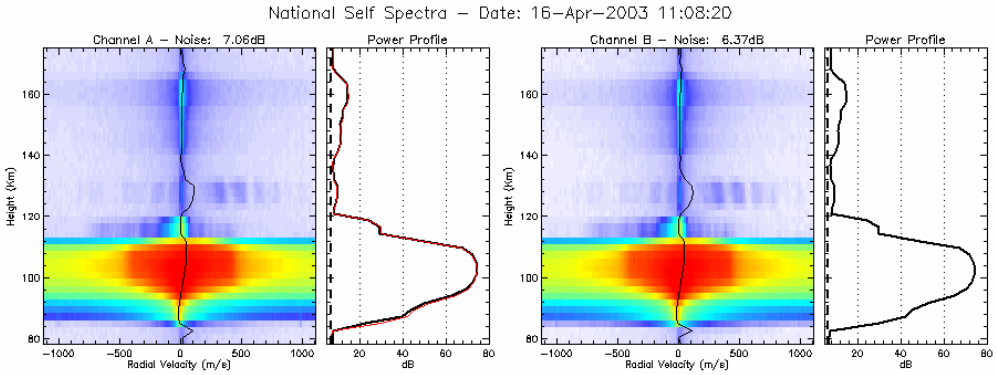

Figure 5 Power spectrum Experiment 2

ELECTRONIC DIGITAL BEAMFORMING IMPLEMENTATION FOR RADARS

R. NEY, S. BONAIMÉ, F. DOLON , J.J. BERTHELIER,
CETP/IPSL, 4 Avenue de Neptune, 94107 Saint-Maur Cedex, France
richard.ney@cetp.ipsl.fr

R. CLAIRQUIN, D. NEVEJANS
BIRA/IASB, Ringlaan 3, B-1180 Brussels, Belgium

C. DUVANAUD
LAII, Université de Poitiers, IUT, 4 Avenue de Varsovie, 16021 Angoulême Cedex, France

A. D'HERMIES
ESIEE, Cité Descartes, BP 99, 2 Bld Blaise Pascal, 93162 Noisy-le-Grand Cedex, France

Introduction.
Beamformers are complex networks used to precisely control the phase and amplitude of RF signals passing through them. They are used either in the transmission or the receiving mode and even in both modes. In RF transmitting systems for radars, beamformers are employed between the RF signal source and the radiating elements to shape the beam illuminating the target to be detected. In receiving systems beamformers are employed between the antenna arrays and the receiver to observe a specific region of space.
Beamformers can be implemented either with analog or digital components. Figure 1 illustrates the analog beamforming concept implemented on the Iceland and Kerguelen islands radars of the SuperDarn network. The beamforming elements are inside the Phasing Matrix box. Each antenna is associated to a power amplifier. Beamforming is performed in both transmitting and receiving mode.

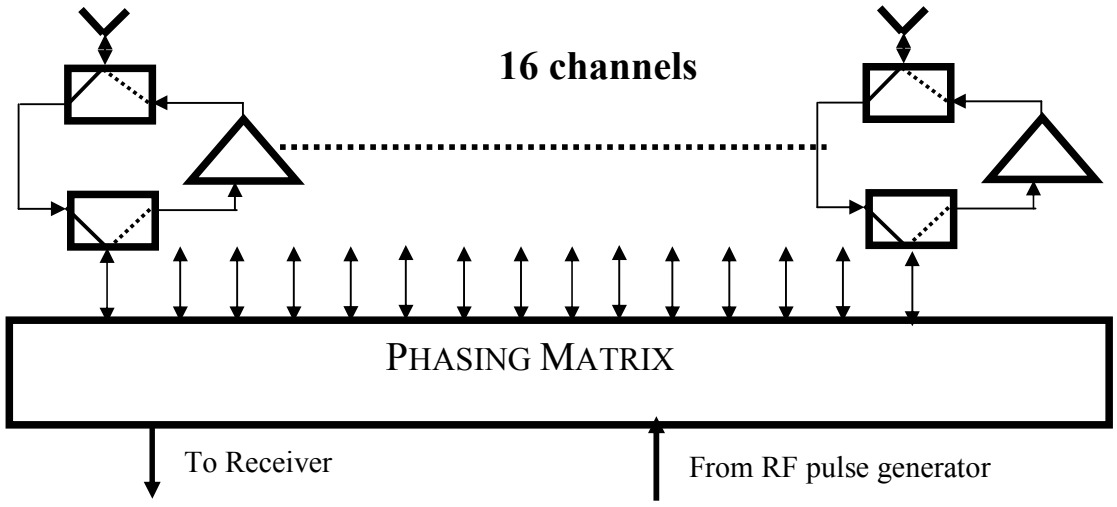

Figure 1: Analog beamforming on the Super DARN (Dual Auroral Radar Network) radars. Operating frequency band: 8-20 MHz, Frequency Agility capability

Digital beamforming.
The classical papers of Barton (1980) and Steyskal (1987) on digital beamforming describe the complete capabilities of the concept. It was emphasized in the 80's that the cost of the whole digital system was beyond the financial capabilities of Research Institutes. The permanent decrease of the cost of digital components in one hand and in the other hand the increase of their performances allow now to many users access to full Digital Beamforming.

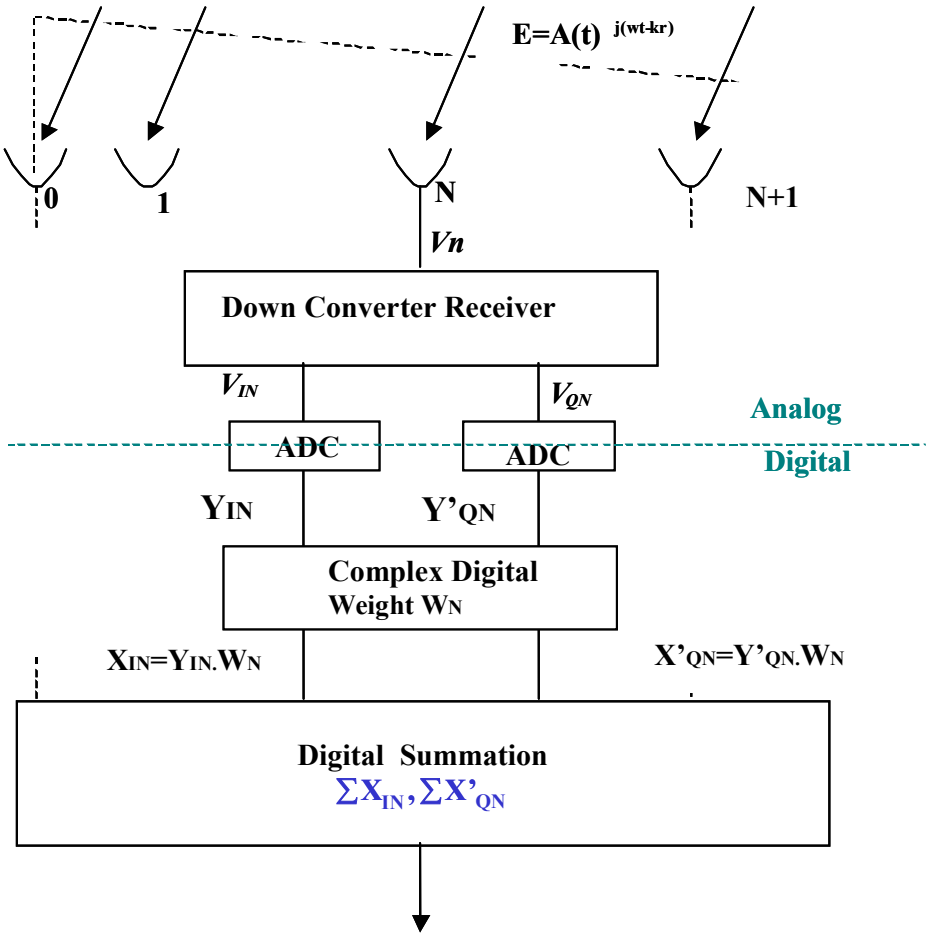

Figure 2 (from Steyskal, 1987) : receiving digital

Figure 2 (from Steyskal, 1987) shows a proposed architecture for a digital implementation in the receiving mode. Each antenna is associated with a complete receiver. After demodulation and analog to digital conversion the time series I and Q go through the unit where beamformer weights are applied. Finally all the signals from all the antennas are summed up.

The GPR of the NetLander mission.
A complete GPR (Ground Penetrating Radar) unit has been developed at CETP for the NetLander space mission devoted to the geophysical exploration of Mars (Ney et al 2002, Berthelier et al 2003). The goal of the radar is twofold: subsurface sounding for mainly water detection and ionospheric sounding for measurement of the ionospheric critical frequency thought to be around 3 MHz during the day and 0.5 MHz during night. The main constraint was the limited available 500g mass for the whole radar including antennas. This led to the development of a very compact unit integrated on two 15x13 cm boards.

The main element of the unit (figure 3) is a FPGA programmed in VHDL language which performs the digital wave generation through a DDS scheme, the full control of the radar operation and interface with a PC and the coherent integrations (up to 2^{24}) of 2500 range gates signals. The frequency range is 0.2 to 5 MHz and the output peak power is 10W. The receiver is a standard analog unit. For the field tests, the ON/OFF, the data transfer, the control parameters of the radar, are achieved through a wireless link between the PC and the radar. The data transfer is done according to a MIL STD 1553-like protocol.

A digital beamforming implementation.

Figure 4 illustrates the concept.

Each antenna of an antenna network has to be associated to an electronic unit. This architecture is very flexible and allows Digital Beamforming for both transmission and reception, or if desired for reception only.

This hardware can be applied to many radars in the HF and VHF bands. The analog receiver can be replaced by a digital receiver which implements the ADC at the HF or VHF level, digital demodulation and matched filtering on the I and Q baseband signals.

Conclusions.

The radar unit developed at CETP allows:

- Digital beamforming in the receiving and transmitting modes.
- A great number of range gates, a great flexibility (frequency generation, ability to oversampling, large range values for parameters…).
- The VHDL program can be implemented in any FPGA.
- Practical user interface.
- Medium cost.
- Extension to VHF frequency range, to higher transmitted power.
- Use of digital receiver (better performances and flexibility).

These features are likely to promote the use of digital beamforming at MF, HF, VHF frequencies in several fields such as ionospheric radars, ST radars, oceanographic radars…

References.

Barton, P., (1980). Digital beam forming for radar. *IEE Proceedings, Vol. 127, Pt. F, N°4, August,* pp. 266-277.

Berthelier,J.J., R. Ney, V. Ciarletti, A. Reineix, B. Martinat, M. Hamelin, F. Costard, W. Kofman, P. Paillou, C. Duvanaud, D. Nevejans, W. Kofman, J.G. Trotignon, G. Grandjean, M. Zamora and A. Nagy (2003). GPR, A Ground Penetrating Radar for the NetLander mission. *J. Geophys. Res., 108,* (E4), 8027.

Ney, R, J.J. Berthelier, V. Ciarletti, B. Martinat, M. Hamelin, M. Rodriguez-Cassola, F. Dolon, S. Bonaimé, A. Reineix, D. Nevejans, C. Duvanaud, F. Costard, and P. Paillou (2002). The Ground Penetrating Radar of the Netlander Misssion. *Proceedings of the Ninth International Conference on Ground Penetrating Radar, University of California, Santa Barbara, USA, Apil 29 – May 2*, pp. 541-5 46.

Steyskal, H. (1987). Digital Beamforming Antennas. *Microwave Journal, January 1987,* pp. 107-124.

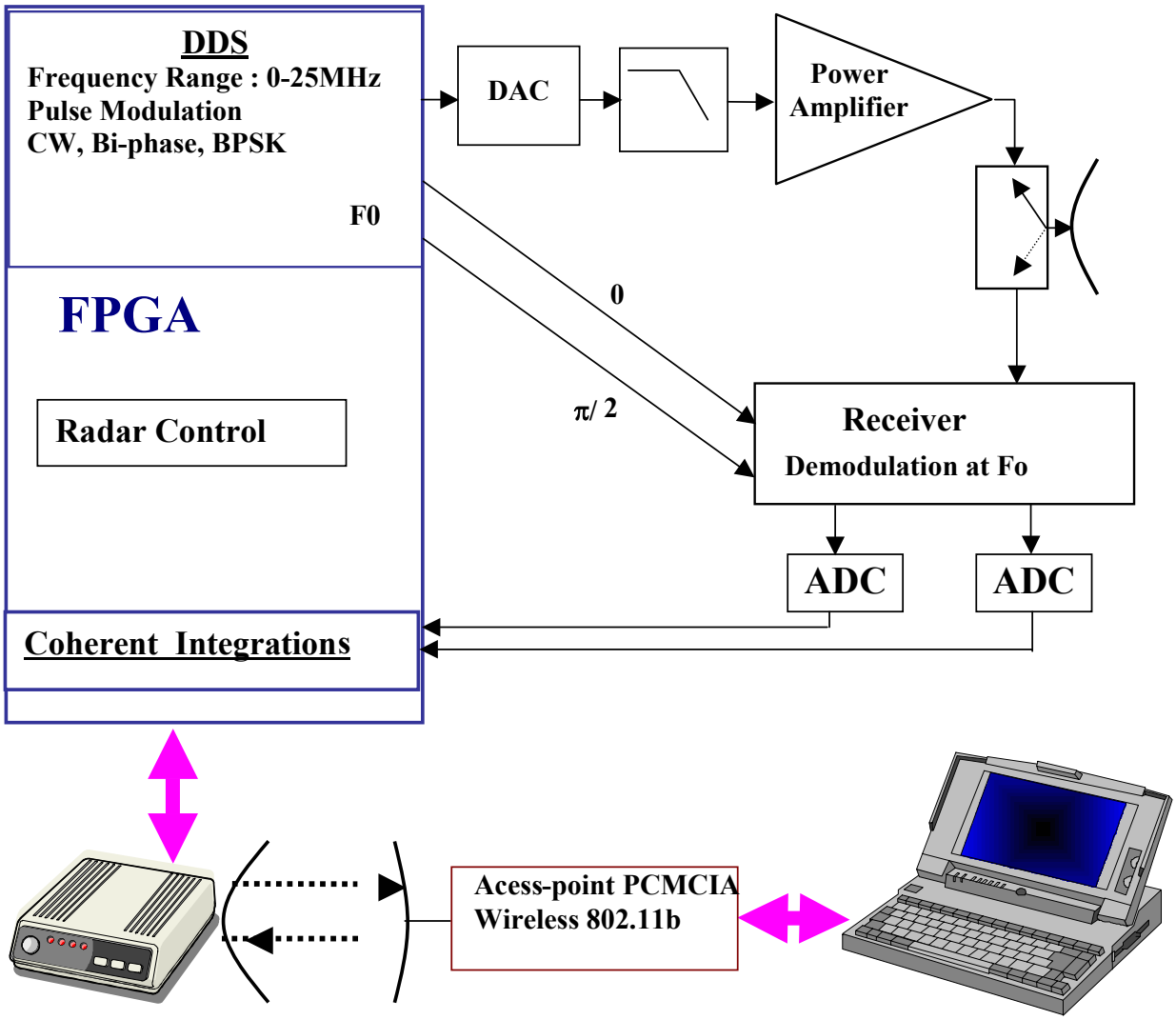

Figure 3 : The NetLander GPR radar architecture

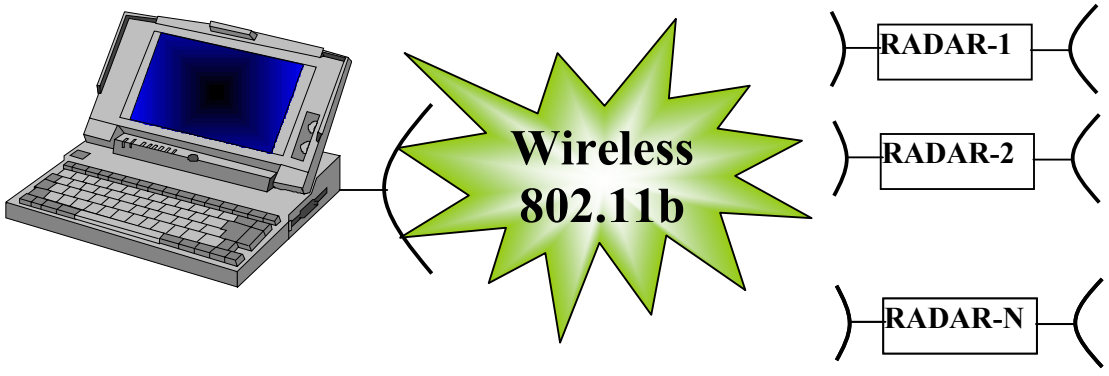

Figure 4: Example of a digital beamforming radar architecture

.

ON-LINE ADAPTIVE DC-GROUND-CLUTTER REMOVAL

Jürgen Röttger
Max-Planck-Institut, 37191 Katlenburg-Lindau, Germany

1. Summary

MST radar observations are frequently affected by partially strong clutter echoes from mountains and other fixed targets. The same holds for and incoherent scatter (IS) radar observations of the D-region. At the EISCAT Svalbard Radar (an incoherent scatter radar for studies of the polar cap upper atmosphere and ionosphere) for instance, the ground clutter even extends out to 100 km. This clutter is usually minimized by antenna optimization by means of suppressing horizontal side-lobes. Sato et al. (this issue, 2003) presented a new method suppressing sidelobes digitally. If there is a still remaining DC component, this can be removed by either interpolating the zero-frequency component (not too elegant method, though) in the Doppler spectrum or by the so-called DC subtraction. The former method eliminates a significant part of the signal or may even fail, when the atmospheric echo has a very narrow Doppler spectrum, comparable to the clutter spectrum. The latter method is usually done off-line on the raw data.

Here the design proposal of a simple digital hardware filter is presented, which allows on-line adaptive narrow-band-pass filtering (notching) for all individual range gates. It can be easily implemented into all MST radar systems and, due to its recursive and adaptive design, removes only a very negligible part of the atmospheric signal. Standard post-detection DC-removal methods are not required after this real-time on-line filtering**.**

2. The problem and solution

Ground clutter is not an unusual phenomenon in many radar applications and there exist several methods to eliminate the destructive effect on atmospheric and ionospheric observations. We will not discuss here the methods used in meteorological radar or MST radar applications, since these are described in the standard literature. These methods apply also for pulse coding, such as complentary codes.

The EISCAT radar systems need different applications, when complex auto-covariance functions are calculated before the ground clutter component is removed. This procedure was successfully used and is described by Röttger (1992) in EISCAT UHF radar observations of the troposphere. For ionospheric observations again another method has to be applied. This holds in particular when phase coding is used and the phase coding sequence changes from pulse to pulse, as it is the case in alternating codes. However, also effects on simple power profile and long pulse modulations are obvious. We present here a method, which will allow to reduce the ground clutter by some orders of magnitude. It will be described here for the most complicated application of alternating codes in the incoherent scatter application, but the principle is also applicable for other kind of coded and single pulse modulations of IS and MST radars.

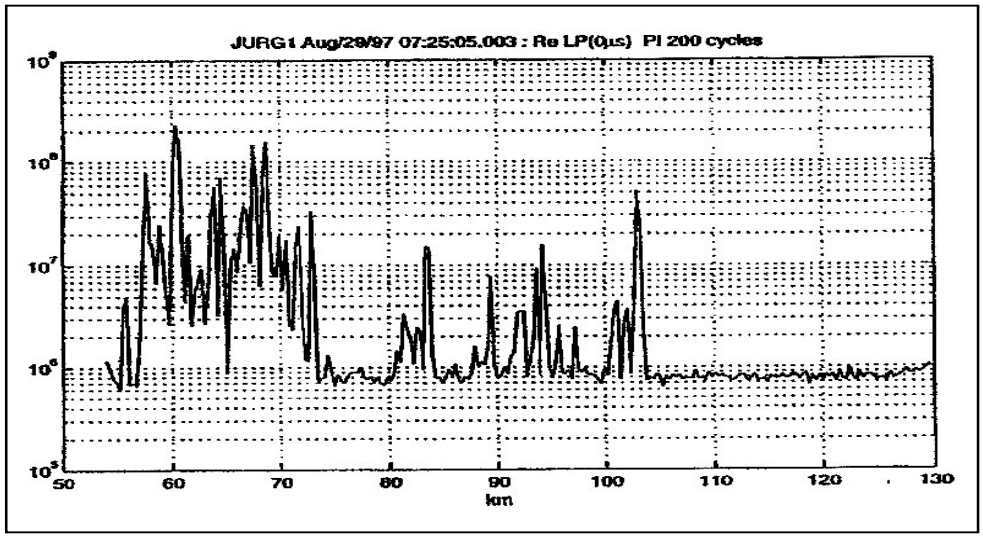

Fig. 1 Ground clutter profile of the EISCAT Svalbard Radar

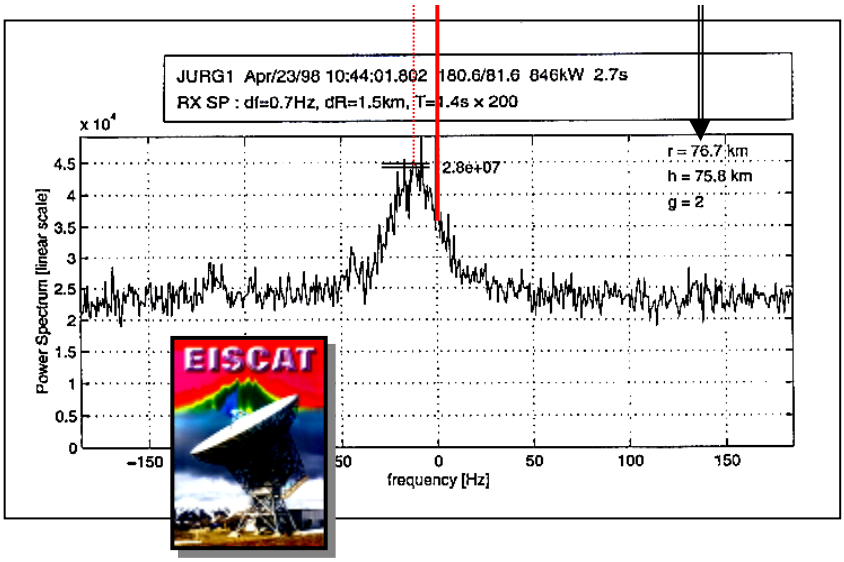

Fig. 2 A spectrum of an incoherent scatter signal from the D-region recorded with complementary coding of the EISCAT Svalbard Radar. The centre line is the ground clutter exceeding the signal level by more than 30 dB.

It is to be noted that this presented method, such as all yet applied methods of clutter removal by signal processing, requires absolute linearity of receiver and ADC. Such conditions should in most cases be fulfilled or the system can be improved to allow for these requirements. The following deliberations hold for mono-static radar measurements, since the ground clutter is not a problem in bi-static applications, such as the EISCAT UHF system.

The upshot of this proposed technique is the fact that the typical signal bandwidth of incoherent scatter signals is much wider than the bandwidth of ground clutter. Although the latter can fade,

resulting in a widening of the bandwidth, this is still much narrower than the incoherent scatter signal bandwidth.

Fig. 1 shows the ground-clutter profile of the EISCAT Svalbard Radar (ESR), which suffers particularly due to its elevated location. This radar uses incoherent scatter for ionospheric studies. An incoherent scatter spectrum is shown in Fig. 2. For simplicity we chose here the Lorentzian-type spectrum of scatter from the D-region. The power in the zero-frequency bin is strongly enhanced in Fig. 2, which indicates a strong ground clutter component. The same feature also applies for a typical double-humped incoherent scatter spectrum of a signal from the E- or F-region. The typical signal bandwidth of scatter from these altitudes is about 5-10 kHz, and the modulation does at most allow a frequency resolution better than a few hundred Hz (corresponding to a long pulse or coded pulse sequence of 1 ms duration). Typically, the total spectrum width can be up to ±25 kHz, corresponding to a code-baud length of 20 μs.

The typical bandwidth of ground clutter is not exceeding a few Hz, even if the clutter from long ranges is fading. The resolution bandwidth in the ISR applications is in the order of some 100 Hz (or less in the D-region applications), which means that in case of ground-clutter, the entire zero-frequency bin in the signal spectrum is spoiled. Since the signal covers usually covers 10-20 frequency bins, this zero-frequency falsification has a substantial effect on the total power and on the shape of the total spectrum, i.e. on the relevance of the analysed data (mostly the analysis would not converge in such cases).

One method to remove this ground clutter in the zero-frequency bin is to apply a spline interpolation using the power in the adjacent non-zero frequency bins. However, this is a fairly crude method, which still leaves a significant error, particularly when the signal spectrum is even narrower than the assumed 10 kHz, i.e. in lower E-region or E-region observations. There are more elegant and methods, which result in much smaller errors and which we will describe now.

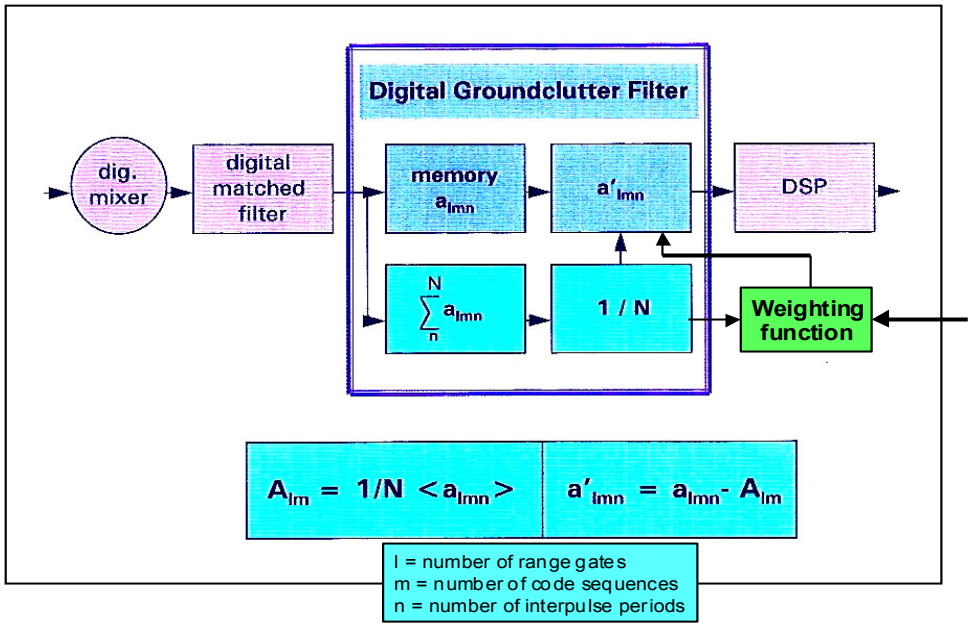

Fig. 3 Block diagram of a hardware DC-clutter filter

The signal bandwidth f_S in standard ISR applications is typically not narrower than 10 Hz (lower D-region) or not narrower than about 1000 Hz (E-region). The modulation is usually adapted to cover this bandwidth. We have measured that the bandwidth of ground clutter f_C is usually less than 0.1 Hz. Thus, the ratio of signal bandwidth and ground clutter bandwidth: $Q_f = f_S / f_C \geq 10$.
In D- and lower E-region ranges the ratio of signal power P_S and clutter power P_C:

$$Q_P = P_S / P_C \leq 0.01$$

Applying a resolution bandwidth f_b, adapted to the signal bandwidth f_S, can usually lead to major malfunctions of the analysis, since the ground clutter power will heavily override the signal power.Usually $f_C << f_S (> f_b) < f_n$ where f_n is the noise bandwidth

However, the resolution bandwidth f_R of any modulation should be adapted to the narrowest bandwidth (i.e., f_C) of the received signals, resulting from the composition of the complex amplitudes $a = a_S + a_C + a_n$ of the IS signal as, the ground clutter a_C and the noise a_n, in order to optimize the separation of these three components. In typical ISR applications this would lead to an enormous amount of data to be stored and analyzed, which may be impossible to be performed on-line, even with the fastest computer, since all complex samples of each range gate and interpulse period would have to be treated. A suitable way around this is the so-called DC-subtraction method, which is a standard applied in the MST radar applications.

Since $f_C << f_S < f_n$ the temporal variations of a_C are very much slower than those of a_S and a_n , we can apply a low-pass filter operation: $a' = a - \langle a_C \rangle$. It has to be considered that this manipulation has to be done for each range sample 1, and each code sequence m, over a suitable time period $T < 1 / f_C$, where $T = N \times T_{ipp}$ with **N =** number of inter-pulse periods T_{ipp}.

Example: Number of range gates l = 1, ..., L (L = 150)
Number of code sequences m = 1, ..., M (M = 32)
Number of interpulse periods n = 1, ..., **N (N =** T / T_{ipp})
For T = 10 s, and T_{ipp} = 5 ms, we get **N** = 2000.

The calculation of $\langle a_C \rangle$ and a' can be done on-line and is principally a digital (low-pass) notch filter with a bandwidth $f_l \sim f_C$. When the clutter fades, the DC-component will widen. The removal then can be accomplished by a corresponding weighting function, which can be changed adaptively using results of data post post-processing.

A hard- or soft-coded microprocessor, which is inserted between the digital matched filter and the digital signal processing (DSP), can be applied for this purpose. The filter output data format is equivalent to the standard input data format. Since f,- << fr, the signal power P_i lost by this notch filter operation is Pi / Ps << 1. Thus, there is negligible loss in signal power, and no loss in significance of the data.

The memory requirement for this digital filter operation is:

$$2 \times 2 \times L \times M \times N = 40 \text{ MB}$$

The throughput depends on Tipp. For the given example and Tipp = 5 ms it is 800 kB / s.

Reference:
J. Röttger "The status of EISCAT as MST radar and plans for the EISCAT Svalbard Radar in the ST mode", Proceedings of the Fifth Workshop on Technical and Scientific Aspects of MST Radar, 501-506, 1992.

ON THE RADIATION EFFICIENCY OF COCO ANTENNAS

Martin F. Sarango, Ronald F. Woodman and Darwin Cordova

Jicamarca Radio Observatory, Apartado 13-0207, Lima 13, Peru

1. Introduction

In the austral summer of 2000-2001 we installed a 4x4 Yagi array at the Artigas Uruguayan Base in King George Is, Antarctica. We originally planned for a simultaneous run with the Peruvian MST radar at Machu-Picchu, also at King George Is. However, due to logistical problems with the latter system the simultaneous observations were not performed. The Machu-Picchu antenna is of the COCO (coaxial-collinear) type with a ~10 dB larger physical antenna aperture than the Yagi array. To our surprise, the PMSE echoes at Artigas were stronger than the ones previously observed at Machu-Picchu (Balsley et al., 1995 and Woodman et al., 1999), for the same time of the year.

In order to determine if the differences can be attributed to antenna performance or to a large PMSE annual variability, we have proceeded to make an experimental calibration of the performance of both systems, mainly of their antennas. This experiment has been carried out at the Jicamarca Radio Observatory using equatorial electrojet echoes and a third common transmitter-receiver antenna for the comparison. We have determined that the COCO antenna gain has to be corrected by an efficiency factor of ~2 dB over whatever is the efficiency of the Yagi array. Part of the loss in efficiency is of ohmic nature and part is due to an uneven current distribution in the COCO line elements.

2. Calibration Experiments

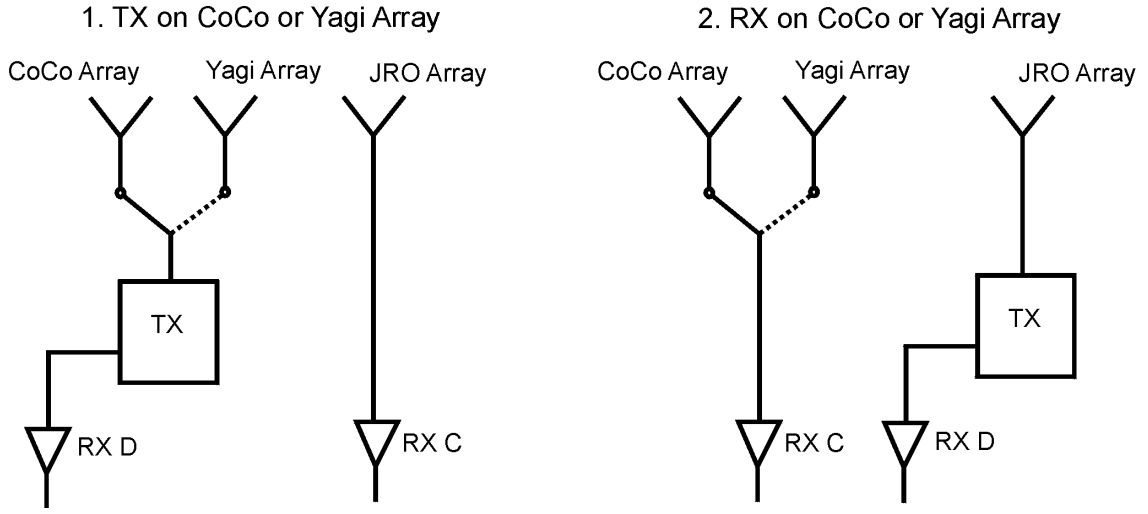

Figure 1: Configuration of the calibration experiments. The left and right panels show the TX and RX configuration respectively.

The calibration experiments were performed using three 50 MHz antenna arrays: a 15x15 m Yagi array (see description in companion paper); a 12x100 m COCO array; and the JRO array (~300x300 m). The two different configurations used for the comparisons are shown in Figure 1.

Experiment #1: Transmission on COCO and Yagi Arrays

In the first configuration/experiment the transmission and reception (RXD) is alternated between the COCO and Yagi arrays, while the JRO array is used as a reference receiving

system (RXC). This configuration allows evaluating the efficiency of the arrays during transmission, as well as the total efficiency for both radar systems.

Experiment #2: Reception on COCO and Yagi Arrays

The second configuration/experiment allows evaluating the receiving efficiency of the two arrays. As shown in Figure 1, the JRO array is used for transmission and the COCO and Yagi arrays are alternated for reception (RXC).

The basic idea for the calibration experiments was to make *quasi* simultaneous observations of the scattering phenomena; i.e., the Equatorial Electrojet, using the Yagi, COCO, and JRO arrays. The three arrays are used according to the experiment configurations described above. The effective antenna dimensions for the COCO and Yagi arrays are shown in Table 1.

Table 1: COCO and Yagi antenna array dimensions

Antenna array	**East-West dimension (*X*)**	**North-South dimension (*Y*)**
COCO Array	$L_{C,X} = 12.0$m	$L_{C,Y} = 100$m
Yagi Array	$L_{Y,X} = 18.6$m	$L_{Y,Y} = 18.6$m

An artist representation of the corresponding antenna patterns for the three arrays is shown in Figure 2. The JRO array is supposed to have a very small radar cross section related to the COCO and Yagi antenna patterns. The elements/lines of the Yagi/COCO arrays are oriented in the North-South magnetic direction (*Y*). The longest dimension of the COCO array (100m) also corresponds to the *Y* direction.

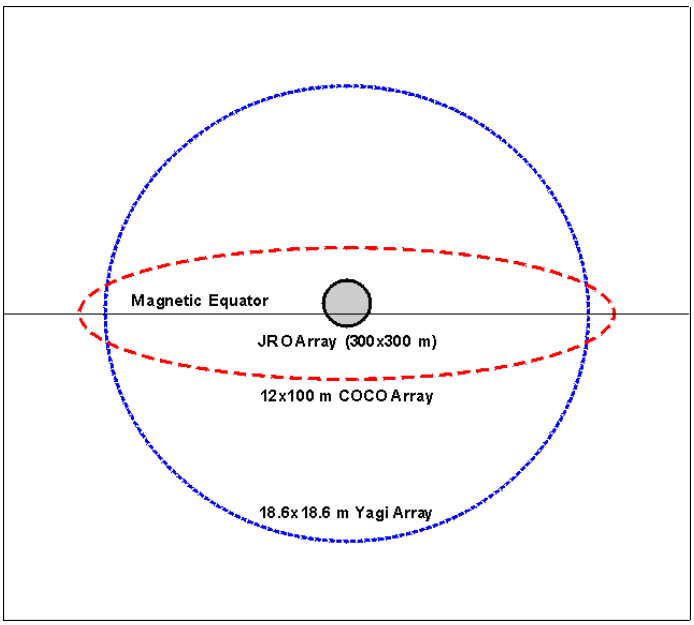

Figure 2: Artist representation of the antenna patterns and the corresponding pointing directions with respect to the Geomagnetic Equator.

3. Experiment Results

Several calibration experiments have been performed after the 2000-2001 Antarctic campaign. The results presented and discussed here correspond to data gathered in December 1st, 2003.

The signal power ratios, S_C/S_Y, for the experiments #1 and #2 are shown in Tables 2 and 3 respectively.

Table 2: Experiment #1 results, Transmission on COCO and Yagi Arrays		
RX Antenna Array	**S_C/S_Y (SNR, dB)**	**S_C/S_Y (Total Power, dB)**
COCO / Yagi (RXD)	13.9237	11.1051
JRO (RXC)	5.4195	5.6255

Table 3: Experiment #2 results, Transmission on JRO Array		
RX Antenna Array	**S_C/S_Y (SNR, dB)**	**S_C/S_Y (Total Power, dB)**
COCO / Yagi (RXC)	5.9739	5.5257

Using the values shown in tables 2 and 3 we can calculate the efficiency ratio between the COCO and Yagi Arrays. If we consider two radar systems that differ only in their antenna arrays, with areas A_Y y A_C and efficiencies ε_Y y ε_C, the ratio of received power S_C/S_Y is given by:

$$\frac{S_C}{S_Y} = \frac{G'_C V_C G'_C}{G'_Y V_Y G'_Y} \tag{1}$$

The antenna gain, G, for an ideal antenna is proportional to its area. The real gain G' is corrected by an efficiency factor (ε), that takes into account: how good is the illumination of the area (ε_B); and any Ohmic loss (ε_Ω).

$$G' = G\varepsilon = kA\varepsilon_B\varepsilon_\Omega = kA\varepsilon \tag{2}$$

Then, we can write,

$$\frac{S_C}{S_Y} = \left(\frac{G'_C}{G'_Y}\right)^2\left(\frac{V_C}{V_Y}\right) = \left(\frac{\varepsilon_C A_C}{\varepsilon_Y A_Y}\right)^2\left(\frac{V_C}{V_Y}\right) \tag{3}$$

If A has a simple geometry, $A \sim Ap$; and the dispersion media is aspect sensitive, with sensitivity angles smaller than the antenna beam-width; and we suppose that δ is the angle in the Y direction; each scattering volume is given by δ and the inverse of the corresponding antenna dimension in the X direction.

$$V_Y = \frac{\delta}{L_{Y,X}} \quad ; \quad V_C = \frac{\delta}{L_{C,X}} \tag{4}$$

We can write:

$$\frac{S_C}{S_Y} = \left(\frac{\varepsilon_C}{\varepsilon_Y}\right)^2\left(\frac{L_{C,X}L_{C,Y}}{L_{Y,X}L_{Y,Y}}\right)^2 \frac{\delta}{\delta}\frac{L_{Y,X}}{L_{C,X}} \tag{5}$$

and then,

$$\left[\left(\frac{\varepsilon_C}{\varepsilon_Y}\right)^2\right] = \left[\frac{S_C}{S_Y}\right] - \left[\left(\frac{L_{C,Y}}{L_{Y,Y}}\right)^2\right] - \left[\frac{L_{C,X}}{L_{Y,X}}\right] \tag{6}$$

where the [] operator denotes 10*Log10 operation. The Total Power results for RXD in table 2 correspond to Transmission and Reception with the COCO and Yagi Arrays; i.e., the radar case. Replacing these results in (6) we obtain:

$$\left[\left(\frac{\varepsilon_C}{\varepsilon_Y}\right)^2\right] = 11.1051 - 14.6 + 1.9 = -1.5949 dB \quad (7)$$

For the independent Transmission and Reception experiments (RXC in Tables 2 and 3), we must consider the areas only one time in equation (5). The calculated efficiency ratios for the transmission and reception experiments are -1.67 dB and -1.7743 dB respectively. These results conform very well to the result in (7).

Finally, as the insertion loss difference between the COCO and Yagi Arrays was 0.5 dB in favor of the COCO; the total efficiency ratio is -2.0949 dB.

4. Conclusions

We have calculated the total efficiency ratio between COCO and 3-element Yagi array, and found that the COCO antenna gain has to be corrected by an efficiency factor of ~2 dB over whatever is the efficiency of the Yagi array.

Acknowledgments: The VHF radar at the Peruvian Antarctic Station "Machu-Picchu" is an important part of the Peruvian research activities in Antarctica. We would like to acknowledge the support received from the Jicamarca Radio Observatory staff.

References

Balsley, B.B., R.F. Woodman, M. Sarango, R. Rodriguez, J. Urbina, E. Ragaini, J. Carey, M. Huaman, and A. Giraldez, On the lack of southern hemisphere polar mesosphere summer echoes, *J. Geophys. Res., 100(D6)*, 11685-11693, 1995

Woodman, R.F., B.B. Balsley, F. Aquino, L. Flores, E. Vasquez, M. Sarango, M. Huaman, and H. Soldi, First observations of polar mesosphere summer echoes in Antarctica, *J. Geophys. Res., 104(A10)*, 22577-22590, 1999

A NEW NARROW BEAM MF RADAR AT 3 MHZ FOR STUDIES OF THE HIGH-LATITUDE MIDDLE ATMOSPHERE: SYSTEM DESCRIPTION AND FIRST RESULTS

W. Singer[(1)], R. Latteck[(1)], D. Holdsworth[(2)], T. Kristiansen[(3)]

(1) Leibniz-Institut für Atmosphärenphysik, Schloss-Str. 6, D-18225 Kühlungsborn, Germany
(2) Atmospheric Radar Systems, 1/26 Stirling St., Thebarton, SA, 5031, Australia
(3) Andøya Rocket Range, Andenes, Norway

Abstract

A new narrow beam MF radar operating at 3 MHz with Doppler beam swinging and spaced antenna capabilities has been installed close to the Andøya Rocket Range as part of the ALOMAR observatory to improve the ground based capabilities for studies of the dynamical structure (small scale features, turbulence) of the upper mesosphere. The characteristics of radio wave scatterers can be studied now in a wider frequency range by common volume observations with the ALWIN MST radar at 53.5 MHz (Latteck et al., 1999). The Saura MF radar is a joint experiment of the Andoya Rocket Range, the Communication Research Laboratory, Tokyo and the IAP. The radar has been developed by Atmospheric Radar Systems (ATRAD). Observations of PMSE signatures at 3 MHz and interleaved Doppler winds and spaced antenna winds using Full Correlation Analysis are presented. First results of interleaved measurements of Doppler and spaced antenna winds, of momentum flux estimates using co-planar beams, of turbulent kinetic energy dissipation rates, and signatures of polar mesosphere summer echoes (PMSE) at 3 MHz are discussed.

System description

The system operating at 3.17 MHz was put into operation nearby Andenes (Fig. 1) in July 2002 applying spaced antenna observations and reached its full Doppler capability in

Table 1: Saura MF radar

Location	69.30°N, 16.04°E
Frequency	3.17 MHz
Peak power transmitter	116 kW
Peak power incl. cable loss	40 kW
Transceiver modules	62 (each 2 kW)
Base band receiver	4
Pulse width	7, 10, 13.3 μs
Range resolution	1, 1.5, 2 km
Sampling resolution	1, 1.5, 2 km
Pulse repetition frequency	max. 200 Hz
Length of time series	min. 60 s

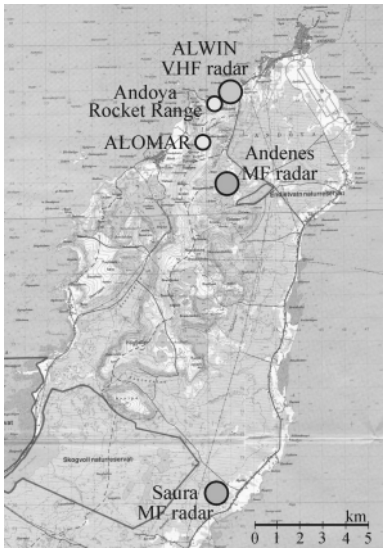

Figure 1: Map of the northern part of the Andøya island/Norway.

Table 2: Antenna system

Typ	*Mills-cross*
Spacing	70 m
Polarization	circular (O, X)
Crossed half wave dipols used on	
- Transmission	1 ... 29
- Reception	
DBS mode	1 ... 26
SA mode	4
user mode	4
Gain	19 dB
Beam width (HPFW, one way)	6.6°/13.8°
Beam directions	
- azimuth	NW, SE, NE, SW
- zenith	vertical, 7.3°, 17.2°
Interleaving modes	O/X polarization co-planar beams

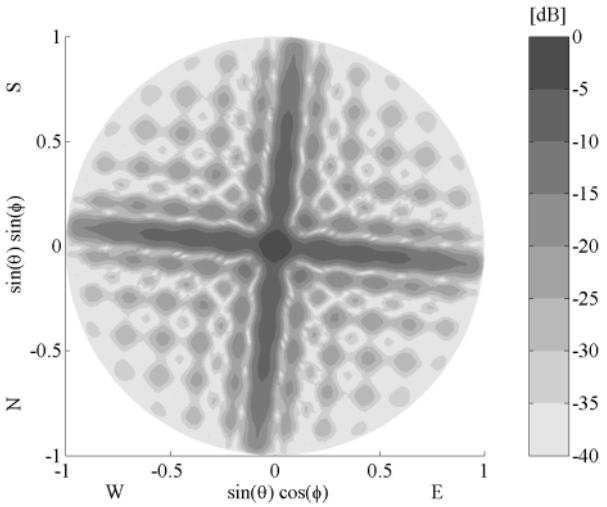

Figure 2: Radiation pattern (top view) of Saura MF radar antenna for a vertically pointed narrow beam.

April 2003. Various Doppler beam steering (DBS) techniques as well as spaced antenna applications can be applied. The main feature of the new radar is the narrow beam transmitting/receiving antenna which is formed by 29 crossed half-wave dipoles arranged as a *Mills-Cross*. The spacing of the crossed dipoles is 0.7 wave lengths resulting in a minimum beam width of 6.6° (**H**alf-**P**ower-**F**ull-**W**idth, one way). Each dipole is fed by its own transceiver unit with a peak power of 2 kW and individually controlled in phase on transmission and reception (Fig. 3). This design provides high flexibility in beam forming and beam pointing as well as capability forming right and left circular polarisation (ordinary and extraordinary magneto-ionic component). The IF outputs of the two transceivers feeding one crossed dipole are combined into one signal and led to a combining unit of the IF signals. In DBS mode, the IF signals of the seven crossed dipoles of each arm of the Mills cross are combined into one receiver (down converter).

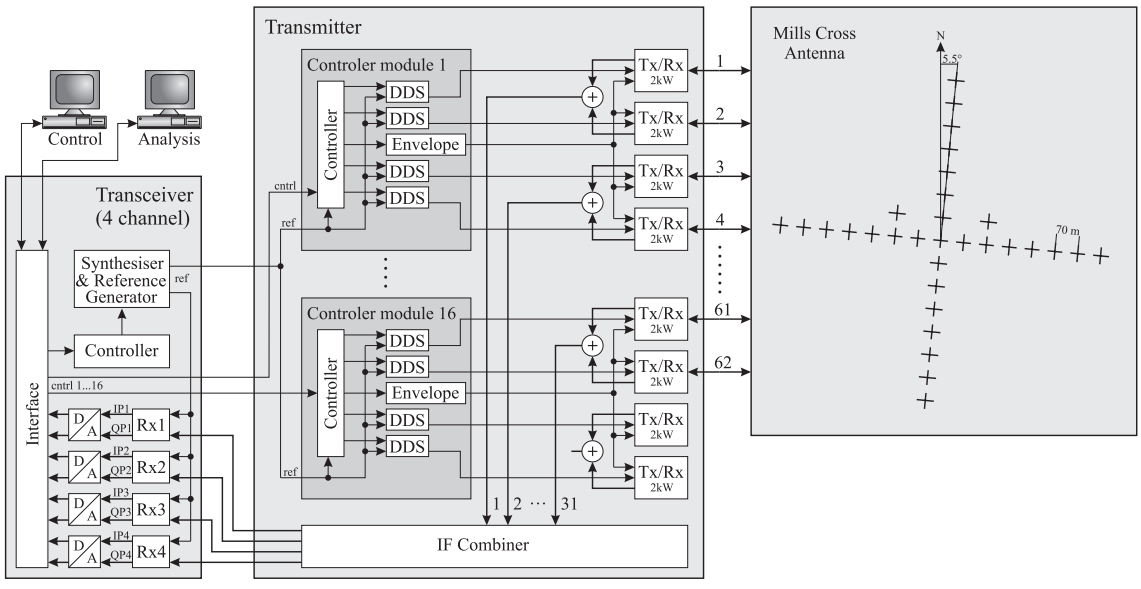

Figure 3: Saura MF radar block diagram

Off-zenith beams towards N, S, E, W and NW, NE, SE, SW at 7.3°/17.2° can be formed. Fig. 2 shows the radiation pattern of the vertically pointed narrow Doppler beam. In addition, beams with different widths at the same pointing angle can be formed. For multiple receiver applications four independent receiving channels and two additional crossed dipole arrangements are available. The parameters of the radar system and of the Mills cross antenna are summarized in Tables 1 and 2.

Radar experiments and first results

Spaced antenna experiments can be performed with four independent receiving channels each connected with a crossed dipole, two additional cross-dipole arrangements outside the Mills cross (see Fig. 3) combined with the center antenna and the second antenna cross of the south arm provide the classical "Y" arrangement for spaced antenna observations using the Full Correlation Analysis (FCA). In addition one crossed dipole can be selected from each antenna arm for Imaging Doppler Interferometry (IDI) experiments and for observations of radar backscatter from meteor trails using the so-called user mode. Fig. 4 presents horizontal winds determined from spaced antenna observations with the narrow beam Saura radar and the broad beam ALOMAR MF radar (Singer et al., 1997) together with narrow beam Doppler winds. The FCA winds are in reasonable agreement with the Doppler winds obtained simultaneously by the Saura radar with indication that the broad beam FCA winds are slightly underestimated.

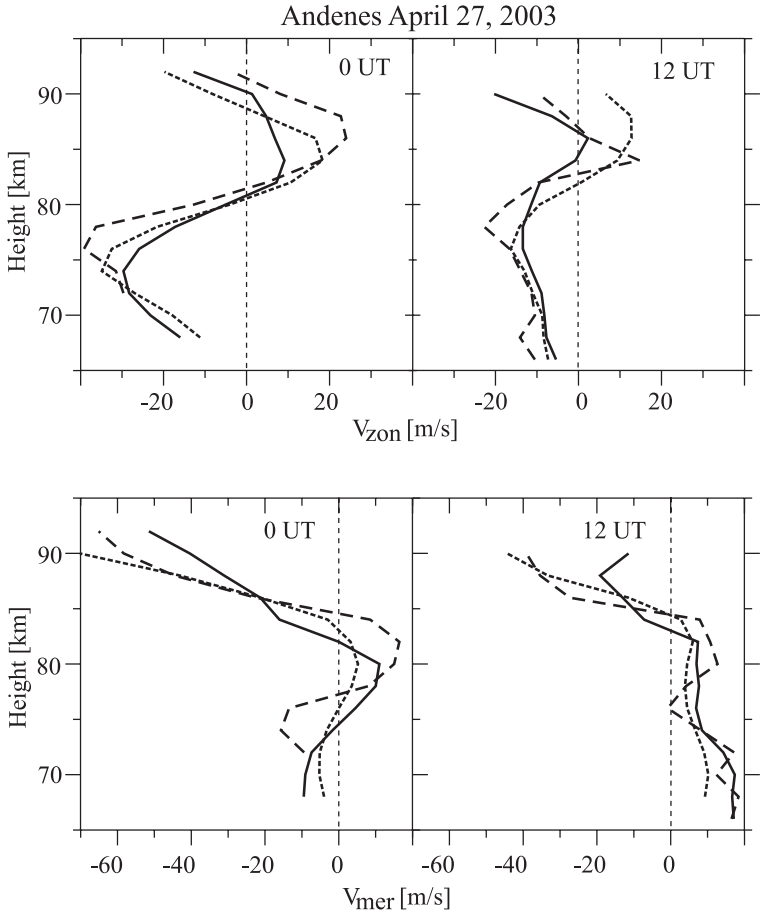

Figure 4: Comparison of simultaneous, co-located Doppler (short dashed lines) and spaced antenna winds from a narrow beam MF radar (long dashed lines) with spaced antenna winds from a wide beam MF radar (solid lines)

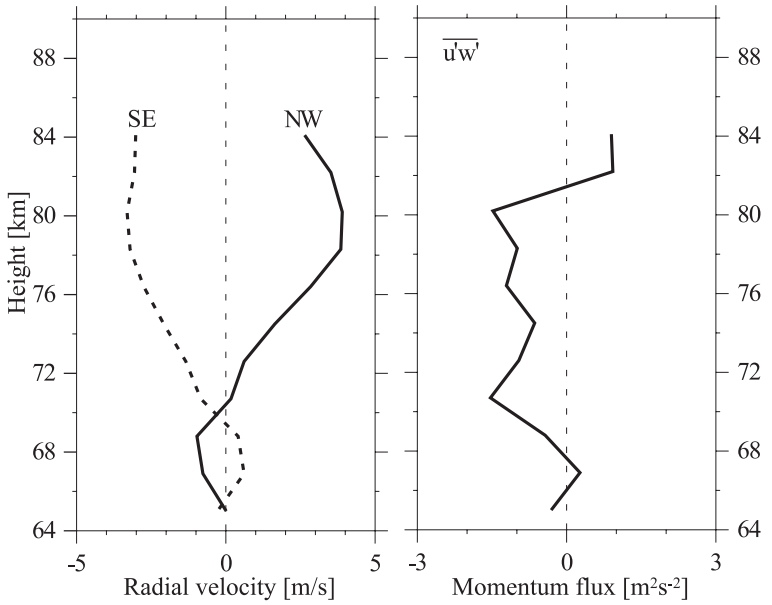

Figure 5: Mean radial velocities and zonal momentum flux obtained with interleaved oblique beams (HPFW=6.6°) directed towards NW and SE at 17.2° zenith angle .

Doppler beam swinging measurements are possible at various off-zenith directions with various beam widths. Two beam widths of 6.6° and 13.8° (**H**alf-**P**ower-**F**ull-**W**idth, one way) can be applied. The radar beam can be steered into the vertical direction and towards 7.2° and 17.2° off-zenith at 8 azimuthal directions with preference into the directions NE, SW, NW, and SE with the lowest background noise levels. The high flexibility of Doppler beam swinging experiments allows Doppler wind measurements with different off-zenith beams, estimation of momentum fluxes and of turbulent spectral widths using different techniques. Mean radial velocities and fluxes of horizontal momentum obtained by interleaved beam swinging from data point to data point in the NW-SE plane are shown in Fig. 5. The application of the nested beams technique (VanZandt et al., 2002),

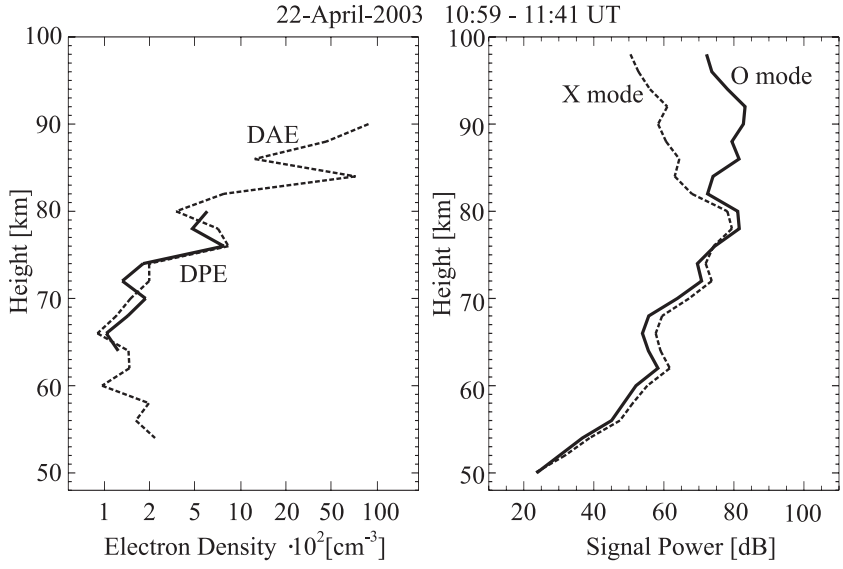

Figure 6: Electron densities derived from the Differential Absorbtion Experiment and the Differential Phase Experiment. Interleaved observations with ordinary (O mode) and extra-ordinary (X mode) polarization.

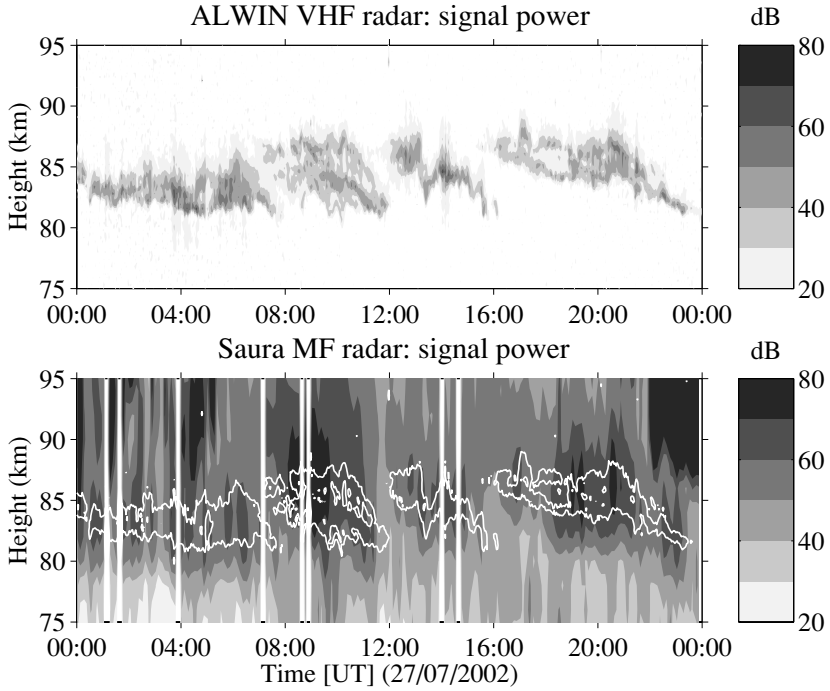

Figure 7: Height-time plots of radar echo power observed with ALWIN VHF radar (53.5 MHz) and Saura MF radar (3.17 MHz) during the appearance of PMSE in the VHF observation. The PMSE signatures in the VHF range are overlayed to the MF radar echo power.

that means soundings with a narrow and a broad beam at an off-zenith angle of 17.2°, provides estimates of the turbulent kinetic energy dissipation rates comparable to the results by rocket soundings (Latteck et al., 2003).

Radar observations of the mesosphere can be done with different polarisations of the transmitted signal. Interleaved transmission of the ordinary and extraordinary polarisation with a change of the polarisation from data point to data point provides differential absorption (DAE) and differential phase (DPE) mesasurements resulting in estimates of the electron number density (Fig. 6). The electron number density profiles derived with the DAE/DPE method are in remarkable good agreement.

Narrow beam MF radar observations during the appearance of polar mesosphere summer echoes (PMSE) detected with the ALWIN VHF radar show clear signatures of excessive signal power at PMSE altitudes during these events (Fig. 7).

Summary and outlook

The Saura MF radar was put into operation in July 2002 with spaced antenna observations and reached its full performance for Doppler beam swinging operations in April 2003. The new system has high flexibility in forming of Doppler beams with various beam widths at different off-zenith angles and azimuths. Spaced antenna and Doppler beam swinging measurements provide 3D winds, estimates of horizontal momentum fluxes and of turbulent kinetic energy dissipation rates. Height profiles of the electron number density are obtained from differential absorption and differential phase measurements. The Saura MF radar, ALWIN MST radar, ALOMAR MF radar, and lidars (ALOMAR RMR lidar, ALOMAR Weber sodium lidar) at the ALOMAR observatory are located within distances by up to 16 km allowing common volume observation in the MF/VHF frequency

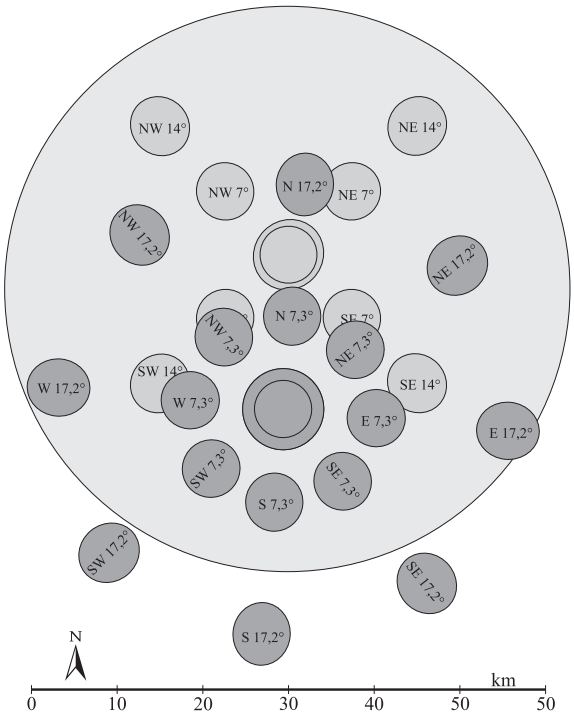

Figure 8: Areas at 85 km altitude illuminated by oblique and vertical beams of ALWIN VHF radar (gray), Andenes MF radar (light gray) and Saura MF radar (dark gray).

range (Fig. 8, see also Fig. 1). Correlative experiments with the co-located radars, lidars, and in-situ measurements from sounding and meteorological rockets launched from the Andoya Rocket Range allow intercomparisons of different remote and in-situ techniques as well as complementary studies of mesospheric/lower thermospheric processes.

Acknowledgments

The authors wish to thank the engineers and technicians of the Leibniz-Institut für Atmosphärenphysik and the Andøya Rocket Range for their engagement building up the new antenna system and installing the radar system. Also, the authors express their appreciation to the staff of Atmospheric Radar Systems, Australia for their cooperative support in solving problems connected with remote radar operation and control.

References

Latteck, R., W. Singer, and H. Bardey, The ALWIN MST Radar - Technical design and performances, in *Proc. 14th ESA Symp. on European Rocket and Ballon Programmes and Related Research*, ed. by B. Kaldeich-Schürmann, vol. SP-437, 179-184, 1999.

Latteck, R., W. Singer, and N. Engler, Application of the dual-beam width method to a narrow beam MF radar for estimation of turbulent spectral width, *in this issue*.

Singer, W., D. Keuer, and W. Eriksen, The ALOMAR MF radar: Technical design and first results, in *Proc. 13th ESA Symp. on European Rocket and Ballon Programmes and Related Research*, ed. by B. Kaldeich-Schürmann, vol. SP-397, 101-103, 1997.

VanZandt, T. E., G. D. Nastrom, J. Furumoto, T. Tsuda, and W. L. Clark, A dual-beamwidth radar method for measuring atmospheric turbulent kinetic energy, *Geophys. Res. Lett.*, Vol. 29, No. 12, 13-1 - 13-3, 2002.

ANTENNA BEAM VERIFICATION USING COSMIC NOISE

T. K. Carey-Smith, A. J. McDonald, W. J. Baggaley, R. G. Bennett, G. J. Fraser and G. E. Plank

Department of Physics and Astronomy, University of Canterbury, Christchurch, New Zealand.

To obtain accurate vertical wind measurements using a VHF radar, the pointing direction of the antenna beam must be known precisely. Antenna beam patterns can be investigated using aircraft, satellites [*Sato et al.*, 1989], the sun [*Graf et al.*, 1971] and extra-solar radio sources [*Campistron et al.*, 2001]. In this study, different methods of beam verification using cosmic noise sources have been investigated. With data obtained from the new Canterbury University Stratosphere Troposphere Atmospheric Radar (CUSTAR) in Christchurch, New Zealand (43° 49.5′ S, 172° 41.5′ E), the antenna's pointing direction has been derived by comparison with discrete radio sources and also a 45 MHz sky map. The comparison has been performed by fitting Gaussian curves to the individual noise sources and also by performing a cross-correlation over the whole sky map. The pointing direction of the beam has also been investigated using measurements of the vertical velocity. The results indicate that if a sky survey is available at a similar frequency and latitude to that of the radar then the optimum method of verifying the beam pattern is to compare the right ascensions and widths of individual noise sources with corresponding peaks in the radar sky noise profile.

1 Calculating the sky noise

CUSTAR operates at 42.5 MHz and uses a square antenna array made up of 128 individual elements. The theoretical half-power full-width of the main beam is 6.35° and the largest sidelobe is 13 dB below the main peak. The sky noise measured by the radar was calculated from the background noise, which was obtained using the method of *Hildebrand and Sekhon* [1974].

On a typical day, for ranges less than 5 km the background noise is contaminated by instrumental noise, mainly due to leakage of the transmitter pulse through to the receiver input. Above 5 km, sky noise becomes the dominant feature. However, enhancements can be observed in this region and are due to other events such as reflections from aircraft. For the CUSTAR data these areas were removed by averaging over the 25 range bins (at each time point) that contained the lowest noise level. Approximately half of the total number of bins were used so that the time series is smoothed considerably, while the possibility of including areas of unwanted noise, such as aircraft reflections, is minimized.

2 Comparison with discrete radio sources

Three strong radio sources pass through the beam of the CUSTAR antenna array, these are the Vela-Puppis region (Vela XYZ), Centaurus A and part of the galactic equator. The galactic equator is a broad ridge of high radio emission so does not have exact coordinates, but

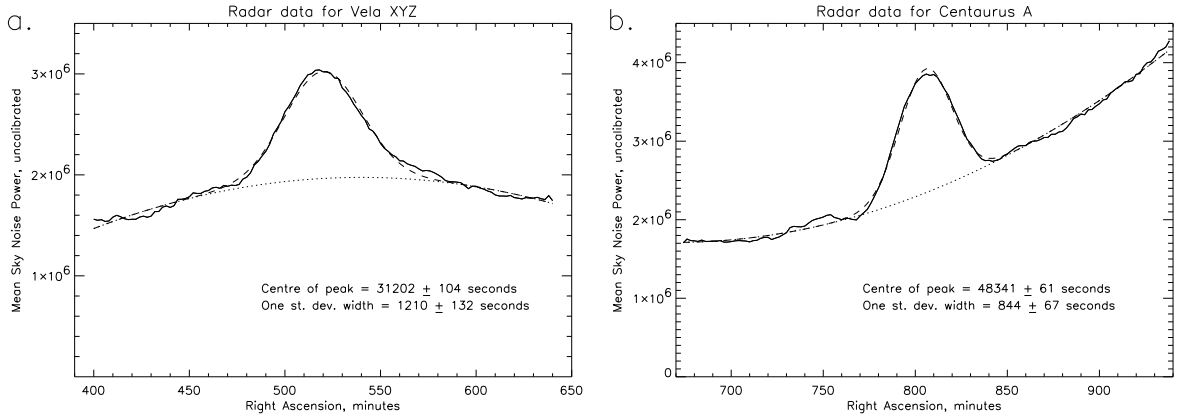

Figure 1: CUSTAR data (solid line) for **(a)** Vela XYZ and **(b)** Centaurus A. The dotted line is the polynomial fit and the dashed line is the Gaussian plus polynomial fit.

Vela XYZ and Centaurus A have relatively small angular sizes, so their positions and widths can be accurately defined.

Sky noise data from the CUSTAR radar was averaged over a 4 month period and the regions associated with Vela XYZ and Centaurus A are shown by solid lines in Fig. 1. A Gaussian plus polynomial curve (dashed line) was fitted to these peaks to ascertain the central point and also the width of the peak.

The differences between the deduced right ascensions and the expected coordinates are $-64\,\mathrm{s} \pm 140\,\mathrm{s}$ and $17\,\mathrm{s} \pm 73\,\mathrm{s}$ for Vela XYZ and Centaurus A, respectively, where the negative sign means that the CUSTAR antenna observed the source earlier than expected. The uncertainties in these values arise mainly from the spread in the CUSTAR data over the four months that were included in the average, giving each point included in the Gaussian fitting routine a large uncertainty. The widths of the fitted Gaussians can also be compared to the widths of the radio sources, and these differences came to $2.7^\circ \pm 1.7^\circ$ for Vela XYZ and $1.7^\circ \pm 0.9^\circ$ for Centaurus A.

3 Comparison with 45 MHz sky map

A 45 MHz sky map was convolved to the theoretical resolution of the CUSTAR antenna [*Alvarez et al.*, 1997]. This is displayed as a solid line in Fig. 2 and the CUSTAR sky noise data is included as a dashed line. The three peaks from left to right correspond to Vela XYZ, Centaurus A and the galactic equator. The two data sets agree very well, which is expected because they are not only of the same resolution and declination, but also at very similar frequencies.

In a similar way to the data shown in Fig. 1, Gaussian curves are fitted to the peaks corresponding to Vela XYZ and to Centaurus A in the sky map data. The differences between the right ascensions are $-20\,\mathrm{s} \pm 104\,\mathrm{s}$ and $-66\,\mathrm{s} \pm 61\,\mathrm{s}$ for Vela XYZ and Centaurus A, respectively. The differences between the widths come to $-1.2^\circ \pm 1.5^\circ$ for Vela XYZ and $-1.1^\circ \pm 0.9^\circ$ for Centaurus A.

These results have similar uncertainty values to those obtained from comparisons with discrete sources, however the results are in some cases quite different. This demonstrates the limitation of this method, which arises from the accuracy of the reference source position. However, all the lags calculated are within $\simeq 1$ minute (or 0.25°).

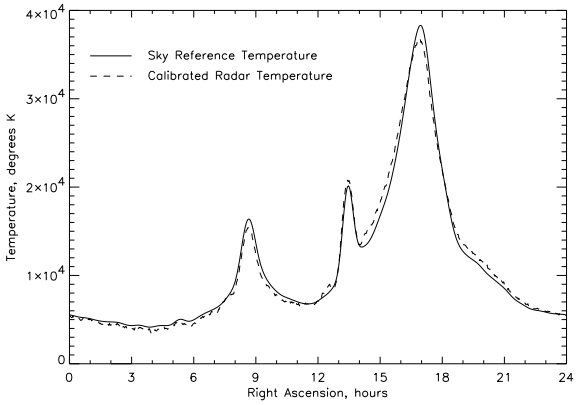

Figure 2: A 45 MHz reference sky temperature map (solid line) and the calibrated radar temperature (dashed line).

The beam direction was also estimated by performing a cross-correlation between the sky map data and radar data (i.e. between the two curves in Fig. 2). This produced a lag of -146 s $\pm$ 120 s, which is much greater than any of the previous methods. This deviation may be due to differences observed on the edges of the galactic equator, where the two curves rise at slightly different rates.

4 Verification using vertical velocity

The pointing direction of the beam can also be estimated by analysing the long-term mean of vertical wind velocities measured using the radar. At mid-latitudes, the mean vertical velocity over a period of three or four months should be near zero[1]. This will not be the case, however, if the radar antenna beam is tilted off-vertical, as a component of the horizontal wind, which is significantly stronger than the vertical wind, will be measured along with the vertical wind.

Figure 3a contains the mean horizontal wind from September 1 to December 28, 2002, obtained from the NCEP/NCAR reanalysis dataset and shows a westerly flow which reaches a maximum velocity at just above 10 km. The magnitude of the vertical bias, Δw, produced by a horizontal wind, v, for an off-vertical beam is given by $\Delta w = v \sin\theta$, where θ is the angle off vertical in the direction of v. The mean vertical velocity as measured by the radar from September 1 to December 28, 2002, is shown in Fig. 3b (solid line). Also included is the expected bias caused by the horizontal wind (dashed line) and its uncertainty (dotted line). There is clearly a significant downward vertical velocity in the radar profile, but the features of the vertical velocity profile do not match those of the expected bias, in fact, the peaks are in quite different locations. This suggests that the non-zero mean vertical velocity is unlikely to be caused by horizontal wind contamination.

5 Conclusion

This paper has described experiments that were performed to verify the beam pattern of the CUSTAR antenna array. A technique which involved measuring the variation of sky noise over

[1]Most long-term means measured using existing VHF radars have, however, shown a typical downward vertical velocity of a few cm s^{-1} [e.g. *Nastrom and VanZandt*, 1994].

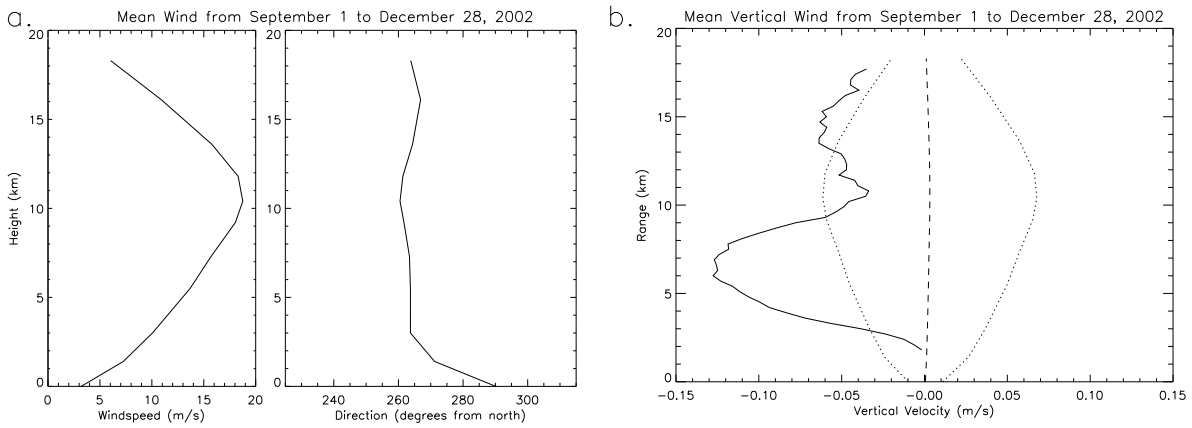

Figure 3: (a) Mean horizontal wind speed and direction from September 2002 to December 2002, obtained from NCEP/NCAR reanalysis dataset. **(b)** Mean vertical wind speed measured by the radar (solid line) and the expected horizontal contamination (dashed line).

the sidereal day was utilized. The results obtained show that the antenna array behaves almost exactly as expected.

It was found that the most accurate method of finding the beam pointing direction and beam-width was the comparison of individual radio source patterns, as measured by the radar, with their expected patterns. It should be noted that excellent sky noise results were obtained while the radar was in normal operation, demonstrating the value of this technique, as it can be used to continuously monitor the antenna beam pattern and also the system stability. The availability of both a 45 MHz sky map and high resolution data allowed for independent estimations of the source locations. The difference in location was comparable to the uncertainty in the radar sky noise data, producing a limitation in accuracy of $\simeq 0.25°$.

References

Alvarez, H., J. Aparici, J. May, and F. Olmos, A 45-MHz continuum survey of the southern hemisphere, *Astron. Astrophys. Suppl. Ser.*, *124*, 315–328, 1997.

Campistron, B., G. Despaux, M. Lothon, V. Klaus, Y. Pointin, and M. Mauprivez, A partial 45 MHz sky temperature map obtained from the observations of five ST radars, *Ann. Geophys.*, *19*, 863–871, 2001.

Graf, W., R. N. Bracewell, J. H. Deuter, and J. S. Rutherford, The sun as a test source for boresight calibration of microwave antennas, *I.E.E.E. Trans. Antennas. Prop.*, *AP-19*, 606–612, 1971.

Hildebrand, P. H., and R. S. Sekhon, Objective determination of the noise level in doppler spectra, *J. Appl. Meteorol.*, *13*, 808–811, 1974.

Nastrom, G. D., and T. E. VanZandt, Mean vertical motions seen by radar wind profilers, *J. Appl. Meteorol.*, *33*, 984–995, 1994.

Sato, T., Y. Inooka, S. Fukao, and S. Kato, Multi-beam pattern measurements of the MU radar antenna by satellite OHZORA, *J. Geomag. Geoelectr.*, *41*, 743–751, 1989.

AN ATTEMPT TO CALIBRATE THE UHF STRATO-TROPOSPHERIC RADAR AT ARECIBO USING NEXRAD AND DISDROMETER DATA

P. Kafando* and M. Petitdidier

CETP/CNRS, Vélizy, France, monique.petitdidier@cetp.ipsl.fr
On leave to Ouagadougou University, Burkina Faso (petronille.kafando@univ-ouaga.bf)

1- Introduction

During the period, September 15th-October 16th 1998, a campaign devoted to thunderstorm observations took place at NAIC, Puerto Rico. Several instruments were deployed on the Observatory site, like a disdrometer. Other instruments, in the eastern part of the island, have been operated by the National Weather Service like the rain gauges, radiosondes and the NexRad Radar.

The goal of this paper is to present an attempt to calibrate the backscattered signal of the UHF radar. Several studies reported such calibrations. They have been done with a collocated disdrometer, reflectivities being compared. The lowest reliable heights are below 500m (Gage et al., 2000; William et al., 2000). The ST radar at NAIC observed from a lowest altitude around 5.9km, that is above the melting layer (4.8km). As a consequence the collocated disdrometer cannot be used to calibrate the radar. Another difficulty comes by the fact that the running parameters like the transmitted power and the attenuation, put in order not to saturate the receiver, may be changed at any time during the same experiment and are not recorded with the data. Then, an attempt has been done to calibrate the UHF radar at Arecibo by using the NexRad radar data located in Cayey (PR). But, one uncertainty may be the NexRad data calibration. In order to avoid any assumption for the Z-R relationship that it is highly variable during one event, reflectivities are compared. Ulbrich and Lee (1999) have shown that a systematic offset in radar constant explains the large discrepancies observed when rainfall amounts, deduced from NexRad reflectivity, are compared to the rain gauge ones. The authors found an offset around -5.4dB. Then the first step has been to compare the NexRad reflectivity with the reflectivity deduced from the disdrometer data. Once this work done, the comparison between the reflectivity observed by the UHF radar and the NexRad radar is carried out. As the attenuation of the UHF backscattered signal varies as a function of time to avoid the receiver saturation the gain of the different period has to be evaluated using the noise power. Then the backscattered signal is corrected by this factor and the comparison is done in the common range.

2- Data set

During that period, there were 18 days out of 29 when rain was detected by the disdrometer but only 7 with a rain amount larger than 10mm. Simultaneous measurements of disdrometer, and NexRad Radar occurred only on 3 days, September 18 and 30 and October 15. Among these 3 days, on two days only, September 30 and October 15, we have simultaneous ST and NexRad data during the thunderstorm activity. Finally, only on October 15 the UHF radar was working, on September 30 there was only the VHF radar working.

3- NexRad Calibration

Calibration set-up

First, from the latitude and longitude of each instrument, using different geoide models we calculate the distance and the azimuth of the disdrometer relatively to the NexRad radar.

The distance between NexRad and the disdrometer is found equal to 75978m, with an angle between both instruments found equal to 289.86°. The final distance and azimuth were adjusted.

At this range from the radar, the central beam is a thousand meters above the surface and is well below the freezing level around 4.8km for all thunderstorms. The beamwidth of the NexRad radar is relatively broad.

Disdrometer data

The data were collected with a Disdromet Joss-Waldvogel disdrometer (Joss and Waldvogel, 1967). One-minute samples of DSDs were collected for 29 days from September 15th to October 15th, 1998. Rain was observed on 18 days, and the total number of DSDs equals 1298 samples.

The JWD records the number of raindrops, nd_i, of diameter D_i, in each of its 20 diameter channels, for a one-minute sampling period.

From the DSD data the radar reflectivity is deduced:

$$\mathbf{Z = 10^{9} \int_{0}^{\infty} D^{6} N(D) dD}$$

Z is expressed in mm^6m^{-3} with D, dD in m and N(D) m^{-4}.

The drawback of the instrument is in presence of strong rains.

NexRad data

The Doppler weather radar, NexRad, is installed atop Cerro Baldios, around 8.15 km east of the city of Cayey, in the south-western part of the island. The WSR-88D units are powerful 10cm wavelength radars with approximately 1° beam width by 250m range resolution and volume scan sampling frequency of 5 or 6mn according to the mode selected (Crum et al., 1993). The discrete values of the elevations provide a relatively poor vertical resolution from 1.26 km to 1.76 at 16km. For the elevation greater than 10°, the vertical resolution goes from 2.8 to 4km. Just above the disdrometer, the radar beamwidth is about 1.3km.

According to the weather conditions, a specific scanning mode is selected. On October 15, the precipitation mode, VCP11, selected consists of volume scans at 14 elevations from 0.4° to 19.5°. The time resolution is 5mn with a pulse length of 1.57µs. On September 30, a precipitation mode, VCP21, was also operating but with only 9 elevations. The time resolution is 6mn.

Comparison

From the relation (3), the reflectivity is deduced for the three days, September 18 and 30, and October 15. Figure 1 presents the variation of the reflectivity, Z_d, observed on October 15, superimposed and indicated by a star the values of the NexRad reflectivity, Z_{Nx}.

Due the height difference between the disdrometer and the central beam axis above the disdrometer, i.e. 1050m, the time delay between the precipitation located into the NexRad beam and the observed one by the disdrometer varies according to the mean diameter from 2 to 4mn. Due to the beamwidth that is quasi perpendicular to the cloud and intercepts a range of 1.3 km around a mean altitude of 1.4km MSL. the time delay could not be precise.

Gage et al. (2000) found a difference of about 2mn between the UHF reflectivity at 327m and the disdrometer one.

The first result points out no significant difference between the computed reflectivity and the observed one by the radar in the event observed. At least, if it exists it will be relatively small.

4- UHF calibration

Calibration set-up

During this experiment the measurements were carried out simultaneously at UHF (430MHz) and VHF (46.7MHz) with a 2µs pulse, the inter pulse period (IPP) being 1ms. The relationship to compute the mean height of the first sample or gate takes into account the zenith angle, and various delays (Cho, Private communication, 1994). In UHF, the first gate

is at 4.7 km, but in the first 4-gates the signal cannot be used. Consequently the lowest useful gate was at 5.9 km, an altitude that does not allow observation of the melting level, which in the tropics is typically around 4-4.5 km. The first 50 gates are consecutive and their sampling starts at 40 μs; the last ten gates correspond to the calibration; the sampling of this group starting at 900 μs. The in-phase and in-quadrature data are recorded without any coherent integration. The UHF radar operated in the near-field. The three-decibel beam radius was 0.085° at UHF.

During this campaign UHF and/or VHF ST radar observations were carried out. We gathered data on 11 storm days of UHF and VHF observations from 14:00 AST until 16:00 AST, 4 days with only the VHF radar and 1 day (October 15) with only the UHF radar.

UHF data

On October 15, the thunderstorm activity is important over the observatory. A strong updraft is observed from 20:05 until 20:15 above 5.9km**.** Due to the lightning activity until 20:40, the attenuation was modified and its variation is clearly detected on the noise level and the calibration. From the mean values of the noise level a correcting factor is applied to the UHF reflectivity data.

Comparison UHF-NexRad data

The corrected reflectivity of the ST UHF radar is averaged over 1.2km in order to be compared to the reflectivity observed by the NexRad Radar. The altitude chosen was 8km From 19:45 until 20:33 on both curves similar variations are observed with more details on the UHF data plot (Fig.2a). This first attempt points out a time delay between the two patterns that could be due to a cut in the NexRad data close to the UHF radar but not just above. The ratio between the peak is different. Further investigations are on going.

Discussion and Conclusion

In this paper, we present the first attempt to calibrate the UHF ST radar at NAIC by using a scanning radar, calibration of which is verified by a disdrometer. The calibration of the NexRad radar does not present a noticeable offset. The comparison between the UHF radar and the NexRad needs more investigation at different heights.

References

Gage, K.S., C.R. Williams, P.E. Johnston, W.L. Ecklund, R. Cifelli, A. Tokay and D.A. Carter, Doppler Radar profilers and calibration tools for scanning radars. *J. Appl. Meteor., 39, 2209-2222*, 2000.

Petitdidier, M., C.W. Ulbrich, P. Laroche, E.F. Campos, and E. Boyer, Tropical Thunderstorm campaign at Arecibo, PR. *Proceedings of the ninth workshop on technical and scientific aspects of MST radar and combined with COST-76 final profiler workshop,. 401-404*, 2000.

Ulbrich, C.W., and Lee, L.G., Rainfall measurement error by WSR-88D radars due to variations in Z-R law parameters and the radar constant. *J. Atmos. Oceanic Tech., 16, 8, 1017- 1024*, 1999.

Ulbrich, C.W., Petitdidier, M., Campos, E.F., Radar properties of tropical rain found from disdrometer data at Arecibo, PR. *Proceedings of the 29th International Conference on Radar Meteorology, pp676- 679*, 1999.

Ulbrich, C.W., and N.E. Miller, Experimental test of the effects of Z-R law variations on comparison of WSR-88D rainfall amounts with surface rain gauge and disdrometer data. *Weather and Forecasting, 16, 369-374*, 2001

Williams, C.R., A. Kruger, K.S. Gage, A. Tokay, R. Cifelli, W.F. Krajewski and C. Kummerow, Comparison of simultaneous rain drop size distributions estimated from two surface disdrometers and a UHF profiler. *Geophys. Res. Lett., 27, 1763-1766*, 2000.

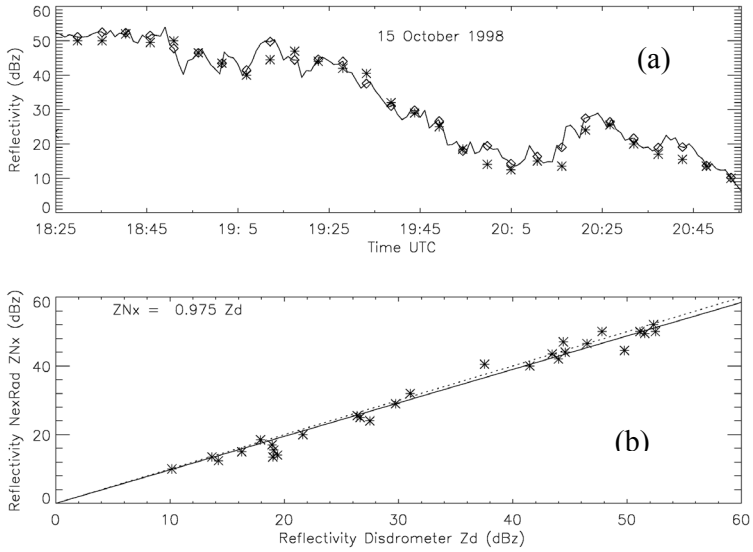

Figure 1: (a) Reflectivity computed from disdrometer data (- and diamonds), and measured by NexRad (*)
(b) Reflectivity NexRad data plotted as a function of the reflectivity computed from disdrometer data.

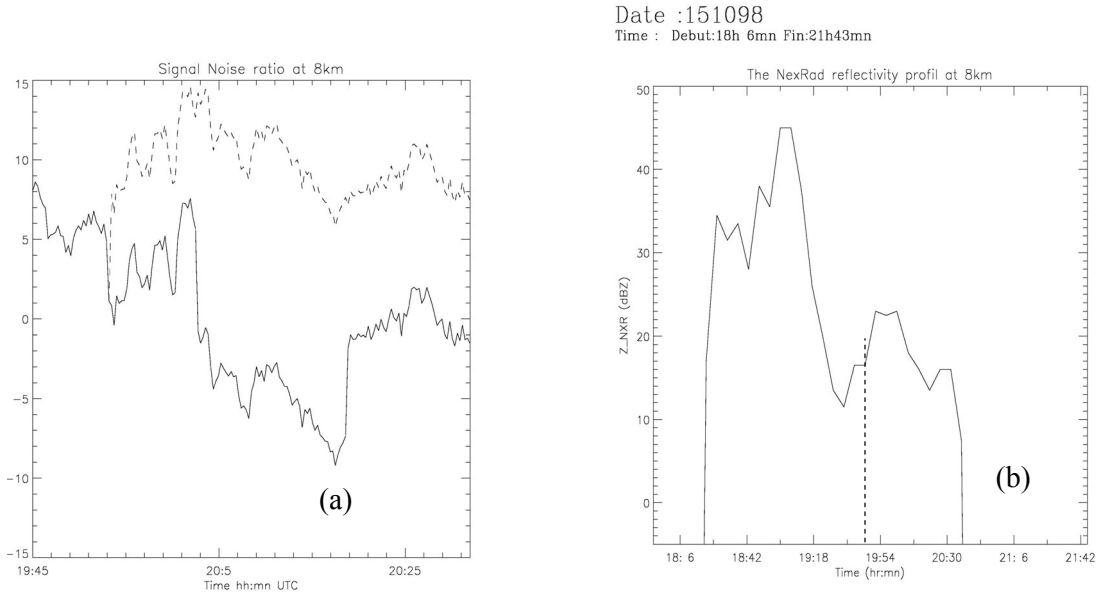

Figure 2 : (a) UHF signal-to-noise ratio expressed in relative dB, dashed line corrected from the attenuation, averaged over 1.2km around 8km.
(b) NexRad reflectivity expressed in dBz at 8km. The dashed line is at the time when the UHF data started.

QUALITY CONTROL FOR DOPPLER WIND PROFILERS USING NIMA

Corinne S. Morse[1], Robert K. Goodrich[1, 2], Larry B. Cornman[1], and Stephen A. Cohn[1]

1. National Center for Atmospheric Research, P.O. Box 3000, Boulder, Colorado 80307 USA
2. Department of Mathematics, University of Colorado, Boulder, Colorado, USA

Introduction

The NCAR Improved Moments Algorithm (NIMA) was developed to support the use of Doppler wind profilers for wind hazard detection in an airport environment. (Cornman, et al., 1998; Morse, et al., 2002) In this application, rapidly updated winds are required and the traditional quality control method of long term moments averaging is not appropriate. Human experts can often discern the atmospheric signal in a spectral plot, rejecting clutter and other contaminants, but this approach is also not practical in a real-time application. NIMA attempts to mimic the performance of the human expert (Cohn, et al., 2001) to detect features within the spectra and identify them as atmospheric, ground clutter, radio-frequency-interference (RFI), or noise, and to do so in a totally automated fashion.

Because each profiler site has some unique characteristics, NIMA was designed to be configurable for each application. The default parameters of the NIMA configuration were developed in response to our primary application on three 915 MHz profilers in Juneau, Alaska. Some other users of NIMA have been able to use these default parameter settings and obtain satisfactory results. Other sites produce spectra with significantly different characteristics and tuning has been required to optimize the performance. This poster illustrates one such case for a profiler operating in a very dry climate.

NIMA Algorithm Overview

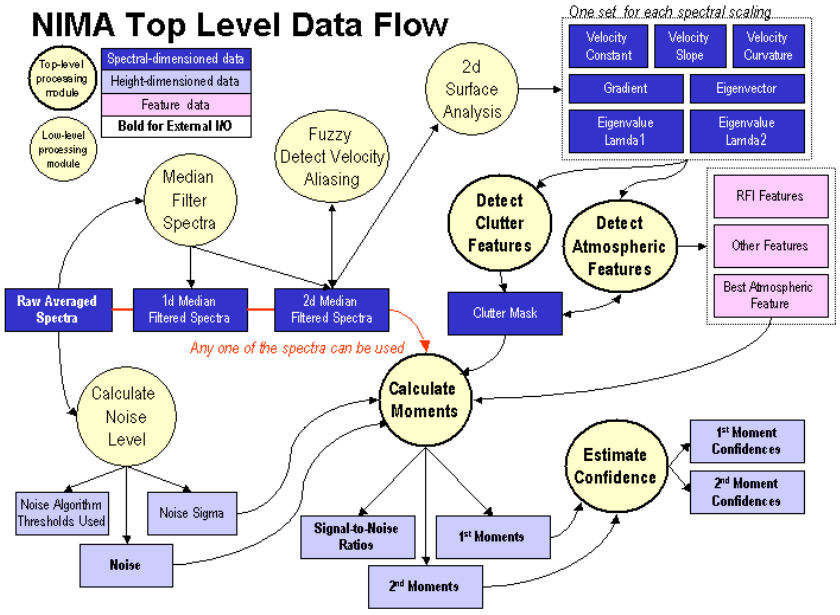

Figure 1. Summary of overall NIMA processing and data flow.

The overall processing flow of the NIMA algorithm is shown in Figure 1. Some of the major processing steps are illustrated in Figures 2-3 using an example spectrum from the north beam of the Juneau Lemon Creek profiler containing ground clutter, RFI, and point target contaminants. Figure 2 shows the averaged spectra both as stacked spectra and as the spectral intensity contour over Doppler velocity (x) and range (y). Median filtering in velocity and range mitigates the effects of point target contamination and smoothes the spectral surface to facilitate mathematical analysis.

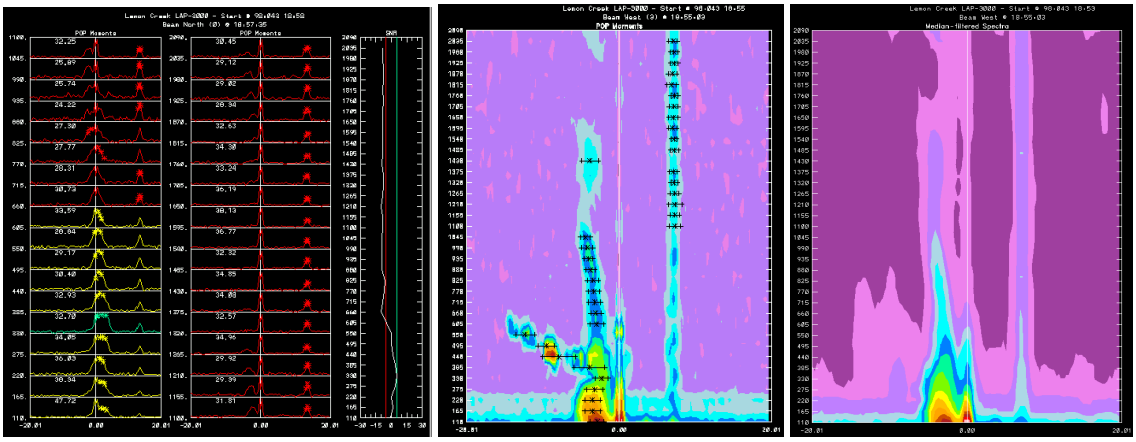

Figure 2. Stacked spectra (left), equivalent spectral intensity contour with POP moments (center), and 2d median-filtered spectra (right) from Lemon Creek profiler.

Spectral intensity scaling is used to emphasize different parts of the spectral surface. Using range-normalized scaling of the 2d median filtered values emphasizes the intensity contour in regions of low signal-to-noise (SNR). Mathematical analysis using equation (1) over a small region surrounding each point of the resulting spectral surfaces yields information about the local curvatures and gradients of the surface.

$$z(x,y) = a(x-x_0)^2 + b(x-x_0)(y-y_0) + c(y-y_0)^2 + d(x-x_0) + e(y-y_0) + f \qquad (1)$$

A number of these derived fields are calculated and membership maps are used to translate each into a "Doppler Peak membership field." Fuzzy logic is then used combine these into a combined Doppler Peak membership field. As illustrated in Figure 3, spectral regions with high Doppler peak membership values are grouped into "features" that can be classified as potentially atmospheric, clutter, and/or RFI. The highest scoring atmospheric feature is used to identify the spectral points from which to calculate the moments.

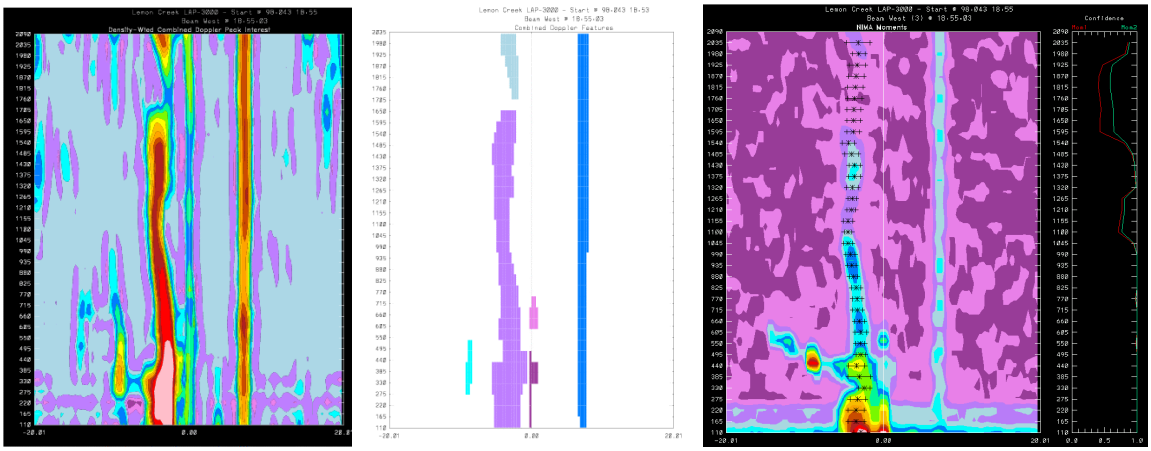

Figure 3. Combined Doppler Peak membership field (left), resulting Doppler peak features (center), and NIMA moments overlaid on the 1d (velocity) median-filtered spectra used to calculate the moments (right). Confidence in the moments is shown in the side plot.

The resulting moments are subjected to a continuity test to identify potential bad values. Confidence is estimated for each moment based on SNR, Gaussian fit of the spectral points used for the moments, the results of the continuity test, and proximity to contaminants.

NIMA Tuning Case Study – January 7, 2003

An example of tuning NIMA for a challenging site is given. The 915 MHz 3-beam profiler with RASS is located in Dugway, Utah where the climate is very dry, resulting in wind profiler spectra that are characterized by very low SNR. RFI and occasional point targets often contaminate the spectra. Examples of typical spectra are shown in Figure 4.

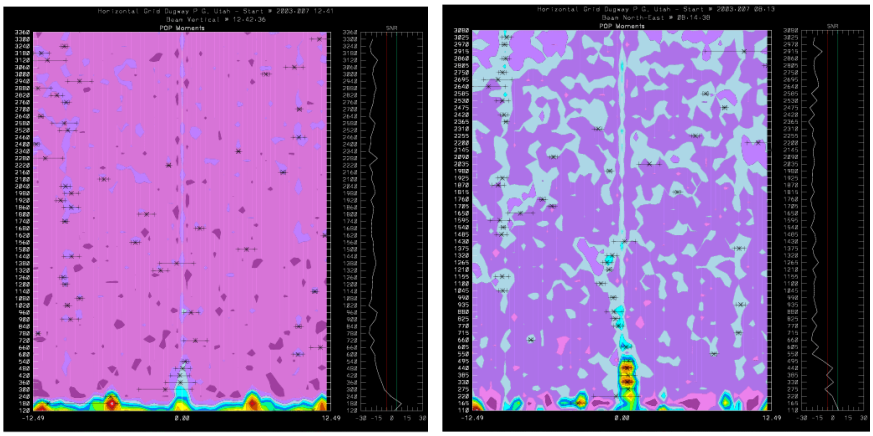

Figure 4. Examples of typical spectra from the Dugway profiler. Note the low signal to noise at most range gates and the RFI-like contamination symmetrically located at roughly ¾ the Nyquist velocity.

The 30-minute consensus winds calculated from the POP moments using a constant wind model are shown in Figure 5. Only at the low ranges are the resulting winds consistent and reasonable. The winds calculated from NIMA moments generated using the default NIMA configuration were also unsatisfactory. These included some large wind speeds that changed direction by 180 degrees between consensus intervals indicating contamination by the apparent symmetric RFI signals at large Doppler velocities. The tuning effort thus focused on detecting the atmospheric signal in the low SNR regions, identifying the weak RFI signals, and improving the preference for the atmospheric signal over the RFI signals.

The Doppler peak detection was tuned to increase the reliance on the curvature fields as these appeared to have higher skill than the some of the spectral intensity fields and the curvature membership maps were modified slightly as well. The overall threshold for Doppler peaks was lowered to allow the detection of the very weak signals.

For RFI detection, the site-specific field was utilized to help detect the RFI signals that appeared consistently in fixed locations. The RFI feature membership maps were modified to allow more tolerance in feature width, width variance, midpoint variance, and intensity variance as the RFI signals were also contaminated with noise.

The membership maps for atmospheric feature detection were also modified to account for the contamination by noise. In particular, the feature SNR and intensity variance maps required tuning. The overall threshold for categorizing a feature as atmospheric was lowered and both the Doppler peak score and feature SNR were de-emphasized while the overlap with RFI was given increased weight to help eliminate the RFI contamination.

The consensus winds from the tuned NIMA moments calculated using a linear wind field model (Goodrich, et al., 2002) are shown in Figure 5. These winds look more consistent and reasonable up to a range of about 1200 m. Above that range, the calculated winds still appear to be unreliable as corroborated by their low (< 0.2) confidence scores. The NIMA tuning exercise that resulted in this significant improvement of the resulting winds required 1-2 days of effort.

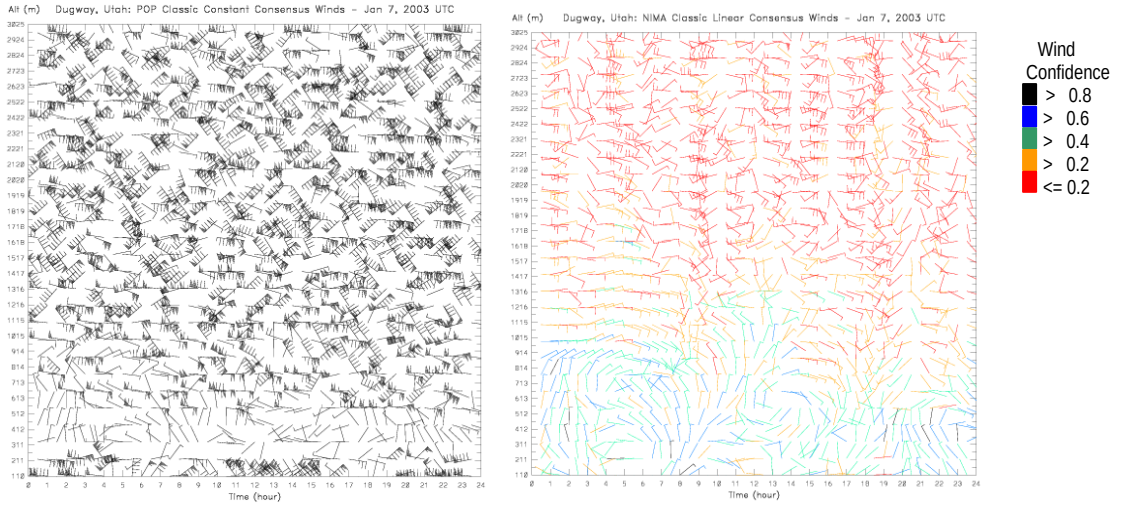

Figure 5. Comparison of the 30-minute winds calculated from POP moments and a constant wind field model (left) and those from tuned NIMA moments using a linear wind field model (right).

References

1. Cohn, S. A., R. K. Goodrich, C. S. Morse, E. Karplus, S. Mueller, L. B. Cornman, and R. A. Weekley, Radial velocity and wind measurements with NIMA: Comparisons with human estimation and aircraft measurements, *J. Appl. Meteor.*, *40*, 709-719, 2001
2. Cornman, L. B., R. K. Goodrich, C. S. Morse, and W. L. Ecklund, A fuzzy logic method for improved moment estimation from Doppler spectra, *J. Atmos. Oceanic Technol.*, *15*, 1287-1305, 1998.
3. Goodrich, R. K., C. S. Morse, L. B. Cornman, and S. A. Cohn, A horizontal wind and wind confidence algorithm for Doppler wind profilers, *J. Atmos. Oceanic Technol.*, *19*, 257-273, 2002.
4. Morse, C. S., R. K. Goodrich, and L. B. Cornman, The NIMA method for improved moment estimation from Doppler spectra, *J. Atmos. Oceanic Technol.*, *19*, 274-295, 2002.

Acknowledgements

The authors wish to thank Volker Lehmann of the Deutsche Wetterdienst, William O. J. Brown of NCAR/Atmospheric Technology Division, and William Shaw of Pacific Northwest National Laboratory for valuable feedback on NIMA performance. Much of this research is in response to requirements and funding by the Federal Aviation Administration (FAA). The views expressed are those of the authors and do not necessarily represent the policy or position of the FAA. Additional funding was provided by the U.S. Army and by the Deutsche Wetterdienst. NCAR is operated by the University Corporation for Atmospheric Research under the sponsorship of the National Science Foundation.

SOUSY RADAR AT JICAMARCA: SYSTEM DESCRIPTION

R.F. Woodman, O. Castillo, G. Micchue, P. Reyes, S. Villegas

Radio Observatorio de Jicamarca, Instituto Geofisico del Perú

The Max Planck Institute fur Aeronomy has donated the SOUSY radar, to the Instituto Geofisico del Peru. This radar was previously working in the Harz mountains, Germany since 1977. The radar has now been installed at the Jicamarca Radio Observatory (JRO) in Lima, Peru (see Figure 1).

Figure 1. The Sousy Radar at Jicamarca in the foreground, with JRO main antenna in the center. The trasnmitter and receiver trailers are in between.

The main characteristics that differentiate the SOUSY radar from the Jicamarca radar are: (1) its bandwidth (4 MHz against 700 KHz for the Jicamarca radar) and (2) its steerability. The wider bandwidth allows an altitude resolution of at least 75 meters. The Sousy radar is a phased array that allows for a wide and agile steerability of its antenna ($\pm$ 15^o). In order to satisfy our scientific need, we have redesigned the antenna to have two main positions, zenithal and 15° south.

The addition of SOUSY to the JRO would make possible the following number of new studies:

1. Measurements of meridional winds at ionospheric heights, taking advantage of the larger zenithal angles that the SOUSY radar can be steered. The meridional wind is the only ionospheric parameter of importance that has not been reliably measured at Jicamarca.
2. High range resolution of Mesospheric, Stratospheric and Tropospheric (MST) measurements, taking advantage of the broad bandwidth of the SOUSY radar and the possibility of a wide frequency allocation in Peru.
3. High–power wide-angle meteor radar interferometric studies. The behavior of meteor trails at the equator, because of the Electrojet electrodynamics, is different than at other latitudes.

In addition, its relative mobility should allow it to be placed, in the future, at other convenient locations near the magnetic equator, for instance the Punta Lobos rocket

ranges, at the edges of the Equatorial Electrojet at (± 300 km from magnetic Equator), etc. This in turn will allow us the following experiments:

1. Concurrent observations, with radar and in situ probes, of the same mesospheric scattering volume probed by rockets launched from the Punta Lobos rocket range. Neutral turbulence in a stratified atmosphere is now being numerically modeled with success. Equatorial mesospheric turbulence is the best testing ground for these simulations since the Reynolds numbers are low and comparable to those of the models. What we will learn at equatorial latitudes should benefit our understanding of the more complicated Polar Mesospheric Summer Echoes.
2. Concurrent rocket and radar observations of *E*- and *F*- region irregularities. Common volume observations have not been done in the past because of the distance between Jicamarca and Punta Lobos rocket range, and moving the SOUSY radar will solve this problem in future rocket campaigns.
3. Measurements of the *E*-region irregularities at the foot of the field lines passing through the "150 km echoes" region above Jicamarca. Such observations might give us a clue about the physical mechanism responsible for these irregularities, for which there is as yet no accepted theory. For such measurements we would have to move the radar to location about 300 km north (or south) of Jicamarca, a location that also happens to be edge of the equatorial electrojet.

Some changes have been made to the original design of the SOUSY radar, as we can see in the block diagrams of Figure 2. As far as the antenna design, we have used the same Yagi elements used in the original SOUSY radar but in a 64 m x 64 m square array (Figure 3) rather than circular. The new antenna is composed of 64 (8 x 8) modules. Each module is composed of a 2 x 2 Yagi array, with fixed phasing. Each module will have a centrally controlled 3 bit phase shifter allowing arbitrary phasing in λ/8 steps. The square array demanded 60 additional Yagi elements than the original circular design, which were constructed locally using the same design.

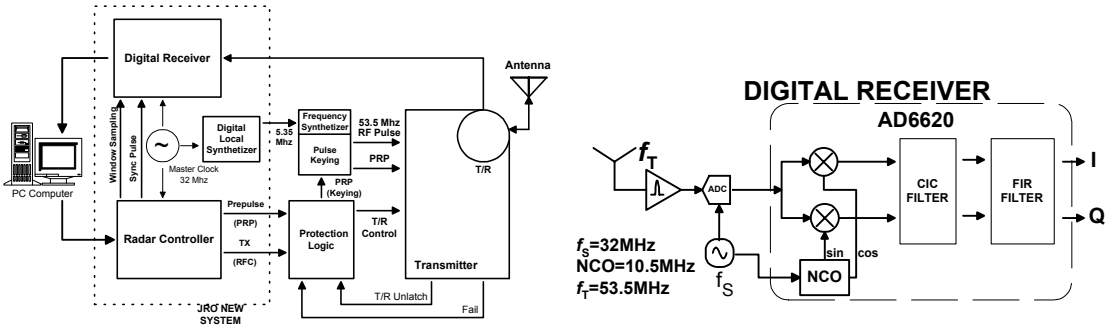

Figure 2: (a) Block diagram of the SOUSY radar (b) Block diagram of the digital receiver

The booms of the Yagis have been bent to allow two main directions (zenithal and 15°S off-zenith). The two pointing positions are obtained by flipping the boom up-side down with respect to the other, as we can see in Figure 4. The antenna modules are phased in accordance to the particular on axis direction, by properly phasing their elements. We achieve this by interchanging the same set of cables feeding each of the four Yagis that conform them. In Figure 5 are presented the radiation patterns for the mentioned main directions.

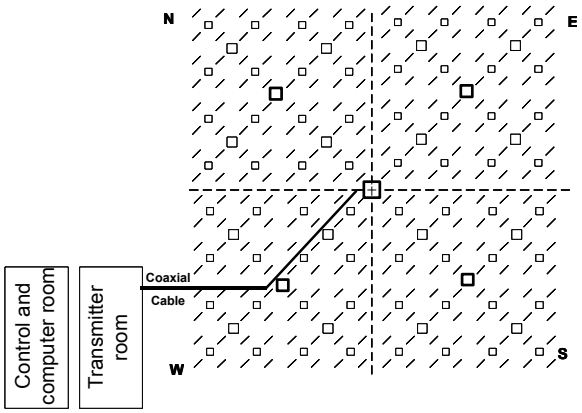

Figure 3. Distribution of the antenna array. The squares represent divide-by-four power dividers. Different sizes correspond to different power levels.

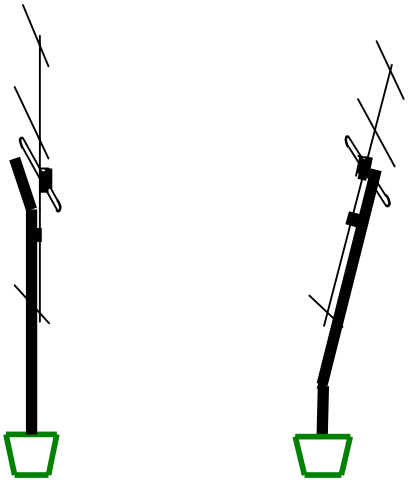

Figure 4. Two alternatives for mechanical mounting of the Yagis. Left point to zenith, right 15^{o} S off-zenith.

At present, we are operating the antenna in a fixed 15°S off-zenith configuration. Fixed cable sections are used instead of the phase shifters. This will allow us to perform the IS experiment to obtain the meridional projection of the ionospheric wind, one of the experiments of maximum priority, without having to wait until the phase shifters are installed in each of the modules

For transmission we are using the original SOUSY transmitter in its own trailer with no modification [See Czechowsky et al., 1976 and Czechowsky et al., 1984]. For the control, signal receiving and processing, we are using a complete new system similar to the one currently being developed for the Jicamarca radar.

For the sampling of the received signal and transmitter control we are using the same design of the radar controller used at Jicamarca (Figure 2(a)). This is a modern version of the first unit designed and built in the earlier 1970's. Similar units are described in Tobaja et al. [1978] and Woodman et al. [1980]. In this new configuration we are using PLD (Programmable Logic Device) technology, which has

the advantage of containing controller electronics in a single chip and can be upgraded by software.

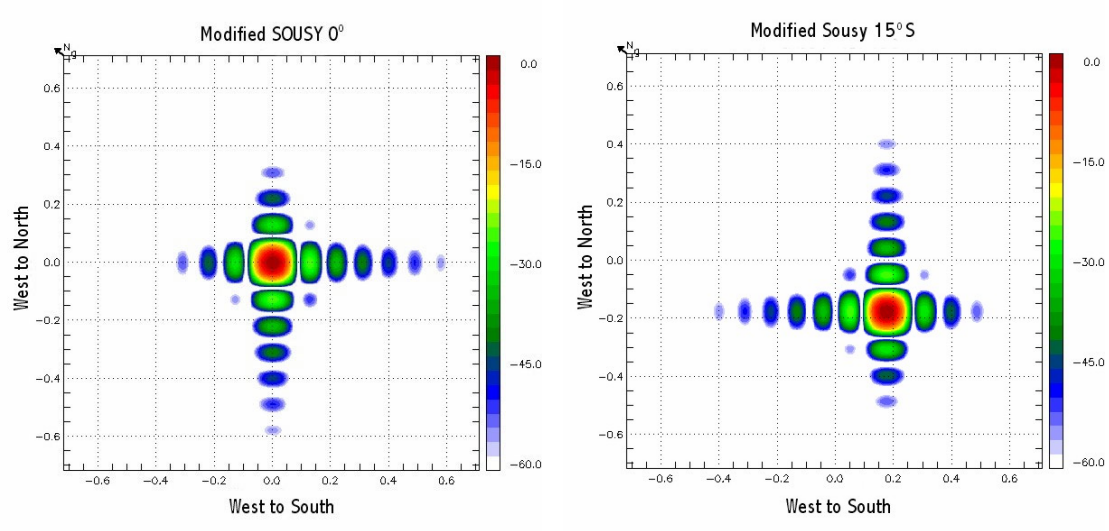

Figure 5. Radiation patterns of Sousy antenna for the 0° and 15° South center modes. Phase shifters set for 0° off-set..

For reception we are using the newly designed Jicamarca digital receiving system (Figure 2(b), for details see Micchue and Woodman this issue). In short, it uses the evaluation card of an Analog Devices chip (AD6620) designed mainly for the cellular phone industry. This board uses software developed by the manufacturer to configure the different chip parameters, such digital filters, NCO (Numeric Controlled Oscillator) and digital attenuation. The main advantages compared with an analog receiver are: 1) high sampling rates, 2) higher dynamic range, 3) programmable filters with very flexible designs, and 4) an ideal quadrature between real and imaginary outputs of the receiver. The output of the receiver is channeled directly to a PCI interface card working at 80 Mbytes per second. Processing is done on a PC working under Windows.

References

Czechowsky, P., J. Klostermeyer, J. Röttger, R. Ruster, G. Schmidt, and R. F. Woodman; The SOUSY-VHF radar for tropo-strato-and mesospheric sounding, *Proceedings of the 17th Conference on Radar Meteorology*, pp. 349-353, American Meteorological Society, Boston, Mass. 1976.

Czechowsky, P., G. Schmidt, and R. Ruster; The mobile SOUSY Doppler radar: Technical design and first results, *Radio Sci., 19*, 441-450, 1984.

Tobaja, E., R.F. Woodman, and D. Haseltine; Synchronous programmable sequencer, S.P.S., *Arecibo Observatory, Technical Report*, September 1978.

Woodman, R. F., R. P. Kugel, and J. Röttger; A coherent integrator-decoder preprocessor for the SOUSY-VHF-Radar, *Radio Sci., 15,* 233-242, 1980.

THE EQUATORIAL ATMOSPHERE RADAR: SYSTEM AND NEW RESULTS

Shoichiro Fukao, Hiroyuki Hashiguchi, and Masayuki K. Yamamoto

Radio Science Center for Space and Atmosphere, Kyoto University
(e-mail:fukao@kurasc.kyoto-u.ac.jp)

Introduction

The Western Pacific region, called the Indonesian Archipelago, is a center of intense atmospheric motions that are considered to be closely associated with the global atmospheric change. The world's most active convective clouds are generated in this region. The mechanisms responsible for these atmospheric changes and fluctuations, however, have not yet been clearly identified because of the sparseness of observational data from that region. A VHF Doppler radar with an active phased-array antenna system, called the Equatorial Atmosphere Radar (EAR), was established at the equator near Bukittinggi, West Sumatra, Indonesia (0.20°S, 100.32°E, 865 m above sea level) in March 2001. In this paper, we will describe the outline of the EAR system.

The EAR System

Table 1 shows the specifications of the EAR system. Its operating frequency is 47.0 MHz and its bandwidth is 4 MHz. The maximum peak and average radiation powers are 100 kW and 5 kW, respectively (the maximum duty ratio is 5%). A subpulse width as short as 0.5 μs can be accommodated by the 4-MHz bandwidth of the system to satisfy the requirement for a maximum range resolution of 75 m. The nominal one way half power antenna beam width is 3.4°.

Figure 1 shows the schematic block diagram of the EAR system. The hardware of the EAR consists mainly of five subsystems; the antenna array (ANT), the transmitter and receiver (TRX), the signal modulator and demodulator (SMD), the signal processor (SP), and the host computer (HC). Figure 2 shows the view of the entire EAR antenna field. The EAR uses a circular antenna array, approximately 110 m in diameter, which consists of 560 three-element Yagi antennas. Each antenna is driven by a solid-state transmitter-receiver module. The TRX is composed of a pre-amplifier (Pre-amp), an indoor divider and combiner unit (DCU), 24 outdoor DCUs, and 560 TR modules. For transmission, the RF (47.0-MHz) signal from the SMD is amplified by the Pre-amp and divided equally into 560 signals by the indoor and outdoor DCUs. Each of the 560 signals is sent at a low power level (0.3 mW or 5 dBm) to a TR module and amplified to the final transmitting power level of 180 W (peak; 52.5 dBm).

The SMD is composed of a stable local oscillator (STALO) of 37 MHz, a coherent oscillator (COHO) of 10 MHz, two frequency conversion units (one of which forms a super-heterodyne receiver), a phase detector, two analog-to-digital converters (A/Ds), and a radar controller (RC). The receiver has a wide dynamic range of more than 70 dB. The IF (intermediate frequency) transmitter source signal of 10MHz is generated by applying a specified phase-modulation and pulse-modulation to the COHO signal in the modulator. The source signal is up-converted to the RF transmitted signal of 47.0 MHz by mixing it with the STALO signal in the frequency conversion unit. On the other hand, the signal received at 47.0 MHz is down-converted to the IF of 10 MHz in the frequency conversion unit. The IF signal is subsequently down-converted to a video signal (analog signal) by COHO and divided into in-phase (I) and quadrature-phase (Q) signals by a phase detector. The I and Q video signals are then converted to 14-bit digital signals by

A/Ds. All timing signals for EAR operation are generated by the timing generator in the RC. The RC sends parameters of operation to the receiver and TRX.

The SP performs a series of signal processing operations (pulse decoding, coherent integration, fast Fourier transform (FFT), incoherent integration), and sends the processed data to the host computer (HC). The digitized I and Q signals are stored in the FIFO (First-In/First-Out) memory (double-buffered memory) in the A/Ds. The output is sent to the pulse decoding and coherent integration units with header data added. After pulse decoding the digitized I and Q signals are coherently integrated for each beam and range. The coherent integration unit adds a specified number of I and Q signals and outputs 32-bit data to double-buffered memory. The data from the ranges to be processed are selected and sent to the digital signal processing (DSP) unit. The integrated I and Q signals are stored in the buffered memory of the DSP unit, and rearranged into time series at respective ranges. The DSP then performs complex FFT and power spectrum calculations on these time series. The DSP also performs a specified number of incoherent integrations of the power spectra. After incoherent integration the power spectra are sent to the HC. The HC sends operating parameters to the RC and controls start/stop of operation of the entire system. It also receives observed data from the SP and store them to digital data storage (DDS) tape.

Conclusion

The EAR has been continuously operated since July 2001, with some intermittent short-term data gaps. The EAR is usually operated with a standard observation mode to observe the whole troposphere and the lower troposphere (2–20 km) with the time and vertical resolution of ∼90 sec and 150 m, respectively. The equatorial cross-tropopause process is considered to play an important role on global stratosphere-troposphere exchange (STE). Observations by the EAR in the tropical tropopause layer (TTL) have been reported [*Fujiwara et al.*, 2003; *Yamamoto et al,*, 2003]. The EAR is also capable of viewing the ionosphere in directions perpendicular to the geomagnetic field, and it is the first one established in the Indonesian-Thai longitude sector (10.63°S, 171.93°E). Studies on field-aligned irregularities (FAIs) in the ionospheric E and F regions also have been reported [*Fukao et al.*, 2003b]. Additionally, the EAR has the capability to observe thin atmospheric structures by the frequency domain interferometry (FDI) or the frequency domain interferometric imaging (FII) techniques. Many phenomena that remains to be uncovered in the equatorial atmosphere will be clarified by the EAR.

References

Fukao, S., H. Hashiguchi, M. Yamamoto, T. Tsuda, T. Nakamura, M. K. Yamamoto, T. Sato, M. Hagio, and Y. Yabugaki, The Equatorial Atmosphere Radar (EAR): System description and first results, Radio Sci., *38(3)*, 1053, doi:10.1029/2002RS002767, 2003a.

Fukao. S., Y. Ozawa, T. Yokoyama, M. Yamamoto, and R. T. Tsunoda, First observations of spatial structure of 3-m-Scale field-aligned irregularities with the Equatorial Atmosphere Radar in Indonesia, In revision, J. Geophys. Res., 2003b.

Fujiwara, M., M. K. Yamamoto, H. Hashiguchi, T. Horinouchi, and S. Fukao, Turbulence at the tropopause due to breaking Kelvin waves observed by the Equatorial Atmosphere Radar, Geophys. Res. Lett., *30(4)*, 1171, doi:10.1029/2002GL016278, 2003.

Yamamoto, M. K., M. Fujiwara, T. Horinouchi, H. Hashiguchi, and S. Fukao, Kelvin-Helmholtz instability around the tropical tropopause observed with the Equatorial Atmosphere Radar, Geophys. Res. Lett., *30(9)*, 1476, doi:10.1029/2002GL016685, 2003.

Table 1: Specifications of the EAR system (from *Fukao et al.*, 2003a)

Item	Specification
Location:	0.20°S, 100.32°E, 865 m above sea level
Geomagnetic latitude and longitude	10.63°S, 171.93°E
Radar system:	Monostatic pulse Doppler radar
Operating frequency:	47.0 MHz
Antenna:	Quasi-circular antenna array of 560 three-elemen t Yagi antennas
Aperture:	110 m in diameter
Beam width:	3.4° (half power width; one way)
Beam direction in azimuth:	0–360° in 0.1° steps
Beam zenith angle:	0–30° in 0.1° steps (no grating lobe)
Gain:	33 dBi
Transmitter	
Peak power:	100 kW (sum of all TR modules)
Average power:	5 kW (max; sum of all TR modules)
Number of TR modules:	560 units (same as Yagi antennas)
Single TR module's power:	180 W/unit
Pulse width:	0.5–256 μs
IPP:	200 μs–10 ms (variable in 200μs steps)
Receiver	
Type:	Single super heterodyne
Noise figure:	5 dB (TR modules)
Pulse compression:	Barker, complementary and Spano codes (1 to 16 bits)
Subpulse width:	0.5, 1.0, 2.0, 4.0, 8.0, 16.0 μs (variable)
Dynamic range:	70 dB
A/D converter:	14 bits
Number of range gates:	256 (max.)

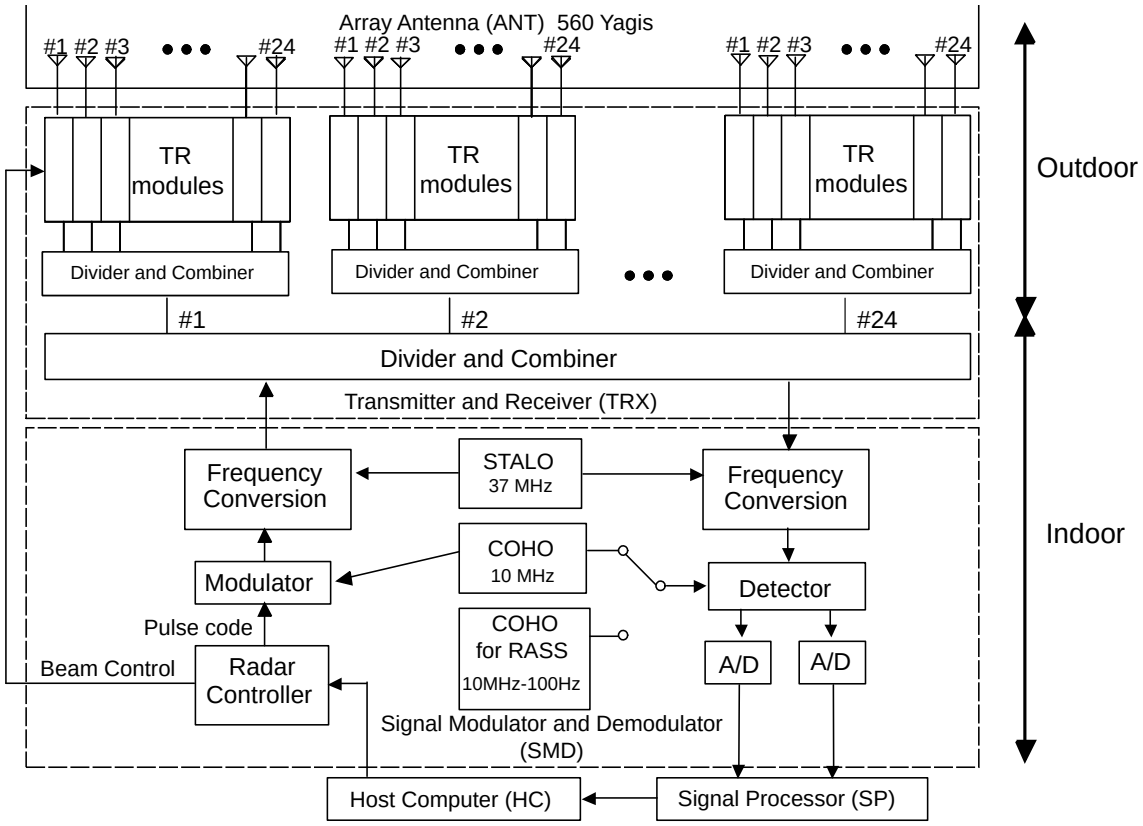

Figure 1: Schematic block diagram of the EAR (from *Fukao et al.*, 2003a).

Figure 2: A view of the entire EAR (from *Fukao et al.*, 2003a).

VHF ATMOSPHERIC AND METEOR RADAR INSTALLATION AT DAVIS, ANTARCTICA: PRELIMINARY OBSERVATIONS

R. J. Morris[1], D. J. Murphy[1], I. M. Reid[2], and R. A. Vincent[2]

[1]Australian Antarctic Division, Kingston 7050, Tasmania, Australia
[2]University of Adelaide, Adelaide 5005, South Australia, Australia

Introduction

A 55 MHz VHF atmospheric radar was commissioned at the high-latitude station Davis (78.0°E, 68.6°S geographic; 74.6°S magnetic), Antarctica during the austral summer of 2002-03. This paper presents an overview of this new facility which has been constructed for the Antarctic environment including, the 12 x 12 array of Yagi antennas, equipment module, and associated infrastructure. Several aspects of the design tailored for the harsh Antarctic conditions are described. The radar specifications as developed by Atmospheric Radar Systems will be given together with an account of the proposed science to be conducted utilizing this new facility. The radar commenced 'spaced antenna' mode observation with 20 kW of transmitted power from mid February 2003, and is scheduled to be upgraded to 120 kW of transmitted power and a beam steering capability from November 2003. Some initial troposphere and stratosphere region wind observations are presented. The facility includes a meteor radar capability and some preliminary mesosphere region results are also presented.

Scientific Objectives

VHF radars have been used extensively and successfully in the northern hemisphere to study the dynamics of the Earth's polar atmosphere, however, with the exception of a short-term experiment at South Georgia, they have not been used in the southern polar-regions. VHF radars allow the measurement of wind speeds in the troposphere and lower stratosphere throughout the year and in the mesosphere during daylight hours. They collect data with a high-time resolution (typically every few minutes) and with high-spatial resolution (typical altitude ranges of a few hundred metres) and operate stand alone with little operator intervention. As a result, they have played a key role in developing our understanding of the energy source regions in the lower atmosphere, energy deposition regions higher up, the coupling between them and the resulting global circulation.

The potential of the VHF radar can be demonstrated through consideration of the following scientific objectives.

Investigations of troposphere, stratosphere and mesosphere dynamics:

- Gravity waves; climatology; case studies; propagation studies; and estimates of momentum flux in these atmospheric regions
- Turbulence
- Meteorology

Studies of Polar Mesospheric Summer Echoes (PMSEs):

- Interhemispheric differences
- Morphology and climatology
- Links to noctilucent clouds
- Theory

Meteor studies:

- Mesosphere temperatures and winds

A detailed account of the science objectives can be found at www.aad.gov.au under AAS Project 2325 "VHF radar studies of the Antarctic mesosphere, stratosphere and troposphere" Drs Ray Morris, Damian Murphy, Andrew Klekociuk, Gary Burns, Iain Reid and Bob Vincent.

VHF Radar Specifications

Array dimensions: 42.43 m x 42.43 m
Antennas: 3 element Yagi's with a folded dipole driver element
Antenna Grouping: Groups of four adjacent antennas are grouped to form 36 sub-arrays
Tranceiver: 6 channel fixed frequency
Meteor Capability: The radar can be switched to a 5 antenna meteor array (with a separate transmit antenna)

Table 1. Description of the Davis VHF Radar.

Frequency	55 MHz	
Array	12x12 grid of 3-element Yagi antennas	0.7 Lambda spacing
Effective Area of Array	2180 m^2	At 55 MHz
One-way beam width	~ 7 degrees	Using whole array
Peak Power	20 kW (2003) 120 kW (2004)	In 6 x 20 kW modules
Average Power	6 kW	5% Duty cycle
Power Aperture Product	~1.5 x 10^7 Wm^2	At peak power

Figure 1. A photograph of the Davis VHF radar installation.

Antenna Array Design and Construction

The project was assessed under a 'preliminary environmental assessment' in compliance with the Madrid Protocol for Protection of the Antarctic Environment. Final site selection was

based upon a geotechnical engineering assessment to protect the array from possible damage due to permafrost and annual freeze and thaw cycles. The 3-element Yagi antennas that make up the array were attached to their vertical 50 mm diameter support posts at varying heights above the ground so as to set the plane of their driver elements horizontal. The posts ranged in length from 2 to 4 metres. The posts were supported at their base by concrete blocks designed to prevent translation and rotation. The strain caused by wind loading on the antennas and posts was taken up by a system of guy ropes. Concrete blocks were placed on small pads of un-reinforced concrete approximately 800 mm x 800 mm x 250 mm. These provided an even surface to support the blocks and were oversized to allow the block to be moved into the correct position on the pad. The guy system consisted of a network of ropes at the height of the top of the poles. After tensioning, the guy ropes were secured to anchor points at the ends of each row and column of antennas. After setting each support post to vertical, the top of each post was clamped to an East-West and a North-South aligned guy. The rope used was a 'braid' made of fibre that has a high strength and a low stretch factor. The radar module has power and fibre optics communications to the main station network.

Radar Operating Schedule for the 2003 Austral Winter with Preliminary Observations

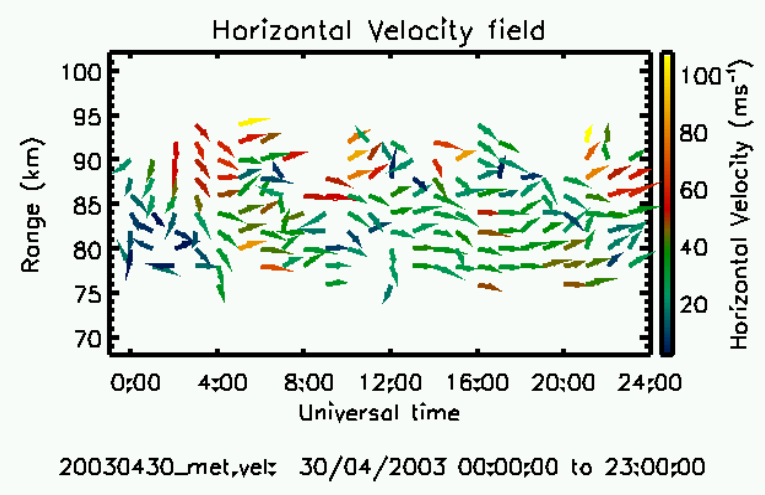

Figure 2. Horizontal wind measurements in the mesosphere and lower thermosphere obtained with the VHF radar operating in meteor mode.

Through the Antarctic winter, the VHF radar schedule emphasises detection of meteor echoes from the mesosphere and lower thermosphere. These echoes are to be used, in conjunction with other instruments at Davis, for wind and temperature comparisons. However, soundings of the lower atmosphere are carried out every 12 minutes. The frequency and duration of lower atmospheric soundings was later increased to every 6 minutes for two hour intervals following ozone-sonde and standard sonde balloon releases.

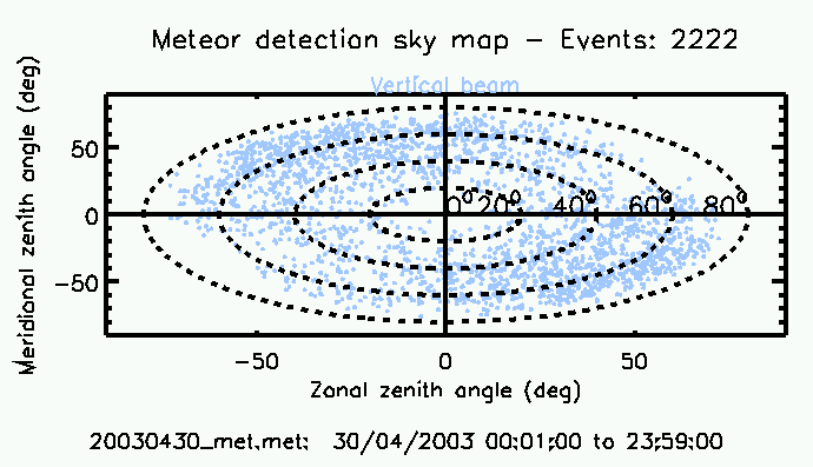

Figure 3. Direction of arrival for meteor detections on 30 April 2003 at Davis.

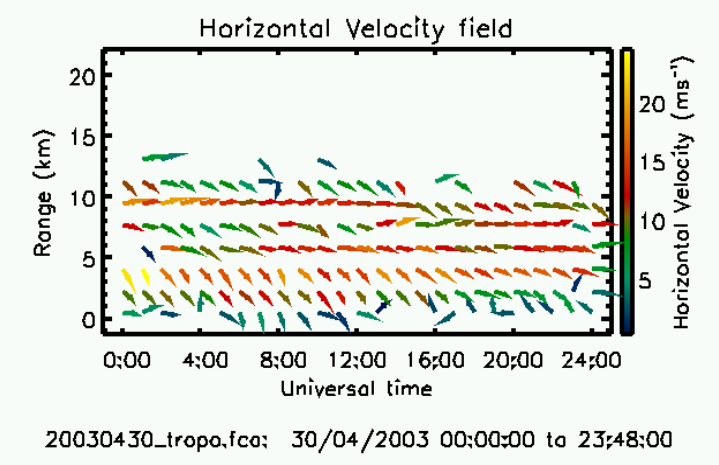

Figure 4. Horizontal velocities in the troposphere and lower stratosphere obtained using the Davis VHF radar. One minute lower atmosphere soundings are carried out at 12 minute intervals.

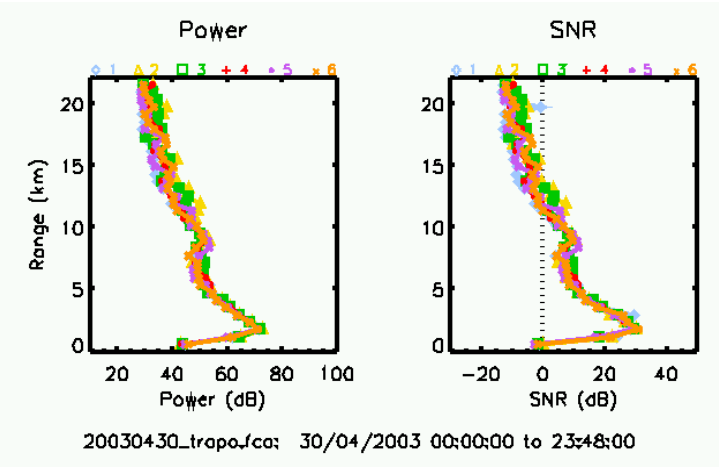

Figure 5. Average echo power and signal-to-noise ratio for tropospheric soundings using the Davis VHF radar.

Davis Station Research Facility

The VHF Radar is located on the shoreline of Heidemann Bay some 2 km from Davis station, Antarctica (78.0°E, 68.6°S geographic; 74.6°S magnetic). The Australian Antarctic Division and the Australian physics community have developed Davis as their primary site for high-latitude middle and upper atmospheric physics research. Finally, the science objectives will be addressed using the suite of instruments at Davis coupled with international collaboration.

Middle atmospheric experiments include:
Rayleigh and Doppler lidar; 2 MHz Medium Frequency Spaced Antenna radar; Czerny-Turner Spectrometer observing OH airglow; Fast Fourier Transform Spectrometer observing OH airglow; Scanning Radiometer; and UV Spectrophotometer.

Upper atmospheric experiments include:
Fabry-Perot Spectrometer; Digital Portable Sounder; Three Field Photometer; Wide Angle Two Field Photometer; Fluxgate Magnetometer; Induction Magnetometer; IRIS Imaging Riometer; 30 MHz Standard Riometer; All Sky Video Camera; Ionospheric Scintillations; Total Electron Content; and Magnetic Absolutes.

Acknowledgments

We acknowledge the support of the Australian National Antarctic Research Expeditions (ANARE) expeditioners at Davis during the 2002-03 austral summer. The VHF radar was installed by Space and Atmosphere Science expeditioners – Damian Murphy, Ray Morris, Lloyd Symons, Danny Ratcliffe and Richard Groncki, and Trade expeditioners – Paul Saxby, Alan Taylor and Chris Heath, under the supervision of Janine Lea. Richard Groncki provided the photograph of the VHF radar at Davis.

VORTICAL MOTIONS OBSERVED WITH THE NEW MCGILL VHF RADAR AND ASSOCIATED DYNAMICAL CHARACTERISTICS

Edwin F. Campos[1] and Wayne Hocking[2]

1. Dept. of Atmospheric & Oceanic Sciences, McGill University, Montreal, Quebec, Canada
2. Dept. of Physics, University of Western Ontario, London, Ontario, Canada

1. Sensor description

The McGill VHF WindTtracker (Wind and Turbulence tracker) radar is a Windprofiler located near the city of Montreal, at 45°24'33"N, 73°56'12"W, at an elevation of 30 m above sea level. This radar has been operational since the summer of 2002. It operates at a frequency of 52.0 MHz and samples at ranges between 1.5 km and 20.5 km with a resolution of typically 500 m, using better resolution at lower heights and poorer resolution at upper altitudes. Maximum useful altitudes achieved are typically 14 to 17 km. (A boundary layer mode will be added in due course.) The signal processing of this radar is basically the same as that described in Hocking [1997]. The details are given in Table 1.

Table 1. General characteristics of the McGill VHF Wind Profiler.

Variable:	*Description:*
Frequency [wavelength]	*52.0 MHz [5.77 m]*
Antenna area [cross shaped]	*2 000 m^2 [100 m long]*
Peak transmitted power	*40 kW*
2-way beam half-width	*1.6°*
Off-vertical angle	*10.9°*
Pulse Repetition frequency	*Normally operates at 3kHz to 10kHz*
Time resolution at one height	*Data recorded at 60 - 100 Hz*
Height resolution [gradually decreasing with height, from 1.5 km]	*500 m [from 0.5 km to 1 km]*
Location [Montreal, Canada]	*45.409° Latitude North, 73.937° Longitude West*

2. Winds Validation

2.1 Weather S-band radar.

The McGill S-band weather radar is located just 2 km from the McGill VHF wind profiler, at an elevation of about 80 m above sea level. It derives operationally (when there is precipitation) vertical profiles of winds using the Velocity-Azimuth-Display method (VAD, e.g., Doviak and Zrnic 1993, section 9.3.3). To construct each wind profile, the following conditions are used (see Fig. 1): The VAD method uses 13 elevation angles (Ø between 0.5° and 14.6°) and 360 azimuth angles. For a given elevation and azimuth, the radial direction is sampled every 10 km until a range r_s is reached. This r_s is obtained when the height h reaches 8.5 km or when the horizontal distance d reaches 50 km, whichever occurs first. Thus, the analyzed volumes correspond to $h < 8.5$ km and $d < 50$ km. For a particular height, the sampling region is an approximately cylindrical volume of depth equal to the range resolution with a circular surface of radius d. In the following comparisons, we use only those observations that have useful weather-radar echoes in at least 50% of this cylindrical volume. Measurements were generated every 5 minutes.

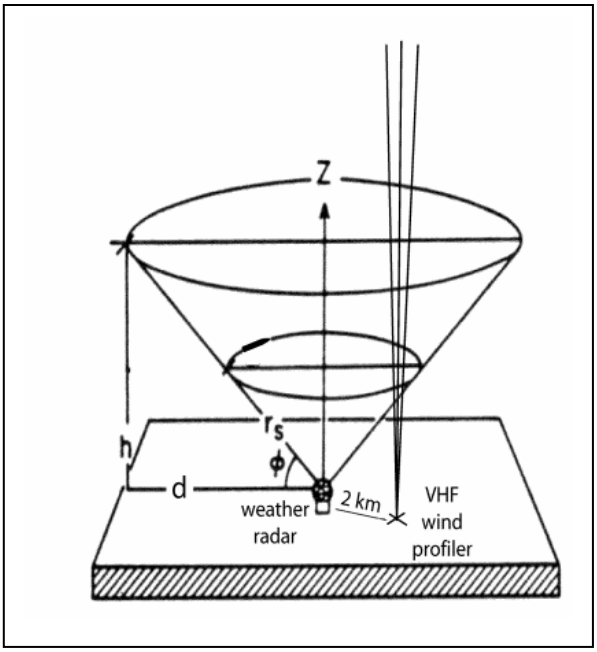

The event of February 4th, 2003, was chosen because it provided widespread precipitation and good height coverage. For this case, Fig. 2 compares the VAD wind profiles (averaged over 30 minutes) with the VHF winds. Note that the sampling volumes of the VAD observations are not completely matched to the corresponding sampling volumes in the VHF observations. However, the times and heights were adjusted in order to match both data-sets.

Although the speeds in the VAD tend to be less than for the VHF radar, there is no clear bias in the comparison of the wind directions.

Fig. 1. VAD Analyses.

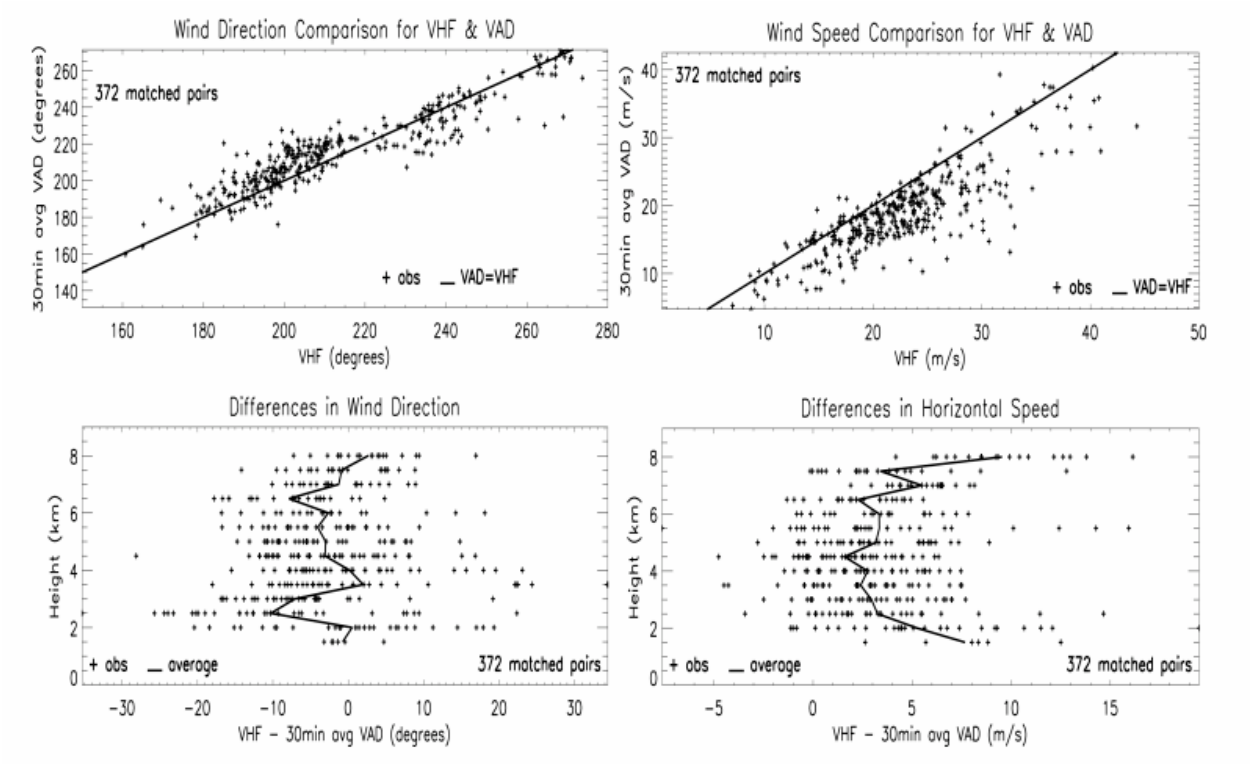

Fig. 2. VHF and VAD comparison. Left: Wind direction. Right: Wind speed. Upper: scatter plot of VAD winds vs. VHF winds. Bottom: Wind difference as a function of height.

2.2 Meteorological numerical model.

The numerical model output from the Rapid Update Cycle (RUC, Benjamin et al., 2002) analysis/model system was also used for comparison with the VHF winds. The RUC model has a horizontal resolution of 20 km, and its vertical resolution corresponds to 18 levels for heights near 16 km or below. A new RUC analysis (0h forecast) is available every hour.

For this comparison, we use 10 different RUC analyses on February 4, 2003 (at 00, 01, 12, 13, 14, 17, 18, 19, 21 and 22 UTC). The RUC wind profiles used were obtained by bilinear

interpolation from the original grid points of the model to give conditions over the radar. These RUC data were averaged in height intervals of 0.5 km, in order to match the vertical resolution of the VHF winds. In addition, the VHF data were averaged in time, in order to match the 1h temporal resolution of the RUC data. Fig. 3. presents the results of this comparison.

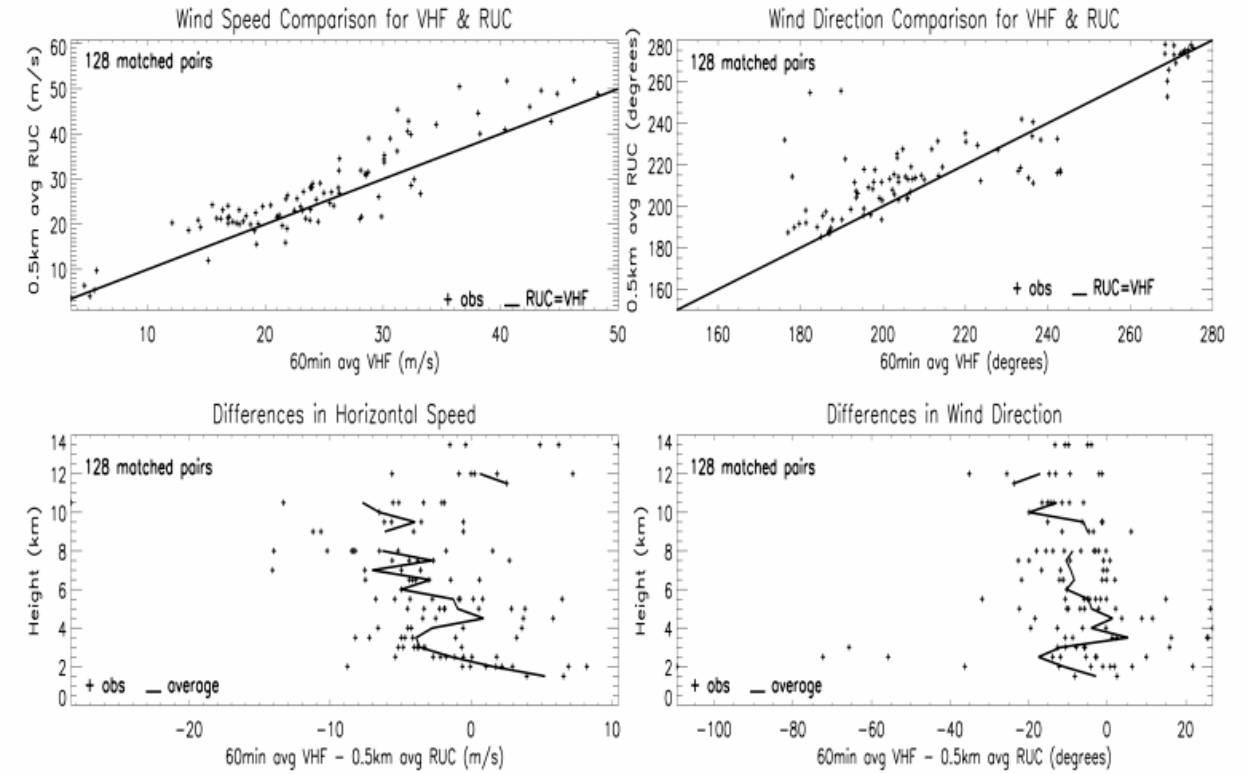

Fig. 3. VHF and RUC comparisons. Left: Wind direction. Right: Wind speed. Upper: scatter plot of RUC winds vs. VHF winds. Bottom: Wind difference as a function of height.

3. Vortical motions.

Due to the geographical location of this VHF radar, the sampling of the upper-troposphere, mid-latitude jet stream is quite frequent. Strong vortical motions have been observed during these events, and wind directions can often rotate by a full 360 degrees in only a few hours. Such structures can be quite deep, extending several kilometers up in the troposphere.

The observations on November 23rd, 2002, near 6 UTC, are an example of these vortical motions. A significant bearing of the wind can be observed through all the troposphere and the lower stratosphere (Figure 4). This particular situation is associated with the passage of a front over the site, as well as an upper tropospheric trough embedded into the jet stream. Although not shown here, this was confirmed by operational analyses from the Canadian Meteorological Centre (CMC-MSC).

In addition, comparisons between the vertical profile of winds measured by our VHF radar and computed by the CMC-MSC operational model (i.e., GEM regional, zero hour forecast) were analyzed (not presented here). It is found that the good agreement is lost during the occurrence of the vortical motion. This suggests the opportunity for data assimilation of VHF wind observations into numerical meteorological models.

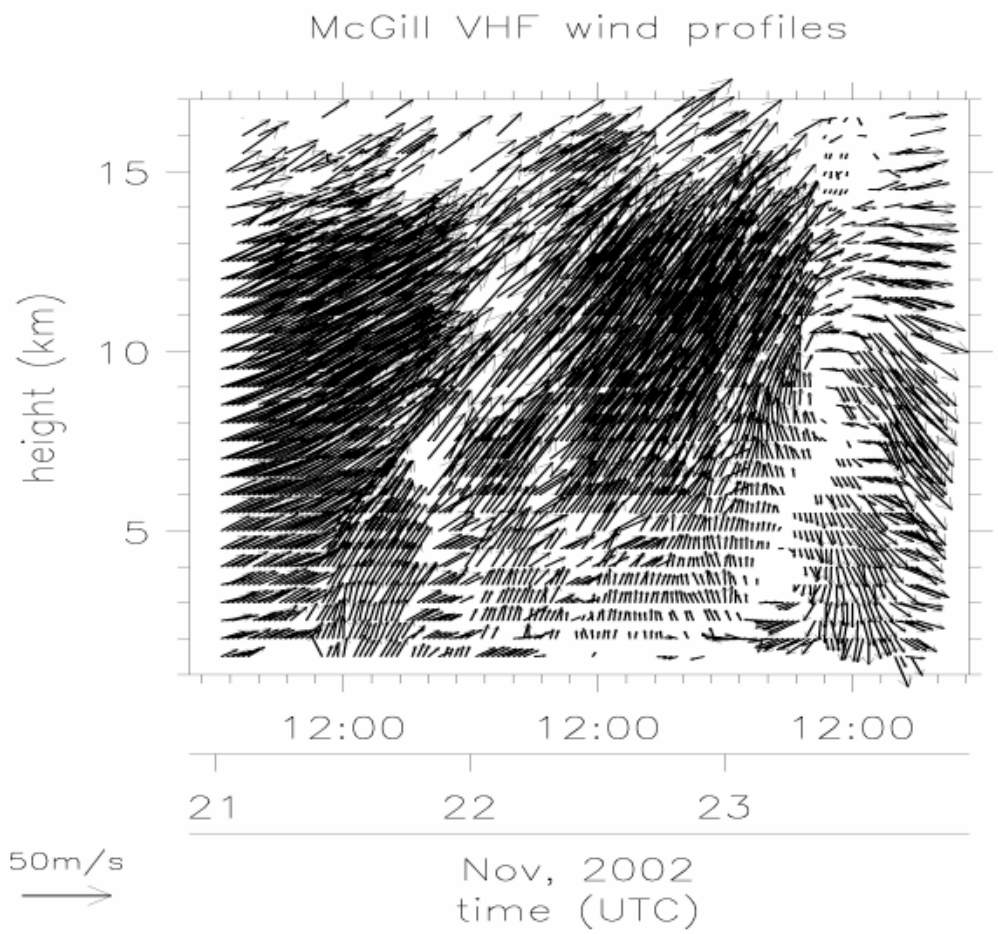

Fig. 4. Vector plot of the evolution of the winds over the McGill radar for 21 to 23 November, 2002. Upward is northward, and horizontal towards the right is eastward.

Acknowledgments:

The GEM data were provided by Tom Robinson, from CMC-MSC. The algorithm of the VAD method used here was developed by Dr. Aldo Bellon, from MRO-McGill. RUC data was made available by Prof. John Gyakum, from AOS-McGill.

References:

Benjamin, S.G., J.M Brown, K.J. Brundage, D. Dévényi, G.A. Grell, D. Kim, B.E. Schwartz, T.G. Smirnova, T.L. Smith, S. S.Weygandt, and G.S. Manikin, RUC20 - The 20-km version of the Rapid Update Cycle. *NWS Technical Procedures Bulletin No. 490.* [Revised version available at http://ruc.fsl.noaa.gov] 2002.

Doviak, R.J., and D.S. Zrnic, Doppler Radar and Weather Observations. 2nd edition. Academic Press, San Diego, California, USA. 562 pp. 1993.

Hocking, W.K., System design, signal processing procedures and preliminary results for the Canadian (London, Ontario) VHF Atmospheric Radar. Radio Sci., 32, 687-706, 1997.

A NEW MINIRADAR TO INVESTIGATE URBAN CANOPY: CURIE CANOPY URBAN RADAR FOR INVESTIGATION OF EXCHANGES

Alain Weill, Christophe Legac, Richard Ney and Laurent Chardenal

CETP 10-12 Avenue de l'Europe 78140, Vélizy, France

Introduction

Inside large cities, air dynamics knowledge is necessary for several kinds of investigations. For example pollution studies have to be connected to the city boundary layer and exchange between the city itself which concerns particularly the city canopy. However due to traffic, acoustic sounding does not seem to be the most relevant technique. Acoustic ambient noise mainly related to automobile traffic prevents from using Sodar. More, Sodar noise itself does not seem to be socially accepted by city inhabitants though as shown by Little (1972), the acoustic backscattering intensity can be considered as the most efficient information to retrieve atmospheric boundary layer turbulence. These considerations indicate an interest to develop an instrument able to give an information equivalent to Sodar but not sensitive to ambient noise and with no acoustic noise generation. About Doppler acoustic sounders abundant literature has been published, see for example Brown et Hall (1978), Neff and Coulter (1985), Weill et al. (1978), Weill and Lehmann (1990). We therefore decided to study the possibility to develop a very cheap low power small radar, to investigate the lower part of the urban canopy. The first idea was to work about the feasibility of a small FMCW radar as those designed by Konrad (1970), Richter (191969) or recently Eaton (1995) but the solution of a pulse system as used by Gossard et al., 1978, Browning (1971) was not excluded.

The aim is to document at least two domains: inside canopy corresponding to a height range from 20 m up to 100 m (with a 20 m gate resolution) and a boundary layer height domain between 100 m and 500 m (with a 50 m gate resolution). The antenna has to be small, with a dish diameter value close to one meter.

At first a low power FMCW radar has been evaluated but eliminated due to the difficulty and high associated cost to limit coupling between transmitter and receiver. The concept of a mobile pulse X band radar has then been chosen which involves to solve several questions as:

ability to perform sounding with a first gate close to 20 m height

systematic elimination of fixed echoes (ground clutter)

feasibility of different sounding modes for both domains (20m-100m and 100m-500m) which corresponds to what was usually performed by acoustic Doppler sounders in quiet atmosphere.

The project therefore aims to realize a miniradar prototype able to perform wind profiling in the lower part of the ABL (Atmospheric Boundary layer) with an orientated antenna.

We point out different topics from which it is necessary to get knowledge such as building vortex documentation, computation of entrainment processes across the canopy top and other questions that have to be solved: measurement of wind profiles upon forests, nuclear plants monitoring and survey, eolian fields speed limit survey, air-sea interactions study.

2. The CURIE radar system

The radar architecture is given on figure 1. The radar frequency is 9.48 GHz and is obtained by the mixing of a 9.6 GHz phase locked source and a 120 MHz signal generated by frequency multiplication from a 10 MHz OCXO. The pulse modulation is performed on the 120 MHz signal. After mixing and filtering the 9.48 GHz pulse can be phase modulated before amplification. The transmitter is a solid state power amplifier delivering a peak power of 100 W. The pulse is radiated by a Cassegrain antenna through a circulator acting as a TR

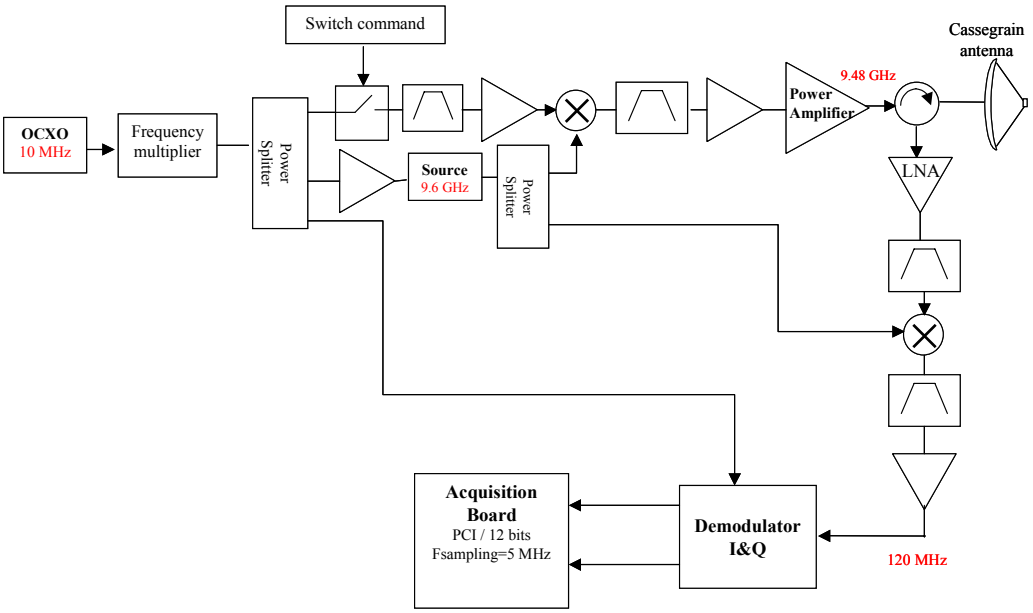

Figure 1. Curie radar architecture

(Transmit-Receive) switch.

The third port of the circulator feeds a LNA (Low Noise Amplifier).After filtering the signal is translated back to the 120 MHz frequency by mixing with the 9.6 GHz frequency. The last stages of the receiver are the 120 MHz band-pass filter, amplifier and the complex demodulator which delivers the I and Q video signals to the sampling and data processing unit. The architecture is rather standard but some features must be emphasized. To obtain a useful first range gate at a height of about 20m a low peak power transmitter has been selected. The choice between solid state or TWT technology is dictated by cost level which leads to a 100W peak power solid state amplifier. A specific design is implemented inside the power amplifier to limit the leakage after the pulse. The side-lobes of the antenna must be very low to limit the power received from ground clutter. High stable frequency sources and frequency multiplication techniques are used to yield very low phase noise X band signals. For the data processing a trade-off is made between the number of coherent additions and the FFT-point number.

3. First results.

The first step was to develop a first realization of the concept to show it was relevant to make atmospheric sounding for range as low as 30m with a 10 watts solid state amplifier.

As shown on the following figures (2 a, b, c) during clear air conditions, we can observe different kinds of Doppler spectra representative of different kinds of atmospheric activities. Let us point out that the central peak is narrow and peaks of small Doppler shift can be easily identified. However, several spurious spectral line attributed to power supplies have to

be eliminated to analyze correctly the Doppler shift.

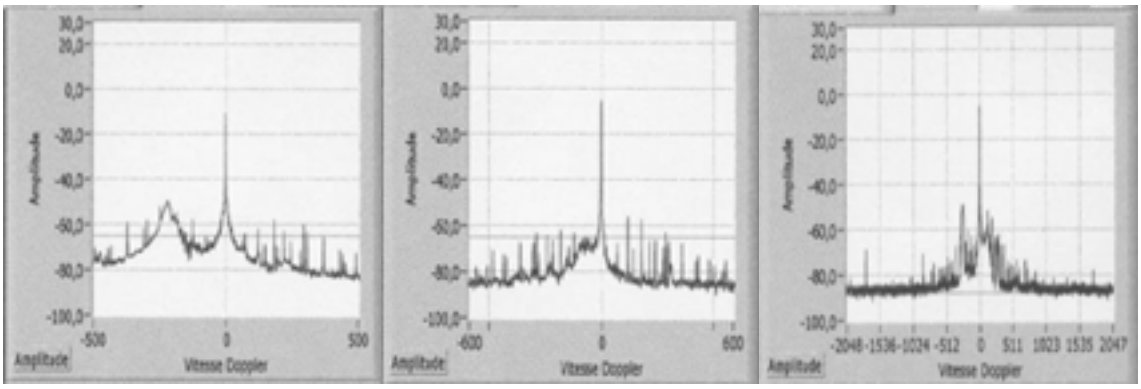

a) b) c)

Figures 2. a, b, c "Classical" Doppler spectrum corresponding to a) a non – atmospheric echo, b) an atmospheric echo (air velocity of .78 m/s and c) several echoes corresponding probably to tree leaves clutter.

.

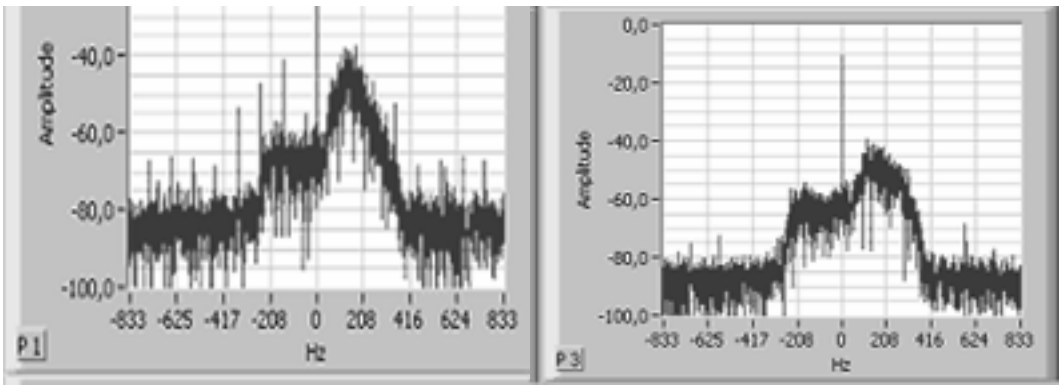

a) b)

Figure 3 a) spectrum during precipitation at gate n°1 (25m height) b) at gate n°3 (90 m height). The two peaks corresponding to precipitation and turbulence are here well separated.

The figures 3 a, b show spectrum obtained during precipitation conditions at 25 m and 90m height respectively taking into account the antenna orientation. On these spectrum two main spectral parts can be identified: one part related to turbulence and one part related to precipitation as already observed with acoustic sounder (Weill et al., 1986). It can be observed that at 90 m height the spectrum seems less noisy and a peak associated with precipitation is better identified

Conclusions.

It is difficult to conclude with these limited results, but we think that the CURIE miniradar is now feasible with two height ranges of observation (with a 100 W power amplifier). It remains a lot of questions to be solved and particularly the backscattering intensity interpretation in case of turbulence since probably as pointed by Kropfli; 1985, packets of particles of small dimensions can produce Bragg scattering just as turbulence does.

Acknowledgements.

The authors wish to thank particularly the CSOA and INSU to help to the development of CURIE. Special thanks are due to Hervé De Feraudy head of CETP for help and stimulation of this study.

References.

Brown E.H. and F.F. Hall,1978, Advances in atmospheric acoustics. *Rev. Geophys.Space Phys.* 16,47-180

Browning K.A., 1971, Structure of the atmosphere in the vicinity of large amplitude Kelvin-Helmoltz billows. *Q.J.R. Metorol. Soc*., 97, 283-299.

Eaton F.D., S.A. Mc Laughlin and J.R. Rhines, 1995, a new frequency- modulated continuous wave radar for studying planetary boundary layer morphology, *radio Science 30(1)*, 75-88.

Gossard E.E., R.B. Chadwick, K.P. Moran, R.G. Strauch, G.E. Morrison and W.C. Campbell, 1978, Observations of winds in the clear atmosphere unsing an FM-CW radar, *radio Science*, 13(2), 285-289.

Konrad, T.G., 1970, The dynamics of the convective process in clear air as seen by radar. *J. Atmos. Sci.* 27, 1138-1147.

Kropfli R.A., 1985, In probing the Atmospheric Boundary Layer, (D.H. Lenschow editor),Radar probing measurement of the planetary boundary layer: part II scattering by particles, *AMS*, 183-199

Neff W.D. and R.L. Coulter, 1985: In probing the Atmospheric Boundary Layer, (D.H. Lenschow editor), Acoustic Remote Sensing, *AMS*, 201-236.

Little C.G., 1972, On the detectability of fog, cloud, and snow by acoustic echo sounding methods. *J. Atmos. Sci.* 28, 748-755.

Richter J.H., 1969, High resolution tropospheric radar sounding, *Radio Science*, 4(12), 1261-1268.

Weill A., F. Baudin, J.P. Goutorbe, P. Van Grunderbeeck and P. Leberre, 1978 ,Turbulence Structure in temperature inversion and in convection fields as observed by Doppler sodar, *Boundary layer Meteorol.*,15, 375-390.

Weill A. and H.R. Lehmann, 1990, Already twenty years of acoustic sounding: some applications, *Zeitschrist für Meteorologie* 40 (4) 241-250.

Weill A., F. Baudin and C. Klapisz 1986:The CRPE minisodar, Applications in micrometeorology and in physics of precipitations, *Atmos. Res.,* 20 (2-4), 317-333.

Session PWG 1: System Calibrations and Definitions

A proper calibration of UHF/VHF wind profilers and MST radars is essential for the determination of atmospheric backscattering cross sections. Knowledge of the cross sections is used, for example, to obtain absolute radar reflectivities and their variation as function of time, location and meteorological condition. The System Calibrations and Definitions Permanent Working Group has the major task of defining such calibration procedures. Invited speakers will provide inputs on such topics as the use of sky maps as means of getting antenna efficiencies, the impact of ionospheric absorption on these sky maps, and the use of noise injection from hot loads. These will lead to open discussions among participants. Additionally, several definitions and terminologies have been introduced into the MST radar and wind profiling community. Based on a summary presented by the PWG chair persons there will be a debate as to which terms should preferably be used for particular parameters and widely applied methods.

Conveners:
P. Chilson and J. Röttger

PWG 1 Abstracts:

J. Röttger — MST RADAR CALIBRATION TO OBTAIN ABSOLUTE SIGNAL POWER

Session PWG 2: Data Analysis, Validation and Parameter Deduction Methods

This working group will examine signal processing techniques used for MST radars. Topics of interest include general pre-processing (e.g., interference and clutter removal, noise level estimation), analysis techniques (e.g. Doppler, full correlation analysis, interferometry) and statistical inversion methods (e.g. maximum-likelihood methods), and post analysis techniques (e.g. consensus averaging, outlier removal, data quality indicators). Related topics such as parameter comparisons and assimilation of multiple source data into physical models for "most likely parameter" estimation will be discussed. Invited speakers will provide presentations on these topics with the aim of stimulating discussion on how current techniques may be improved.

Conveners:
D. Holsworth, M. Yamamoto, and E. Kudeki

PWG 2 Abstracts:

W. Hocking	PARAMETER COMPARISON METHODS IN GEOPHYSICAL STUDIES
C. Meek	FULL CORRELATION ANALYSIS: ANALYSIS MODEL, DATA SELECTION, QUALITY INDICATORS FOR SASKATOON-TYPE MFR DATA
F. Kuo, C. Liu, K. Chen et al.	NEW METHODS TO DEDUCE GRAVITY WAVE PARAMETERS FROM RADAR DATA
E. Boyer, M. Petitdidier and P. Larzabal	PARAMETRIC ESTIMATION OF SPECTRAL MOMENTS OF OVERLAPPED WEATHER DOPPLER ECHOES BY THE USE OF HIGH-RESOLUTION

PARAMETRIC ESTIMATION OF SPECTRAL MOMENTS OF OVERLAPPED WEATHER DOPPLER ECHOES BY THE USE OF HIGH-RESOLUTION ALGORITHMS

E. Boyer[1], M. Petitdidier[2], and P. Larzabal[1,3]

[1] SATIE/ENS Cachan, UMR CNRS 8029, 61 avenue du président Wilson, 94235 Cachan Cedex France
[2] CETP 10-12 Avenue de l'Europe78140 Vélizy France
[3] IUT de Cachan, CRIIP, Université Paris Sud, 9 avenue de la division Leclerc, 94 234 Cachan cedex, France

I- INTRODUCTION

The purpose of this work is the estimation of the spectral moments of Doppler echoes even in the case of strongly overlapped echoes. In such cases, Fourier like techniques provide poor results because of the lack of resolution. Boyer et al.(2001) proposed the MUSIC algorithm for the estimation of the first spectral moment of the echoes and pointed out the very good resolution of this estimator in comparison with Fourier-like techniques. However, this method doesn't provide the two other spectral moments of interest for meteorological studies (the zeroth and the second moment of the echoes). To fill this lack, we propose the use of Stochastic Maximum Likelihood (SML) for a joint estimation of spectral moments. This method is based on a parametric modelization of the covariance matrix of the time series.
The proposed method is validated on the VHF and UHF times series obtained during Thunderstorm observations at the National Astronomy and Ionosphere Center, Arecibo, PR during September and October 1998. The results obtained confirm the great potential of the method. The algorithm is applied on the UHF time series and the step after consists of determining what echo corresponds to the wind and the hydrometeor ones. The reconstructed wind and reflectivity profiles are in a fairly good qualitative agreement with the corresponding profiles obtained by the use of a classical Fourier technique based on both VHF and UHF time series.

II- PRESENTATION OF THE METHOD

II.1 signal model

The SML method is based on following hypotheses:

- the *N* echoes contained in the power spectrum $P_S(f)$ of the time series *x(t)* are Gaussian:

$$P_S(f) = \left(\sum_{i=1}^{N} S_i(f) + \sigma_n^2 \right) |\beta|^2 ,$$

with

$$S_i(f) = \frac{P_i}{\sigma_i \sqrt{2\pi}} \exp\left(-\frac{1}{2} \left(\frac{f - f_i}{\sigma_i} \right)^2 \right), \qquad (1)$$

where σ_n^2 is the power of an additive white Gaussian circular noise, β is a Gaussian random variable with unit standard deviation, and where P_i, f_i and σ_i are the three unknown spectral moments of the i^{th} Gaussian echo.

- the time series vectors **x***(k)* of dimension $m \times 1$ obtained from independent recording data is a Gaussian stochastic vector with mean zero and covariance matrix $\mathbf{R}_x$: $\mathbf{x} \in \mathcal{N}(\mathbf{0}, \mathbf{R}_x)$.

It follows that the covariance matrix $\mathbf{R}_x$ can be written:

$$\mathbf{R}_x(\boldsymbol{\mu}) = \sum_{i=1}^{N} \left[P_i . \mathbf{A}(f_i) \mathbf{B}(\sigma_i^2) \mathbf{A}^*(f_i) \right] + \sigma_n^2 \mathbf{I}, \tag{2}$$

with

$$\mathbf{A}(f_i) = diag\left(1 \quad e^{2j\pi f_i T_s} \quad \ldots \quad e^{2j\pi f_i (m-1) T_s}\right), \tag{3}$$

$$\mathbf{B}_{k,l}(\sigma_i^2) = e^{-2\pi^2 \sigma_i^2 (k-l)^2 T_S^2}, \tag{4}$$

where $j^2 = -1$, $\mathbf{I}$ is the identity matrix, T_S the pulse repetition time of the radar, $(.)^*$ denotes the conjugate transpose and where $\boldsymbol{\mu}$ is parameter of dimension $3N+1$ to be estimated:

$$\boldsymbol{\mu} = \left[f_1 \quad \sigma_1^2 \quad P_1 \quad \ldots \quad f_N \quad \sigma_N^2 \quad P_N \quad \sigma_n^2 \right]. \tag{5}$$

II.2 the SML algorithm

The Maximum Likelihood (ML) estimates $\hat{\boldsymbol{\mu}}$ of $\boldsymbol{\mu}$ are calculated as the values of $\boldsymbol{\mu}$ that minimize the negative log-likelihood function $L(\boldsymbol{\mu})$,

$$\hat{\boldsymbol{\mu}} = \arg\min_{\boldsymbol{\mu}} \left(L(\boldsymbol{\mu}) \right), \tag{6}$$

with

$$L(\boldsymbol{\mu}) = \log\left(\left| \mathbf{R}_x(\boldsymbol{\mu}) \right| \right) + Tr\left\{ \mathbf{R}_x^{-1}(\boldsymbol{\mu}) \widehat{\mathbf{R}_x} \right\}, \tag{7}$$

and where the notations $\log(.)$, $|.|$ and Tr(.) denote the natural logarithm, the matrix determinant and the trace operator. $\hat{\mathbf{R}}_x$ is the sample covariance matrix

$$\hat{\mathbf{R}}_x = \frac{1}{K} \sum_{k=1}^{K} \mathbf{x}(k) \mathbf{x}(k)^*. \tag{8}$$

The SML algorithm is initialized with different values of the parameter vector space and is optimized with a second-order steepest descent method. For more details about that algorithm, see Boyer et *al.* (2003).

III- EXPERIMENTAL RESULTS

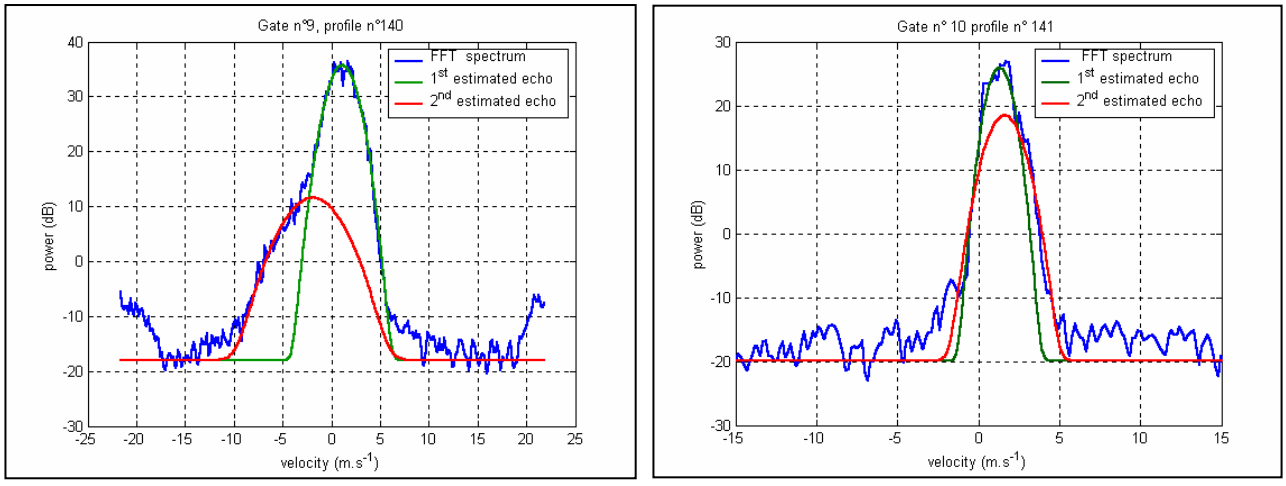

Fig. 1: MVS estimation of the two echoes with UHF data (*Nfft*=256, *Ncoh*=8 and *Ninc*=8)

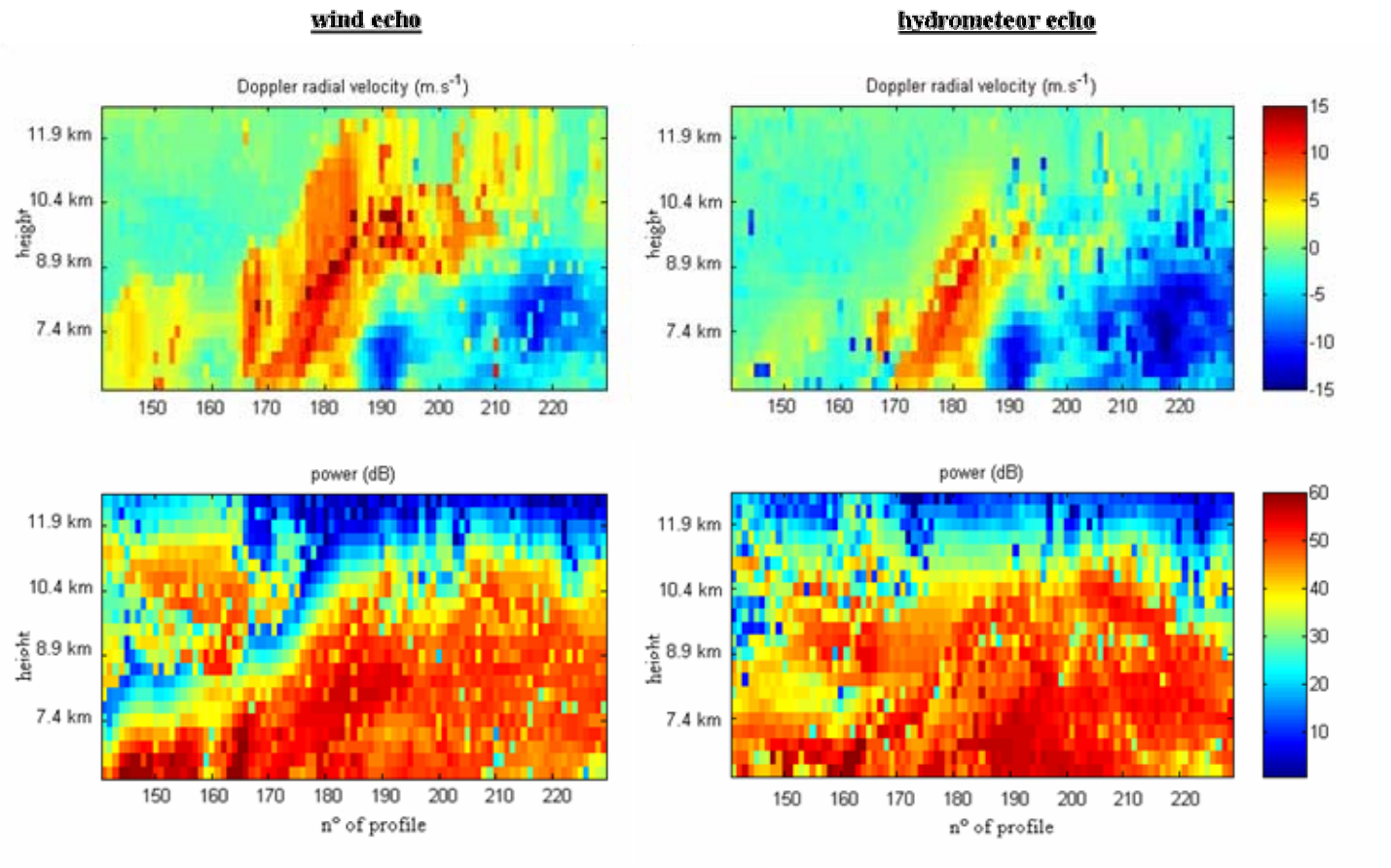

Fig. 2: Doppler radial velocity and power of the wind echo and hydrometeor echo

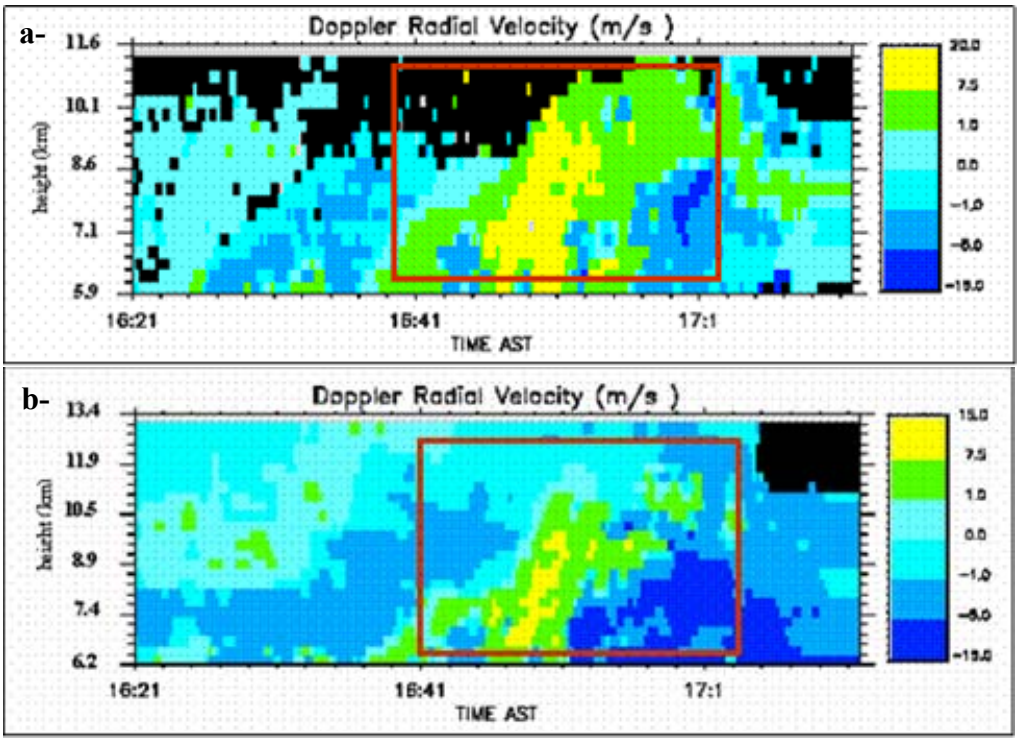

Fig. 3: a- wind echo (from VHF data)
b- hydrometeor echo (from UHF data)

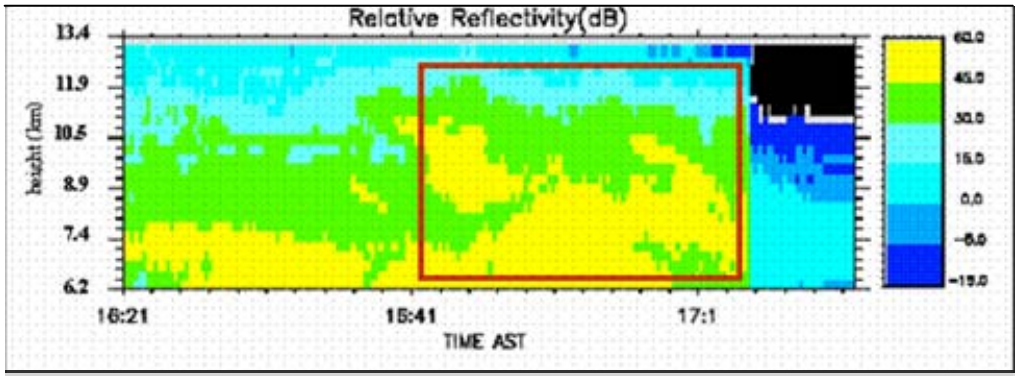

Fig. 4: reflectivity of the hydrometeor echo

Figure 1 presents the results of the MVS reconstruction of UHF spectra of two strongly overlapped echoes. The estimated echoes are in perfect adequacy with the FFT spectrum (which is not calculated with the SML algorithm). Figure 2 presents the velocity and reflectivity fields of both wind and hydrometeor echoes retrieved by the SML algorithm from only the UHF data on the 8th October. As the thunderstorm, characterized by a large vertical air-motion, is above the radar the method proposed by Williams et al. (2000) is not efficient because not adapted to this case. Then, the vertical velocity is used to separate in UHF data the wind echoes from the hydrometeor ones. In figure 3 and figure 4 are presented the velocity and reflectivity fields retrieved by a "standard" method applied on the UHF and VHF spectra. The squares drawn in these figures delineate the zone corresponding to figures 2 obtained with the SML algorithm. The agreement is qualitatively fairly good, i.e. the same features are observed.

III- CONCLUSION AND PROSPECTIVE

The MVS algorithm appears to be a very attractive method for the estimation of the three spectral moments of strongly overlapped Gaussian echoes. These first results have to be confirmed by the study of other cases and by the comparison of the method applied successively on VHF and UHF data. This is an ongoing work.

ACKNOWLEDGEMENTS

The National Astronomy and Ionospheric Center is operated by Cornell University under contract with the National Science foundation.

REFERENCES

Boyer E., Petitdidier M., Corneil W., Adnet C. and Larzabal P., Application of model-based spectral analysis to wind profiler radar observations, *Ann. Geophys.*, 19, 815-824, 2001.

Boyer E., Larzabal P., Adnet C. and Petitdidier M.., Parametric Spectral Moments Estimation for Wind Profiling Radar, *IEEE Trans. On Geosci. and Remote Sens.*, 41, 1859-1868, 2003.

Williams C. R., Ecklund W. L., Johnston P. E. and Gage K. S., Cluster Analysis Techniques to Separate Air Motion and Hydrometeors in Vertical Incident Profiler Observations, *J. Atmos. Oceanic Technol.*, 17, 949-962, 2000.

Session PWG 3: Accuracies and Requirements for Meteorological Applications

Observations from MST radars are finding increased application in meteorology. This workshop will deal with the accuracy, precision, and sampling requirements for those applications. Discussions will include known practical or theoretical limitations of the technique as applied in various climatic/synoptic settings (such as mid-latitude vs. tropical, tropospheric vs. stratospheric, etc.) and for observation of various meteorological variables (wind, temperature, humidity, precipitation, tropopause height, frontal surfaces, etc.). Other general or specific topics are welcome; please send your suggestions to the conveners.

Conveners:
G. Nastrom and J. Chau

PWG 3 Abstracts:

P. Johnston	PROFILER ACCURACY
C. Lucas	SOUTHERN HEMISPHERE SYNOPTIC METEOROLOGY
K. Takahashi.	RADARS AND THEIR APPLICATION TO METEOROLOGICAL PROBLEMS IN PERU
C. Gaffard	NETWORKS OF RADARS AND THEIR APPLICATION TO METEOROLOGICAL PROBLEMS
C. La Hoz	NEUTRAL WINDS IN THE D-E REGION

Session PWG 4: International Collaborations

The session on international collaborations would be devoted primarily to four topics of current interest:

- On geographic dependence of Polar Mesospheric Summer Echoes (PMSE) - An International Observing Program. The discussion on this would aim at evolving a coordinated multi-national program for a comparative study of the intensity of PMSE at different latitudes and longitudes.
- International Multi-instrumented Campaigns: Under this the outcome of three major campaigns, a. SEEK-2 (Sporadic E Experiment in Kyushu-2), b. MUTSI (MU radar Temperature Sheets and Interferometry) and c. CPEA (Coupling Processes in the Equatorial Atmosphere), would be reviewed and recommendations made for possible follow-up campaigns.
- Multinational Atmospheric radar Projects: Collaborations of developed and developing countries. Two specific topics have been identified for detailed discussions under this item: a. TRAINER (TRopical Atmosphere INdonesian Equatorial Radar) - a potential RASC-DLR-LAPAN-ISRO collaborative program and b. ISAR (International Schools on Atmospheric Radar).
- Future direction of international collaboration with EISCAT. The discussions on this would be aimed at formulating EISCAT - based collaborative programs on middle and lower atmosphere research.

Conveners:
P.B. Rao, S. Fukao, R. Woodman & J. Röettger

PWG 4 Abstracts:

S. Fukao	AN ONGOING JAPANESE PROJECT: COUPLING PROCESSES IN THE EQUATORIAL ATMOSPHERE
J. Röttger	REPORT ON THE THIRD INTERNATIONAL SCHOOL ON ATMOSPHERIC RADAR – ISAR3 – HELD IN NOVEMBER/DECEMBER AT THE ABDUS SALAM INTERNATIONAL CENTER FOR THEORETICAL PHYSICS IN TRIESTE, ITALY
D. Narayana Rao	TROPICAL NETWORK OF RADARS
C. Gaffard	NETWORKS OF RADARS AND THEIR APPLICATION TO METEOROLOGICAL PROBLEMS
I. Reid	WUHAN MST RADAR

Session II.E: NOVEL PERSPECTIVES AND UNSOLVED ISSUES

A brain-storming session was included in this workshop with the aim to highlight open questions and potential solutions, to produce proposals for innovative approaches, define new programs and prepare recommendations. To review and outline such research directions and to stimulate such discussions the following invited papers were presented".

Conveners:
P. Chilson, S. Fukao & J. Röttger

AN ADAPTIVE CLUTTER REJECTION SCHEME FOR MST RADARS

Toru SATO and Kazunori KAMIO

Department of Communications and Computer Engineering
Graduate School of Informatics, Kyoto University,
Kyoto 606–8501, Japan
E-mail: tsato@kuee.kyoto-u.ac.jp

1 Introduction

Sidelobe cancelling is an important issue in various fields of antenna engineering. In atmospheric radar applications, where a sharp antenna beam is usually configured by a large array antenna, strong clutter echoes from surrounding mountains are the major source of interference.

A clear advantage of the adaptive antenna is that it makes use of an extra information of the direction of arrival in discriminating undesired echoes in contrast to other clutter rejection schemes based on signal processing of the received echoes, such as adaptive filtering. However, conventional algorithms for the adaptive antenna had a serious defect of distorting the antenna main beam pattern when they are directly applied to atmospheric radars.

Original sidelobe canceller by Howells (1965) may cancel the output of the main beam under extremely strong interference signal. This effect is mitigated by adding a limiter in its feedback loop (Abe *et al.*, 1995), but the threshold should be controlled according to the interference level. Since the sidelobe canceller is regarded as a type of adaptive antenna, Directionally Constrained Minimum Power (DCMP) algorithm (Takao *et al.*, 1976) can be used to suppress the sidelobe echoes while maintaining the desired signal. The same principle is also known as Minimum Variance Distortionless Response (MVDR) (Haykin, 2001). This idea is further utilized in a variety of Generalized Sidelobe Canceling (GSC) algorithms (Griffiths and Jim, 1982), which assure the response in the desired direction by controlling the weight of an output which does not contain desired signal. Efforts have been made to effectively delete the desired signal in this output by means of block filters (Fudge and Linebarger, 1996, Chu and Fang, 1999, Wang and Fang, 2000).

Performance of these algorithms depend on the characteristics of the desired signal, and the shape of the main beam may be altered when the cancellation is not complete. The main beam pattern is an essential design factor in the atmospheric radars since the target is widely distributed in space, and the 'desired signal' is defined as the echoes which return from the main lobe region. A slight change of the shape of the main beam will result in an offset of the estimated wind velocity.

Here we introduce a new sidelobe cancelling algorithm (Kamio and Sato, 2003), which extended DCMP by introducing another constraint on the weight of the receiving array so that the main beam pattern of the radar is conserved. We demonstrate its effectiveness by applying the technique to actual data taken with the MU (Middle and Upper atmosphere) radar. Its performance in rejecting the clutter echoes from surrounding mountains is examined, and the optimum choice of the controlling parameter is discussed with actual data as well as numerical considerations.

2 Proposed Algorithm

Received signal of a phased array is given by

$$y = W^H X \tag{1}$$

where X and W are the complex input signal vector and the weight vector, respectively. The output power is expressed in terms of the covariance matrix R_{xx} as

$$P = \frac{1}{2}[|y|^2] = \frac{1}{2}W^H X X^H W = \frac{1}{2}W^H R_{xx} W \tag{2}$$

Principle of DCMP algorithm(Takao *et al.*, 1976) is to minimize the output power under the constraint

$$W^H C = H^* \tag{3}$$

where C is the desired direction vector, and H is the constraint. Here we further apply an alternate condition

$$W^H W \leq U \tag{4}$$

which forces that the norm of the weight should be less than a given value U, which is set to be sufficiently lower than the main lobe level, but not to affect the weight control of the sidelobe region. This second constraint assures that the entire main lobe pattern is not affected by the weight control. Here we call this algorithm as 'DCMP Constrained Norm' (DCMP-CN) in contrast to conventional DCMP.

The principle of DCMP-CN is thus expressed as

$$\min_W \left(P_{\text{out}} = \frac{1}{2}W^H R_{xx} W \right) \tag{5}$$

$$\text{subject to } C^T W^* = H \;\&\; W^H W \leq U \tag{6}$$

This minimization problem with an equality constraint and an inequality condition is solved by using penalty function method. The cost function is expressed as

$$Q_k(x) = f(x) + \rho_k(\sum_{i=1}^{r}(g_i(x))^2 + \sum_{r+1}^{m}(g_i(x))_-^2) \ , \tag{7}$$

where $f(x)$ is the function to be minimized, $g_i(x) = 0$ gives an equality constraint, and $g_i(x)_- = 0$ gives an inequality constraint. Here $(a)_- = \min\{0, a\} = (a - |a|)/2$, r is the number of equality constraints, and $(m - r)$ is the number of inequality constraints.

We choose an arbitrary increasing series $\{\rho_k\}$ of the penalty factor which vanishes to ∞. For each k, we minimize $Q_k(x)$ with a non-linear unconstrained optimization algorithm to obtain x_k starting from x_{k-1}. This procedure is iterated from x_0 by increasing the penalty factor so that x_k converges to the allowed region.

The cost function for the current case is given by

$$\begin{aligned} Q_k(W) &= \frac{1}{2}W^H R_{xx} W + \rho_k[|W^H C - H|^2 + (U - W^H W)_-^2] \\ &= \frac{1}{2}W^H R_{xx} W + \rho_k[(W^H C - H)(C^H W - H^*) + (U - W^H W)_-^2] \ . \end{aligned} \tag{8}$$

The gradient of $Q_k(W)$ in terms of the weight vector W is given by

$$\nabla_w Q_k(W) = R_{xx} W + \rho_k[2C(C^H W - H^*) - 4W(U - W^H W)_-] \ . \tag{9}$$

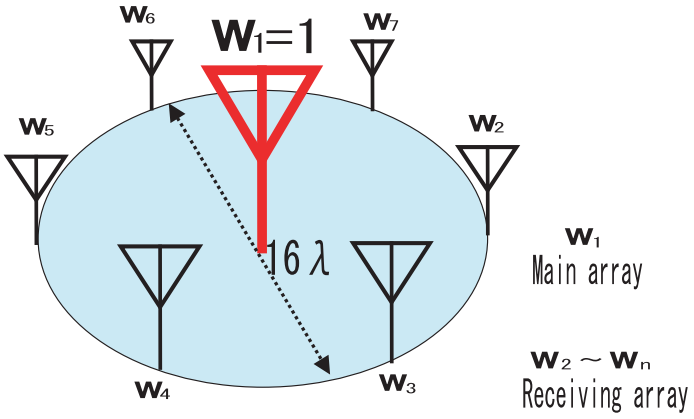

Figure 1: Configuration of a high-gain antenna and the sub-array.

3 Application to High Gain Arrays

Here we consider the application of DCMP-CN to the case of a high-gain antenna array consisting of several hundred elements. In such a case, it is not practical to control all of the elements. Instead, we select several antennas at the outer edge of the array to configure a sub-array, and only control the weights of its elements as shown in Fig. 1, keeping the weight of the main array output to 1. In the radar application, the main array is used both for transmission and reception, and the sub-array is used only for reception. This configuration is useful in suppressing the clutter echoes of existing radar by adding several receiving antenna elements. In this case, the output power is rewritten as

$$P_{\text{out}} = \frac{1}{2} W^H R_{xx} W = \frac{1}{2}(x_1 x_1^* + W_{2:n}^H X_{2:n} x_1^* + x_1 X_{2:n}^H W_{2:n} + W_{2:n}^H \tilde{R}_{xx} W_{2:n}) \ , \qquad (10)$$

where subscript 1 denotes the output of the main array, and 2 to n correspond to sub array. Since the constraints are given only to the sub-array elements, the problem is expressed as

$$\min_W \left(P_{\text{out}} = \frac{1}{2}(x_1 x_1^* + W_{2:n}^H X_{2:n} x_1^* + x_1 X_{2:n}^H W_{2:n} + W_{2:n}^H \tilde{R}_{xx} W_{2:n} \right)$$
$$\text{subject to } C_{2:n}^T W_{2:n}^* = H \ \& \ W_{2:n}^H W_{2:n} \leq U \ . \qquad (11)$$

The cost function is then given by

$$Q_k(W) = \frac{1}{2}(x_1 x_1^* + W_{2:n}^H X_{2:n} x_1^* + x_1 X_{2:n}^H W_{2:n} + W_{2:n}^H \tilde{R}_{xx} W_{2:n})$$
$$+\rho_k [(W_{2:n}^H C_{2:n} - H)(C_{2:n}^H W_{2:n} - H^*) + (U - W_{2:n}^H W_{2:n})_-^2 \ . \qquad (12)$$

4 Observations

We applied this algorithm to the data taken with the MU (Middle and Upper Atmosphere) radar. It is a large atmospheric radar with a flexible active phased array antenna consisting of 475 Yagi-Uda antennas. The antenna array consists of 25 groups of hexagonal sub-array with 19 crossed 3-element Yagi antennas. A transmit/receive module is connected to each Yagi antenna. On reception, RF signal of 46.5 MHz is converted to IF of 5 MHz at each module, and the output of 19 modules are combined at each group. Combined IF signals from 25 groups

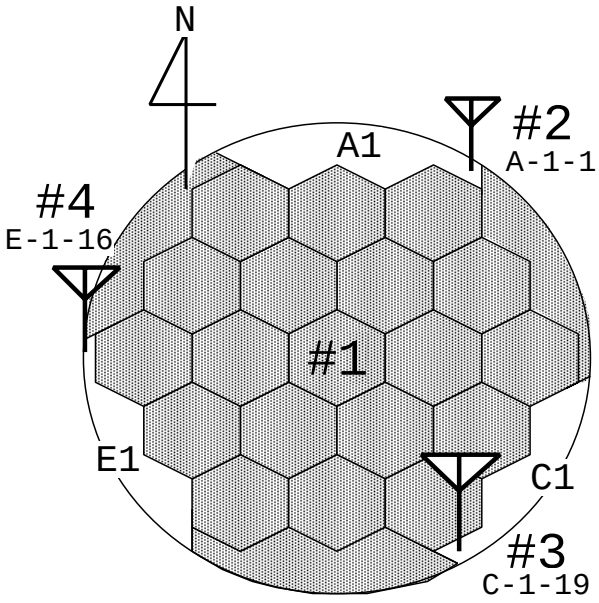

Figure 2: Antenna position for observation.

are sent to the control building, divided for 4 receiver channels. Each receiver can select and combine output from 25 groups at an arbitrary selection.

We made an experiment making use of this flexibility. Output from all groups except for 3 groups at the outer edge of the array is fed to a receiver as shown in Fig. 2. For the rest of 3 groups, only one antenna is activated in each group, and connected to three receivers.

Observation was made for about two hours of 6:45–7:56 JST and 17:18–18:21 JST on 26 December 2002 with 1-μsec pulse transmissions at 400 μsec intervals. The antenna beam was tilted 10° from the zenith, and tropospheric echoes were sampled from 1.5 km to 9.6 km height region at 150-m sampling intervals. The received time series was averaged for 19 pulses for each range gate and recorded for off-line processing.

5 Clutter Suppression Using Real Data

Here we use the above data to examine the effectiveness of our proposed algorithm. The entire antenna array is regarded as the main antenna, and three antennas connected to other three receivers constitute the sub-array. The weight of the main channel is fixed, and the complex weight of the output from other three channels are varied so that the clutter echo is suppressed. By controlling the weight of only the sub-array, complexity of the adaptive processing is drastically reduced. Also, this system can be easily applied to existing radar systems.

The maximum constraint of the weight norm U is set to 0.5. In generating the covariance matrix R_{xx}, instantaneous samples are averaged with a forgetting factor of β=0.997, which is roughly equivalent to take the average of 1,000 samples. The appropriate values of U is discussed in more details in section 6.

Fig. 3 shows an example of the echo power spectrum. The spectrum was generated by applying 128-point FFT to a time series of 9.7 s after coherent integration of 190 pulse samples. No incoherent integration is applied. The vertical scale is in an arbitrary unit, and the galactic background noise level is about 100dB. The dashed line shows the original spectrum with the main antenna. The sharp spike at zero Doppler velocity is the clutter component, while a broad peak with positive Doppler shift is the desired echo. The solid line shows the result

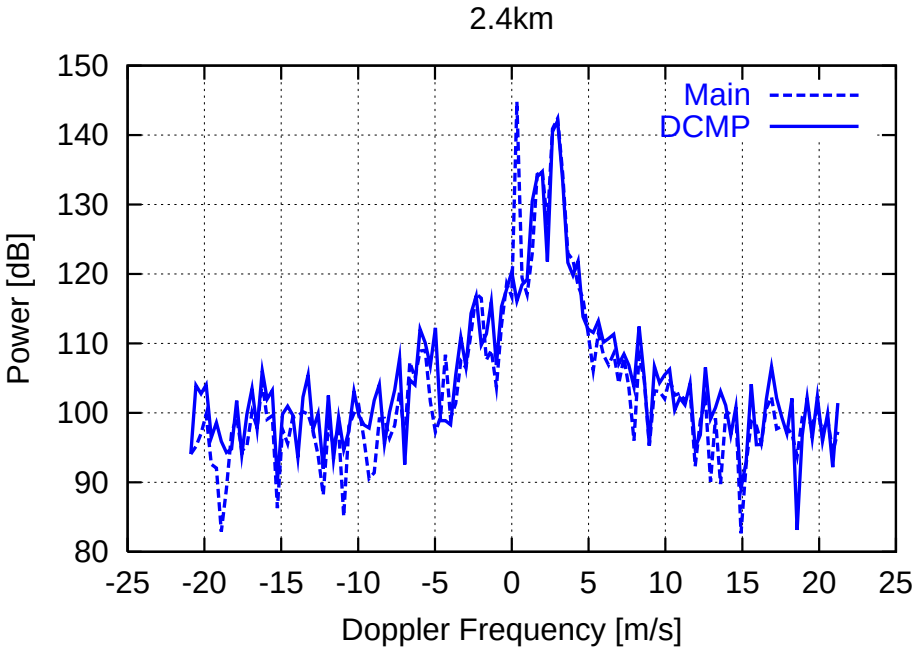

Figure 3: Doppler echo power spectrum at the range of 2.4km processed with conventional DCMP algorithm.

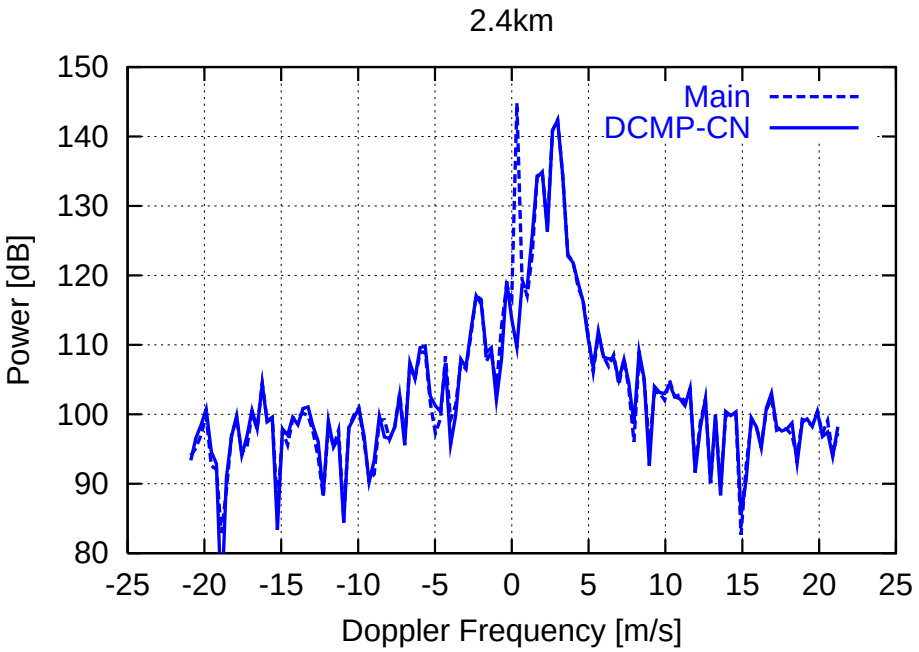

Figure 4: Doppler echo power spectrum at the range of 2.4km processed with the proposed DCMP-CN algorithm.

of conventional DCMP, with which the clutter is suppressed with a penalty of increased noise level.

Fig. 4 shows the same spectrum processed with the proposed DCMP-CN algorithm. The solid line exactly follows the desired signal component by rejecting the clutter component only. It should be noted that we assume no information on the echo power spectrum such as the narrow clutter spectrum. It is therefore possible to cancel not only the DC clutter, but also clutters with fading as far as its time constant is long enough compared to the time required to obtain the covariance matrix.

The increased noise level with the conventional algorithm is due to large weight of the sub-array elements, which enhanced the galactic noise level and also atmospheric echoes entering low elevation sidelobes, which spreads out in a broad Doppler spectrum. On the other hand, the proposed DCMP-CN algorithm effectively suppresses such increase by controlling the weight of the sub-array elements. This example clearly demonstrates the usefulness of adaptively controlling the antenna pattern with a sub-array configuration.

It should be noted that the adaptive cancellation needs to be applied separately for different range gates and beam directions. In this manner, clutters from various directions can be suppressed with a small number of sub-array elements, as far as they have different range from the radar. As the computational load of the proposed algorithm is very light, more than 1,000 time series corresponding to different range gates and beam directions can be handled simultaneously with a personal computer.

6 Considerations on the Constraints

In the previous section, we set the maximum norm constraint U to 0.5. Here we examine the appropriate range of this value, and also the relative importance of the norm constraint over the directional constraint.

The proposed DCMP-CN algorithm has an advantage that the control parameter U can be chosen regardless to the strength of the desired and undesired signals, since it is determined simply by the relative pattern of the main and sub-array antennas. However, there is a certain range of U that gives the best performance.

If we set U to a too large value, the DCMP-CN algorithm approaches to DCMP, and thus becomes unable to suppress the increase of the noise level as shown in Fig. 3. On the other hand, if we set U to a too small value, the algorithm may not be able to cancel the clutter component by the combined output of sub-array elements.

We first consider a case where the output of a sub-array element is added to that of the main array consisting of M elements. We assume that the sub-array element is the same as that of the main array, and the output is in phase for the main beam direction. Also, in Eq. (10) we implicitly assumed that the output of the sub-array element is normalized to that of the main array at the uniform-gain level. At VHF range, where the noise is dominated by the galactic background radiation, it is equivalent to normalize them by their noise level.

In this case, the signal power after adding the sub-array element increases by $(\sqrt{M}+1)^2$ times, while the noise level increases by a factor of 2. The gain of the signal-to-noise ratio by adding a sub-array element is thus given by

$$G_{\mathrm{SNR}} = \frac{(\sqrt{M}+1)^2}{2} \quad , \tag{13}$$

which is roughly -3dB for a large M.

Next we consider a more general case where the sub-array element has a relative gain of G_{s} in the main beam direction of the main-array element, the output power of the sub-array

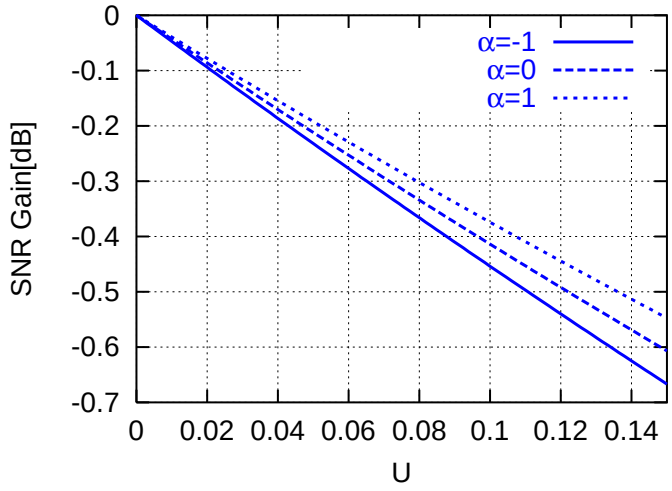

Figure 5: SNR loss as a function of constrained norm value U.

element is multiplied by U before addition, and it may not be in phase with the main array. In this case, Eq. (13) becomes

$$G_{\rm SNR} = \frac{(\sqrt{M} + \alpha\sqrt{G_{\rm s}U})^2}{1+U} \quad , \tag{14}$$

where α takes a value between -1 and 1, and is 1 for the case where two signals are in phase, 0 for the orthogonal phase, and -1 for the opposite phase. This situation corresponds to the worst possible case of the proposed algorithm with norm constraint value of U. Although we have examined only the case of one antenna element, Eq. (14) can also be applied to a sub-array consisting of multiple antenna elements, because the norm constraint U limits the sum of the weight of sub-array elements.

In the case shown in Fig. 4, $G_{\rm s} = 1$ (0dB) and $U = 0.5$, which gives $G_{\rm SNR}$ of -1.5dB. However, the actual loss is much less than this value as is clear from the figure, because Eq. (14) gives the worst case. Fig. 5 shows $G_{\rm SNR}$ versus U for the case of $M = 475$, assuming the MU radar, and $G_{\rm s} = U$.

Apparently, a small constraint is desirable in order to assure a small loss in SNR. If we allow a loss of up to 0.5dB, the norm constraint U should be set to 0.135, 0.120, and 0.105 for the in-phase, orthogonal, and the out-of-phase cases, respectively. As we assumed that the antenna element used for the sub-array has a gain of $G_{\rm s} = U$ relative to that for the main-array element, it means that the sub-array element should have a relative gain of -9.2dB in the main lobe direction for $U = 0.12$. In the case of the MU radar, as a typical example of VHF MST radars, 3-element Yagi antenna elements with an isotropic gain of 7.2dB are pointed to the zenith, and the main lobe is steered in an angular region of 30° from the zenith. An isotropic gain of less than -2dB is easily achieved in this angular region by pointing the same element to the horizontal direction, for example. If a specially designed antenna element which has less sensitivity to the main lobe region is used for the sub-array element, a larger value of U becomes acceptable.

If we apply the proposed DCMP-CN algorithm, the sub-array elements should always be kept in phase with the main antenna because of the directional constraint. The orthogonal and the out-of-phase cases examined above correspond to situations where this constraint is not applied. Fig. 5 shows that if we remove the directional constraint from the algorithm with $U = 0.12$, we further loose about 0.13dB, or 3%, of the sensitivity. The advantage of not

applying the directional constraint is that a simpler algorithm with only the norm constraint can be used, and that no phase calibration is required for the sub-array elements.

7 Summary

In this paper, we applied an adaptive sidelobe suppression algorithm developed for a high-gain antenna to actual data taken by the MU radar, and confirmed its effectiveness in suppressing the clutter echoes from mountains.

By constraining the weight norm of the sub-array as well as the response of the main antenna to the desired direction, good cancellation of undesired signal is achieved without disturbing the main beam pattern. It should be noted that the proposed algorithm does not require any knowledge on the input signal spectrum.

The proposed method can be easily implemented to existing high-gain antenna systems by adding a small number of receiving antenna elements and a personal computer which performs all necessary computation and control.

Considerations are made on the value of the norm constraint U to achieve the best performance. One of the advantages of the proposed algorithm over other adaptive antenna algorithms is that the controlling parameter is independent from the strength of the interference signal, and depends only on the antenna pattern of the main antenna and the sub-array.

References

Abe, K., K. Hirasawa, and H. Watanabe, Radar sidelobe canceller characteristics in high power interference, *IEICE Trans. Commun.*, **E78-B**, 1507–1512, 1995.

Chu, Y., and W. Fang, A novel wavelet-based generalized sidelobe canceller, *IEEE Trans. Antennas Propagat.*, **47**, 1485–1495, 1999.

Fudge, G. L., and D. A. Linebarger, Spatial blocking filter derivative constraints for the generalized sidelobe canceller and MUSIC, *IEEE Trans. Signal Processing*, **44**, 51–61, 1996.

Griffiths, L. J., and C. W. Jim, An alternative approach to linearly constrained adaptive beamforming, *IEEE Trans. Antennas Propagat.*, **30**, 27–34, 1982.

Haykin, S. S., *Adaptive filter theory*, 4th Ed., Prentice Hall, New York, 995pp, 2001.

Howells, P. W., Intermediate frequency sidelobe canceller, U. S. Patent No.3202990, 1965.

Kamio, K., and T. Sato, An adaptive sidelobe cancellation algorithm for high-gain antenna arrays, *IEICE Trans. Commun.*, **J86-B**, 790–797, 2003 (in Japanese).

McWhirter, J.G., Data-domain penalty function algorithm for stabilized adaptive beamforming, *IEE Proc. Radar, Sonar Navig.*, **147**, 265–269, 2000.

Takao, K., M. Fujita, and T. Nishi, An adaptive antenna array under directional constraint, *IEEE Trans. Antennas Propagat.*, **24**, 662–669, 1976.

—, and N. Kikuma, Tamed adaptive antenna array, *IEEE Trans. Antennas Propagat.*, **34**, 388–394, 1986.

Wang, Y., and W. Fang, Wavelet-based broadband beamformers with dynamic subband selection, *IEICE Trans. Commun.*, **E83-B**, 819–826, 2000.

Yang, H., and M. A. Ingram, Design of partially adaptive arrays using the singular-value decomposition, *IEEE Trans. Antennas Propagat.*, **45**, 843–850, 1997.

THREE-METRE-SCALE TURBULENCE ANISOTROPY AS A PRECURSOR TO RAIN

Anna Hocking[1] and W.K. Hocking[2]

1. Mardoc Inc., London, Ontario, Canada.
2. Dept. of Physics and Astronomy, University of Western Ontario, London, Ontario. Canada.

Abstract.
It is shown that the anisotropy parameter, θ_s, which is often measured with VHF radars, can serve as a forecast diagnostic for the occurrence of local liquid precipitation. We demonstrate this effect using VHF and S-band radars at McGill University, near Montreal, QC, Canada, for the months of October and November, 2002. The study is preliminary, and is to be extended to include other months of the year. Current observations suggest that the statement is true for non-winter months, but is not valid once the precipitation becomes predominantly snow and ice. It is not clear whether this phenomenon is specific to the McGill site, or can be applied to other locations as well.

Introduction.
It has long been recognized that atmospheric scatter detected by ~50 MHz VHF windprofiler radars is anisotropic in nature, with scatter from overhead generally being stronger than scatter observed when off-vertical beams are used. The phenomenon is especially dominant in the stratosphere (e.g. Liu and Roettger, 1978; Gage and Green, 1978, Tsuda et al., 1986; Hocking et al., 1990). Discussions about this phenomenon often revolve around consideration of specular reflectors, but anisotropic turbulence can also contribute to the differences in relative powers. Hocking and Hamza (1997) have discussed the differences between specular reflections and anisotropic turbulence, and described some methods which can help distinguish the phenomena.

Tropospheric observations of the aspect sensitivity have also been made. The troposphere is generally less stable than the stratosphere on average, and it is not unreasonable to suppose that tropospheric aspect sensitivity might be considered to be due mainly to anisotropic turbulence. However, most observations of anisotropy are only made over relatively short time frames, since the studies have often been considered to be primarily for curiosity-based research.

In this paper, we present data from a VHF ST radar system which routinely measures the aspect-sensitivity on a continuous basis. The radar works at a frequency of 52 MHz, and receives its greatest scatter from Fourier scales of about 3 metres. This corresponds to turbulent eddies with typical depths of the order of 2 to 3 metres (see Hocking (1987), and references therein). The radar is located close to a large S-band radar which is sensitive to precipitation, and the comparisons between the two radars form the basis of this paper.

Method.
The aspect sensitivity of radar scatter is most simply measured by comparing the signal strengths determined on an off-vertical bean and a vertical beam. For a very narrow beam, the relative powers are of the form

$$P_{ratio} = exp\{ -sin^2\theta/sin^2(\theta_s)\}$$

while for a beam of finite width, the parameter θ_s is found according to the expression

$$\theta_s = \arcsin\{\sqrt{[\sin^2\theta_t/\{\ln(P(0)/\ln(P(\theta_t)\} - \sin^2\theta_0]}\}$$

where θ_t is the tilt of the off-vertical beam, θ_0 is the 1/e half-width of the beam, $P(0)$ and $P(\theta_t)$ are the powers received on the vertical and off-vertical beams respectively (e.g. Hocking, 1988; Hooper and Thomas, 1995). The parameter θ_s is small when the scatterers are highly stretched horizontally relative to their vertical extent, and θ_s is large when the scatterers are close to isotropic. Hocking and Hamza (1997) have described how θ_s relates to the length-to-depth ratio of the scatterers in greater detail.

The parameter θ_s is a standard output from the McGill VHF windprofiler radar. This instrument has been described by Campos and Hocking (this issue). A typical height-time diagram of this parameter is shown in fig. 1. Notice in particular that there are frequent occurrences where θ_s exceeds 20^o. The transition is often quite sharp, changing rapidly between values of the order of 9^o or less and values of over 20^o within less than one hour.

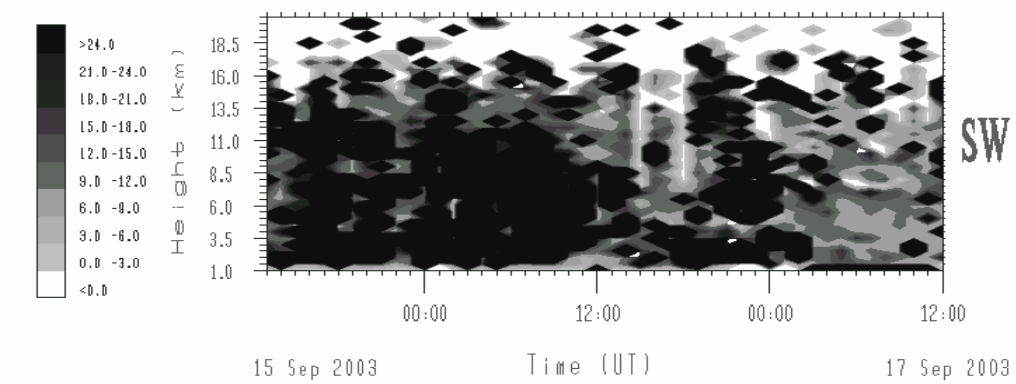

Fig. 1. θ_s parameter plotted vs height and time from 1200 on 15 September to 1200 on 17 September, 2003.

An S-band Doppler radar operates within close proximity to the windprofiler radar. It scans out to distances of typically 240 km, and is very sensitive to the occurrence of precipitation. Early observations suggested that when the radar detected precipitation, the VHF radar showed its largest values of θ_s, indicating greater isotropy. We have therefore carried out a detailed comparison between the θ_s parameter measured with the VHF radar and the occurrence of precipitation determined with the S-band radar. An example of a typical precipitation map seen with the S-band radar is shown in fig.2, and this map coincides with the occurrence of strong isotropy seen in fig. 1.

In order to compare the two radar sets, we decided to develop simple parameters to represent each data type. For the VHF radar, we examined the aspect sensitivity parameter within any given hour, and found the percentage of the height range between 1 km and 10 km (approximately the tropopause) in which θ_s exceed 20^o. We assigned a value of 1 if this number was less than 25%, 2 if it lay between 25% and 50%, 3 if it lay between 50% and 75%, and 4 if it exceeded 75%. This parameter will be referred to as the "isotropy index". We then performed a 5-point running mean of this parameter, in order to introduce a small level of smoothing. At the same time, we examined the hourly precipitation maps and searched for signs of precipitation within 200 km of the S-band radar. If precipitation existed in at least 10% of the viewing area, a number 1 was assigned to that hour. If no precipitation

was present, or precipitation was present in only small quantities, the period was assigned a value of 0. This parameter is called the precipitation index.

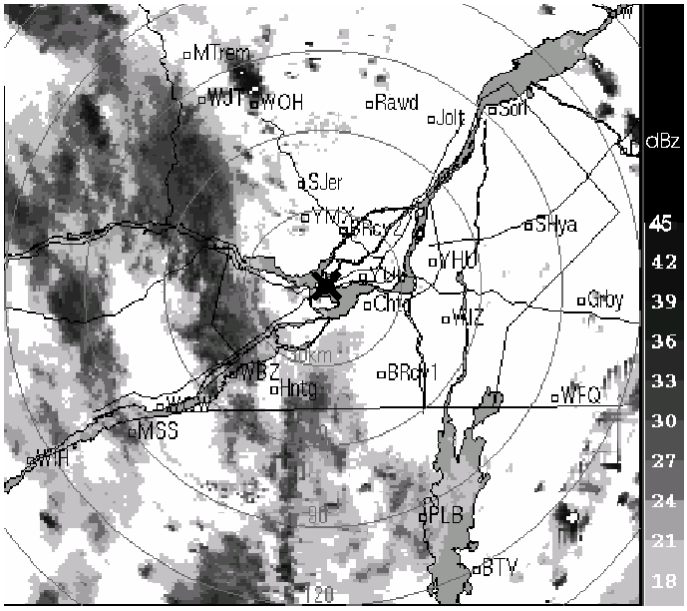

Fig. 2. S-band radar map of precipitation, 16 September. 2003, 0600UT.

Results.

A comparison of these two parameters for the period from Oct. 18 to Nov. 18 is shown in fig. 3. It is apparent from this graph that for most of the time frame, incidences of enhanced isotropy correspond to occurrences of precipitation. Vertical broken lines show times where precipitation starts shortly after the onset of an increase in θ_s to values in excess of 20^o.

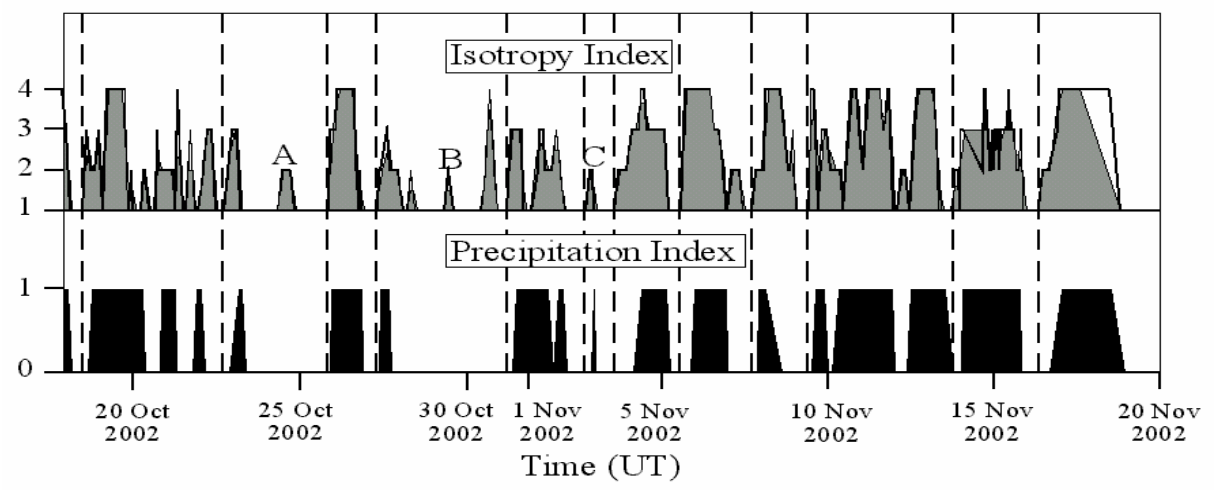

Fig. 3. Plots of the isotropy index (upper graph) and precipitation index (lower graph) as a function of time in October and November, 2002. In the upper graph, the solid line shows the raw values of the isotropy index, and the gray shading shows the 5-point running mean.

Fig. 3 shows that if the isotropy index equals 3 or 4, precipitation is generally found. If the precipitation index is 2, there may be some precipitation (e.g., case C) or there may be none (cases A and B). If the isotropy index is 0, there is no precipitation. Generally the isotropy parameter increases before the precipitation index rises to 1, so that enhanced isotropy is a precursor to the precipitation. The delay varies between 3 and 12 hours. The incidences of enhanced θ_s often also persist for a short time after the precipitation has disappeared.

In order to make the process more quantitative, we have also calculated the cross-correlation coefficient between the two parameters, and the results are shown in fig. 4.

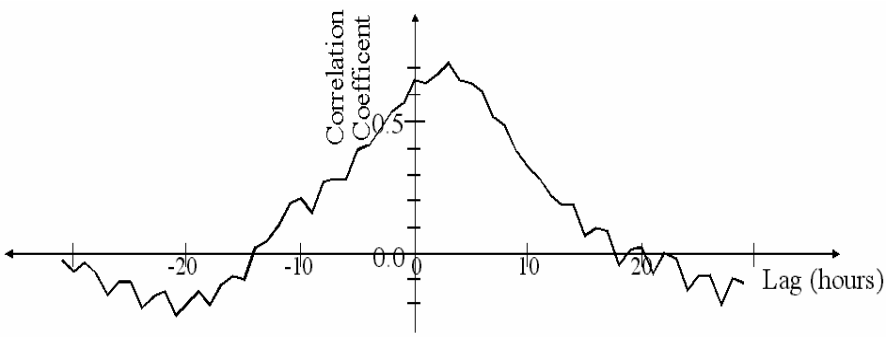

Fig. 4. Cross-correlation between the isotropy index and the precipitation index.

The cross-correlation coefficient at zero lag is 0.656, and it is in fact slightly larger at a lag of 3-4 hours, being 0.722 at the peak. Typically there are about 200 points per correlation, although this number varies depending on the degree of overlap of data in the two data sets (in some cases one or other parameter had missing data). The 95% confidence limits on these estimates are 0.570 and 0.723 at zero lag, and 0.652 and 0.782 at a lag of 3 hours, indicating a strong correlation. The fact that the cross-correlation function peaks at a temporal lag of 3-4 hours arises because the isotropy parameter usually reaches values of 20^o before the precipitation arrives, as discussed in regard to fig. 3.

It therefore appears that the aspect-sensitivity parameter is often a precursor to precipitation. We expect that the reason for this is because much of the non-winter rain arises due to convection, and we expect enhanced convection to correspond to greater isotropy for the turbulent eddies. We envisage that the convection may encompass a much larger area than the precipitation, with the region of precipitation embedded inside it. This explains why the enhanced anisotropy precedes the precipitation – it covers a larger area, and so as the region drifts across the radars, the outskirts, where there is no precipitation, cross the radars first.

We plan to extend this study to cover a longer time-frame.

Acknowledgments:
We especially acknowledge the support of Prof. Isztar Zawadzki, Director, J.S. Marshall Radar Observatory, Dept. of Atmospheric and Oceanic Sciences, McGill University, Canada.

References:
Campos, E., and W. Hocking, Vortical Motions observed with..., *this issue*.
Gage, K.S., and J.L. Green, Evidence for specular ..., , *Radio Sci., 13*, 991-1001, 1978
Hocking W.K. Radar studies of small ..., *Advances in Space Res*., **7**(10), 327-338, 1987.
Hocking, W.K. Target Parameter Estimation, *MAP Handbook*, **30**, 228-268, 1989.
Hocking, W.K., et al., Aspect sensitivity of stratospheric..., *Radio Sci*., **25**, 613-627, 1990
Hocking, W.K., and A.M. Hamza, , *J. Atmos. Solar Terr. Phys*., **59**, 1011-1020, 1997.
Hooper, D., and L. Thomas, Aspect sensitivity of..., *J. Atmos. Terr. Phys., 57*, 655-663, 1995.
Roettger, J., and C.H.Liu, Partial reflection and..., Geophys. Res. Lett., 5, 357-360, 1978
Tsuda, T., et al., MU radar observations of the aspect ..., Radio Sci., 21, 971-980, 1986.

WHAT IS THE FUTURE OF THE MULTI-FREQUENCY TECHNIQUES?

Hubert Luce

LSEET/Toulon University, France

Since the radial resolution of MST radars is limited by their pulse length, dual frequency-domain interferometry (FDI) and multi-FDI (called FII/RIM) techniques have been proposed by different authors and applied to different VHF and UHF radars with various high-resolution data processing methods. Simulations and observations proved in the past that these techniques have considerable potentialities for detecting very thin atmospheric structures, invisible when using the standard mode. Some recent results will be shown. However, can we be confident about the (multi) FDI observations? Especially at VHF, are the images the signature of real atmospheric structures? Should we introduce new filtering methods and/or other approaches for processing the data? All the questions will be debated during the brain-storming.

WHAT IS TURBULENCE SEEN BY VHF RADARS ?

J. Röttger, Max-Planck-Institut, 37191 Katlenburg-Lindau, Germany

At the 9th Workshop on Technical and Scientific Aspects of MST Radar - MST9 - Hocking and Röttger (2001) had reviewed the structure of turbulence in the middle and lower atmosphere seen by and deduced from MF-, HF- and VHF-radars with special emphasis on small-scale features. Here I want to expand on this by recollecting some more historical ideas on scattering and reflection and very initial VHF MST (mesosphere-stratosphere-troposphere) radar observations. I also like to address frequently asked questions, and elaborate on simple new methods to improve our understanding of these echoes. Here are a few of these questions:

(1) Can the ensemble of refractive index irregularities, causing VHF radar echoes, be described by a Gaussian process ?

(2) How much does intermittency, inhomogeneity and anisotropy affect the interpretation of the echoes and the deduction of atmospheric parameters ?

(3) How coherent are the "scatterers" or “partial reflectors”, which lead to echoes from the mesosphere, stratosphere and troposphere ?

(4) What is "turbulent" and "non-turbulent" scatter or “specular-type” partial reflection ?

(5) How deeply must (can) we investigate the microstructure of scattering/reflection processes to improve our understanding of VHF MST radar echoes and the applied analysis methods and interpretations ?

The first high-resolution spectra of VHF MST radar (Fig. 1) showed that there are strong monochromatic lines on top of what one may regard as a weak Gaussian background spectrum. This lead to the assumption that partial specular-type reflection would have to be considered, as Atlas (1964) had suggested already. The question then came up: How sharp have the gradients of radar reflectivity to be to create such strong echoes and what the reason for these gradients could be. It was also noticed that there exists a high aspect sensitivity (Figs. 2a and 2b), which let conclude that there is a pronounced horizontal stratification of these gradient structures.

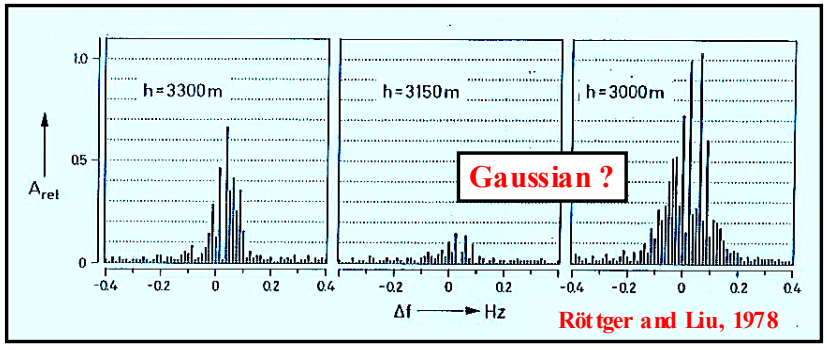

Fig. 1 Spectra of early SOUSY VHF Radar observations, which were not regarded to be of Gaussian shape.

The mean received radar echo power P_r for volume scatter is given by the radar equation:

$$P_r = \frac{\alpha^2 A_E P_t \delta r}{4 \pi r^2} \cdot \eta \qquad (10)$$

where P_t is the transmitter power, A_E the effective antenna area, r the distance to the centre of the scattering volume, δr is the range gate width *[corresponding to the radar pulse length]*, and η the radar reflectivity.

Since it is assumed that partial reflections from steep vertical gradients of the refractive index are also observed by vertically beaming *VHF* radars, the radar equation has to be extended for this condition. Then the power received by reflection is:

$$P_r = \frac{\alpha^2 P_t A_E^2}{4 \lambda^2 r^2} \cdot |\rho^2| \qquad \rho_i^2 = \frac{1}{4}\left|\int \frac{dn}{dz} e^{-2ikz} dz\right|^2 \qquad (11)$$

where $|\rho^2|$ is the amplitude reflection coefficient.

Following these early observations the two extreme cases, scattering from isotropic turbulence and partial reflection from steep refractive index gradients, attracted wide attention. The governing parameters, turbulence refractive index structure constant, determining the radar reflectivity η, and the reflection coefficient ρ were treated in many publications (see inset above). It soon was recognized that the real atmosphere is not behaving properly enough to allow description of the MST VHF radar echoing mechanism by these two parameters. The whole issue is much more complicated, and is not even finally solved yet.

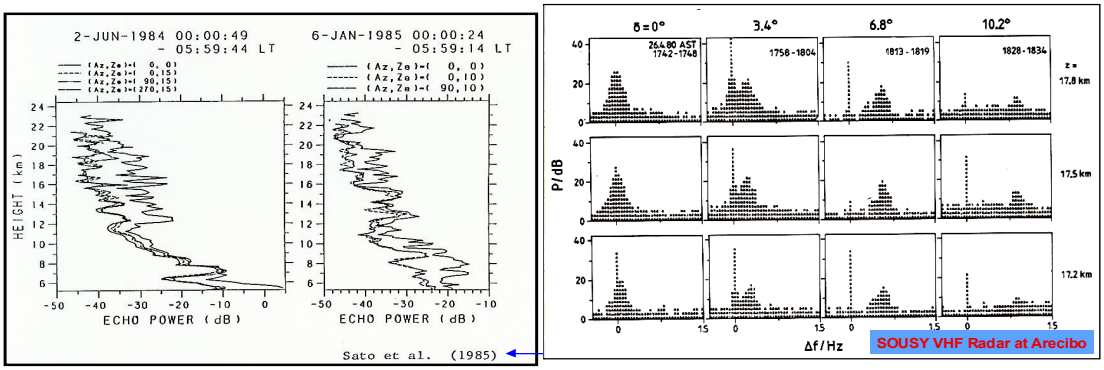

Fig. 2 (a) The left-side shows echo power differences between vertical and off-vertical beam measured with the MU Radar; (b) the right-side shows power spectra of vertical to 10 degrees off-vertical bema pointing, measured with the SOUSY VHF radar at the Arecibo Observatory.

It was also shown, that there are very thin layers (then called sheets or laminae) of echo power, which usually cannot be resolved by the best available standard range resolution of 150 m. Fig. 3 shows an example. A technique of pulse scanning and complex de-convolution was implemented (Röttger and Schidt, 1979), which allowed to estimate the thickness of sheets; some of these were only several tens meters thin.

Intermediate summary: How can these VHF radar observations of thin sheets, which are highly anisotropic, persistent and not immediately turbulent, and also the broader more turbulent layers be explained properly by atmospheric processes?

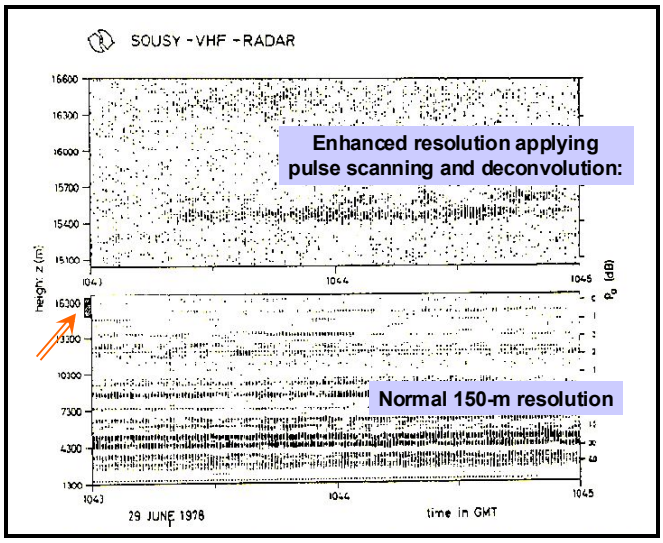

Fig. 3 Height-time-intensity plot of radar echoes from the troposphere and lower stratosphere showing sheets and laminae, which are thinner than 150 m and often persist over many tens of minutes. The arrow in the lower panel points to the height region 15100-16600 m, which is expanded by pulse scanning yielding enhanced resolution (upper panel).

Already 40 years ago Beckmann and Spizzichino had examined the scattering and reflection from rough surfaces of refractive index in the lower atmosphere. The upper-left inset in Fig. 4 shows how they introduced the appearance of stable laminae embedded in a turbulent background. There are different scenarios which could explain these laminae (Röttger, 1980); one of these is the establishment of temperature gradients at the edges of turbulent layers, as originally proposed by Bolgiano (1968). This original proposal was the basis for many models, which followed subsequently. The generation of sheet ensembles is sketched in the main panel of Fig. 4, which base on the mixing of potential temperature gradient by turbulence. Browning and Watkins (1970) mentioned that stretched filaments and double layers result from Kelvin-Helmhotz-Instability as shown in the upper right-hand panel of Fig.4. Röttger (1987) implemented a scheme on the decay of turbulence into multiple temperature sheets.

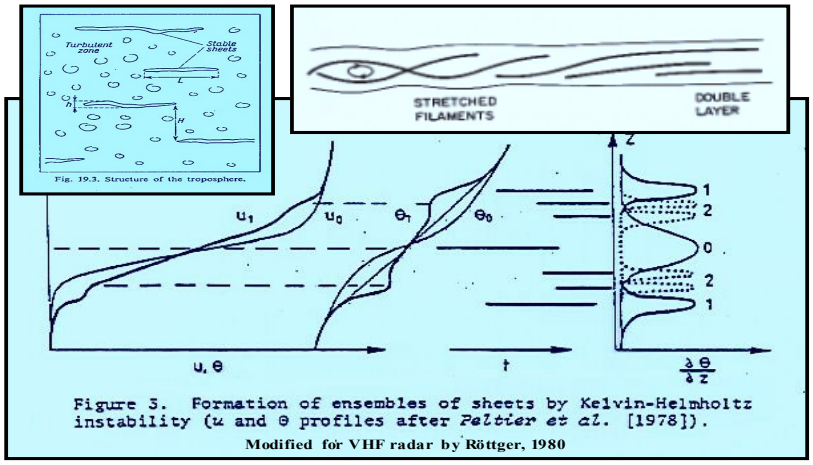

Fig. 4 Sheets, laminae or stretched filaments in a turbulent background. (Beckmann and Spizzichino, 1963 (upper left); Browning and Watkins, 1970 (upper right) and others referenced therein; Peltier et al., 1978; Röttger, 1981).

In the following (Figs. 5, 6, and 7) we repeat some more models, which all base on the original idea of Bolgiano (1968). We note in all these models that the horizontal dimensions of refractivity variations are mostly larger than the vertical ones, in particular close to the edges of turbulent layers. The corresponding vertical gradients, which characterize this structure, can be quite steep as in-situ temperature measurements have shown (Luce et al., 1995). Nothing is really known about their horizontal extent other than the deduction of scale estimates, which follow from VHF radar observations. It is prudent that these sheets with small vertical extent and much larger horizontal extent, which are corrugated by surrounding turbulence, can be regarded as rough surfaces. Again, Beckmann and Spizzichino (1963) have treated the corresponding reflection and scattering, which we show in Fig. 8.

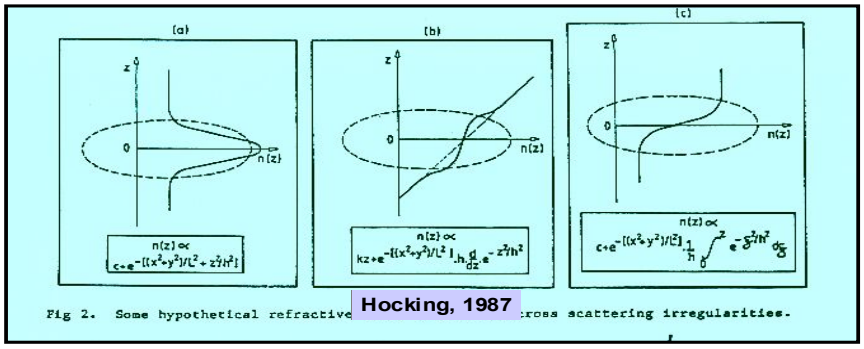

Fig. 5 Refractive index shaping (Hocking, 1987)

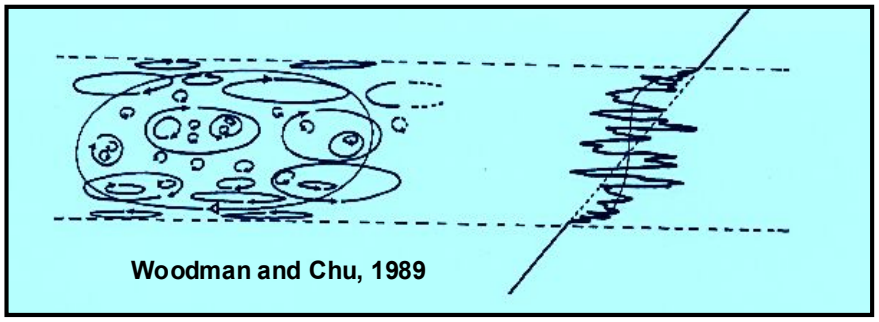

Fig. 6 A turbulence layer containing large- and small-scale eddies (Woodman and Chu, 1989).

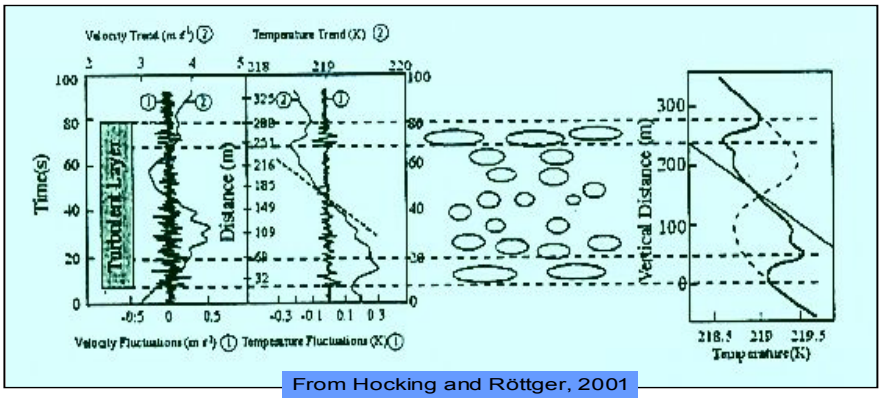

Fig. 7 Velocity, temperature and refractive index inhomogeneities in a turbulent layer, proposed by Hocking and Röttger (2001) following Klaasen and Peltier (1985), and Dalaudier and Sidi (1987) and others.

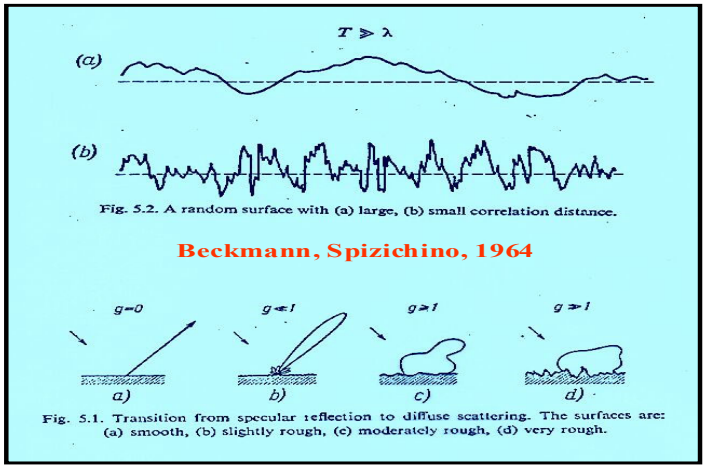

Fig. 8 Polar diagrams of forward scatter from refractive index surfaces of different roughness (a) very smooth surface to (d) very rough surface. From Beckmann and Spizzichino (1964).

The models of Beckmann and Spizzichino show the two extremes, namely specular-type reflection and diffuse scattering from a very rough surface. They did their models for oblique incidence, which we immediately can revert into partial (specular-type) reflection at vertical incidence and monostatic backscatter as well, which determines the signals detected by VHF MST radars. Experience over the past two decades directs us to interpret our observations not in terms of pure backscatter from isotropic homogeneous turbulent refractive index variations, described by a Gaussian process, as is the condition for determining the turbulence refractive index structure constant C_n^2, as adequately developed by Ottersten (1969). The following new type of radar observations and data representation should manifest this presumption.

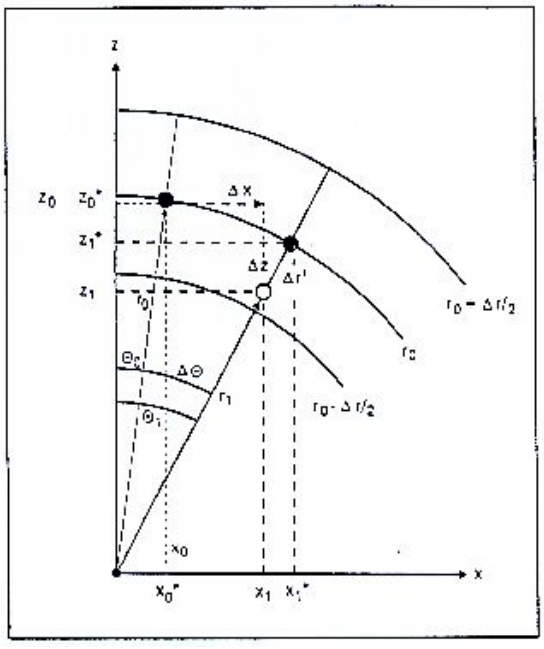

Fig. 9 Geometry of positions determined by the SDI and FDI technique.

This method bases on the combination of spatial-domain-interferometry (SDI) and frequency-domain-interferometry (FDI), as it was applied by Röttger (2000) for studying the three-dimensional motions of scattering locations on lightning channels. These are regarded as small-extent localized radar targets. The standard range gating allows only the localization within (the beam width and) the range gate $r_0 \pm r/2$ (see Fig.9). Additional spatial-domain-interferometry allows the determination of position x_0^* in the horizontal plane, and a simultaneous frequency-domain-interferometry allows to position z_0^* within the range gate (with unknown initial position). Tracking of the target area as function of time is possible by combining :

$$x_1^* = x_0^* + \Delta x \quad \text{(from SDI)}$$
$$z_1^* = z_0^* + \Delta z \quad \text{(from FDI).}$$

This can be extended into the y-plane as well.

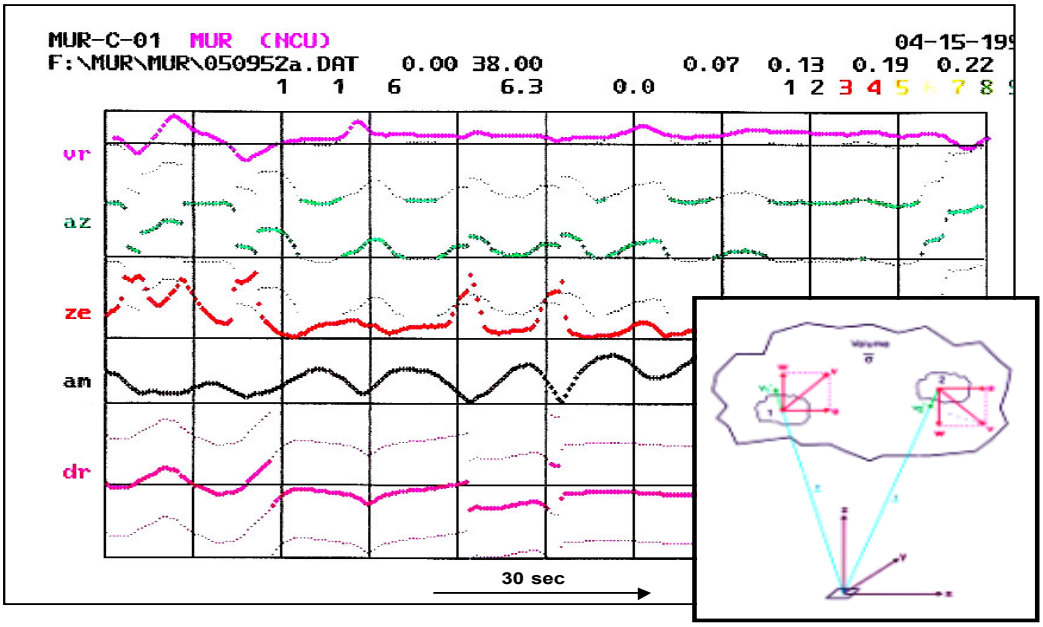

Fig. 10 Temporal variation of SDI-FDI-determined parameters: dr = $(\Delta x^2 + \Delta y^2 + \Delta z^2)^{1/2}$ = radial distance in the radar range gate volume (at 6.3 ± 0.15 km), am = signal amplitude, ze = zenith incidence angle, az = azimuth incidence angle, vr = radial velocity. These measurements were done with the MU radar in October 1998 (Röttger et al., 2000). The lower right-hand-side inset shows the model of scattering/reflecting regions as discussed by Röttger (1998).

The combination of the SDI with the FDI technique allows three-dimensional tracing of locations of normal MST radar echoes from the clear and cloudy air as well. Here we have to regard, though, the fact that we do not have a localized (hard) target as in the case of lightning echoes, but a volume (soft) target. This was considered by Röttger (1998), who pointed out that one can only measure the phase center location and its spatial and temporal variation. The phase center is the mean location of the vector sum of signals from a certain number of individual, maybe even overlapping, targets in the radar volume. Unless one has a very-high-resolution, large-baseline spaced antenna system (or an extremely narrow antenna beam), which allows high spatial resolution in the SDI mode, and a very wide frequency range in the FDI mode (or a very short pulse allowing range resolutions of some ten meters), one cannot separate the individual targets. A usual SDI spaced-antenna set-up of 3-4 receiving arrays and a limited number of FDI frequencies then allows to determine only the mean phase center as so-called effective target location.

Fig. 10 shows the temporal variations of the parameters, which can be measured with this technique. The display is in arbitrary units, since we consider only the mutual variations of these parameters. The amplitude variations have the characteristics of beating (superposition) of two signals, i.e. here we observed just two dominating target echo regions. This is a very common observation. Several amplitude minima occur when the zenith angle is large, the azimuth angle changes or even jumps, and the radial distance changes as well. This is regarded as additional prove that signals from two dominating regions were beating each other.
To understand more about the scattering-reflection mechanism we regard this technique essential, looking into the micro-scale variations of the refractivity structures overhead.

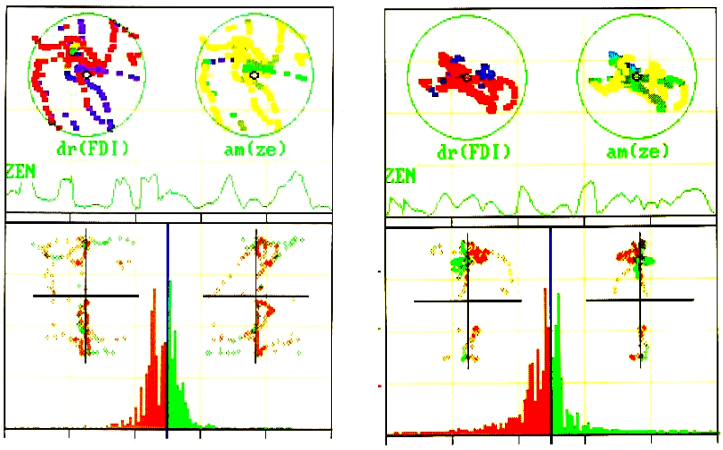

Fig. 11 Plots of temporal variations of target locations in the horizontal plane (upper circles, which represent about the beam width) and the positions in vertical (z) and horizontal (x) and (y) planes; the color codes indicate negative/positive dr/dt and amplitudes as function of zenith angle, deduced over a period of 30 seconds. In the lower part the spectra are shown, which correspond to the other displays above. The vertical scale corresponds to the range resolution of 300 m and the x, and y-scales are determined by the antenna beamwidth.

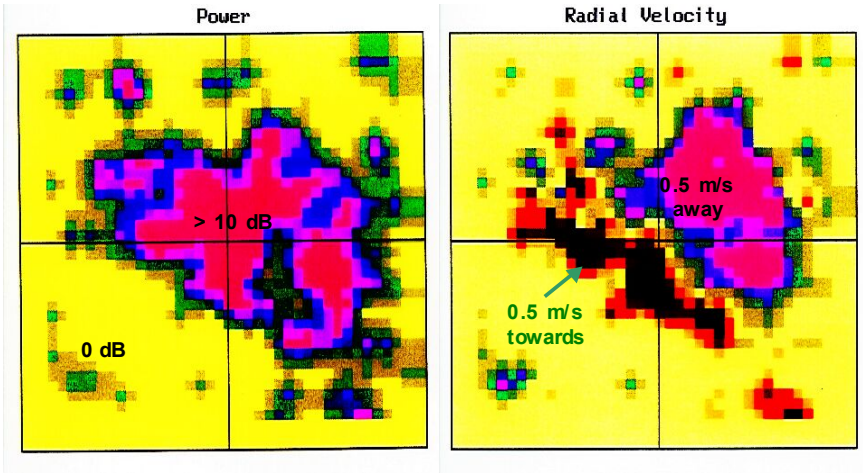

Fig. 12 A 30-sec average projection of power and radial velocity of a signal from one range gate at 6.3 km height into the horizontal plane measured with the MU radar with the SDI-FDI combination, applying a Fresnel zone filter. The centre is the vertical direction and the outer scales are determined by the beamwidth (±200m at 6 km height). The upper right-hand corner are NE etc.

In Fig. 11 data of this kind are presented in polar plots (upper panels). The left-hand one shows that dr/dt (i.e. changes in position of the mean scattering center) are depending on azimuth. Also the maximum signal amplitude is close to the vertical direction. The lower left-hand panels show that the scattering centers are located all over the range gate, and the lower right-hand panel shows that they are mostly confined to a part of the range gate (about one third of the range gate width of 300 m). The former is an indication of a “wide layer” and the latter indicates a “thin layer”, which we also call sheet or lamina. Comparing this thin layer and the instantaneous radial velocities measured by this technique with the corresponding Doppler spectra shown in that graph, it is noticed that negative velocities come from one side of the vertical and positive from the other side. This is an indication that the width of the

spectrum results mainly from beam width broadening. An explanation of these analyses is, that we observe partial specular-type reflection from rough surfaces of refractivity. Of course these may not fill the radar volume, there may be separate centers with different cross section and different velocity, which then are called individual scatterers, sheets, laminae or stretched filaments adding up in the volume. In shorter time-scales than such averages over 30 seconds, individual scatterers (i.e. shorter-lived sheets or filaments (see original suggestion of Beckmann and Spizzichino, 1967, in Fig. 4) may dominate, which then cause strong spikes in the Doppler spectra, as regularly observed (Figs. 1 and 11). We note that either the positions in the range gate volume (Fig. 11) nor the Doppler spectra have a Gaussian shape.

Since we know that partial reflection requires the size of the refractivity structure to be in the order of a Fresnel zone, we have applied a spatial filter to the data points represented in the upper panels (circles) of Fig. 11. This filter has a width of half the first Fresnel zone (150m). The result is shown in Fig. 12. We notice that the power distribution (left-hand panel) is not Gaussian. The right hand panel shows the radial velocity for this case. We recognize the opposite signs of velocities in the SW and the NE part of the volume.

We should note here that this SDI-FDI method has the advantage to determine the positions and their variations in the x, y and z-direction within the radar beam. In order to support this conclusion we have introduced another extension of this new combined SDI-FDI method, which determines the distributions of mean positions within a given time period. As shown in Figs. 13 and 14 the distributions of positions (in vertical direction) are not Gaussian shaped either. One may argue that long averages may yield Gaussian distributions. However, there is no means to average longer than about 30 seconds, since the mean position changes over this time scale. We even recognize several peaks in the distributions, i.e. they are not Gaussian. The instantaneous width of these distributions (over 27 seconds) is less than one third of the range gate in the beginning and about half the range gate towards the end of this period. This corresponds to widths much less than 150 m.

Whichever method we apply in our analyses, the “width” or “thickness” of such refractivity structures is just given by the width of the distribution of the average of the locations of individual scatterers (sheets, laminae or whatever we call them). The individual scatterers can have a much thinner width than this average “thickness”. Thus, the term “thickness”, as commonly used, is not the thickness of any kind of layer but just the width of the distribution of phase centers, which change their position within the range gate. VHF radar observations, done so far, cannot say too much about the real “thickness” of refractivity structures.

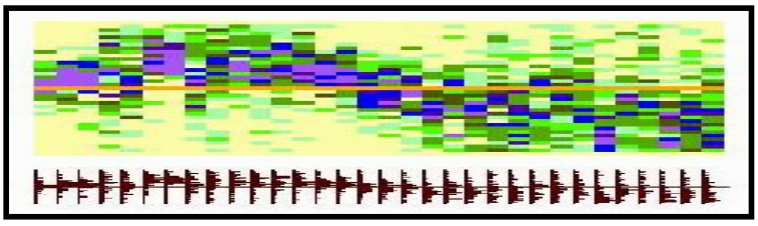

Fig. 13 Temporal variations of distributions of vertical position of scattering centers deduced by SDI-FDI combination of tropospheric data collected with the Chung-Li VHF radar. The vertical scale covers the range gate width of 300 m (range gate center is in red color). The individual distributions are obtained from 256 samples taken within 27 seconds. The total time span of this graph is 850 seconds. The upper panel shows the distributions in color coding.

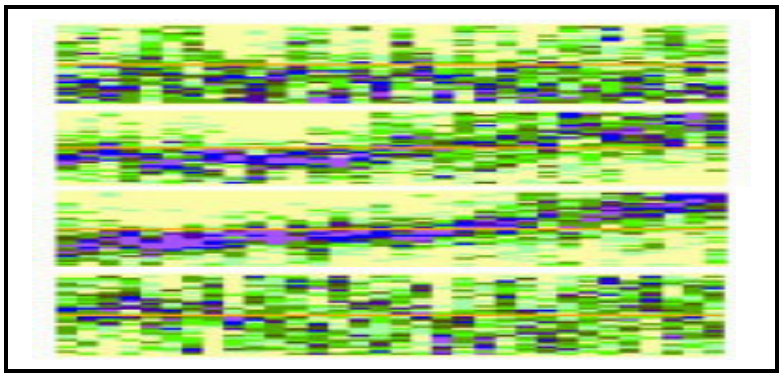

Fig. 14 Distributions of phase centers in vertical direction for range gates 5.0 - 6.2 km observed with the Chung-Li VHF radar in the combined SDI-FDI method (same procedure as in Fig. 13). The center panels show that the "width" can be as "thin" as some 50-80 m, and that the mean position changes as function of time. The upper and lower panel show much more irregular variations of the positions.

This presented SDI-FDI method does not need any assumptions, such as other methods which are frequently applied for atmospheric radar imaging (e.g., Chilson et al., 2003). It is further quite simplistic and yields the maximum, undistorted and unbiased information available from these observations. We can well qualify the characteristics of the radar echo, such as mean position, its variability and variation as function of time, reflectivity and velocity distributions, and the "width" of structures. To quantify these needs careful piece-by-piece interpretation. Another versatile method, pulse scanning, was only applied once (Röttger and Schmidt, 1979). This allows higher resolution than the pulse width by applying complex deconvolution. It was shown that this yields an almost three times resolution improvement. One can also apply short coded pulses, which requires broader-band transmitters and antennas than used so far**.**

Possible answers to the initially asked questions:

(1) Most of the echoes detected by VHF MST radars cannot be described by a Gaussian process but are often highly deterministic.

(2) The morphology of these echoes is extensive, which means that standard analysis methods have to be adopted with greatest care.

(3) Mostly the spatial and temporal coherency of the echoes cannot be explained by isotropic, homogeneous turbulence.

(4) We prefer the quantification into Bragg scatter, Fresnel scatter and Fresnel reflection (Fig. 14, Table 1). Fresnel scatter may most often occur, which is the composite of specular-type reflection from several smaller-scale rough sheets or laminae.However, discriminating clearly between these is rather complex still.

(5) Apply most unsophisticated analysis methods. Each assumption (how does it replicate nature?) introduces further uncertainties. Nature already confronts us with quite some perplexity, which we cannot disentangle by further conjectures.

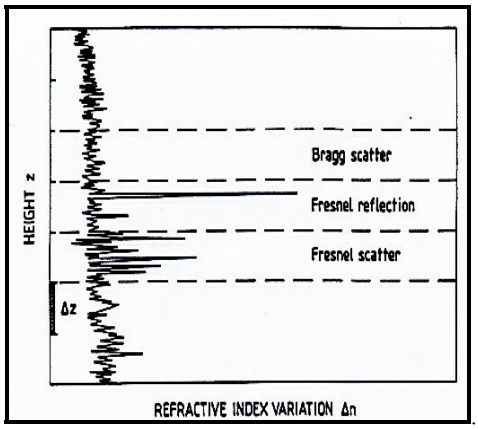

Model for Scatter/Reflection Mechanisms of MST Radar Signals

(*conceptual synopsis*)

Mechanism	Angular Spectrum	Coherence Time	Reflectivity Structure
BRAGG SCATTER (a) isotropic (b) anisotropic	constant wide	short short	random turbulence (a) isotropic (b) anisotropic
FRESNEL SCATTER (a) stratified (b) spread	narrow wide	intermediate intermediate	multiple laminae in stable environment (a) horizontally stratified (b) range, angle spread
FRESNEL (partial) REFLECTION (a) specular (b) diffuse	narrow very narrow	long very long	one dominating laminae in stable environment (a) very smooth (b) corrugated (rough)

Fig. 15 after Röttger and Larsen (1990). Table 1 after Röttger (1989).

Final remarks: Quite some progress has been made over the past two decades in understanding MST VHF radar returns. We were able to show that simplistic assumptions about scattering and reflection can at most be applied in exceptional cases. What we see is not immediately convertible into refractivity structure of the atmosphere. We have mostly used our observations to trace atmospheric structure and dynamics. Combination with other observations, such as those made in-situ and modeling is highly valuable. One may even have to do "backward modeling or simulation" by adjusting model parameters in such a way that they replicate all the parameters of individual radar observations. The initial observations, interpretations and visions made some 20-40 years ago are still basic and valid. New approaches, such as the Direct Numerical Simulation (Fritts, 2003) bring us forward and verify the early visions with modern computing techniques.

References:

Atlas, D., Advances in radar meteorology, Adv. Geophys., Academic Press, 317-478, 1964.

Beckmann, P., and A. Spizzichino, The scattering, of electromagnetic waves from rough surfaces, 418-453, Pergamon Press, 1963.

Bolgiano, R., The general theory of turbulence: Turbulence in the atmosphere, in Wind and Turbulence in Stratosphere, Mesosphere and Ionosphere, North Holland Publ., 371-400, 1968.

Browning, K.A., and C.D. Watkins, Observations of Clear Air Turbulence by High Power Radar, Nature, 227, 260-263, 1970.

Chilson, P.B., T.Y. Yu, R.G. Strauch, A. Muschinski, and R.D. Palmer, Implementaton and validation of range imaging on a UHF radar wind profiler, J. Atmos. Ocean. Tech., 20, 987-996, 2003.

Dalaudier, F. and C. Sidi, Evidence and interpretation of spectral gap in the turbulent atmospheric temperature spectra, J. Atmos. Sci., 44, 3121-3126, 1987.

Fritts, D., Ímplications of Direct Numerical Simulations of turbulence generation and Morphology for dynamics and radar backscatter, paper presented at 10th Workshop Techn. Scient. Aspects MST Radar, Piura, 13-20 May 2003.

Hocking, W.K., Radar studies of small-scale structure in the upper atmosphere and lower ionosphere, Adv. SpaceRes., 7(1), 327-338, 1987.

Hocking, W.K., and J. Röttger, The structure of turbulence in the middle and lower atmosphere seen by and deduced from MF-, HF- and VHF-radars with special emphasis on small-scale features, Ann. Geophys., 19, 933-944.

Klaassen, G.P., and W.R. Peltier, Evolution of finite amplitude Kelvi-Helmholz billows in two spatial dimensions, J. Atmos. Scie., 42, 1321-1339, 1985.
Luce, H., Crochet, M., Delaudier, F., and C. Sidi, Interpretation of VHF ST radar vertical echoes from in-situ temperature sheet observations, Radio Sci., 30, 1002-1025, 1995.

Ottersten, H., Radar backscattering from the turbulent clear air, Radio Sci., 4, 1251-1255, 1969.

Peltier, W.R., J. Halle, and T.L. Clark, Geophys. Astrophys. Fluid Dyn., 10, 53, 1978.

Röttger, J., and C.H. Liu, Partial reflection and scattering of VHF radar signals from the clear atmosphere, Geophys. Res. Lett., 5(5), 357-360, 1978.

Röttger, J., and G. Schmidt, High-resolution VHF radar sounding of the troposphere and stratosphere, IEEE Trans. Geosci. Electr., GE-17(4), 182-189, 1979.

Röttger, J., Structure and dynamics of the stratosphere and mesosphere revealed by VHF radar observations, Pageoph, 118, 494-527, 1980.

Röttger, J., The dynamics of stratospheric and mesospheric fine structure investigated with an MST VHF radar, Handbook for MAP, 2, 341-350, 1981.

Röttger, J., VHF radar measurements of small-scale and meso-scale dynamical processes in the middle atmosphere, Phil. Trans. Roy. Soc. London, A323, 611-628, 1987.

Röttger, J., The interpretation of MST radar echoes: The present knowledge of the scattering/reflection and the irregularity generation mechanism, Handbook for MAP 28, 68-82, 1989.

Röttger, J., and M.F. Larsen, UHF/VHF radar techniques for atmospheric research and wind profiler applications, in Radar in Meteorology, AMS, 235-281, 1990.

Röttger, J., A microscopic view on VHF radar returns from the troposphere, Proc. 8th Workshop Techn. Scie. Aspects MST Radar, SCOSTEP, 21-24, 1998.

Röttger, J., Combined high-time resolution SDI-FDI experiments with VHF radars, Proc. 9th Workshop Techn. Sci. Aspects MST Radar, SCOSTEP, 47-50, 2000.

Woodman, R.F. and Y.H. Chu, Aspect sensitivity measurements of VHF backscatter made with the Chung-Li radar: plausible mechanisms, Radio Sci., 24, 113-125, 1989.

APPLICATIONS OF A WORLD-WIDE NETWORK OF MESOSPHERIC RADARS, WITH SPECIAL EMPHASIS ON THE COLUMBIA SPACE SHUTTLE DISASTER

W. K. Hocking[1], S. Franke[2], N. Mitchell[3], D. Pancheva[3], P. Batista[4], B. Clemesha[4], B. Fuller[5], B. Vandepeer[5], T. Nakamura[6], T. Tsuda[6], J. MacDougall[1]

1. University of Western Ontario, Canada.
2. University of Illinois, USA.
3. Bath University, UK.
4. INPE, Brazil.
5. Genesis Software Pty. Ltd., Australia.
6. RASC, Japan.

Dynamical motions in the mesosphere are some of the most intense in the Earth's atmosphere. Gravity waves, tides and planetary waves are in continual complex motion, and hurricane-strength winds exceeding 80 m/s (300 km/hr) are not unusual. Intense turbulence dissipation is not uncommon. The region is, however, often ignored, largely because (i) it is high above our heads and (ii) densities are so low that the impact of the motions are diminished compared to interactions in the much more dense troposphere.

The region also has the possibility to affect rocket and Shuttle launches, but in general the effects are not severe because of the diminished densities at these heights. However, extrema in dynamical quantities can possibly have an impact. In this talk, we demonstrate the value of a world-wide network of middle atmosphere radars for understanding this region, and as a particular example we use data from a network of equatorial radars to reconstruct the wind field experienced by the Space Shuttle Columbia during its final minutes. An important result is a large wind shear deduced to have occurred at 60 to 65 km altitude over Texas at the time that Columbia passed through, due to an unfortunate alignment of the 2-day wave and the diurnal tide. The extent to which this may have contributed to the destruction of Columbia is under investigation.

THE STRUCTURE FUNCTION-BASED APPROACH TO DATA ANALYSIS FOR SPACED ANTENNA RADARS: A COMPARISON WITH TRADITIONAL TECHNIQUES

Alexander Praskovsky[1] and Eleanor Praskovskaya[2]

[1]National Center for Atmospheric Research, 3450 Mitchell Lane, Boulder, CO 80501, USA
[2]Colorado Research Associates, 3380 Mitchell Lane, Boulder, CO 80501, USA

INTRODUCTION

During the last four decades, spaced antenna (SA) methods for measuring characteristics of a scattering medium at altitudes from the low troposphere to the high mesosphere and ionosphere have become widely used, and a diversity of the methods has been developed; for reviews see, e.g., Hocking et al. (1989), Fukao and Palmer (1991), Palmer (1994), and Doviak et al. (1996). The methods are based on the analysis of cross and auto correlation functions (CF) of signals from multiple receiving antennas, and each CF-based method has its spectral counterpart. For example, Full Spectral Analysis in the frequency domain corresponds to Full Correlation Analysis (FCA) in the time domain; Briggs and Vincent (1992), and Briggs (1984), respectively. The most advanced CF-based SA techniques were originated by Liu et al. (1990); the Liu et al. theory was generalized and further expanded by Doviak et al. (1996), below referred to as DLH. The technique based on the Doviak et al. theory is referred to below as the Holloway and Doviak (HAD) method; see Holloway et al. (1997b), below referred to as HDC.

As emphasized by many authors, e.g., Briggs and Vincent (1992), Sheppard et al. (1993), Hocking et al. (1989), all SA methods are basically similar in that they utilize the same initial information: time series of amplitude and phase of signals from several receivers. The methods differ by: (1) mathematical functions for analyzing multiple signals; (2) parameters of these functions to be estimated; (3) equations for relating these parameters to characteristics of the scattering medium; and (4) assumptions which are adopted for deriving the operational equations. Although basically similar, all methods produce important information about a scattering medium. Multiple signals from several receivers provide an enormous amount of raw information. Each mathematical function (spectrum, CF, wavelet, etc.) extracts only a small part of useful information from multiple random signals; therefore, different techniques do not compete but rather complement each other.

A structure function (SF)-based SA method UCAR-STARS (University Corporation for Atmospheric Research -- STructure function Analysis of Received Signals) has been developed recently by Praskovsky and Praskovskaya (2003a, b), below referred to as PPa and PPb. The goal of this paper is to compare STARS to the HAD method. The latter is basically similar to FCA (Holloway et al., 1997a); therefore, the results of a comparison can be applied to any CF-based SA technique. As shown in PPa, equations for SF of any order $p \geq 2$ can be derived and applied to practical measurements. On the contrary, only the second order CF have been used in SA methods, and spectra are second-order functions as well. To compare STARS and HAD techniques, cross and auto SF at only $p = 2$ are considered in this paper.

ESTIMATING WIND AND TURBULENCE

In this section we summarize the basic equations for estimating the mean horizontal winds and turbulence characteristics with STARS and HAD techniques as well as the assumptions

which are adopted for deriving the equations. Detailed derivation of the equations and discussion of the assumptions can be found in PPa, PPb, and DLH, HDC, respectively.

The transmitter of a SA profiling radar sends pulses of radio waves vertically upwards into the atmosphere and these are scattered by the refractive index irregularities to form a moving and changing diffraction pattern on the ground. Following PPa, the irregularities are referred to as scatterers independent of their physical nature. Therefore, the scatterer is defined as the refractive index irregularity scattering the transmitted waves of a specific frequency, and it is a property of the atmosphere to which the radar is sensitive. Following such a definition, each scatterer is characterized by its instantaneous location $\vec{x}_i(t) = \{x_i(t), y_i(t), z_i(t)\}$, velocity $\vec{W}_i(t) = \{U_i(t), V_i(t), W_i(t)\}$, and reflectivity $\Delta n_i(t)$. Hereafter t is time, i = 1, 2, ..., M, and M is the number of scatterers in the illuminated volume. The geophysical coordinate system with z axis directed upwards, x axis towards east, and y axis towards north is used hereafter; the values in the brackets $\{\ \}$ denote the Cartesian components of a vector.

The magnitude and phase of the diffraction pattern is sampled with $N \geq 3$ spatially separated receiving antennas with the phase centers $\vec{x}_{a,k}$ where k = 1, 2, ..., N denotes the receiver number. Each antenna provides a complex received signal

$$E(\vec{x}_{a,k}, t) = I(\vec{x}_{a,k}, t) + \sqrt{-1}Q(\vec{x}_{a,k}, t) \tag{1}$$

where I and Q are the in-phase and quadrature components of the pure return from the scatterers with no noise or clutter. Without loss of generality, one can consider $\left\langle I(\vec{x}_{a,k}) \right\rangle = \left\langle I(\vec{x}_{a,k}) \right\rangle = 0$; hereafter the brackets $\langle\ \rangle$ denote the ensemble averages. Equations for pure signals can be used directly in practical measurements while noise can be taken into account while calculating SF and CF; see PPa and HDC for details.

UCAR-STARS: equations and assumptions. Consider a pair of receivers with the phase centers $\vec{x}_{a,k}$ and $\vec{x}_{a,m}$, $(k \neq m)$ = 1, 2, ..., N. The non-dimensional second order cross SF can be defined as (Tatarskii, 1971, chap. 1A):

$$D(\Delta\vec{x}_{mk}, \tau) = \left\langle \left[S(\vec{x}_{a,k}, t) - S(\vec{x}_{a,k} + \Delta\vec{x}_{mk}, t + \tau) \right]^2 \right\rangle \Big/ \left\langle \left[S(\vec{x}_{a,k}, t) - \left\langle S(\vec{x}_{a,k}, t) \right\rangle \right]^2 \right\rangle \tag{2}$$

where

$$S(\vec{x}_{a,k}, t) = I^2(\vec{x}_{a,k}, t) + Q^2(\vec{x}_{a,k}, t) \tag{3}$$

is the instantaneous power of pure received signals; $\Delta\vec{x}_{mk} = \vec{x}_{a,m} - \vec{x}_{a,k}$ is a spatial separation between the antenna centers, and τ is a temporal separation between the signals. The auto SF $D_{auto}(\vec{x}_{a,k}, \tau)$ is a particular case of (1) at $\Delta\vec{x}_{mk}$ = 0. For any atmospheric profiling radar at $\tau \to 0$ and small enough $\left|\Delta\vec{x}_{mk}\right|$, SF (2) can be presented in the following form (PPa):

$$D(\Delta\vec{x}_{mk}, \tau) = d_0(\Delta\vec{x}_{mk}) + d_1(\Delta\vec{x}_{mk})\hat{\tau} + d_2(\Delta\vec{x}_{mk})\hat{\tau}^2 + O(\tau^3) \tag{4}$$

$$D_{auto}(\vec{x}_{k,a}, \tau) = d_{auto}(\vec{x}_{a,k})\hat{\tau}^2 + O(\tau^3) \tag{5}$$

where $\hat{\tau} = \tau / \delta t$, and δt is the inter-sample time interval. Eqs. (4) and (5) were derived in PPa using the only Assumption 1S: the characteristics of each scatterer $x_i(t)$, $y_i(t)$, $z_i(t)$, $U_i(t)$, $V_i(t)$, $W_i(t)$, and $\Delta n_i(t)$, i = 1, 2, ..., M, are locally statistically stationary random processes. The term "locally stationary" is used in the paper in the same sense as in a theory of the fine-scale turbulence, e.g., Monin and Yaglom (1975, sec. 21). It stands for stationarity over a time period which is much smaller than the integral time scale of the random process. Following Assumption 1S, the instantaneous velocity of each scatterer can be presented as a sum of the mean and turbulent components:

$$\{U_i(t), V_i(t), W_i(t)\} = \{\langle U_i \rangle, \langle V_i \rangle, \langle W_i \rangle\} + \{u_i(t), v_i(t), w_i(t)\} \quad (6)$$

Projection of the instantaneous velocity $\vec{W}_i(t)$ on the baseline $\Delta\vec{x}_{mk}$ can be defined as follows:

$$U_{i,mk}(t) = \langle U_{i,mk} \rangle + u_{i,mk}(t) = \left(\vec{W}_i(t) \bullet \Delta\vec{x}_{mk}\right) \Big/ \left|\Delta\vec{x}_{mk}\right| \quad (7)$$

where the bullet $\bullet$ denotes a scalar product of two vectors. To derive practically useful equations for the coefficients d_0 and d_1, two more assumptions were adopted in PPa. Assumption 2S: the instantaneous location of all scatterers $x_i(t)$ and $y_i(t)$ in the illuminated volume is statistically uniform in any horizontal direction. Assumption 3S: the mean motion of all scatterers in the volume is statistically homogeneous in any horizontal direction, that is, $\langle U_i \rangle = \langle U \rangle$, $\langle V_i \rangle = \langle V \rangle$, and $\langle U_{i,mk} \rangle = \langle U_{mk} \rangle$ for i = 1, 2, …, M. Using Assumptions 1S - 3S, the following equations were derived in PPa:

$$d_0(\Delta\vec{x}_{mk}) = 2\left[1 - \exp\left(-4\pi^2\gamma^2 \left|\Delta\vec{x}_{mk}\right|^2 / \alpha^2 D^2\right)\right] \quad (8)$$

$$d_1(\Delta\vec{x}_{mk}) = -\left[32\pi^2\gamma^2 \left|\Delta\vec{x}_{mk}\right| \langle U_{mk} \rangle \delta t / \alpha^2 D^2\right] \exp\left(-4\pi^2\gamma^2 \left|\Delta\vec{x}_{mk}\right|^2 / \alpha^2 D^2\right) \quad (9)$$

Hereafter D is the transmitter diameter; $\alpha^2 = 1 + (\sigma / \sigma_a)^2$; σ and σ_a are the transmitted beam and the receiver's field of view linear widths; λ is the radar wavelength; and γ is the antenna factor. Combining Eqs. (8) and (9), one can get:

$$\langle U_{mk} \rangle = \left[\left|\Delta\vec{x}_{mk}\right| d_1(\Delta\vec{x}_{mk})\right] \Big/ \left\{8\delta t\left[1 - d_0(\Delta\vec{x}_{mk})/2\right] \ln\left[1 - d_0(\Delta\vec{x}_{mk})/2\right]\right\} \quad (10)$$

This equation relates the projection of the scattering medium's mean speed $\langle U_{mk} \rangle$ on the baseline $\Delta\vec{x}_{mk}$ to "measurable" coefficients d_0 and d_1 in Eq. (4) for cross SF. The mean horizontal wind speed components $\langle U \rangle$ and $\langle V \rangle$ can be estimated uniquely by applying Eq. (10) to the coefficients $d_0(\Delta\vec{x}_{mk})$ and $d_1(\Delta\vec{x}_{mk})$ for any two non-parallel baselines $\Delta\vec{x}_{mk}$ at $(m \neq k)$ = 1, 2, …, N.

To derive practically useful equations for the coefficients d_2 and d_{auto}, the following additional assumptions were adopted in PPa and PPb. Assumption 4S: turbulent motion of all scatterers inside the illuminated volume is statistically homogeneous, that is $\langle w_i^p \rangle = \langle w^p \rangle$, $\langle u_{i,mk}^p \rangle = \langle u_{mk}^p \rangle$, $\langle u_i^j v_i^{p-j} \rangle = \langle u^j v^{p-j} \rangle$ for i = 1, 2, ..., M, and j = 0, 1, ..., p. Assumption 5S: the integral scale of the vertical turbulent velocity $w_i(t)$ is smaller than σ_r or/and σ, and that of the horizontal velocities $u_i(t)$ and $v_i(t)$ is approximately equal to, or larger than σ. Using Assumptions 1S - 5S, the following equations were derived in PPa and PPb:

$$\frac{d_2(\Delta\vec{x}_{mk})}{1 - d_0(\Delta\vec{x}_{mk})/2} = 32\pi^2\delta t^2 \left[\frac{\langle w^2 \rangle}{\lambda^2} + \frac{\gamma^2\left(\langle U \rangle^2 + \langle V \rangle^2\right)}{\alpha^2 D^2} - \frac{8\pi^2\gamma^4 \left|\Delta\vec{x}_{mk}\right|^2 \left(\langle U_{mk} \rangle^2 + \langle u_{mk}^2 \rangle\right)}{\alpha^4 D^4}\right] \quad (11)$$

$$d_{auto}(\vec{x}_{a,k}) = 32\pi^2\delta t^2 \left[\langle w^2 \rangle \Big/ \lambda^2 + \gamma^2\left(\langle U \rangle^2 + \langle V \rangle^2\right) \Big/ \alpha^2 D^2\right] \quad (12)$$

Eq. (12) relates the intensity of the vertical turbulent velocity $\langle w^2 \rangle$ to the "measurable" coefficient d_{auto} in Eq. (5) for the auto SF. Using Eqs. (8), (11), and (12), one can derive the following equation (PPb):

$$\left(\left\langle u^2\right\rangle+\left\langle U\right\rangle^2\right)\Delta x_{mk}^2+2\left(\left\langle uv\right\rangle+\left\langle U\right\rangle\left\langle V\right\rangle\right)\Delta x_{mk}\Delta y_{mk}+\left(\left\langle v^2\right\rangle+\left\langle V\right\rangle^2\right)\Delta y_{mk}^2$$
$$=\frac{\left(\Delta x_{mk}^2+\Delta y_{mk}^2\right)^2}{16\ln^2\left[1-a_2(\Delta\vec{x}_{mk})/2\right]\delta t^2}\left[d_{2,auto}(\vec{x}_{a,k})-\frac{c_2(\Delta\vec{x}_{mk})}{1-a_2(\Delta\vec{x}_{mk})/2}\right] \quad (13)$$

This linear equation relates three unknown values, the turbulence characteristics $\left\langle u^2\right\rangle$, $\left\langle v^2\right\rangle$, and $\left\langle uv\right\rangle$ to "measurable" coefficients d_0, d_2, and d_{auto} in Eqs. (4) and (5) for the second-order cross and auto SF. The characteristics $\left\langle u^2\right\rangle$, $\left\langle v^2\right\rangle$, and $\left\langle uv\right\rangle$ can be estimated uniquely by applying Eq. (13) to the coefficients $d_0(\Delta\vec{x}_{mk})$, $d_2(\Delta\vec{x}_{mk})$, and $d_{auto}(\vec{x}_{a,k})$ for any three non-parallel baselines $\Delta\vec{x}_{mk}$ at $(m\neq k)=1, 2, \ldots, N$. Eqs. (2) - (5), (10), (12), and (13) are the major operational equations for measuring the mean horizontal winds and the second-order turbulence characteristics with the UCAR-STARS method.

HAD: equations and assumptions. The non-dimensional second order cross CF for a pair of receivers with the phase centers $\vec{x}_{a,k}$ and $\vec{x}_{a,m}$, $(k\neq m)$ = 1, 2, ..., *N*, can be defined as:

$$C(\Delta\vec{x}_{mk},\tau)=\left\langle E(\vec{x}_{a,k},t)E^*(\vec{x}_{a,k}+\Delta\vec{x}_{mk},t+\tau)\right\rangle\Big/\left\langle E(\vec{x}_{a,k},t)E^*(\vec{x}_{a,k},t)\right\rangle \quad (14)$$

The auto CF $C_{auto}(\vec{x}_{a,k},\tau)$ is a particular case of (14) at $\Delta\vec{x}_{mk}=0$. Notations in this paper differ from those in DLH and HDC to match notations for SF. Following HDC, the magnitude of cross and auto CF can be presented in the form:

$$\left|C(\Delta\vec{x}_{mk},\tau)\right|=\exp\left[-c_0(\Delta\vec{x}_{mk})-c_1(\Delta\vec{x}_{mk})\hat{\tau}-c_2(\Delta\vec{x}_{mk})\hat{\tau}^2-O(\tau^3)\right] \quad (15)$$

$$\left|C_{auto}(\vec{x}_{a,k},\tau)\right|=\exp\left[-c_{auto}(\vec{x}_{a,k})\hat{\tau}^2-O(\tau^3)\right] \quad (16)$$

where the coefficients are given as follows:

$$c_0(\Delta\vec{x}_{mk})=2\pi^2\gamma^2\left|\Delta\vec{x}_{mk}\right|^2\Big/\alpha^2D^2 \quad (17)$$

$$c_1(\Delta\vec{x}_{mk})=-8\pi^2\gamma^2\left|\Delta\vec{x}_{mk}\right|\left\langle U_{mk}\right\rangle\delta t\Big/\alpha^2D^2 \quad (18)$$

$$c_2(\Delta\vec{x}_{mk})=c_{auto}(\vec{x}_{a,k}) \quad (19)$$

$$c_{auto}(\vec{x}_{a,k})=8\pi^2\delta t^2\left[\left\langle w^2\right\rangle\Big/\lambda^2+\gamma^2\left(\left\langle U\right\rangle^2+\left\langle V\right\rangle^2\right)\Big/\alpha^2D^2\right] \quad (20)$$

Combining Eqs. (17) and (18), one can get:

$$\left\langle U_{mk}\right\rangle=-\left(4\left|\Delta\vec{x}_{mk}\right|/\delta t\right)\left[c_1(\Delta\vec{x}_{mk})/c_0(\Delta\vec{x}_{mk})\right] \quad (21)$$

Equations (21), (19), and (20) relate the mean speed $\left\langle U_{mk}\right\rangle$ and intensity of the vertical turbulent velocity $\left\langle w^2\right\rangle$ to "measurable" coefficients c_0, c_1, c_2, and c_{auto} in Eqs. (15) and (16) for the second-order cross and auto CF. The characteristics $\left\langle U\right\rangle$, $\left\langle V\right\rangle$, and $\left\langle w^2\right\rangle$ can be estimated uniquely by applying Eqs. (14) - (16) and (19) - (21) to any two non-parallel baselines $\Delta\vec{x}_{mk}$ at $(m\neq k)=1, 2, \ldots, N$.

Eqs. (14) - (16) and (19) - (21) are the major operational equations for measuring the mean horizontal winds and intensity of the vertical turbulent velocity with the HAD method. The assumptions that were adopted for deriving Eqs. (15) - (20) are not listed systematically in DLH but rather scattered throughout the paper. Below we try to systemize the assumptions to the best of our ability as well as present them in the terms of those for STARS whenever is possible.

Assumption 1H: the characteristics of each scatterer $x_i(t)$, $y_i(t)$, $z_i(t)$, $U_i(t)$, $V_i(t)$, $W_i(t)$, and $\Delta n_i(t)$, i = 1, 2, ..., *M*, are globally statistically stationary random processes; DLH (p.

161). Assumption 2H: the instantaneous location of all scatterers is statistically uniform in the illuminated volume; DLH (pp. 158 and 161). Assumption 3H: the mean motion of all scatterers is statistically homogeneous in the illuminated volume; that is, $\langle U_i \rangle = \langle U \rangle$, $\langle V_i \rangle = \langle V \rangle$, and $\langle W_i \rangle = \langle W \rangle$ (DLH, p. 163). Assumption 4H: the instantaneous reflectivity of all scatterers is statistically homogeneous in the illuminated volume; DLH (pp. 158 and 161). Assumption 5H: turbulent motion of all scatterers inside the illuminated volume is statistically homogeneous and isotropic; DLH (p.163 and Sec. 4). Following this assumption, the turbulence intensity was characterized in DLH and HDC by $\sigma_t^2 = \langle w^2 \rangle = \langle u^2 \rangle = \langle v^2 \rangle$. As shown in DHL (sec. 5.3), σ_t is related to the spectral width in the Doppler method, therefore, the measured value in Eq. (19) is $\langle w^2 \rangle$ (DHL, p. 169). Assumption 6H: specific functional form of CF or spectrum for the reflectivity Δn_i of scatterers in the illuminated volume; e.g., the Gaussian CF with the correlation lengths ρ_{ch} and ρ_{cz} in the horizontal and vertical directions (DLH, sec. 4), a power law of the Kolmogorov type with specified parameters (DHL, sec. 5), or another. Assumption 7H: the vertical correlation length ρ_{cz} is much smaller than the range resolution σ_r. Assumption 8H: specific horizontal correlation length ρ_{ch}; e.g., $\rho_{ch} << D$ (DHL, pp. 159, 166), $\rho_{ch} \geq D$, $\rho_{ch} >> \rho_{cz}$ (DLH, p. 170), or another.

Relations between STARS and HAD. To relate the second order CF and SF, one can apply the standard set of assumptions about the received signals $E(\vec{x}_{a,k}, t)$; the assumptions are presented and discussed by Ishimaru (1997, sec. 4-9). Let us consider the in-phase and the quadrature components $I(\vec{x}_{a,k}, t)$ and $Q(\vec{x}_{a,k}, t)$ in Eq. (1) as two statistically stationary and independent Gaussian random processes, and the phase of the signals $E(\vec{x}_{a,k}, t)$ to be uniformly distributed over 2π. Let us further consider the joint distribution of $I(\vec{x}_{a,k}, t)$, $Q(\vec{x}_{a,k}, t)$, $I(\vec{x}_{a,k} + \Delta\vec{x}_{mk}, t+\tau)$, and $Q(\vec{x}_{a,k} + \Delta\vec{x}_{mk}, t+\tau)$ to be Gaussian as well, and the antenna centers to be close to each other. The relevant consequences from these assumptions can be reproduced from Ishimaru (1997, sec. 4-9) in our notations as follows:

$$\left\langle S(\vec{x}_{a,k}, t) \right\rangle = \left\langle S(\vec{x}_{a,k} + \Delta\vec{x}_{mk}, t+\tau) \right\rangle = \langle S \rangle \tag{22}$$

$$\left\langle E(\vec{x}_{a,k}, t) E(\vec{x}_{a,k}, t) \right\rangle = \left\langle E(\vec{x}_{a,k}, t) E(\vec{x}_{a,k} + \Delta\vec{x}_{mk}, t+\tau) \right\rangle \approx 0 \tag{23}$$

Using Eqs. (2), (3), (14), (22), and (23), one can derive the following relation between the second order CF and SF for received signals (Praskovsky et al., 2003e):

$$D(\Delta\vec{x}_{mk}, \tau) = 2\left[1 - \left|D(\Delta\vec{x}_{mk}, \tau)\right|^2\right] \tag{24}$$

This equation provides a "bridge" between SF and CF-based SA techniques, e.g., direct relations between HAD and STARS. It follows from Eqs. (4) and (5) that:

$$\begin{aligned} &d_0(\Delta\vec{x}_{mk}) = D(\Delta\vec{x}_{mk}, 0), \qquad && d_1(\Delta\vec{x}_{mk}) = \left[\partial D(\Delta\vec{x}_{mk}, \tau)/\partial\tau\right]_{\tau=0} \\ &2d_2(\Delta\vec{x}_{mk}) = \left[\partial^2 D(\Delta\vec{x}_{mk}, \tau)/\partial\tau^2\right]_{\tau=0}, && 2d_{auto}(\vec{x}_{a,k}) = \left[\partial^2 D_{auto}(\vec{x}_{a,k}, \tau)/\partial\tau^2\right]_{\tau=0} \end{aligned} \tag{25}$$

Combining Eqs. (24), (25), and (15) - (20), one can estimate coefficients d_0, d_1, d_2, and d_{auto} using the cross and auto CF as follows (the estimates are denoted by the tilde):

$$\tilde{d}_0(\Delta\vec{x}_{mk}) = 2\left[1 - \left|C(\Delta\vec{x}_{mk}, 0)\right|^2\right] = 2\left\{1 - \exp\left[-2c_0(\Delta\vec{x}_{mk})\right]\right\} = d_0(\Delta\vec{x}_{mk}) \tag{26}$$

$$\tilde{d}_1(\Delta\vec{x}_{mk}) = -2\left[\partial\left|C(\Delta\vec{x}_{mk}, \tau)\right|^2/\partial\tau\right]_{\tau=0} = 4c_1(\Delta\vec{x}_{mk})\exp\left[-2c_0(\Delta\vec{x}_{mk})\right] = d_1(\Delta\vec{x}_{mk}) \tag{27}$$

$$\tilde{d}_2(\Delta\vec{x}_{mk}) = -\left[\partial^2 \left|C(\Delta\vec{x}_{mk},\tau)\right|^2 / \partial\tau^2\right]_{\tau=0} = 4\left[c_2(\Delta\vec{x}_{mk}) - c_1^2(\Delta\vec{x}_{mk})\right]\exp\left[-2c_0(\Delta\vec{x}_{mk})\right]$$
$$= d_2(\Delta\vec{x}_{mk}) + \left(256\pi^4\gamma^4 \left|\Delta\vec{x}_{mk}\right|^2 \delta t^2 \left\langle u_{mk}^2 \right\rangle / \alpha^4 D^4\right)\exp\left(-4\pi^2\gamma^2 \left|\Delta\vec{x}_{mk}\right|^2 / \alpha^2 D^2\right) \quad (28)$$

$$\tilde{d}_{auto}(\vec{x}_{a,k}) = -\left[\partial^2 \left|C_{auto}(\vec{x}_{a,k},\tau)\right|^2 / \partial\tau^2\right]_{\tau=0} = 4c_{auto}(\vec{x}_{a,k}) = d_{auto}(\vec{x}_{a,k}) \quad (29)$$

where d_0, d_1, d_2, and d_{auto} are given by Eqs. (8), (9), (11), and (12).

COMPARISON OF THE TECHNIQUES

A good agreement between STARS and CF-based SA techniques FCA and HAD in measuring the mean horizontal winds $\langle U \rangle$, $\langle V \rangle$, and intensity of the vertical turbulent velocity $\langle w^2 \rangle$ was found for the NCAR Multiple Antenna profiler and the Middle and Upper Atmosphere radar, respectively (Praskovsky et al., 2003c, d, e). The agreement seems to be expected because STARS is related to the CF-based techniques; see the previous section. However, the relations between the SF and CF do not indicate the equivalence between STARS and HAD (or any other) CF-based technique. Below we show that the CF and SF-based SA techniques are conceptually different in spite of being formally related to each other for a particular case of the second order functions.

CF can be applied only to the *globally* statistically stationary random processes. Real physical processes are almost never globally stationary while practically any process can be safely considered as being the locally statistically stationary; e.g., Tatarskii (1971), and Monin and Yaglom (1975). The basic STARS Assumption 1S about a local stationarity is much less restrictive than the basic HAD Assumption 1H about a global stationarity. Another important feature of SF is the presence of a small parameter $\tau \to 0$. The small parameter always significantly simplifies a physical task by both leading to the asymptotically exact solutions, and requiring a smaller number of less restrictive assumptions; e.g., Migdal (1977). Indeed, the STARS Assumptions 2S and 3S for estimating the mean horizontal winds are less restrictive than the HAD Assumptions 2H - 4H. Furthermore, STARS requires only two additional Assumptions 4S and 5S for deriving operational equations for turbulence characteristics $\langle w^2 \rangle$, $\langle u^2 \rangle$, $\langle v^2 \rangle$, and $\langle uv \rangle$ while HAD requires four much restrictive additional Assumptions 5H - 8H for estimating the only turbulence characteristic $\langle w^2 \rangle$.

CF characterizes fluctuations of a random process at all scales but mainly at the large ones of the order of the process's integral time scale T_{cor}. Fluctuations at large scales are heavily affected by external conditions, and the functional form of CF can never be universal; e.g., Townsend (1956, secs. 1.8, 1.9). In particular, the Gaussian functions (15) and (16) in the HAD technique are merely good approximations near the peak values of the auto and cross CF; in practice the rigorous validity of Eqs. (15) and (16) over a wide range of τ would be more an exception than a rule. SF characterizes fluctuations at small scales $\tau << T_{cor}$. The small-scale fluctuations of random processes are typically quite universal (e.g., Tatarskii, 1971; and Monin and Yaglom, 1975), and the decompositions (4) and (5) for cross and auto SF are valid almost always in practical measurements. On the other hand, CF is a more general characteristic of a random process than SF because it describes all scales. Indeed, Eqs. (26) - (29) express coefficients d_0 - d_2, and d_{auto} in Eqs. (4) and (5) for cross and auto SF using Eqs. (15) - (20) for cross and auto CF. Reverse operation, expressing coefficients c_0 - c_2, and c_{auto} in Eqs. (15), (16) for CF using equations for SF is impossible because the latter are valid only at $\tau \to 0$.

Only the second order SF are considered in this paper. As shown in PPa, SF of any order $p \geq 2$ can be derived for a pair of received signals and applied to practical measurements while CF at only p = 2 are used in SA techniques. It is important that equations for SF at p > 2, for example those for estimating the higher-order turbulence characteristics $\langle w^3 \rangle$, $\langle u^3 \rangle$, $\langle v^3 \rangle$, $\langle w^4 \rangle$, $\langle u^4 \rangle$, $\langle v^4 \rangle$, and so on, can be derived using the same Assumptions 1S - 5S as at p = 2 (PPa). Therefore, SF is a more powerful theoretical tool than CF which has been well recognized in the turbulence research; e.g., Tatarskii (1971), and Monin and Yaglom (1975).

However, the major difference between CF and SF-based SA techniques is not in the above theoretical details but rather in the physical concept beneath the techniques. The cross CF (14) describes the *similarity* between signals from two receivers $E(\vec{x}_{a,k} + \Delta\vec{x}_{mk}, t+\tau)$ and $E(\vec{x}_{a,k}, t)$ at all temporal separations $-\infty < \tau < \infty$. For example, the maximum value $\left|C(\Delta\vec{x}_{mk}, \tau_p)\right|_{\max}$ defines the lag τ_p for which the signal $E(\vec{x}_{a,k} + \Delta\vec{x}_{mk}, t+\tau)$ is the *mostly similar* to the signal $E(\vec{x}_{a,k}, t)$. A specific technique for relating CF for received signals (that is, CF of the diffraction pattern on the ground) to characteristics of a scattering medium could be very simple as in the plane drift method for the ``frozen'' field of scatterers (e.g., Briggs et al., 1950, Hocking, 1983b, Briggs, 1984), or rather sophisticated as in the FCA and HAD techniques. The latter could take into account spatial/temporal decorrelation due to turbulence, anisotropy of scatterers, and many other important aspects of a scattering medium as well as specific radar parameters; e.g., Briggs (1984), Hocking (1989), Hocking et al. (1989), Briggs and Vincent (1992), DLH, Holloway et al. (1997a). However, the physical concept underneath all CF-based techniques is uniquely defined by the CF as a mathematical tool, and it is the following: *tracking the diffraction pattern and its changes*, and, therefore, *tracking a scattering medium and its changes* in the illuminated volume. The cross SF (2) describes the *difference* between the signals $S(\vec{x}_{a,k} + \Delta\vec{x}_{mk}, t+\tau)$ and $S(\vec{x}_{a,k}, t)$. The increment $S(\vec{x}_{a,k} + \Delta\vec{x}_{mk}, t+\tau) - S(\vec{x}_{a,k}, t)$ is a band-pass filter that extracts fluctuations with spatial and temporal scales around $\left|\Delta\vec{x}_{mk}\right|$ and τ, respectively. At $\Delta\vec{x}_{mk} = 0$ and $\tau \to 0$, the increment tends to the temporal derivative $\partial S(\vec{x}_{a,k}, t)/\partial t$. At $\tau = 0$ and $\left|\Delta\vec{x}_{mk}\right| \to 0$ it tends to the spatial derivative $\partial S(\vec{x}_{a,k}, t)/\partial\left|\vec{x}_{a,k}\right|$ of the signal $S(\vec{x}_{a,k}, t)$ with the receiver center $\vec{x}_{a,k}$ being moved in the direction $\Delta\vec{x}_{mk}$; see PPa for details. Therefore, a SF-based technique is intrinsically differential while a derivative characterizes the rate of change in the function. Independent of a specific technique for relating SF for received signals to characteristics of a scattering medium, the physical concept underneath SF-based techniques is uniquely defined by the SF as a mathematical tool, and it is the following: *evaluating the rates of spatial and temporal changes in the diffraction pattern*, and, therefore, *evaluating the rates of spatial and temporal changes in a scattering medium* in the illuminated volume. Therefore, CF and SF-based techniques utilize conceptually different physical features of the diffraction pattern and a scattering medium; some practical consequences from the difference are discussed below.

To increase sensitivity of measurements with CF, one should apply a CF-based technique at the range of separations $\left|\Delta\vec{x}_{mk}\right|$ and τ close to the maximum gradient of the functions. For the Gaussian CF (15) and (16), the maximum gradient is at such separations where cross and auto CF are around 0.5. To ensure high measurement accuracy, "it is undesirable to work with very high values of correlation" (Briggs, 1984, p. 174), therefore, the receiver separation $\left|\Delta\vec{x}_{mk}\right|$ should not be too small. Another reason for applying sufficiently large $\left|\Delta\vec{x}_{mk}\right|$ with CF-based SA technique is referred to as the triangle effect; e.g., Meek (1980), Holdsworth and Reid (1997). Typical separation between the antenna centers for applying CF-based SA

techniques is usually chosen in such a way as to ensure $|C(\Delta\vec{x}_{mk},0)| \approx 0.2$ - 0.7; e.g., Awe (1964), Vincent (1984), Hocking et al. (1989). The range of temporal separations for fitting Eqs. (15) and (16) to experimental data is typically chosen in such a way as to cover CF from approximately 0.05, and higher. Tens, or even hundreds of data points including rather large values of τ are employed into the fitting. On the contrary, the SF requires as small separations as possible to approximate the derivatives. The smaller are τ and $|\Delta\vec{x}_{mk}|$, the better one can estimate the derivatives $\partial S(\vec{x}_{a,k},t)/\partial t$ and $\partial S(\vec{x}_{a,k},t)/\partial|\vec{x}_{a,k}|$, and the more accurate are the SF-based measurements; see PPa for details. For this reason, only a few separations, typically not more that $\tau = \pm\delta t$, $\pm 2\delta t$, and $\pm 3\delta t$ are used in STARS. Therefore, CF and SF-based techniques use the *different parts* of the functions: those at large and small separations, respectively.

Utilizing different physical features of the diffraction pattern and using different ranges of temporal separations, CF and SF-based techniques are differently affected by noise. Theoretically CF are unaffected by white noise (except for the auto CF at zero lag) while are strongly affected by any noise with a finite temporal scale, especially with a large one such as ground clutter. As any differential values, both auto and cross SF are strongly affected by any noise with a small temporal scale at all lags, in particular by a white noise. On the other hand, SF is not sensitive to noise with a large temporal scale such as ground clutter, or hard targets; this STARS feature was found theoretically in PPa (sec. 4), and then demonstrated experimentally in Praskovskaya et al. (2003) and Praskovsky et al. (2003c). The feature can be easily understood from the definition of SF, Eq. (2). A statistical difference between two signals at separation τ cannot "sense" a process with a temporal scale $T_{cor} >> |\tau|$ because such a process is merely filtered by the increment.

As shown in the previous section, the coefficients d_0, d_1, d_2, and d_{auto} in the cross and auto SF (4) and (5) can be obtained from Eqs. (14) - (20) for the cross and auto CF at $\tau \to 0$. However, Eqs. (11) and (28) for the coefficient $d_2(\Delta\vec{x}_{mk})$ and its CF-based estimate $\tilde{d}_2(\Delta\vec{x}_{mk})$ differ by the term with $\langle u_{mk}^2 \rangle$. This term describes intensity of the turbulent velocity along the baseline $\Delta\vec{x}_{mk}$ and plays a very important role in the STARS method. It leads to the operational Eq. (13) for estimating intensity of the horizontal turbulent velocities and the momentum flux $\langle uv \rangle$. Similar terms at $p > 2$ would lead to equations for estimating $\langle u^4 \rangle$, $\langle v^4 \rangle$, $\langle u^2 v^2 \rangle$, and so on. One can see from Eqs. (11) - (13) that measuring characteristics of the horizontal turbulent velocities with STARS is possible because $d_2(\Delta\vec{x}_{mk}) \neq d_{auto}(\vec{x}_{a,k})$. The term $\langle u_{mk}^2 \rangle$ appears in the derivation of Eq. (11) from Eq. (7) as $\langle U_{i,mk}^2(t) \rangle = \langle U_{i,mk} \rangle^2 + \langle u_{i,mk}^2 \rangle$. From a physical point of view, the term $\langle U_{i,mk}^2(t) \rangle$ reflects rather obvious fact: the *rates* of spatial and temporal changes in the diffraction pattern along $\Delta\vec{x}_{mk}$ are proportional to the square of the *instantaneous* velocity component along the baseline. This can be obtained from simple dimensional considerations, and it is proven rigorously in PPa for any scalar random field. At the same time, the HAD coefficients $c_2(\Delta\vec{x}_{mk})$ and $c_{auto}(\vec{x}_{a,k})$ in the cross and auto CF are identical; Eq. (19). It is noteworthy that Eq. (19) is the major operational equation in the FCA technique; Briggs (1984, p. 176). One can see that $c_2(\Delta\vec{x}_{mk})$ does not contain $\langle u_{mk}^2 \rangle$ which is quite natural. Cross CF $|C(\Delta\vec{x}_{mk},\tau)|$ reveals a statistical similarity between the signals $E(\vec{x}_{a,k} + \Delta\vec{x}_{mk}, t+\tau)$ and $E(\vec{x}_{a,k},t)$; it tracks the diffraction pattern in its motion from $\vec{x}_{a,k}$ to $\vec{x}_{a,k} + \Delta\vec{x}_{mk}$. It is quite obvious that

fluctuations $u_{mk}(t)$ along the baseline $\Delta\vec{x}_{mk}$ cannot affect the statistical similarity between the signals but only make $E(\vec{x}_{a,k}+\Delta\vec{x}_{mk},t+\tau)$ more ``blurring", that is, only the mean speed $\langle U_{mk}\rangle$ can be detected while tracking motion of the pattern as a whole. To get a formal explanation of the above statement, one should note that the term with $\langle U_{mk}\rangle^2 + \langle u_{mk}^2\rangle$ in Eq. (11) for $d_2(\Delta\vec{x}_{mk})$ is simulated by the term $c_1^2(\Delta\vec{x}_{mk})$ in Eq. (28). The latter contains only $\langle U_{mk}\rangle$, Eq. (18). One can obtain from simple dimensional considerations that $c_1(\Delta\vec{x}_{mk}) \propto \langle U_{mk}\rangle + \langle u_{mk}\rangle$ although the last term is zero by definition. This is the place where the horizontal turbulent velocity formally disappears from the coefficient $c_2(\Delta\vec{x}_{mk})$ in Eq. (15) for cross CF.

Therefore, the conceptual difference between CF and SF-based approaches to analyzing received signals for SA radars, namely tracking the diffraction pattern and evaluating the rates of changes in the pattern, respectively, lead to significant practical differences. In particular, one can potentially estimate the different order moments of all turbulent velocity components separately with the SF-based SA techniques while only $\langle w^2\rangle$ can be estimated with the CF-based techniques. Other characteristics such as the turbulent kinetic energy, eddy dissipation rate, and so on can be estimated with CF-based techniques only by assuming the isotropy, the dynamic equilibrium, or a specific functional form of the turbulence spectrum, and/or with other restrictive assumptions; e.g., Briggs (1980), Hocking (1983a, 1989), Hocking et al. (1989), DLH.

One can conclude that CF and SF-based SA techniques do not compete but rather complement each other. The UCAR-STARS method could become a useful alternative to the traditional, CF and spectra-based data analysis techniques for SA radars.

Acknowledgements. The NCAR is sponsored by the National Science Foundation (NSF). The first author (AP) was sponsored by the NCAR/RAP Director's fund, and the second author (EP) was sponsored by the NSF Grant ATM-0122877.

REFERENCES

Awe, O., Effects of errors in correlation on the analysis of the fading of radio wave, *J. Atmos. and Terr. Phys*., *26*, 1257-1271, 1964.

Briggs, B. H., Radar observations of atmospheric winds and turbulence: a comparison of techniques, *J. Atmos. and Terr. Phys*., *42*, 823-833, 1980.

Briggs, B. H., The analysis of spaced sensor records by correlation techniques, *MAP Handbook*, *13,* 166-186, 1984.

Briggs, B. H., G. J. Phillips, and D. H. Shinn, The analysis of observations on spaced receivers of the fading radio signals, *Proc. Phys. Soc. London*, *63*, 106-121, 1950.

Briggs, B. H., and R. A. Vincent, Spaced-antenna analysis in the frequency domain, *Radio Sci*., *27*, 117-129, 1992.

Doviak, R. J., R. J. Lataitis, and C. L. Holloway, Cross correlations and cross spectra for spaced antenna wind profilers, 1, Theoretical analysis, *Radio Sci*., *31*, 157-180, 1996.

Fukao, S., and R. D. Palmer, Spatial and frequency domain interferometry using the MU radar: A tutorial and recent developments, *J. Geomag. Geoelectr*., *43*, 645-666, 1991.

Hocking, W. K., On the extraction of atmospheric turbulence parameters from radar backscatter Doppler spectra--I. Theory, *J. Atmos. Terr. Phys*., *45*, 89-102, 1983a.

Hocking, W. K., The spaced antenna drift method, *MAP Handbook*, *9*, 171-186, 1983b.

Hocking, W. K., Target parameter estimation, *MAP Handbook*, *30*, 228-268, 1989.

Hocking, W. K., P. May, and J. Röttger, Interpretation, reliability, and accuracies of

parameters deduced by the spaced antenna method in middle atmosphere applications, *PAGEOPH*, *30*, 571-604, 1989.
Holdsworth, D. A., and I. M. Reid, An investigation of biases in the full correlation analysis technique, *Adv. Space Res*., *20*, 1269-1272, 1997.
Holloway, C. L., R. J. Doviak, and S. A. Cohn, Cross correlations of fields scattered by horizontally anisotropic refractive index irregularities, *Radio Sci*., *32*, 1911-1920, 1997a.

Holloway, C. L., R. J. Doviak, S. A. Cohn, R. J. Lataitis, and J. S. Van Baelen, Cross correlations and cross spectra for spaced antenna wind profilers, 2, Algorithms to estimate wind and turbulence, *Radio Sci*., *32*, 967-982, 1997b.
Ishimaru, A., *Wave Propagation and Scattering in Random Media*, Oxford Univ. Press, 1997.
Liu, C. H., J. Röttger, C. J. Pan, and S. J. Franke, A model for spaced antenna observational mode for MST radars, *Radio Sci*., *25*, 551-563, 1990.
Meek, C. E., Triangle size effect in spaced antenna wind measurements, *Radio Sci*., *25*, 641-648, 1980.
Migdal, A. B., *Qualitative Methods in Quantum Theory*, W. A. Benjamin, Inc., 1977.
Monin, A. S., and A. M. Yaglom, *Statistical Fluid Mechanics: Mechanics of Turbulence*, Vol. 2, MIT Press, 1975.
Palmer, R. D., Multiple-receiver techniques for atmospheric wind profiling, *IEEE Geosci. Remote Sens. Soc. Newsl*., 9-17, 1994.
Praskovskaya, E. A., A. A. Praskovsky, J.-S. Chen, and Y.-H. Chu, Wind measurements by the Chung-Li radar in the presence of strong clutter and hard targets, *this volume*, 2003.
Praskovsky, A. A., and E. A. Praskovskaya, Structure-function-based approach to analyzing received signals for spaced antenna radars, *Radio Sci*., *38*(4), 7-1 - 7-25, 2003a.
Praskovsky, A. A., and E. A. Praskovskaya, Towards the advanced measurements of atmospheric turbulence by spaced antenna radars, *this volume*, 2003b.
Praskovsky, A. A., E. A. Praskovskaya, W. O. J. Brown, S. A. Cohn, and S. Oncley, Advanced measurements of atmospheric turbulence with a UHF spaced antenna wind profiler, Submitted to *Ann. Geophys*., MST-10 Special Issue, 2003c.
Praskovsky, A. A., E. A. Praskovskaya, G. Hassenpflug, Y. Yamamoto, and S. Fukao, Wind and turbulence measurements by the Middle and Upper Atmosphere radar using UCAR-STARS method, *this volume*, 2003d.
Praskovsky, A. A., E. A. Praskovskaya, G. Hassenpflug, Y. Yamamoto, and S. Fukao, Wind and turbulence measurements by the Middle and Upper Atmosphere radar: comparison of techniques, Submitted to *Ann. Geophys*., MST-10 Special Issue, 2003e.
Sheppard, E. L., M. F. Larsen, R. D. Palmer, S. Fukao, M. Yamamoto, T. Tsuda, and S. Kato, A statistical comparison of spaced antenna and spatial interferometry wind estimation, *Radio Sci*., *28*, 585-593, 1993.
Tatarskii, V. I., *The Effects of the Turbulent Atmosphere on Wave Propagation*, UDC 551.510, U.S. Dep. of Commerce, Washington, D.C., 1971.
Townsend, A. A., *The Structure of Turbulent Shear Flow*, Cambridge Univ. Press, 1956.
Vincent, R. A., Relationship of spaced antenna and Doppler techniques for velocity measurements, *MAP Handbook*, *14*, 126-130, 1984.

VHF PARASITIC RADAR INTERFEROMETRY FOR MST ZENITH SOUNDING

John D. Sahr

University of Washington
Department of Electrical Engineering
Paul Allen Center – Room AE100R
Campus Box 352500
Seattle, WA 98195-2500
jdsahr@u.washington.edu

Abstract

In this report we describe the technique of parasitic or passive radar, and how it may be applied to observation of MST targets. Passive radars carefully observe the scatter of uncooperative, commercial VHF and UHF broadcast services, providing range-Doppler profiles which are equivalent those of conventional active radars. Although passive radar is not replacement for conventional MST radars, passive radars offer an inexpensive means to create a large network of low-cost, unattended instruments, especially for the stratosphere and mesosphere[1].

1 Introduction

For the past several years, the Manastash Ridge Radar (MRR) has been making high quality range profiles of the Doppler velocity spectra of auroral electrojet echoes [*Lind et al.*, 1999]. Although data of this kind are not new, the technique employed at MRR is quite novel: we rely commercial broadcasts of analog stereo FM near 100 MHz.

Although the passive radar transmitters are uncooperative, some emitters provide two key features: high average power, and low ambiguity waveforms.

[1]This report will appear in the Technical Reports of the Department of Electrical Engineering at the University of Washington. You may retrieve this report by searching `https://www.ee.washington.edu/techsite/papers/`.

In the case of commercial FM, stations emitting 100 kW ERP are ubiquitous; this power level is comparable to that of incoherent scatter radars! Of course the broadcast antenna directivity is much lower than that of ISR or MST systems. The second feature is subtle; it is highly likely that efficient communications and broadcast signals have excellent range-Doppler ambiguity. Thus it is possible to fully resolve the range of targets consistent with the transmitter bandwidth (as in conventional radar waveforms). It is also possible to estimate the Doppler power spectrum. For non periodic waveforms (such as FM, and the newer digital modulations used in wireless communications and broadcast), these data can be estimated without suffering any range or Doppler aliasing. The mathematical basis for these statements has been demonstrated by *Sahr and Lind* [1997]. Similar efforts using random waveforms in active radars were undertaken by *Hagfors and Kofman* [1991] and *Sulzer* [1986]. .

1.1 Technology Advances

Passive radar detection algorithms are computationally intensive compared to those of most conventional radars. Fortunately, recent progress in computing hardware has effectively eliminated this challenge for illuminators with effective bandwidth less than about 250 kHz. *Morabito and Sahr* [2004] are preparing a report which describes efficient numerical schemes for evaluating the range-Doppler profiles.

The MRR uses a "distributed" topology, which requires two synchronization of two receivers separated by 150 km, as well as transport of the data from each receiver to the computational detection engine. The former problem has been solved inexpensively with GPS clocks, and the data transport is achieved with internet connectivity. A distributed receiver is necessary for MST applications, which will be described below.

Although not strictly necessary, modern digital receivers offer very high performance as well as convenience in synchronization. Their use is strongly recommended.

1.2 Practical Benefits of Passive Radar

By ceding the operation of a transmitter to others, a number of benefits accrue.

- All the costs of transmitter procurement and operation are eliminated.
- A passive system requires no license.
- A passive system is inherently much safer than an active radar.
- A passive system requires little electric power.
- A passive system may require a large antenna, but the antenna need not bear high power, and needs no T/R switch.
- A passive system naturally accomodates unattended operation.

1.3 Aerospace Development

Passive radars are naturally stealthy, and their relatively long wavelength offers potential utility in detection of low-observable targets. Thus, aerospace firms and military agencies have been investigating passive radar for many years; it is only in recent years that these efforts have begun to appear in open literature. See *Howland* [1995] and *Griffiths et al.* [1992] for prior art in aerospace applications of passive radar, and *Port* [2003] and *Leavitt* [1999] for aerospace applications of passive radars in news reports. In the commercial aerospace arena, commercial products are nearing the market from Lockheed Martin Mission Systems (Silent Sentry™) and Roke Manor Research Ltd. (CELLDAR™).

2 Manastash Ridge Radar Operations

The Manastash Ridge Radar consists of two identical receiver systems which are separated by 150 km and the Cascade Mountains ($\sim$ 2000 m). One receiver at the UW gathers the direct broadcast from transmitters illuminating the Seattle area; the second but otherwise identical receiver is significantly shielded from the transmitter by the mountains, and is exposed to signals scattered back from the upper atmosphere.

A matched filter-based signal processor yields range-Doppler profiles like those in Fig. 1. The scatter receiver can collect signals on several antennas. When the 16 λ baseline antennas are interferometrically analyzed, the scattering region can be distributed in azimuth as well as range, as in Fig. 2.

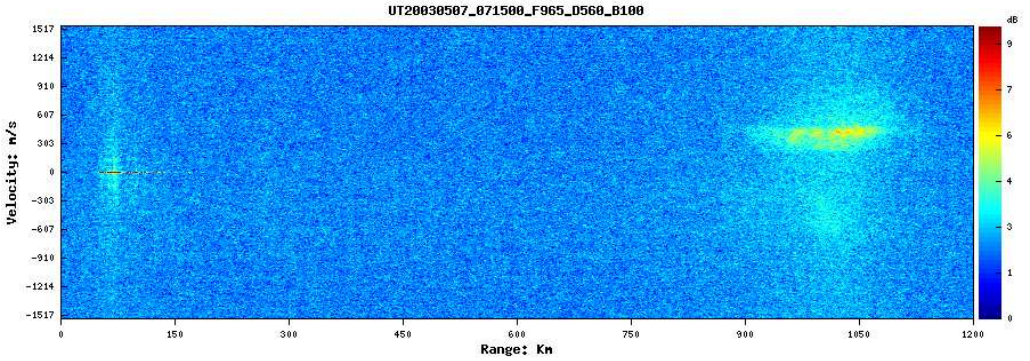

Figure 1: Example of Range-Doppler distribution from the Manastash Ridge Radar. The horizontal axis is range from 0 to 1200 km in 1.5 km increments; the vertical axis is Doppler velocity covering 3000 m/s with 12 m/s resolution. The data were collected for 10 seconds at 96.5 MHz.

The azimuth resolution is approximately 0.2° for signals whose signal to noise ration exceeds unity.

The MRR operates nearly unattended, automatically acquiring data for 10 seconds every 4 minutes, performing the range-Doppler processing, and building a WWW page showing the results[2].

3 Zenith Sounding for MST applications

The technique used at MRR can be applied to MS (and perhaps T) targets by keeping the following issues in mind.

MST scatterers are predominantly zenith oriented. This means that strong forward scatter bistatic geometries are required for passive radar. This geometry is illustrated in Fig. 3.

In strong forward scatter geometry, the range delay to the desired target is not substantially different from the shortest path from transmitter to receiver. This means that the signal scattered from the target will arrive at the receiver at very soon after any ground clutter signals. Thus, it is quite important that the direct path be offer significant attenuation. It is also important that there be little ground clutter on paths off the direct path, as those signals will arrive at the same time as the desired signal. In Fig. 4 we

[2]see `http:rrsl.ee.washington.edu/Data`

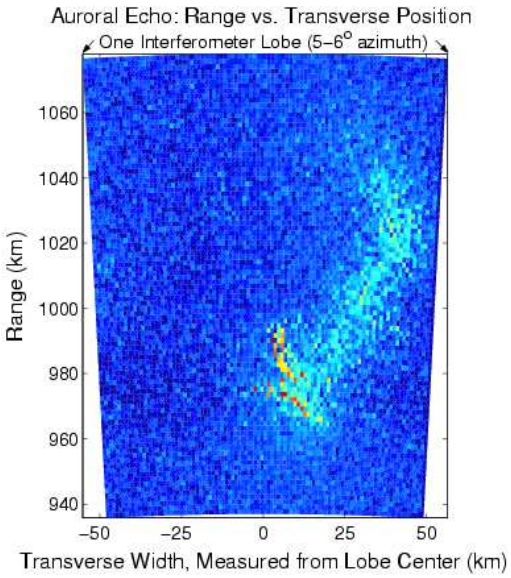

Figure 2: Example of range-azimuth interferometry from Melissa Meyer's Master's thesis [2003]. By computing the passive radar extention to otherwise conventional interferometric cross-spectra, the scatterer can be located in azimuth and range. In this figure, dark blue is the noise background, with light blue, yellow, and red indicating progressively stronger signals. The resolution in this imate is 1.5 km in range and 1.0 km in azimuth. At 1000 km range this corresponds to 0.001 radian, about 0.2°.

plot the additional propagation delay for targets at MST altitude, for several transmitter–receiver separation distances.

There is an additional challenge. The strong forward scatter path causes "geometric dilution of precision" in range (altitude), as illustrated in Fig. 5. A dilution of precision factor of 10 means that, if the range resolution of a backscatter radar is 1 km, then in the forward scatter application the range (altitude) resolution would be 10 km. This means that analog FM waveforms, with a bandwidth of 150 kHz and an intrinsic range resolution of about 1 km, provide little altitude discrimination, and strong coincidence with ground clutter. Therefore, much higher bandwidth illuminators would be useful.

Digital television, has a bandwidth of about 6 MHz, and an intrinsic range resolution of about 25 m. Thus a GDOP of 10 produces an altitude resolution of about 250 m, which is quite acceptable.

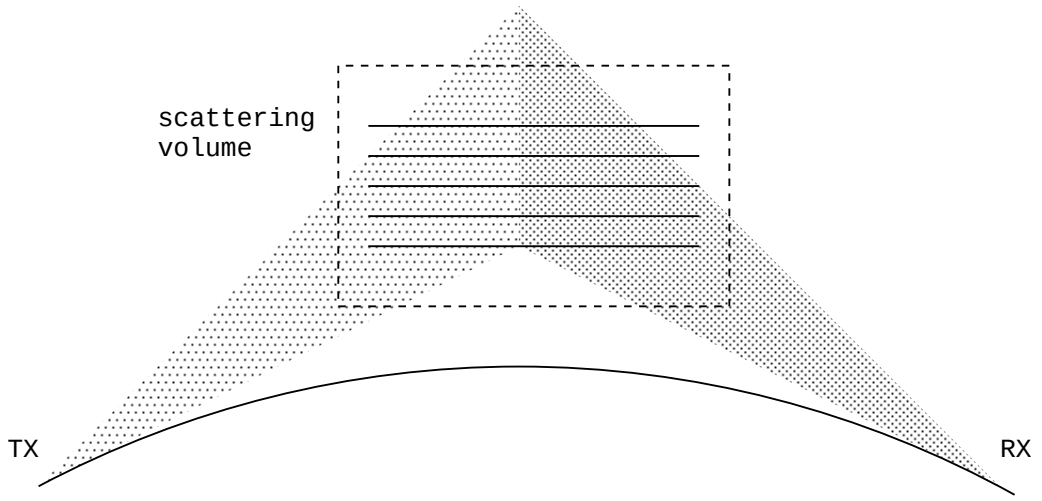

Figure 3: Sketch of the forward scattering geometry for passive bistatic MST operation.

Conventional TV broadcasts are ordinarily of little use for atmospheric sounding because the high amplitude sync pulse appears about every 63 μs, resulting in a backscatter range ambiguity of 9.5 km. However the GDOP factor applies to this, too. Taking a typical GDOP of 10 we observe that the altitude ambiguity increases to about 100 km. Although analog TV is "less interesting" as a waveform, it more resembles a simple periodic pulse waveform, and will be quite simple to detect and proces.

The GDOP factor also applies to the effective wavelength sampled (for a Bragg-like scattering process). In a conventional backscatter radar, operating at a frequency of 50 MHz, radio waves are strongly scattered from irregularities whose wavelength is about 3 m. However, in a forward scatter system with GDOP of 10, the sampled wavelength would be 30 m. Thus, relatively high transmitter frequencies can sample scatterers associated with relatively large wavelength/small $\vec{k}$, for which the scattering cross section is still large. Also, it is simpler to build high gain antennas at UHF than VHF, which makes it more possible to exclude undesired signals (from ground clutter, or other interferors at other azimuths).

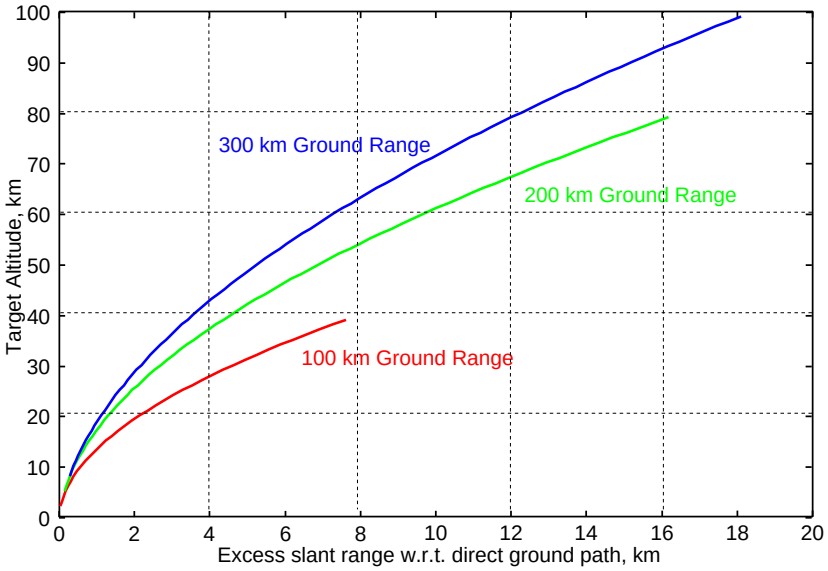

Figure 4: Plot of the excess propagation delay on a forward scatter path vs. altitude of scatter, for several different transmitter–receiver separations.

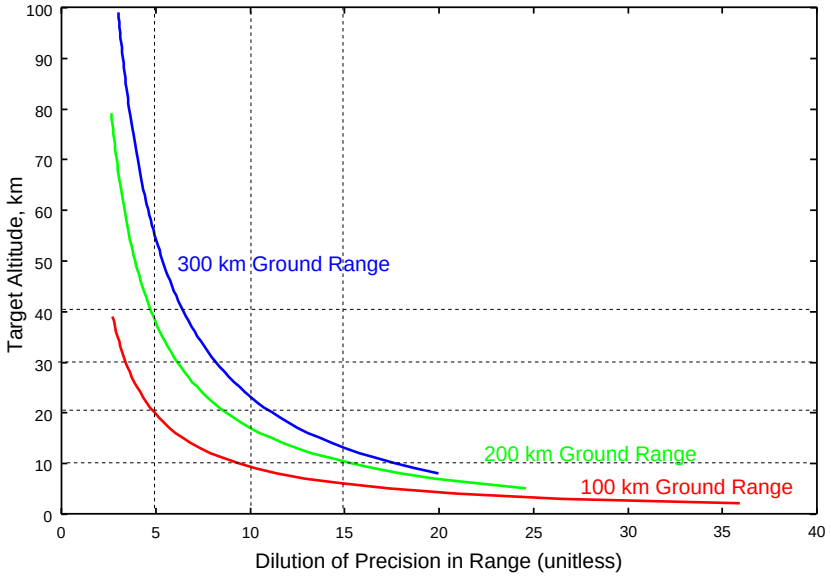

Figure 5: Sketch of the forward scattering geometry for passive bistatic MST operation.

4 Discussion and Conclusion

We have briefly described the circumstances in which one might use transmitters of opportunity to synthesize fairly sensitive MST radars with relatively low cost receive-only systems. This idea is motivated by success in using passive radar to observe ionospheric turbulence at high latitudes by observing bistatic scatter of commercial FM broadcasts at 100 MHz.

Two key experimental issues need to be addressed: the proximity of ground clutter to the desired scatter; and the geometric dilution of precision (GDOP) on the forward scatter path. However, the GDOP provides an opportunity to use higher frequency, UHF television broadcasts, both current NTSC and future digital waveforms. These signals have very high average power and should provide net altitude resolution of about 250 m.

Ultimately such systems are unlikely to offer the resolution and sensitivity of conventional active MST systems. However, the low cost, safety, and simplicity of passive systems may make them very useful for networked coverage over wide areas. As computing becomes larger and internet connectivity becomes more ubiquitous and faster, the passive or parasitic radar becomes more and more attractive.

Acknowledgement

The author wishes to express his gratitude to the US National Science Foundation for its support of this work.

References

Griffiths, H. D., A. J. Garnett, C. J. Baker, and S. Keaveney, Bistatic radar using satellite-borne illuminators of opportunity, in *International Conference Radar 92*, pp. 276–279, IEE, London, 1992.

Hagfors, T., and W. Kofman, Mapping of overspread targets in radar astronomy, *Radio Sci.*, *26*, 403–416, 1991.

Howland, P. E., Passive tracking of airborne targets using only doppler and doa information, in *IEE Colloquiam 'Algorithms for Target Tracking'*, vol. 7, p. 1, 1995.

Lind, F. D., J. D. Sahr, and D. M. Gidner, First passive radar observations of auroral E region irregularities, *Geophys. Res. Lett.*, *26*, 2155–58, 1999.

Meyer, M. G., Passive VHF radar interferometer implementation, observation, and analysis, Master's thesis, Univ. of Wash., Seattle, 2003.

Morabito, A., and J. D. Sahr, Efficient algorithms for estimation of range-doppler profiles in passive radar observation of deep fluctuating targets, *(in preparation)*, 2004.

Sahr, J. D., and F. D. Lind, The Manastash Ridge Radar: A passive bistatic radar for upper atmospheric radio science, *Radio Sci.*, *32*, 2345–2358, 1997.

Sulzer, M. P., A radar technique for high range resolution incoherent scatter autocorrelation function measurements utilizing the full average power of klystron radars, *Radio Sci.*, *21*, 1033–1040, 1986.

Participants List

Avery, James P.
University of Colorado
United States
james.avery@colorado.edu

Bahcivan, Hasan
Cornell University
United States
hb53@ece.cornell.edu

Balsley, Ben
CIRES/University of Colorado
United States
balsley@cires.colorado.edu

Barbin, Yves J.
LSEET/CNRS
France
yves.barbin@lseet.univ-tln.fr

Bénech, Bruno
Observatoire Midi-Pyrénées
France
benb@aero.obs-mip.fr

Boyer, Eric
ENS de Cachan
France
eric.boyer@wanadoo.fr

Caccia, Jean-Luc
LSEET
France
caccia@lseet.univ-tln.fr

Castillo, Otto
ROJ/IGP
Peru
ocastillo@jro.igp.gob.pe

Chau, Jorge L.
ROJ/IGP
Peru
j*chau@geo.igp.gob.pe*

Chen, Chung L.
Institute of Space Science, National Central University
Taiwan
harechen@ms46.hinet.net

Chen, Jenn-Shyong
Chienkou Institute of Technology
Taiwan
jamse.chen@msa.hinet.net

Chocos, Jorge A.
ROJ/IGP
Peru
jchocos@jro.igp.gob.pe

Choudhary, Raj Kumar
University of Western Ontario
Canada
rajkumar@uwo.ca

Chu, Yen-Hsyang
National Central University
Taiwan
yhchu@jupiter.ss.ncu.edu.tw

Clark, Wallace L.
AL/NOAA
United States
Wallace.L.Clark@noaa.gov

Currier, Philipp E.
ETS Degreane Horizon
France
currier@wanadoo.fr

Dalaudier, Francis
Service d'Aéronomie du CNRS
France
Francis.Dalaudier@aerov.jussieu.fr

Doviak, Richard J.
National Severe Storms Laboratory/NOAA
United States
dick.doviak@noaa.gov

Farley, Donald T.
Cornell University
United States
donf@ece.cornell.edu

Fernandez, Jose R.
University of Nebraska-Lincoln
United States
jose@doppler.unl.edu

Fernandez, Leonardo
Centro Meteorológico Provincial de Camaguey
Cuba
leonardo@met.cmw.inf.cu

Flores, Luis A.
Universidad de Piura
Peru
lflores@udep.edu.pe

Fritts, David C.
Colorado Research Associates/NWRA
United States
dave@cora.nwra.com

Fukao, Shoichiro
RASC, Kyoto University
Japan
fukao@kurasc.kyoto-u.ac.jp

Fuller, Brian M.
Genesis Software
Australia
bfuller@gsoft.com.au

Furumoto, Jun-ichi
RASC, Kyoto University
Japan
furumoto@kurasc.kyoto-u.ac.jp

G, Mrudula
Cochin University of Science and Technology
India
gkmrudu@yahoo.com

Gaffard, Catherine
Met Office
United Kingdom
catherine.gaffard@metoffice.com

Gage, Kenneth S.
AL/NOAA
United States
Kenneth.S.Gage@noaa.gov

Ganoza, Marco A.
Gobierno Regional de Piura
Peru
mage60us@msn.com

Gavrilov, Nikolai M.
Saint-Petersburg State University
Russia
gavrilov@pobox.spbu.ru

Haldoupis, Christos
University of Crete
Greece
chald@physics.uoc.gr

Hashiguchi, Hiroyuki
RASC, Kyoto University
Japan
hasiguti@kurasc.kyoto-u.ac.jp

Hassenpflug, Gernot
RASC, Kyoto University
Japan
gernot@kurasc.kyoto-u.ac.jp

Heo, Bok-Haeng M.
Korea Meteorological Administration
Korea
happyheo@kma.go.kr

Hermawan, Eddy
The Indonesian National Institute of Aeronautics and Space (LAPAN)
Indonesia
eddy_lapan@yahoo.com

Hocking, Anna
Mardoc Inc.
Canada
mardoc-inc@rogers.com

Hocking, Wayne K.
University of Western Ontario
Canada
whocking@uwo.ca

Hoffmann, Peter
Leibniz-Institut für Atmosphärenphysik, Kühlungsborn
Germany
hoffmann@iap-kborn.de

Hooper, David A.
Rutherford Appleton Laboratory
United Kingdom
D.A.Hooper@rl.ac.uk

Hussey, Glenn C.
University of Saskatchewan
Canada
Glenn.Hussey@usask.ca

Hysell, David L.
EAS/Cornell University
United States
dlh37@cornell.edu

Johnston, Paul E.
CIRES/NOAA
United States
Paul.E.Johnston@noaa.gov

Kawano, Noriyuki
RASC, Kyoto University
Japan
kawano@kurasc.kyoto-u.ac.jp

Kishore Kumar, Karanam
National MST Radar Facility
India
dilkash_kish@rediffmail.com

Kolatkar, Aditi B.
University of Alaska - Fairbanks
United States
ftabk@uaf.edu

Krishna Reddy, K.
Frontier Observational Research System for Global Change
Japan
kkreddy@jamstec.go.jp

Kudeki, Erhan
University of Illinois at Urbana-Champaign
United States
erhan@uiuc.edu

La Hoz, Cesar
University of Tromso
Norway
Cesar.La.Hoz@phys.uit.no

Latteck, Ralph
Leibniz-Institut für Atmosphärenphysik, Kühlungsborn
Germany
latteck@iap-kborn.de

Lau, Elias M.
University of Colorado
United States
Elias.Lau@Colorado.edu

Lehmacher, Gerald A.
Clemson University
United States
glehmac@clemson.edu

Lind, Frank D.
MIT Haystack Observatory
United States
flind@haystack.mit.edu

Liu, Jann-Yenq
National Central University
Taiwan
jyliu@jupiter.ss.ncu.edu.tw

López Dekker, Paco
University of Massachusetts
United States
paco@mirsl.ecs.umass.edu

Lucas, Christopher
University of Adelaide
Australia
clucas@physics.adelaide.edu.au

Luce, Hubert
LSEET/Toulon University
France
luce@lseet.univ-tln.fr

McDonald, Adrian J.
University of Canterbury
New Zealand
adrian.mcdonald@canterbury.ac.nz

Meek, Chris E.
University of Saskatchewan
Canada
meek@dansas.usask.ca

Michhue, Gabriel P.
ROJ/IGP
Peru
gmichhue@jro.igp.gob.pe

Milla, Marco A.
ROJ/IGP
Peru
mmilla@jro.igp.gob.pe

Morris, Raymond J.
Australian Antarctic Division
Australia
ray.morris@aad.gov.au

Morse, Corinne S.
National Center for Atmospheric Research
United States
morse@ucar.edu

Narayana Rao, Daggumati
National MST Radar Facility
India
profdnrao2001@yahoo.com

Nastrom, Gregory D.
St. Cloud State University
United States
nastrom@stcloudstate.edu

Ney, Richard
CETP/CNRS/IPSL
France
richard.ney@cetp.ipsl.fr

Ogawa, Tadahiko
Nagoya University
Japan
ogawa@stelab.nagoya-u.ac.jp

Palmer, Robert D.
University of Nebraska-Lincoln
United States
bpalmer@unl.edu

Peña, Arturo
Centro Meteorológico Provincial de Camaguey
Cuba
arturo@met.cmw.inf.cu

Petitdidier, Monique
CNRS/CETP
France
monique.petitdidier@cetp.ipsl.fr

Praskovskaya, Eleanor A.
Colorado Research Associates (CORA)
United States
epraskov@cora.nwra.com

Praskovsky, Alexander A.
National Center for Atmospheric Research
United States
praskov@ucar.edu

Pulache, Wilmer
SENAMHI
Peru
wpulache@senamhi.gob.pe

Reid, Iain M.
University of Adelaide
Australia
ireid@atrad.com.au

Reyes, Pablo M.
ROJ/IGP
Peru
preyes@jro.igp.gob.pe

Riggin, Dennis
Colorado Research Associates (CORA)
United States
riggin@colorado-research.com

Rodriguez, Rodolfo
Universidad de Piura
Peru
rrodrigu@udep.edu.pe

Röttger, Jürgen
Max-Planck-Institut für Aeronomie
Germany
roettger@linmpi.mpg.de

Sahr, John D.
University of Washington
United States
jdsahr@u.washington.edu

Saito, Susumu
RASC, Kyoto University
Japan
susaito@kurasc.kyoto-u.ac.jp

Sarango, Martin F.
ROJ/IGP
Peru
m*sarango@jro.igp.gob.pe*

Sato, Toru
Kyoto University
Japan
tsato@kuee.kyoto-u.ac.jp

Scipión, Danny E.
ROJ/IGP
Peru
dscipion@jro.igp.gob.pe

Shibagaki, Yoshiaki
Osaka Electro-Communication University
Japan
sibagaki@maelab.osakac.ac.jp

Shimomai, Toyoshi
IFSE/Shimane University
Japan
shimomai@ecs.shimane-u.ac.jp

Silva, Robert R.
ATRAD
Australia
rsilva@atrad.com.au

Singer, Werner
Leibniz-Institut für Atmosphärenphysik,
Kühlungsborn
Germany
singer@iap-kborn.de

Takahashi, Ken
Instituto Geofísico del Perú
Peru
ken@atmos.washington.edu

Teshiba, Michihiro
RASC, Kyoto University
Japan
teshiba@kurasc.kyoto-u.ac.jp

Thorsen, Denise
University of Alaska - Fairbanks
United States
ffdt@uaf.edu

Tsutsumi, Masaki
National Institute of Polar Research
Japan
tutumi@nipr.ac.jp

Umemoto, Yasuko
Kobe University
Japan
umemoto@ahs.scitec.kobe-u.ac.jp

Urbina, Julio
University of Arkansas at Little Rock
United States
jvurbina@ualr.edu

Van Zandt, Thomas E.
NOAA
United States
vanzandt@al.noaa.gov

Vandepeer, Brenton G.
Genesis Software
Australia
bvandepe@gsoft.com.au

Vogt, Siegfried
Institut für Meteorologie und Klimaforschung
Germany
siegfried.vogt@imk.fzk.de

Wilson, Richard
Service d'Aeronomie
France
richard.wilson@aero.jussieu.fr

Woodman, Ronald F.
ROJ/IGP
Peru
ronw@geo.igp.gob.pe

Yokoyama, Tatsuhiro
RASC, Kyoto University
Japan
yokoyama@kurasc.kyoto-u.ac.jp

Zecha, Marius
Leibniz-Institut für Atmosphärenphysik,
Kühlungsborn
Germany
zecha@iap-kborn.de

Authors Index

A

Adachi, A. 298
Anandan, V. K. 58, 130
Arvelius, J. 42

B

Baggaley, W. J. 391
Bahcivan, H. 110
Batista P. 460
Bénech, B. 294, 310
Bennett, R G. 391
Berthelier, J. J. 373
Bhaskara Rao, S. V. 342
Bonaimé, S. 373
Bourdillon, A. 118
Boyer, E. 426
Bremer, J. 146
Brown, W. 62

C

Caccia, J.-L. 294
Campistron, B. 294, 310, 346
Campos, E. F. 415
Carey-Smith, T. K. 391
Carrión, M. 66
Carter, D. 262, 361
Castillo, O. 403
Chardenal, L. 419
Chau, J. L. 76, 98, 134, 326, 357
Chen, C. L. 94
Chen, J.-S. 230
Cheong, B. L. 50
Chilson, P. B. 138
Chu, Y.-H. 230
Chung, L. J. 274
Clairquin, R. 373
Clark, W. L. 208, 298, 361
Clemesha, B. 460
Cohn, S. A. 399
Córdova, D. 381
Cornman, B. 399

D

D'Hermies, A. 373
Dalaudier, F. 204
Das, S. S. 58, 70
Dolon, F. 373
Drobinski, P. 294
Duvanaud, C. 373
Dyson, P. L. 122

E

Engler, N. 245

F

Fernandez, J. R. 138
Flores, L. A. 102, 326, 357
Franke, S. J. 90, 460
Fraser, G. J. 391
Frasier, S. J. 50
Fricke-Begemann, C. 142
Fujiwara, M. 218, 266
Fujiyoshi, Y. 314
Fukao, S. 106, 126, 152, 156, 218, 222, 234, 258, 266, 314, 352, 407
Fuller, B. 460
Furumoto, J.-I. 208

G

Gaffard, C. 365
Gage, K. 262, 298, 361
Gavrilov, N. M. 168, 234
Geng, B. 322
Ghosh, A. K. 58, 70
Girard-Ardhuin, F. 310
Goodrich, R. K. 399
Guénard, V. 294

H

Häggström, I. 138
Haldoupis, C. 86, 118, 164
Harten, L. 262
Hashiguchi, H. 258, 266, 314, 352, 407
Hassenpflug, G. 152, 156
Heo, B.-H. 346
Hewison. T. 365
Hocking, A. 444
Hocking, W. K. 214, 415, 444, 460
Hoffman, M. W. 50
Hoffmann, F. 146
Höffner, J. 142
Holdsworth, D. A. 122, 385
Hooper, D. A. 42, 46, 334
Horinouchi, T. 266
Hsu, M. L. 185, 274
Hussey, G. C. 86, 118
Hyde, M. R. 122
Hysell, D. L. 76, 98, 110

I

Igarashi, K. 342
Ishihara, M. 352

J

Jain, A. R. 58, 70, 249, 270, 282, 338
Jaubert, G. 290
Johnston, P. 262, 361

K

Kafando, P. 395
Kamburelis, A 118
Kamio, K. 436
Kartasasmita, M. 266
Kelley, M. C. 86
Kim, K. E. 346
Kiran Kumar, N. V. P. 181, 226, 278
Kishore Kumar, K. 70, 270, 338
Kishore, P. 342
Kita-Fukase, M. 258
Klaassen, G. P. 189
Klaus, V. 254, 346
Kobayashi, T. 298
Koehler, J. A. 118
Kozu, T. 282, 314, 318, 330
Krishna Reddy, K. 282, 318, 322, 330, 342
Kristiansen, T. 385
Kubo, K. 106, 222
Kudeki, E. 90

L

La Madrid, J. 326
Lal, S. 330
Larsen, M. F. 98
Larzabal, P. 426
Latteck, R. 245, 385
Legac, C. 419
Liu, L. 160
Lohou, F. 310
López, F. J. 50
Lübken, F. 142
Luce, H. 448

M

MacDougall, J. 460
Madhu Chandra Reddy, K. 249
Maekawa, Y. 258
Manson, A. 238
McDonald, A. J. 391
Meek, C. 238
Michhue, G. 369, 403
Milla, M. A. 76, 134
Mitchell, N. 460
Monselesan, D. P. 122
Mori, S. 314
Morris, R. J. 122, 411
Morse, C. S. 399
Müllemann, A. 142
Murphy, D. J. 122, 411
Muzirwan, M. 266

N

Naja, M. 330
Nakamura, K. 70, 282, 318, 330
Nakamura, T. 460
Namboothiri, S. P. 342
Narayana Rao, D. 58, 70, 177, 181, 226, 249, 278, 282, 318, 330, 342
Narayana Rao, T. 318
Narendra Babu, A. 177
Nash, J. 365
Nastrom, G. D. 208, 210
Nevejans, D. 373
Ney, R. 373, 419
Ning, B. 160

O

Ohno, Y. 249, 282, 330

P

Palmer, R. D. 50, 138
Pan, C. J. 94, 114, 130, 185, 274
Pancheva, D. 164, 460
Patra, A. K. 58
Pavelin, E. 46, 334
Petitdidier, M. 254, 395, 426
Pfaff, R. F. 126
Plank, G E. 391
Praskovskaya, E. 152, 230, 302, 461
Praskovsky, A. 152, 230, 302, 461
Puygrenier, V. 310

R

Rajalakshmi, T. 130
Ramachandra Reddy, G. 130
Rao, P. B. 114, 210, 241
Reid, H. J. 334
Reid, I. M. 411
Reyes, P. 403
Rietveld, M. T. 138
Rodríguez, R. 66
Röttger, J. 54, 106, 142, 185, 222, 274, 306, 377, 449

S

Sahr, J. 471
Saïd, F. 310
Sarango, M. F. 102, 381
Sato, T. 436
Scipión, D. 357
Seto, T. H. 266
Shalimov, S. 86
Shibagaki, Y. 258, 314
Shimomai, T. 314
Singer, W. 245, 385
Sivakumar, V. 210, 241
Sosa, F. 66
Stebel, K. 42
Subba Reddy, I. V. 177, 181, 226, 342

T

Tabary, P. 254
Takahashi, K.....286
Tellabati, V.....50
Thurai, M.....282
Tong, H.....50
Tsai, W. C.....185
Tsuda, T.....208, 460

U

Urbina, J. 90
Uyeda, H.....322

V

Vandepeer, B.....460
VanZandt, T. E.. 208
Vasantha, B. 181, 226
Venkat Ratnam, M. 177
Vijaya Bhaskara Rao, S.....177
Villegas, S. 102, 403
Vincent, R. A.....411
Vogt, S.....290

W

Wei, W..... 160
Weill, A. 419
Williams, C..... 361
Wilson, R..... 194, 204
Woodman, R. F.....102, 134, 369, 381, 403
Wu, J..... 185, 274

X

Xiong, J..... 160

Y

Yamada, H..... 322
Yamamoto, M.....126, 152, 156, 266
Yamamoto, M. K.....218, 266, 314, 407
Yamanaka, M. D..... 258, 314
Yokoyama, T. 126
Yu, T.-Y..... 62

Z

Zecha, M..... 142, 146